Precision measurements of jet quenching in relativistic heavy ion collisions at the LHC

Laura Havener

Submitted in partial fulfillment of the
requirements for the degree
of Doctor of Philosophy
in the Graduate School of Arts and Sciences

COLUMBIA UNIVERSITY

2019

ABSTRACT

Precision measurements of jet quenching in relativistic heavy ion collisions at the LHC

Laura Havener

Jets are a useful probe of the hot, dense medium produced in heavy ion collisions since partons are expected to lose energy in interactions with the medium through a phenomena called jet quenching. Recent results studying jet quenching in relativistic heavy ion collisions at the LHC with the ATLAS detector are presented here. The jets are reconstructed using the anti-k_t algorithm with a background subtraction that removes the large underlying event. A fully unfolded measurement of the dijet asymmetry in Pb+Pb and pp collisions with an integrated luminosity of 0.14 nb^{-1} and 4.0 pb^{-1}, respectively, at $\sqrt{s_{\text{NN}}} = 2.76$ TeV is shown. The dijets are found to be highly asymmetric in central Pb+Pb collisions and become more symmetric, or like pp, in more peripheral collisions. A strong p_{T} dependence to the asymmetry is also observed. This measurement is shown to have similar qualitative features at jet radii of $R = 0.3$ and $R = 0.4$, implying that the underlying event is under control. Measurements of the nuclear modification factor, R_{AA}, for $R = 0.4$ jets in Pb+Pb and pp collisions with an integrated luminosity of 0.49 nb^{-1} and 25 pb^{-1}, respectively, at $\sqrt{s_{\text{NN}}} = 5.02$ TeV are also presented. The R_{AA} shows the strongest suppression in central collisions and the least suppression in peripheral collisions. It shows a slight increase with jet p_{T} and a decrease with increasing rapidity at high p_{T}. Finally, the dijet asymmetry for $R = 0.4$ jets is also reported in Xe+Xe collisions at $\sqrt{s_{\text{NN}}} = 5.44$ TeV compared to Pb+Pb and pp collisions at $\sqrt{s_{\text{NN}}} = 5.02$ TeV. No difference is observed between Pb+Pb and Xe+Xe collisions, within the uncertainties of the measurement, as a function of the number of participants or the collision centrality.

Table of Contents

List of Figures

List of Tables

Acknowledgments

First and foremost I would like to thank my adviser, Brian Cole. Your passion and enthusiasm for physics and determination to work tirelessly to address a question, despite the challenges an analysis presents, is contagious. You taught me to always "dig deeper" even when a solution seemed impossible and that doing so is what produces good science. You continuously pushed and challenged me beyond what I thought was possible, but at the same time were always supportive, understanding, caring, and immensely patient.

I would like to thank the past and present members of the Columbia Heavy Ion group who I've had the privilege of interacting with: Aaron Angerami, Sarah Campbell, Felix Clark, Soumya Mohapatra, Dennis Perepelitsa, Yun Tian, Xiao Tu, Tingting Wang, Bill Zajz. From useful discussions and analysis insight, to conferences and heavy ion runs at CERN, you all made my research experience at Columbia exceptional. I am especially thankful to Aaron for being so patient with me and for teaching me all about jets and how to be a good experimentalist. I appreciate the advice, encouragement, guidance, and friendship through the years. Your example has, and will continue, to serve as inspiration. Thank you to the women in heavy ions who have been my role models and whose advice and encouragement has been invaluable, especially Sarah, Jaki Noronha-Hostler, Christine Nattrass, and Eliane Epple. I am grateful to members of the ATLAS Heavy Ion group, especially Martin Spousta, Radim Slovak, Martin Rybar, Peter Steinberg, and Anne Sickles, for analysis help, collaboration on projects, and of course a "heavy ion beer" or two. The research in this thesis would not have been possible without you all.

My time at Columbia has been shaped by many wonderful people. I would like to thank Jeremy Dodd for being a tireless advocate for women and Lam Hui for starting Reading Team Math which has been enriching and fun. I also owe a huge amount of gratitude to my fellow graduate students, particularly Matt, Ryne, Felix, Zach, and Russell, for being there through quals, coursework, and the ups and downs of research and life. Because of this, you all have become some of dearest friends. I am deeply appreciative to my academic brother, Felix, for traveling with me all over Europe and for simply being there for me as a colleague and close friend. I am lucky to have had you as a constant in this journey.

I have been surrounded by a strong group of supportive girl friends (and sisters), in the order that I met them: Amanda, Sara, Kailyn, Halie, Katie, Spenser, Dimitra, Blaire, Meredith, Kelsey, Susan, Alex, Alee, Karo. You ladies inspire me every day in all that you do and have been my rock through all the milestones in my life.

I am thankful to a superstar physicist and dear friend, Susan Clark. From problem set all-nighters at UNC, to being roomies and graduate students together at Columbia, we've been through it all and this thesis wouldn't exist if it wasn't for your support and friendship. Thank you for being the only person at times who truly "gets it" and for always believing in me and saying "you can do it" when I needed it most. Despite you no longer being in NYC, your success and encouragement from afar has inspired me more than you can know.

I owe everything to the unconditional love and support of my parents, Henry and Georgiana. You pushed me in all my endeavors and always believed in me, despite how crazy my goals seemed. Thank you for answering every panicked phone call about exams, conference deadlines, and finally this thesis, and for always telling me that you are proud of me no matter what. Thank you to my wonderful, intelligent, hilarious sisters, Sara and Halie - you are my biggest fans and knowing you are routing for me keeps me going when continuing seems impossible. Thank you to my grandparents, David, Georgiana, Pen, and Laura, whose passion for education and investment in my own inspired me to pursue graduate studies. I'm grateful for my parents-in-law, Betty and Bob, who even made a trip to CERN to see where I do research. They, along with Kurt, Ryan, Alex, Alee, and my nephew, James, have been the supportive, loving, and fun-advocating family I needed while living far from home. And to my dog Chloe, thanks for making me smile and laugh every day.

Finally, to my wonderful, intelligent, supportive husband, Matt, thank you for being the push I need to reach for goals way beyond those I set for myself, including encouraging me to apply to Columbia for graduate school. You've picked me up and kept me going when I was convinced otherwise. Thank you for struggling through every practice qual problem with me and reading every email, application, and stressed out text I sent your way. You inspire me every day by example. Thank you for being there, with champagne, to celebrate even the tinniest of successes and for never failing to make me laugh. This thesis wouldn't exist without your love and support, and I'm thrilled to finally join you on the other side.

for my parents, Georgiana and Henry, and my husband, Matt

Chapter 1

Introduction

This purpose of this thesis is to discuss precision measurements of jet quenching in experimental relativistic heavy ion collisions with the ATLAS detector. Jet quenching is the phenomena where partons inside jets lose energy in the hot, dense medium produced in heavy ion collisions. Quantum Chromodynamics (QCD) is the theory of the strong interaction between quarks and gluons, where quarks and gluons are confined inside of hadrons. QCD predicts that at high temperatures the quarks and gluons will become asymptotically free and a new state of matter where the quarks and gluons are deconfined will form, called quark-gluon plasma (QGP). Heavy ion (HI) collisions at the LHC (specifically Pb+Pb collisions) are used to produce and study the dynamics of the QGP. The medium will be strongly coupled in the temperatures produced at the LHC, which means it should have a low viscosity and expand collective as a nearly perfect fluid. The medium will also be very opaque which allows for large parton energy loss. This large parton energy loss in the QGP (or jet quenching) is the topic of this thesis.

Jets are highly collimated clusters of partons from a QCD high momentum (hard) scattering. They are an effective probe of the QGP since the initial state of the hard processes are mostly understood such that any final state differences from what is expected in standard pp collisions can be attributed to in-medium effects. Many measurements of jet quenching have been performed at RHIC and at the LHC. The measurements presented in this thesis are improvements over previous results because they are more precise due to unfolding for detector effects, increased statistics, and better determined systematic uncertainties. The

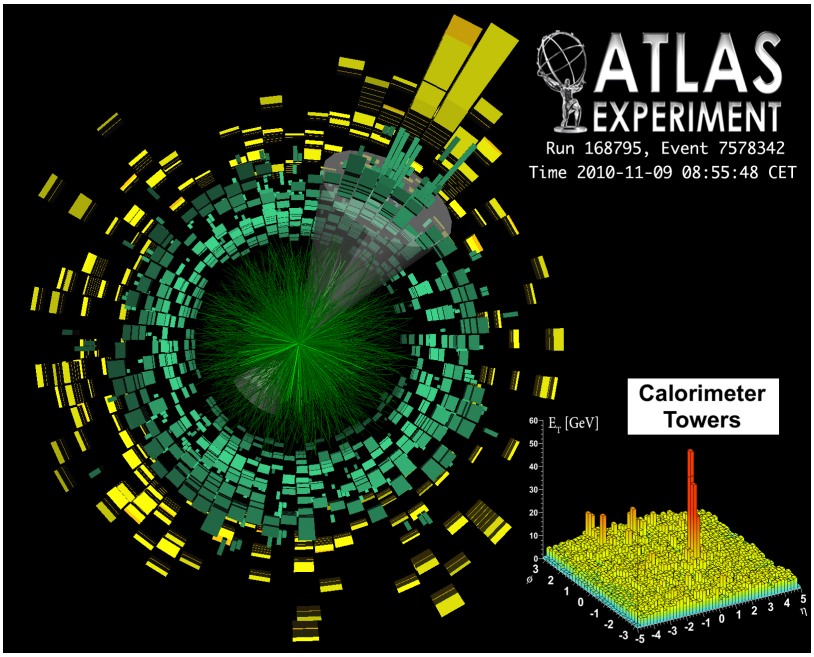

Figure 1.1: An ATLAS heavy ion event display of a dijet event in 2010 Pb+Pb collisions at 2.76 TeV at the LHC [3].

increased statistics also allow for more differential measurements in jet kinematics which probe the flavor and path length dependence of energy loss, as well as reach significantly higher values in the jet p_{T}. The unfolded measurements can be compared directly to theoretical models of jet energy loss to help constrain our understanding of jet quenching.

Jets are used to study inclusive energy loss through the suppression of single jets and differential energy loss through jet correlations. The latter can be seen directly in an event display of a dijet event in the ATLAS detector in Figure 1.1, where one high p_{T} jet is clearly observed and the other has disappeared. This imbalance is a consequence of energy loss since the jets travel different paths in the plasma and thus lose different amounts of energy. This imbalance is quantified through the variable $x_{\mathrm{J}} = p_{\mathrm{T}_1}/p_{\mathrm{T}_2}$, where p_{T_1} is the higher energy jet (or leading jet) and p_{T_2} is lower energy jet (or sub-leading jet). This dijet asymmetry was first observed by ATLAS in Ref. [1], but this measurement was not corrected for detector effects. The jet imbalance measurements in this thesis are fully unfolded for detector effects and are measured differential in the leading jet p_{T} [2] to probe the flavor dependence of energy loss.

Jet imbalance can be used to study the collision system dependence of energy loss by comparing the x_{J} distribution in Pb+Pb (A = 208) and Xe+Xe collisions (A = 129). The different atomic masses will create mediums of different densities and sizes, where in this case the medium density and size will be larger in the Pb+Pb collisions. This thesis presents a measurement of the x_{J} comparison in Pb+Pb and Xe+Xe collisions [4] to probe the path length and medium density dependence, as well as the collision geometry dependence, of energy loss.

Single jets are expected to be suppressed inclusively at a fixed value of the jet momentum when compared to jets in standard *pp* collisions. This suppression is quantified by comparing the number of jets in Pb+Pb collisions to that in *pp* through the nuclear modification factor (R_{AA}), which is just the ratio of the jet yield in Pb+Pb collisions to the cross section in *pp* collisions scaled by a factor to account for differences in the nuclear geometry. ATLAS previously measured jet suppression through the nuclear modification factor in Ref. [5]. This thesis presents a new measurement of the R_{AA} at a different center-of-mass energy with significantly reduced systematics, a much further reach in jet p_{T}, and the ability to measure differentially in the jet rapidity [6]. The rapidity dependence studies the flavor dependence of energy loss, and the higher statistics and reduced uncertainties allow for detailed comparisons to theoretical models.

This thesis is organized as follows. Chapter 2 describes the theoretical and experimental background of QCD, HI collisions, jets, and jet quenching. It also motivates the measurements presented in this dissertation. Chapter 3 describes the LHC and the components of the ATLAS detector. Chapter 4 outlines how the jets are measured including a description of the jet reconstruction and performance, as well as general details about unfolding. Chapter 5 presents the fully unfolded measurement of the dijet asymmetry in Pb+Pb and *pp* collisions. Chapter 6 details the measurement of jet suppression through the R_{AA} in Pb+Pb collisions. Chapter 7 also discusses a dijet asymmetry measurement, but now in Xe+Xe collisions. Finally, Chapter 8 provides a summary and discussion of the results.

Chapter 2

Background

2.1 Quantum Chromodynamics

2.1.1 Fundamentals

Quantum Chromodynamics (QCD) is the theory of the strong interaction between quarks and gluons. It is a SU(3) Yang-Mills theory [7] which is a non-abelian gauge theory [8, 9, 10, 11]. QCD differs from QED (Quantum Electrodynamics) in that it is non-abelian instead of abelian and that the force carrier is a gluon with color charge instead of a photon with no charge. The color charges are conserved like electric charges in QED. The spin-$\frac{1}{2}$ quarks can have three color charges (red, green, and blue) can interact via the strong nuclear force that is mediated by a spin-1 gluon. The QCD Lagrangian is given by

$$\mathcal{L}_{\text{QCD}} = \sum_f \overline{\psi}^i_f (i\gamma^\mu D_{\mu,ij} - m_f \delta_{ij}) \psi^j_f - \frac{1}{4} F^a_{\mu\nu} F^{\mu\nu}_a \tag{2.1}$$

where f is the quark flavor (in the Standard Model there are six: up, down, charm, strange, top bottom), a is the gluon color index (with 8 possible values), i and j are the color charges (with 3 possible values), γ_μ is the Dirac matrix which connects the spinor to the vector representation of the Lorentz group, and m_f is the quark mass.

The spin-$\frac{1}{2}$ quark field, ψ_f, is in the fundamental representation of the SU(3) gauge group. It has local gauge symmetry and transforms under the SU(3) space-dependent rotation

$$\psi^i = e^{i\sum_a \theta^a(x) t^a_{ij}} \psi^j = U(x)_{ij}\psi^j \tag{2.2}$$

where i and j are again the quark charges. This local symmetry is non-commuting which makes it non-abelian. The generator t^a of the gauge group (represented by eight 3×3 matrixes called Gell-Mann matrixes) obey the Lie algebra

$$[t^a, t^b] = i f_{abc} t^c \tag{2.3}$$

where f_{abc} are the structure constants of SU(3).

The gauge covariant derivative D_μ is defined as

$$D_\mu = \partial_\mu - igt^a A^a_\mu \tag{2.4}$$

where A^a_μ is the gluon field and g is the coupling strength between the quarks and the gluons (represented by the gauge field). It is defined in this way because the covariant derivative must be gauge invariant, i.e.

$$D_\mu \rightarrow U(x) D_\mu U(x)^\dagger \, . \tag{2.5}$$

Since the partial derivative ∂_μ is not invariant, the potential A needs to be added to the partial derivative ∂ to form a covariant operator D. The potential A_μ transforms under a local gauge transformation as

$$A^a_\mu \rightarrow U(x)(A^a_\mu t^a + \frac{i}{g}\partial_\mu) U(x)^\dagger \, . \tag{2.6}$$

The gluon field tensor, $F^a_{\mu\nu}$, from Equation 2.1 is given by

$$F^a_{\mu\nu} = \partial_\mu A^a_\nu - \partial_\nu A^a_\mu - g f_{abc} A^b_\mu A^c_\nu \tag{2.7}$$

and is defined by

$$[D_\mu, D_\nu] = -igF^a_{\mu\nu} t^a \, . \tag{2.8}$$

The fields of the Lagrangian are in representations of the gauge group G, which is allowed once the local symmetry group is defined. The fermion fields ψ are in the fundamental representation of SU(3) and thus have dimension 3 corresponding to the three colors (red, blue, green). The vector boson fields A^a_μ are in the adjoint representation of SU(3), which has dimensions equal to $8 = 3^2 - 1$. Physically in QCD, the bosons are the gluons which must represent interactions between the colors since the gluons are the mediators between the quark interactions (red-green, blue-red, etc.). Naively, nine would be expected since there would be 3×3 possible interactions but the states need to be linearly independent and it turns out that only 8 are needed. The ninth state would be a color singlet state which has a color charge of zero. This is not physical since the states need color charge to interact in the theory.

Setting $g = 0$ in equation 2.1 gives the free field Lagrangian without interactions. The free field theory has the number of vector bosons equal to the number of generators of the gauge group (8) and the number of free fermions equal to the dimension of the representation of the gauge group (3). The free field Lagrangian $\mathcal{L}_0$ becomes

$$\mathcal{L}_0 = \mathcal{L}_0^{\text{quarks}} + \mathcal{L}_0^{\text{gluons}} \tag{2.9}$$

where the free quark Lagrangian is given by only the parts that contain fermion fields

$$\mathcal{L}_0^{\text{quarks}} = \sum_f \overline{\psi}^i_f (i\gamma^\mu \partial_{\mu,ij} - m_f \delta_{ij}) \psi^j_f \tag{2.10}$$

and the gluon Lagrangian is given by only the parts that contain the vector boson fields

$$\mathcal{L}_0^{\text{gluons}} = -\frac{1}{2}(\partial_\mu A^a_\nu \partial^\mu A^\nu_a - \partial_\nu A^a_\mu \partial^\nu A^\mu_a) \, . \tag{2.11}$$

The rest of the Lagrangian are the interaction terms

$$\mathcal{L}_{\text{int}} = \sum_f g A^a_\mu \overline{\psi}_f \gamma^\mu t^a \psi_f - g f_{abc} (\partial_\mu A^a_\nu) A^\mu_b A^\nu_c - \frac{1}{4} g^2 f_{abc} A^b_\mu A^c_\nu f_{ade} A^\mu_d A^\nu_e \, . \tag{2.12}$$

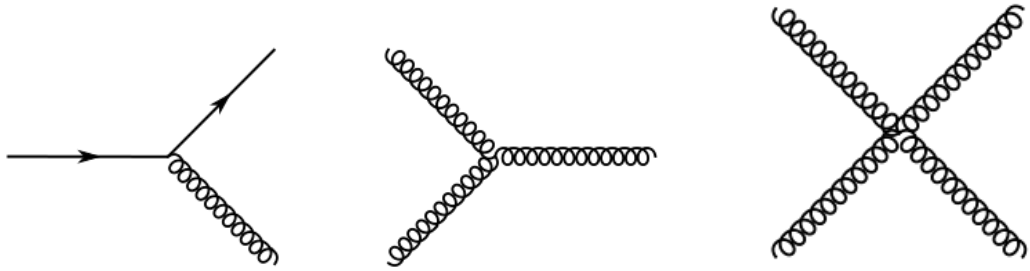

Figure 2.1: The possible QCD interactions from the QCD Lagrangian: quark-gluon (left), three-gluon (center), and four-gluon (right).

The three terms represent three possible interactions between the fields. The first is the quark-gluon vertex with strength proportional to g. The second and third represent gluon-gluon interactions, where the second term is between three gluons (with strength proportional to g) and the third term is between four gluons (with strength proportional to g^2). The gluon-gluon interactions are from the non-abelian gauge theory where the gluon has a color charge and can interact strongly and thus self-interacts. This is different than QED, where the structure constants $f_{abc} = 0$, because the photon has no charge and doesn't interact with itself. These are represented by Feynman diagrams in Figure 2.1.

The covariant gauge-fixing term must be supplemented by a ghost Lagrangian term. This additional Fadeev-Popov ghost term is added to be consistent with the path integral formalism since this is typically used to quantize the theory. The path intergral over-counts solutions for the same physical state which leads to unphysical degrees of freedom. The ghost term

$$\mathcal{L}_{ghost} = \partial_\mu \overline{c}^a D^\mu c^a \tag{2.13}$$

where c^a is a ghost field, serves to cancel it out. Ghosts show up as virtual particles in internal closed loops and only couple to gluons.

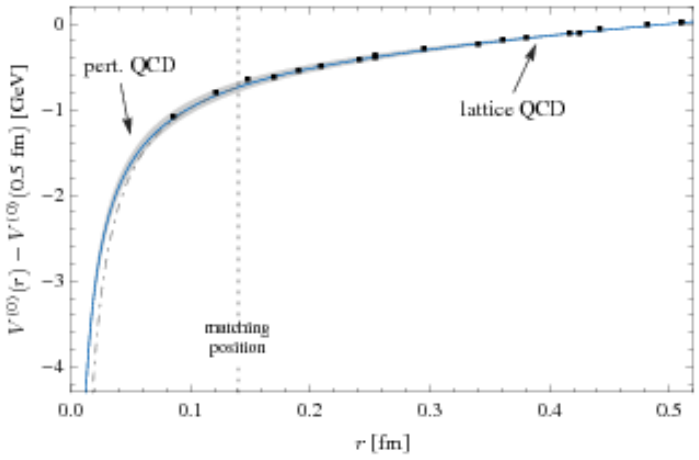

Figure 2.2: The QCD potential as a function of r, where a QCD potential calculated in perturbative QCD from Ref. [15] has been matched to a calculation from lattice QCD from Ref. [16].

2.1.2 Confinement and Asymptotic Freedom

QCD predicts both confinement and asymptotic freedom. Confinement is the idea that quarks and gluons are always bound inside of hadrons. They will not be found in an isolated state under normal conditions since there needs to be zero color charge because of the gluon self-interactions. This can be understood qualitatively by writing the potential between $q\bar{q}$ pairs in the following way,

$$V_{q\bar{q}} = \frac{-4}{3}\frac{\alpha_s(r)}{r} + kr \tag{2.14}$$

which is derived in Lattice QCD (described more in Section 2.1.3.1) [12, 13, 14].

At large distances the second term dominates, which shows that the potential grows with distances, as seen in Figure 2.2. This means the interaction between two quarks does not weaken the further away they are from each other. When the quarks are pulled away from each other a narrow flux tube (or string) exists between the two quarks where the strong force is constant between the two of them. As the two quarks are separated it eventually becomes more energetically favorable for a $q\bar{q}$ pair to pop out of the vacuum than for the flux tube to grow anymore. These then form additional $q\bar{q}$ pairs with the original quarks

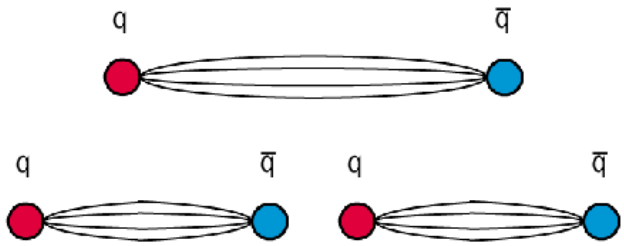

Figure 2.3: Diagram of what happens to quark anti-quark pairs when they are pulled apart because of confinement.

as shown in Figure 2.3.

At short distance scales the potential in equation 2.14 becomes dominated by the first term which is Coulomb-like. In this regime the potential is much weaker and thus the force is weaker. The field lines start to spread out and the quarks become less bound. This phenomena is called asymptotic freedom, where the interactions between the quarks and gluons become weaker at short distance scales (or high energies).

This can be derived using the running coupling constant,$\alpha_s(Q^2)$ which depends on the momentum transfer Q^2 and represents the strength of the strong interaction. It is smaller at small distances or high energy and larger at large distances or low energy, which is in contrast with the strength of the QED interaction. In field theory renormalization is used to make the coupling in the field theory depend on some energy scale such that that changes of the physical system can be observed at different scales. This particular renormalization scheme is used to remove infinities in observables calculated from Lagrangians that are present due to self-interactions of fields in the Lagrangian.

Renormalization of QCD theory involves a renormalization scale called μ and a renormalized coupling constant, α_s or g. A dimensionless physical quantity R in renormalization must follow [11, 17]

$$\mu^2 \frac{dR}{d\mu^2} = [\mu^2 \frac{\partial}{\partial \mu^2} + \mu^2 \frac{\partial \alpha_s}{\partial \mu^2} \frac{\partial}{\partial \alpha_s}]R = 0 \, . \tag{2.15}$$

If a β function is defined in the following way

$$\beta(\alpha_s) = \mu^2 \frac{\partial \alpha_s}{\partial \mu^2} \tag{2.16}$$

then the following differential equation results from equation 2.15:

$$\frac{\partial R}{\partial \log \frac{Q^2}{\mu^2}} = \beta(\alpha_s) \frac{\partial R}{\partial \alpha_s} \tag{2.17}$$

Solving this partial differential equation and introducing the running coupling $\alpha_s(Q)$ gives the relation

$$\frac{\partial \alpha_s(Q)}{\partial \log \frac{Q^2}{\mu^2}} = \beta(\alpha_s(Q)) \tag{2.18}$$

where $\beta(\alpha_s)$ can be expanded perturbatively as

$$\begin{aligned} \beta(\alpha_s) &= -\beta_0 \alpha_s^2 (1 + \beta_1 \alpha_s + O(\alpha_s^2)) \\ \beta_0 = \frac{33 - 2N_f}{12\pi}, \beta_1 &= \frac{153 - 19N_f}{2\pi(33 - 2N_f)} \end{aligned} \tag{2.19}$$

where N_f is the number of degrees of freedom and $\alpha_s = g^2/4\pi$. Combining equation 2.19 and 2.18 gives

$$\frac{\partial \alpha_s(Q)}{\partial \log \frac{Q^2}{\mu^2}} = -\beta_0 \alpha_s^2(Q)(1 + \beta_1 \alpha_s(Q) + O(\alpha_s^2(0))) \ . \tag{2.20}$$

Solving the one-loop beta equation (i.e. dropping the β_1) yields the following equation for the running coupling

$$\alpha_s(Q) = \frac{\alpha_s(\mu)}{1 + \beta_0 \alpha_s(\mu) \log \frac{Q^2}{\mu^2}} \ , \tag{2.21}$$

It can be seen in this equation that if Q^2 increases the running coupling decreases to zero, which is the property of asymptotic freedom. If β was negative (as it is in QED) then the coupling would increase with increasing Q^2. Note that the decrease is gradual because of the natural log. This can be rewritten as

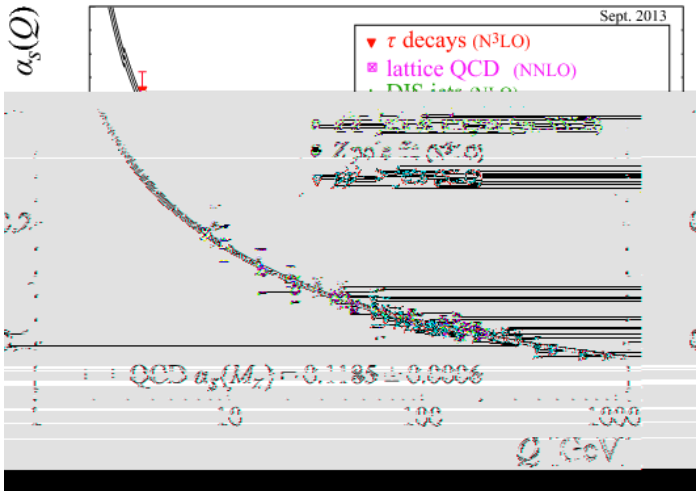

Figure 2.4: The QCD running coupling as a function of Q^2 compared to data [8].

$$\alpha_s(Q) = \frac{1}{\beta_0 \ln \frac{Q^2}{\Lambda^2_{QCD}}} \tag{2.22}$$

where $\Lambda_{QCD} = \mu^2 e^{-\frac{1}{\alpha_s(\mu)\beta_0}}$. Λ_{QCD} becomes the mass scale of QCD at approximately 200 GeV and replaces the dimensionless coupling constant. It is like a dividing scale between low and high energy QCD, where the low energy behavior can be described using perturbative QCD (pQCD) which will be described in detail in Section 2.2 and the high energy behavior is described by non-perturbative QCD through frameworks like lattice QCD (Section 2.1.3.1) and effective field theories. Figure 2.4 demonstrates this phenomena with the running coupling shown as a function of Q^2. At low energies ($Q << \Lambda_{QCD}$) and large distances, $\alpha_s(Q) \to \infty$ and confinement occurs in a non-perturbative regime. At high energies ($Q >> \Lambda_{QCD}$) and small distances, $\alpha_s(Q) \to 0$ and asymptotic freedom occurs in the pQCD regime. This one-loop β-function for SU(N) non-abelian gauge theory was first calculated in 1973 by Gross, Politzer, and Wilczek [18, 19] and earned them the Nobel Prize in Physics in 2004.

2.1.3 Non-perturbative QCD

QCD at low energies and strong coupling can not be described by perturbative techniques and thus requires non-perturbative QCD methods. The current models to describe non-perturbative effects are Lattice QCD [20], AdS/CFT correspondance [21, 22, 23], QCD sum rules [24], and effective field theory models like the Nambu-Jona-Lasinio (NJL) model [25, 26], the chiral perturbation theory [27], and soft collinear effect field theory (SCET) [28].

2.1.3.1 Lattice QCD

Lattice QCD begins with a Euclidean space-time grid or lattice of points [29]. The quark fields are the lattice sites and the gluon fields are the links between each site (also called Wilson lines). The spacing between the lattice is denoted as a and the momentum cut-off in the theory becomes $1/a$. A schematic of the spacing is shown in Figure 2.5. To make the theory continuous instead of discrete, the sites are taken to be infinitesimally close to each other ($a \to 0$) and the overall size of the lattice is infinitely large. Lattice calculations use a Feynman path integral approach with the QCD action. A complication known as fermion doubling arises from the fermion fields on the lattice which creates 2^4 spurious states instead of just one [30, 31]. This can be remedied by using Wilson fermions or staggered fermions.

Lattice QCD calculations are done using Monte-Carlo simulations but they are very computationally intensive and require the use of supercomputers. The simulations have statistical errors due to the MC and systematic errors due to the discrete lattice. Lattice QCD was used to calculate the equation for the $q\bar{q}$ potential in equation 2.14.

2.1.3.2 AdS/CFT Correspondance

Anti-de Sitter/conformal field theory (AdS/CFT) correspondance relates two theories in a gauge/string duality: the AdS spaces where quantum gravity is formulated in string theory and CFT which are quantum field theories like those that describe particles. It describes a weak-strong duality such that it can be used to study strongly coupled field theories since when the quantum field theory is weak the gravitational theory is strong, and vice-versa. Therefore, the difficult problems in strongly-interacting nuclear physics can be translated into problems that are more easily solved in a weakly-interacting grav-

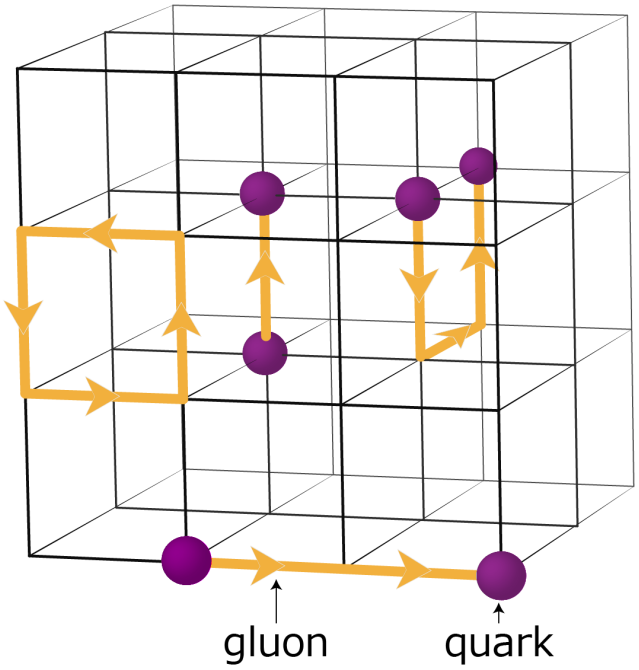

Figure 2.5: A schematic of the lattice in Lattice QCD.

itational theory. Non-abelian gauge theories can be described as gravitation theories in $4+1$-dimensional space-time with a black hole horizon. For the strongly interacting QCD phase at nonzero temperature, the simplest model is a $N = 4$ supersymmetric Yang Mills (SYM) theory where holographic calculations can be performed to gain a better qualitative understanding of strongly-coupled QCD.

2.1.3.3 Effective Field Theory

Effective field theories (EFT) are approximations to field theories that can be solved in certain physical limits. The QCD partition function is not solvable to date so approximations are necessary to solve it. Chiral perturbative theory is an EFT for low energy properties of QCD and has a chiral symmetry in QCD. SCET is an EFT for soft (low energy) or collinear (moving in the same direction as other particles in the process) particles. It models highly energetic quarks interacting with soft gluons. The NJL model parallels superconductivity where Cooper pairs are formed from electrons except Dirac fermions interact with chiral symmetry. It doesn't actually model confinement but there will be a chiral condensate.

2.2 Perturbative QCD

Section 2.1.2 showed that at high energies (or Q^2) and small distances, the quarks and gluons become asymptotically free. Perturbation theory techniques [32, 11, 33, 34] can be used when $\alpha_s << 1$ and the infinite number of possible interactions in QCD can be approximated by a finite number of terms.

2.2.1 Parton Model and Factorization

In the parton model, a hadron can be thought of as being made of many pointlike particles that move together colinearly. It can be applied to any process that has a large momentum transfer Q. In this model the cross section for a hard (or high momentum) process can be described by the cross sections of the partons inside the hadrons interacting convolved with parton distribution functions (PDFs), which are the probability distributions of partons in side of hadrons. The cross section is given by,

$$\sigma_{A+B}(p_A, p_B) = \sum_{ij} \int_0^1 dx_a dx_b f_i(x_a, \mu_f) f_j(x_b, \mu_f) \sigma_{ij}(p_a, p_b, \alpha_s(\mu), Q) \tag{2.23}$$

where $x_{a,b}$ is the parton's momentum fraction of the total hadron's momentum ($0 \leq x \leq 1$), $f_{i,j}(x, \mu)$ are the PDFs where i and j represent quarks, anti-quarks, and gluons, μ_f is the factorization scale, μ is the renormalization scale (discussed in Section 2.1.2), $p_a = x_a p_A$, and σ_{ab} is the partonic scattering cross section where Q is the characteristic scale of the hard scattering. The cross section for parton scattering is a short distance cross section and can be calculated in perturbation theory as an expansion in α_s. This needs to be factorized from the long-distance, non-perturbative behavior since the short distance cross section does not depend on the long-distance behaviors in the PDFs or the details of the initial and final state hadrons. The ability to separate these is called factorization [35]. This is useful because the short-distance cross sections can be calculated perturbatively and the long-distance behavior can be measured experimentally. A more generalized form of equation 2.23 that includes all the long-distance behavior is written as

$$d\sigma_{A+B\to h+X}(p_A,p_B) = \sum_{abcd}\int_0^1 dx_a dx_b dz f_a(x_a,\mu_f) f_b(x_b,\mu_f)\sigma_{ab\to cd}(p_a,p_b,\alpha_s(\mu),Q)D_c^h(z,\mu_f) \tag{2.24}$$

where now the fragmentation functions (FFs), $D_c^h(z,\mu_f)$, are included in the calculation which are how the final state partons fragment into a hadron (described more in Section 2.2.4), where z is the fraction of the momentum that the parton carries of the fragmented hadron. The FFs and PDFs are the non-perturbative parts that are separated out by the factorization scale μ_f from the perturbative cross section. The factorization scale μ_f is usually defined to be equal to Q.

The factorized part of the cross section in equation 2.24 is computed in perturbation theory in the following way

$$\sigma(Q^2/\mu^2, m^2/\mu^2, \alpha_s(\mu)) = \sum_{n=0}^{\infty} a_n(Q^2/\mu^2, m^2/\mu^2)\alpha_s^n(\mu)\ . \tag{2.25}$$

It is shown be infrared safe, meaning that it doesn't depend on any long distance behavior and the coefficients a_n are finite. An infrared divergent cross section has infinities that blow up since the gluon mass and light quark masses are close to zero but infrared safe quantities have a finite limit for the vanishing mass. The distributions should have no sensitivity to emissions of low momentum gluons (stable in the soft limit) or to collinear splitting (stable in the collinear limit where all particles are moving parallel)

$$\begin{aligned} \sigma(Q^2/\mu^2, m^2/\mu^2, \alpha_s(\mu)) &= \sigma(Q^2/\mu^2, 0, \alpha_s(\mu))(1 + O(m^2/\mu^2)) \\ \sigma(Q^2/\mu^2, 0, \alpha_s(\mu)) &= \sigma(1, 0, \alpha_s(\mu))\ . \end{aligned} \tag{2.26}$$

The momentum dependence is contained within the running coupling which vanishes when Q is large such that the perturbative calculation keeps getting more precise. The PDFs and FFs contain the infrared divergent part and depends on the initial hadron but are independent of the hard scattering process.

2.2.2 Parton Distribution Functions

PDFs are functions that describe the probability density of finding a parton inside of a hadron with momentum fraction x and Q^2. They represent the initial state of the hadron before a collision occurs. The 13 functions are for the gluon and each quark and anti-quark, where the heavy quarks evolve from the gluon and light quark PDF. They can be written in terms of a formal correlator function as

$$f_{a/A}(x,Q) = \frac{1}{4\pi}\int dy^- e^{-xP^+y^-}\langle P|\bar{\psi}(0,y^-,0_T)\gamma^+\psi(0,0,0_T)|P\rangle \tag{2.27}$$

but the momentum state of the hadron $|P\rangle$ is not known so these can't be directly calculated. Everything discussed so far has been at a fixed value of Q^2 but a PDF at one scale μ can be used to predict a PDF at another scale μ', as long as μ and μ' are both large enough such that that $\alpha_s(\mu)$ and $\alpha_s(\mu')$ are small. The evolution of the PDFs with Q^2 can be described using the Dokshitzer-Gribov-Lipatov-Altarelli-Parisi (DGLAP) equations [36, 37, 38]

$$\begin{aligned}
\frac{\partial f_{q_i}(x,Q^2)}{\partial \ln Q^2} &= \frac{\alpha_s(Q^2)}{2\pi}\int_x^1 \frac{dx'}{x'}(f_{q_j}(x',Q^2P_{q_iq_j}(\frac{x}{x'}) + f_g(x',Q^2)P_{q_ig}(\frac{x}{x'})) \\
\frac{\partial f_g(x,Q^2)}{\partial \ln Q^2} &= \frac{\alpha_s(Q^2)}{2\pi}\int_x^1 \frac{dx'}{x'}(f_{q_j}(x',Q^2P_{gq_j}(\frac{x}{x'}) + f_g(x',Q^2)P_{gg}(\frac{x}{x'}))
\end{aligned} \tag{2.28}$$

where $P_{ab}(\frac{x}{x'})$ are the splitting functions (equation 2.29) for a parton a with momentum fraction x from a parton b with momentum fraction x', shown in Figure 2.6. The q represents quarks and the g represents gluons. The DGLAP equations in equation 2.28 are leading order (LO) calculations. The splitting functions are given by the following formulas, where z is the fraction of momentum in the split parton of the original parton and $C_F = 4/3$, $C_A = 3$, and $T_R = 1/2$

$$\begin{aligned}
P_{qq} &= C_F\left[\frac{1+z^2}{(1-z)_+}\right] & P_{gq} &= C_F\left[\frac{1+(1-z)^2}{z}\right] \\
P_{qg} &= T_R\left[z^2+(1-z)^2\right] & P_{gg} &= 2C_A\left[\frac{z^2+(1+z^2)(1-z)^2}{z(1-z)}\right]_+ .
\end{aligned} \tag{2.29}$$

where "+" is defined as $\int_0^1 \frac{f(x)}{(1-x)_+}dx = \int_0^1 \frac{f(x)-f(1)}{1-x}dx$ for a generic function $f(x)$.

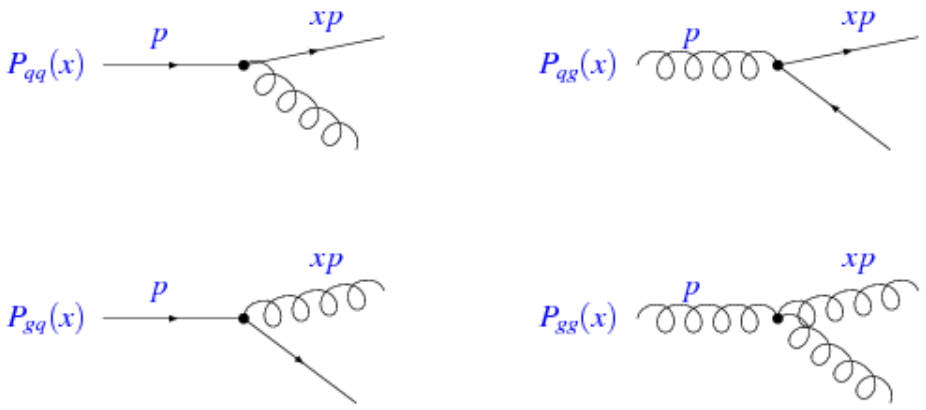

Figure 2.6: Diagrams of the different kinds of splitting that can occur in the DGLAP functions for LO PDF calculations [39].

The PDFs are calculated by doing a global fit to data and then the evolution with Q^2 is used to find the value at another Q^2. The data available from different fixed target experiments and colliders span a large range of Q^2 and x, as shown in Figure 2.7. PDFs can also be fit to next-to-leading order (NLO) and next-to-next-to-leading order (NNLO) and are calculated in various groups including MMHT [40], NNPDF [41], CTEQ [42], HERAPDF [43], ABMP [44], and JR [45]. An example of PDFs from the NNLO NNPDF analysis [46] is shown in Figure 2.8, where the PDF is shown as function of x for the different types of partons at $\mu^2 = 10$ GeV^2 and 10^4 GeV^2. In general, the gluon PDF dominates over the quarks at low values of x such that it is more likely to find gluons with a lower momentum fraction of the hadron and thus the soft parts of the hadron are more likely to be gluons. The quarks dominate over gluons at high x indicating that the harder partons within the hadron tend to be quarks, in particular up and down quarks. Also, the PDFs decrease with increasing x indicating that it is less likely to find particles having more of the momentum of the hadron. Finally, at low x, the PDF increases with increasing values of μ^2.

2.2.3 Deep Inelastic Scattering

Deep inelastic scattering (DIS) of a high energy lepton off of a hadron is an example of a process calculable in pQCD using factorization. A DIS process is represented by

$$l(k) + h(p) \rightarrow l'(k') + X \tag{2.30}$$

where the momentum of the incoming and outgoing lepton are k^μ and k'^μ and p^μ is the momentum of the hadron. The four momentum transfer is $q^\mu = k^\mu - k'^\mu$ and the Lorentz-invariant magnitude is given by $Q^2 = -q^2 > 0$. The Bjorken scaling variable (or total momentum fraction of the struck quark of the total momentum of the target in the infinite momentum frame) is

$$x = \frac{Q^2}{2p \cdot q} = \frac{Q^2}{2M(E - E')} \tag{2.31}$$

and the ratio of the energy transferred to the hadronic system to the total leptonic energy is

$$y = \frac{p \cdot q}{p \cdot k} = \frac{E - E'}{E} \tag{2.32}$$

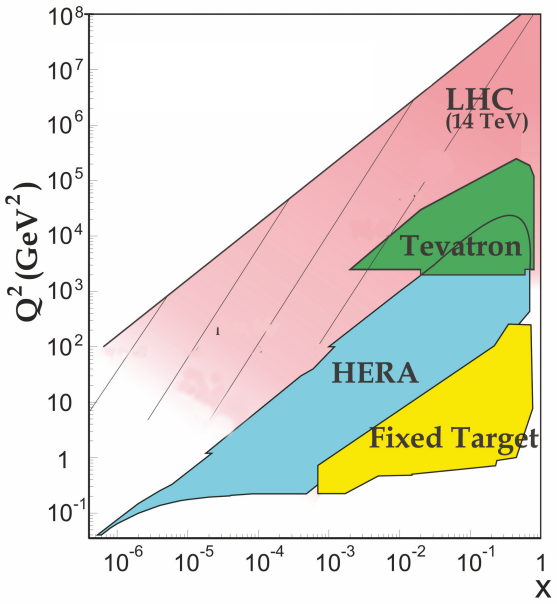

Figure 2.7: The kinematic reach in x and Q^2 for different colliders and fixed target experiments [8].

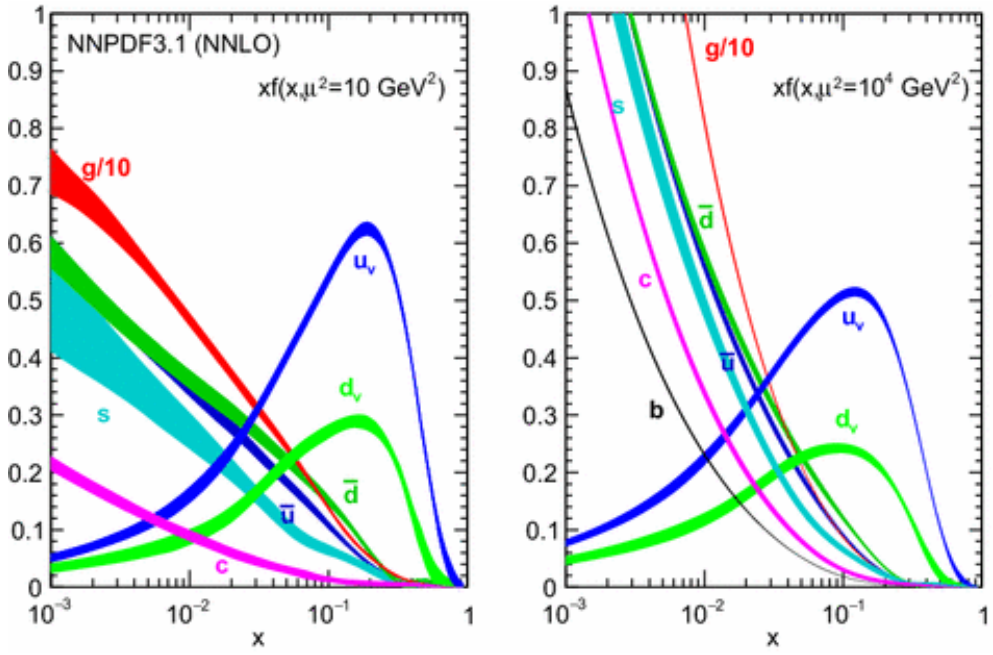

Figure 2.8: The NNPDF3.1 NNLO PDFs at $\mu^2 = 10$ GeV^2 and 10^4 GeV^2 [46].

The energy in both equations refers to the energy in the rest frame of the target. The invariant mass of the hadronic state, $W^2 = (p+q)^2$, becomes

$$W^2 = m^2 + \frac{Q^2}{x}(1-x). \tag{2.33}$$

This will be much larger than m^2 and thus the collision is deeply inelastic. The differential cross section for DIS can be written as

$$\frac{d\sigma}{dxdy} = \frac{4\pi\alpha_{EM}^2}{Q^2}\left[yF_1(x,Q^2) + (\frac{1-y}{xy} - \frac{2M^2xy}{Q^2})F_2(x,Q^2)\right] \tag{2.34}$$

where $F_i(x,Q^2)$ are structure functions that describe the structure of the target as seen by the virtual photon. The virtual photon is exchanged in the interaction between the lepton and the hadron as seen in Figure 2.9.

Experiments of electron-proton scattering were performed at SLAC (Standford Linear Accelerator Center) to try to measure the structure functions as a function of x and Q^2 [48, 49]. Similar experiments have been performed at other accelerators and the findings are

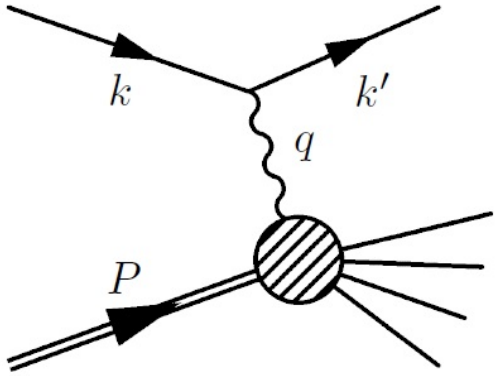

Figure 2.9: Diagram of a lepton and a hadron DIS process, where the squiggle represents a virtual photon [47].

shown in Figure 2.10. This shows the structure functions as a function of Q^2 for different values of x. At intermediate values of x the structure function is shown to be independent of x. This phenomenon is called Bjorken scaling [50] and is the idea that as $Q^2 \to \infty$ the structure functions no longer depend on Q^2. This doesn't hold for lower values of x or higher values of x. Finding this in experiment is what prompted the acceptance of the parton model and the discovery of asymptotic freedom since the scaling implies that no matter how hard the proton is probed, the structure is the same and consists of point-like particles.

For spin-$\frac{1}{2}$ partons, the Callan-Gross relation was shown to hold by experiment which says

$$2xF_1(x, Q^2) = F_2(x, Q^2) \tag{2.35}$$

The structure functions can be computed from the PDFs in the following way

$$\begin{aligned} F_1(x, Q^2) \approx &\quad \frac{1}{2}\sum_a Q_a^2 f_{a/A}(x) + \mathcal{O}(\alpha_s) + \mathcal{O}(m/Q) \\ F_2(x, Q^2) \approx &\quad \sum_a Q_a^2 x f_{a/A}(x) + \mathcal{O}(\alpha_s) + \mathcal{O}(m/Q) \end{aligned} \tag{2.36}$$

where $f_{a/A}$ are the PDFs discussed in Section 2.2.2.

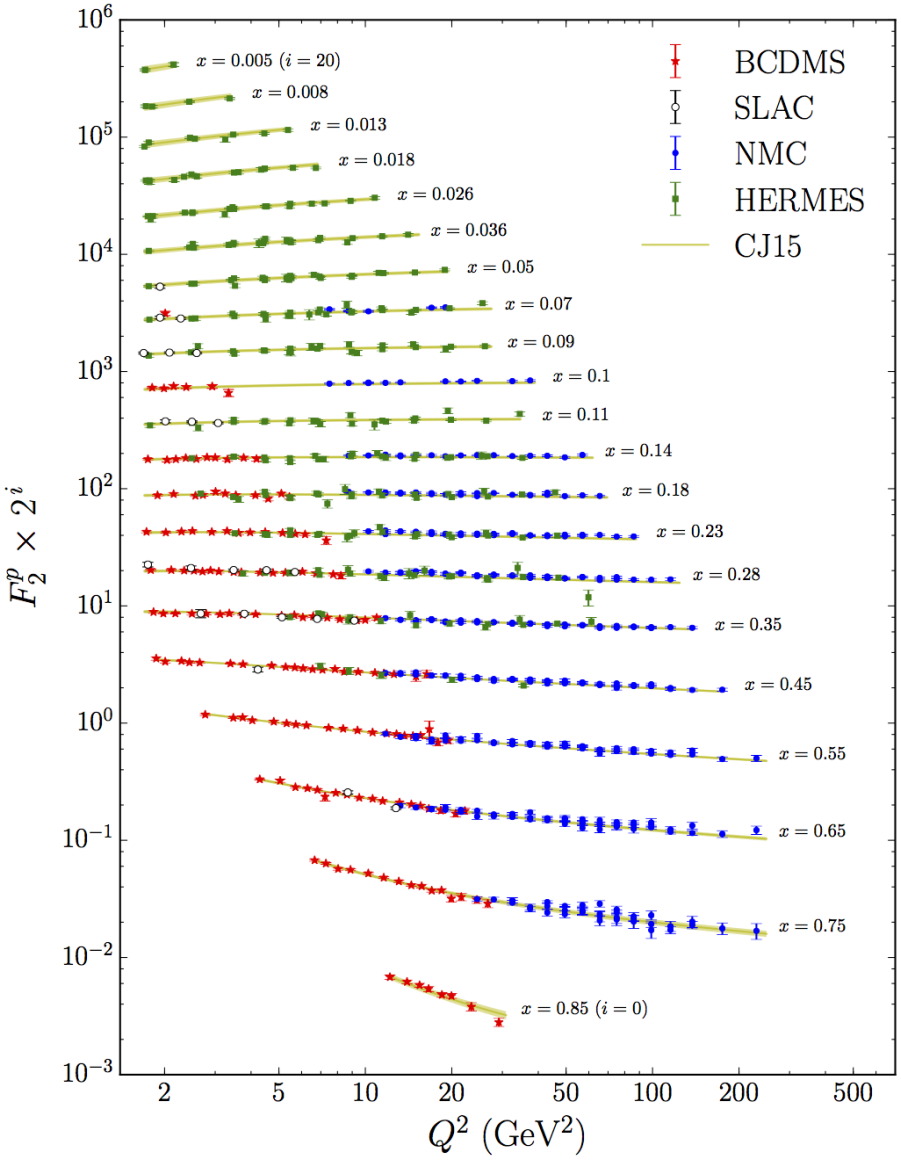

Figure 2.10: The structure function, F_2, of the proton as a function of Q^2 for different values of x. Data is taken from different experiments and all plotted on the same graph.

2.2.4 Fragmentation and Hadronization

The FFs describe the final state of the partons after a collision in the same manner as the PDFs describe the initial state [51, 8]. They are defined as the probability that a parton i will fragment into a hadron h with momentum fraction $z = \frac{p_i \cdot p_h}{|p_i|^2}$. It describes how the color-carrying quarks and gluons transform into color neutral particles. This transformation happens because of color confinement (Section 2.1.2) which says that quarks and gluons should be confined into color neutral hadrons. The cross section for $e^+e^- \to h + X$ can be written as

$$\frac{d\sigma_h}{dx} = \sum_i \int_x^1 \frac{dz}{z} C_i(z, \alpha_s(Q^2)) D_i(z, Q^2) \tag{2.37}$$

where C_i are the coefficients for particular processes. FFs are not calculable perturbatively but they do evolve via the DGLAP equations in the same way as the PDFs do in equation 2.28 where the splitting functions now depend on z instead of x. These functions are independent of the factorization scheme when they retain the parton model momentum sum rule

$$\sum_h \int_0^1 dz \; z D_i^h(z, Q^2) = 1 \; . \tag{2.38}$$

The process by which fragmented partons are recombined into final-state hadrons is called hadronization. Two processes contribute to hadronization [52]. The first process begins with the idea that when partons are produced in a parton scattering they have color and color confinement requires them to be colorless. Thus the partons are connected by a "gluon string" or "flux tube" which is a strong QCD field between them. When the string is stretched it produces quark and anti-quark pairs between the partons which then form many hadrons in the final state that are color neutral [53]. The second is from QCD bremsstrahlung radiation which is gluon radiation from the production and scattering of colored partons that occurs when the partons experience an acceleration. This can occur before the partons interact (initial state radiation) or after (final state radiation). These gluons can split into more gluons or quarks as well, producing a cascade. The cascading parton shower from both parton splitting and gluon radiation tend to form into narrow

cones around the original parton and the partons in the shower eventually come together and hadronize. Clusters of these final state hadrons are what are experimentally measured as jets, described in more detail in Section 2.2.5. The gluon radiation that is produced at large angles and high energy can actually become another jet leading to multi-jet events. Others will be soft and/or collinear along the jet axis and become secondary partons inside the jet. There can also be interjet contributions, which can change the structure of the jet.

QCD predicts color coherence which is the idea that a gluon radiating from partons may not be able to resolve the partons as two separate partons [54, 53]. There are two types of coherence, intrajet and interjet. Interjet processes involve three or more partons interacting and can lead to drag effects which is the depletion of particle flow between two quarks relative to between a quark and a gluon. Intrajet coherence leads to angle ordering and also suppresses the production of very soft gluons. Angular ordering is a condition where the opening angles of the partons in a cascade have to decrease with sequential splittings, as shown in the left panel of Figure 2.11. This phenomenon leads to the hump-back plateau, which is seen in the right panel of Figure 2.11 [53] where the jet FFs as a function of the logarithm of their energy is shown. The shaded grey area represents what it would look like with no gluon radiation in the simple parton model. Adding in gluon radiation leads to the dashed line where the multiplicity will rise significantly. Finally, accounting for coherence effects, gives the black line which shows the soft gluon suppression due to angular ordering.

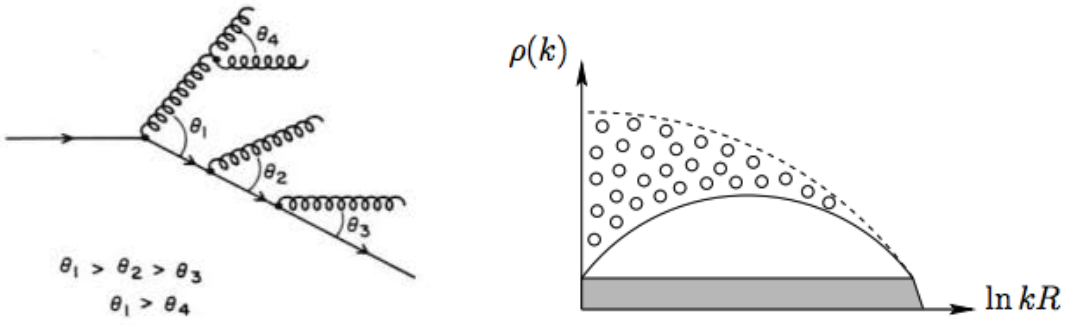

Figure 2.11: Left: A diagram depicting angular ordering. Right:The multiplicity of the FFs as a function of $\ln kR$, where k is the particles energy and R is the size of the jet. The shaded grey region shows the distribution with no bremsstrahlung radiation, the dotted line shows it with radiation (incoherent), and the solid line shows it for coherent radiation [53].

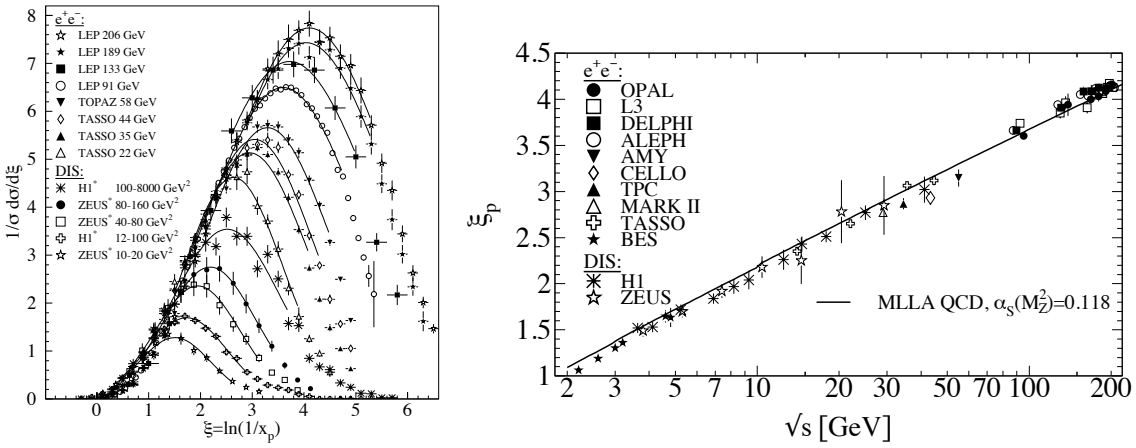

Figure 2.12: The FFs as a function of $\ln 1/x$ at different center-of-mass energies and Q^2 values, including the hump-back plateau structure, is shown on the left. The distributions on the left are fit with a gaussian and the peak position is plotted as a function of s on the right [8].

Higher-order corrections can be enhanced by large logarithms at small x. A modified-leading-log approximation (MLLA) [55, 56, 53, 51] is used where the single and double logarithms ($[\alpha_s \ln 1/x]^m$ terms) are both summed. It takes into account all of the parton multiplication up to NLO including the parton splitting functions, the dependence of the split partons transverse momentum on the running coupling, and the exact angle ordering. This is necessary because even though these soft particles at low x take away a negligible portion of the jet energy, there are many of them such that they contribute the most to the jet multiplicity. The MMLA is compared to experimental data for the FFs as a function of $\ln 1/x$ in the left-hand side of Figure 2.12, where the peak is seen at $\sim \frac{1}{2} \ln s$, where s is the center-of-mass energy (or Q^2) [8]. The distributions can be fit with a gaussian and the peak value can be extracted. The right-hand side shows this peak position plotted as a function of s, where it is seen to increase with increasing energies. Observing the hump-back plateau in data is confirmation of jet fragmentation in pQCD.

There are two main models for hadronization [51, 57], the string and cluster, which are both shown in Figure 2.13. In general it is assumed that the momentum and color flow is similar at the parton level and at the hadron level. The cluster model starts with pre-confinement [58], where partons that are color-connected are lumped together into color-

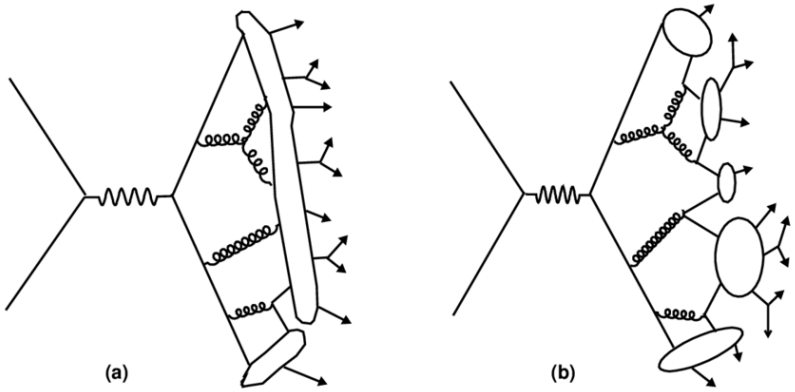

Figure 2.13: The string hadronization model is shown on the left and the cluster hadronization model is shown on the right.

singlet clusters that have finite masses. These clusters then decay into hadrons during confinement. The string model is based on the idea that there is a colour flux in the form of a string connecting the partons. The string is stretched and breaks into hadron pieces from $q\bar{q}$ pairs. Gluons represent kinks on the string that gives rise to a stronger color force on the gluons than the quarks.

2.2.5 Jets

Jets are collimated streams of particles from the hadronization of a parton shower from QCD hard (high momentum) scatterings. A depiction of the entire evolution of a jet from a QCD hard scattering is shown in Figure 2.14. The process starts with partons confined inside of a proton with a PDF, as described in Section 2.2.2. The partons then interact through a hard scattering with a cross section. Before and after the collision the partons can experience initial and final state radiation (ISR and FSR) due to gluon radiation. After the collision the partons undergo a parton shower and then form hadrons during the hadronization process, as described in Section 2.2.4. The hadrons tend to form narrow cones which can be grouped together to form jets in the final state.

Jets are defined through a particle jet clustering algorithm which clusters the hadrons together in a particular way and assigns a momentum that gives a close estimate of the original parton momentum [60, 61]. They are a useful experimental and theoretical quantity,

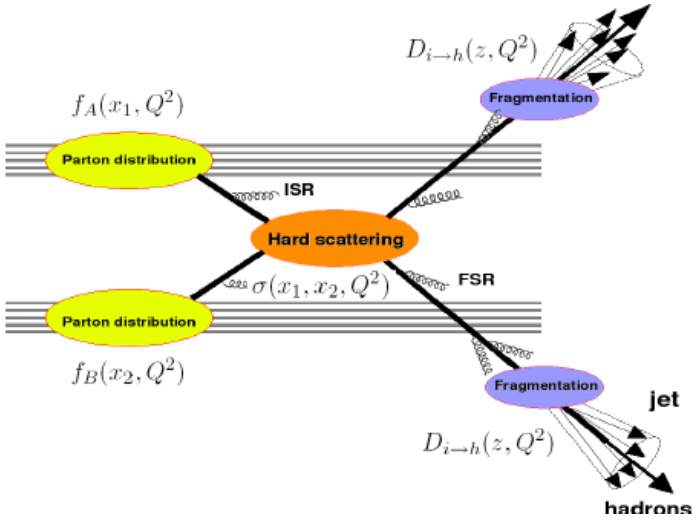

Figure 2.14: Diagram of the evolution of a jet originating from a QCD hard scattering [59]

but they need to be well defined theoretically in the context of pQCD and be simple to implement theoretically or experimentally. The jet should be infrared and collinear safe (IRC), which means the jet's observables need to remain unchanged by the addition of a collinear splitting ("collinear safe") or a soft emission ("infrared safe"). The definition also needs to be sensitive to the underlying physics of interest. There are two different types of algorithms: cone, or "top down", and sequential recombination, or "bottom up". The cone algorithms were one group of the earlier suggested algorithms and work by simply groups particles together into cones around peaks in energy, but many turned out to not be IRC safe.

Many of the sequential recombination algorithms were found to be IRC safe. They combine pairs of nearby partons, mimicking the physics of the parton shower. These algorithms start with a list of particles in an event and define $\Delta R_{ij}^2 = (\phi_i - \phi_j)^2 + (y_i - y_j)^2$ as the distance between the particles, where y is the particle rapidity and ϕ is the azimuthal angle. For each pair, a p_{T}-weighted distance is defined as

$$d_{ij} = \min(p_{\mathrm{T}i}^{2p}, p_{\mathrm{T}j}^{2p}) \frac{\Delta R_{ij}^2}{R^2} \tag{2.39}$$

where R is the size of the jet and can be any fixed value. At the LHC, the R values typically

range from 0.2 up to 1.0 (0.4 is the most common radius in this thesis). The exponent p can be set to different values that each represent different algorithms. A value of $p = 1$ corresponds to the k_t algorithm [62], $p = -1$ corresponds to the anti-k_t algorithm [63], and $p = 0$ corresponds to the Cambridge-Aachen algorithm [64]. The algorithm works in the following way, starting from a list of jets in a given event:

1. Calculate the d_{ij} values for each possible pair. Also, determine the distance of each particle to the beam $d_{iB} = p_{\mathrm{T}i}^{2p}$.
2. Find the minimum between d_{ij} and d_{iB}.
3. If d_{ij} is the minimum, combine i and j and return to step 1.
4. If the minimum is d_{iB} then i is a final state jet and it is removed from the list of particles. Return to step 1.
5. Repeat until there are no more particles.

The k_t algorithm is not preferred by experimentalists since it is slow (N^3 or $N \log N$ in `FastJet` [65]) and leads to some irregular geometries in the jet shape (see the left panel of Figure 2.15). The Cambridge-Aachen only uses the geometry of the particles to cluster the jet. It has the same speed and shape issues as the k_t algorithm, but is useful because it reflects the angular ordering of the hadrons inside the jet. The anti-k_t algorithm starts with the hard part of the jet, unlike the k_t which starts with the soft part, and grows outward from hard "seeds". This creates more realistic circular jets with a hard core as shown in Figure 2.15, but the substructure from the clustering in this algorithm doesn't reflect the QCD branching like in the other algorithms. The anti-k_t algorithm is the jet algorithm used in this thesis.

2.2.6 MC generators

Monte-Carlo (MC) generators are useful in high energy physics to compare experimental results to predictions from theoretical models. A MC is any model that uses random numbers to solve a problem. Specifically in high energy, it corresponds to a simulation of

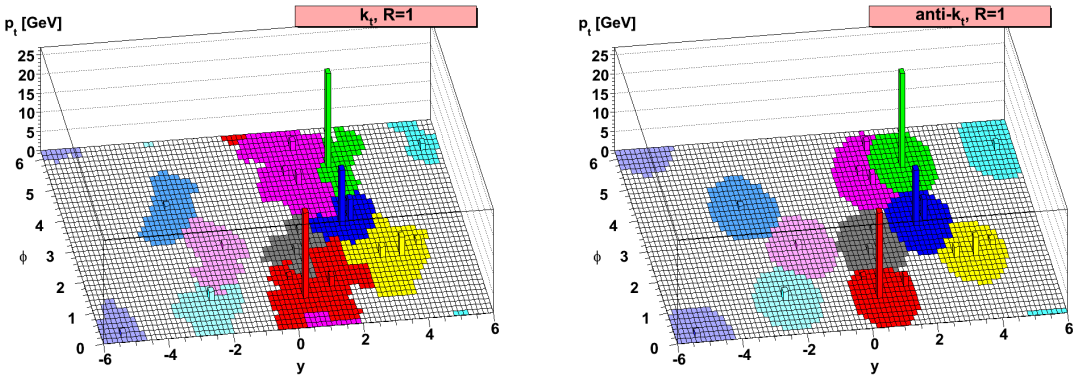

Figure 2.15: The two panels show the y-ϕ distributions of cells in an event where the left panel clusters the cells to form jets using the k_t algorithm and the right panel uses the anti-k_t algorithm. The colors represent the jets defined by the algorithms [63]

high energy reactions with random numbers using physical models to generate a MC event. This is why they are called MC event generators [59, 66, 67]. MC generators can represent a theory or a phenomenological model where a parameter needs to be tuned to the data. HI simulations fall in the latter category and jets in a vacuum fall somewhere in the middle (closer to the former). MC generators are useful to gain some insight into the underlying theory and what mechanisms are at play (discussion in Section 2.5.2.5). They are also used for experimental corrections, background, and unfolding (discussed in Chapter 4).

The most common generators for jets in high energy physics are Pythia [68], Herwig [69] (or Herwig++ [70] which is the same but written in C++ instead of Fortran), Sherpa [71], and more recently Powheg [72]. MC generators can simulate many aspects of an event (tracks, bosons, etc.) but here the focus will be on jets. The main elements of a MC generator are matrix elements (ME), initial state radiation (ISR) or the initial state parton shower, final state radiation (FSR) or the final state parton shower, and hadronization. ME are fixed order calculations in perturbation theory at leading (LO) or next-to leading order (NLO). ISR and FSR were defined in the beginning of Section 2.2.5 and hadronization was discussed in Section 2.2.4.

MC generators model the parton shower where splitting functions (equation 2.29) determine how a parton may branch into two partons. The MC establishes random jet pa-

rameters to evaluate the splitting for each event. The probability of not splitting during an evolution between two scales (Q_a^2 and Q_b^2) is called the Sudakov form factor [73], $\exp - \int \frac{dQ}{Q^2} \int \frac{\alpha_s}{2\pi} P_{a\to bc}(z, Q^2) dz$. The integral over z has an infared cut-off below which the parton splittings are not resolvable. For each event the probability for scattering can be calculated from those factors and the splitting continues until the cut-off is reached. PYTHIA 6 [68] uses coherent scattering where the parton shower is angle ordered (discussed in Section 2.2.4) and HERWIG and Pythia 8 [74] use dipole showering where instead of a parton splitting there is a dipole radiation pattern for gluon emission. For the hadronization, PYTHIA uses the Lund string model and HERWIG uses the cluster model which are both discussed in Section 2.2.4. There is also an underlying event (UE) contribution from collisions of partons in the incoming hadrons that don't directly participate in the hard processes (most common is from multiple parton interactions) and thus are not part of the shower. This UE is larger in minimum bias events in high energy collisions than events that are triggered on hard processes. HERWIG and PYTHIA are typically for LO calculations, whereas POWHEG includes NLO.

2.3 Quark Gluon Plasma

2.3.1 Phase Diagram and Transition

The fact that QCD predicts confinement and asymptotic freedom suggests that there are two states of QCD matter that can be described by a phase diagram and a phase transition. Figure 2.16 shows the QCD phase diagram as temperature versus baryon density. It demonstrates that at low temperatures and baryon density the quarks and gluons are confined inside hadrons but at higher temperatures and baryon densities the quarks become free in a new state of matter called quark-gluon plasma [75]. This transition occurs at a temperature of about ~ 154 MeV and an energy density ϵ above ~ 0.2 GeV/fm^3 [76].

The conditions for this QGP phase to form existed in the early Universe right after the big bang [77]. During the expansion of the universe, the temperature was high enough right after the big bang for the quarks and gluons to be deconfined in a hot phase of matter, as shown in Figure 2.17 (age of leptons). This phase lasted until around 1 μs when the

temperature was cool enough for the quarks and gluons to confine into hadrons.

High temperatures and pressures can cause this phase transition to occur. At low baryon density the transition is a smooth crossover where there is no distinct phase transition [78,

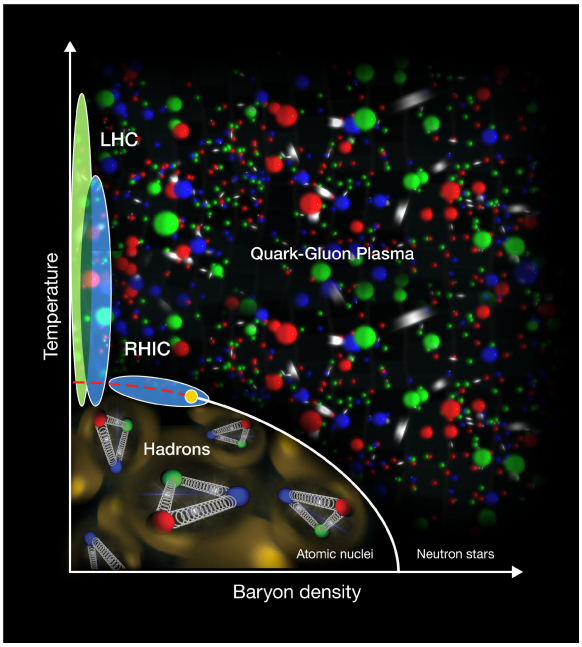

Figure 2.16: A schematic of the QCD phase diagram.

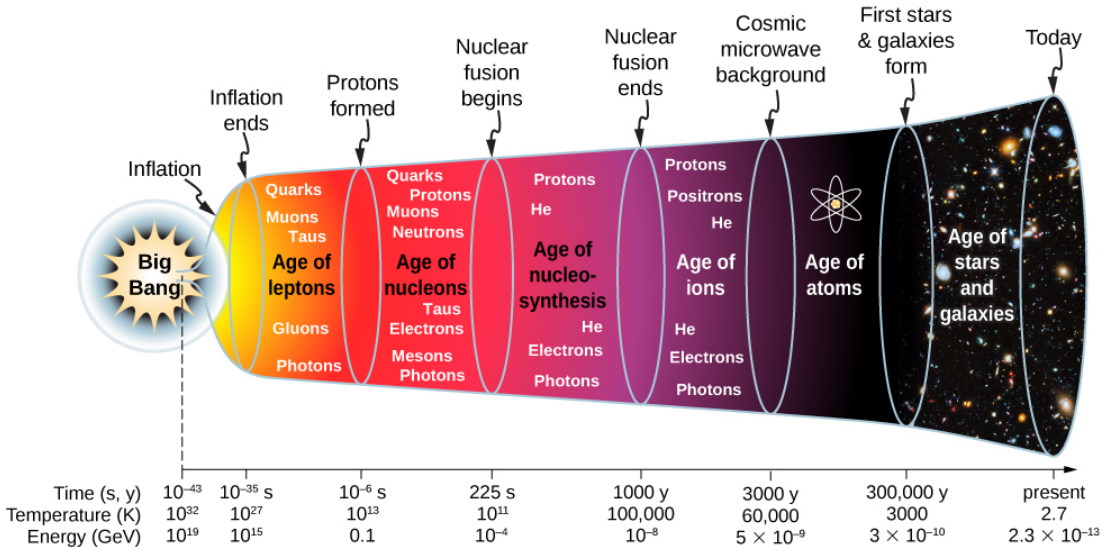

Figure 2.17: A timeline for the expansion of the Universe after the big bang.

79, 80], indicated by the dashed lines in Figure 2.16. At higher baryon density the transition is expected to become a first order phase transition [81, 82], indicated by the solid line. This means that there must be a critical point at the boundary between the crossover and the first order phase transition, which is indicated by the orange dot on the figure. Finding the critical point is crucial for understanding the full phase structure of QCD. This is being targeted experimentally by the Beam Energy Scan (BES) at RHIC [83, 84].

The dynamics of the phase transition can be calculated and understood in different ways including through thermodynamics and statistical mechanics or lattice QCD.

2.3.1.1 Bag Model

The MIT bag model [85, 86], which uses the physics of confinement along with thermodynamics and statistical mechanics, can describe the basic features of the hadronic and QGP phases of QCD matter. In the model, quarks are massless particles confined inside a bag and infinitely massive outside of the bag. A bag pressure B that is directed inward balanced with the stress from the kinetic energy of the quarks inside the bag represents confinement. The gluons are also confined inside the bag in this model and the total color of the bag is colorless. The bag pressure B represents the non-perturbative aspects of QCD. The bag pressure B can be calculated by considering the total energy of the gas (where the partons are the particles in the gas) to be the energy from the bag pressure, or the pressure times the volume, and the internal energy of the gas, or radiation energy.

$$E = B\frac{4\pi}{3}r_0^3 + \frac{N}{V^{1/3}} \tag{2.40}$$

The second term comes from $E = \hbar c/\lambda$, where λ can be approximated as the cubed root of the volume and $\hbar = c = 1$. To find B, E should be minimized:

$$\frac{dE}{dr} = B4\pi r_0^2 - \frac{N}{(\frac{4\pi}{3})^{1/3}}\frac{1}{r_0^2} = 0 \tag{2.41}$$

Solving for B and setting $N = 3$

$$B = \frac{3}{4\pi}^{4/3}\frac{1}{r_0^4} = (\frac{4\pi}{3}r_0^3)^{-4/3} \tag{2.42}$$

or $B \approx V^{-4/3}$. The bag pressure B ends up being approximately 200 MeV/fm^3. In the bag model, there are two balancing pressures but eventually the outward pressure becomes greater than the inward bag pressure. When this happens the bag no longer confines the partons and a new state of matter is produced. This outward pressure can become large by either increasing the temperature or the baryon density. Thus to understand the two phases it is useful to compare the pressure and energy density of both.

Starting with the density of states, the energy density is

$$\epsilon = \int_0^\infty E(p)n(p)dp \tag{2.43}$$

where $n(p)dp$ is the number density and $E(p)$ is the energy, which in the relativistic realm is just the momentum. The number density is

$$n(p) = \frac{g}{e^{(p-\mu)/kT} \pm 1} \frac{4\pi p^2}{h^3} \tag{2.44}$$

which comes from the Fermi-Dirac distribution, where the $+$ sign is used for fermions, and the Bose-Einstein distribution, where the $-$ sign is used for bosons. The constant g represents the number of internal degrees of freedom. The energy density then becomes

$$\epsilon = \frac{g}{2\pi^2} \int_0^\infty \frac{p^3 dp}{e^{(p-\mu)/kT} \pm 1} \, . \tag{2.45}$$

Once the energy density is obtained, the pressure can also be found using $P = \frac{1}{3}\epsilon$. The integral is done separately for gluons, which are treated as bosons, and quarks, which are fermions. The results are as follow:

$$\begin{aligned} \epsilon_q &= \frac{7}{8}\frac{\pi^2}{30} g_q T^4 \quad P_q = \frac{7}{8}\frac{\pi^2}{90} g_q T^4 \\ \epsilon_g &= \frac{\pi^2}{30} g_g T^4 \quad P_g = \frac{\pi^2}{90} g_g T^4 \end{aligned} \tag{2.46}$$

The energy density and pressure for hadrons can be easily found since they are bosons. If pions are used, $g_\pi = 3$ since there are three pions states.

$$\epsilon_H = \frac{\pi^2}{10} T^4 \quad P_H = \frac{\pi^2}{30} T^4 \tag{2.47}$$

For the quark-gluon plasma, the pressures for the quarks and gluons need to be added together and the bag pressure should be subtracted, $P_{QGP} = P_q + P_g - B$.

$$P_{QGP} = \frac{\pi^2}{90}(\frac{7}{8}g_q + g_g)T^4 - B \tag{2.48}$$

The number of degrees of freedom for gluons in the QGP is $2 \times 8 = 16$ since there are 8 gluons with two possible polarizations. The number of degrees of freedom for quarks is $2 \times 2 \times 2 \times 3 = 16$ since there are two flavors, two spin states, three colors, and two $q\bar{q}$ states.

$$P_{QGP} = 37\frac{\pi^2}{90}T^4 - B \tag{2.49}$$

The energy density is derived the same way except the bag pressure is added.

$$\epsilon_{QGP} = 37\frac{\pi^2}{30}T^4 + B \tag{2.50}$$

The state with the higher pressure at a particular value of the temperature will be the state that the matter will be in. The two pressures can be plotted as a function of temperature, as shown in Figure 2.18. These pressures can be used to determine the critical temperature for the phase transition to occur by setting them equal, $P_H = P_{QGP}$,

$$\begin{aligned} \frac{\pi^2}{30}T_C^4 &= 37\frac{\pi^2}{90}T_C^4 - B \\ T_C &= (\frac{45B}{17\pi^2})^{1/4} \end{aligned} \tag{2.51}$$

which makes $T_C \approx 158$ MeV. The critical temperature is at zero baryon density on the phase diagram in Figure 2.16. For non-zero baryon density the critical temperature will be somewhere between 0 and T_C. This temperature can be plugged into equation 2.50 to determine the minimum energy density of the plasma ($\epsilon_{QGP} \approx 1.6$ GeV/fm^3).

2.3.1.2 Lattice Thermodynamics

To obtain a more accurate description of the phase transition and the thermodynamics of the QGP state, lattice calculations [88, 89, 76] (previously described in Section 2.1.3.1) are used. As mentioned earlier, these require significant computing resources which limits the extend

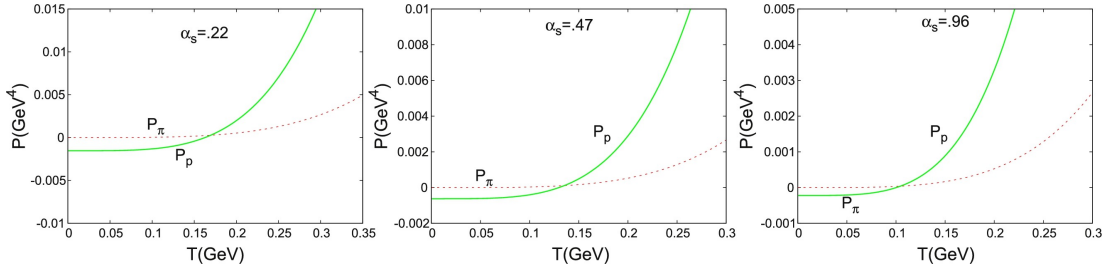

Figure 2.18: Curves of pressure versus temperature for the hadronic (P_π) and QGP (P_p) phase of QCD matter, where the QGP phase is calculated using the MIT bag model [87]. The panels are for different values of α_s.

to which calculations can be made. Lattice calculations are performed by doing a Feymann path integral in four-dimensional Euclidean space-time with $N_s^3 N_\tau$ lattice sites and a as the lattice spacing (N_s is spatial and N_τ is time). The formalism involves the calculation of a partition function Z using the sum of the gauge and the fermionic actions. The gauge action is the Wilson gauge action [20]. The fermionic action is given by $S_f = \sum_q \bar{\psi}(D + m_q)\psi$, where $D + m_q$ is the fermionic matrix and q is summed over all quark flavors. Integrating over the fermion fields results in the fermion determinant which can be negative sometimes for non-zero chemical potential μ. This fact, referred to as the sign problem, makes it hard to do calculations at finite chemical potential, so most lattice calculations are done for $\mu = 0$. In order to do the calculation for non-zero temperature the temperature has to be related to the lattice spacing $T = 1/(N_\tau a)$ and then $N_\tau \to \infty$.

The equation of state can be derived from the partition function by calculating the trace of the energy-momentum tensor (called the trace anomaly of the interaction measure).

$$\begin{aligned} \frac{\Theta^{\mu\mu}(T)}{T^4} &= \frac{\epsilon - 3p}{T^4} = T\frac{d}{dT}\left(\frac{p}{T^4}\right) \\ \Theta^{\mu\mu}(T) &= \epsilon - 3p = -\frac{T}{V}\frac{d\ln Z}{d\ln a} \end{aligned} \tag{2.52}$$

After calculating $\Theta_{\mu\mu}$ from the partition function Z, the value of p/T^4 and thus the pressure can be found by performing the intergral

$$\frac{p(T)}{T^4} = \frac{p_0}{T_0} + \int_{T_0}^{T} \frac{\Theta_{\mu\mu}}{T^5} dT \tag{2.53}$$

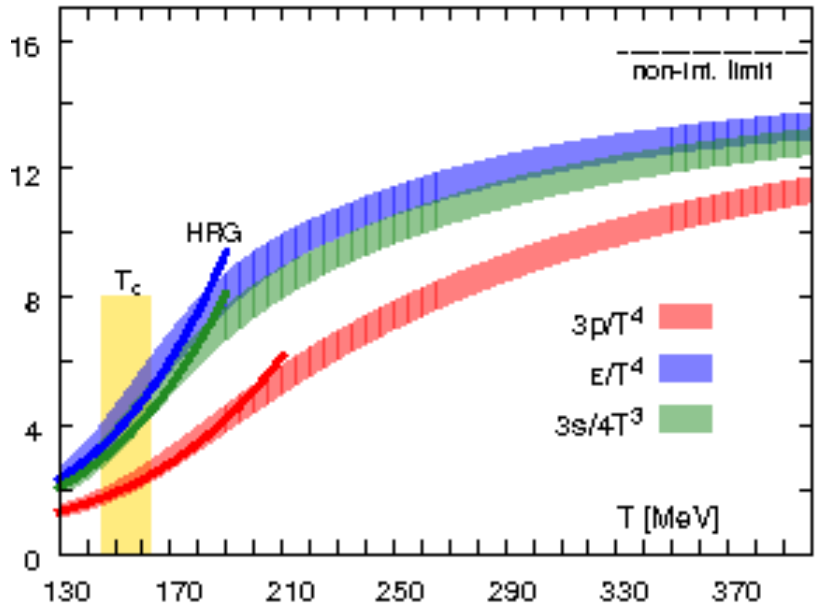

Figure 2.19: The pressure, energy density, and entropy density divided by T^4 as a function of temperature using Lattice calculations. The yellow band indicates the transition region between 145 and 163 MeV [76].

where T_0 is chosen in the low temperature regime where the pressure is suppressed by a Boltzmann factor. It is sometimes chosen to be $T = 0$ such that $p = 0$. Given the pressure and $\Theta_{\mu\mu}$, the energy density can be found since $\Theta_{\mu\mu} = \epsilon - 3p$. The entropy can be found using $\frac{s}{T^4} = \frac{\epsilon - 3p}{T^4}$ and the speed of sound using $c_s = dp/d\epsilon$. The pressure and energy density divided by T^4 as a function of temperature are shown in Figure 2.19. They demonstrate a rapid but continuous rise with a large increase in the number of degrees of freedom at $T_C \approx 154$ MeV, which is indicative of a crossover and not a first or second order phase transition. The sign problem makes it hard to study the first order phase transition and critical point for non-zero chemical potential using Lattice calculations.

2.4 Relativistic Heavy Ion Collisions

The phase diagram in Figure 2.16 shows that the Large Hadron Collider (LHC) [90] at CERN and the Relativistic Heavy Ion Collider (RHIC) at Brookhaven National Lab (BNL) reach energies that can access the formation of the QGP. Therefore, high energy particle

accelerators are used to study the plasma and also the phase transition back to hadronic matter (also depicted on the diagram). Heavy ions are collided at high energies in an attempt to produce the plasma. Heavy ions are used because they consist of many protons and neutrons that when smashed together at high temperatures and pressures will break apart and form a plasma of their constituent quarks and gluons.

The evolution of a heavy ion collisions is shown in Figure 2.20 and described briefly here [91]. First the heavy ions are accelerated towards each other at speeds close to the speed of light such that they are Lorentz contracted into pancakes. After they hit, there is a pre-equilibrium phase that creates the initial energy density and its fluctuations. The initial state can be modeled initially as a Color Glass Condensate (CGC) [92] before the ions collide, where the valence quarks are surrounded by dense clouds of gluons. After the collision the CGC briefly becomes a Glasma, which are longitudinal color electric and magnetic fields [93, 94]. The Glasma then forms a QGP phase after ~ 1 fm/c. This plasma is a strongly-coupled QGP (sQGP) that behaves as a nearly perfect fluid in contrast to an ideal gas which would be the case for weakly-coupled. The plasma quickly hadronizes to form a Hadron Gas phase as the system cools and the temperature drops below T_c. The hadrons are formed at the chemical freeze-out temperature T_{chem} and interact with each-other until they reach the kinetic freeze-out temperature T_{kin}. The hadrons are formed through recombination and coalesce at low p_{T}, where the quarks and anti-quarks combine into mesons and baryons, or fragmentation and hadronization at high p_{T} (discussed in Section 2.2.4). These become the final state particles that are detected in a particle detector. Throughout the evolution the system is expanding collectively due to the strong coupling of the plasma that gives the system a low shear viscosity, making it a nearly perfect fluid. The expansion can be described using viscous hydrodynamics (Section 2.4.3.1). The strong coupling also makes the system very opaque, which allows for large parton energy loss (Section 2.4.3.2). This large parton energy loss is the focus of this thesis.

The first evidence of the QGP was at CERN's Super Proton Synchrotron (SPS) at $\sqrt{s_{\text{NN}}} = 20$ GeV with Pb+Pb collisions [95]. At RHIC, Cu+Cu and Au+Au collisions at $\sqrt{s_{\text{NN}}} = 200$ GeV are used and measurements to study the QGP have been made by the STAR, PHENIX, BRAHMS, and PHOBOS collaborations. At the LHC, Pb+Pb and

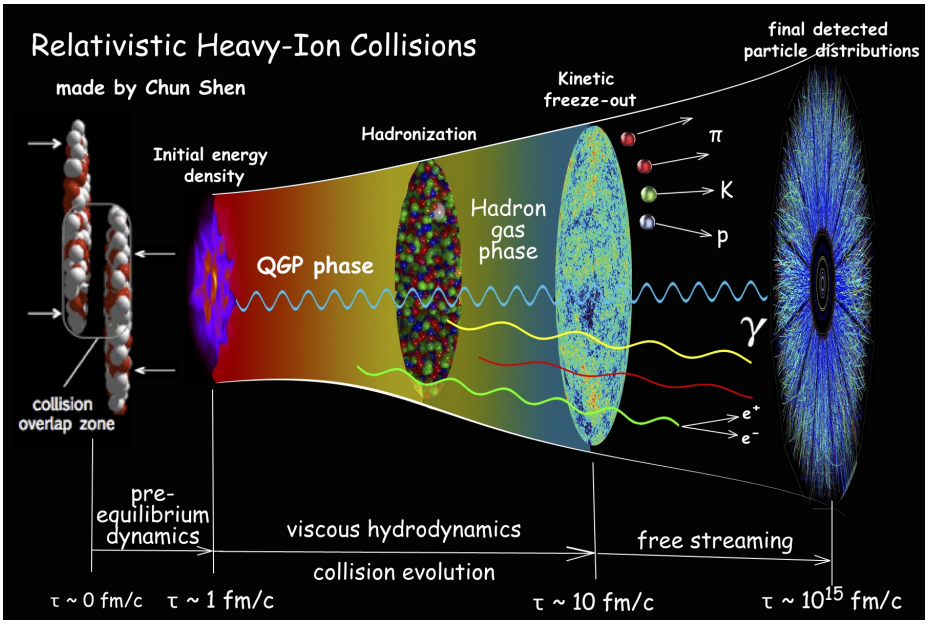

Figure 2.20: The evolution of a relativistic heavy ion collision.

Xe+Xe collisions are used to probe the QGP at $\sqrt{s_{\rm NN}} = 2.76$ and 5.02 TeV and measurements have been made by the ALICE, ATLAS, and CMS collaborations.

The initial energy density can be estimated using a geometrical model proposed by Bjorken [91]. In the model, after the collision there will be two pancakes moving away from each other and the energy density is between the two pancakes in the form of a cylinder. Take a slab of length $2d$ between the pancakes and the volume of the slab becomes $2d\pi R^2$, where R is the nuclear radius, $1.2A^{1/3}$ fm, and A is the atomic mass. The spatial information can't be measured so it needs to be related to the rapidity y since the energy can be measured experimentally as dE_T/dy. Then $dy = d\theta \approx 2d/ct_f$, where $c = 1$ and t_f is the formation time of the plasma. The energy density E/V becomes

$$\epsilon = \frac{(\frac{dE_T}{dy}\frac{2d}{t})}{2d\pi R^2} = \frac{1}{t_f \pi R^2}\frac{dE_T}{dy} \tag{2.54}$$

For Au+Au collisions at $\sqrt{s_{\rm NN}} = 130$ GeV the dE_T/dy was found to be about 680 GeV by PHENIX [96]. This value, along with a formation time of 1 fm, can be used to calculate an energy density of about 5 GeV/fm^3 which is larger than the $\epsilon_{QGP} = 1.6$GeV/fm^3 from Section 2.3.1.1. This indicates that the phase transition can happen at RHIC energies.

The energy density at the LHC will be larger (by about a factor of 5) and thus the phase transition can happen there as well.

2.4.1 Hydrodynamics

It was already mentioned that the space-time evolution of the medium can be described by hydrodynamics since it flows like a nearly perfect fluid. For zero viscosity (an ideal fluid) the evolution of the system is modeled by the following equation

$$\partial_\mu T^{\mu\nu} = \partial_\mu(\epsilon + P)u^\mu u^\nu - P g^{\mu\nu} \tag{2.55}$$

where $g^{\mu\nu}$ is the metric tensor, $T_{\mu\nu}$ is the energy momentum tensor, and u^μ is the local four velocity. The viscosity is not necessarily zero, just low, such that viscous hydrodynamics is typically used instead of the ideal fluid case just described. Here the ideal version of the energy momentum tensor is expanded using the second-order Israel-Stewart formalism [97]. In order to model the evolution via viscous hydrodynamics, numerical hydro frameworks are used like the 3+1D viscous hydro model [97, 98]. These models need specific inputs including event-by-event distributions of in the initial geometry of the system, a description of the evolution of the medium before equilibrium, and information about hadronization. It also needs transport coefficients the value of the ratio of the shear viscosity to the entropy of the system η/s or the ratio of the bulk viscosity to the entropy. This was calculated using AdS/CFT (described in Section 2.1.3.1) to be $\eta/s \geq 1/4\pi$ [99, 100].

2.4.2 Nuclear Geometry

When the ions collide in heavy ion collisions they can overlap by different amounts. This degree of overlap is used to characterize events because the geometry of the collision (and thus the physics) changes with this value. The degree of overlap is given by the impact parameter b, which is the distance between the center of the two nuclei in the transverse direction. This is demonstrated in Figure 2.21, where the colliding nuclei are shown in orange and blue and b is the distance between the centers. The beam-line view shows how much of the nuclei actually overlap and the shape of that overlap region. The smaller

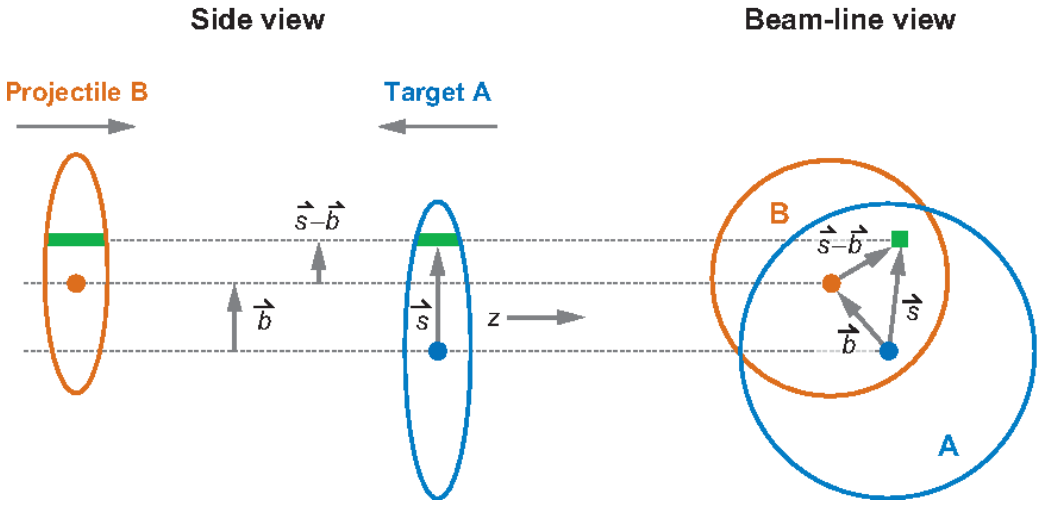

Figure 2.21: Diagram of the geometry for the Glauber model where the left side (a) is the longitudinal view and the right side (b) is the transverse view [101]. The impact parameter b is also shown.

the impact parameter the larger the nucleon flux which forms a larger, denser plasma. In experiment, events with similar overlap are grouped into centrality classes, where central collisions are events with the largest amount of overlap and peripheral events are events with the least amount of overlap.

Given the importance of the nuclear geometry to the experimental measurements in heavy ion collisions it is necessary to have a good model for describing it. The Glauber model [101, 102, 103] framework is typically used to describe the nuclear geometry in heavy ion experiments. It assumes that the inelastic collision of the nuclei can be treated as a superposition of the same number of individual nucleon-nucleon collisions. The calculations are performed in the optical limit where the overall phase shift is a sum over all the possible two-nucleon phase shifts. The model assumes the Woods-Saxon distribution for the nuclear density ρ,

$$\rho = \rho_0 \frac{1}{1 + e^{\frac{r-R}{a}}} \tag{2.56}$$

where R is the nuclear radius, a is the skin depth, and ρ_0 is the density at the center of the nucleus. The Glauber Model is used to derive the nuclear thickness function $T_{\mathrm{AB}}(\boldsymbol{b})$ which

represents the flux of the nucleons determined by the amount of overlapping geometry. It is used to normalize many quantities in heavy ion collisions to account for the nuclear geometry in different centralities. The calculation begins by evaluating the transverse density or the expected number of nucleons at position $\boldsymbol{s}$

$$T_{\mathrm{A}}(\boldsymbol{s}) = \int \rho(\boldsymbol{s}, z_A) dz_A \tag{2.57}$$

where $\rho(\boldsymbol{s}, z_A)$ is the probability per unit volume (normalized to unity) and z_A is the distance along the beam-line. T_{AB} is found by taking the product of this value for nuclei A and B to get the probability of finding nucleons in both at position b.

$$T_{AB} = \int T_A(s) T_B(\boldsymbol{s} - \boldsymbol{b}) d^2 s \tag{2.58}$$

The T_A values have units of inverse area, such that the probability for an interaction to occur becomes $T_A \sigma_{\mathrm{inel}}^{\mathrm{NN}}$, where $\sigma_{\mathrm{NN}}^{\mathrm{inel}}$ is the nucleon-nucleon inelastic cross section. The probability of having n nucleon-nucleon interactions between nucleus A with A nucleons and nucleus B with B nucleons at position b is given by the binomial distribution

$$P(n, \boldsymbol{b}) = \binom{AB}{n} [T_{\mathrm{AB}}(\boldsymbol{b}) \sigma_{\mathrm{inel}}^{\mathrm{NN}}]^n [1 - T_{\mathrm{AB}}(\boldsymbol{b}) \sigma_{\mathrm{inel}}^{\mathrm{NN}}]^{AB-n} \tag{2.59}$$

where the first term is the number of combinations for n out of AB possible interactions. The probability for having at least one nucleon collision at b is

$$\frac{d^2 \sigma_{\mathrm{inel}}^{AB}}{db^2} = \sum_{n=1}^{AB} P(n, \boldsymbol{b}) = 1 - [1 - T_{\mathrm{AB}}(\boldsymbol{b}) \sigma_{\mathrm{inel}}^{\mathrm{NN}}]^{AB} \tag{2.60}$$

and the total cross section can be found by integrating. The total number of nucleon-nucleon collisions becomes $N_{\mathrm{coll}}(\boldsymbol{b}) = AB T_{\mathrm{AB}}(\boldsymbol{b}) \sigma_{\mathrm{inel}}^{\mathrm{NN}}$. The expected number of participants, or the number of nucleons in the nuclei that interact, (also "number of wounded nucleons") at b can be found from

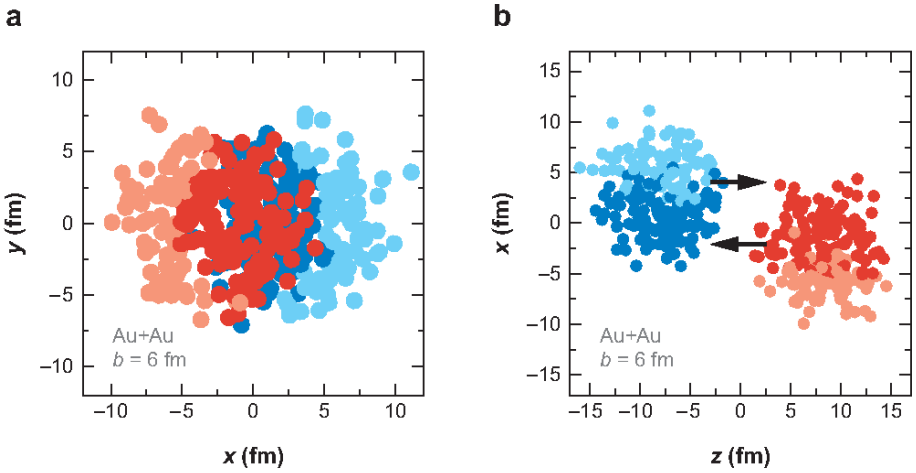

Figure 2.22: Outcome of the MC Glauber simulation for a Au+Au event at $\sqrt{s_{\rm NN}} = 200$ GeV with $b = 6$ fm viewed in the transverse plane on the left and the longitudinal plane on the right. The darker nucleons are the participating nucleons [101].

$$N_{\rm part} = A \int T_A(\boldsymbol{s})(1-[1-T_B(\boldsymbol{s}-\boldsymbol{b})\sigma_{\rm inel}^{\rm NN}]^B)d^2s + B\int T_B(\boldsymbol{s}-\boldsymbol{b})(1-[1-T_A(\boldsymbol{s})\sigma_{\rm inel}^{\rm NN}]^A)d^2s\ . \tag{2.61}$$

This analytical integral approach in the optical limit assumes the nucleon density distributions are continuous. Another approach is the MC formalism which allows for per event local density fluctuations. The nucleons inside nuclei A and B are distributed in a 3D space based on the full Woods-Saxon distribution. Then a random b value is sampled and a collision takes place if their distance d in the transverse plane satisfies the following constraint

$$d \leq \sqrt{\sigma_{\rm inel}^{\rm NN}/\pi}\ . \tag{2.62}$$

The number of collisions $N_{\rm coll}$ is the number of times this happened and the number of participants $N_{\rm part}$ is number of nucleons where this was satisfied at least once. An exampled is shown in Figure 2.22.

In experiment, b is not directly measurable so it needs to be related to a measurable quantity and then that quantity has to be translated back into Glauber quantities. Exper-

imental quantities with similar distributions to the N_{part} and N_{coll} distributions are used. Some examples are the multiplicity (number of charged particles) and transverse energy distributions. These distributions are then broken up into centrality quantiles that correspond to a value of b (and thus N_{part} and N_{coll}). The most central collisions (or most degree of overlap) are the lower percentiles and the most peripheral (or least degree of overlap) are the higher percentiles. Figure 2.23 shows a multiplicity distribution from the MC Glauber model broken up into centrality percentiles. ATLAS heavy ion measurements use the total transverse energy in the forward calorimeter of the detector to classify centrality (discussed further in Section 5.1.1.1).

2.4.3 Signatures of QGP

There are some signatures for the formation of the QGP in experiment. These signatures span the soft and hard sector, as well as utilize a variety of final state particle species. They stem directly from consequences of the sQGP, where the plasma expands collectively and

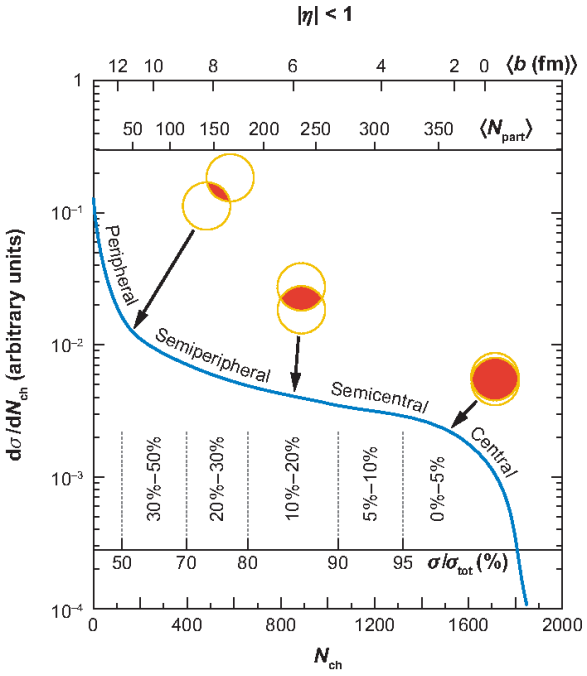

Figure 2.23: An example of a MC Glauber calculation of the dN_{evt}/dN_{ch} with the centrality quantiles, b values, and N_{part} indicated [101].

is very opaque with large parton energy loss.

2.4.3.1 Collective flow

The collective expansion of the medium that is modeled via hydrodynamics can be studied through a phenomenon called flow. Collective flow is apparent in measurements of soft particle correlations and is a global property of the system. The system has an initial anisotropy that causes transverse pressure gradients in specific directions. These pressure gradients are larger where the thickness of the medium is smaller and thus pushes particles in that direction [104]. This causes more particle production in these locations in the detector. This is shown in Figure 2.24, where the overlap region between the colliding nuclei in orange creates particle flow out along the transverse plane (azimuthally) in both the geometric and momentum space. This azimuthal anisotropy is typically flat along η since the particles are correlated with the event plane along each longitudinal direction, but varies along the azimuthal angle ϕ. Therefore, it is measured by the angular distribution of particles [105, 106]

$$\frac{1}{N}\frac{dN}{d\Delta\phi} = \frac{1}{2\pi}(1 + \sum_{n=1}^{\infty} 2v_n(p_{\mathrm{T}})\cos n(\phi - \Psi_n)) \tag{2.63}$$

This is a Fourier decomposition where v_n is the amplitude of the modulations and Ψ_n is the event plane angle, shown in Figure 2.24. The different flow harmonics correspond to different initial shapes as shown in Figure 2.25, where the second order harmonic is elliptical flow, the third order is triangular, the fourth order is square, etc.

Correlations between two particles are used to study properties of the medium through the correlation function defined in terms of the relative azimuthal angle, $\Delta\phi = \phi_a - \phi_b$, and pseudorapidity, $\Delta\eta = \eta_a - \eta_b$. The distribution of pairs can also be decomposed in a Fourier series and the amplitude $v_{n,n} = v_n^a v_n^b$ factorizes [107]

$$\frac{dN_{\mathrm{pair}}}{d\Delta\phi} \propto 1 + 2\sum_{n=1}^{\infty} v_n(p_{\mathrm{T}}^a)v_n(p_{\mathrm{T}}^b)\cos n\Delta\phi\ . \tag{2.64}$$

This distribution is shown on the left side of Figure 2.26 in a measurement in Pb+Pb collisions at $\sqrt{s_{\mathrm{NN}}} = 2.76$ GeV by ATLAS. It is flat with $\Delta\eta$ and has a modulation with

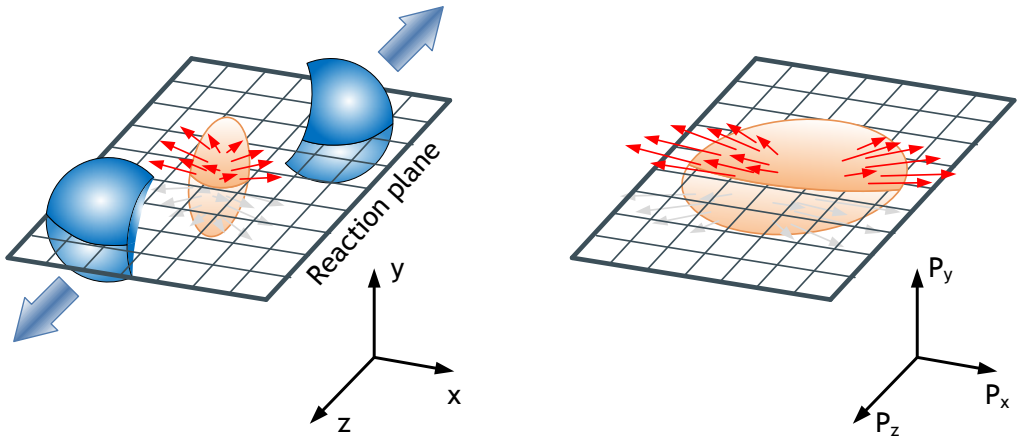

Figure 2.24: A diagram of the flow of soft particles (red vectors) after the collision of two nuclei that create an elliptical initial geometry indicated by the orange almond shape. The event plane is also indicated on the figure and the event plane angle (Ψ) is the azimuthal angle of the event plane to the x-axis. The left panel shows what happens geometrically and the right panel shows what happens in momentum space.

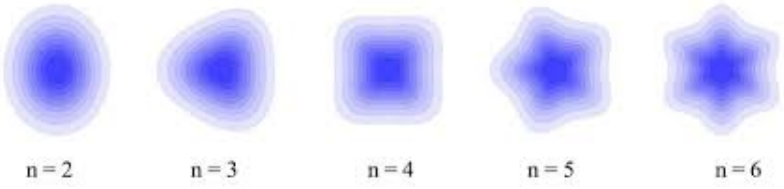

Figure 2.25: A diagram of the shape of the initial geometry for the different flow harmonics.

$\Delta\phi$, except for the jet peak on the near-side ($\Delta\eta \sim 0$). This distribution is projected in $\Delta\phi$ in the away-side $\Delta\eta$ region ($2 < \Delta\eta < 5$) and fit to extra the Fourier components (shown on the right side of Figure 2.26). This shows the typical "ridge" structure of the correlations. The v_n values are then extracted using a discreet Fourier transform

$$v_{n,n} = \langle \cos n\Delta\phi \rangle \tag{2.65}$$

where $v_n = \sqrt{v_{n,n}}$. Results from ATLAS for these v_n are plotted as a function p_{T} and in different centrality bins in Figure 2.27. All the v_n values increase with p_{T} until 3–4 GeV where they begins to decrease. This is consistent with the idea that the flow is coming from the azimuthal anisotropy at low p_{T} and from path-length dependent energy loss at higher p_{T}. The v_n values also decrease with increasing n such that the elliptical flow is the dominant effect, except in the most central collisions where the v_3 is the highest. This is because the nuclei are almost completely overlapping here and thus the initial geometry wouldn't be dominantly almond-shaped. The v_2 value increases with centrality and is largest in the mid-central bins before it starts to decrease, which can be explained by the collisions being the most almond-shaped in mid-central configurations.

2.4.3.2 Hard Processes

High momentum processes are produced early on in the collisions such that their initial state is mostly understood when considering cold nuclear matter (CNM) effects (discussed in Section 2.4.4). Thus the products from the hard interactions (hard probes) are used to probe the properties of the QGP in HI collisions since any differences from standard pp collisions can be attributed to interactions with the medium. The initial state effects from CNM can be separated out from the medium effects by comparing p+Pb collisions to pp collisions since little to no medium is expected to be produced in p+Pb, but CNM effects will be present due to the lead ion. The hard probes include electro-weak bosons, heavy flavor, jets, hadrons, and quarkonia.

Electroweak (EW) bosons like photons, Z, and W bosons are useful controls in HI collisions since they are colorless and only interact electromagnetically and thus won't interact strongly with the medium. They should exit the medium unscathed with no modification

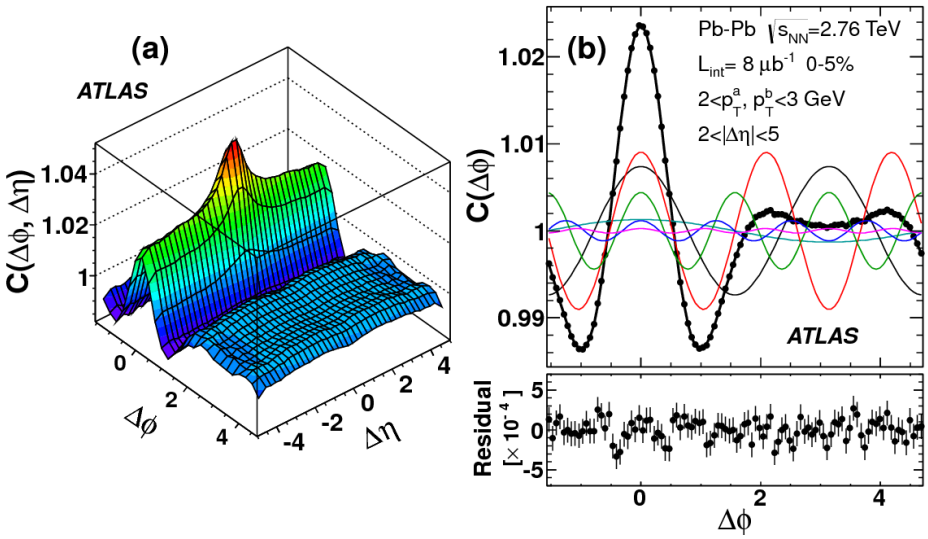

Figure 2.26: The left panel shows the $\Delta\phi$-$\Delta\eta$ distribution of the two particle correlations measured with ATLAS for 2-3 GeV and 0–5% centrality. The right panel shows the correlation function projected on $\Delta\phi$ for $2 < |\Delta\eta| < 5$ overlaid with the different Fourier components (colored lines) and their sum (black line). The residual between the data and sum is shown in the bottom panel [107].

to their production rates as shown in the left panel in Figure 2.28. They are useful for verifying that we understand the nuclear geometry of the collision (from Section 2.4.2) by looking at the nuclear modification factor, R_{AA}, (discussed in detail in Section 2.5.3) for EW bosons. The R_{AA}

$$R_{\mathrm{AA}} = \frac{\frac{1}{N_{\mathrm{evt}}^{\mathrm{tot}}} \frac{\mathrm{d}N_{\mathrm{Pb+Pb}}}{\mathrm{d}y}|_{\mathrm{cent}}}{\langle T_{\mathrm{AA}} \rangle \frac{\mathrm{d}\sigma_{pp}}{\mathrm{d}y}|_{pp}} \tag{2.66}$$

should be close to unity since there should be no modification but if the $\langle T_{\mathrm{AA}} \rangle$ factors are wrong the R_{AA} will not be one. They can also be used to study CNM effects since any deviations from unity could be attributed to this. The Z boson production from the di-muon decay channel in 5.02 TeV Pb+Pb and pp collisions with ATLAS was used to calculate the Z boson rates, which are compared through the R_{AA} [108]. The R_{AA} as a function of N_{part} is shown in the right panel in Figure 2.28. It is consistent with unity, within the statistical and systematic uncertainties in the measurement, indicating that the $\langle T_{\mathrm{AA}} \rangle$ factor is under control.

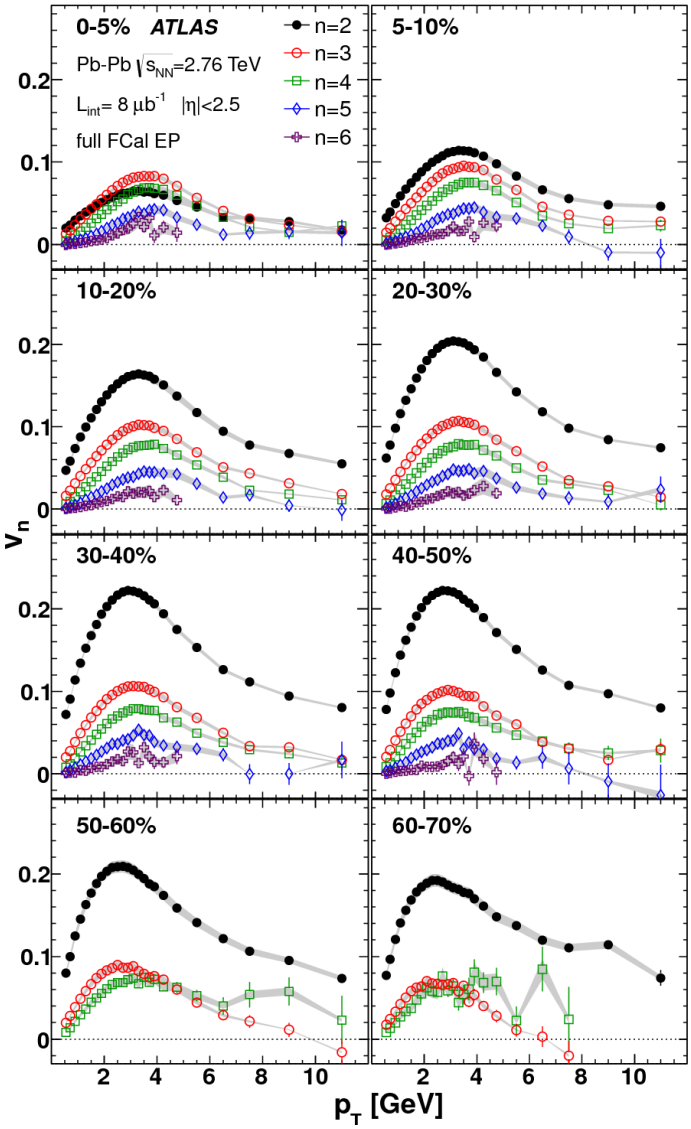

Figure 2.27: The v_n (nth harmonics in the different colors) as a function of p_{T} as measured by the ATLAS detector for different centrality bins in the panels [107].

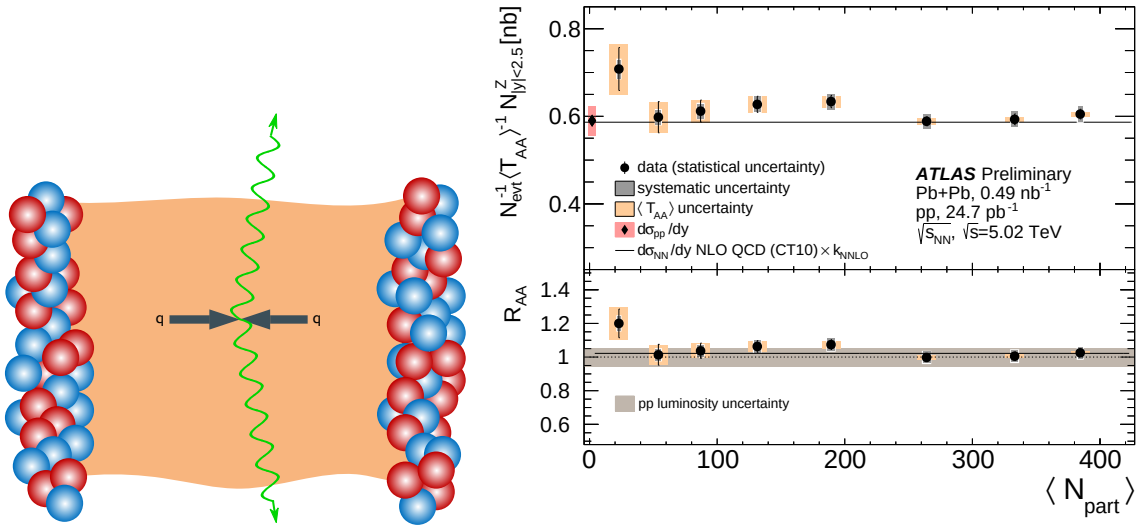

Figure 2.28: The left panel shows a diagram of a boson moving through the plasma produced in HI collisions (image credit: Martin Rybar). The right panel shows the Z-boson yield in Pb+Pb collisions divided by $\langle T_{\mathrm{AA}}\rangle$ as a function of N_{part} and the cross section for pp collisions at $N_{\mathrm{part}} = 2$ on the top and the R_{AA} as a function of N_{part} in the bottom [108].

Quarkonia are flavorless mesons with a heavy quark and its anti-quark as its constituents. An example is J/ψ which is a ground state of charmonia ($c\bar{c}$). Quarkonia serve as another probe of the QGP because it experiences color charge screening where bound quarkonia states screen themselves from the medium as they move through it [109]. This is because the formula for the strong potential (equation 2.14) in the presence of a medium includes an exponential Debye screening $e^{-\frac{r}{\lambda_D(T)}}$ on the first term. The quarkonia states will eventually break up, resulting in a suppression in that bound state. Quarkonia states have different bound states and the more loosely bound the state is, the easier it is to break up (or melt) and the stronger the suppression will be at a fixed temperature of the plasma. This phenomenon is called sequential melting and can be used as a probe of the temperature of the medium since the different quarkonia states will "melt" at different temperatures as shown in the left side of Figure 2.29. The right side of Figure 2.29 shows the ratio of the prompt (immediate formation of composite $c\bar{c}$ states) R_{AA} for $J/\psi \to \mu^+\mu^-$ and $\psi(2S) \to \mu^+\mu^-$ charmonia production ($\rho_{\mathrm{PbPb}^{\psi(2S)/J/\psi}}$) as a function of p_{T} in Pb+Pb collisions at 5.02 TeV with ATLAS [110]. The ratio is less than unity indicating the that $\psi(2S)$ is more suppressed than the J/ψ, which is consistent with sequential melting since the excited $\psi(2S)$ state is

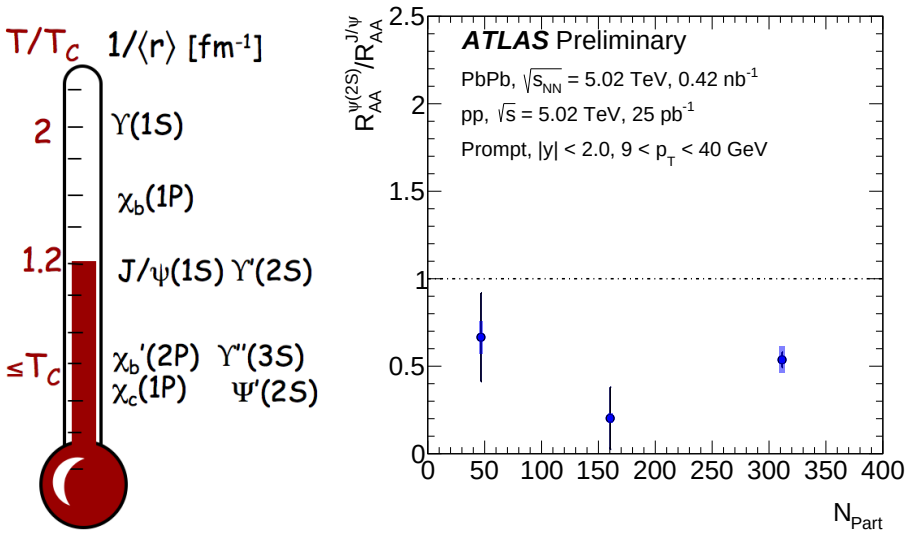

Figure 2.29: The left panel shows a diagram of the temperatures that different quarkonia states melt in the plasma, where the charmonia states $J/\psi(1S)$ and $\psi(2S)$ are shown [111]. The right panel shows the ratio of the R_{AA} for prompt $\psi(2S)$ to J/ψ, $\rho_{\mathrm{PbPb}^{\psi(2S)/J/\psi}}$, in Pb+Pb collisions with ATLAS [110].

less bound than the ground state J/ψ.

2.4.4 Cold Nuclear Matter Effects

As previously mentioned, cold nuclear matter (CNM) effects can affect the initial state in a heavy ion collision. The CNM effects can modify the rates and processes due to a nuclear environment but not necessarily a QGP medium. The CNM effects include the isospin effects, the Cronin effect, parton energy loss, and shadowing. The isospin effect is a consequence of protons having a different up and down quark content than nuclei which consist of both protons and neutrons. The Cronin effect was observed in p+A collisions, where high p_{T} particles were enhanced in p+A collisions when compared to pp [112, 113]. There are a few ideas of what could cause this, but a popular one is through transverse momentum broadening due to multiple particle elastic scatterings in the nuclear matter. Parton energy loss is due to the partons moving through the nuclear matter elastically and inelastically (bremsstrahlung radiation) scattering with the nucleons. These processes are described in more detail in Section 2.5.1.1 in the context of energy loss in the QGP, but similar effects

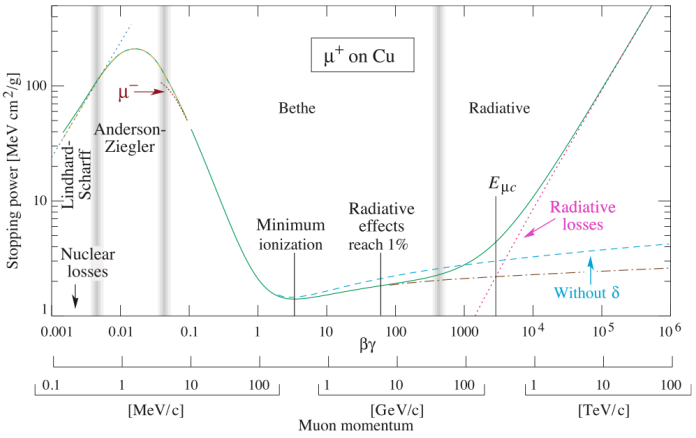

Figure 2.30: The energy loss per unit length dE/dl for positive muons in copper as a function of the momentum or $\beta\gamma$ [8].

are at play here in the QED realm [8, 59]. This is also shown in Figure 2.30, where the energy loss is shown as a function of momentum for muons in copper. It demonstrates that inelastic, or radiative, energy loss dominates at high momentum and elastic (collisional or Bethe-Bloch) dominates at low momentum.

The nuclear PDFs (nPDFs) represent the probability of finding a parton inside a nucleon that is inside a nucleus. This is different than that for a free nucleon (PDFs) and thus comparing the two can be used to see the effects of CNM. The comparison is done through the nuclear modification factor $R_i^A(x, Q^2)$

$$R_i^A = \frac{f_i^A}{f_i^p} \tag{2.67}$$

where f_i^A are the nPDFs and f_i^p are the PDFs. This is shown in Figure 2.31 as a function of x, which is the momentum fraction of the parton of the total nucleon. In this figure there are four regions with different features. The first is a suppression at low x, or the shadowing region. The second is an enhancement at intermediate x, or the anti-shadowing region. The third is another suppression at large x, or the EMC region. Finally, there is another enhancement at very high x due to Fermi motion. Shadowing is the destructive interference of multiple soft scatterings which hides the inner nucleons by the exterior nucleons [114]. Anti-shadowing is due to energy-momentum conservation with the suppression from shad-

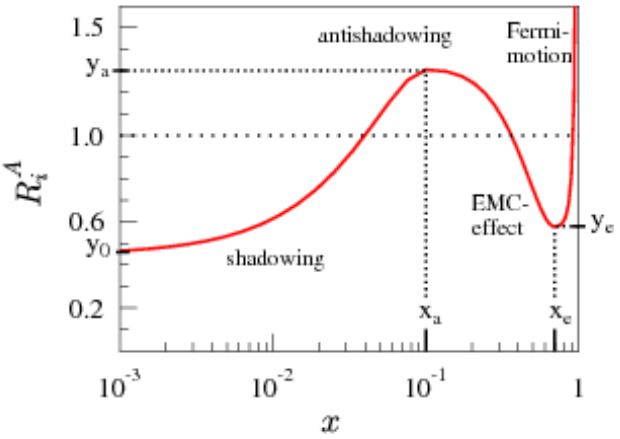

Figure 2.31: The nuclear modification factor as a function of x [117].

owing and is from the constructive interference of the multiple soft scatterings. The EMC effect [115] may be due to either the mean-field effect where the components of different nucleons interact directly leading to structure modification or short-range correlations between nucleons [116].

2.5 Jet Quenching

Hard processes that have a large transverse momentum or mass (larger than $\Lambda_{\mathrm{QCD}} \approx 0.2$ GeV) are useful for studying the QGP. They have cross sections that are predicted by QCD such that the initial state is mostly understood and are produced at time scales that are short enough to allow them to propagate through the medium and potentially interact [59]. When a parton moves through, it will lose energy through strong interactions with the dense medium produced. This is a final state effect, such that any differences from the initial state results from QCD calculations with possible CNM effects (Section 2.4.4) are due to the QGP. There are many hard processes that could be used (discussed in Section 2.4.3.2) but jets are particularly useful because of the large modifications expected from the medium. The idea to use jets specifically was first suggested by Bjorken [118]. He proposed that dijets should be a strong signature of jet quenching since the two back-

to-back jets would travel through different path lengths of the plasma and thus experience different amounts of energy loss, resulting in an imbalance.

The jets can interact with the medium in different ways depending on the energy of the jet and the scale of the coupling to the plasma [119]. Although the jet production at high momentum is weakly coupled and thus can be described by pQCD, the medium produced is strongly coupled for the temperatures produced in our current heavy ion colliders (as discussed in Section 2.4.3.1). Therefore, energy loss can be described in two limits, the weakly coupled limit (or pQCD) and the strongly coupled limit (the non-perturbative regime), and the dynamics of the jet in the strongly coupled medium is based on an interplay between the different scales. The jet evolves perturbatively as in the vacuum but the branches of the parton shower are at low enough momentum that the interactions of those partons with the medium are not weak, making part of the jet evolution not calculable in pQCD. Thus the jet is a probe of both the strong and weak regimes of QCD and any model must incorporate aspects of both to properly describe the jet energy loss. Section 2.5.1 will describe the different energy loss mechanisms in detail and Section 2.5.2 will describe the current theoretical models.

2.5.1 Energy Loss Mechanisms

Before discussing the mechanisms it is useful to define a few common variables that are used in discussions of how different aspects of the medium and the jet can affect how the jet loses energy [59]. The energy loss ΔE depends on characteristics of the jet like its energy, mass and charge and also on properties of the plasma like it's temperature T, thickness L, and the particle-medium interaction coupling α (which can be $\alpha_s = g^2/4\pi$ or $\alpha_{em} = e^2/4\pi$). The mean free path is defined as

$$\lambda = \frac{1}{\rho\sigma} \tag{2.68}$$

where ρ is the density of the medium, which for an idea gas is proportional to T^3, and σ is the integrated cross section of the particle-medium interactions, $\sigma_{el} \propto \alpha/T^2$. Thus the path length is proportional to $1/(\alpha T)$ for an ideal gas. The opacity, or the number of scatterings a particle experiences in a medium with thickness L is

$$N = \frac{L}{\lambda} \, . \tag{2.69}$$

The Debye mass m_D gives the typical momentum exchanges in the medium and the order of the thermal mass of the plasma constituents

$$m_D \approx gT \, . \tag{2.70}$$

The transport coefficient $\hat{q}$ is the average transverse momentum squared transferred to particle moving through the matter per unit path length and gives an idea of how strong the scattering is

$$\hat{q} = \frac{m_D^2}{\lambda} = m_D^2 \rho \sigma \, . \tag{2.71}$$

In the approximations from above it becomes proportional to $4\pi\alpha_s^2 T^3$. A typical value for a strongly coupled plasma ($\alpha_s \approx 0.5$) and a temperature of 400 MeV would be around 2 GeV^2/fm.

There can also be CNM effects that contribute to energy loss in the initial state. These are described in more detail in Section 2.4.4.

2.5.1.1 Weakly-coupled Limit

In the weakly-coupled limit there are two ways the particles can lose energy, radiatively (inelastic collisions) or collisional (elastic collisions), shown in Figure 2.32. Collisional energy loss (e-loss) dominates at low momentum and radiative energy loss dominates at high momentum. The total energy loss ΔE is the sum of these two contributions.

Collisional E-loss:

Collisional energy loss is when the particles moving through the medium elastically scatter with particles in the plasma. It is subdominant for hard partons but has been shown to be important, especially for heavy quarks. It was first calculated by Bjorken [118] and then later improved in further calculations [120, 121, 122, 123, 124, 125]. The average energy loss per unit length is given by

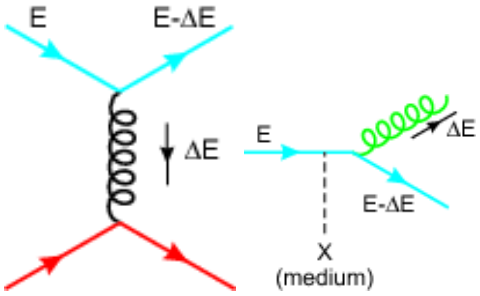

Figure 2.32: Diagram of collisional energy loss (left) and radiative energy loss (right) [59].

$$\frac{dE}{dx} = \int d^3k\rho_i(k)\Phi \int_{t_{min}}^{t_{max}} \frac{d\sigma_{ij}}{dt}(E - E')dt \tag{2.72}$$

where $t = Q^2$, $E-E'$ is the energy loss in the collision, ρ_i is the number density, $\Phi = 1-\cos\theta$ is the flux where θ is the angle between the momentum of the incoming parton and the medium, and k is the momentum of the target particle in the medium. The momentum transfer $t = -2(1-\cos\theta)k(E-E')$ and the cross section is

$$\frac{d\sigma_{ij}}{dt} = 2\pi\frac{\sigma_s^2}{t^2}C_{ij} \tag{2.73}$$

where $C_{gg} = 9/4$, $C_{gq} = 1$, and $C_{qq} = 4/9$. Plugging this into equation 2.72 and integrating over t gives

$$\begin{aligned}\frac{dE}{dx} &= \int d^3k\rho_i(k)\int_{t_{\min}}^{t_{\max}} \frac{d\sigma_{ij}}{dt}\frac{-\pi\sigma_s^2 C_{ij}}{kt}dt = -\pi\sigma_s^2 C_{ij}\ln\frac{t_{\max}}{t_{\min}}\int d^3k\frac{\rho_i(k)}{k} \\ &= -\pi C_R\alpha_s^2 T^2(1+\frac{1}{6}N_f)\ln\frac{t_{\max}}{t_{\min}}\end{aligned}$$

The $t_{\max}$ can be set to $2\langle k\rangle E$ and $\langle k\rangle \approx T$ such that $t_{\max} = 4ET$ and $t_{\min} = m_D^2$. The color factor C_R is 4/3 for quarks and 3 for gluons. Thus the final energy loss formula becomes

$$\frac{dE}{dx} = -\pi C_R\alpha_s^2 T^2(1+\frac{1}{6}N_f)\ln\frac{4ET}{m_D^2} \tag{2.74}$$

Equation 2.74 shows that the energy loss is proportional to the medium thickness ($\Delta E_{col} \propto L$) and depends logarithmically on the energy of the initial parton ($\Delta E_{col} \propto \ln E$).

It also depends on the temperature of the medium and on the flavor (quark vs. gluon) ($\Delta E_{col} \propto C_R$). Recent models have found that the average collisional loss remains significant over a large range in parton p_{T} and thus can not be neglected for hard probes [66].

Radiative E-loss:

Radiative energy loss is due to inelastic collisions of the particles with the medium via medium-induced gluon emission (or bremsstrahlung radiation as discussed in Section 2.2.4). This dominates at high momentum and thus is the dominant contribution to energy loss for hard jets. The energy loss in one scattering is found by integrating over the gluon bremsstrahlung spectrum [59, 126, 119]

$$\Delta E_{rad} = \int^{E} \int^{k_T^{max}} \omega \frac{d^2 I_{rad}}{d\omega dk_T^2} d\omega dk_T^2 \tag{2.75}$$

where ω is the energy and k_T is the momentum of the emitted gluon. Then the total energy loss when there are multiple incoherent scatterings is $\Delta E_{rad}^{tot} = N\Delta E_{rad}$, where N is the opacity of the medium. The energy loss per unit length becomes

$$\frac{dE}{dx} = -\frac{\langle \Delta E_{rad}^{tot} \rangle}{L} = -\frac{\langle \Delta E_{rad} \rangle}{\lambda} \, . \tag{2.76}$$

The radiated gluon spectrum is proportional to the DGLAP splitting functions P_{qg} and P_{gg} from equation 2.29 and has been computed using various approximations. The treatment of the spectrum is different depending on if the medium is thick ($L >> \lambda$) or thin ($L << \lambda$) compared to the mean free path. In the thin case the Bethe-Heitler (BH) [127] formalism is used to describe processes with a single hard momentum transfer and in the thick case the Landau-Pomeranchuk-Migdal (LPM) [128] formalism is used to describe processes with multiple soft momentum transfers [66, 129, 130].

For the LPM region there are multiple soft scatterings that experience Brownian motion. In the path intergral formulation it is equivalent to a harmonic oscillator with the "spring constant" being the transport coefficient $\hat{q}$. Thus the scale of the radiated energy distribution is set by $\omega_c = \frac{1}{2}\hat{q}L^2$, which is the characteristic energy of the gluon bremsstrahlung radiation [126] with a formation time of $t_f = 2\omega/k_T^2$. A gluon is emitted if it obtains a

significant amount of transverse momentum to decohere from the original parton. These gluons will have $\omega > \omega_c$ and pick up a phase of

$$\phi = \langle \Delta z / t_f \rangle = \langle \frac{k_T^2}{2\omega} \Delta z \rangle \approx \frac{\hat{q}L}{2\omega} L = \frac{\omega_c}{\omega} \, . \tag{2.77}$$

The spectrums becomes

LPM ($L >> \lambda$):

$$\omega \frac{dI_{rad}}{d\omega} \approx \alpha_s C_R \begin{cases} \sqrt{\frac{\omega_c}{\omega}} & \omega < \omega_c \\ \frac{\omega_c}{\omega} & \omega > \omega_c \end{cases} \tag{2.78}$$

Here there is a suppression of the coherent radiation, relative to the incoherent radiation, above ω_c, where coherence is when the parton shower is angle-ordered and decoherence is when this ordering is broken up by the medium. Plugging into equation 2.75 results in

$$\Delta E_{rad}^{LPM} \approx \alpha_s C_R \begin{cases} \omega_c & \omega < \omega_c \\ \omega_c \ln \frac{E}{\omega_c} & \omega > \omega_c \end{cases} \tag{2.79}$$

For the BH region, there are very few single hard scatterings within the length L in an incoherent superposition. The behavior will be different depending on if ω is larger or smaller than the typical gluon energy $\omega' = \frac{1}{2} m_D^2 L$, which comes from the formation length of the gluon being $2\omega/(\mu^2 L)$ and the formation length being greater than or less than L.

BH ($L << \lambda$):

$$\omega \frac{dI_{rad}}{d\omega} \approx \alpha_s C_R \begin{cases} \frac{L}{\lambda} \ln \frac{L\mu^2}{\omega} & \omega < \omega' \\ \frac{\omega_c}{\omega} & \omega > \omega' \end{cases} \tag{2.80}$$

Plugging into equation 2.75 and integrating gives

$$\Delta E_{rad}^{BH} \approx \alpha_s C_R \omega_c \log \frac{E}{\omega'} \, . \tag{2.81}$$

Combining both regions and replacing ω_c and ω' with a dependence on L gives

$$\Delta E_{rad} \approx \alpha_s C_R \hat{q} L^2 \begin{cases} \ln \frac{E}{\hat{q}L\lambda} & \omega < \frac{1}{2}\hat{q}L\lambda \\ 1 & \frac{1}{2}\hat{q}L\lambda < \omega < \frac{1}{2}\hat{q}L^2 \\ \ln \frac{E}{\hat{q}L^2} & \omega > \frac{1}{2}\hat{q}L^2 \end{cases} \tag{2.82}$$

Equation 2.82 shows that the energy loss is proportional to the medium thickness squared ($\Delta E_{rad} \propto L^2$) and depends logarithmically on the energy of the initial parton in the soft and hard part of the spectrum ($\Delta E_{rad} \propto \ln E$). It also depends on the flavor ($\Delta E_{rad} \propto C_R$). Finally, it depends linearly on $\hat{q}$ which is proportional to the density of the medium ρ ($\Delta E_{rad} \propto \rho$).

The radiative energy loss of heavy quarks is different from massless partons (described above) [59]. The radiation is suppressed at angles smaller than $\theta_0 = M_{\text{quark}}/E$, where

$$\omega \frac{dI^Q_{rad}}{d\omega} = \omega \frac{dI_{rad}}{d\omega}(1 + \frac{\theta_0}{\theta}) \tag{2.83}$$

This is the "dead cone effect" [131] where the total gluon emission is reduced for radiation off a heavy quark. This means that there is a hierarchy in the energy loss for heavy quarks, light quarks, and gluons [66]. The gluon vs. quark difference comes from the C_R factor in equation 2.82.

$$\Delta E_{\text{gluon}} > \Delta E_{\text{lightquark}} > \Delta E_{\text{heavyquark}} \tag{2.84}$$

2.5.1.2 Strongly-coupled Limit

The strongly-coupled limit uses non-perturbative calculations like the AdS/CFT correspondance discussed in Section 2.1.3.2, where a strongly-coupled gauge theory corresponds to a weakly-coupled gravity. It says that a string theory in an AdS space times a 5-dimensional sphere are the same as a CFT on the 4D boundary of this space [59, 132, 133, 134]. The simplest way this has been applied to the QGP is with $N = 4$ supersymmetric Yang Mills (SYM) for large number of colors (N_c) or large 't Hooft coupling ($\lambda = g^2_{SYM} N_c >> 1$). In this regime, calculations can be made analytically in gravity and then mapped to gauge theory. For finite temperature calculations, the AdS_5 space can be replaced with an AdS Schwarzchild black hole. Then the temperature in gauge theory is the same as the black-hole hawking temperature, $T = r_0/(\pi R^2)$, where r_0 is the black-hole horizon and R is the AdS metric. This representation can determine the energy loss and modification of jets as they move through the the sQGP and to calculate the $\hat{q}$ parameter of jet quenching using holographic calculations. The jets are treated as if they are moving through the medium

with a drag force acting on them slowing them down. The parton moving through the plasma is modeled using Wilson lines and stretching a string along the black hole. The $\hat{q}$ becomes

$$\hat{q}_{SYM} = \frac{\pi^{3/2} T(3/4)}{T(5/4)} \sqrt{g^2 N_c} T^3 \, . \tag{2.85}$$

In one picture [119, 135] the partons are described as a string moving in the dual gravity spacetime whose endpoint is attached to a brane and thus the string can fall into the horizon. In this set-up, a quark jet is incident on a 'slab' of strongly-interacting plasma with temperature T and thickness L. In the dual gravity the jet is represented by a falling string into the bulk, as shown in Figure 2.33. The dragging of the string to the horizon is what causes the energy loss. In this formalism the energy loss can be calculated, where the initial energy is E_{in} and the distance the jet could move through the plasma without stopping is

$$x_{stop} = \frac{1}{2\kappa_{SC}} \frac{E_{in}^{1/3}}{T^{4/3}} \tag{2.86}$$

where $\kappa_{SC} = 1.05\lambda^{1/6}$ is the strong coupling constant. This is different for gluons than quarks, where $\kappa_{SC}^{G} = \kappa_{SC}(\frac{9}{4})^{1/3}$. The energy loss is given by

$$\frac{1}{E_{in}} \frac{dE}{dx} = -\frac{4}{\pi} \frac{x^2}{x_{stop}^2} \frac{1}{\sqrt{x_{stop}^2 - x^2}} \, . \tag{2.87}$$

In the limit where L is small, $\frac{dE}{dx} \propto x^2$ and $\Delta E \propto L^3$. When L is approaching x_{stop}, $\frac{dE}{dx} \propto \frac{1}{\sqrt{x_{stop}^2 - x^2}}$ and the energy loss gets larger and larger. The energy loss also depends on the flavor since $x_{stop} \propto (C_A/C_F)^{1/3}$, where C_A/C_F is 9/4 for gluons and 1 for quarks. The energy loss is also independent of the initial energy of the parton in the limit where L is small compared to x_{stop}.

In this theory the jet also exits the plasma with a larger opening angle than it started with and since $\theta \approx m/E$, the final mass is expected to be larger than the initial mass.

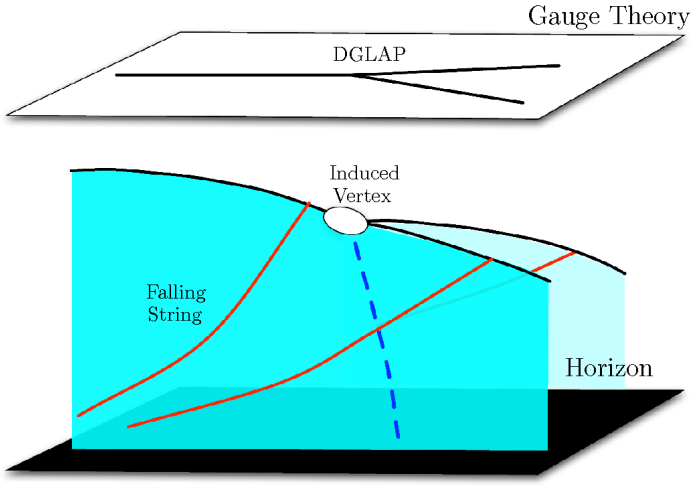

Figure 2.33: Depiction of a parton moving through a strongly-coupled plasma in the gauge theory on the white plane, with strings that represent the soft interactions of jet with the plasma that pull the parton down to the horizon (in black) in the dual gravitational view [119].

2.5.2 Theoretical Models

The descriptions of energy loss in Section 2.5.1.1 is for the ideal case where the medium is static and uniform. The medium properties like $\hat{q}$ and m_D are both space and time dependent and the medium is expanding with large longitudinal and transverse velocities. There are various approaches including path-integral (BDMPS-Z), reaction operator (DGLV), higher twist (HT), finite temperature field theory (AMY, SCET), and various MC implementations. The models make different assumptions about the dynamics of the medium and the relationship between the parameters involved in energy loss like the energy of the parton and the extent of the medium. Most models use pQCD approaches unless otherwise specified.

Outside of the MC simulations, there are two different groups of models. The first, which includes BDMPS-Z and GLV, involve calculating the radiated gluon spectrum or the energy loss from a parton. These can be used for both thin and thick mediums but don't account for energy flowing into the medium from the propagating parton (no recoil). The second, which includes HT and AMY, involve calculating the final distribution of the transversing parton. HT is only useful for thin mediums but can directly calculate the

FFs and di-hadron correlations. AMY accounts for thermal gluons being absorbed by the propagating parton and can include elastic energy loss but doesn't take into account vacuum radiation or medium-vacuum interference. The models can also differ in the approximations they make, the types of physical processes they use, the fitting parameters allowed, and the description of the medium. Each model depends on a fit to data for a different parameter to run the model that will be mentioned in their descriptions below.

2.5.2.1 BDMPS-Z

The Baier, Dokshitzer, Mueller, Peigne and Schiff (BDMPS) [129, 136, 137] approach solves energy loss in the multiple soft-scattering limit as in the LPM effect (Section 2.5.1.1) for radiative energy loss. It uses a finite length of hot matter, where $L < \sqrt{\lambda E/m_D^2}$, and the radiated gluon spectrum $\omega\frac{dI}{d\omega}$ is treated as a Schrodinger-like equation with a potential in terms of the single scattering cross section. The energy loss ϵ distribution [138] becomes

$$D(\epsilon) = \alpha\sqrt{\frac{\omega_c}{2\epsilon}}e^{-\frac{\pi\alpha^2\omega_c}{2\epsilon}} \ . \tag{2.88}$$

This determined that

$$\Delta E = -\frac{\alpha_s C_R}{8}\hat{q}L^2 \ln L/\lambda \tag{2.89}$$

which has a L^2 dependence for the energy loss but no dependence on the energy of the parton. The same L^2 dependence was found by Zakharov [139, 140, 141] for the LPM regime but using a path integral approach where the propagation of the partons are described by Green's functions that are obtained from a path integral over the field. The two formalisms together are called BDMPS-Z. It also found that jets broaden in the QGP and the momentum broadening of the jet is $p_T^2 \propto \frac{m_D^2}{\lambda}L$ such that the jet gets wider the further it moves through the plasma.

The FFs in the medium can be determined from the FsF in a vacuum using quenching weights $P_E(\epsilon, \hat{q})$, where ϵ is the fraction of energy loss, derived by Armesto, Salgado and Wiedemann (ASW) [130].

$$D^{med}_{a\to h}(z,Q^2) = P_E(\epsilon,\hat{q})D^{vac}_{a\to h}(z,Q^2) \tag{2.90}$$

These calculations are done for a static medium, but in this model for an expanding medium that is time dependent, τ,

$$\hat{q}(\tau) = \hat{q}_0(\frac{\tau_0}{\tau})^\alpha \tag{2.91}$$

where $\alpha = 0$ is for a static medium and $\hat{q}_0$ is the maximum value at the time of highest density when the medium is formed at the formation time τ_0. The average $\bar{\hat{q}}$ becomes

$$\bar{\hat{q}} = \frac{2}{L^2}\int_{\tau_0}^{\tau_0+L} d\tau(\tau-\tau_0)\hat{q}(\tau)\ . \tag{2.92}$$

When $\tau_0 << L$, $\bar{\hat{q}} = 2\hat{q}_0\tau_0/L$. The value of $\hat{q}$ is extracted from experimental data before running the model.

2.5.2.2 DGLV

The Gyulassy-Levai-Vitev (GLV) [142, 143, 144] or DGLV [145, 146] approach is similar to the BDMPS-Z except it starts with a single hard radiation spectrum that is expanded in opacity for gluon emission from multiple scattering. This is done using a reaction operator $\hat{R}_n$ to derive the recursion relations for the inclusive gluon distribution. This approach tries to calculate the energy loss for in between the thick and thin plasmas, where the "thick" case with multiple soft scatterings is done by BDMPS-Z. The ASW formalism from Section 2.5.2.1 can be done for both multiple scatterings and hard single scatterings, where for the latter case it is equivalent to the DGLV formalism to first order in opacity. The energy loss becomes

$$\Delta E = \frac{C_R\alpha_s}{N(E)}\hat{q}L^2\ln\frac{E}{m_D} \tag{2.93}$$

where $N(E)$ is determined numerically. It has a dependence on the natural log of the energy, unlike BDMPS-Z in equation 2.89. In equation 2.93, $\hat{q} \propto \rho$, where the density, $\rho = n/A_T$ (A_T is the surface area and n is the opacity). The opacity $n \propto dN^g/dy$ where dN^g/dy is

the initial gluon density and is the medium property that is extracted from fits to the data in this formalism.

2.5.2.3 Higher Twist

The higher twist (HT) [147, 148, 149] formalism describes the multiple scatterings of a parton by replacing the vacuum splitting functions (equation 2.29) with in-medium splitting functions, which are found from power corrections to the leading-twist cross section for parton scattering

$$\Delta P_{a\to b} \propto P_{a\to b} C_A \alpha_s T^A_{qg} \tag{2.94}$$

where T^A_{qg} is a correlator that contains all the medium effects. The normalization C of the correlator is what is extracted from experimental data and ends up being a measure of the average energy lost. The in-medium FFs can then be found from an additive contribution from the vacuum FFs

$$D^{med}_{a\to h}(z, Q^2) = D^{vac}_{a\to h}(z, Q^2) + \Delta D^{med}_{a\to h}(z, Q^2) \, . \tag{2.95}$$

The energy loss has a simple L^2 dependence and at minimum is $\Delta E = \frac{1}{2}\hat{q}L^2$.

2.5.2.4 Field Theory Approaches

Field theory approaches were discussed briefly in Section 2.1.3.3 but are discussed in the context of jets here. The Arnold, Moore, and Yafte (AMY) [150] formalism uses Hard Thermal Loop (HTL) effective field theory to describe the medium and the interactions and dispersion relations of the quark gluon constituents. It describes a parton scattering off medium partons and inducing collinear radiation. The collinear enhanced radiation terms are identified and resummed to calculate the rate of gluon emission. The jet has the same virtuality as the mass of the thermal parton ($\approx gT$). The change in the distribution of hard partons with time is calculated in the Fokker-Planck equation (shown here for a quark)

$$\frac{dP_{qq}}{dt}(p) = \int_{\infty}^{\infty} dk P_{qq}(p+k)\frac{dT^{q}_{qg}(p+k,k)}{dkdt} - P_{qq}(p)\frac{dT^{q}_{qg}(p,k)}{dkdt} + 2P_{g}(p+k)\frac{dT^{g}_{qq}(p+k,k)}{dkdt} \tag{2.96}$$

where k is the gluon momentum, p is the quark momentum, T^{q}_{qg} are the transitions rates for a quark to a gluon and a quark. The $dT/dkdt$ include the Bose-Einstein (gluons) or Fermi-Dirac (quarks) temperature dependent exponentials. The FFs can be calculated by convoluting the vacuum FFs with the hard parton distributions

$$D^{med}_{a\to h}(z) = \int dp_f \frac{z'}{z} \sum_{a} P_a(p_f.p_i) D^{vac}_{a\to h}(z') \tag{2.97}$$

where $z = p_h/p_i$ and $z' = p_h/p_f$, and p_i and p_f are the initial and final momenta of the partons before and after they interact with the plasma. The rates depend on the temperature T of the medium, which is the parameter extracted from data in this formalism. This is the only formalism so far that naturally incorporates the medium reacting to the partons moving through it.

Another field theory approach uses soft collinear effective field theory (SCET) [151, 28, 152, 153, 154] (discussed briefly in Section 2.1.3.3). SCET involves QCD calculations that are soft and collinear to try to control for infared divergences by integrating out all the hard modes and leaving only high energy quarks interacting with the soft or collinear gluons. It was extended to include jets propagating in a medium by modeling the interactions with the medium as being mediated by a Glauber gluon exchange (transverse t-channel gluons) (SCET$_G$) [155, 156, 157]. SCET$_G$ uses medium-modified DGLAP evolution equations for the FFs in a dense strongly-interacting matter. This formalism is useful because other models that use only the radiative energy loss approach (HT and DGLV) only work in the soft gluon emission limit (small x limit) where the parent parton can not change its identity and large energy loss can only come from multiple gluon emission. Large energy loss can also come from collisional energy loss or strong coupling. This limit also doesn't allow for the incorporation of higher-order calculations and resummation. The SCET framework for QCD evolution does not make the soft gluon approximation so is valid for all x, including changes to the parton flavor. SCET agrees with the energy loss formalisms in the soft gluon

limit. In this model, including CNM effects gives better agreement with data. The coupling g is the fit parameter in this theory.

2.5.2.5 MC implementations

There are many MC implementations of energy loss that try to model a prescription of how the jets lose energy in the plasma. The previous models are based on some final energy-rescaling of the FFs but the MC models try to implement the evolution of the FFs in a medium using the DGLAP evolution equations for FFs (equation 2.28). The MC models allow for calculations of the modification beyond the leading parton including how the medium is modified by the jet which provides a better understanding of the background. Section 2.2.6 discusses the MC implementation of jets in a vacuum in PYTHIA and HERWIG. These can be modified to include medium effects by modifying the splitting functions (equation 2.29). There are two main issues when doing this: specifying the length and time scales for the probe and the medium and specifying the interactions between the probe and the medium. The medium is important because the parton energy loss depends strongly on the path it takes in the medium. The interactions matter because the amount that the FFs are modified depends on the strength and the kinematics of the interactions, the relative amount of inelastic and elastic collisions, and the probability that the interactions will occur. There are many MC models on the market that make different choices on how to implement the energy loss (collisional and radiative), how to model the medium, and how to model the hadronization of the final state particles after moving through the medium [59, 66, 67]. Common HI models are listed and described below:

- `HIJING` [158, 159]: This generator simulates complete HI events with both hard and soft components. The hard partons are simulated with PYTHIA and the soft parts are modeled based on the formation and decay of color strings. The model uses radiative but not collinear energy loss that is modeled with collinear parton splitting. The medium is modeled through the mean free path and screening length in the energy loss calculations and the hadronization is from the Lund string model.

- `HYDJET` [160]: This generator is very similar to `HIJING` in that it simulates full HI

events and that it uses the Lund model for hadronization but it models the soft component with a hydrodynamical model. The jets and interactions of the jets in the medium are modeled with `PYQUEN` [161], which is built off of PYTHIA and modifies the branching ratios to include radiative and collisional energy loss, where the former samples a BDMPS radiation spectrum at each scattering and the latter uses LO parton scattering matrix elements. The medium is modeled with the Bjorken model which treats the medium as a fluid of quarks and gluons that is longitudinally expanding with boost invariance.

- `JEWEL` [162]: This generator models final state parton showers and hadronization. It uses BDMPS-Z for radiative energy loss and implements elastic scattering in the DGLAP evolution. The medium can be modeled with hydrodynamics or the Bjorken model and the Lund string model is also used for hadronization.

- `Q-PYTHIA/HERWIG` [163, 164]: These models add on quenching to the splitting functions of the final state parton shower in PYTHIA and HERWIG. The radiative energy loss uses BDMPS-Z to calculate the additive contribution to the splitting function from medium-interactions such that $P_{a\to bc} = P^{vac}_{a\to bc} + \Delta P^{med}_{a\to bc}$. There is no collisional energy loss. The medium model can vary and the hadronization is modeled with the Lung string for `Q-PYTHIA` and `Q-HERWIG` uses the HERWIG implementation of cluster hadronization.

- YAJEM [165, 166]: This model modifies the `PYTHIA` parton shower. It increases the virtuality of the partons by an amount given by a local $\hat{q}$ for radiative energy loss and has a local drag coefficient for collisional energy loss. The medium is also modeled by hydrodynamics and the hadronization by the Lund model.

- `Martini` [167]: This model is built on the AMY model for energy loss where the transition rates are used to calculate radiative and collisional energy loss. Again the medium is modeled by hydrodynamics and hadronization by the Lund model.

- Lorentz Boltzmann Transport (LBT) [168, 169]: This model describes the scattering of partons in a thermal medium using the Boltzmann equation and energy loss models. It

incorporates both radiative and collisional energy loss by calculating their probabilities and combining them. The elastic scattering probability is $P_{el} = 1 - e^{-T_{el}\Delta t}$, where T_{el} is the elastic scattering rate. The inelastic scattering probability is $P_{inel} = 1 - e^{-<N_g>}$, where $\langle N_g \rangle$ is the average number of emitted gluons from a hard parton. The total is $P_{tot} = P_{el} + P_{inel} - P_{el}P_{inel}$. Using this probability and the kinematics of the jet, a MC determines what type of interaction it will be. This model also includes hydrodynamical calculations of the background and it accounts for jet-medium interactions and the recoil of the thermal partons from the jet.

- Holographic jets [134]: Models of holographic jets use MC to simulate AdS/CFT for the strong coupling regime of energy loss.

- Hybrid model [119]: This model uses MC to implement radiative and collisional energy loss, as well as AdS/CFT for the non-perturbative regime, with a cut-off that determines the transition between the two regions.

2.5.3 Consequences of E-loss

The effects of energy loss from the interactions of jets with the plasma will result in differences between collisions involving heavy nuclei (AA) and standard *pp* collisions where no medium is produced and the jets behave as if in a vacuum. The energy loss will cause jets at a particular transverse momentum to lose energy with respect to jets that don't move through a plasma. This is demonstrated in Figure 2.34, where two quarks collide in two different cases. The left-hand side shows two jets in standard *pp* collisions where no jet quenching should occur and the right shows two jets in AA collisions that propagate through the plasma. The vacuum jets stay narrow and balanced in energy, whereas the medium jets interact with the plasma, lose energy, and spread out.

This energy loss leads to a suppression on average of the p_{T} spectra, dN/dp_{T}, at a fixed p_{T} in AA compared to *pp* collisions. This can be seen through the suppression of single hard scattering rates for inclusive jets (all the jets in the event). This suppression can be quantified by comparing the actual number of jets in the AA collisions (with quenching) to the expected number (with no quenching) as a function of p_{T}. The expected number of jets

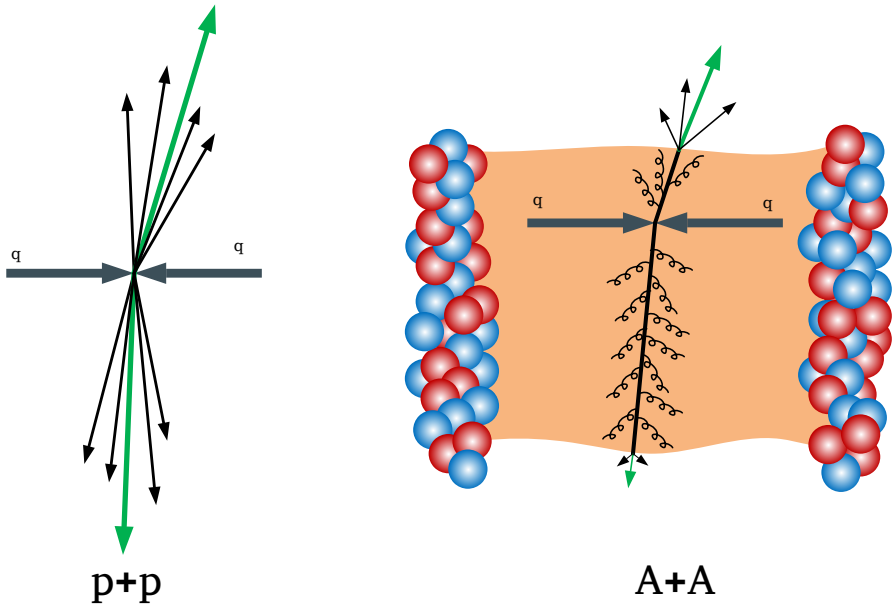

Figure 2.34: Dijet in pp (left) and AA (right) collisions, where in AA collisions the jets move through a medium (Image credit: Martin Rybar).

is just a superposition of A independent nucleons (where A is the mass number). The PDFs become $f_{a/A} \approx A f_{a/p}$, where p is a proton. This means that the expected cross section in AA collisions is a scaled version of the cross section in pp first given in equation 2.24, $d\sigma_{AA} = A^2 d\sigma_{pp}$. From Section 5.1.1.1, the jets in AA collisions are measured in centrality classes so to get the expected number of jets in a given centrality class, the $\langle T_{\mathrm{AA}} \rangle$ factor is used, which is just the amount of nuclear overlap between the colliding nuclei. The expected number of jets in each centrality class becomes

$$dN_{AA}(\mathrm{cent}) = N_{\mathrm{evt}} \langle T_{\mathrm{AA}} \rangle_{\mathrm{cent}} d\sigma_{pp} \tag{2.98}$$

where N_{evt} is the number of events in that particular centrality class. The R_{AA} is the ratio of the number of events found in AA collisions (when the quenching effects are present) $dN_{\mathrm{jet}}|_{\mathrm{cent}}$ to the expected number

$$R_{\mathrm{AA}}(\mathrm{cent}) = \frac{\mathrm{d}N_{\mathrm{jet}}|_{\mathrm{cent}}}{\mathrm{d}N_{AA}|_{\mathrm{cent}}} = \frac{\mathrm{d}N_{\mathrm{jet}}|_{\mathrm{cent}}}{N_{\mathrm{evt}} \langle T_{\mathrm{AA}} \rangle_{\mathrm{cent}} d\sigma_{pp}} \tag{2.99}$$

The $R_{\rm AA}$ is typically evaluated as a function of rapidity y and $p_{\rm T}$ such that the numbers become the differential yields $\mathrm{d}N/\mathrm{d}y\mathrm{d}p_{\rm T}$, where the yield in a particular centrality bin is $\frac{1}{N_{\rm evt}}\frac{\mathrm{d}^2N_{\rm jet}}{\mathrm{d}y\mathrm{d}p_{\rm T}}|_{\rm cent}$. The $R_{\rm AA}$ becomes

$$R_{\rm AA}(p_{\rm T}, y, \text{cent}) = \frac{\frac{1}{N_{\rm evt}}\frac{\mathrm{d}^2N_{\rm jet}}{\mathrm{d}y\mathrm{d}p_{\rm T}}|_{\rm cent}}{\langle T_{\rm AA}\rangle_{\rm cent}\frac{\mathrm{d}^2\sigma^{pp}_{\rm jet}}{\mathrm{d}y\mathrm{d}p_{\rm T}}} \tag{2.100}$$

The meaning of the $R_{\rm AA}$ is simple: $R_{\rm AA} > 1$ indicates an enhancement in AA collisions, $R_{\rm AA} < 1$ indicates a suppression, and $R_{\rm AA} = 1$ means there is neither an enhancement or a suppression.

The $R_{\rm AA}$ can be used to determine various jet quenching parameters and thus gives information about the plasma. The amount of energy loss $\epsilon_{loss} = \Delta p_{\rm T}/p_{\rm T}$ can be extracted from the $R_{\rm AA}$ since the yield follows a power law in the jet $p_{\rm T}$ in both pp and AA collisions, $dN/dp_{\rm T} \propto p_{\rm T}^{-n}$. For pp collisions the $p_{\rm T}$ remains unchanged and thus

$$\frac{\mathrm{d}N}{\mathrm{d}p^f_{\rm T}}_{pp} \propto (p^f_{\rm T})^{-n} = (p^i_{\rm T})^{-n}_{pp} \tag{2.101}$$

For AA collisions, the $p_{\rm T}$ was modified from $p^i_{\rm T\,AA}$ to $p^f_{\rm T}$, where the initial $p_{\rm T}$ in AA and pp are not equivalent but their final $p_{\rm T}$ is since they are being compared at a fixed $p_{\rm T}$. The yield in AA becomes

$$\frac{\mathrm{d}N}{\mathrm{d}p^f_{\rm T\,AA}} = \frac{\mathrm{d}N}{\mathrm{d}p^i_{\rm T\,AA}}\frac{\mathrm{d}p^i_{\rm T\,AA}}{\mathrm{d}p^f_{\rm T}} \propto (p^i_{\rm T})^{-n}_{\rm AA}\frac{\mathrm{d}p^i_{\rm T\,AA}}{\mathrm{d}p^f_{\rm T}} \tag{2.102}$$

The initial $p_{\rm T}$ in AA collisions can be written in terms of the final $p_{\rm T}$ in AA collisions using the energy loss formula

$$\epsilon_{loss} = \frac{\Delta p_{\rm T}}{p^i_{\rm T}} = 1 - \frac{p^f_{\rm T}}{p^i_{\rm T}} \rightarrow p^i_{\rm T} = \frac{1}{1-\epsilon_{loss}}p^f_{\rm T} \rightarrow \frac{dp^i_{\rm T}}{dp^f_{\rm T}} = \frac{1}{1-\epsilon_{loss}} \tag{2.103}$$

Then equation 2.102 becomes

$$\frac{\mathrm{d}N}{\mathrm{d}p^f_{\rm T\,AA}} \propto (1-\epsilon_{loss})^n\frac{1}{1-\epsilon_{loss}}(p^f_{\rm T})^{-n} = (1-\epsilon_{loss})^{n-1}(p^f_{\rm T})^{-n} \tag{2.104}$$

and the $R_{\rm AA}$ becomes

$$R_{\mathrm{AA}} = \frac{\frac{dN}{dp_{\mathrm{T}}^{f}\,AA}}{\frac{dN}{dp_{\mathrm{T}}^{f}\,pp}} = \frac{(1-\epsilon_{loss})^{n-1}(p_{\mathrm{T}}^{f})^{-n}}{(p_{\mathrm{T}}^{f})^{-n}} = (1-\epsilon_{loss})^{n-1} \tag{2.105}$$

Therefore, the energy loss can be calculated from the R_{AA},

$$\epsilon_{loss} = 1 - {R_{\mathrm{AA}}}^{1/(n-1)} \tag{2.106}$$

Using $\epsilon = \Delta E/E$, the energy loss ΔE can be obtained for a given value of energy (or p_{T}). From ΔE, the value of $\hat{q}$ can be extracted since the energy loss models from Section 2.5.1.1 showed that $\Delta E \propto C_R \alpha_s \hat{q} L^2$ if radiative energy loss is assumed and $L \propto A^{1/3}$. Information about the path dependence, flavor dependence, density dependence, and p_{T} dependence can be obtained and help constrain the models and type of energy loss (radiative, collisional, or strong coupling) since they have different dependencies on these factors.

It is important to note that a couple of assumptions were made in the above derivation. First, the energy loss was taken to be a constant fractional shift in the jet p_{T} as $\Delta E = \epsilon_{\mathrm{loss}} E$, making it linear in the jet p_{T}. Second, a power law distribution for the p_{T} spectra was used where the power n was assumed to be constant. Finally, it assumes that quarks and gluons lose the same amount of energy. A phenomenological model in Ref. [170] shows that this interpretation is not the full picture. In the reference, an analytical model was used that includes the flavor dependence of energy loss through different "shifts" in their p_{T}, where the gluon "shift" is larger than the quark "shift". In addition, the power n in the power-law distribution has a dependence on the jet p_{T} ($n = \beta \ln p_{\mathrm{T}}^{\mathrm{jet}}/p_{\mathrm{T}}^{0}$). Including these two factors results in a fractional shift that increases slower than linearly with jet p_{T}. This will be discussed in more detail in Section 6.5.3.

Figure 2.34 shows that for standard pp collisions the jets are back-to-back and approximately balanced in energy. In AA collisions, where the jets are moving through the dense plasma, the jets travel different paths in the plasma and thus lose different amounts of energy. This is due to the path-length dependence of energy loss where energy loss can depend on the distance traveled in the plasma and different fluctuations in the medium. Therefore, jets in dijet configurations may experience unbalanced azimuthal correlations $dN_{\mathrm{pair}}/d\phi$. This imbalance can also be seen by comparing the p_{T} of the jets since one jet

loses more energy than the other. This can be studied quantitatively with the variables A_{J} or x_{J} which are given by the following equations where p_{T_1} is the p_{T} of the highest momentum jet in the event and p_{T_2} is the p_{T} of the second highest momentum jet in the event.

$$A_{\mathrm{J}} = \frac{p_{\mathrm{T}_1} - p_{\mathrm{T}_2}}{p_{\mathrm{T}_1} + p_{\mathrm{T}_2}} \tag{2.107}$$

$$x_{\mathrm{J}} = \frac{p_{\mathrm{T}_1}}{p_{\mathrm{T}_2}} \tag{2.108}$$

A value of $A_{\mathrm{J}} > 0$ or $x_{\mathrm{J}} < 1$ indicates an energy imbalance. These variables can be compared to standard pp collisions where $A_{\mathrm{J}} \approx 0$ and $x_{\mathrm{J}} \approx 1$. The dijet asymmetry gives us insight into relative energy loss since it is a measure of how one jet loses energy with respect to the other. It also shines light on the path length dependence of energy loss due to the different paths the jets move through.

Jets also have an internal structure that is complicated even in a vacuum. The internal structure of the jet is expected to be modified in the medium. The FFs can be used to investigate this modification by comparing the FFs in AA collisions to those in standard pp collisions. This is measured by looking at the distribution of charged particles inside of the jet. The jet mass can also be used which is expected to be larger due to the modification of jets in the medium. Other variables like the jet shape and the splitting of the jet have been used as well. Jet structure is not the focus of this thesis so the details are left out of this discussion.

The flavor dependence of jet quenching can be investigated since the different models for jet quenching have different dependencies on the flavor factor, C_R. Also, a hierarchy is expected for the energy loss, given by equation 2.84, where in general, comparing gluons and quarks gives $\Delta E_{\mathrm{g}} \propto \frac{9}{4}\Delta E_q$ for weakly-coupled energy loss. The flavor dependence can be probed by varying the kinematics of the jet including the jet p_{T} and the jet rapidity y because the fractions of the quarks and gluons vary with p_{T} and y. This is shown on the left side of Figure 2.35, where the gluon fraction for inclusive jets is plotted as a function of $|y|$ and p_{T}. The gluon fraction decreases with increasing rapidity and p_{T}, meaning that there

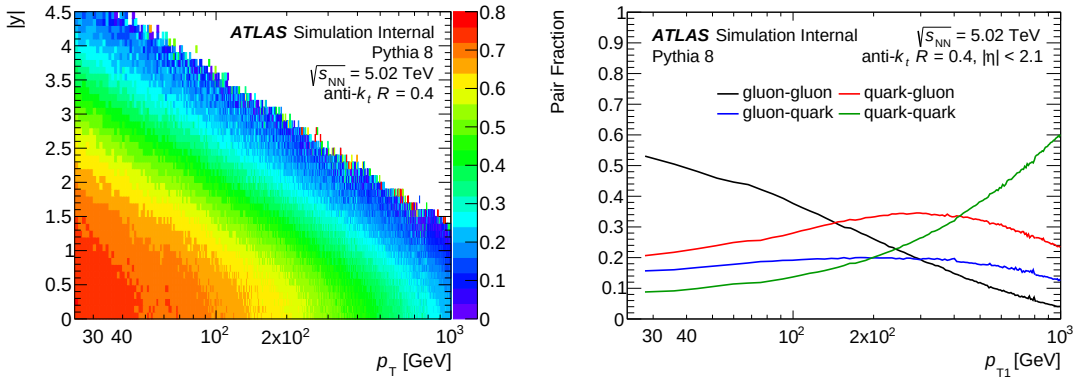

Figure 2.35: The left panel shows the gluon fraction for single jets as a function of jet p_{T} and $|y|$ in Pythia 8. The right panel shows the pair fractions (gg, qq, gq, qg) for dijets in Pythia 8.

are more gluon jets at low p_{T} and central rapidity and there are more quark jets at high p_{T} and forward rapidity. The flavor dependence can also be investigated for dijets by looking at the fraction of different flavor composition in pairs of jets. The right side of Figure 2.35 shows the fraction of qq, qg, gq, and gg pairs in dijet events as a function of leading jet p_{T}, where the qq pairs dominate at high p_{T} and the gg pairs dominate at low p_{T}. Since gluons are expected to lose more energy than quarks, the pairs where the quark is the leading jet and the gluon is the sub-leading jet (qg) should be the most imbalanced on average, which dominate at a p_{T} range between 80 and 200 GeV.

The jet-medium interactions can change the structure of the jet as it propagates through the medium. The jet interacts with the medium causing soft gluons to radiate from the jet which changes the momentum perpendicular to the jet axis through a phenomenon called momentum broadening. This widens the jet and allows the jet to lose energy outside of the defined jet cone as shown in the before and after images in Figure 2.36. This was predicted by BDMPS-Z to have the dependence $k_T^2 \propto \hat{q}L$ in Section 2.5.2.1.

The medium also responds to the jet as the jet moves through it with a recoil in the form of a wake of low energy gluons (second panel of Figure 2.37). The wake is like a Mach cone (shockwave) induced in the medium fluid along the direction of the jet that carries energy and momentum and enhances particle emission around the jet [171, 172, 173, 174]. These particles are soft and spread out but are correlated with the jet. Therefore, there

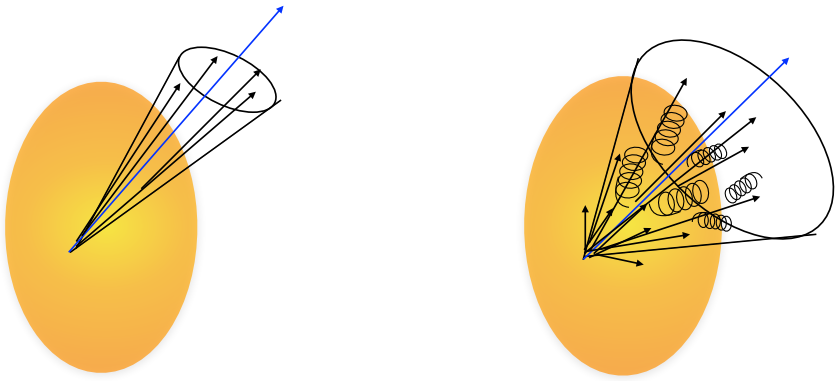

Figure 2.36: Diagram of a jet moving through a medium before (left) and after (right) experiencing momentum broadening.

are soft particles added in the direction of the jet that will contribute energy back inside the jet cone (third panel of Figure 2.37). Many jet quenching models include this effect into their calculations including Martini (AMY energy loss), LBT (HT energy loss), and JEWEL (BDMPS-Z energy loss).

The collision system dependence of energy loss is also interesting because it probes both the path length, density, and geometrical dependence of energy loss. For example, in this thesis Pb+Pb will be compared to Xe+Xe collision. Xenon has a lower mass number of 129 than lead at 208 which will result in a lower medium density and smaller path lengths due to the smaller size plasma produced in xenon collisions. In Section 2.5.1.1 radiative energy loss predicted a linear dependence on the density of the medium such that a lower density should lead to less energy loss. This is shown in Figure 2.38, where the left-hand side depicts the

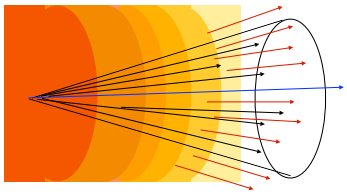

Figure 2.37: Diagram of a the medium recoiling as a jet moves through it and the soft particles (red) that get added back into the jet cone as a result of the wake from the recoil.

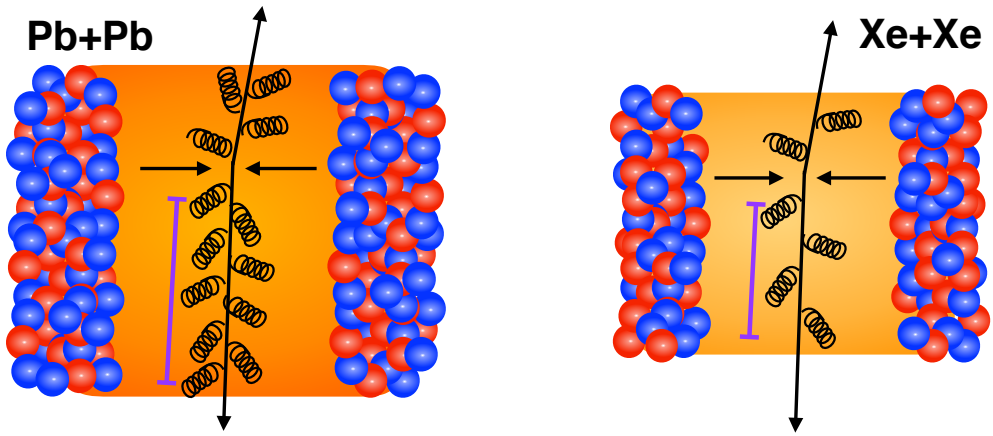

Figure 2.38: Diagram of the medium produced in Pb+Pb collisions (left) and Xe+Xe collisions (right). The darkness of the orange medium represents how dense the medium is and the purple line represents the path length.

medium produced in Pb+Pb collisions and the right-hand side depicts the medium produced in Xe+Xe collisions. The darker orange color indicates a denser medium for the Pb and the purple line depicts a longer path length. The geometry dependence is probed by comparing the collision systems at a fixed density (or N_{part} since $\rho \propto \frac{1}{A_T}\frac{dN_g}{dy} \propto \frac{A}{A^{2/3}} = A^{1/3} \propto N_{\text{part}}^{1/3}$) but at different centralities since the different centralities have different geometry (circular, almond shaped, triangular, etc.) as discussed in Section 2.4.3.1.

$$A_{\text{Xe}} < A_{\text{Pb}} \rightarrow \rho_{\text{Xe}} < \rho_{\text{Pb}} \text{ and } L_{\text{Xe}} < L_{\text{Pb}} \rightarrow \Delta E_{\text{Xe}} < \Delta E_{\text{Pb}} \tag{2.109}$$

In general, it is expected that any jet observable should have a centrality dependence since the larger the degree of overlap the larger the medium produced will be. The more peripheral the system becomes the more the system is like the standard pp collisions and the observables should start to behave more like they would in a vacuum.

2.5.4 Experimental Results

Different measurements at RHIC and at the LHC that investigate the above expectations will be discussed below. Measurements that motivate the studies of this thesis will also be presented.

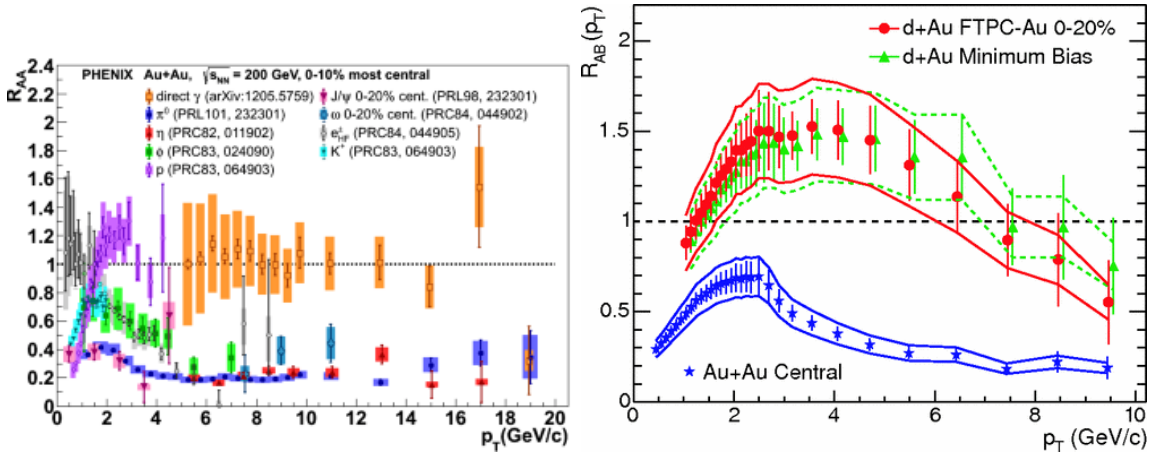

Figure 2.39: The R_{AA} as a function of p_{T} for different mesons in PHENIX [180] on the left and for inclusive hadrons in STAR [181] on the right in d+Au and Au+Au collision systems.

2.5.4.1 RHIC

The first observations of jet quenching was made at RHIC using the nuclear modification factor R_{AA} to measure the high p_{T} suppression of hadrons. The R_{AA} was measured with PHENIX [175, 176] (shown on the left-hand side of Figure 2.39), STAR [177, 178] (shown on the right-hand side of Figure 2.39), and BRAHMS [179]. It was seen in both STAR and PHENIX that for Au+Au collisions the R_{AA} is less than one for hadrons. The PHENIX figure shows the R_{AA} for many different types of final state particles. The mesons are shown to have a strong suppression, whereas the direct photons shown no suppression which is expected since they only interact electromagnetically.

Jet quenching was also first observed at RHIC through di-hadron correlations at STAR [181, 177] as shown in Figure 2.40. This is a measurement of the azimuthal angular difference $\Delta\phi$ between hadrons, where $\Delta\phi = 0$ is when the hadrons come from the same jet (near side peak) and $\Delta\phi = \pi$ is when one hadron is from one jet and the other is from a jet on the opposite side (away side peak). The measurement shows a suppression of the away-side peak in central Au+Au collisions which is indicative of one jet losing more energy in the plasma than the other jet due to the different paths traveled in the medium. The suppression is especially significant when compared to pp and d+Au collisions where no plasma (and thus

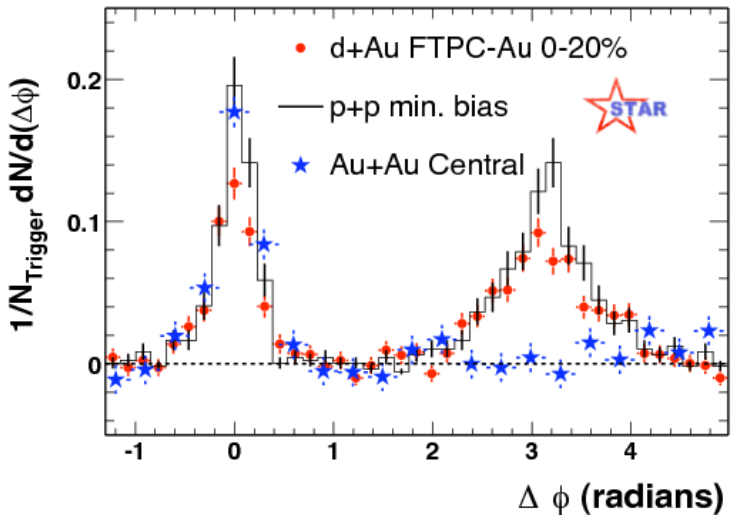

Figure 2.40: Di-hadron azimuthal correlations as a function of p_{T} for pp, d+Au, and central Au+Au collisions measured by STAR at $\sqrt{s_{\mathrm{NN}}} = 200$ GeV [182].

no energy loss) is expected.

In general hadrons are not the most direct way to measure jet quenching since the energy loss happens to the partons, not the final state hadrons. The final state hadrons are formed during hadronization after the propagation of the parton shower and thus a particular hadron is not directly connected to the initial parton since multiple hadrons form from one parton shower. A more direct measurement of energy loss is through fully reconstructed jets which are more experimentally challenging. Recently, many measurements of fully reconstructed jets have been performed at RHIC and at the LHC. Some of the first jet measurements at the LHC will be discussion in Section 2.5.4.2.

RHIC also performed the first measurements comparing energy loss in different colliding systems to probe the path and density dependence of energy loss. Figure 2.41 shows the π_0 R_{AA} at $\sqrt{s_{\mathrm{NN}}} = 200$ GeV for Au+Au collisions in the top panel compared to Cu+Cu collisions in the bottom panel in the 0–10% centrality interval [183]. The Au+Au collisions show a larger suppression than Cu+Cu collisions which is consistent with the picture that the denser, larger system (Au+Au) will have more energy loss than the smaller system (Cu+Cu).

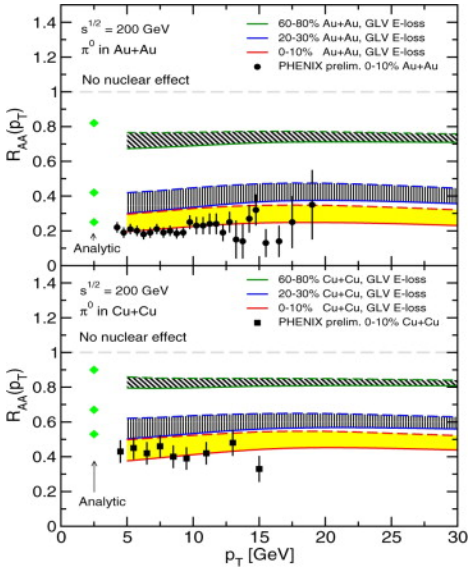

Figure 2.41: The R_{AA} as a function of p_{T} for π_0 in the 0–10% centrality interval in Au+Au collisions (top panel) and Cu+Cu collisions (bottom panel) at $\sqrt{s_{\mathrm{NN}}} = 200$ GeV [183].

2.5.4.2 LHC

The LHC opened a new horizon for studying the QGP, especially for jet measurements. It operates at a much higher center-of-mass energy (2.76 TeV compared to 200 GeV) and luminosity. The state of the art detectors (ATLAS, CMS, and ALICE) allow for more precise measurements that extend further in azimuth and pseudorapidity and also reach much higher values of the jet p_{T}. Combining measurements at RHIC and the LHC gives a better understanding of the full spectrum of energy loss in the QGP since RHIC probes the lower energy scale and the transition region, whereas the LHC probes the highest energies possible to date.

The first jet measurement from the LHC was a measurement of the dijet asymmetry through the variable A_{J} [1] (equation 2.107) by ATLAS. The A_{J} was measured in Pb+Pb collisions at $\sqrt{s_{\mathrm{NN}}} = 2.76$ TeV in 2010 and compared to $\sqrt{s} = 7$ TeV pp collisions and a HIJING+PYTHIA MC generator. The jets were selected by looking for back-to-back jets with $\Delta\phi = |\phi_1 - \phi_2| > \pi/2$ and $|\eta| < 2.1$. The leading jet, or p_{T_1}, had to be greater than 100 GeV and the sub-leading jet, or p_{T_2}, had to be greater than 25 GeV. The A_{J} was evaluated as a function of centrality in four centrality intervals (0–10%, 10–20%, 20–40%, and 40–100%)

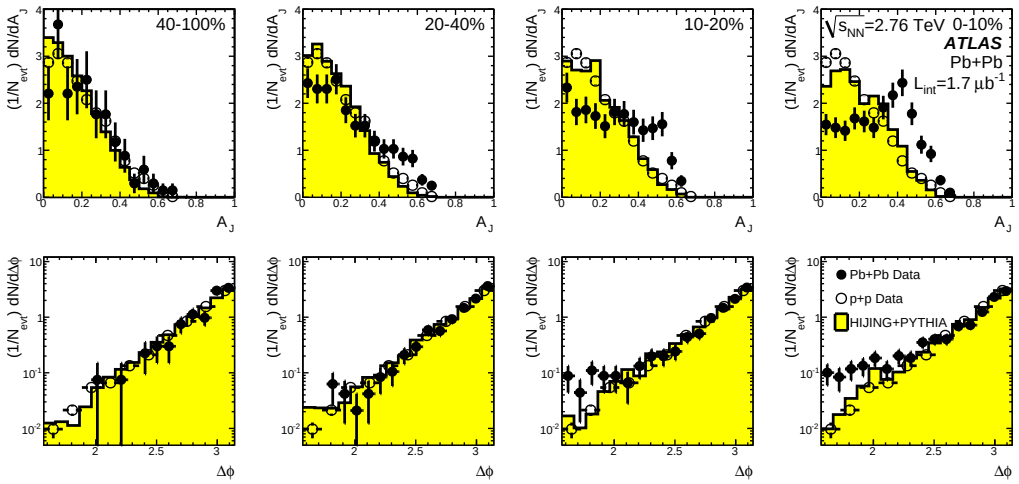

Figure 2.42: The distributions of the dijet asymmetry measured by ATLAS in Pb+Pb data at 2.76 TeV (black closed circles), pp data at 7 TeV (black open circles), and MC (yellow) in different centralities is shown on the top 4 panels. The bottom 4 panels show the same thing but for the distribution in $\Delta\phi$ [1].

as shown in Figure 2.42. The jets are shown to be more asymmetric in central collisions as compared to pp and MC as expected from predictions of energy loss in the QGP. The jets also become more symmetric with decreasing centrality where they become like the jets in pp in the most peripheral collisions. Although this measurement was very enlightening and was the first direct measurement of fully reconstructed jets, it has limitations. First, it was not unfolded (unfolding discussed in Section 4.6) for detector effects such that features could be smeared out by the detector resolution. Also, this measurement had limited statistics compared to the full collection of datasets taken in 2011. It is compared to a pp reference at a different center-of-mass energy and should be compared to a pp reference at $\sqrt{s} = 2.76$ TeV. The results presented in this thesis will improve upon this result to better understand relative energy loss.

ALTAS measured jet suppression using the nuclear modification factor R_{AA} at $\sqrt{s_{\mathrm{NN}}} = 2.76$ TeV withPb+Pb collision data from 2011 and pp collision data from 2013 [5]. This measurement is fully unfolded for detector effects. The jets were selected inclusively, meaning all jets in the event that pass kinematic selections. The kinematic selections were jets with a p_{T} above 40 GeV (50 GeV in central collisions) and a rapidity of $|y| < 2.1$. The mea-

surement was performed differentially in four rapidity intervals, $|y| < 0.3$, $0.3 < |y| < 0.8$, $0.8 < |y| < 1.2$, and $1.2 < |y| < 2.1$, and six centrality intervals, 0–10%, 10–20%, 20–30%, 30–40%, 40–60%, and 60–80%. Figure 2.43 shows the R_{AA} as a function of jet p_{T} overlaid for different centrality intervals and in different rapidity intervals in the panels. The jets are found to be suppressed more in central collisions than in peripheral collisions, where in central collisions the suppression factor is about 0.5. The R_{AA} has a weak, smooth p_{T} dependence and no dependence on rapidity within the statistical limitations of the measurement. This measurement could be improved upon by using the 2015 Pb+Pb data with increased statistics to try to investigate the rapidity dependence and go to higher p_{T}. The results presented in this thesis will also improve upon this result by using a larger collection of data from 2015 with reduced systematic uncertainties to better understand how single jets lose energy in the QGP.

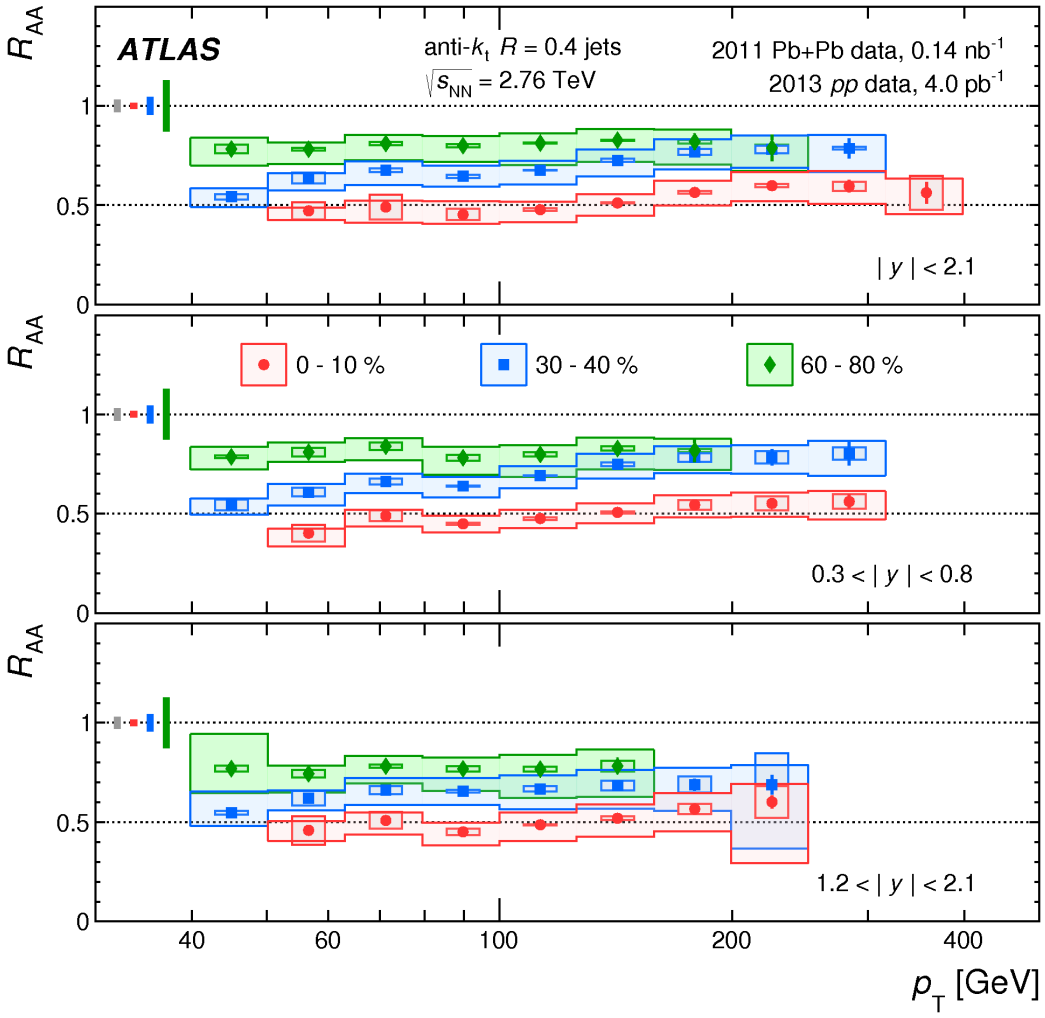

Figure 2.43: The R_{AA} as a function of the jet p_{T} measured by ATLAS at 2.76 TeV, with different centrality bins indicated by different markers and colors and a different rapidity intervals in each panel [5].

Chapter 3

Experimental Setup

3.1 The Large Hadron Collider

The Large Hadron Collider (LHC) [90, 184, 185, 186] is a particle accelerator located at the European Organization for Nuclear Research (CERN) near Geneva, Switzerland on the Swiss-French border. The LHC is the largest particle accelerator in the world at 26.7 kilometers in circumference and is located in a deep underground tunnel between 45 and 170 m below the surface. The LHC has taken data for two runs, with a long shut-down in between, indicated by Run 1 (2010-2013) and Run 2 (2015-2018). This thesis uses results from both runs and thus both are discussed in the following sections.

3.1.1 LHC Injection Chain

The LHC typically collides protons, but also collides heavy ions including both lead ions (Z = 82, A = 208), starting in 2010, and more recently, xenon ions (Z = 54, A = 129) in October 2017. The colliding species are accelerated through stages that each increase the energy of the particles as shown in Figure 3.1. The protons start as a hydrogen gas which is then stripped of it's electrons using an electric field to become hydrogen ions, or protons, that are injected into the linear particle accelerator (LINAC 2) where they reach an energy of 50 MeV. From there they reach the Proton Synchrotron Booster (PSB) where they are accelerated to 1.4 GeV. Next, the protons are injected into the Proton Synchrotron (PS) where they reach 450 GeV. Finally, they are injected into the main ring where they reach

their peak energy. Protons have been collided at 3.5 or 4 TeV per beam in 2013 (or 7 to 8 TeV total) and 6.5 TeV per beam in 2015 (or 13 TeV total), as well as 2.76 TeV in 2013, 5.02 TeV in 2015, and 8.02 TeV in 2017 to serve as reference to heavy ion data. The Pb^{208} ions follow a similar path as the protons except they start in the Linac 3 where they are accelerated to 4.2 MeV per nucleon (/n) and are injected into the Low Energy Ion Ring (LEIR) where they reach 72.2 MeV/n. The ions are then accelerated to 5.9 GeV/n in the PS and 177 GeV/n in the SPS. From the SPS they are injected into the main ring where they have been collided at a center-of-mass energies of 2.76 and 5.02 TeV/n. The Xe^{129} ions follow the same pattern as the lead ions and have been collided in the main ring at 5.44 TeV/n [186].

3.1.2 Main Ring Design

The main ring, or the LHC, consists of two parallel beam pipes where particles can travel in opposite directions around the ring. The LHC was built inside the already existing tunnel

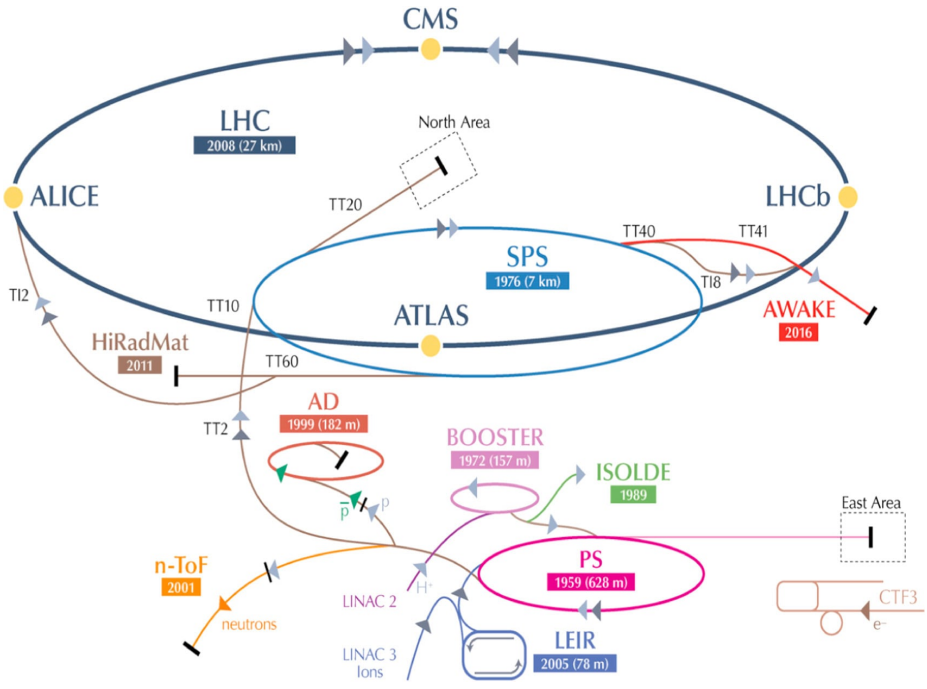

Figure 3.1: The LHC injection chain for both ions and protons. The location of the different LHC experiments are also indicated [187].

that previously contained the Large Electron-Positron collider [188]. The beams are kept inside the beam using 1,232 superconducting dipole magnets that produce an 8.3 T field, which bend the beam so the particles move around the ring in a circle. There are also 392 quadrupole magnets with an alternate-gradient focusing scheme that focuses the beam in both the horizontal and vertical directions. These are spaced throughout the tunnel but are stronger near the places where the beams will interact. The magnets are made of niobium-titanium (NbTi) and are cooled to an operating temperature of 1.9 K using superfluid helium-4 (He-4) [184].

The LHC groups ions together into tight bunches spaced along the beam. The tight bunches increase the chance of a collision happening each time the beam crosses and allows time for the machine and detectors to process the collision before another collision occurs. Each bunch contains about 100 billion protons or 10 million ions. The LHC uses 16 superconducting RF cavities along the ring, 8 for each beam, with a 400 MHz oscillating electric field to accelerate the particles to their peak energies and to focus them together into bunches. This allows for $(400\text{MHz} \times 26.7\text{km}/(3 \times 10^8\text{m/s}) =)$ 35650 RF "buckets" that can contain ions. The SPS actually limits the LHC to 40 Hz or 25 ns bunch spacing, which results in 3560 bunches, called Bunch Crossing IDs (BCIDs). This results in 10 RF "buckets" per BCID. Only a maximum of 2808 BCIDs are occupied when the LHC is running because there needs to be spaces to allow the beam to be dumped which takes a significant amount of time. In Run 1 the design limitation of 25 ns was not reached and the smallest spacing used for protons was 50 ns. In Run 2, 25 ns has been used for protons but for lead ions the smallest bunch spacing was 150 ns [184, 189].

3.1.3 Detectors

The LHC has eight arcs and straight regions with an interaction reaction in the middle of each. At each interaction region the beams are either brought together for a collision at an interaction point (IP) or there are services and utilities performed. There are four IP with four main detectors located at each one, which can be seen in Figure 3.1. ATLAS (A Toroidal LHC ApparatuS) [190] and CMS (Compact Muon Solenoid) [191] are general-purpose, high-luminosity detectors and are the largest of the four, located at IP 1 and IP 5, respectively.

ALICE (A Large Ion Collider Experiment) [192] is a dedicated heavy ion detector located at IP 2 and LHCb (LHC-beauty) [193] specializes in b-physics experiments and is located at IP 8. In addition to ALICE, ATLAS and CMS are used for heavy ion experiments. There are three additional detectors located near the IPs of the main detectors: TOTEM (TOTal Elastic and diffractive cross section Measurement) [194], LHCf (LHC-forward) [195], and MoEDAL (Monopole and Exotics Detector At the LHC) [196].

3.1.4 Luminosity

The luminosity is a major factor in determining the performance of the collider. It is a measure of number of events per cm^2, or per cross section, where the number of events is given by

$$N = \sigma L \tag{3.1}$$

where σ is the cross section for a given process and L is the integrated luminosity. The instantaneous luminosity, or the luminosity per unit time, is $\mathcal{L} = \mathrm{dL/dt} = R/\sigma$, where $R = \mathrm{dN/dt}$. In general, the more luminosity the larger the number of events for a given cross section will be and the more data can be taken for a particular analysis. Thus it is important to try to maximize the luminosity of the collider.

The luminosity of a collider can be expressed in terms of the beam parameters in the following way

$$\mathcal{L} = \frac{n_\mathrm{b} f_\mathrm{r} n_1 n_2}{2\pi \Sigma_\mathrm{x} \Sigma_\mathrm{y}}, \tag{3.2}$$

where n_b is the number of colliding bunches, n_1 and n_2 are the number of particles per bunch, f_r is the revolution frequency, and Σ_x and Σ_y are the gaussian widths of horizontal and vertical profiles of the colliding beams [197].

The Σ_x and Σ_y can be measured using "van der Meer" (vdM) scans [198]. vdM scans are a special running period during which the the beams are stepped through a sequence of separations, first horizontally and then vertically, that span the full profile in each direction. Each horizontal and vertical sweep is referred to as a scan and there are multiple scans performed in a given vdM run. In the vdM scan analysis, the instantaneous lumi-

nosity can also be defined in terms of a number of collisions per bunch crossing (BCID, see Section 3.1.2), μ, and the inelastic cross section for the collisions σ_{inel}in the following way:

$$\begin{aligned} N &= n_{\text{b}}\mu \\ R &= \frac{\text{d}N}{\text{dt}} = f_{\text{r}} n_{\text{b}}\mu \\ \mathcal{L} &= R/\sigma_{\text{inel}} = \frac{f_{\text{r}} n_{\text{b}}\mu}{\sigma_{\text{inel}}} \end{aligned}$$

Detectors that measure luminosity are not fully efficient, thus the total inelastic cross section is not seen by the detectors. The σ_{inel} can be written in terms of the detector efficiency as $\sigma_{\text{inel}} = \varepsilon\sigma_{\text{vis}}$. The same is true for the number of bunch crossings so $\mu = \varepsilon\mu_{\text{vis}}$ and thus,

$$\mathcal{L} = \frac{f_{\text{r}} n_{\text{b}}\mu_{\text{vis}}}{\sigma_{\text{vis}}} \,. \tag{3.3}$$

The μ_{vis} is obtained by luminosity detectors using event counting algorithms. There are two main luminosity detectors in ATLAS, LUCID and BCM, that are described in more detail in Section 3.2.4.1. Event counting algorithms determine the fraction of bunch crossings where an event was registered that satisfies selection criteria. When $\mu_{\text{vis}} << 1$, it can be written as

$$\mu_{\text{vis}} \approx \frac{N}{N_{\text{BC}}} \tag{3.4}$$

where N is the number of events passing a selection criteria and N_{BC} is the number of bunch crossings, both in a specific time interval. When μ_{vis} does not meet this requirement poisson statistics are needed. This is done in two different ways: EventOR (inclusive) or EventAND (coincidence). In EventOR, a bunch crossing is counted if the sum of the hits on both sides of the detector is at least one. In EventAND, a bunch crossing is counted if there is at least one hit on both sides of the detector. The detector+algorithm used is depicted as one label. For example, the Lucid detector and the EventOR algorithm is written as `LucidEventOR` [197].

In the *vdM* analysis, the σ_{vis} is calculated as function of the BCID by measuring the

Σ_x and Σ_y since, by rearranging Equations 3.2 and 3.3

$$\sigma_{\text{vis}} = \mu_{\text{vis}}{}^{\max} \frac{2\pi\Sigma_x\Sigma_y}{n_1 n_2} \ . \tag{3.5}$$

Measurements of the collision rates R_{sp} as a function of separation allows for the direct evaluation of Σ_x and Σ_y, where the $\Sigma_{x,y}$ can be found by integrating the fit functions over the distributions shown in Figure 3.3:

$$\Sigma_{x,y} = \frac{1}{\sqrt{2\pi}} \frac{\int \Delta_{x,y} R_{\text{sp}}(\Delta_{x,y})}{R_{\text{sp}}(\Delta_{x,y}^{\max})} = \frac{1}{\sqrt{2\pi}} \int \Delta_{\text{x,y}} f_{\text{x,y}}(\Delta_{\text{x,y}}). \tag{3.6}$$

The distributions are fit in two-dimensions, the horizontal and vertical directions, for both beams and for each BCID. For example the fits can be uncorrelated (Eq. 3.8) or correlated (Eq. 3.9) double gaussians [199].

$$g_{x,y;1,2} = e^{(-\Delta_{x,y} - \Delta_{x,y;1,2}^{\max})^2 / 2\sigma_{x,y;1,2}^2} \tag{3.7}$$

$$f(\Delta_x, \Delta_y) = A[f g_{x1} g_{y1} + (1-f) g_{x2} g_{y2}] + C \tag{3.8}$$

$$f(\Delta_x, \Delta_y) = A[f g_{x1} + (1-f) g_{x2})(f g_{y1} + (1-f) g_{y2}] + C \tag{3.9}$$

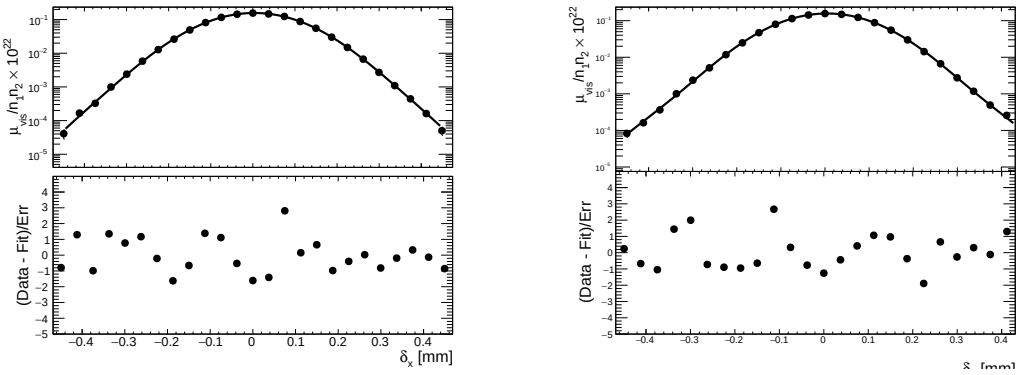

Figure 3.2: The horizontal and vertical vdM scan profiles in the horizontal (left) and vertical (right) directions from a vdM scan from reference [199]. This is for the first scan, the lucidEvtOR detector, and BCID 41.

The σ_{vis} values as a function of BCID can be extracted from this and a direct measurement of n_1 and n_2. They are shown in Figure 3.3. The overall σ_{vis} values are obtained from a constant fit and then are used, along with the μ_{vis} values, to calculate the luminosity under the conditions of the *vdM* scans. Then, the luminosity measured during the *vdM* scan is used to calibrate the response of the luminosity detectors since the σ_{vis} are the same [197, 199].

The σ_{vis} values required various corrections and background subtractions before being used to calibrate. The background comes from noise, after-glow which is from time-delayed particles hitting the detector, and beam-gas interactions or interactions between residual gas and the beam. The beam currents, n_1 and n_2, are corrected for "ghost" charge when charge occupies unfilled bunches and "satellite" charge when charges are outside of the nominal RF buckets. Also, there are corrections to the beam positions and β^* due to electromagnetic interactions between the bunches as the beams sweep past each other at non-zero separation. There is an additional correction to the beam seperation due to the orbit drift where the beams drifts due to changes in the magnetic field of the LHC [200, 201, 199].

The *vdM* scan is also used to determine the systematic uncertainty for the luminosity.

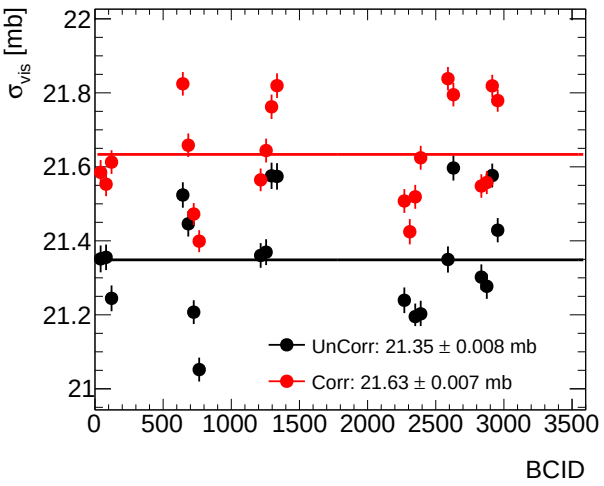

Figure 3.3: The σ_{vis} values as a function of BCID for both the uncorrelated fit (Eq. 3.8) in black and the correlated fit (Eq. 3.9) in red from the vdM scan in reference [199]. The result of a constant fit for both sets of points are given on the legend.

These can be due to many factors including the consistency of the σ_{vis} with BCID which can be seen in Figure 3.3, scan-to-scan reproducibility, and algorithm dependence. There are uncertainties due to the differences in the fit model and the difference between correlated and uncorrelated fits (Eq. 3.8– 3.9) called transverse coupling. There are also uncertainties in the corrections applied, as well as many others [200, 201, 199].

The final luminosity along with it's systematic uncertainty is used for any measurements of cross sections. The luminosities for the datasets used in this thesis, along with their uncertainty when available, is shown in Table 3.1. It is important to mention that only measurements of cross sections need the luminosity value and uncertainty although, it is still useful for other measurements to get an idea of the statistics of the sample. An example of the total integrated luminosity as a function of time for the 2015 Pb+Pb data at 5.02 TeVis shown in Figure 3.4.

Collision type	**Year**	**center-of-mass energy [TeV]**	**Luminosity**	**Uncertainty**
Pb+Pb	2011	2.76	0.14 nb^{-1}	N/A
pp	2013	2.76	4 pb^{-1}	3.1%
Pb+Pb	2015	5.02	0.49 nb^{-1}	6.1%
pp	2015	5.02	25 pb^{-1}	5.4%
Xe+Xe	2017	5.44	3 μb^{-1}	N/A
pp	2017	5.02	278 pb^{-1}	N/A

Table 3.1: The luminosity and uncertainty for the 2011 Pb+Pb data at 2.76 TeV, the 2013 *pp* data at 2.76 TeV [200], the 2015 Pb+Pb data at 5.02 TeV [201], the 2015 *pp* data at 5.02 TeV [199], the 2017 Xe+Xe data at 5.44 TeV, and the 2017 *pp* at 5.02 TeV.

3.2 The ATLAS Detector

The ATLAS detector [190] is a general purpose detector that collects data from proton (pp) and heavy ion (Pb+Pb, p+Pb, Xe+Xe, etc.) collisions at the LHC. It is located at IP1 along the LHC ring. The ATLAS detector is the largest volume detector ever constructed, measuring 46 m long, 25 m high, and 25 m wide, and weighing 7000 tons. It is a forward-backward detector with respect to the interaction point that has 2π azimuthal coverage. The detector is shown in Figure 3.5, where the size can be compared to the size of a person

in the figure. It was built to take advantage of the high energy and luminosity from the LHC that will produce increased cross sections and measurements out to a TeV in energy scale. It needs to take large amounts of data to look for rare phenomena and be very precise to take precision measurements. ATLAS is designed to search for the Higgs boson, which was discovered in July 2012, look for physics beyond the Standard Model, and measure Standard Model particles and interactions to better precision, as well as study the properties of the strongly interacting matter at high densities (QGP) that can be produced in heavy ion collisions.

The coordinate system used for the ATLAS detector is described here and will be used throughout this thesis. It is defined with the interaction point as it's origin, the beam direction as the z-axis, and the x-y plane is transverse to the beam direction. The $+z$ direction is towards the "A" side of the detector and the $-z$ direction is towards the "B" side. The "+x" direction is towards the center of the LHC ring and the "+y" points upwards. The azimuthal angle ϕ is around the beam, or z-axis, and the polar angle θ is around the x-axis defined from the beam. The polar angle is typically reported in terms of the pseudorapidity $\eta = -\ln\tan(\theta/2)$. In the limit where the particle is moving at close the the speed of light, the mass can be treated as negligible and $E \approx p$. Thus,

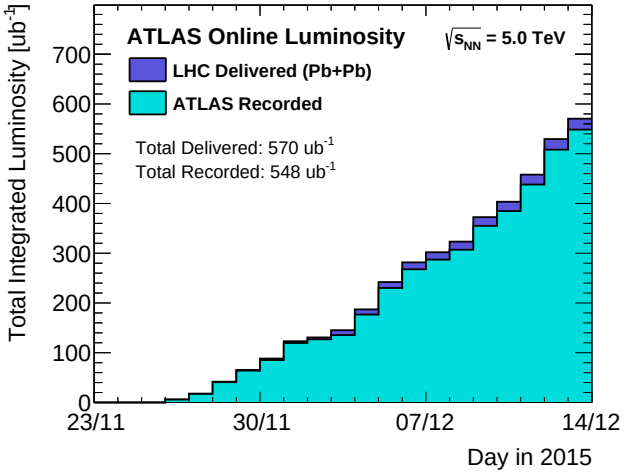

Figure 3.4: The total integrated luminosity as a function of time for the 2015 Pb+Pb run at 5.02 TeV. The luminosity delivered by the LHC is shown in dark blue and the total luminosity that ATLAS recorded is shown in light blue.

$$\eta = \frac{1}{2}\ln\left(\frac{|\mathbf{p}| + p_z}{|\mathbf{p}| - p_z}\right) \approx \frac{1}{2}\ln\left(\frac{E + p_z}{E - p_z}\right) = y \tag{3.10}$$

where y is the rapidity, which is a lorentz invariant quantity. High pseudorapidity is along the beam axis and is referred to as forward, such that $\eta = \infty$ is at $\theta = 0$. Low pseudorapidty is perpendicular to the beam axis and is referred to as central, such that $\eta = 0$ at $\theta = \pi$. The angular seperation between particles in the detector is defined as $\Delta R = \sqrt{\Delta\eta^2 + \Delta\phi^2}$. The transverse energy (E_{T}) and transverse momentum (p_{T}) are projections on the transverse, or x-y plane. This is how the momenta and energy are typically expressed in particle physics since they are lorentz invariant and separate the transverse momentum out from the momentum along the beam-line that might be leftover from beam particles.

After the particles collide at ATLAS many new particles are produced that fly out in all directions with a large range of energies into the detector. The path, momentum, energy and charge of each particle needs to be determined so that each particle can be identified. This requires a large azimuthal and psuedoprapidity coverage, as well as high detector granularity. ATLAS is made up of six different subsystems, organized in layers,

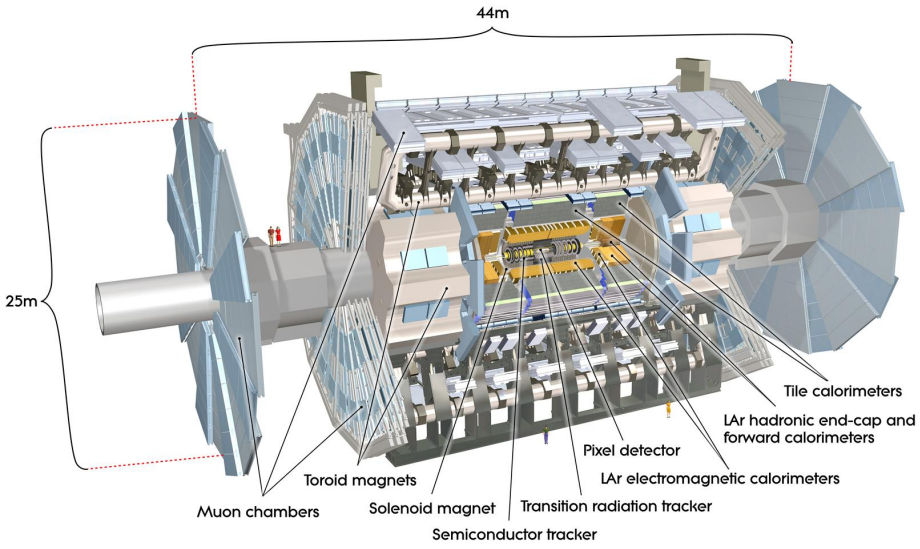

Figure 3.5: A cut-away view ATLAS detector is shown, with a person included for scale. The main detector components are indicated [190].

that are each designed to detect different types of particles. The innermost part is called the Inner Detector (ID), which is immersed in a 2T solenoidal magnetic field, and is used to measure charged particle momentum, reconstruct vertexes, and identify electrons. This is surrounded by the calorimeter which measures energy deposition to determine the energy and position of particles. It consists of both electromagnetic (EM) calorimetry for electron and photon identification and hadronic calorimetry for measuring hadrons in the form of jets. The calorimeter is surrounded by a muon spectrometer which is used to identify and measure the momentum of muons by utilizing the strong toroidal magnetic field surrounding the detector. The subsystems relevant to this work are described in the next sections, with a focus on calorimetry (Section 3.2.3) which is the main part of the detector used in this thesis. The muon spectrometer is not used in this work so it is not discussed beyond mentioning it's purpose above.

Due to the large number of collisions that happen (over a billion interactions per second), ATLAS needs to be able to take data fast, select only interesting data to record, and be able to store large amounts of data for processing. This requires a vast "trigger" system that selects only about one million of those events that are interesting and a data acquisition system (DAQ) that channels the data from the detectors to storage. These are both discussed in more detail in Section 3.2.5.

3.2.1 Magnet system

ATLAS has a large magnet system that allows for charged particle momentum measurements by bending the particles trajectories in the field. The magnet system consists of a solenoid magnet in the center that supports the ID and three toroids (barrel and two endcaps) that support the muon spectrometer. The central solenoid has a 2T magnetic field directed along the beam axis with a current of 7.3 kA. It sits right outside the ID and right inside the calorimeter and is only $\approx 0.66X_0$, where X_0 is the radiation length, to make sure the calorimeter has optimal performance. The cylinder consists of a single layer of coil made of Al-stabilized NbTi conductor that sits inside of a 12 mm thinking Al support chamber. It has an inner diameter of 2.46 m and 2.56 m, with a length of 5.8 m and a weight of 5 tonnes. An image of the central solenoid and the map of the magnetic field dependence on

the radius and the z position is shown in Figure 3.6.

The barrel toroid consists of eight coils, as shown in Figure 3.7, and produces a 0.5 T magnetic field with a 20.5 kA current. The coils are made of Al-stabilized Nb/Ti/Cu conductor. It has an inner diameter of 9.4 m and an outer diameter of 20.1 m, with a length of 25.3 m and a weight of 830 tonnes. The end cap toroids consist of a single coil mass made of the same conductor as the barrel toroid and produces a magnetic field of 1T and a current of 20.5 kA. They are both 5.0 m long and have a 1.7 m inner diameter and a 10.7 m outer diameter. They both weigh 240 tonnes. A map of the field integral as a function of $|\eta|$ is shown in Figure 3.7.

3.2.2 Inner Detector

The purpose of the ID is for charged particle tracking which involves using the solenoidal field to bend the particles into the detector and then determine their position and momentum based on their track trajectories. There are thousands of particles that emerge from a collision point in every event, with significantly more tracks in heavy ion events than in standard pp events. The ID can measure charged particle with track $p_{\mathrm{T}}^{\mathrm{trk}} > 0.5$ GeV, within $|\eta| < 2.5$, and 2π in azimuth. The ID is also used for electron identification and primary and secondary vertex reconstruction. It is cylindrical with a length of 5.3 m and a diameter of 2.5 m. It consists of three subsystems: the pixel tracker, Silicon Microstrip

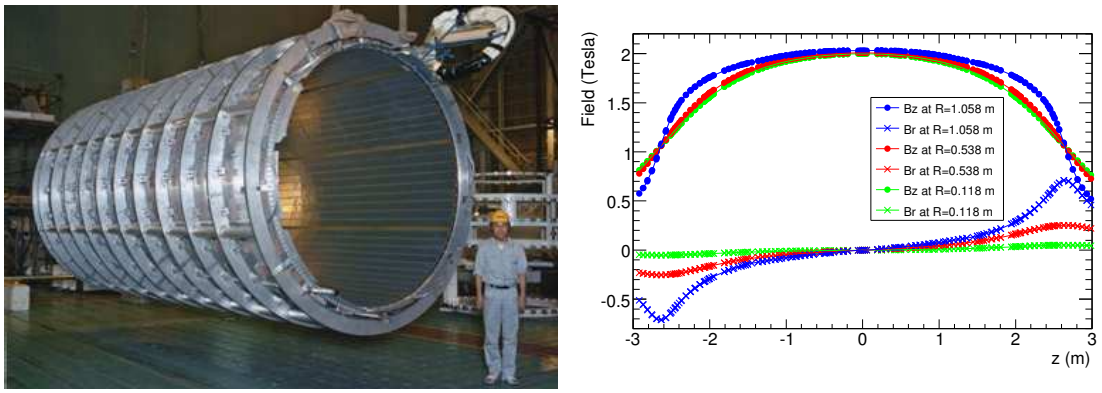

Figure 3.6: The left panel shows the ATLAS central solenoid magnet before installation. The right panel shows the central solenoid magnetic field as a function z for different values of the radius from the center axis. [190].

Tracker (SCT), and the Transition Radiation Tracker (TRT). Figure 3.8 shows the layout and positions of each sub-component, including their psuedorapidity coverage. The high radiation environment puts strict requirements on the ID design. The pixel and SCT components must be kept at an operating temperature of $-5°$ to $-10°$, while the TRT is kept at room temperature.

3.2.2.1 Pixel Detector

The pixel detector consists of pixel modules that are arranged cylindrically in three barrel layers (ID0–2) and two end-cap layers consisting of three disk layers each. The barrel layers are located at radial distances of 50.5, 88.5, and 122.5 mm and the end-cap layers are located at z distances along the beam line of 495, 580, and 650 mm on one side. The layout can be seen for the barrel and end-cap on the left and right side of Figure 3.9, respectively. There are 1744 identical pixel sensors that are each ~ 250 μm thick and 19×63 mm^2. The sensors are oxygenated n-type wafers with readout pixels on the n$\pm$ implanted side of the detector. They operate at a bias voltage of $\sim$ 150 V, but will take up to 600 V during operation. Each pixel module is organized in a stack consisting of electronic chips on the bottom, then bump bonds which connect the electronic channels to pixel sensor elements, then the sensor tile area, and then a printed circuit board on top. There are 47,232 pixels

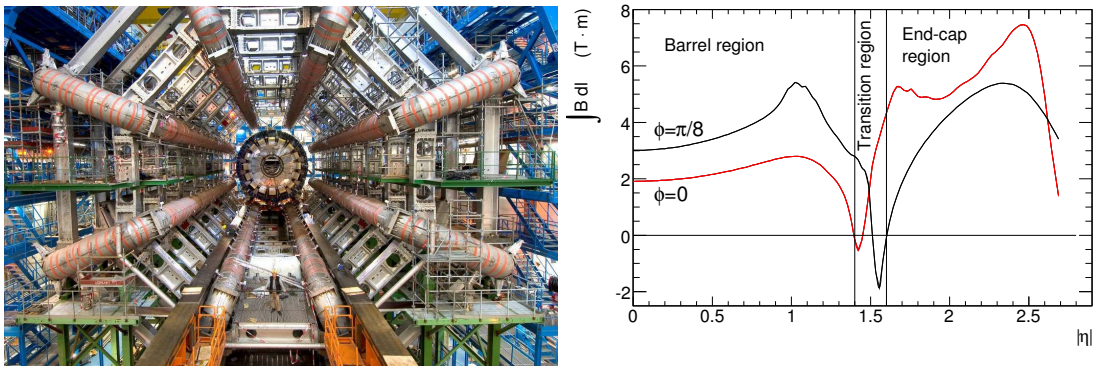

Figure 3.7: The left panel shows the ATLAS barrel toroid magnets after installation is shown, next to a physicist for scale. The right panel shows the intergral of the magnetic field as a function of rapidity for both the barrel and the endcap regions of the magnet system [190].

on each sensor, which makes a total of 80 million pixel channels (there are some ganged pixels on the front-end caps that lead to slightly less read-out channels). The nominal pixel size on each sensor is 50 μm^2. The pixel detector has a resolution of 14 μm in the transverse plane by 115 μm in the z direction.

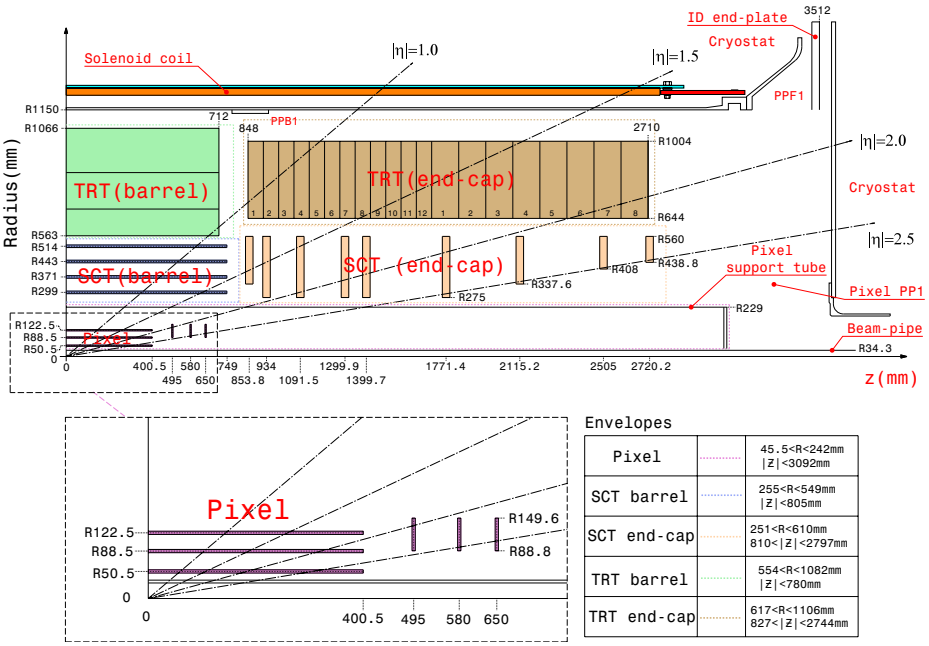

Figure 3.8: Schematic of the inner detector showing the various components' locations in radius and z [190].

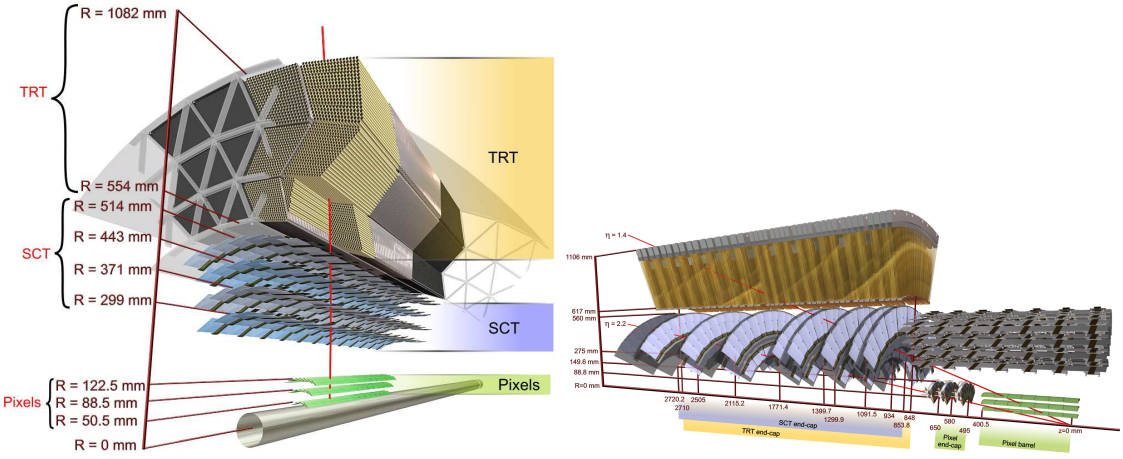

Figure 3.9: The left panel shows a cut-out view of the barrel ID and the right panel shows a cut-out view of the end cap ID [190].

3.2.2.2 Silicon Microstrip Tracker

The SCT consists of four cylindrical barrel layers (ID3–6) and two end-cap layers with nine disk layers each. The barrel layers are located at radial distances of 284, 355, 427, and 498 mm and the end-cap layers are located at z distances 854 and 2720 mm. The layout can be seen for the barrel and end-cap on the left and right side of Figure 3.9, respectively. There are 4,088 modules (2112 in the barrel and 988 in each end-cap) that are 285±15 μm thick and cover 60 m^2 of silicon. The module planes in the barrel are rectangular shape and are at an angle of approximately 11° with respect to the tangent of the cylinder. Each module consist of two 6 cm sensors daisy–chained together at an angle of 40 mrad and strip pitch of 80 μm. The end-cap sensors are trapezoidal and have radial strips of constant azimuth. The end-cap mean pitch is 80 μm. The sensors use a p-in-n technology meaning p-type implanted in n-type bulk, with AC-coupled readout strips. The sensors will operate at a $\sim$ 150 V bias, but will take from 250–350 V during operation. Each sensor has 768 readout strips, which means that in total there are over 6 million implanted readout strips (6 million channels) in both the barrel and end-cap. The SCT has a resolution of 17 μm in the transverse plane by 580 μm in the z direction.

3.2.2.3 Transition Radiation Tracker

The TRT is the remaining part of the ID and sits radially further out than the others. It has a barrel and two end-cap components. It can detect charged tracks with $p_{\mathrm{T}} > 0.5$ GeV with 36 hits per track in $|\eta| < 2$ (22 hits per track in the barrel/end-cap transition region from 0.8< $|\eta|$ <1.0). It is also used for electron identification using transition radiation (TR). The barrel is located at 780 mm in the z direction and extends radially from 554-1084 mm. One of the end-caps is located between 927 and 2744 mm in the z direction and extends radially from 615 to 1106 mm. The TRT consists of multiple layers of about 300 thousand gaseous straw tubes with transition radiation material in between. The barrel has 96 modules in 73 layers with 52544 total straws. The modules are divided into three rings with 32 modules per ring, all surrounded by a carbon-fiber lament shell. The straws are 144 cm long and form an axial array with about 7 mm spacing and fiber in between. Each straw has electronic read-out on both ends. The end-caps have 20 modules in 160 layers

with 122880 total straws in each. The modules are divided into two independent wheels where the first set has 12 wheels with 8 layers that are 8 mm apart. The second set has 8 wheels with 8 layers that are 15 mm apart. Each layer has 768 straws radially oriented that are 37 cm long with foil in between. Each straw contains electronic read-out at the outer radial end.

The straws are made of polyimide and are 4 mm in diameter. The wall of the straws is made of two 35 μm thick films that are bonded together. Each film has a 25 μm layer of polyimide in the center with one side being a 0.2 μm Al layer with a 5-6 μm graphite polyimide layer on top and the other side being a 5 μm polyurethane layer that is heated to seal the two sides of the films together. The walls of the straw are kept at -1.53 kV and serve as the cathode. The anode is a 31 μm diameter tungsten wire in the center of the straw coated in 0.5-0.7 μm gold that is kept at ground potential. The straws are filled with a Xenon gas mixture that consists of 70% Xe, 27% CO_2 and 3% O_2. The gas detects transition radiation photons that are used for electron identification and have larger signal amplitude than the minimum-ionizing charged particles used for tracking. Thus the TR and the tracking hits can be discriminated using high and low thresholds in the electronics. The position resolution determined in the individual straws is 130 μm.

3.2.3 Calorimeters

The ATLAS calorimeter system consists of both electromagnetic (EM) and hadronic calorimetry since photons and electrons shower differently than hadrons. It is a sampling calorimeter that incorporates both liquid-argon and scintillating tile calorimeter designs. They use dense layers, called absorbers, that cause the particles to shower, along with active layers in between to collect the energy deposition. The calorimeter has full azimuthal coverage and covers a pseudorapidity range of $|\eta| < 4.9$. The layout of the calorimeters is shown in Fig. 3.10. The EM calorimeter overlaps with the ID and consists of a LAr EM barrel for mid-rapidity and an end-cap for forward rapidity coverage. It has a very fine granularity for precision measurements of electron and photons. The hadronic calorimeter consists of a tile barrel for mid-rapidity coverage, an extended tile barrel and LAr hadronic end-cap for forward rapidity coverage, and a forward calorimeter (FCal) for even more forward mea-

surements. It covers the full rapidity of the detector to enable full reconstruction of energy deposites to form jets. The locations and granularity of the various parts of the calorimeter are described in detail in Table 3.2. The LAr needs to be kept cold so the calorimeter structures are supported by cryostats. One central cryostat contains the EM barrel along with the central solenoid. There are also two end-cap cryostats on each side that each contain both the EM and hadronic end-cap wheels as well as an FCal. The barrel tile then supports the central cryostat and the extended tile supports the end-cap cryostats.

3.2.3.1 Particle Showers

The calorimetry system is designed to collect all of the energy from leptons and hadrons except for muons which are detected in the muon spectrometer outside the calorimeter. The neutrinos will fly out undetected. Electrons traveling through matter at low energy primarily lose energy through ionization but also through Möeller scattering (electron-electron scattering), Bhabha scattering (electron-positron scattering), and e^+ and e^- annihilation (yields two photons), which all fall logarithmically with energy. Electrons at high energy

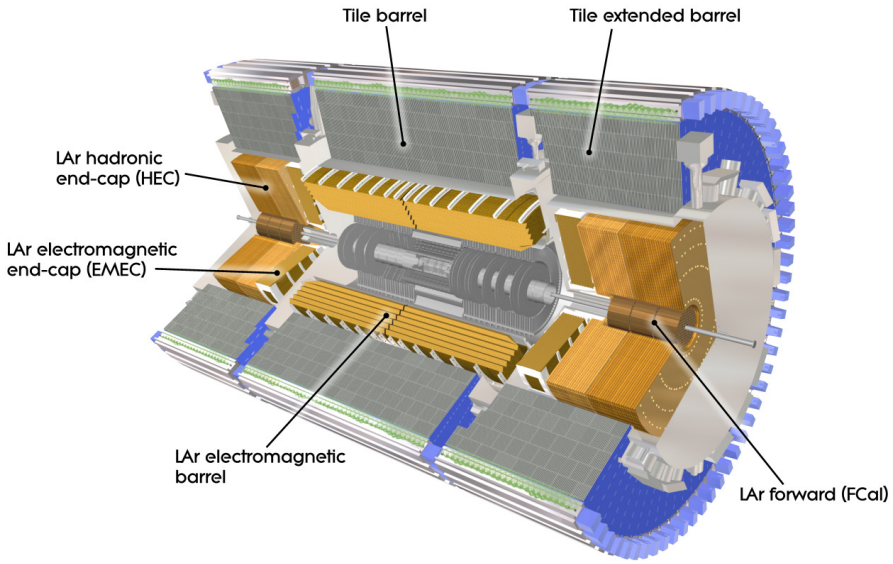

Figure 3.10: Diagram of the Liquid Argon and Tile Calorimeters which sit outside the Inner Detector and solenoid magnet [190].

Layer	$\lvert\eta\rvert$**-coverage**	**Granularity** $\Delta\eta \times \Delta\phi$
EM Barrel Presampler	$\lvert\eta\rvert < 1.52$	0.025×0.1
EM Barrel 1	$\lvert\eta\rvert < 1.475$	0.003×0.1 ($\lvert\eta\rvert < 1.40$) 0.025×0.025 ($1.40 < \lvert\eta\rvert < 1.475$)
EM Barrel 2		
EM Barrel 3	$\lvert\eta\rvert < 1.35$	0.025×0.025
EM End-cap Presampler	$\lvert\eta\rvert < 1.35$	0.025×0.025
EM End-cap 1	$1.375 < \lvert\eta\rvert < 3.2$	0.050×0.1 ($1.375 < \lvert\eta\rvert < 1.425$) 0.025×0.1 ($1.475 < \lvert\eta\rvert < 1.5$) 0.003×0.1 ($1.5 < \lvert\eta\rvert < 1.8$) 0.004×0.1 ($1.8 < \lvert\eta\rvert < 2.0$) 0.006×0.1 ($2.0 < \lvert\eta\rvert < 2.4$) 0.025×0.1 ($2.4 < \lvert\eta\rvert < 2.5$) 0.1×0.1 ($2.5 < \lvert\eta\rvert < 3.2$)
EM End-cap 2	$1.375 < \lvert\eta\rvert < 3.2$	0.050×0.1 ($1.375 < \lvert\eta\rvert < 1.425$) 0.025×0.1 ($1.425 < \lvert\eta\rvert < 2.5$) 0.1×0.1 ($2.5 < \lvert\eta\rvert < 3.2$)
EM End-cap 3	$1.5 < \lvert\eta\rvert < 2.5$	0.050×0.025
Hadronic End-cap 0	$1.5 < \lvert\eta\rvert < 3.2$	0.1×0.1 ($1.5 < \lvert\eta\rvert < 2.5$) 0.2×0.2 ($2.5 < \lvert\eta\rvert < 3.2$)
Hadronic End-cap 1		
Hadronic End-cap 2		
Hadronic End-cap 3		
Forward Cal 1	$3.1 < \lvert\eta\rvert < 4.9$	$\approx 0.2 \times 0.2$
Forward Cal 2		
Forward Cal 3		
Tile Barrel 1	$\lvert\eta\rvert < 1.0$	0.1×0.1
Tile Barrel 2		
Tile Barrel 3		0.2×0.1
Tile Extended 1	$0.8 < \lvert\eta\rvert < 1.7$	0.1×0.1
Tile Extended 2		
Tile Extended 3		0.2×0.1

Table 3.2: Layers, coverage, and granularity of the ATLAS calorimeter system.

lose energy though bremsstrahlung (photon emission through radiation during deceleration or acceleration when scattering) which rises approximately linearly with energy as shown in Figure 3.12. High energy photons lose energy primarily through e^+e^- pair production. Hadrons lose energy differently than electrons and photons in that they interact via the strong force and produce showers that look different and are harder to detect (see Figure 3.11).

The radiation length X_0 is the mean distance over which a particle loses 1/e of it's original energy through bremsstrahlung radiation. It is also defined as 7/9 the mean free path over which a photon travels before it undergoes pair production. It is the appropriate length scale for electromagnetic cascades and has units of g/cm^2. It depends on the specifications of the material the particle is propagating through and increases with increasing atomic number A and decreases with increasing Z ($\sim A/Z^2$) [8]. The transition between where electron energy loss is dominated by bremsstrahlung and ionization is called the critical energy E_c. For an electron in lead it is about 7.6 MeV [202].

When electrons and photons move through the detector they produce electromagnetic showers. Bremsstrahlung radiation by electrons produces photons and e^+e^- pair production

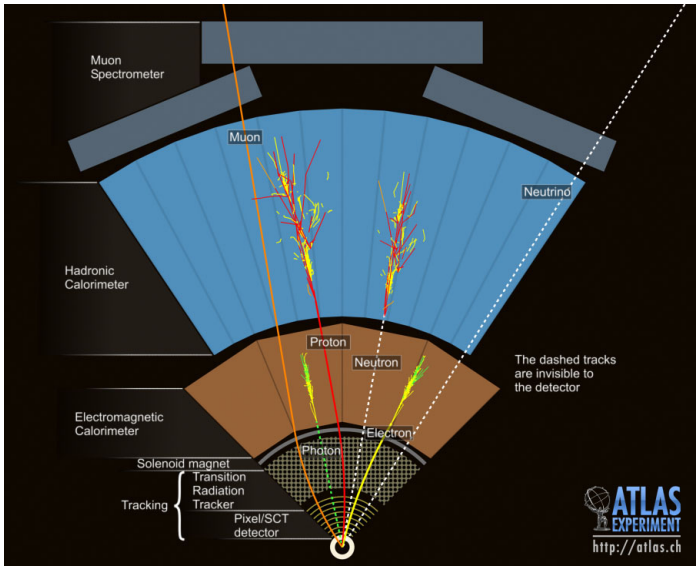

Figure 3.11: A diagram of how each type of particle showers and is detected in the ATLAS detector.

produces positrons and electrons. These electrons and photons then undergo these processes again and again, which produces a shower of many particles in the detector. As the shower progresses the energy of the initial particle is distributed to the showering particles and once those particles in the shower are at energies below the critical energy they no longer radiate and thus no longer contribution to the shower. This can be described using the simplified cascade model, where each photon travels one radiation length and then gives up half it's energy into a photon and each electron travels one radiation length and gives up half it's energy into both an electron and a positron [203]. This is demonstrated in Figure 3.13. This keeps happening until the photon and electron energies drop below E_c. Thus the energy drops by a factor of two each radiation length, resulting in the relation $E = E_0/2^t$, where t is the number of radiation lengths traveled, x/X_0, and x is the total shower depth. Using this relationship, the shower depth for EM showers is given in Eq. 3.11, which shows that the shower varies logarithmically with the original energy of the particle. More complicated models describe this in more detail and it has also been observed experimentally. This describes the longitudinal size of the shower but the transverse size is also important. This is given by the Moliére radius, $R_M = X_0(21\ \text{MeV}/E_c)$ [8].

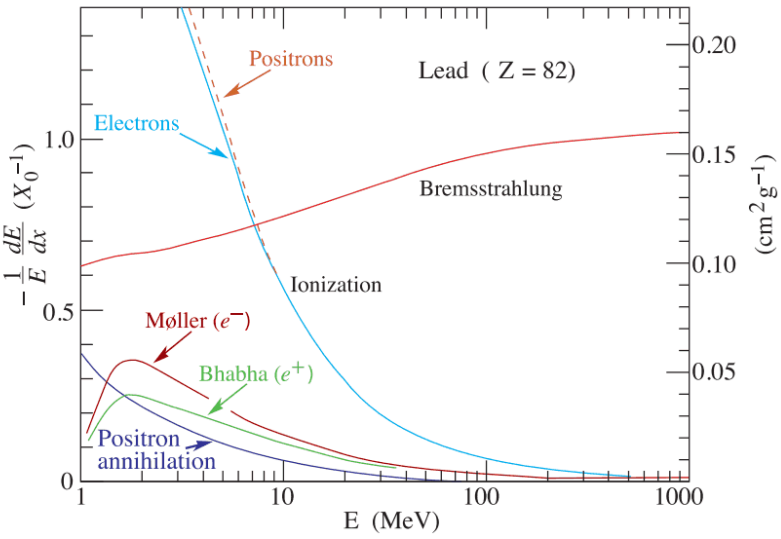

Figure 3.12: The fractional energy loss per radiation length of an electron/positron in lead as a function of the energy of the particle [8].

$$x = X_0 \frac{\log\left(E_0/E_c\right)}{\log 2} \tag{3.11}$$

Particles that are not electrons or photons, or particles that decay into them like π_0, are measured through hadronic showers instead of exclusively EM showers. The processes that dictate hadronic showers are much more complicated than those for EM showers because they involve the strong interaction from QCD. Hadronic showers come from both charged and neutral hadrons like pions, kaons, protons, and neutrons that undergo mainly inelastic hadronic interactions that result in multiple secondary particles. About 1/3 of the time the resulting hadrons produce EM showers (from neutral particles like π_0) and decay into photons and electrons. The hadrons also lose energy via ionization, excitation, and interactions with the nuclei. The ionizing particles and photons from de-excitation produce energy in the calorimeter but recoiling nuclei do not. Neutrons interact via elastic collisions then thermalize and are captured, thus their energy isn't detected. This lost energy that is not detected is called "invisible" energy and accounts for about 30% of the total. A diagram of a hadronic shower and the different components (or types of energy) is shown in Figure 3.14. Hadronic showers are slower than EM showers and are longitudinally and transversely larger

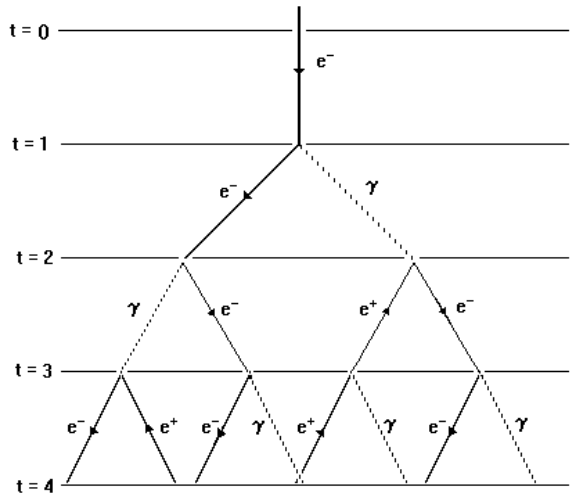

Figure 3.13: A diagram of the simple cascade model for an EM shower [203].

so the hadronic calorimeter sits behind the EM calorimeter in the ATLAS detector so the EM calorimeter can catch some of the shower that is EM. The large fluctuations in the fraction of the shower that is EM and the "invisible" energy make the hadronic showers more challenging to measure.

The nuclear interaction length λ is the mean path length over which a hadron loses 1/e of it's original energy. It is proportional to $A^{1/3}$, thus is about $A^{4/3}$ longer than X_0. For lead that means that the hadronic shower has a depth 30 times the EM shower.

The radiation lengths in the EM calorimeters in ATLAS are shown in Figure 3.15. In the barrel EM calorimeter X_0 is always greater than 22 (left) and in the end-cap it is always greater than 24. The nuclear interaction length in the hadronic calorimeters in ATLAS is shown in Figure 3.16. In the barrel it is approximately 9.7λ and in the end-cap it is approximately 10λ. The calorimeter is this thick to avoid "punch through" where the shower is not contained in the calorimeter and goes into the muon spectrometer making the shower not fully reconstructed.

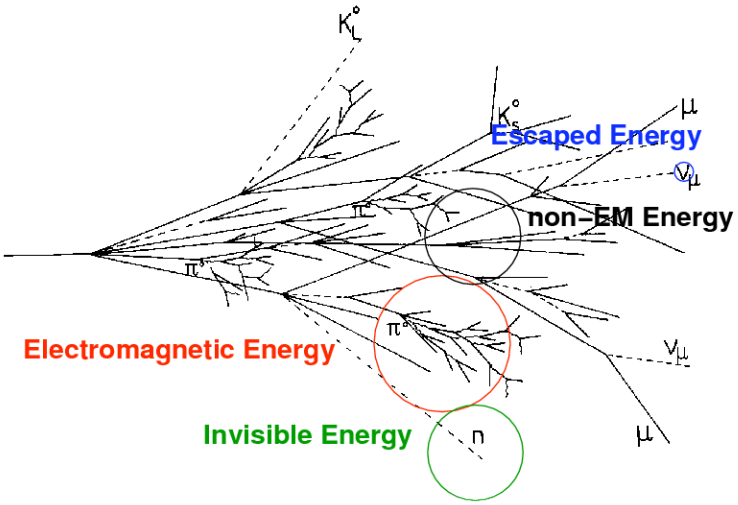

Figure 3.14: A diagram of the components of a hadronic shower [204, 205].

3.2.3.2 EM Calorimeters

The ATLAS EM calorimeter [206] consists of a barrel component (EMB) that covers $|\eta| < 1.475$ and the two-end caps (EMEC) that cover $1.375 < |\eta| < 3.2$ each. All the systems use LAr technology with lead plates as the absorber and LAr as the active medium. The LAr is kept at around 80 K by nitrogen refrigeration. When a particle hits the absorber it's energy is converted into a shower of particles. The particles ionize the LAr gas, which

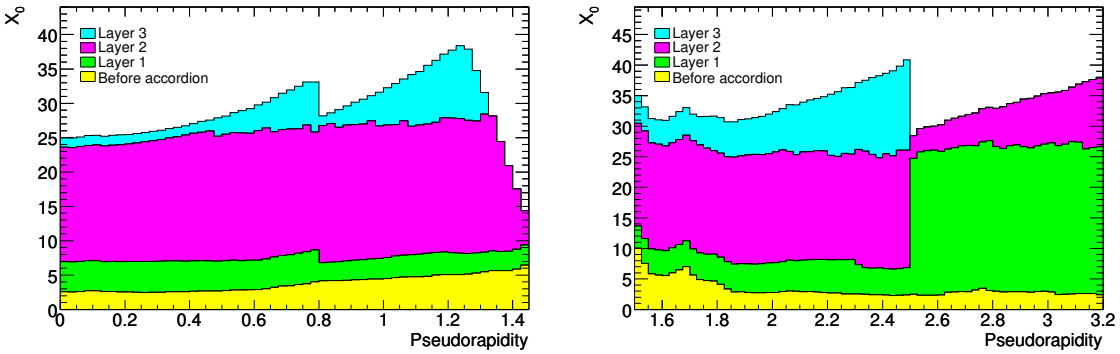

Figure 3.15: The $|\eta|$ dependence of the radiation length in the EM calorimeter at ATLAS. The left shows the barrel region and the right shows the end-cap.

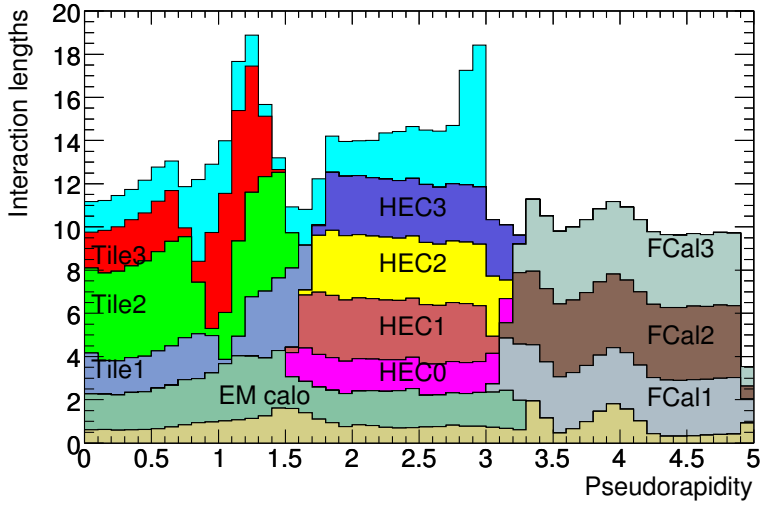

Figure 3.16: The $|\eta|$ dependence of the nuclear interaction length in the hadronic calorimeter at ATLAS.

frees electrons that can be read out as a measurable current. The calorimeter alternates between the absorber and LAr layers in regular intervals to make sure it is deep enough to capture the energy of the full shower.

The EMB consists of two identical half barrels that are separated in the center by 4 mm at $\eta = 0$. The total length of the barrel is 3.2 m with an inner radius of 2.8 m and an outer radius of 4 m. Each of the half barrels have 16 modules. The EMEC has two coaxial wheels with a boundary at $|\eta| = 2.5$ of 3mm, where the outer wheel covers $1.375 < |\eta| < 2.5$ and the inner wheel covers $2.5 < |\eta| < 3.2$. Each wheel is 63 cm thick with an external radius of 2098 mm and an internal radius of 330 mm and is divided into 8 modules that are shaped like a wedge.

The lead absorbers are accordion shaped and interweaved with kapton electrodes. This particular geometry allows for full ϕ coverage and symmetry with no cracks. The EMB has 1024 accordion absorbers and the EMEC has 768 absorbers in the outer wheel and 256 in the inner wheel. The folds of the accordion are axial in the barrel and radial in the end-cap and the sizes and angle of the folds change with the radius in order to keep the LAr gaps even. The accordion geometry is demonstrated in Figure 3.17. In the EMB the lead plates are 1.55 mm thick for $|\eta| < 0.8$ and 1.13 mm thick for $|\eta| > 0.8$ which keeps the fraction of the energy sampled from decreasing with increasing $|\eta|$. In the EMEC the plates are 1.7 mm thick for $|\eta| < 2.5$ and 2.2 mm thick for $|\eta| > 2.5$. The read-out electrodes consist of three layers of conductive copper with polyimide sheets in between. The outer layers are kept at a high voltage potential of 2000 V which allows the electrons to drift across a gap of 2.1 mm with a drift time of 450 ns, to the inner layer that is then used for reading the signal. In the end-cap the gap sizes increases with radius in order to keep the response constant. The η granularity is determined by etching the cells onto the readout boards.

The EMB region within $|\eta| < 2.5$ is where the precision physics can be measured. Therefor, this region has been split into three layers with different granularity, shown in Table 3.2. The granularity and interaction lengths of the layers have been optimized to measure the full calorimeter shower's energy and position. The first layer in finely segmented in pseudo-rapidity (0.003×0.1) to measure the details of the shower over a shorter interaction length. The fine η granularity helps separate photons from neutral pions decaying to photons. The

second layer is coarser in pseudorapidity but finer in azimuth, covering the majority of the interaction length (0.025×0.025) to absorb the largest part of the shower. The third layer captures the remainder of the shower from particles with high energies and covers different lengths depending on the psuedorapidity. It has a coarser granularity (0.05×0.025). The EMEC has a similar depth and granularity design as in the EMB.

Both the EMB and the EMEC have a presampler detector ($|\eta| < 1.8$) that corrects for the energy lost by electrons and photons upstream of the calorimeter. There is a 1.1 cm LAr layer in front of the barrel and a 0.5 cm layer in front of each end-cap. The barrel has 64 sectors in azimuth that are 3.1 m long and 0.28 m wide. The end-caps have 32 modules in azimuth.

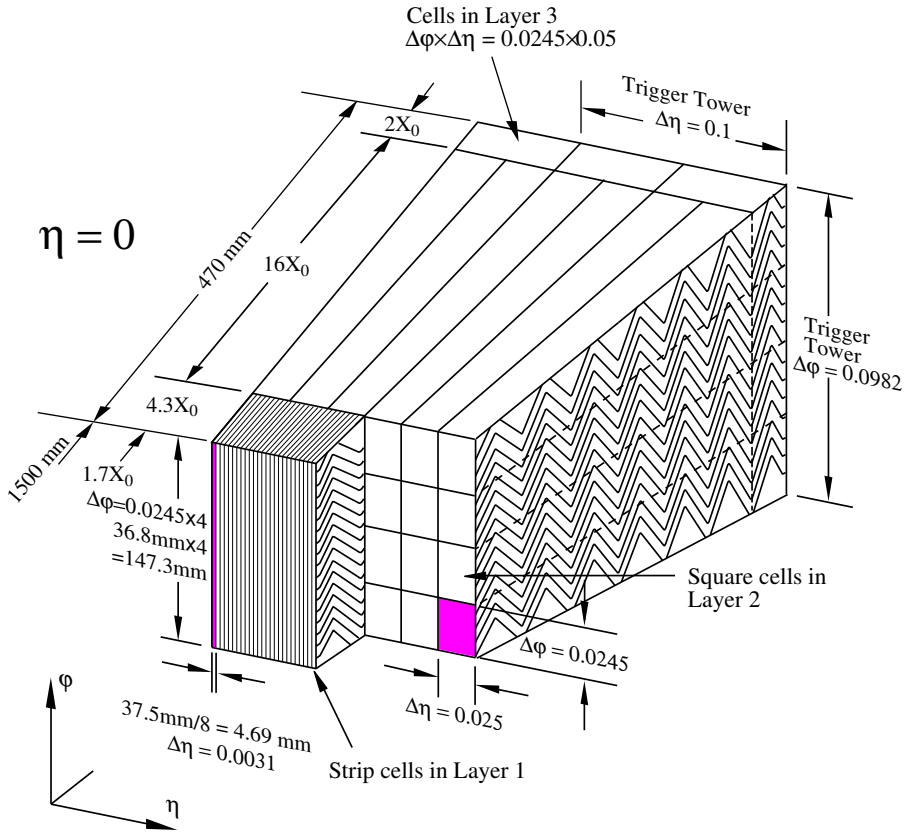

Figure 3.17: The segmentation of a barrel module in the EM calorimeter depicting the accordion geometry. The granularity of the layers are shown.

3.2.3.3 Hadronic Calorimeters

The hadronic calorimeter consists of Tile Calorimeters with a barrel portion that covers $|\eta| < 1.0$ and an extended barrel that covers $0.8 < |\eta| < 1.7$ which sit behind the EMB. There is also a LAr hadronic end-cap (HEC) component that uses similar technology to the EM LAr calorimeters described in Section 3.2.3.2 which covers $1.5 < |\eta| < 3.2$ and sits behind the EMEC. Finally, there is a forward calorimeter (FCal) which covers $3.1 < |\eta| < 4.9$ and has the first layer for EM calorimetry and the next two for hadronic calorimetry.

The Tile Calorimeter [207] is a sampling calorimeter that uses alternating layers of steel as the absorber and scintillating tile made of poylysterene plastic as the active material. It contains a central barrel that is 5.8 m in length and two extended barrels that are 2.8 m in length, both with an inner radius of 2.28 m and an outer radius of 4.25 m. The gaps between the barrel and the extended barrel are filled with smaller steel scintillators which allow for partial recovery of the energy lost in the gaps. Each barrel has 64 modules in azimuth with wedge sizes of $\Delta\phi \approx 0.1$ that have 11 layers of tile stacked on top of each other. Each tile is 3 mm long and have radii that vary between 97 and 187 mm and azimuthal lengths between 200 and 400 m. In order to obtain full azimuthal coverage the tiles are laid out radially normal to the beam line. The high energy particles hit the scintillating tile and are ionized, creating UV scintillating light. The UV light is then converted to visible light using wave-length shifting fibers at the end of tiles for read-out. The fibers are 1 mm in diameter and are grouped together into photomultiplier tubes (PMTs) that collect the light. The groupings make up three layers of depth that are 1.5, 4.1, and 1.8λ thick for the barrel and 1.5, 2.6, and 3.3 λ for the extended barrel, each with different granularities. A diagram of a tile module is shown in Figure 3.18.

The HEC is very similar to the LAr EM calorimeter components except that it uses copper plates as absorbers instead of lead and does not use the accordion geometry. It simply has alternating stacks of absorbers and LAr medium that are perpendicular to the beam axis. The HEC covers the overlap between the Tile Calorimeter and the FCal. It consists of two independent wheels per end-cap that each have 32 wedge-shaped modules. Each wheel is divided into two layers in depth so that there are four layers total in each end-cap, where the front wheel has four times finer granularity than the back wheel. The

front wheel contains 24 copper plates that are 25 mm thick and the back wheel contains 16 copper plates that are 50 mm thick. The plates extend radially from 0.475 m (except for the first nine which start at 0.372 m) to 2.03 m. The LAr gaps are 8.5 mm thick and have three electrodes with four drift zones that are each 1.8 mm wide. The outer electrodes hold the high voltage at 1800 V and the center electrodes are the read-out. Figure 3.19 shows a diagram of the HEC.

The FCal contains three layers, which are shown on the left panel of Figure 3.20. The first layer is for EM calorimetry and have copper as the absorber. The next two layers are for hadronic calorimetry and have tungsten as the absorber. They all have LAr as the active medium. It sits 1.2 m back from the EM calorimeter very close to the beam pipe so it experiences large particle fluxes and thus needs to have a high density design in order to capture all the energy in less material. Each of the layers have a 45 cm depth and the LAr

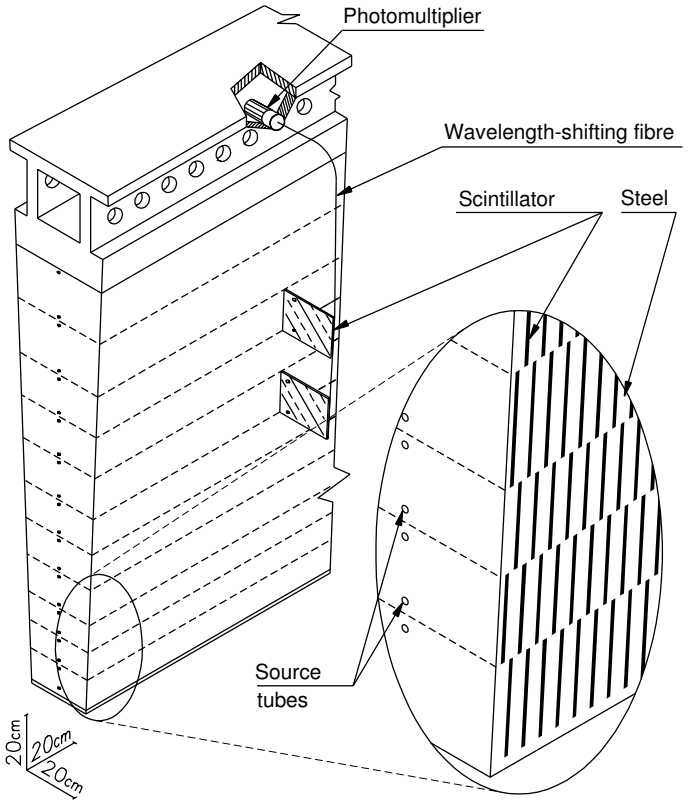

Figure 3.18: A diagram of the a tile module in the Tile Calorimeter.

gaps are much smaller so the calorimeter is denser. The first layer has holes drilled into the plates where cylindrical electrodes that are parallel to the beam-pipe sit. The electrodes consist of a copper rod inside a copper tube separated by a plastic fiber wrapped around the rod. The space between the electrodes are filled with LAr and make 0.249 mm gaps. The layout of the electrodes in the first FCal is shown in the right panel of Figure 3.20. The second and third layer have a similar geometry except the electrodes have a tungsten rod inside a copper tube to maximize the number of interaction lengths for the layers. The FCal is extremely important for heavy ion collisions since it is used to measure centrality.

3.2.4 Forward Detectors

There are a number of detectors that sit at very forward psuedorapidity, close to the beam line, in order to measure global quantities such as luminosity or centrality or to perform a global trigger. The location of the forward detectors is summarized in Table 3.3. The luminosity detectors consist of LUCID, BCM, and ALFA. The ZDC is another forward

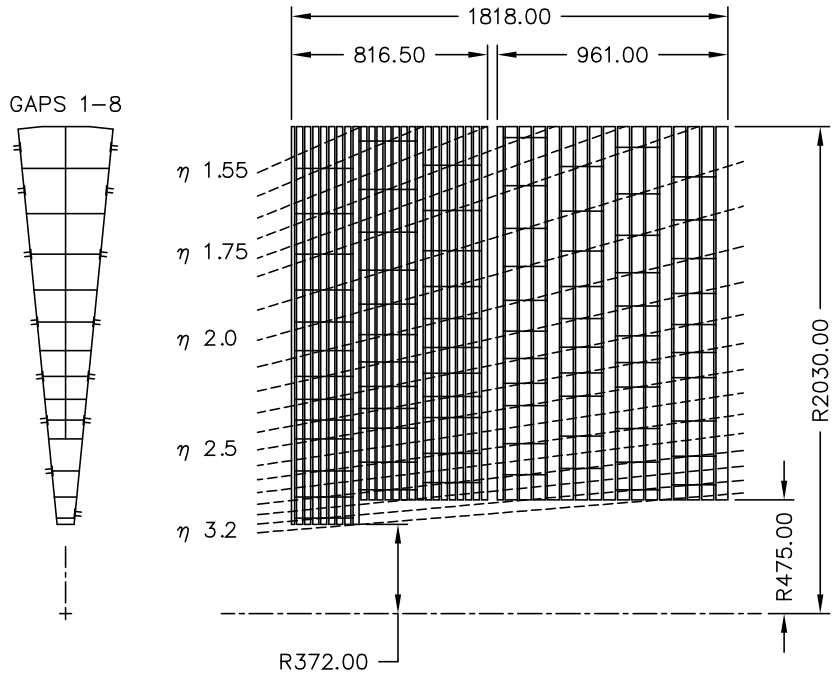

Figure 3.19: A diagram of the HEC, where the left image is in the radial and azimuth direction and the right image is in the radial and z direction.

detector useful for measuring centrality in heavy ion collisions and the MBTS is a detector that serves as a trigger.

Detector	Coverage	Dist. from IP ($\|z\|$ [m])
LUCID	$5.6 < \|\eta\| < 5.9$	17
BCM	$\|\eta\| \approx 4.2$	1.9
ZDC	$8.3 < \|\eta\|$	140
ALFA	$10.6 < \|\eta\| < 13.5$	240

Table 3.3: Location and coverage of the forward detectors.

3.2.4.1 Luminosity Detectors

LUCID stands for LUminosity measurement using Cherenkov Integrating Detector and is located 17 m from the interaction point on either side of the detector. It is the main relative luminosity monitor in ATLAS. It detects inelastic scattering in the forward direction to perform measurements of the integrated luminosity and the online instantaneous luminosity and beam conditions. The detector needs to be radiation hard and have good timing resolution because of the short bunch spacings in Run 2 (25 ns). The detectors are located

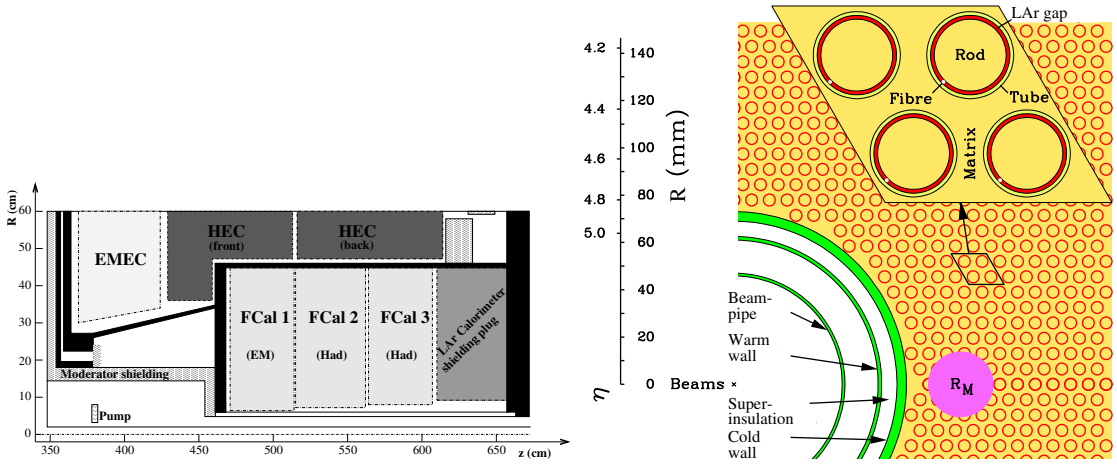

Figure 3.20: The left panel is a diagram of the FCal showing the location of the three layers with respect to the EM end-cap and HEC. The right panel is a schematic of the electrode structure in the copper plates of the first layer of the FCal. The tubes and rods, along with the LAr gaps are indicated. The Moliere Radius (R_M) is shown for scale.

at a radial distance of about 10 cm from the beam which corresponds to a pseudorapidity of about 5.8. It is made of 20 aluminum tubes that surround the beam pipe directed toward the interacting point. Each tube is 1.5 m long and 15 mm in diameter and is filled with C_4F_{10} at a constant pressure of 1.2 to 1.4 bar. This allows for the measurement of Cherenkov radiation from the incident particles that is then collected in the PMTs. The pulse-height of the read-out is then used to count the number of particles that entered a tube and the number of particles is proportional to the number of interactions per bunch crossing μ which can be used to calculate the luminosity as described in Section 3.1.4. LUCID uses two algorithms (see Section 3.1.4): `LucidEvtOR` algoritm which requires greater or equal to one hit on either side of the interaction point and the `LucidEvtAND` which requires greater than or equal to one hit on both sides.

The BCM (Beam Condition Monitors) [208] are located 1.9 m from the interaction point on either side. Their primary purpose is the detect multiple proton bunches hitting collimators that are supposed to protect the detector systems and trigger an abort before radiation detector damage can happen. They also serve as complementary luminosity monitors to LUCID. There are four BCM detectors on each side of the interaction point that are positioned at a radius of 55 mm outside of the beam-pipe, which corresponds to a pseudorapidity of about 4.2. at equal locations in azimuth. They are made of Chemical Vapour Deposited (CVD) diamond sensors which ionizes when charged particles pass through them. The diamond is useful because it is very radiation hard which is needed for detectors that sit close to the beam pipe. At 5 cm radially out from the diamonds there are RF amplifiers that collect the signal from the diamonds. The BCM uses two different algorithms (briefly described in Section 3.1.4) `BCMVEvtOR` and `BCMVEvtOR` which correspond to one hit on either side of the interaction point in the horizontal or vertical pairs of detectors, respectively.

The ALFA (Absolute Luminosity For ATLAS) detectors are located 240 m from the interaction point on either side. They are used to determine the absolute cross section and luminosity by measuring elastic scattering a small angles since the optical theorem relates the elastic-scattering amplitude in the forward direction directly to the total cross-section. They can get very close to the beam (1 mm away) in order to measure at the very small angle of 3 μrad. They are made of scintillating fiber trackers inside of Roman pots. A

Roman pot is a detector volume (the pot) that is separated from the vacuum system of the beam but is connected to the beam-pipe such that it can be moved very close to the beam. Each detector is made of ten double-sided modules that each have 64 fibers with a width of 0.5 mm. This detector can only be ran with special conditions where there is low emittance and high β^*.

3.2.4.2 Zero-Degree Calorimeters

The ZDC (Zero-Degree Calorimeters) measure neutral particles at $|\eta| > 8.2$ and are located 140 m in both directions from the interaction point. There are four modules on each side where the first is an EM module and the last three are hadronic modules. Each module consists of 11 tungsten plates whose faces are perpendicular to the beam direction alternating with steel absorbers and 1.5 mm quartz strips. The incident particles shower when they hit the absorber and produce Cherenkov light in the quartz that are fed through air light-guides to the PMTs at the top of the detectors. There are additional quartz rods that penetrate the tungsten to measure the position of incident particles.

Each side produces a L1 trigger signal called `ZDC_A` and `ZDC_C` that are made by passing the signal through a discriminator to the Central Trigger Processor (CTP) (more details in Section 3.2.5). The coincidence trigger, `ZDC_A_C`, is the logical `AND` of these two triggers. It's main purpose is to look for forward neutrons in heavy ion collisions to measure centrality and more recently to perform measurements in ultra-peripheral collisions (UPC).

3.2.4.3 Minimum Bias Scintillating Trigger

The MBTS, which stands for Minimum Bias Scintillating Trigger [209], is used as a trigger on minimum bias events, which are events selected with as little bias as possible, and to remove background events offline. It consists of 32 octagonal scintillator counters that are each 2 cm thick separated into two disks on each side of the ATLAS detector (A and C). They are located in front of the EMEC cryostats at 3560 mm in either direction from the interaction point so the surface of the disks are perpendicular to the beam-pipe. The disks have an inner and outer ring from 153 to 426 mm and 426 to 890 mm, respectively. The inner ring covers a range of $2.82 < |\eta| < 3.84$ and the outer ring covers a range of $2.09 < |\eta| < 2.82$.

The rings were divided into eight independent trapezoidal sectors in azimuth that are $\pi/4$ radians each. When particles hit the detectors, light from the scintillators is transferred through wavelength-shifting fibers to the PMTs.

The signals from the PMT are amplified by the Tile Calorimeter electronics and put through a leading edge discriminator that sends a pulse to the CTP (see Section 3.2.5). A hit in the MBTS is a signal above the discriminator threshold. This is done separately for each module over the threshold. Coincidence triggers are made from the individual hits to make L1 triggers (see Section 3.2.5) named `MBTS_N`, which is a total of N hits in either of the sides, or `MBTS_N_N`, which is N hits in each side.

In additional to a minimum bias trigger, the MBTS is used for timing. A time is reported for each side of the detector (t_A and t_C) relative to the LHC clock that is the average time over the wedges that have a hit. The time difference ($t_A - t_C$) is used as a cut offline to reject out of time background which is background that is not connected to a collision or left-over signal from previous bunch crossings.

3.2.5 Trigger and Data Acquisition

At the LHC the events are so large (25 MB per event) and the rate is so high (40 million Hz) that the amount of data per second (1 thousand TB/s) is too large to be recorded due to processing power limitations and storage. Triggers are a way to quickly select a small portion of the total that are useful events for physics to record so that all of the events do not have to be processed and stored. Triggers use a combination of hardware level and software level criteria, where the hardware decisions are made in μs and use data from subsets of the detector and the software decisions make subsequent decisions with more detailed information from all the detectors with more complicated algorithms. The trigger system at ATLAS [210, 211] has three components: Level 1 (L1), Level 2 (L2), and event filter (EF) triggers. The L1 trigger is hardware based and the L2 and EF trigger are software based and make up the HLT (High-Level Trigger). Each layer of the trigger builds on each other and adds additional selection criteria when necessary. The L1 trigger makes the decision in less than 2.5 μs (which is 100 bunch crossings) and reduces the rate to 75 kHz in Run 1 and 100 kHz in Run 2. The HLT triggers reduce the rate again to 200 Hz in

Run 1 and 1 kHz in Run 2 and to an event size of 1.6 MB in Run 1 and 2.4 MB in Run 2.

The L1 trigger looks for high p_{T} jets, photons, muons, electrons, τ-leptons that decay into hadrons, and large $E_{\mathrm{T}}^{\mathrm{miss}}$ and $E_{\mathrm{T}}^{\mathrm{tot}}$. It utilizes reduced granularity information from a subset of detectors that include muon spectrometer components, all the calorimeter sub-systems for EM clusters, jets, τ-leptons, $E_{\mathrm{T}}^{\mathrm{miss}}$, and total transverse energy. The L1 Calorimeter Trigger (L1Calo) tries to find high-E_{T} objects using information from all the calorimeter components and sums of 7000 trigger towers with a granularity of $\Delta\eta \times \Delta\phi = 0.1 \times 0.1$. This information is moved to the Cluster Processor (CP) which identifies photons and electrons and the Jet/Energy-sum Processor (JEP) which uses jet trigger components to identify jets and calculate scalar E_{T} and $E_{\mathrm{T}}^{\mathrm{miss}}$. There is also a L1Muon that is not relevant to this thesis and thus not described. This information is then sent to the Central Trigger Processor (CTP) where the final L1 trigger decision is made. The CTP can process 512 items in a trigger menu with different requirements on the detector signals. The trigger items can be prescaled so that a fraction of the events that pass a given trigger are randomly ignored to reduce the rate of triggers that produce a high number of events regardless. The CTP also gives the number of the current luminosity block which is the smallest interval over which the instantaneous luminosity can be measured.

The Data Acquisition System (DAQ) is what receives all the information from readout electronics at L1 trigger rates. The data from the event is buffered until the L1 trigger decision is given and when it is accepted the data is transmitted over point-to-point Readout Links (ROL's) to the L2 trigger where event building is performed. This data is then moved again by the DAQ to the event filter, which are then moved to permanent storage. The DAQ also monitors, controls, and provides configurations for the ATLAS detector.

The L1 trigger defines Regions-of-Interest (RoI) which are η and ϕ regions in the detector that have been selected to have interesting features. This information is then used by the HLT. The L2 trigger uses the detector information, like energy, position, and signature type, within the RoIs at full granularity and precision. The information from the RoI contain information on energy deposited in the calorimeter which improves threshold cuts and information from the inner detector so tracks can be reconstructed to improve particle identification. Events that pass the L2 trigger are then fully reconstructed and the events

that do not are removed from memory. The next step is the Event Filter (EF) which looks at fully built events and can make more sophisticated cuts like on fully reconstructed jets (including subtraction procedures) or tracks. The ROIs are seeds to about 2500 "trigger chains" which are EF items seeded on an L1 and L2 trigger. Events the pass the EF are then passed to be recorded at TIER-0 by the DAQ so they can be fully reconstructed offline.

An overview of the ATLAS TDAQ (Trigger and DAQ) system in run 2 is shown in Figure 3.21.

In this thesis, both Run 1 and Run 2 data is used, including *pp*, Pb+Pb, and Xe+Xe collisions systems. Each system in each run utilizes different trigger streams that will be detailed in dedicated dataset sections of their corresponding chapters. There are two main streams that are used: `MinBias` stream which contains data from the MBTS or ZDC triggers and `HardProbes` stream which contains high energy heavy ion objects like jets or photons that do not happen as often. The `HardProbes` triggers can be used to select events with a

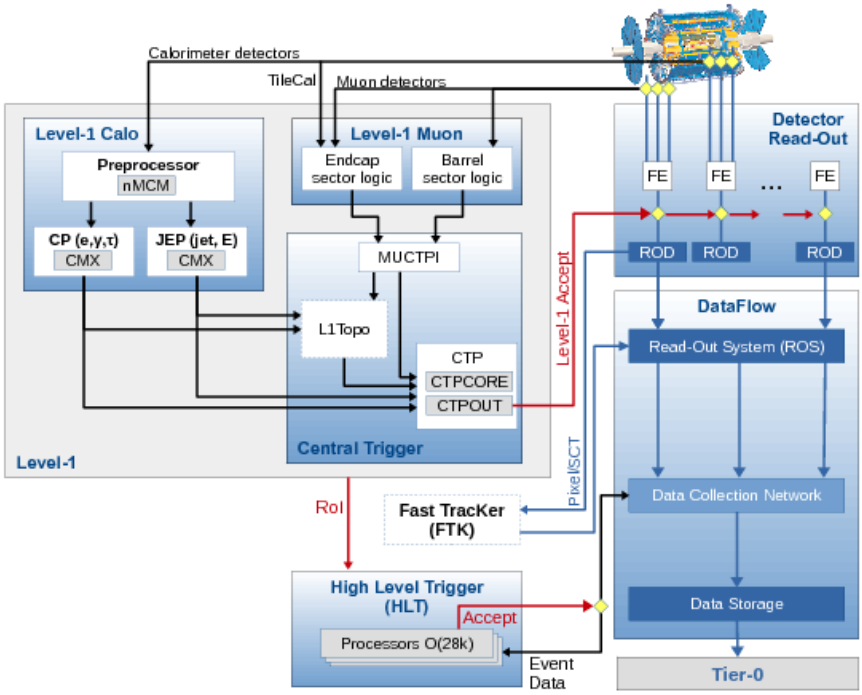

Figure 3.21: A diagram of the ATLAS TDAQ system in run 2 showing the trigger and DAQ components and the flow of data from one to the other.

reconstructed jet above some energy threshold and since these events are rare, saving the data only when this occurs allows more events to be stored.

Chapter 4

Jet Reconstruction and Performance

Jets need to be reconstructed from energy deposits in the calorimeter of the detector and calibrated before being used in a measurement. The jets in this thesis have been reconstructed in ATLAS using a similar reconstruction procedure detailed in Section 4.1 (and in Ref. [212]), that is developed specifically for heavy ions. Despite the measurements in this thesis being from different runs (Run 1 and Run 2), different center-of-mass energies (2.76, 5.02, and 5.44 TeV) and different collision systems (Pb+Pb, Xe+Xe, and pp), they all use a similar reconstruction procedure. This procedure will be discussed generally here and the jet performance will be shown for all the energies and systems used in the measurements with a focus on Run 2 in Section 4.5. Unfolding procedures will also be discussed in general (with some references to examples in the analysis chapters) in Section 4.6.

Jets in ATLAS HI collisions (and pp collisions) are constructed from 0.1×0.1 towers in the calorimeter using the anti-k_t algorithm [63] (discussed in Section 2.2.5). They can be grouped into various radii like $R = 0.2, 0.3, 0.4, 0.5$. This is shown in Figure 4.1, where the parton-level jets after the collision hadronize and then deposit energy in the calorimeter. These energy deposits are grouped together to form the jets. The energy of the towers are constructed from cells within the towers that are at the electromagnetic scale.

The jets in HI collisions have a large background due to the underlying event (UE) that

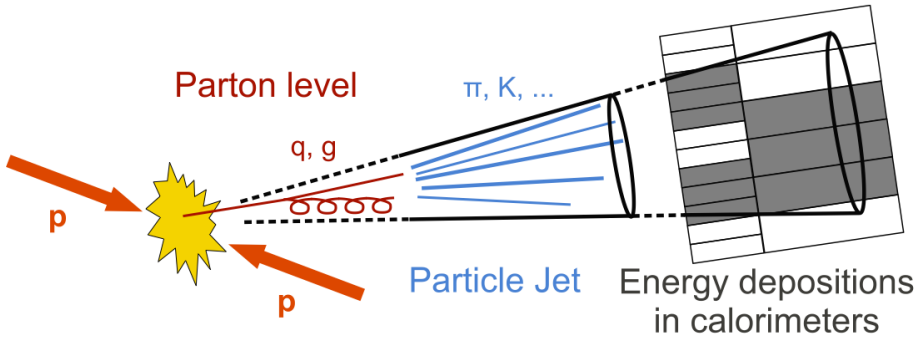

Figure 4.1: A diagram of how energy deposits in a calorimeter are grouped together to form jets.

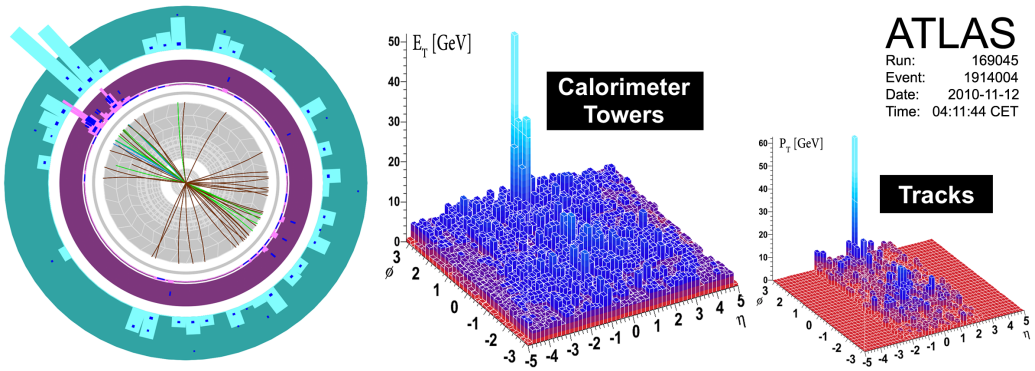

Figure 4.2: An ATLAS heavy ion event is shown from the 2.76 TeV Pb+Pb run in 2010. The left panel shows the calorimeter towers and tracks in the detector in the transverse plane. The center panel shows the E_{T} values of the calorimeter towers in η-ϕ space. The right panel shows the same thing but for the p_{T} of the tracks [1].

contributes energy inside the jet cone. It needs to be removed from the jet before the jets are used in a measurement. Figure 4.2 shows the E_{T} for each calorimeter tower in η and ϕ in the center panel. In this figure a jet can be seen above the large UE, where the UE varies largely with η and ϕ (and also event-by-event). This background needs to be subtracted from the jet shown in the figure. There can also be jets hidden underneath the background that need to be found by removing the background. The procedure for removing this UE background is detailed in Section 4.1.

4.1 Background Subtraction Procedure

The UE is subtracted from each cell in each calorimeter layer within the towers inside of jets. The procedure is iterative and uses a per-event average UE that is modulated by harmonic flow [106]. The energy density of the background is estimated by,

$$\frac{\mathrm{d}^2 E_{\mathrm{T}}}{\mathrm{d}\eta \mathrm{d}\phi} = \frac{\mathrm{d}E_{\mathrm{T}}}{\mathrm{d}\eta}(1 + 2\sum_{n} v_n \cos n(\phi - \Psi_n)) \tag{4.1}$$

where Ψ_n is the angle with respect to the event plane of the different flow harmonics and v_n are the amplitudes of the different flow harmonics (discussed in detail in Section 2.4.3.1). This energy density is additive to the actual jet energy density

$$\frac{\mathrm{d}^2 E_{\mathrm{T}}}{\mathrm{d}\eta \mathrm{d}\phi}^{\mathrm{total}} = \frac{\mathrm{d}^2 E_{\mathrm{T}}}{\mathrm{d}\eta \mathrm{d}\phi}^{\mathrm{jet}} + \frac{\mathrm{d}^2 E_{\mathrm{T}}}{\mathrm{d}\eta \mathrm{d}\phi}^{\mathrm{UE}} \tag{4.2}$$

so it can be subtracted in each cell in each layer within the jet. The subtraction is done layer-by-layer and cell-by-cell and the background density and harmonics values are determined in each layer to get the best estimate of the final jet energy. The subtraction is done in the following way

$$E_{\mathrm{T}}^{j}|_{\mathrm{sub}} = E_{\mathrm{T}}^{j} - A_{ij}\rho_i(\eta_j)(1 + 2v_{ni}\cos 2(\phi_j - \Psi_n)) \tag{4.3}$$

where j represents the cells, i represents the layers, and $A_{ij} = \Delta\phi\Delta\eta$ is the area of the cell. The $\rho(\eta)$ is the per-event average energy density measured in strips of η and over the full 2π in azimuth.

The jets bias the estimation of the UE by overestimating the background since the jet's energies will be part of the total background. This causes an underestimation in the jet energy once this background is removed, called self energy bias (SEB). Therefore, this procedure is iterative so that the jets can be first found and then removed before estimating the background density. These jets are referred to as seeds. The procedure is described step-by-step below (and in Ref. [213]) with Figure 4.3 illustrating each step.

1. Find jet seeds: The jet finding algorithm is run on towers in the calorimeter without any background subtraction (left-most panel of Figure 4.3). This will find many jets

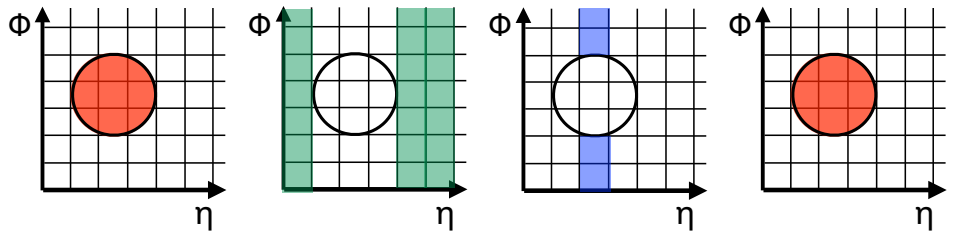

Figure 4.3: Diagrams depicting the UE event subtraction procedure.

that could be real or background so a "seed" is defined to try to distinguish the two. Here the seeds are defined to be $R = 0.2$ jets with at least one tower inside the jet with $E_{\mathrm{T}} > 3$ GeV. A discriminant factor,

$$D = \frac{E_{\mathrm{T}}^{\mathrm{max}}}{\langle E_{\mathrm{T}} \rangle} \tag{4.4}$$

where $E_{\mathrm{T}}^{\mathrm{max}}$ is the maximum tower E_{T} and $\langle E_{\mathrm{T}} \rangle$ is the average tower E_{T} inside the jet, is required to be greater than 4 ($D > 4$). These selections find jets with denser cores because the background jets will have a more uniformly distribution of E_{T} values and a real jet will have core particles within that carry most of the energy.

2. Remove seeds and estimate v_n and Ψ_n: The jet seeds are removed from the distribution of towers in the calorimeter and the amplitude and the phase of the background modulation are estimated. In Run 1 only the $n = 2$ harmonics were used but in Run 2, $n = 2 - 4$ were used to get a better estimate of the background. This decision will be discussed in more detail in Section 4.5. The event plane angles, Ψ_n, are calculated using [214]

$$\Psi_n = \frac{1}{n} \tan^{-1} \frac{\sum_j E_{\mathrm{T}}^j w_j \sin 2\phi_j}{\sum_j E_{\mathrm{T}}^j w_j \cos 2\phi_j} \tag{4.5}$$

where w_j are tower weights that correct for local variations in the detector response. The index j represents summing over all the towers that are not in η regions where there are jets (as shown in the center right panel of Figure 4.3). This exclusion is done so that the harmonic modulation is not overestimated by the presence of the

jets. The amplitude is calculated in each layer of the calorimeter using

$$v_n^i = < \cos 2(\phi - \Psi_n) >^i = \frac{\sum_{j \in i} E_{\mathrm{T}}^j \cos 2(\phi_j - \Psi_n)}{\sum_{j \in i} E_{\mathrm{T}}^j} \tag{4.6}$$

where the towers are again only outside of η regions containing jets. The harmonic variables are only calculated in the FCal region in Run 1 and in the full calorimeter in Run 2.

3. Estimate $\rho(\eta)$: The average density is estimated in each layer in strips of η using

$$\rho_i(\eta) = \frac{1}{N} \sum_{j \in i} \frac{E_{\mathrm{T}}^j}{A_{ij}} \frac{1}{1 + 2v_n^i \cos 2(\phi_j - \Psi_n)} \tag{4.7}$$

where the cells are only used if they are not inside or within $\Delta R < 0.4$ of the jet seeds (as shown in the center left panel of Figure 4.3).

4. Subtract the background: Using equation 4.3 the background is subtracted from each cell in each layer of the calorimeter.

5. Re-find jet seeds: The cells are grouped back into towers. Any negative energy cells from an over subtraction should be averaged out in this sum. The jet finding algorithm is then run again to find new jet seeds with $R = 0.2$ (as shown in the right-most panel of Figure 4.3). These new jets seeds are defined to be jets with $E_{\mathrm{T}} > 25$ GeV in Run 1 and > 30 GeV in Run 2. Track jets (defined in Section 4.2) that have $p_{\mathrm{T}} > 10$ GeV in Run 1 and $p_{\mathrm{T}} > 7$ GeV in Run 2 were also stored as seeds in this iteration step.

6. Determine the $\rho(\eta)$, v_n, and Ψ_n again excluding the new seeds and subtract this new background estimate from the original calorimeter cells using equation 4.3 but with these new variables.

7. Run the jet reconstruction again at any jet radii $R = 0.2, 0.3, 0.4, 0.5$. These are the final jets that come out of the jet reconstruction.

8. SEB and mutual energy bias (MEB) corrections: Although the jets were removed from the UE estimation to remove the SEB, the jets around the seed selection can

still have some impact from the SEB if the final jets don't match the seeds used. A SEB correction is applied to any jet that was not associated with a seed (this information is stored during the reconstruction). This selection classified jets as either biased or not, but there is an in between case where the region around the jet seed doesn't contain the entire geometry of a jet (just part of it). There can be a bias from the region where there is no overlap. There is also a MEB where any jet that isn't excluded from the background can cause an over subtraction of energy in another jet in the same η interval. The procedure to remove these effects looks at strips of η for jets that pass fake rejection (described in Section 6.2.1) but that have towers that weren't associated with a seed ($\Delta R > 0.4$) and sums the energies of those towers. This over subtracted energy is then added back into the real jets in that η strip. For jets correlated with seeds this is negligible but for jets with no overlap with the seeds the effect is 10 %. This is a geometric effect that comes from a scale of the areas since the new added energy would be $\rho' A_{\text{jet}}$, where ρ' is the density of the correction which is the summed energy found (or the original energy of the jet, E_{T}^{old}) divided by the area of the η slice $2 * R * 2\pi$. The energy added the becomes, $\Delta E = E_{\text{T}}^{old} * (\pi R^2/4R\pi) = E_{\text{T}}^{old} * (R/4) = E_{\text{T}}^{old} * (0.4/4) = 0.1 * E_{\text{T}}^{old}$ such that $E_{\text{T}}^{new} = E_{\text{T}}^{old} + \Delta E = E_{\text{T}}^{old}(1 + 0.1)$, which is a 10 % effect.

9. Calibration: The jets are at the EM scale after the reconstruction and need to be calibrated to the hadronic scale. This is done using a multiplicative constant that depends on the jet's energy and η. The details of the calibration procedure is discussed in Section 4.4.

After this procedure the jets can be used in an analysis. In this thesis, jets using $R = 0.3$ and $R = 0.4$ from both Run 1 and Run 2 are used.

4.2 Track jets

It was mentioned that track jets are also stored which are used as a cross-check on the calorimeter jet energies. Track jets are jets that have been reconstructed from the energy of charged particle tracks using the anti-k_t algorithm at $R = 0.4$. The tracks included in

the sum are required to have a $p_{\mathrm{T}} > 4$ GeV in order to suppress the UE. The tracks were also required to pass some track selection requirements.

4.3 MC samples

The measurements in this thesis use different MC samples. MC generators were discussed in Section 2.2.6) and the specific MC samples used in the different analyses are discussed in their respective MC sections. Here a general description of what type of MC samples are used for HI collisions will be discussed.

Typically in HI collisions the MC simulations start with some signal of "truth" (or generator level) jets in pp collisions. These jets usually come from some version of Pythia, where the jets are constructed from a parton shower modeled by the MC generator. These "truth" jets are then embedded into some background meant to represent the HI background in data. In some cases minimum bias `HIJING` (discussed in Section 2.5.2.5) Pb+Pb events are used with an afterburner to simulate the flow modulation using v_n values from data. A more effective way to simulate the background is to embed the jets into real minimum bias Pb+Pb data so that the MC has the same UE as the data. The MC generator signal and background are put through a GEANT4 [215] simulation of the ATLAS detector. The signals are then combined during the digitization state and reconstructed together as a combined event. This combined event is reconstructed in the same way as the data so that the effects of the UE and detector response can be seen in MC. The resulting jet after the reconstruction is called a "reconstructed" jet. The "truth" and "reconstructed" jets can be used to derive the calibration and also to evaluate the jet performance.

The Pythia samples are divided into J samples with fixed ranges on the jet $\hat{p_{\mathrm{T}}^{\mathrm{min}}}$ to $\hat{p_{\mathrm{T}}^{\mathrm{max}}}$ in the hard scattering with each having the same number of events. This allows the full p_{T} spectrum in the MC to have good statistics instead of relying on the power law behavior of jet p_{T} spectrum that will have low statistics at high p_{T}. A single background event is used once in each of the J samples. The ranges could be different for the different samples used in the analyses and are thus given in their respective analysis chapters. The J samples are then combined using cross-section weights from Pythia.

An issue can arrise when the overlaid background contains real jets that get reconstructed on top of the truth jets. In this case the energy of the reconstructed jet comes from both the truth jet and the real jet in the background and thus doesn't correspond to the original jet energy. In order to remove this effect a `MinBiasOverlay` stream [216] is produced, where the events used in the MC overlay from the minimum bias data or `HIJING` are separately analyzed to identify real jets. This sample was then used to remove all truth jets that overlapped with a real jet in the `MinBiasOverlay`.

The MC samples now have a background distribution with a $\Sigma E_{\mathrm{T}}^{\mathrm{FCal}}$ distribution like in the `MinBias` data, not like in the jet-triggered `HardProbes` jet data (discussed in Section 3.2.5), since the `MinBias` data was used for the overlay. The $\Sigma E_{\mathrm{T}}^{\mathrm{FCal}}$ distribution is used to characterize centrality and is discussed in Section 5.1.1.1. The events in the MC are re-weighted at a given $\Sigma E_{\mathrm{T}}^{\mathrm{FCal}}$ value using weights derived by taking the ratio of the $\Sigma E_{\mathrm{T}}^{\mathrm{FCal}}$ in the jet-triggered sample to the minimum bias sample. An example of this procedure is described in Section 6.3.1.1.

4.4 Calibration derivation

As already mentioned the jets have to be calibrated from the EM to the hadronic scale. This is done through a MC-based procedure called "EM+JES" [217] that is used in standard pp collisions. The procedure derives a multiplicative constant that can be applied to the jet four-momentum that depends on the η and p_{T} of the jet. It uses a numerical inversion procedure and is derived using HI jets in pp MC with data overlay. Standard EMTopo pp jets are different than HI jets (the jets described in all the steps above) in that the EMTopo jets use topological clusters of energy to form jets instead of the calorimeter towers. The calorimeter towers are used for HI jets because the conditions in the HI environment make the topo-clusters ill-defined. The calibration procedure for HI jets is described in Ref. [218]. The calibration calculates a response

$$R = \frac{E_{\mathrm{T}}^{\mathrm{EM}}}{E_{\mathrm{T}}^{\mathrm{truth}}} \tag{4.8}$$

which is evaluated for all calorimeter jets that are isolated from other calorimeter jets and that match a truth and a track jet (within $\Delta R < 0.3$). This response is evaluated as a function of the truth E_{T} and η. For each truth jet E_{T} and η the values of the mean response $\langle R \rangle$ and the mean EM-scale reconstructed E_{T}, $\langle E_{\mathrm{T}}^{\mathrm{EM}} \rangle$, is found using gaussian fits. The mean response is fitted as a function of $\langle E_{\mathrm{T}}^{\mathrm{EM}} \rangle$ for each truth E_{T} and η bin using a fourth-order polynomial in $\log E_{\mathrm{T}}^{\mathrm{EM}}$. This function, $F_{\mathrm{calib}}(E_{\mathrm{T}}^{\mathrm{EM}})$, is used as the multiplicative factor on the EM scale E_{T} to obtain the EM+JES scale energy,

$$E_{\mathrm{T}}^{\mathrm{EM+JES}} = \frac{E_{\mathrm{T}}^{\mathrm{EM}}}{F_{\mathrm{calib}}(E_{\mathrm{T}}^{\mathrm{EM}})} \tag{4.9}$$

This calibration is applied in AA and pp in both data and MC. An additional "cross calibration" is applied to the data to account for the difference between the calorimeter response in data and MC since the calibration factors are derived in MC. It is found by comparing the response between HI jet and EMTopo jets, since the EMTopo jets have a well-defined energy scale, in data and MC through the ratio

$$R_{\mathrm{xcalib}}(p_{\mathrm{T}}^{\mathrm{HI}}) = \frac{\langle \frac{p_{\mathrm{T}}^{\mathrm{HI}}}{p_{\mathrm{T}}^{\mathrm{EMTopo}}} \rangle|_{\mathrm{data}}}{\langle \frac{p_{\mathrm{T}}^{\mathrm{HI}}}{p_{\mathrm{T}}^{\mathrm{EMTopo}}} \rangle|_{\mathrm{MC}}} \tag{4.10}$$

and fitting it to a polynomial. The fit contants as a function of $p_{\mathrm{T}}^{\mathrm{HI}}$ and η are then used as multiplicative factors to the jet p_{T}.

4.5 Jet Performance

In this section the performance will mainly be discussed in the context of Run 2 jets at $\sqrt{s_{\mathrm{NN}}} = 5.02$ TeV in 2015 Pb+Pb and pp data and MC from Powheg+Pythia 8 with minimum-bias data overlay. The jet performance in Run 1 at $\sqrt{s_{\mathrm{NN}}} = 2.76$ TeV in 2011 Pb+Pb and 2013 pp data and MC from Pythia with minimum-bias data overlay has previously been investigated for the analysis in Ref. [5], but some results are shown here as well. Run 2 jets at $\sqrt{s_{\mathrm{NN}}} = 5.44$ TeV in 2017 Xe+Xe data and $\sqrt{s_{\mathrm{NN}}} = 5.02$ TeV in 2017 pp data and MC from Pythia 8+`HIJING` are also discussed.

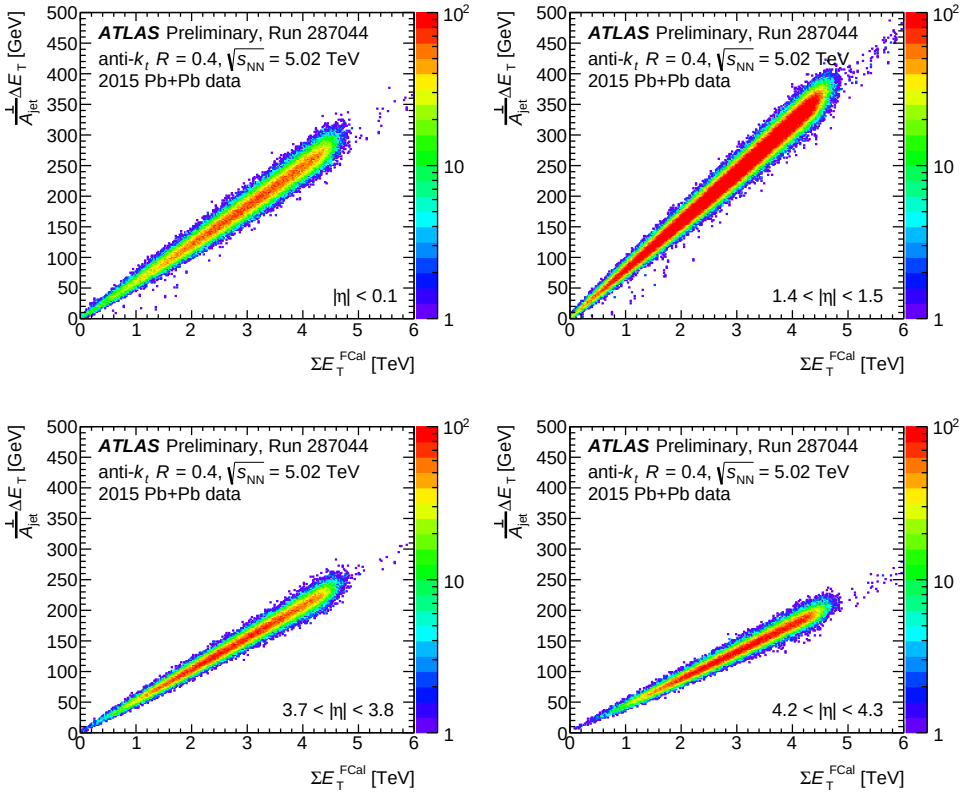

Figure 4.4: The subtraction energy ΔE_{T} as a function of $\Sigma E_{\mathrm{T}}^{\mathrm{FCal}}$ in four different η intervals for 2015 Pb+Pb data at $\sqrt{s_{\mathrm{NN}}} = 5.02$ TeV.

4.5.1 Subtracted E_{T}

The background subtraction procedure can be verified in HI data by looking at the energy that was subtracted, ΔE_{T}, as a function of $\Sigma E_{\mathrm{T}}^{\mathrm{FCal}}$. The UE is expected to increase with centrality or increasing $\Sigma E_{\mathrm{T}}^{\mathrm{FCal}}$. This is shown for Run 2 jets in Pb+Pb collision in Figure 4.4 in different η intervals since the UE varies with η as well as centrality. The subtracted E_{T} is shown to be linearly correlated with the $\Sigma E_{\mathrm{T}}^{\mathrm{FCal}}$ as expected.

This is also shown for the Xe+Xe data in run 2 in Figure 4.5 for jets having subtracted transverse momenta $p_{\mathrm{T}} > 35$ GeV. The η intervals use here are wider than the intervals used for the Pb+Pb case because of the limited statistics in Xe+Xe. The distributions also show the expected behavior.

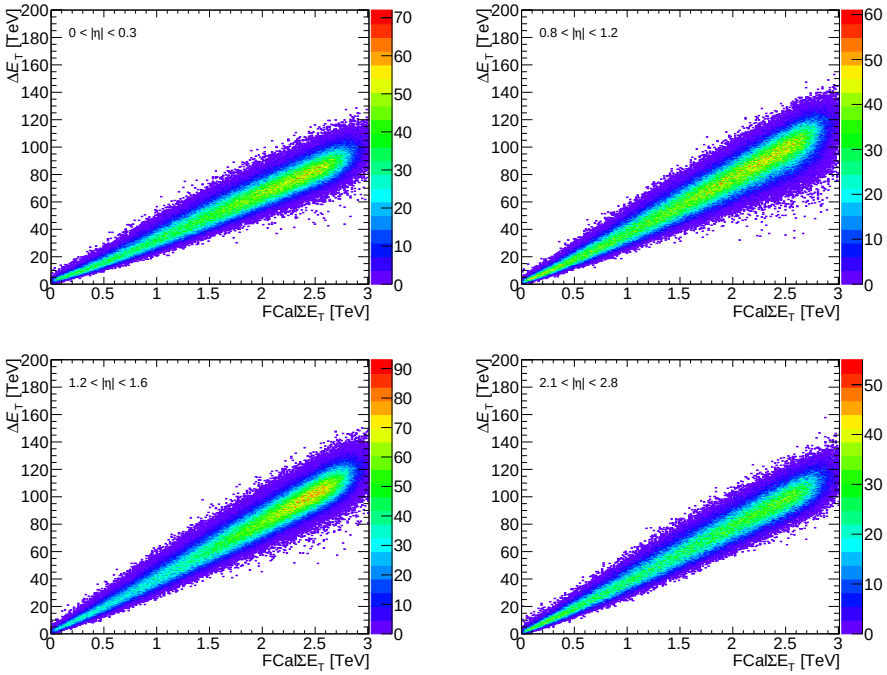

Figure 4.5: Distributions of subtracted jet transverse energy, ΔE_{T}, vs $\Sigma E_{\mathrm{T}}^{\mathrm{FCal}}$ for jets having $p_{\mathrm{T}} > 35$ GeV in different intervals of jet rapidity.

4.5.2 JES and JER

After the jet reconstruction, the jet performance is evaluated to determine how well any jet measurement can be done. The MC samples described in Section 4.3 are used where the Pythia jets are embedded in real minimum bias data (or `HIJING` for the Xe+Xe analysis) and reconstructed in the same way as data. This way the jets in the MC have the same UE as in the data. If the background subtraction is working, the energy of the jet after reconstruction should be back to energy of the before ("truth"). This is evaluated by looking at the jet energy scale (JES) and jet energy resolution (JER), which are found by evaluating the distribution of $p_{\mathrm{T}}^{\mathrm{reco}}/p_{\mathrm{T}}^{\mathrm{truth}}$ as a function of $p_{\mathrm{T}}^{\mathrm{truth}}$. If the background was completely removed this would be a gaussian centered at unity with the width of the gaussian equal to the detector resolution. Any deviations from unity are due to imperfections in the background subtraction procedure.

In MC the $p_{\mathrm{T}}^{\mathrm{reco}}/p_{\mathrm{T}}^{\mathrm{truth}}$ is found by matching truth and reconstructed jets within a $\Delta R = \sqrt{\Delta\eta^2 + \Delta\phi^2} < 0.3$. This is done in bins of η in pp collisions and in bins of centrality and η

in Pb+Pb collisions. The 2D distribution is shown in Figure 4.6, with the mean indicated in the black circles.

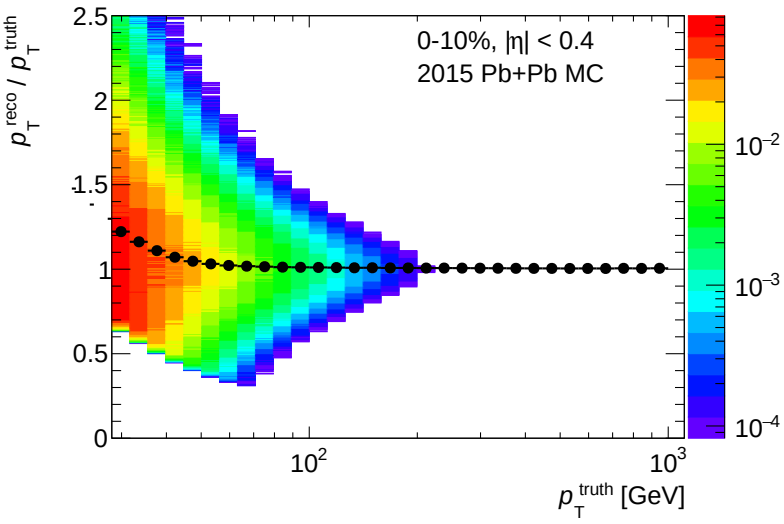

Figure 4.6: The $p_{\mathrm{T}}^{\mathrm{reco}}/p_{\mathrm{T}}^{\mathrm{truth}}$ as a function of $p_{\mathrm{T}}^{\mathrm{truth}}$ for 0-10% 2015 Pb+Pb MC at $\sqrt{s_{\mathrm{NN}}} =$ 5.02 TeVin $|\eta| < 0.4$. The mean of the distribution is shown in the black circles.

The JES and JER are the mean and width of this distribution, respectively. These are found by fitting gaussians in slices of $p_{\mathrm{T}}^{\mathrm{truth}}$. A schematic of this is shown in Figure 4.7 with the JES and JER indicated. Figure 4.8 shows some examples of gaussian fits to the slides in the 2D distribution. The fit is performed by fitting the gaussian once to get an estimate of the mean and width, which are used to truncate the distribution to remove non-gaussian tails. The distribution is then fit with a gaussian again to extract a new mean and width. The gaussian also needs to be truncated at low $p_{\mathrm{T}}^{\mathrm{truth}}$ where the kinematic cuts are reached.

The means and widths of each slice in η and centrality (including pp) are extracted and plotted as a function of the $p_{\mathrm{T}}^{\mathrm{truth}}$ in Figure 4.9, where the left shows the JES and the right shows the JER. The JES (or closure) is shown to be at most 1% at high p_{T}. It has a small centrality dependence which is expected since the UE is harder to remove in central collisions where it is the largest. The JER is shown to be largest in the most central collisions as well, where it is $\sim 16\%$ at 100 GeV and decreases to a value of about 5–6% at high p_{T}.

The JES in different η bins for different centralities in Pb+Pb are shown in Fig 4.10.

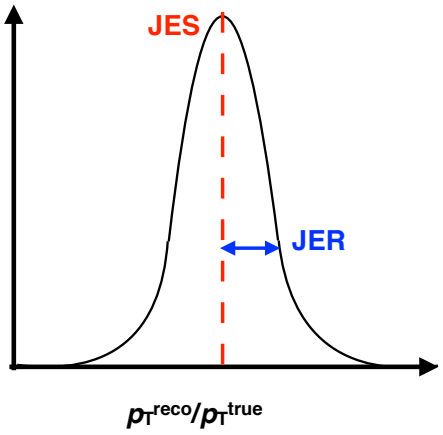

Figure 4.7: A diagram of a slice of the $p_{\mathrm{T}}^{\mathrm{reco}}/p_{\mathrm{T}}^{\mathrm{truth}}$ distribution where the mean (JES) is shown in red and the width (JER) is shown in blue.

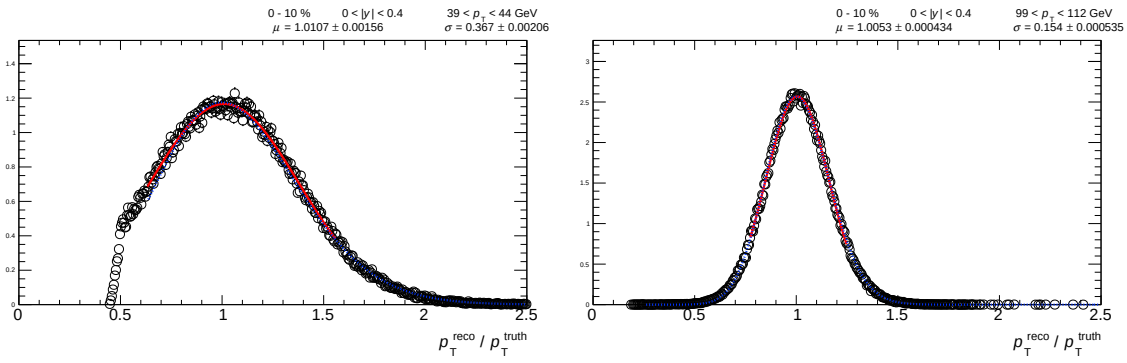

Figure 4.8: Two $p_{\mathrm{T}}^{\mathrm{truth}}$ slices of $p_{\mathrm{T}}^{\mathrm{reco}}/p_{\mathrm{T}}^{\mathrm{truth}}$ distribution for 0-10% 2015 Pb+Pb MC at $\sqrt{s_{\mathrm{NN}}} = 5.02$ TeVin $|\eta| < 0.4$ fit to a gaussian.

The JES tends to be worse in more forward rapidity where the detector response is less understood.

The JER in different η bins for different centralities in Pb+Pb are shown in Fig 4.11. The JER can be parameterized as

$$\sigma(\Delta p_{\mathrm{T}}) = a\sqrt{p_{\mathrm{T}}} \oplus b \oplus c p_{\mathrm{T}} \tag{4.11}$$

where a, b, and c are free parameters.

The parameters a and c are sensitive to the detector response and are expected to be

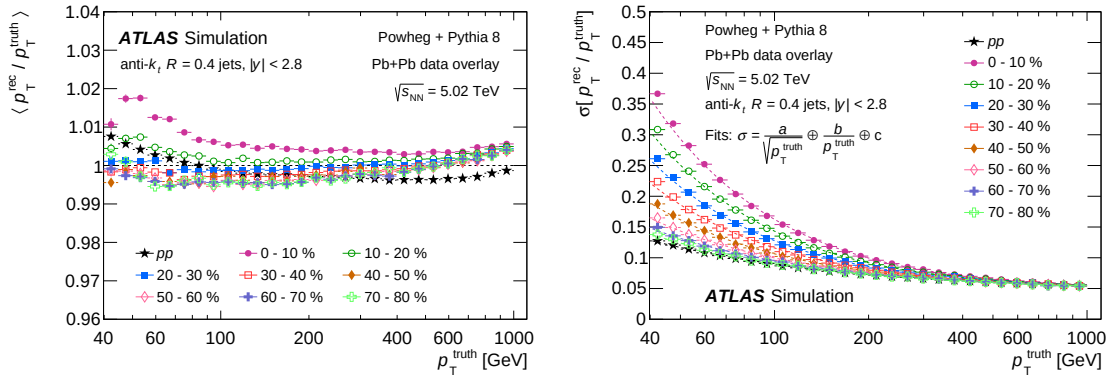

Figure 4.9: The left panel shows the JES as a function of $p_{\mathrm{T}}^{\mathrm{truth}}$ and the right panel shows the JER as a function of $p_{\mathrm{T}}^{\mathrm{truth}}$. Both are for jets inclusive in $|\eta| < 2.8$. The curves are for pp and Pb+Pb with different centralities in 2015 at $\sqrt{s_{\mathrm{NN}}} = 5.02$ TeV.

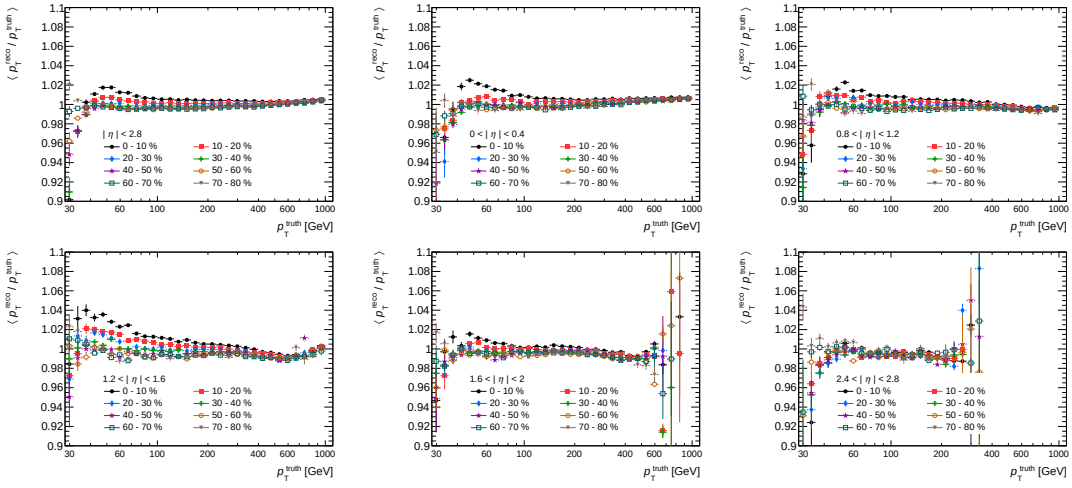

Figure 4.10: The JES as a function of $p_{\mathrm{T}}^{\mathrm{truth}}$ in different η bins and centralities.

independent of centrality. The b term is from fluctuations uncorrelated with the jet p_{T}. It is called the "noise" term because it is expected to be from electronic or pileup noise, but in HI (in all but the most peripheral HI collisions) it is actually from the UE fluctuations and the noise terms are small in comparison. The JER distributions are fit using equation 4.11 and the values for a and c are shown in Fig. 4.12 to be independent of centrality. The b term is shown in Fig. 4.13 to have a strong centrality dependence. The b term can be directly compared to an independent study of fluctuations in the data. This study is described in Section 5.5.2 and 7.2.

The JES and JER in $\sqrt{s_{\mathrm{NN}}} = 2.76$ TeV Pb+Pb and pp collisions from Run 1 data is

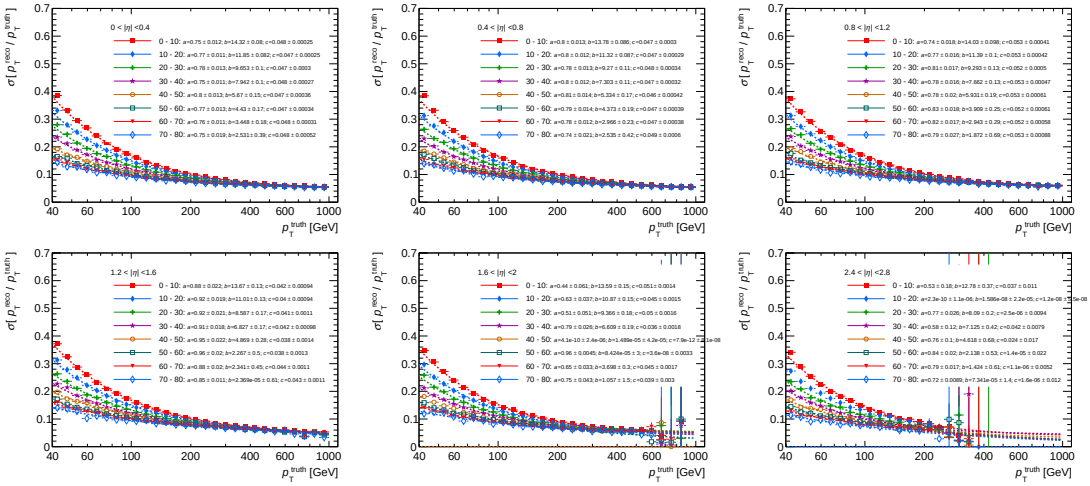

Figure 4.11: The JER as a function of $p_{\mathrm{T}}^{\mathrm{truth}}$ in different η bins and centralities.

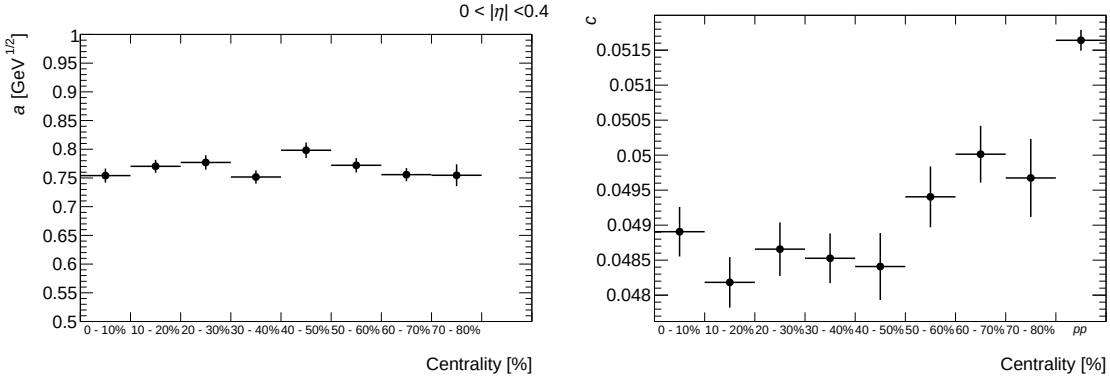

Figure 4.12: The a (left) and c (right) parameters from the fits of the JER using equation 4.11.

shown in Figure 4.14. Both the JES and JER have similar trends to the Run 2 results but the resolution is slightly lower due to the different center-of-mass energy that should produce a lower UE. The same thing is shown for $\sqrt{s_{\mathrm{NN}}} = 5.44$ TeV Xe+Xe and pp collisions from Run 2 data in Figure 4.15. The JER shows similar trends to Pb+Pb data except it is slightly low, which is expected due to the smaller system size. This is quantified in Section 7.2. The JES has a slight shift downward (corrected for in the analysis) that could be due to the fact that this analysis uses `HIJING` for the background.

The performance can have a flavor dependence since the detector can respond differently to quark and gluon jets. The difference between the JES and JER for quarks and gluons

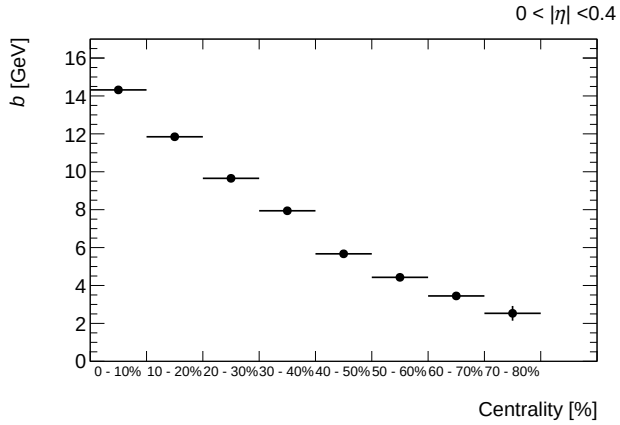

Figure 4.13: The b parameter from the fits of the JER using equation 4.11.

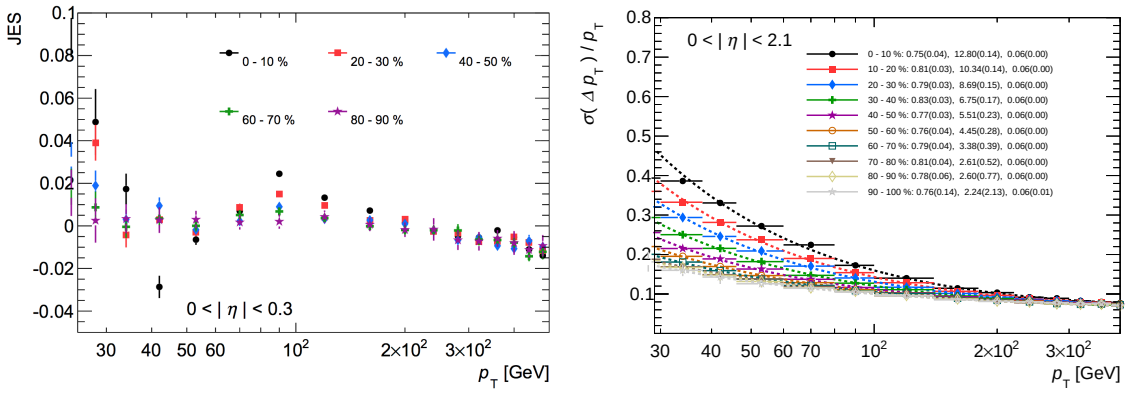

Figure 4.14: The left panel shows the JES as a function of $p_{\mathrm{T}}^{\mathrm{truth}}$ and the right panel shows the JER as a function of $p_{\mathrm{T}}^{\mathrm{truth}}$. The curves are for Pb+Pb with different centralities in 2011 at $\sqrt{s_{\mathrm{NN}}} = 2.76$ TeV.

in central and peripheral Pb+Pb collisions in shown in Figure 4.16. The top panel shows the difference in the JES between central and peripheral collisions, where the quarks have a slightly higher JES (especially at lower p_{T}) than gluons. The bottom panel shows the JER for central collisions on the left and peripheral on the right, where for central collisions the resolution is worse for gluon jets at low p_{T} and worse for quark jets at high p_{T}. In peripheral collisions the quark jet resolution tends to be worse.

As mentioned in Section 4.1, the reconstruction does a lot of work to remove the background due to the UE that is modulated by the harmonic flow. It was also mentioned that in Run 1 only $n = 2$ was used, but that in Run 2 the subtraction was extended to include $n = 3 - 4$ because it was found to improve the jet performance. The effectiveness of the

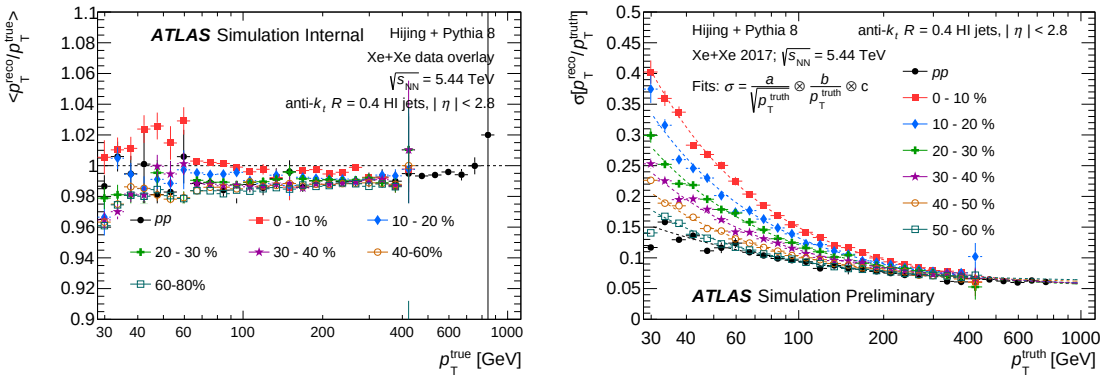

Figure 4.15: The left panel shows the JES as a function of $p_{\mathrm{T}}^{\mathrm{truth}}$ and the right panel shows the JER as a function of $p_{\mathrm{T}}^{\mathrm{truth}}$. The curves are for Xe+Xe with different centralities in 201y at $\sqrt{s_{\mathrm{NN}}} = 5.44$ TeV.

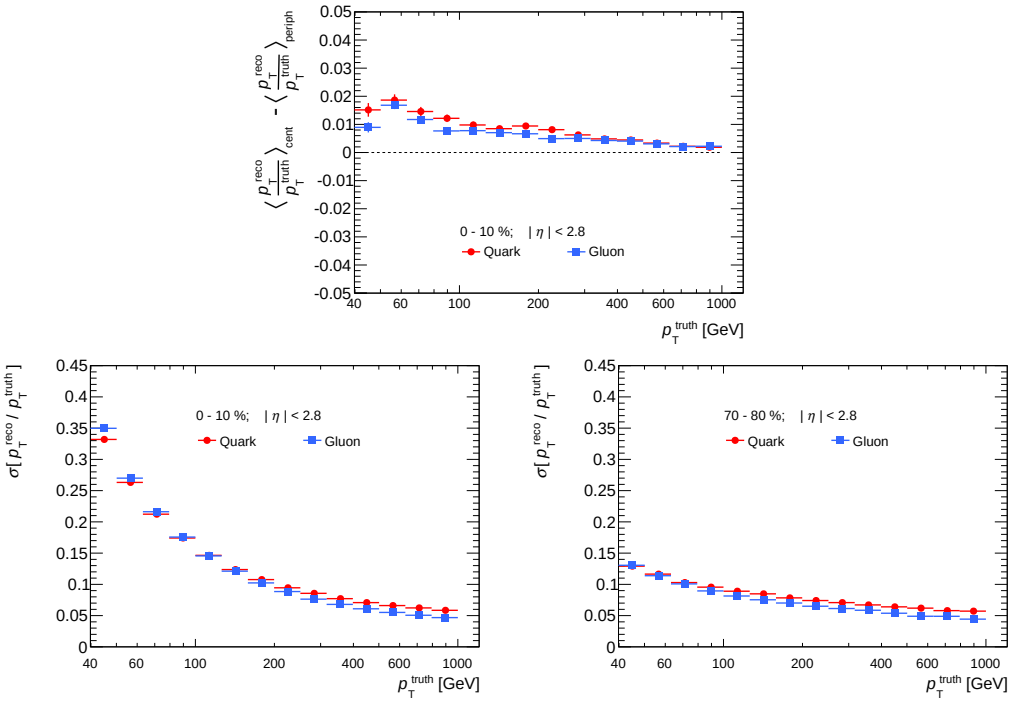

Figure 4.16: The top panel shows the difference in the JES between central and peripheral Pb+Pb collisions as a function of $p_{\mathrm{T}}^{\mathrm{truth}}$ for quark and gluon jets. The bottom panel shows the JER as a function of $p_{\mathrm{T}}^{\mathrm{truth}}$ for central Pb+Pb on the left and peripheral on the right for quark and gluon jets. The curves are for 2015 Pb+Pb data at $\sqrt{s_{\mathrm{NN}}} = 5.02$ TeV.

background subtraction procedure can be investigated by looking at the JES relative to the $n = 2$ and $n = 3$ phase, $n|\Psi_n - \phi|$, where Ψ_n is the phase of the harmonic modulation due to flow as described in Section 2.4.3.1 and shown in equation 4.1. This is shown in the

left and right panel of Figure 4.17, where the open black points on each figure show the distribution without including harmonic flow in the UE subtraction and the filled points show the impact of including the harmonic flow correction. It can be seen that including the harmonics greatly reduces the JES $\Delta\phi_n$ dependence and results in only a small residual dependence on event plane angle. This translates into a substantial improvement in the overall JER, which is shown in Figure 4.18.

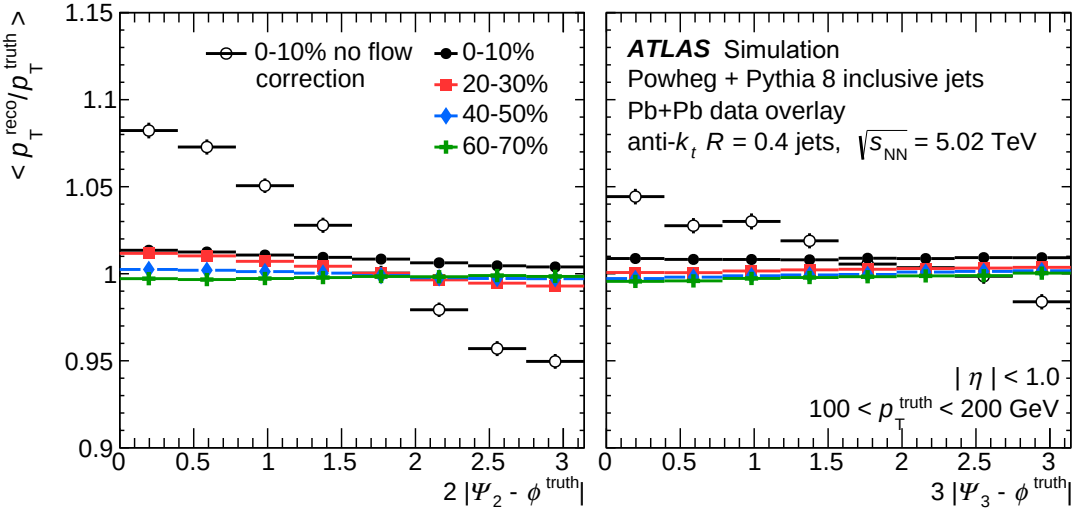

Figure 4.17: The JES as a function of $2|\Psi_2 - \phi^{\text{truth}}|$ (left) and $3|\Psi_3 - \phi^{\text{truth}}|$ (right) for jets with $p_{\text{T}}^{\text{truth}}$ between 100-200 GeV. The black unfilled points are for centrality of 0-10% without the flow subtraction. The filled points show the JES with the flow subtraction applied for different centralities.

The motivation for including higher harmonics is shown in Figure 4.19. The colors represent turning on different aspects of the jet reconstruction, where "no flow" represents no harmonic flow in the subtraction, "vnonlybarrel" means that only that particular nth harmonic was turned on and it was estimated in the barrel, "v2v3barrel" means that just the $n = 2$ and 3 harmonics were turned on, "v2v3v4barrel" means that $n = 2-4$ were turned on, and "ARA06v2v3v4barrel" means that remodulation was turned on. Remodulation is when the flow harmonics are recalculated in the second iteration of the background subtraction (step 6 in Section 4.1). In the left panel the JES as a function of $\Delta\phi_2$ is shown for turning on different aspects of the jet reconstruction, where turning on the v_2 subtraction significantly improves the JES. The center panel shows the JES as a function of $\Delta\phi_3$, where turning on

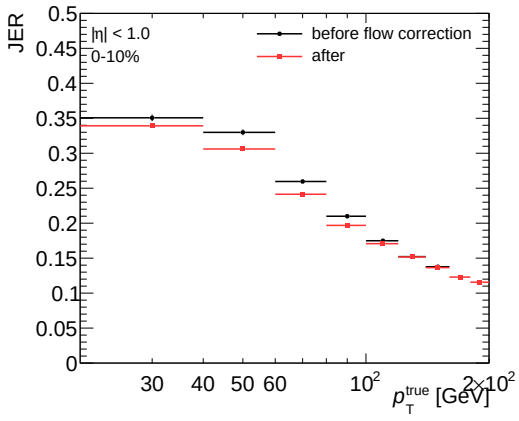

Figure 4.18: The JER as a function of $p_{\mathrm{T}}^{\mathrm{truth}}$ for 0-10% centrality with and without the flow subtraction included in the reconstruction.

the v_3 subtraction improves the JES. Finally, the right panel shows the JES as a function of $\Delta\phi_4$, where turning on the $n = 2 - 3$ subtraction reduces the JES but turning on the v_4 subtraction starts to over subtract (including $n = 2 - 4$ instead of just $n = 4$ reduces this effect a bit).

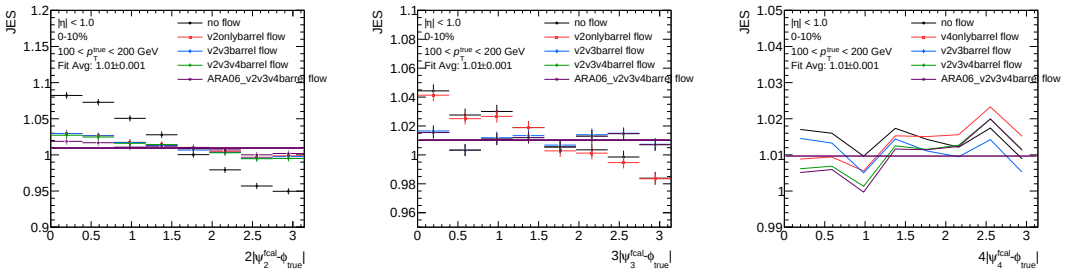

Figure 4.19: The JES as a function of $n|\Psi_n - \phi^{\mathrm{truth}}|$ (n=2 left, n=3 middle, n=4 right) for jets with $p_{\mathrm{T}}^{\mathrm{truth}}$ between 100-200 GeV in 0-10% centrality. The colors indicated the effects of turning on different aspects of the background subtraction in the reconstruction.

Despite the slight over subtraction, the $n = 4$ harmonic is still included in the subtraction because it improved the JER as shown in Figure 4.20. The left panel shows the JER as a function of $p_{\mathrm{T}}^{\mathrm{truth}}$, where the v_2 is shown to significantly reduce the JER, especially at low $p_{\mathrm{T}}^{\mathrm{truth}}$. Adding in additional harmonics also reduces the JER but it is difficult to see which ones have the biggest effect so the right side of Figure 4.20 shows the difference in the squares of the JER for each successive improvement to the reconstruction. It can be

seen that the v_2 shows the most improvement, but that the v_3 and even v_4 also show an improvement.

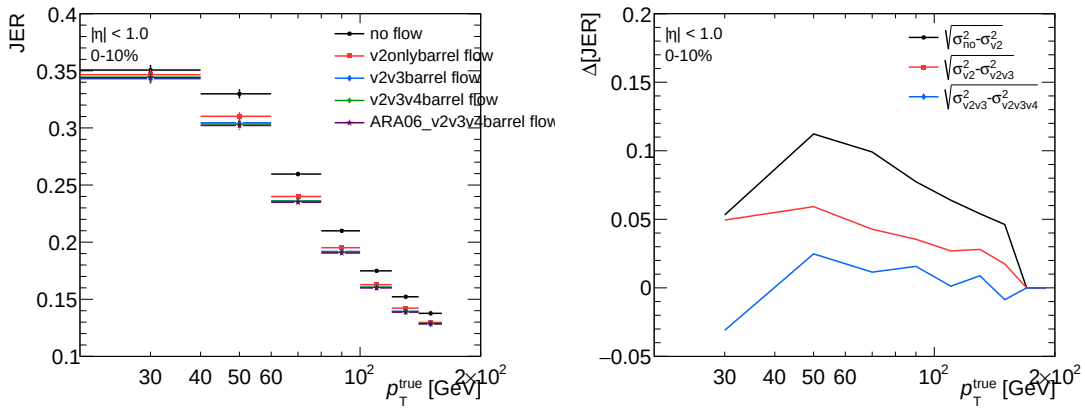

Figure 4.20: The left panel shows the JER as a function of $p_{\mathrm{T}}^{\mathrm{truth}}$ for 0-10% centrality with different types of UE subtraction in the reconstruction, where each curve represents an improvement to the previous curve. The right panel shows the difference in the final and initial JER ($\sqrt{\sigma_f^2 - \sigma_i^2}$) for the successive improvements to the reconstruction.

Figures 4.9, 4.14, and 4.15 shows the status of the jets after the reconstruction and how well the jets are measured for any jet measurement. The remaining effects of the JES and JER are removed through an unfolding procedure discussed in Section 4.6.

4.5.3 Reconstruction Efficiency

The efficiency of the jet reconstruction for reconstructing a jet at a given $p_{\mathrm{T}}^{\mathrm{truth}}$ is evaluated by taking the ratio of the distribution oftruth jets that are matched to a reconstructed jet to all of the truth jets. This is shown for Run 2 jets in Pb+Pb and pp collisions in Figure 4.21 for different η intervals. This demonstrates that the reconstruction is efficient above 100 GeV for central collisions (where the efficiency is the worst). The reconstruction efficiency is also shown for Run 2 jets in Xe+Xe collisions in Figure 4.22, where the reconstruction is also fully efficient above 100 GeV.

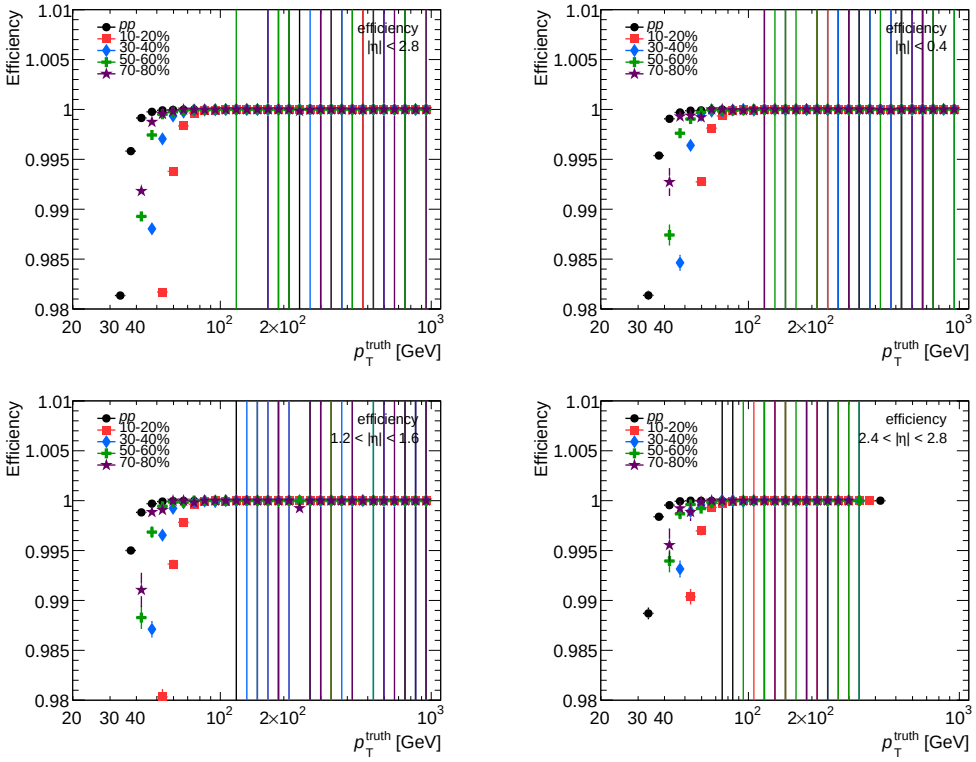

Figure 4.21: The jet reconstruction efficiency for $\sqrt{s_{\mathrm{NN}}} = 5.02$ TeV jets as a function of $p_{\mathrm{T}}^{\mathrm{truth}}$ in different η bins with pp and different Pb+Pb centrality overlaid.

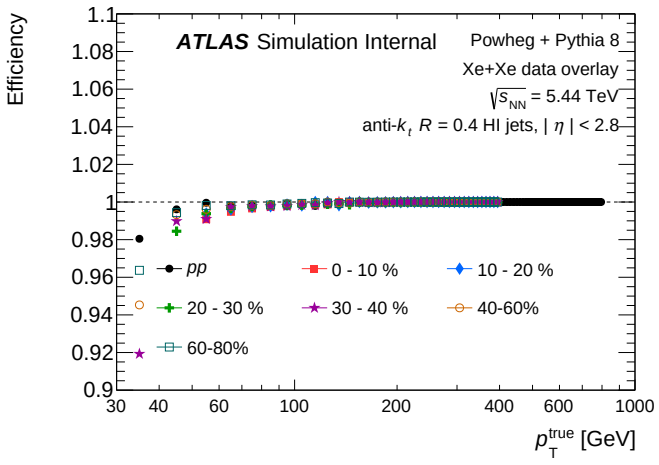

Figure 4.22: The jet reconstruction efficiency as a function of $p_{\mathrm{T}}^{\mathrm{truth}}$ for $|\eta| < 2.8$ for pp and the different centralities in Pb+Pb.

4.6 Unfolding

The jets are unfolded to remove residual detector and UE effects. The unfolding is under better control the more effective the background subtraction is at removing the UE. Unfolding corrects the data from the detector to a generator (or truth) level distribution. The data is reconstructed and is thus at the reconstructed level in the same vein as the reconstructed MC. This correction is achieved by using the response between the truth and reconstructed distributions. The unfolding works as follows

$$\boldsymbol{R}\vec{p_{\mathrm{T}}}^{\,\mathrm{truth}}_{\mathrm{MC}} = \vec{p_{\mathrm{T}}}^{\,\mathrm{reco}}_{\mathrm{MC}} \tag{4.12}$$

where $\boldsymbol{R}$ is the response between truth and reconstructed jets (example in Figure 6.22). To find the $\vec{p_{\mathrm{T}}}^{\,\mathrm{truth}}_{\mathrm{data}}$ from the $\vec{p_{\mathrm{T}}}^{\,\mathrm{reco}}_{\mathrm{data}}$ (the measured data), the response matrix needs to be inverted.

$$\vec{p_{\mathrm{T}}}^{\,\mathrm{truth}}_{\mathrm{data}} = \boldsymbol{R}^{-1}\vec{p_{\mathrm{T}}}^{\,\mathrm{reco}}_{\mathrm{data}} \tag{4.13}$$

It is not this simple though because sometimes the p_{T} distributions are actually distributions of multiple variables and the response matrix has to be inverted in a controlled way. This can be done using Bayesian unfolding techniques. Specifically, iterative Bayesian unfolding [219] uses the Bayesian method, which says

$$t_j^{\mathrm{data}} = t_j^{\mathrm{MC}} \sum_i \frac{A_{ij}}{\epsilon_j} \frac{r_i^{\mathrm{data}}}{r_i^{\mathrm{MC}}} \tag{4.14}$$

where A_{ij} is the response between the truth and reconstructed MC, $\epsilon_j = \sum_i A_{ij}$, t represents truth level and r represents reconstructed level. The truth level MC or t_i^{MC} is called the prior and a good unfolding procedure should not depend on the prior. This is because any dependence on an input truth level distribution can bias the eventual truth level data distribution. Therefore, Bayesian iterative unfolding iterates on the truth distribution by replacing t_i^{MC} by t_i^{data} and r_i^{MC} by $\sum_j A_{ij} t_j^{\mathrm{data}}$. This is then repeated until convergence.

Unfolding can be done in multiple dimensions but this thesis includes unfolding problem in 1D and 2D. For a 1D unfolding problem, where the data is a one-dimension distribution

like a p_{T} spectrum, the response is in 2D. For example, the p_{T} spectra in the R_{AA} result discussed in Chapter 6. For a 2D unfolding, where the data is a two-dimensional distribution between two variable v_1 and v_2, the response is a 4D distribution between v_1^{truth}, v_2^{truth}, v_1^{reco}, and v_2^{reco}. An example of a 2D unfolding problem is the leading/sub-leading (p_{T_1}-p_{T_2}) distribution that produces the x_{J} distributions in Chapter 5. When unfolding a binned distribution, counts are moved around and redistributed through an effect called bin migration.

Any unfolding problem requires a detailed understanding of the response and the more diagonal the response is the easier it is to unfold. A diagonal response comes from jets that have high resolution, meaning the JER is smaller. The effect of unfolding can vary depending on the variable at hand and how different the data is from the MC. For example, the effect of unfolding on jet R_{AA} isn't that large, especially at high p_{T} (shown in Section 6.3.3.5), but the x_{J} distribution changes significantly with unfolding (shown in Section 5.4). The response must also include bins outside of the kinematic ranges desired for the final results because bin migration will cause counts to move in and out of the kinematic boundaries during unfolding.

Unfolding is useful because the unfolded response can be compared directly to theoretical calculations since unfolding removes the effect of the detector and thus the bias in the measurement to the particular detector used. This is particularly useful for jets where there are numerous theories and questions about which jet energy loss mechanisms and jet-medium interaction effects are important and dominant in different kinematic regimes (described in detail in Section 2.5). Thus comparisons to theory can help constrain different models to better understand how the jets lose energy in the QGP. This comparison can also be achieved by smearing out theoretical models using a MC response to produce a "reconstructed" version of the theory that can be compared directly to the data without unfolding. This method can be useful to constrain models but sometimes distinct features in data are lost in unfolding, or unfolding can reveal features that can tell us something about what the medium is doing to the partons. This is particularly true in the x_{J} analysis and will be discussed in detail in Section 5.4. Unfolding is also more useful than smearing when trying to compare results between experiments.

Unfolding problems can be hard to solve and there are some common issues that come up in each unfolding problem which will be discussed in general here and in detail for specific examples in the analysis sections of this thesis.

4.6.1 Convergence and Prior

In the Bayesian unfolding method detailed above, the unfolded result must converge with the number of iterations. In theory, this means that the data could be iterated until infinity but the statistical uncertainties in the data actually increase with the number of iterations. Therefore, the point of convergence needs to be found so that the iterating can stop and a reasonable estimate of the statistical uncertainties can be made. In an unfolding problem, a check that the unfolding is working is looking at the stability of the results to number of iterations meaning that the result can not change much within a certain amount of iterations from the nominal result. The "nominal" refers to the distribution at the fixed number of iterations determined to be the final unfolded result.

As mentioned previously, when discussing the Bayesian unfolding method, an unfolded result should not depend on the prior or original truth level MC distribution. Therefore, any number of priors should be able to be used in an unfolding problem and the same "truth" should come out. In theory, a flat prior could be used and convergence to "truth" would still happen. The prior used for the nominal result should also be carefully chosen to be as close to the data as possible since the result converges faster the closer the prior is to the "truth" and the faster the convergence the less the statistical uncertainties blow up. The dependence on the prior must always be checked with a carefully selected number of priors that fully encapsulates plausible changes to the reconstructed MC. An "alternative" prior is then used as for a systematic uncertainty in the final measurement.

A method for deciding when the result has converged to the truth is needed in each unfolding problem. For simpler unfolding problems, where the data and the MC aren't that different, the "nominal" is chosen when the result is stable with the number of iterations. This method is used in the R_{AA} analysis and is discussed in Section 6.3.3.4. For more complicated unfolding problems the convergence criterion is based on a comparison between dependence on the prior and the statistical uncertainties. The dependence on the prior is

determined by comparing the result with two different priors at a fixed number of iterations and is expected to decrease with the number of iterations. Since the statistical uncertainties increase with number of iterations, a number of iterations can be found that collectively minimizes the two. This is used for the x_{J} analysis and is described in detail in Section 5.4.6.

4.6.2 Statistics

Unfolding requires a careful treatment of both how the statistics in the data and MC are propagated to the final unfolded results and how the limited statistics can affect the unfolding. The statistics on the final unfolded result are determined through pseudo-experiments on the data, where a new data distribution is generated and re-unfolded N times based on the statistical uncertainties in the data. The same thing is done for the response based on the statistical uncertainties in the MC. The difference between the nominal result and the pseudo-experiments is taken as the statistical uncertainty in the data.

Sometimes the MC samples have limited statistics, like in the x_{J} analysis discussed in Section 5.5.5, which can cause the edges of the response distributions to be sparse. This can result in fluctuations in the response matrix that are propagated through the unfolding and cause fluctuations in the unfolded result. This effect is accounted for by building a factorized response that is generated by sampling the response between the truth and reconstructed jets to fill out all the edges of the response distributions. The response is factorized because it is filled without taking into account the correlation between the individual variables in a 2D unfolding problem. The difference between the result from unfolding with the factorized response and the nominal is taken as a systematic uncertainty.

4.6.3 Distribution Shape

Abnormal shapes in the data like kinks or changes in curvature can make the unfolding more difficult. These shapes typically come from some residual background in the data like fake or combinatoric jets. These backgrounds need to be removed before unfolding the data. These background contributions usually come into the distributions in unique ways depending on the analysis and thus the procedures to remove them can be different in each individual measurement. “Fake” jets or “UE jets” are jets that are reconstructed

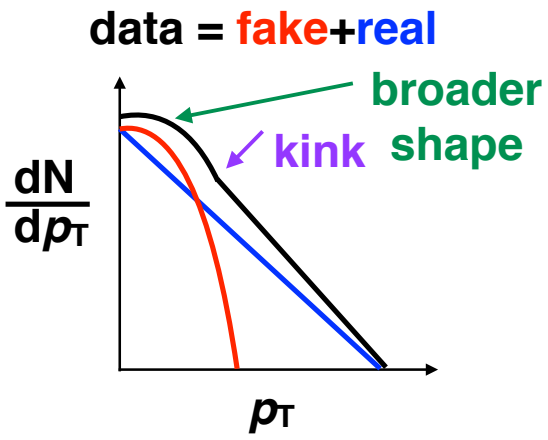

Figure 4.23: A diagram showing the effect of the fakes on a steeply falling p_{T} spectrum. The fake rate is shown in red, the real distribution in blue, and the fake+real distribution in black.

from fluctuations in the UE. An over exaggerated demonstration of the effect of this on a p_{T} spectrum is shown in Figure 4.23. The fakes typically have a gaussian shape in jet p_{T} and are more prominent at lower p_{T} where the background subtraction is more difficult due to the UE size being more comparable to the size of the jets. The data with the fakes included is shown to cause a broader shape and kink due to a curvature change when added to the real distribution. This is discussed in more detail in Section 6.2.1. There can also be combinatoric jets that do not originate from the same hard scattering due to uncorrelated hard scatterings in the same event as the signal jets. This is relevant in the x_{J} analysis and the method to remove them is discussed in Section 5.3.1.3.

4.6.4 Systematic Uncertainties

The systematic uncertainties are treated in a specific way in an unfolding problem, where the dominant uncertainties are due to the JES and JER (discused in detail in Section 5.5) since the dominant uncertainty is from the UE. The systematic uncertainties are evaluated by building a new response with a systematically varied relationship between the truth and reconstructed jet kinematics and re-unfolding the data with the new response. The systematic uncertainty then becomes the quadratic difference between the nominal and systematically varied results. There are analysis specific systematic uncertainties that will

be discussed in the corresponding analysis sections. Finally, there are specific uncertainties due to the unfolding procedure that were already mentioned above: sensitivity to the prior discussed in Section 4.6.1 and sensitivity to MC statistics discussed in Section 4.6.2.

Chapter 5

Dijet Asymmetry

5.1 Data and MC Samples

This analysis used data from 2011 Pb+Pb collisions and 2013 pp collisions at $\sqrt{s_{\mathrm{NN}}}$ = 2.76 TeV.

5.1.1 2011 Pb+Pb Data

The Pb+Pb data used is this analysis was taken during run 1 in 2011 at $\sqrt{s_{\mathrm{NN}}} = 2.76$ TeV with a total luminosity of 0.14 $\mu\mathrm{b}^{-1}$. A combination of minimum bias and jet-triggered triggers were used. The minimum bias events were selected using a logical OR between the `EF_L1TE50_NoAlg`, which is a transverse energy (TE) trigger with an $E_{\mathrm{T}}^{\mathrm{tot}} = 50$ GeV and `EF_mbZdc_a_c_L1VTE50_trk`, which is ZDC coincidence trigger. When just the ZDC trigger is fired, empty events are removed by imposing a requirement of at least one track. This trigger was prescaled by a factor of 18, which means that a factor of 18 less data was stored, and was fully efficient for the kinematic ranges in this analysis. The jet-trigger `EF_j20_a2hi_EFFS_L1TE10` [220] was used to improve the statistics at high p_{T}. It is an unprescaled trigger that is seeded off of the `L1TE10` trigger. This is also a TE trigger with $E_{\mathrm{T}}^{\mathrm{tot}} = 20$ GeV that had the full jet reconstruction applied to it (Section 4.1) during data taking. The trigger then selects events with at least one jet with $E_{\mathrm{T}} > 20$ GeV at the electromagnetic scale. This trigger is fully efficient above the threshold at 20 GeV for $R = 0.2$ jets (the radius that the reconstruction was performed at), but larger R jets that

are reconstructed offline (offline being not during data-taking) will have an efficiency with a broad turn-on around the threshold. The trigger efficiencies are discussed in Section 5.3.1.1.

The events were also required to pass typical HI event-level selection criteria which try to remove non-collisional background and EM inelastic interactions between the nuclei:

- At least one reconstructed primary vertex.
- A MBTS timing cut of $\Delta t_{\mathrm{MBTS}} < 5$ ns which is determined by a timing difference between the two MBTS detectors on the A and C sides of the detector.
- Good data quality selections which include being in a running period with stable beam and detector conditions by selecting on lumi-blocks specified in the HI good runs list (GRL).
- Removal of events containing detector or DAQ errors.

After all of the event level selections the minimum bias data contained 53 million events with an integrated luminosity of 8 $\mu\mathrm{b}^{-1}$ and the jet-triggered data contained 14 million events with an integrated luminosity of 0.14 nb^{-1}. The average number of collisions per bunch crossing μ was less than 0.001.

5.1.1.1 Centrality Determination

As mentioned in Section 2.4.2, HI events are divided into centrality classes based on the degree of overlap of the colliding nuclei. The centrality is used as a proxy for the impact parameter b. The more overlap, the more central the collision, and the less overlap, the more peripheral the collision. In-medium effects are expected to have a dependence on the centrality since the more overlap the more medium is created and the less overlap the more the collision is like a standard pp collision. Section 2.4.2 described how experiments use measurable quantities with similar distribution to the Glauber variables N_{part} and N_{coll} to classify centrality. These quantities are somehow representative of the total particle production in the event. In ATLAS the sum of the transverse energy in the forward calorimeter (FCal) is used $\Sigma E_{\mathrm{T}}^{\mathrm{FCal}}$ which covers $3.2 < |\eta| < 4.9$. It is located very far forward so is separated from the centrality-dependent physics but is correlated with the remaining energy

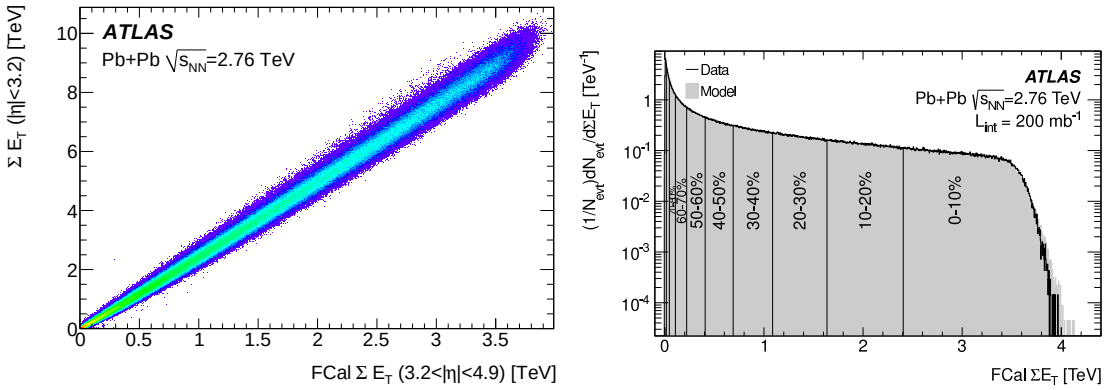

Figure 5.1: The left-hand side shows the sum of the total transverse energy in the calorimeter within $|\eta| < 3.2$ ($\sum E_{\mathrm{T}}$) as a function of the $\Sigma E_{\mathrm{T}}^{\mathrm{FCal}}$ [1]. The right-hand side shows the $\Sigma E_{\mathrm{T}}^{\mathrm{FCal}}$ partitioned into centrality quantiles [214].

Table 5.1: The centrality ranges used to the analysis with their corresponding $\Sigma E_{\mathrm{T}}^{\mathrm{FCal}}$ values.

Centrality [%]	$\Sigma E_{\mathrm{T}}^{\mathrm{FCal}}$ [TeV]
0–10	>2.423
10–20	1.661–2.433
20–30	1.116–1.661
30–40	0.716–1.116
40–60	0.239–0.716
60–80	0.053–0.239

in the rest of the calorimeter ($|\eta| < 3.2$) which represents the total event activity. This is shown in the left-hand side of Figure 5.1.

The right-side of Figure 5.1 shows the $\Sigma E_{\mathrm{T}}^{\mathrm{FCal}}$ distribution in minimum bias, where all the minimum bias cuts defined above are applied. This ends up being about 98% of the total minimum bias data. The distribution was partitioned in 10% centrality intervals except for 40–80% which is divided into 20% intervals. In this analysis six centrality intervals are used: 0–10%, 10–20%, 20–30%, 30–40%, 40–60%, and 60–80% and their $\Sigma E_{\mathrm{T}}^{\mathrm{FCal}}$ values are given in Table 5.1.

5.1.2 2013 *pp* Data

The *pp* data used in this analysis was taken during run 1 in 2013 at $\sqrt{s_{\mathrm{NN}}} = 2.76$ TeV with a total luminosity of 4.1 pb^{-1}. It is composed of multiple triggers from the `HardProbes`

Table 5.2: Trigger scheme in the pp data, listing which triggers were used in the p_{T} bins and the total luminosity sampled.

Trigger	$p_{\mathrm{T}}^{\mathrm{min}}$	$p_{\mathrm{T}}^{\mathrm{max}}$	$\mathcal{L}_{\mathrm{int}}$ [nb^{-1}]
EF_j10_a4tchad_EFFS_L2mbMbts_L1RD0	20	32	11.268
EF_j20_a4tchad_EFFS_L2mbMbts_L1RD0	32	50	12.478
EF_j40_a4tchad_EFFS_L1J5	50	65	277.38
EF_j50_a4tchad_EFFS_L1J10	65	79	800.455
EF_j60_a4tchad_EFFS_L1J15	79	100	1594.7
EF_j75_a4tchad_EFFS_L1J15	100	–	3935.65

stream that have different p_{T} thresholds and different prescales. These triggers were reconstructed in the same way as standard pp jets [220]. The lowest threshold triggers were seeded off the L1RD0 trigger and the higher thresholds were seeded of the L1 jet triggers. Table 5.2 lists the trigger names and luminosities.

The pp data was alo required to have a reconstructed primary vertex and be in the GRL. The μ was between 0.3 and 0.6.

5.1.3 Monte Carlo samples

The MC samples in this analysis use a signal from Pythia version 6.423 [68] with AUET2B tune [221] and CTEQ6L1 PDFs [222]. As mentioned in Section 4.3, the Pythia events are divided into ranges of $\hat{p_{\mathrm{T}}}$, which is the p_{T} of the outgoing partons in a $2 \rightarrow 2$ hard scattering, and combined using weights from their cross sections. Separate samples are generated for the Pb+Pb and pp data analyses because of the different detector conditions during the different recording periods. The J slices and their cross sections for the Pythia used to generate the HI MC are shown in Table 5.3. The pp samples are overlaid with minimum bias pp collisions generated by Pythia 8 version 8.160 [74] using the A2 tune [223] and CT10 PDFs [224] to account for pile-up which are additional collisions in the same bunch crossing. The JZ slices and their cross sections for the MC used for the pp is shown in Table 5.4. Here JZ samples, instead of J, are used, where the JZ ranges are on the p_{T} of the hard scattering. The Pb+Pb MC is overlaid with real minimum bias Pb+Pb data as discussed in Section 4.3.

There are some additional pp datasets used to compare to the unfolded pp result which

Table 5.3: Definitions of PYTHIA samples used in embedding for the Pb+Pb MC and the names of the overlaid datasets.

J Slice	$\hat{p}_{\mathrm{T}}^{\mathrm{min}}$ [GeV]	$\hat{p}_{\mathrm{T}}^{\mathrm{max}}$ [GeV]	σ [nb]
0	8	17	3576900
1	17	35	187600
2	35	70	8279
3	70	140	294.2
4	140	280	6.445
5	280	560	0.06388

Table 5.4: Definitions of PYTHIA samples used in embedding for the *pp* MC and the names of the overlaid datasets.

JZ Slice	$\hat{p}_{\mathrm{T}}^{\mathrm{min}}$ [GeV]	$\hat{p}_{\mathrm{T}}^{\mathrm{max}}$ [GeV]	σ [nb]
0	0	20	41300000
1	20	80	41300000
2	80	200	3226.2
3	200	500	33.335
4	500	1000	0.12851

include Pythia 8 with the AU2 tune, Herwig++ [70] with the UE-EE-3 tune [225], and Powheg+Pythia 8 which is generated using Powheg-Box 2.0 [72, 226, 227] interfaced with Pythia 8. They all use CTEQ6L1 PDFs except for the Powheg+Pythia 8 which uses CT10 PDFs. These different generators were described in Section 2.2.6.

Finally, the detector's response to quenching jets (used for a systematic uncertainty) is quantified using `PYQUEN` [161], which was described in Section 2.5.2.5.

5.2 Jet Reconstruction

The jet reconstruction procedure was described in detail in Section 4.1 and in this analysis the run 1 jet reconstruction was used. In addition to all the corrections mentioned in that section, there was some additional corrections applied.

The first is a residual correction at the tower level that accounts for a slight deviation from uniformity of the calorimeter response in ϕ. There is also a small over-subtraction in certain regions of the calorimeter, especially in regions where the geometry of the detector changes, that is corrected for. Figure 5.2 shows the average additive correction applied to the leading jet, as a function of η and ϕ.

The run 1 reconstruction only corrects for v_2, but in this analysis the higher order harmonics can affect the $\Delta\phi$ distributions, especially when one of the jets has $p_{\mathrm{T}} \lesssim 45$ GeV,

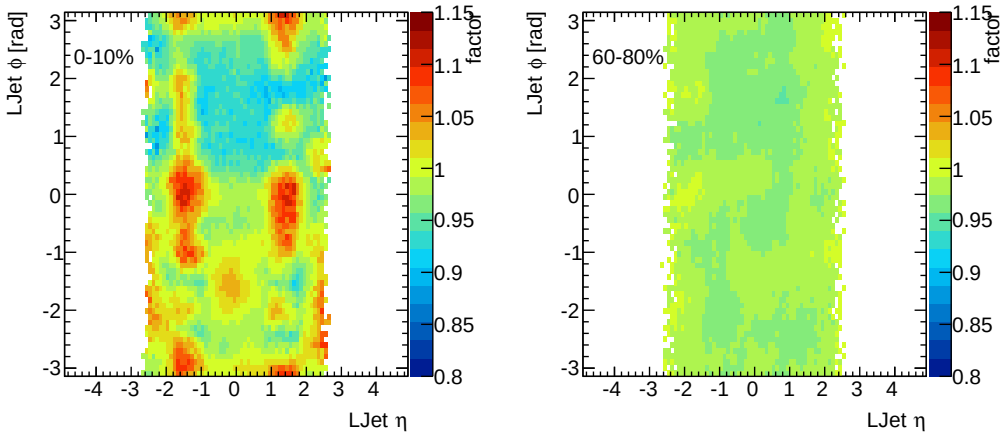

Figure 5.2: Correction factors applied to the leading jet p_{T} as a function of η and ϕ in 0-10% and 60-80% collisions in the left and right panels, respectively.

since this region is dominated by fakes jets. The UE fluctuations that are above the (averaged) subtracted background are largest at ϕ values that are in phase with the higher order harmonics, so there are more fakes in those regions. In the regions where one or both jets is likely to be a fake, the pairs are more likely to occur when both jets are in phase with the higher order flow harmonics. Therefore, they have a $\cos n\Delta\phi$ modulation to their $\Delta\phi$ correlations. This is shown in Figure 5.3 in the 0–10% centrality interval for different selections on the leading jet p_{T}. The third and fourth order flow harmonics are clearly visible in the red curve on top of the expected dijet contribution.

To account for this, a correction was applied to each tower within a jet. The v_3 and v_4 (and $\Psi_{3,4}$) are measured event-by-event in the FCal (described in Section 3.2.3), where the influence from jets is small, and used to modulate the average UE in the following way

$$\Delta E_{\mathrm{T}}{}^{\mathrm{tower}} = \rho(\eta^{\mathrm{tower}})A^{\mathrm{tower}} \sum 2\, c_n(\Sigma E_{\mathrm{T}}^{\mathrm{FCal}}) v_n^{\mathrm{FCal}} \cos n(\phi^{\mathrm{tower}} - \Psi_n^{\mathrm{FCal}}). \tag{5.1}$$

where $c_n(\Sigma E_{\mathrm{T}}^{\mathrm{FCal}})$ is the correlation between the mean v_n in the region $|\eta| < 3.2$ as a function of the v_n^{FCal} in narrow bins of $\Sigma E_{\mathrm{T}}^{\mathrm{FCal}}$. This correlation is needed because the harmonic modulation in two different η regions can be different due to uncorrelated particle multiplicity fluctuations. The correlation is the slope between these two quantities which increases with $\Sigma E_{\mathrm{T}}^{\mathrm{FCal}}$. These slopes as a function of $\Sigma E_{\mathrm{T}}^{\mathrm{FCal}}$ were parametrized using a

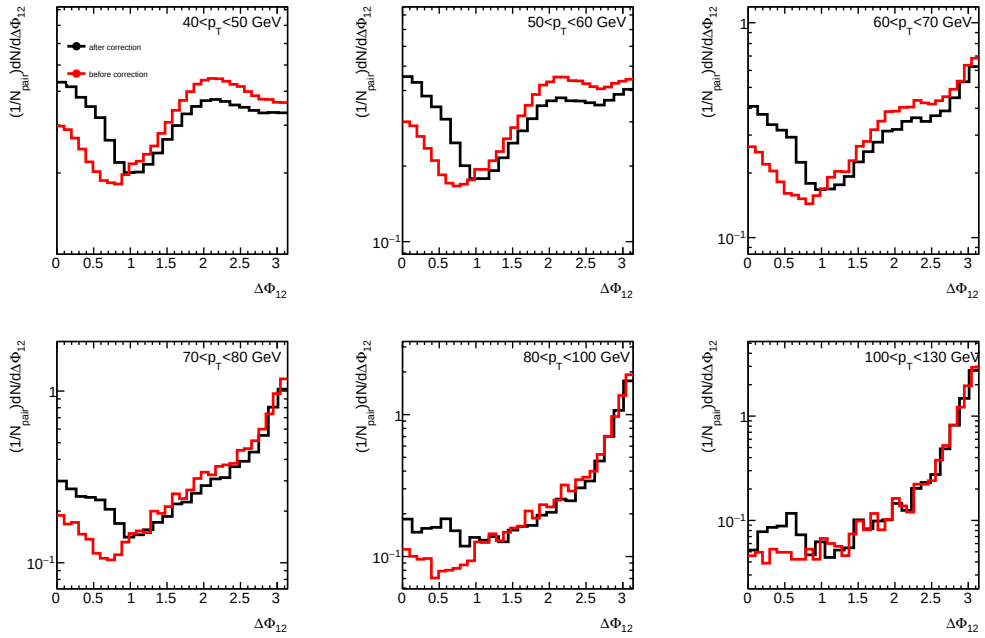

Figure 5.3: The dijet $\Delta\phi$ distribution in different bins of leading jet p_{T} before and after the v_n subtraction for the 0–10% centrality interval.

fourth order polynomial. This correction was performed for $n = 3$ and 4, and higher order flow harmonics were found to be negligible. The $\Delta E_{\mathrm{T}}^{\mathrm{jet}}$ vs $n(\phi^{\mathrm{jet}} - \Psi_n^{\mathrm{FCal}})$ distributions are shown for $n = 3$ and 4 in Figures 5.4 and 5.5, respectively for different centrality bins. The black line in Figure 5.3 shows the effect of the correction, where the correction reduces the modulation at low p_{T} and helps reveal the dijet peak.

5.3 Data Analysis

5.3.1 Pb+Pb Data Analysis

In the Pb+Pb data the jets were reconstructed and calibrated as described Section 4.1 and in Section 4.4. In this analysis dijet pairs were selected from the raw data and then unfolded using a response built from the MC. The final unfolded results will have a p_{T} cut at 100 GeV on the leading jet but the raw data needs to include all the pairs to allow for bin migration from lower p_{T} bins to higher p_{T} bins. Therefore, a 2D distribution in p_{T_1} and p_{T_2} was filled where both jets are required to have p_{T} >25 GeV. In each event, p_{T_1}

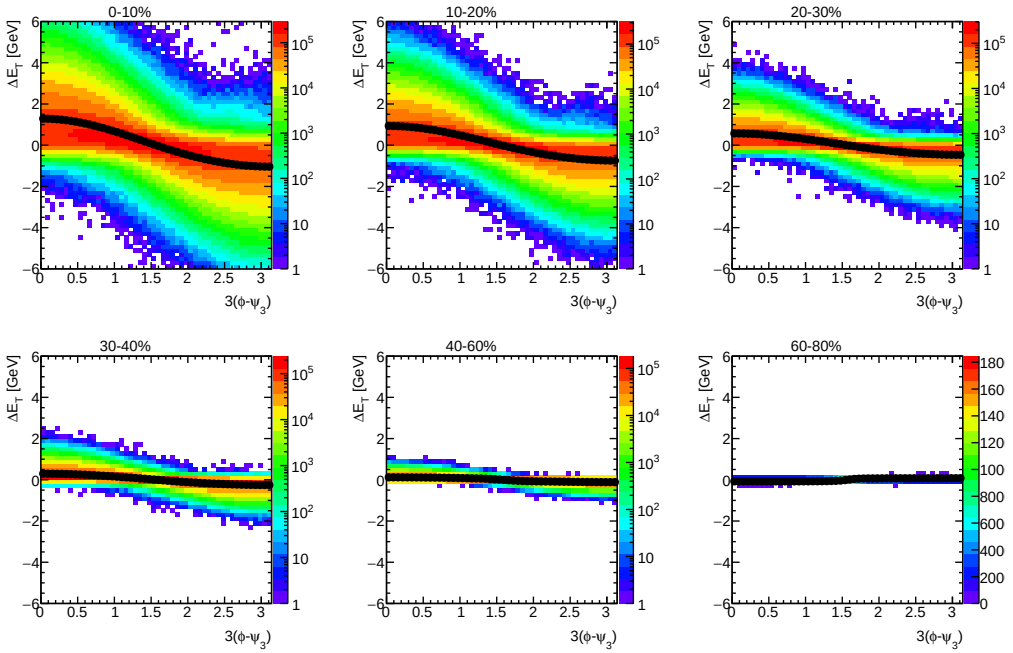

Figure 5.4: ΔE_T for the contribution that is subtracted for the v_3 modulation in the background in the minimum bias sample in different centrality bins.

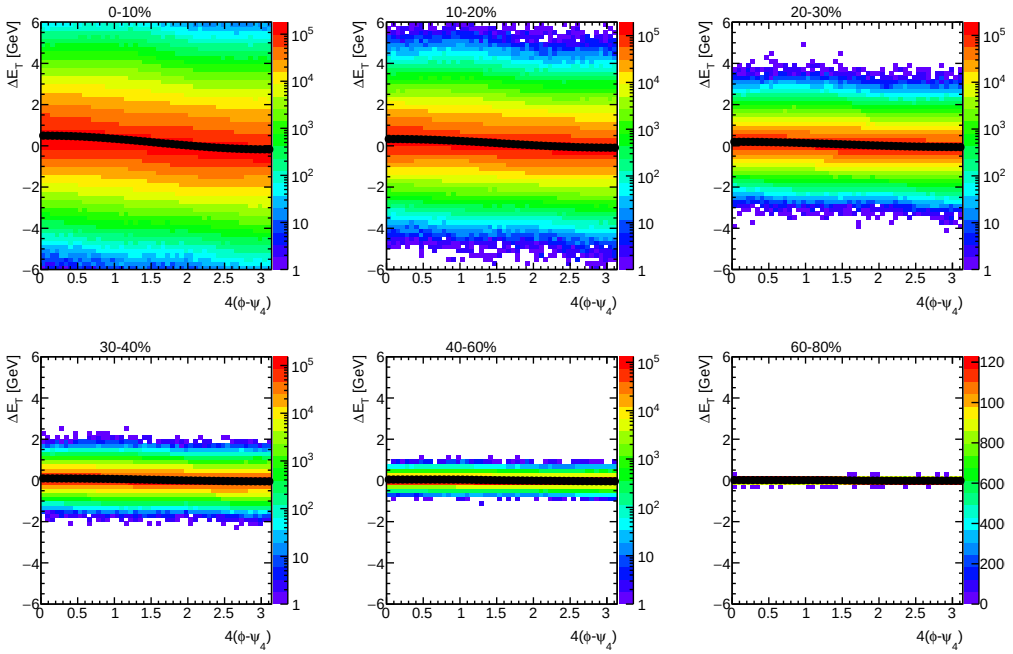

Figure 5.5: ΔE_T for the contribution that is subtracted for the v_4 modulation in the background in the minimum bias sample in different centrality bins.

is the highest p_{T} jet with $|\eta| < 2.1$ and p_{T_2} is the second highest. The leading jets must match a trigger jet (either minimum bias or jet triggered depending on the p_{T} of the jet) within $\Delta R < 0.4$. In order for the jet pair to be considered a dijet in the analysis they must be back-to-back, or within $\Delta\phi > 7\pi/8$, where $\Delta\phi \equiv |\phi_1 - \phi_2|$. This cut was chosen to guarantee that the dijets have minimal background contribution and the least amount of bias. A tighter cut could bias the distribution to select more balanced jets and a looser cut could introduce fake background into the data. The binning was chosen such that there are 40 logarithmic bins with 10 GeV as the lowest bin boundary and 1 TeV is the highest bin boundary. This guarantees that our cut in the leading jet p_{T} at 100 GeV is at a bin boundary.

The Pb+Pb analysis was performed on both $R = 0.4$ and $R = 0.3$ jets. The $R = 0.3$ analysis serves to verify the result in the $R = 0.4$ since the $R = 0.3$ jets have less background in the jet selection because smaller jet radii will lead to less fake contribution. The $R = 0.3$ jets have a potential bias because the jet radius can broaden as the energy of the jet decreases. This could cause the analysis to miss quenched jets in the $R = 0.3$ jets. The data analysis is the same for both the $R = 0.4$ and $R = 0.3$ so the $R = 0.4$ jets are shown in the following sections and the $R = 0.3$ figures are included in Appendix A.

5.3.1.1 Combining Trigger Samples

The first step in the data analysis is to use the Pb+Pb jet triggered (hard probes jet trigger) data to select the jets in the way described above. It was found that at low p_{T} the jet triggered data has a large inefficiency that is steeply falling as seen in Figure 5.6. Therefore, the minimum bias sample (which has no inefficiency due to the trigger) was used instead of the jet triggered sample in the low p_{T} region. The minimum bias sample has less statistics, especially at higher p_{T}, so it could not be used for the full spectrum. Thus, at high p_{T} the analysis switches back to the jet triggered sample with a trigger efficiency correction. The samples were combined by selecting specific p_{T} regions from the samples and then scaling the minimum bias data up by its pre-scale of 12. The inefficiency in the jet triggered data is determined by fitting the efficiency distribution between 60 and 100 GeV (where the efficiency goes to 1) as shown in Figure 5.6.

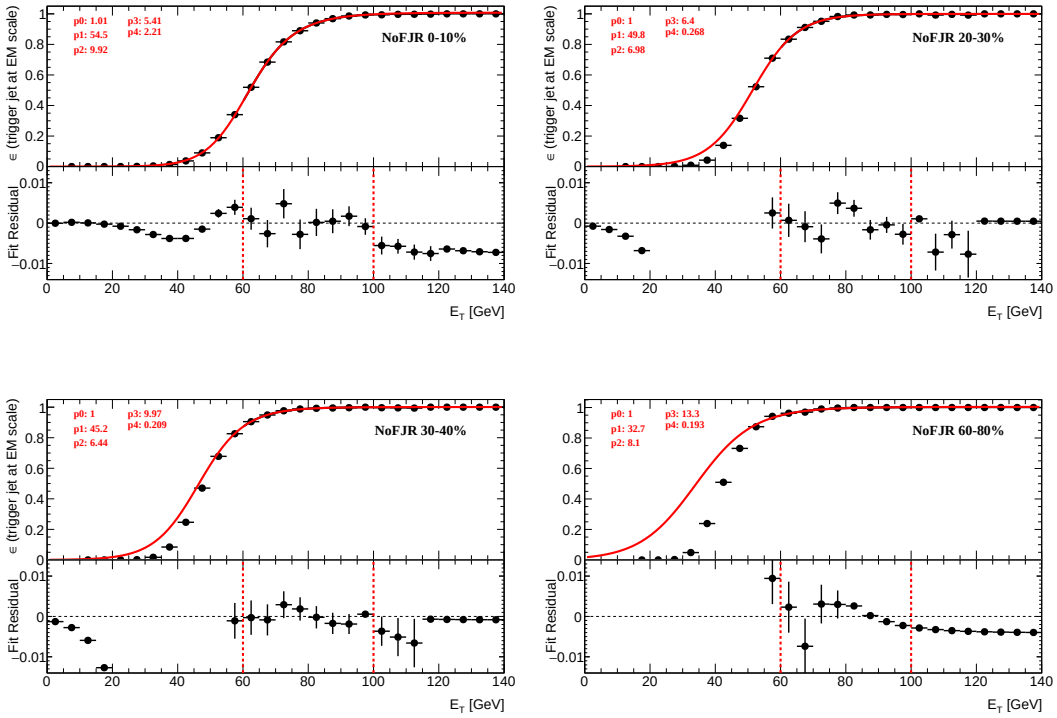

Figure 5.6: Trigger efficiencies fit between 60-100 GeV for different centralities in $R = 0.4$ jets. The fit parameters are given on each plot in red. The fit residuals (data-fit) are shown below each efficiency distribution.

The function used to fit the efficiency is given by:

$$\epsilon(E_T) = \frac{p_0}{1 + \exp\frac{E_T - p_1}{p_2} + p_4 \exp\frac{E_T - p_1}{p_3}} \tag{5.2}$$

The fit residual shown in Figure 5.6 demonstrates that the fit represents the data within less than 1%. In order to choose the transition p_{T} value between the two samples the ratio of the samples for all p_{T} was taken as shown in Figure 5.7. The location where the ratio fluctuates around 1 without being systematically above or below 1 is where the crossover was chosen. Here the value was selected to be 85 GeV.

The combined spectra are shown in Figure 5.8. The 2D distribution needed to be symmetric before it can be unfolded so the distribution is reflected over the diagonal as shown in Figure 5.9.

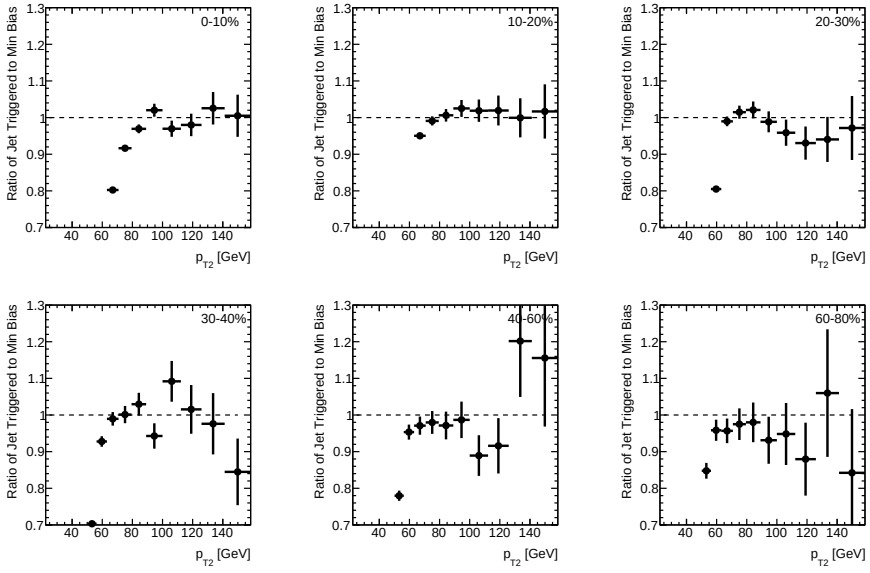

Figure 5.7: Ratio of the minimum bias to jet triggered samples in centrality bins for $R = 0.4$ jets. The transition region was chosen from this plot to be 85 GeV.

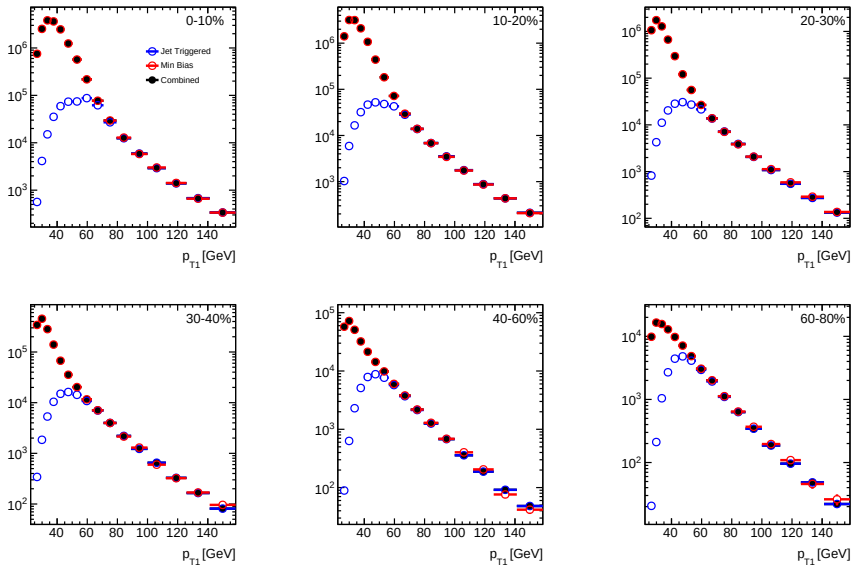

Figure 5.8: The minimum bias, jet triggered, and combined samples overlaid in centrality bins for $R = 0.4$ jets.

The left and center panels of Figure 5.10 show the 2D distribution (p_{T_1}, p_{T_2}) before unfolding, where the trigger boundary between the minimum bias and hard probe trigger

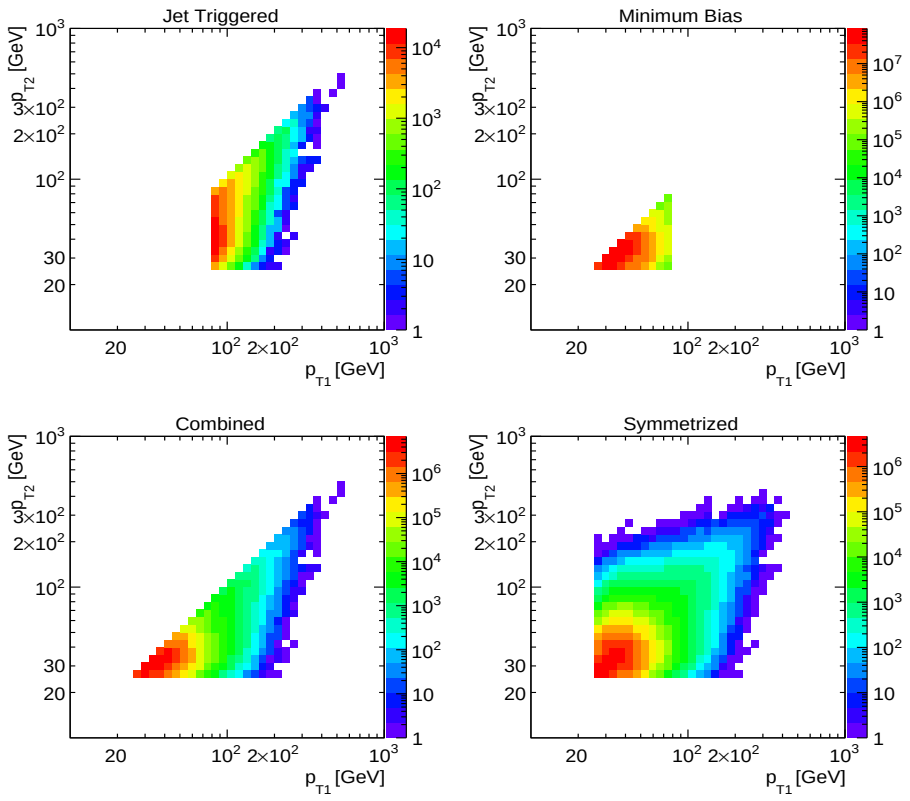

Figure 5.9: The 2D distributions for the minimum bias, jet triggered, and combine samples for $R = 0.4$ jets. The symmetric distribution is also shown after it was reflected over the diagonal.

is indicated with the black dashed line.

5.3.1.2 v_n Subtraction

The flow contribution to the underlying event were subtracted in the jet reconstruction and also a correction was applied after the fact to remove the $n = 3$ and 4 contributions (described in Section 5.2). This correction does not completely remove all of the contribution from v_3 and v_4 so an additional modification to the $\Delta\phi$ distribution was made. This can be seen in Figure 5.11, where the $\Delta\phi$ distributions for $R = 0.4$ jets show a clear residual modulation, especially at low p_{T_1}. This demonstrates that at low p_{T} a modulation in the background remains after the flow subtraction.

This can also be seen in Figure 5.12 where the red distributions have a $\Delta\eta$ cut greater

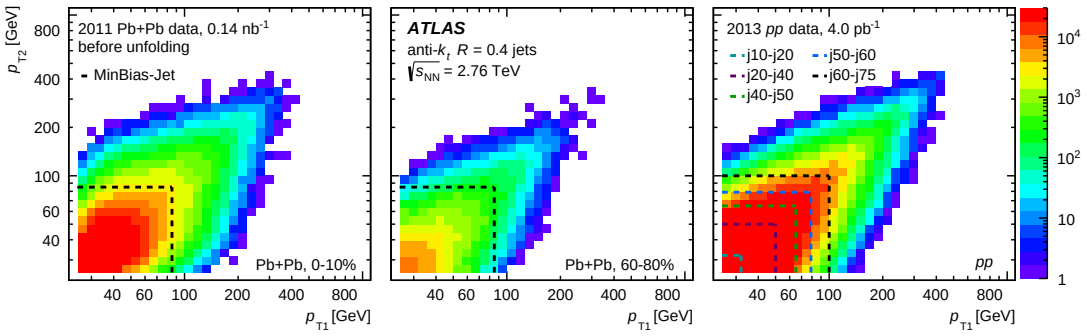

Figure 5.10: The two-dimensional $(p_{\mathrm{T}_1}, p_{\mathrm{T}_2})$ distributions after correction and symmetrisation for Pb+Pb data in the 0–10% (left) and 60–80% (center) centrality bins and for pp data (right) for $R = 0.4$ jets. The dashed lines indicate the boundaries used in selecting the different triggers where, for example, the line called j10–j20 indicates the boundary between the j10 and j20 triggers. The Pb+Pb data distributions have their combinatoric contribution subtracted.

than 1.0 to remove the contribution from nearby jets, where $\Delta\eta$ is the distance in η between the two jets in the pair. This contribution was fit to the following function:

$$C(\Delta\phi) = Y(1 + 2c_3 \cos 3\Delta\phi + 2c_4 \cos 4\Delta\phi) \tag{5.3}$$

The c_3 and c_4 were extracted using this fit and then applied when calculating the background that will eventually be subtracted from the data (described in Section 5.3.1.3). This is done in each (p_{T_1}, p_{T_2}) bin for low p_{T} and then integrated over more bins for higher p_{T} where the statistics are lower.

Figure 5.13 shows a summary of the fit and correction for central collisions for p_{T_1} between 80 and 100 GeV. The black points show a clear nearby jet peak when zoomed in on in the square. The distributions with the η cut that were fit (fit shown in blue) show the nearby jet peak removed. This blue fit was used to extract the c_n values of the modulation that were then used to perform a combinatoric subtraction described in Section 5.3.1.3.

5.3.1.3 $\Delta\phi$ Combinatoric Subtraction

A method was developed to remove the combinatoric background from the raw 2D (p_{T_1}, p_{T_2}) distributions used in the unfolding. The combinatoric background comes from jets not originating from the same hard scattering, which can be independent hard scatterings

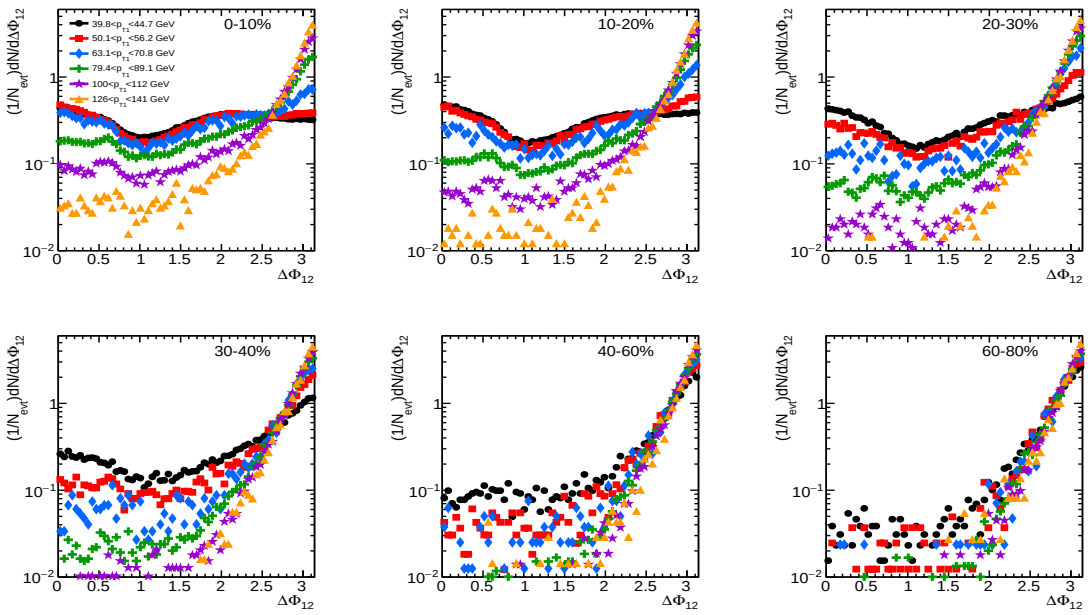

Figure 5.11: The $\Delta\phi$ distribution binned in centrality as a function of leading jet p_{T} for $R = 0.4$ jets.

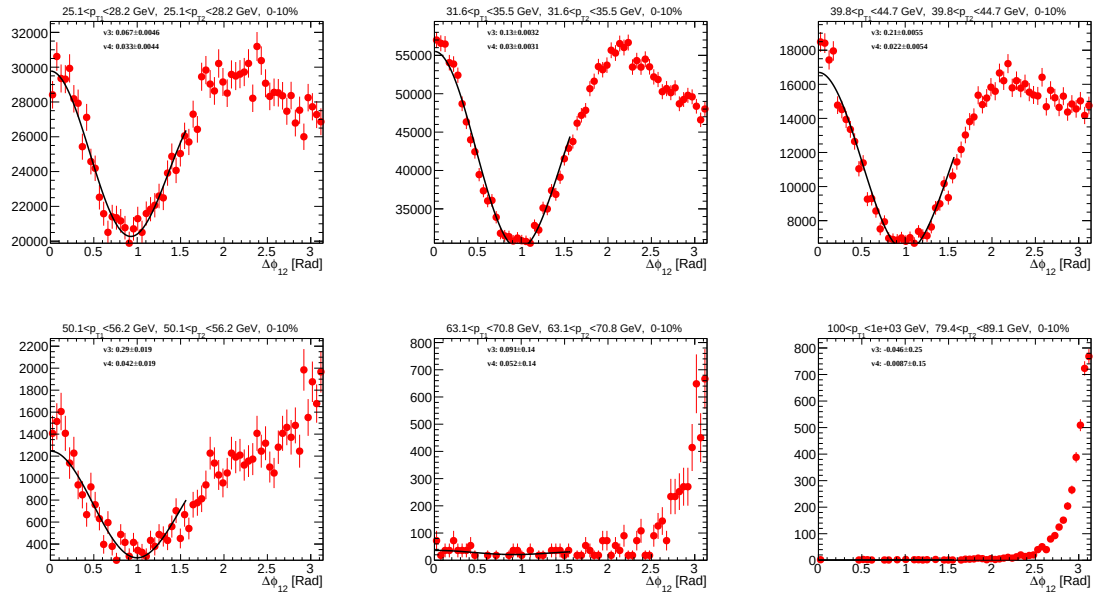

Figure 5.12: Sample of bins in the 2D jet p_{T} distribution with the background in red fit to a flow modulation. This is for the 0-10% centrality bin and for $R = 0.4$ jets.

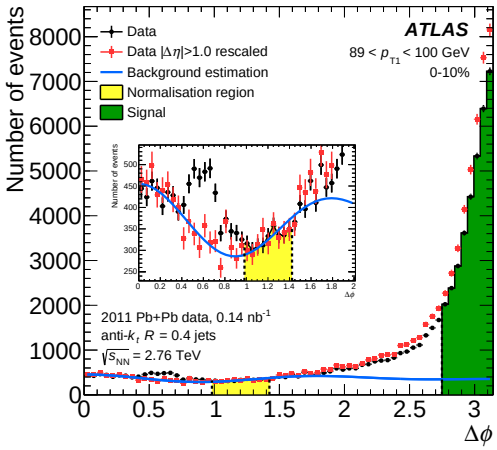

Figure 5.13: The $\Delta\phi$ distribution for $R = 0.4$ jet pairs with $89 < p_{\mathrm{T}_1} < 100$ GeV in the 0–10% centrality interval. The distribution for all jet pairs is indicated by the black circles. The combinatoric contribution given by Eq. 5.3 is shown as a blue line. The ranges of $\Delta\phi$ used to fix the value of Y and to define the signal region ($\Delta\phi > \frac{7\pi}{8}$) are indicated by yellow and green shaded regions, respectively. The parameters c_3 and c_4 are obtained by fitting the $\Delta\phi$ distribution for jet pairs with $|\Delta\eta| > 1$ in the region $0 < \Delta\phi < \frac{\pi}{2}$, which is indicated by the red squares (scaled to match the black circles in the yellow region for presentation purposes). The error bars denote statistical errors.

or fake jets (described in Section 4.6.3). This is a replacement for using fake rejection to eliminate the background since fake rejection is inefficient at low p_{T}. The background was estimated using the $\Delta\phi$ distribution between the leading and sub-leading jet in the region where the jets are uncorrelated ($\Delta\phi < \pi/2$). The $\Delta\phi$ distributions were compared between dijet pairs with and without fake rejection as shown in Figure 5.14. The distribution without fake rejection has a clear background where the distribution with fake rejection does not. The background decreases with decreasing centrality until the most peripheral dijet pairs have no background contribution. Figure 5.14 indicates in yellow the background between $\phi_{\mathrm{min}} = 1.0$ and $\phi_{\mathrm{max}} = 1.4$ that was selected for the analysis. The ϕ_{min} was chosen to be 1.0 because when determining the background a ΔR cut at 1.0 ($\Delta R_{12} > 1.0$) was made between the leading and sub-leading jets to eliminate split jets. The ϕ_{max} was chosen to be 1.4 in order to get the largest background region possible without going into the correlated region that begins around $\pi/2$.

The background is modulated by the residual flow contributions especially at low p_{T}.

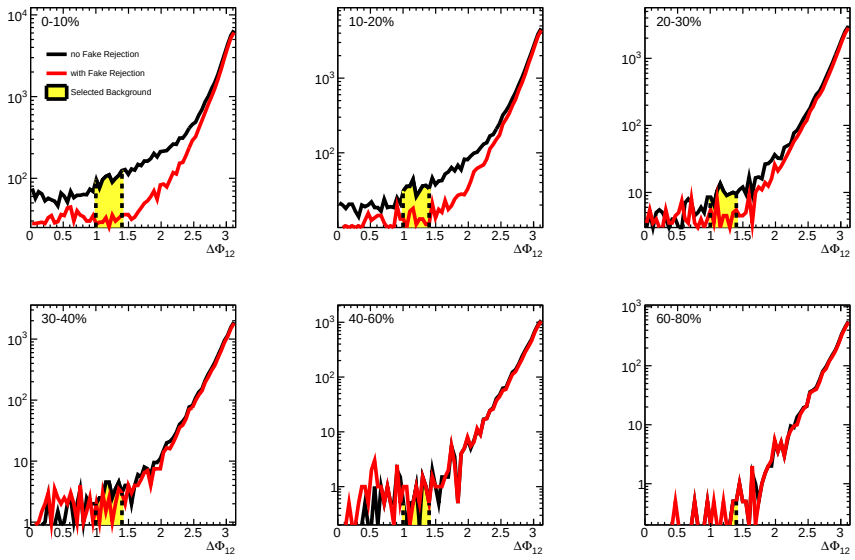

Figure 5.14: The $\Delta\phi$ distributions for dijet pairs with fake rejection and without fake rejection in different centrality bins for $R = 0.4$ jets. The background region is selected between 1.0 and 1.4.

Corrections were made to reduce this contribution as described in Section 5.3.1.2 including fitting the residual background in a region of large $\Delta\eta$ to extract v_3 and v_4. The background was estimated by using these values in the full background region (no $\Delta\eta$ cut) between $\Delta\phi$ of 1.0 to 1.4 to determine the amplitude of the flow modulation. This amplitude is the same throughout the full $\Delta\phi$ range. This was done through the following integral where A is the amplitude and N_{bkgr} is the number of counts in the $\Delta\phi$ distribution between $\Delta\phi_{\text{min}} = 1.0$ and $\Delta\phi_{\text{max}} = 1.4$:

$$
\begin{aligned}
N_{\text{bkgr}}|_{\Delta\phi_{\text{min}}}^{\Delta\phi_{\text{max}}} &= \int_{\Delta\phi_{\text{min}}}^{\Delta\phi_{\text{max}}} A[1 + 2v_3\cos(3\Delta\phi) + 2v_4\cos(4\Delta\phi)] \\
\Delta\phi_{\text{bkgr}}^{-} &= \Delta\phi_{\text{max}} - \Delta\phi_{\text{min}} \\
\Delta\phi_{\text{bkgr}}^{+} &= \Delta\phi_{\text{max}} + \Delta\phi_{\text{min}} \\
N_{\text{bkgr}}|_{\Delta\phi_{\text{min}}}^{\Delta\phi_{\text{max}}} &= A[\Delta\phi_{\text{bkgr}}^{-} + \frac{4v_3}{3}\cos(\frac{3\Delta\phi_{\text{bkgr}}^{+}}{2})\sin(\frac{3\Delta\phi_{\text{bkgr}}^{-}}{2}) + v_4\cos(\frac{4\Delta\phi_{\text{bkgr}}^{+}}{2})\sin(\frac{4\Delta\phi_{\text{bkgr}}^{-}}{2})] \\
A &= \frac{N_{\text{bkgr}}|_{\Delta\phi_{\text{min}}}^{\Delta\phi_{\text{max}}}}{\Delta\phi_{\text{bkgr}}^{-} + \frac{4v_3}{3}\cos(\frac{3\Delta\phi_{\text{bkgr}}^{+}}{2})\sin(\frac{3\Delta\phi_{\text{bkgr}}^{-}}{2}) + v_4\cos(\frac{4\Delta\phi_{\text{bkgr}}^{+}}{2})\sin(\frac{4\Delta\phi_{\text{bkgr}}^{-}}{2})}
\end{aligned}
$$

Then the amplitude A was used to determine the contribution of the background to the signal region of back-to-back correlated jets by integrating the same function between $\Delta\phi_{\text{signal}} = 7\pi/8$ to π:

$$
\begin{aligned}
N_{\text{bkgr}}|^{\pi}_{\Delta\phi_{\text{signal}}} &= \int_{\Delta\phi_{\text{signal}}}^{\pi} A[1 + 2v_3\cos(3\Delta\phi) + 2v_4\cos(4\Delta\phi)] \\
\Delta\phi^{-}_{\text{signal}} &= \pi - \Delta\phi_{\text{signal}} \\
\Delta\phi^{+}_{\text{signal}} &= \pi + \Delta\phi_{\text{signal}} \\
N_{\text{bkgr}}|^{\pi}_{\Delta\phi_{\text{signal}}} &= A[\Delta\phi^{-}_{\text{signal}} + \frac{4v_3}{3}\cos(\frac{3\Delta\phi^{+}_{\text{signal}}}{2})\sin(\frac{3\Delta\phi^{-}_{\text{signal}}}{2}) + v_4\cos(\frac{4\Delta\phi^{+}_{\text{signal}}}{2})\sin(\frac{4\Delta\phi^{-}_{\text{signal}}}{2})] \\
N_{\text{bkgr}}|^{\pi}_{\Delta\phi_{\text{signal}}} &= N_{\text{bkgr}}|^{\Delta\phi_{\text{max}}}_{\Delta\phi_{\text{min}}} \frac{\Delta\phi^{-}_{\text{signal}} + \frac{4v_3}{3}\cos(\frac{3\Delta\phi^{+}_{\text{signal}}}{2})\sin(\frac{3\Delta\phi^{-}_{\text{signal}}}{2}) + v_4\cos(\frac{4\Delta\phi^{+}_{\text{signal}}}{2})\sin(\frac{4\Delta\phi^{-}_{\text{signal}}}{2})}{\Delta\phi^{-}_{\text{bkgr}} + \frac{4v_3}{3}\cos(\frac{3\Delta\phi^{+}_{\text{bkgr}}}{2})\sin(\frac{3\Delta\phi^{-}_{\text{bkgr}}}{2}) + v_4\cos(\frac{4\Delta\phi^{+}_{\text{bkgr}}}{2})\sin(\frac{4\Delta\phi^{-}_{\text{bkgr}}}{2})}
\end{aligned}
$$

Figure 5.13 shows a summary of the procedure for 0–10% centrality in a p_{T_1} range between 80 and 100 GeV. The fit is shown in the blue and the area used to estimate the amplitude of the background A is shown in the yellow shaded region. The location where the background was removed from the signal is shown in green.

In the 2D (p_{T_1},p_{T_2}) distributions each bin has a background in the signal region so this background was calculated bin-by-bin. Then the background was subtracted bin-by-bin from the signal region for $\Delta\phi > 7\pi/8$ to obtain the data to unfold in the analysis. The signal before and after the background subtraction is overlaid with the background in the $100 < p_{\text{T}_1} < 112$ GeV bin as a function of centrality in Figure 5.15 and in the 0–10% centrality bin as a function of leading jet p_{T} in Figure 5.16. The background is the largest for the most central bins and for the lowest leading jet p_{T}. The background is significantly less than the signal for leading jets greater than 100 GeV which is the region of interest for this analysis.

The systematics on the background subtraction were examined by comparing results using a different $\Delta\phi$ range to estimate the amplitude of the modulation to the nominal one from 1.0 to 1.4. Figures 5.17 and 5.19 compares the two ranges for the data with the background subtracted (signal). The small difference between the different ranges in the signal indicate that this is small effect but the ratios to the nominal range were evaluated to quantitatively assess the magnitude of the difference. The ratios are shown in Figures 5.18

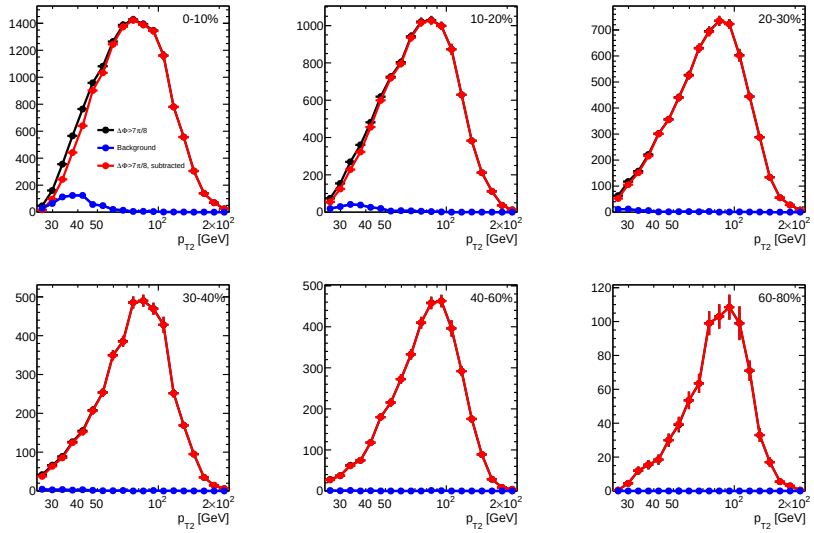

Figure 5.15: The background subtraction method in different centrality bins for $100 < p_{T_1} < 112$ GeV for $R = 0.4$ jets. The red curve is before subtraction for $\Delta\phi > 7\pi/8$, the blue curve is the contribution to the background between $\Delta\phi = 7\pi/8$ to π, and the black is the data with the background subtracted.

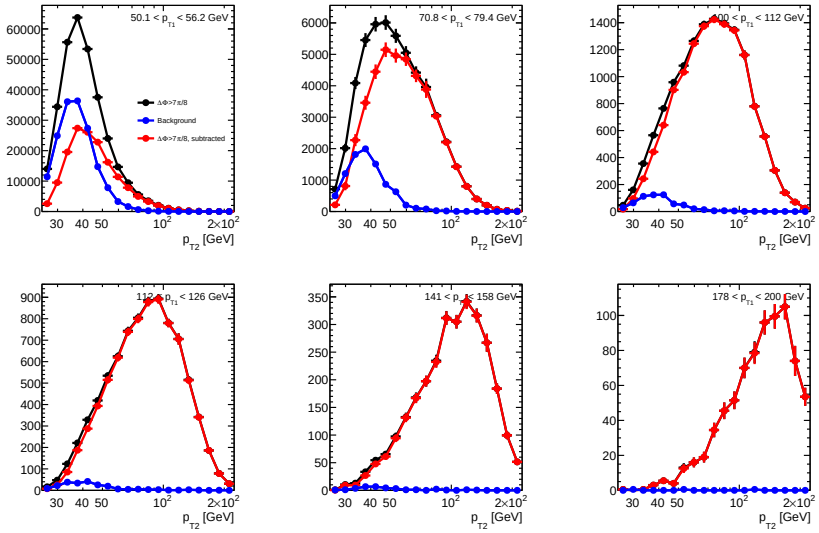

Figure 5.16: The background subtraction method in different p_{T_1} bins for 0-10% centrality for $R = 0.4$ jets. The red curve is before subtraction for $\Delta\phi > 7\pi/8$, the blue curve is the contribution to the background between $\Delta\phi = 7\pi/8$ to π, and the black is the data with the background subtracted.

and 5.20. The biggest difference is in the most central bin for the lowest p_{T} leading jets. The difference for leading jets around 50 GeV in the 0–10% centrality bin is greater than 10% for sub-leading jets less than 30 GeV then becomes less than 1% for sub-leading jets above 70 GeV. For leading jets greater than 100 GeV, which is the region of interest for this analysis, the difference is about 10% for sub-leading jets less than 30 GeV and becomes less than 3% for sub-leading jets greater than 30 GeV (and less than 1% for sub-leading jets greater than 50 GeV). The data will be unfolded for this different $\Delta\phi$ range and compared to the nominal result to calculate the final systematic from this effect.

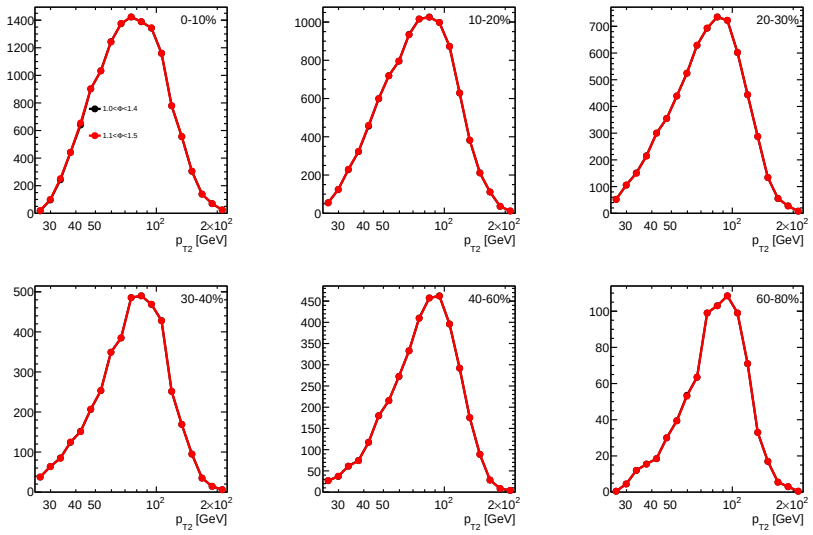

Figure 5.17: The data with the background subtracted for $\Delta\phi$ regions of 1.0-1.4 (nominal) in black and 1.1-1.5 in red in different centrality bins for $100 < p_{\mathrm{T}_1} < 112$ GeV for $R = 0.4$ jets.

The combinatoric subtraction leads to an inefficiency because there will be real pairs that have a sub-leading jet that is lower p_{T} than the combinatoric sub-leading jet. This causes the pair to be subtracted as background when it is actually real and should be in the signal. The data after the combinatoric subtraction was corrected for this inefficiency on a pair-by-pair basis. The inefficiency was calculated by first estimating the number of times there is a jet in an event above a particular p_{T} value using the inclusive jet spectrum. This number was then used to calculate the probability this occured zero times using the Poisson distribution for zero events. This probability becomes the inefficiency at that particular value of p_{T}

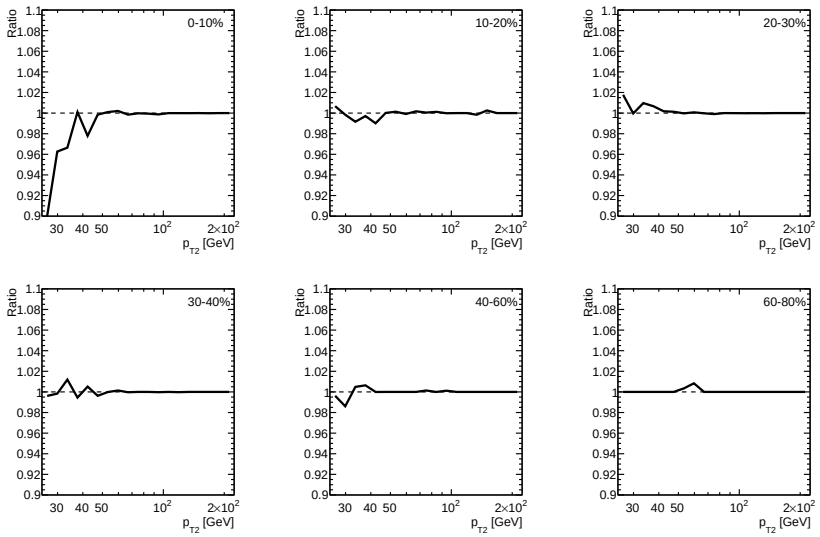

Figure 5.18: Ratio of the data with the background subtracted for $1.1 < \Delta\phi < 1.5$ to $1.0 < \Delta\phi < 1.4$ in different centrality bins for $100 < p_{\mathrm{T}_1} < 112$ GeV for $R = 0.4$ jets.

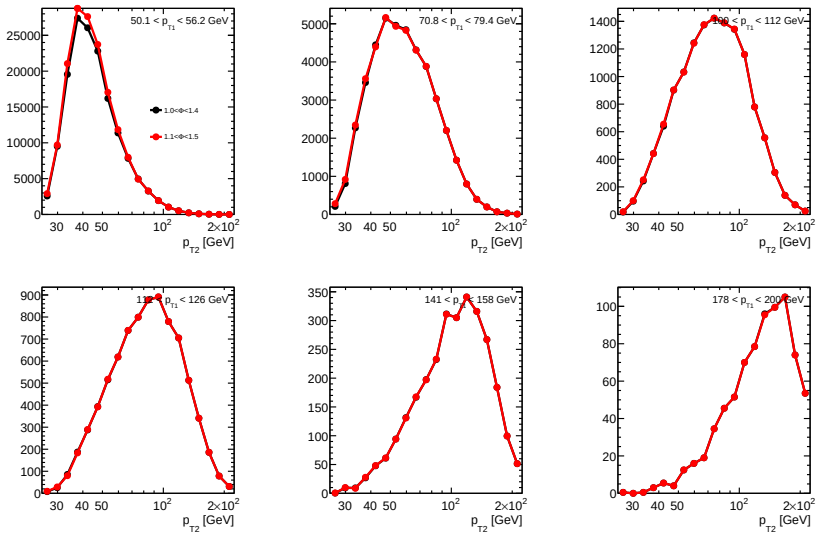

Figure 5.19: The data with the background subtracted for $\Delta\phi$ regions of 1.0-1.4 (nominal) in black and 1.1-1.5 in red in different p_{T_1} bins for 0-10% centrality for $R = 0.4$ jets.

and this was calculated for all possible sub-leading jet p_{T} values. The inefficiency as a function of the sub-leading jet p_{T} is shown in Figure 5.21 in different centrality bins. It is independent of the leading jet p_{T}. The effects of the combinatoric jet pairs are accounted

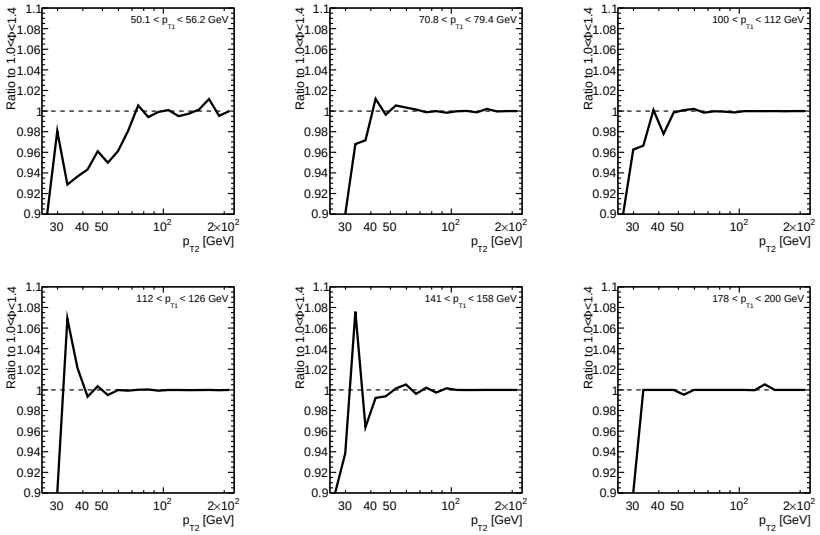

Figure 5.20: Ratio of the data with the background subtracted for $1.1 < \Delta\phi < 1.5$ to $1.0 < \Delta\phi < 1.4$ in different p_{T_1} bins for 0-10% centrality for $R = 0.4$ jets.

for by first subtracting the estimated background and then correcting for the efficiency, ε, in each $(p_{\mathrm{T}_1}, p_{\mathrm{T}_2})$ bin. The number of jet pairs corrected for such effects is defined to be:

$$N^{\mathrm{corr}} = \frac{1}{\varepsilon}\left(N^{\mathrm{raw}} - B\right),$$

where N^{raw} is the number of jet pairs after correcting for trigger efficiency.

5.3.1.4 Raw Spectra

The final raw (before unfolding) data in Pb+Pb collisions is shown in Figure 5.22 and Figure 5.23. Figure 5.22 shows sub-leading jet distributions in different centrality bins with selections on the leading jet p_{T}. It demonstrates that as the p_{T} of the leading jet is increased, the peak in the sub-leading jet distribution increases and widens. Figure 5.23 is the same plot except now the distribution is binned in leading jet p_{T} and the projections are shown as a function of centrality. At higher p_{T} the peak in the sub-leading jet distribution decreases with increasing centrality such that the most peripheral jet pairs are the most balanced in energy.

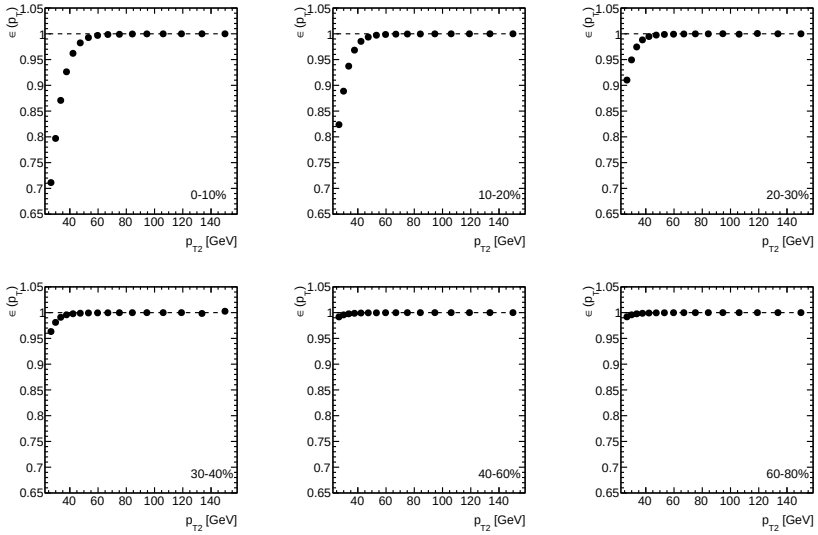

Figure 5.21: The inefficiency as a function of sub-leading jet p_{T} in different centrality bins centrality for $R = 0.4$ Pb+Pb jets.

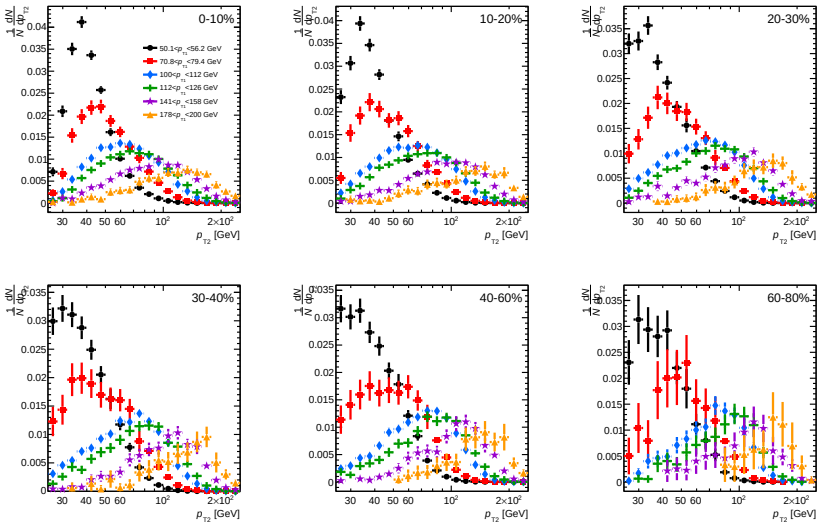

Figure 5.22: The raw (before unfolding) data sub-leading jet distributions binned in centrality as a function of leading jet p_{T} for $R = 0.4$ jets.

5.3.1.5 x_{J} Projection

The final measurement will be the x_{J} distribution of the dijet pairs which is calculated from the leading and sub-leading jet in the following way, where p_{T_1} is the leading jet and p_{T_2} is

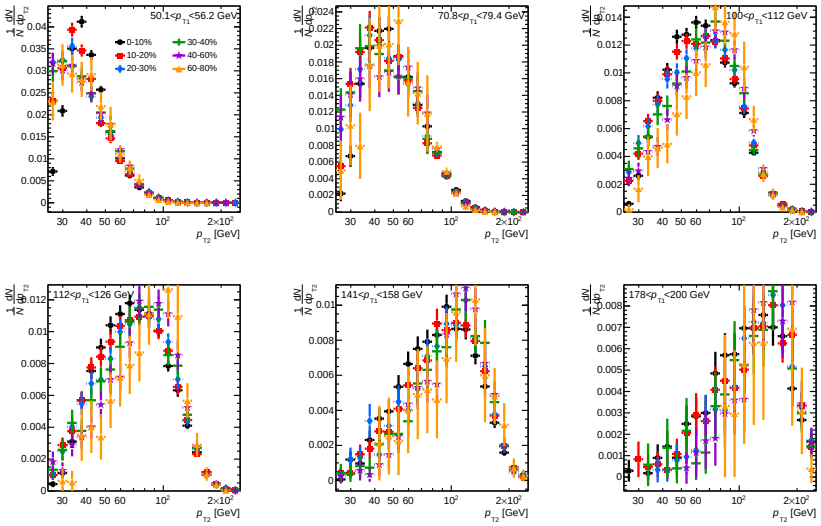

Figure 5.23: The raw (before unfolding) sub-leading jet distributions binned in leading jet p_{T} as a function of centrality for $R = 0.4$ jets.

the sub-leading jet:

$$x_{\mathrm{J}} = \frac{p_{\mathrm{T}_2}}{p_{\mathrm{T}_1}} \tag{5.4}$$

This is a quantity that goes from 0 to 1 where 1 is fully symmetric dijets and anything less than 1 indicates an asymmetry. In the analysis the x_{J} was generated from the 2D p_{T_1} and p_{T_2} distribution by first folding over the diagonal and then projecting into a 1D x_{J} distribution. This is demonstrated in the cartoon in Figure 5.24. In the first panel the 2D distribution after the different trigger samples are combined is shown. This was symmeterized in panel 2 because a symmetric distribution is needed in order to unfold. Panel 3 shows the distribution folded back over the diagonal after unfolding to obtain a leading/sub-leading jet distribution again. Notice that the number of jets in the diagonal bin doesn't change in the first 3 panels. This is so that the total number of jets is always the same regardless of whether the distribution is symmetric or folded. Panel 4 shows what the distribution looks like with more bins filled (numbers were added arbitrarily so that the projection into x_{J} can be better described). The diagonal lines across the 2D distribution indicate where the bin boundaries of the x_{J} distribution will be. These bin boundaries

divide the bins in half so the counts have to be distributed accordingly. The way the counts in the bins are combined is shown in the panel 5. Here the counts in each 2D bin are divided by two so half goes to one x_{J} bin and the other half goes to the other. The first and the last bin in x_{J} are unique in that the first bin is only half the counts and the last bin (x_{J}=1) includes the full diagonal bin plus half of the first off diagonal bin. Then the projection into x_{J} is shown panel 6 with the counts evaluated correctly.

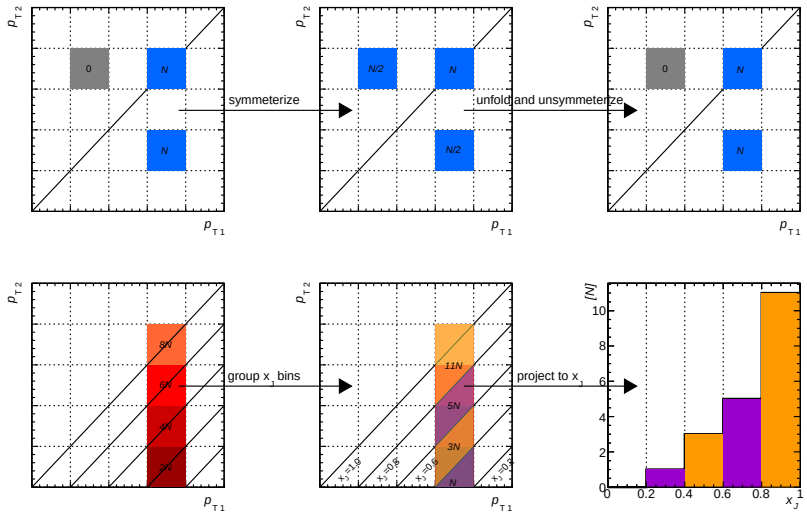

Figure 5.24: A schematic demonstrating the procedure to project a symmetric 2D $p_{\mathrm{T}_1}/p_{\mathrm{T}_2}$ distribution into x_{J}.

A mathematic description of the binning choices and how the projection is achieved is as follows. The two-dimensional distribution uses binning in both the x and y axis such that the upper edge of the i^{th} bin obeys

$$p_{\mathrm{T}\,i} = p_{\mathrm{T}\,0}\,\alpha^{i}\,, \quad \alpha = \left(\frac{p_{\mathrm{T}\,N}}{p_{\mathrm{T}\,0}}\right)^{1/N}$$

where N is the total number of bins and $p_{\mathrm{T}\,0}$ and $p_{\mathrm{T}\,N}$ are the minimum and maximum bin edges, respectively. The bins are actually the same size when plotted on a logarithmic axis. In this binning scheme, the range of x_{J} values in any given $(p_{\mathrm{T}_1}, p_{\mathrm{T}_2})$ bin is completely contained within two adjacent x_{J} bins, which have boundaries at $x_{\mathrm{J}\,i} = \alpha^{i-N}$.

This procedure introduces an inherent bias since the counts are divided by two and

distributed into the corresponding x_J bins. This assumes that the counts are distributed in an approximately constant manner across the 2D bins which is not necessarily true. The accuracy of this procedure was evaluated by sampling a 2D distribution in the MC to directly fill a x_J distribution and fill a new 2D distribution. Then the 2D distribution was projected into x_J using the above procedure and the two distributions were compared in the left panel of Figure 5.25 (making sure the binning in the two curves are the same). The ratio in the bottom part of the panel indicates good closure until very low x_J values where it differs up to a few percent. This analysis does not use x_J below 0.3 where the agreement is less that 1%. Then the original 2D distribution in the MC was weighted by $1/{x_J}^2$ and the check described above was repeated. This weighting was done to verify that the projection procedure works for a x_J distribution with a wider shape. This again demonstrated good closure in the method above 0.3.

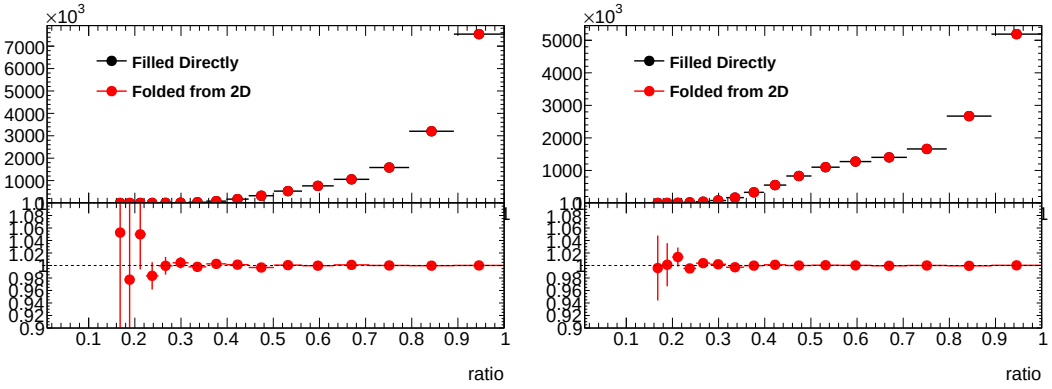

Figure 5.25: Comparison between x_J distributions filled directly and filled by projecting from a 2D distribution. The ratio of the two is shown in the bottom part of the panel. The left demonstrates the comparison in the MC and the right is the MC reweighted by $1/{x_J}^2$.

Figure 5.26 and Figure 5.27 demonstrate what the x_J distributions look like for the raw data. The raw data doesn't need to be symmeterized or folded because the projection into x_J can be evaluated from the raw 2D distributions after the trigger samples are combined. These distributions demonstrate similar qualitative effects as the slices in the previous section but the spectra are smeared out. At high p_T the dijet pairs become more asymmetric in more central collisions and with increasing leading jet p_T.

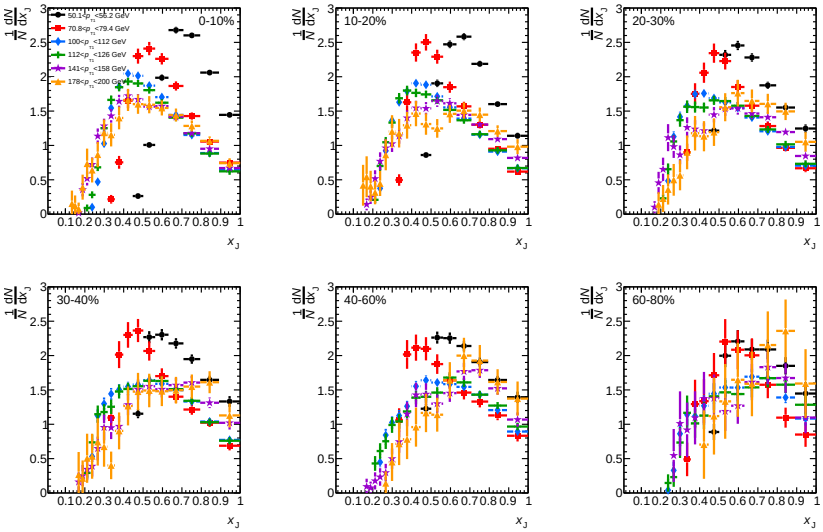

Figure 5.26: The raw (before unfolding) x_{J} distributions binned in centrality as a function of leading jet p_{T} for $R = 0.4$ jets.

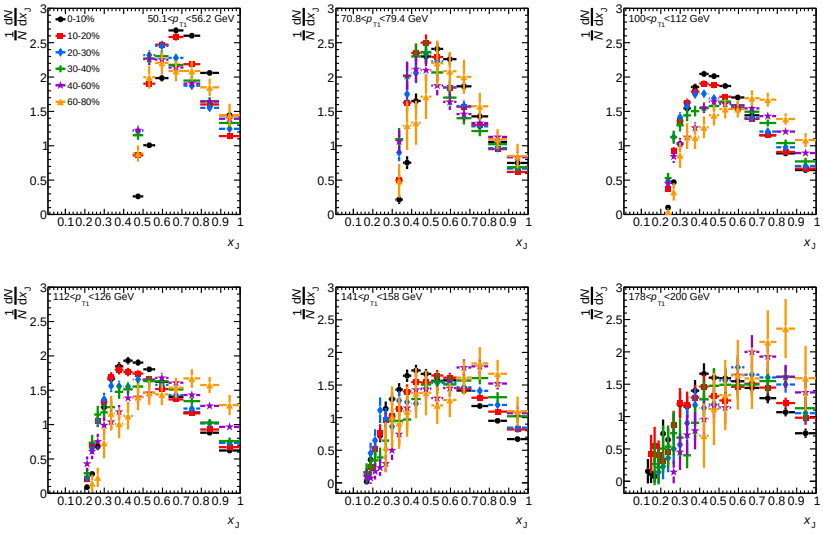

Figure 5.27: The raw (before unfolding) x_J distributions binned in leading jet p_{T} as a function of centrality for $R = 0.4$ jets.

5.3.2 *pp* Data Analysis

The *pp* data is generated in almost the same way as the Pb+Pb data with respect to the jet selection and corrections. The difference in the corrections is that for the *pp* there is no

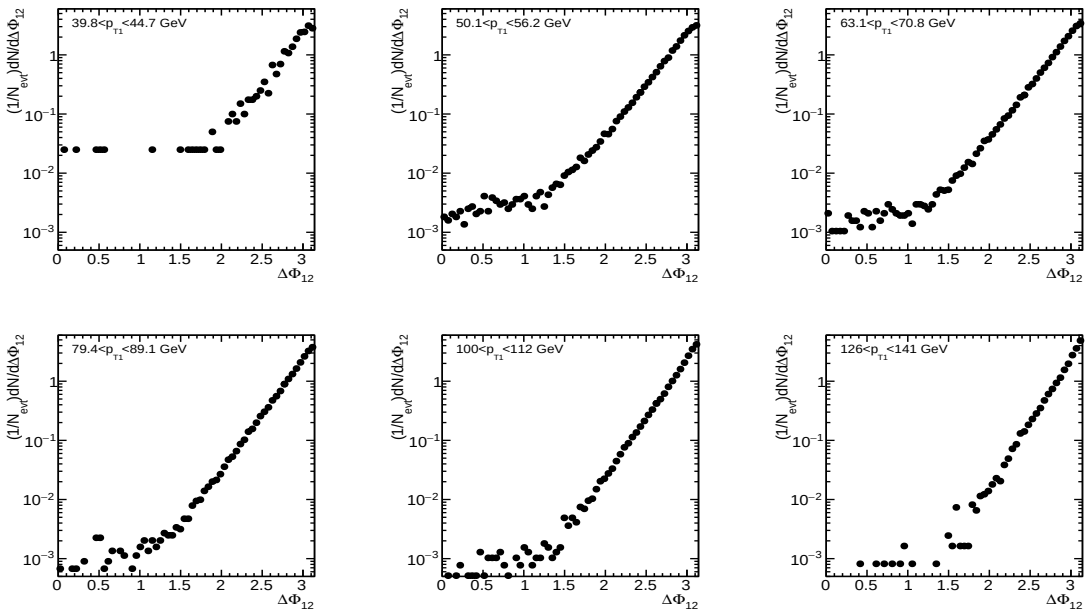

Figure 5.28: The $\Delta\phi$ distribution binned in leading jet p_{T} for the pp data.

η-ϕ, self-energy bias, or flow correction. There is no combinatoric background subtraction in the pp jets because there is a negligible background as seen in Figure 5.28.

The pp jets are required to pass "isUgly" and "isBadMedium" cleaning cuts. The "isUgly" cut is designed to reject jets depositing a majority of their energy in the Tile Barrel to Tile Extension transition region or in dead cells, since the total energy is not well measured in these cases. The "isBadMedium" cut rejects jets consistent with noise spikes in the HEC, coherent noise in the EM calorimeter and out-of-time energy deposits from cosmic rays and beam backgrounds. The efficiency for these cuts in the different trigger samples is shown in Figure 5.29.

The pp data was generated by combining 6 different trigger samples. They were combined using the same method that was used for the Pb+Pb minimum bias and jet triggered data except here the trigger samples are scaled by the luminosity of the different triggers. Table 5.2 shows the luminosity for the different samples and the p_{T} ranges over which they are efficient to $> 99\%$.

The different trigger samples were generated by finding the events and jets in the sample

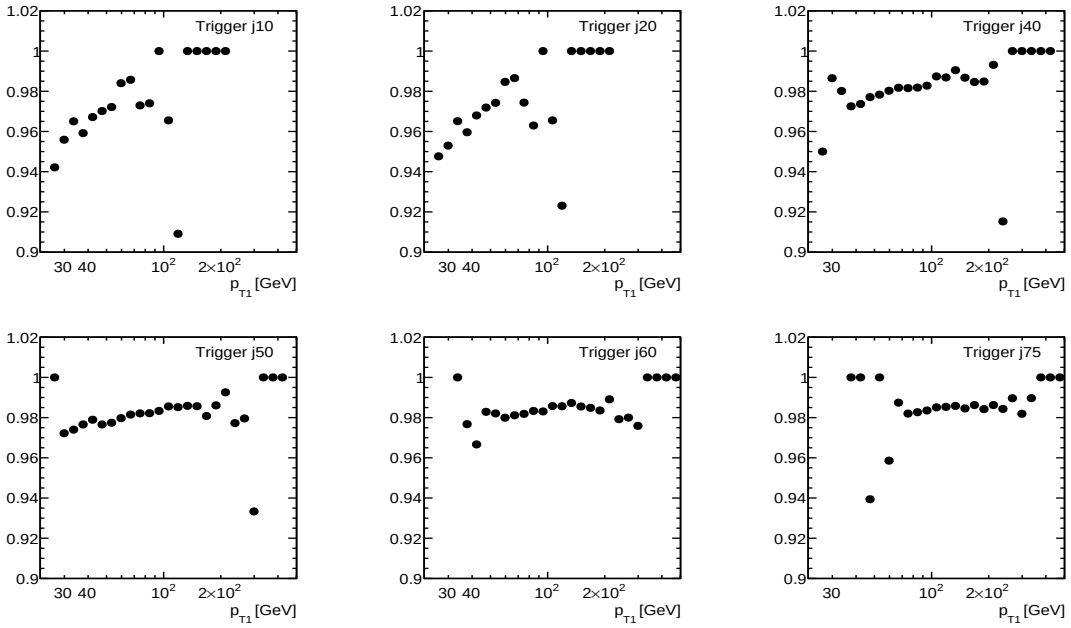

Figure 5.29: Efficiency of the jets for applying the "isUgly" and "isBadMedium" cleaning cuts for the different triggers.

that fired each corresponding trigger in the following way:

- Check that the event fired the trigger by checking the PID of the event.
- For each event check if the leading jet matches to a trigger jet:
  - Find the trigger jets that pass a4tchad branch .
  - Check that the trigger jet E_{T} is above the corresponding trigger threshold:
    - j10: 10 GeV
    - j20: 20 GeV
    - j40: 40 GeV
    - j50: 50 GeV
    - j60: 60 GeV
    - j75: 75 GeV
  - Check that the leading jet is within $\Delta R = \sqrt{\Delta\phi^2 + \Delta\eta^2}$ of 0.4 of the trigger jet.

Then the samples were combined by selecting on the leading jet p_{T} as shown in Figure 5.30. On the top panel in the plot each trigger sample matches the combined spectrum in black in the region over which it is efficient and then falls off around a specific value.

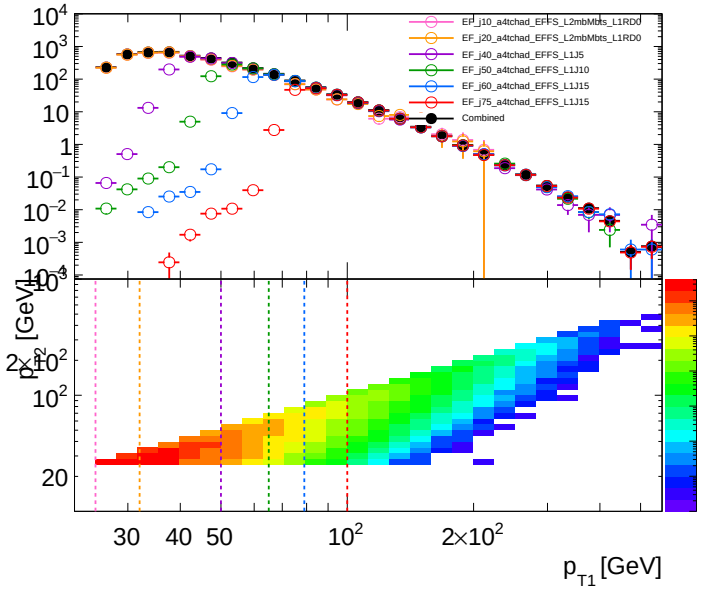

Figure 5.30: The top panel is an overlay of the different $R = 0.4$ trigger sample leading jet p_{T} spectrums with the combined spectrum in black. The bottom panel is the combined spectrum 2D jet 1/jet 2 distribution.

The 2D distribution (shown in the bottom panel) demonstrates that when the samples are combined and weighted by the luminosity the distribution is smooth. Ratios were evaluated between the different trigger samples in order to visualize how well the samples match. The left panel of Figure 5.31 shows the ratio of each trigger sample to the previous trigger sample for $R = 0.4$ and $R = 0.3$. In the regions where both samples are efficient the ratio fluctuates around one which indicates that the scaled samples match. The right panel of Figure 5.31 shows the ratio of the high p_{T} triggers to the j40. This was investigated because the region we care the most about is at high p_{T}. Again the ratio fluctuates about 1 in the regions where the triggers are efficient indicating that the spectra were combined correctly.

Figure 5.10 shows the final 2D $(p_{\mathrm{T}_1}, p_{\mathrm{T}_2})$ distributions in central Pb+Pb, peripheral Pb+Pb, and pp. The trigger boundaries for the pp data are shown in the colored lines on the figure. In a given event, the p_{T} resolution may result in the jet with the highest true p_{T} being measured with the second highest p_{T} and vice-versa. To properly account for such migration effects, $(p_{\mathrm{T}_1}, p_{\mathrm{T}_2})$ distributions are symmetrized before unfolding by reflecting

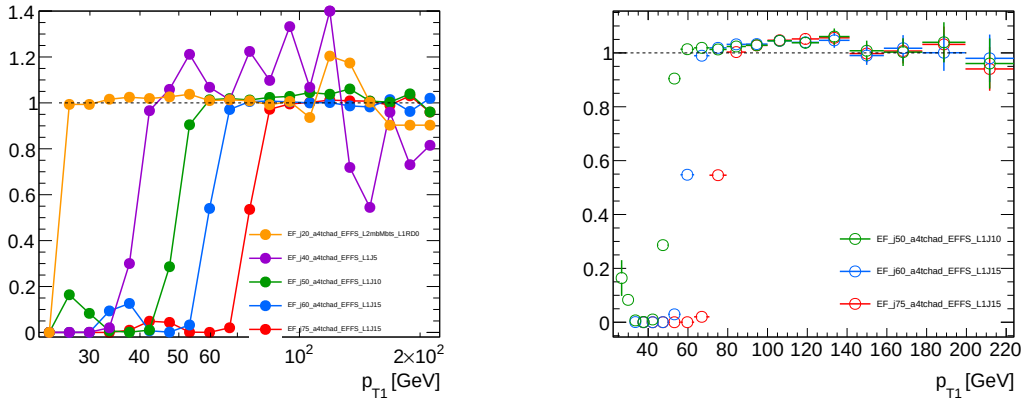

Figure 5.31: The left panel shows the ratio of each $R = 0.4$ trigger sample leading jet p_{T} distribution to the lower p_{T} sample (for example j75/j60 and j20/j10. The right panel shows the ratio of the j75, j60, and j50 trigger samples leading jet p_{T} distribution to the j40.

half the distribution over the diagonal as demonstrated in the figure.

Slices in the leading jet p_{T} were taken to investigate how the spectrum changes as the leading jet p_{T} was increased. This is shown in Figure 5.32 in the left panel. The peak of the sub-leading jet spectrum increases as the leading jet p_{T} increases. The x_{J} was also evaluated in the same way as for Pb+Pb. The right side of Figure 5.32 shows what the distributions look like when projected into x_{J}.

A comparison of the Pb+Pb centrality dependence in x_{J} before unfolding to pp data is shown in Figure 5.33. The pp agrees with the Pb+Pb in more peripheral collisions and then starts to differ in more central.

5.4 Unfolding

The results are unfolded using a two-dimensional Bayesian iterative unfolding method based on Bayes theorem [219] from the `RooUnfold` software package [228] (described in more detail in Section 4.6. The results are unfolded to account for bin migration due to the finite jet energy resolution from intrinsic detector resolution. The order of the leading jet p_{T} can be reversed due to bin migration over the diagonal so the results are unfolded simultaneously in 2D with a four-dimensional response matrix built from the MC that is filled symmetrically. The response matrix for the unfolding is generated separately in the Pb+Pb and pp and

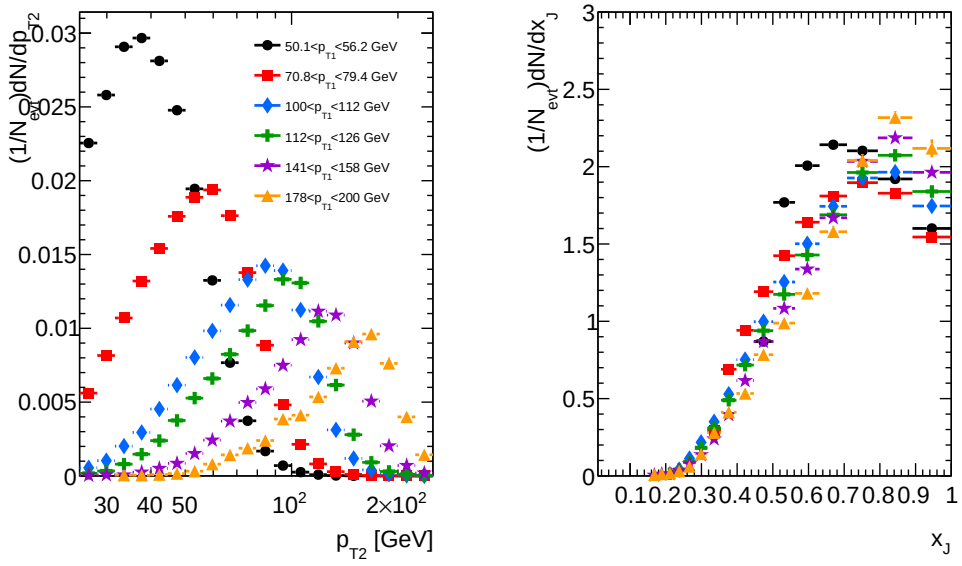

Figure 5.32: Left panel is the distribution of the sub-leading jet p_{T} in bins of leading jet p_{T} for $R = 0.3$ jets. Right panel is the x_{J} distributions in bins of leading jet p_{T}.

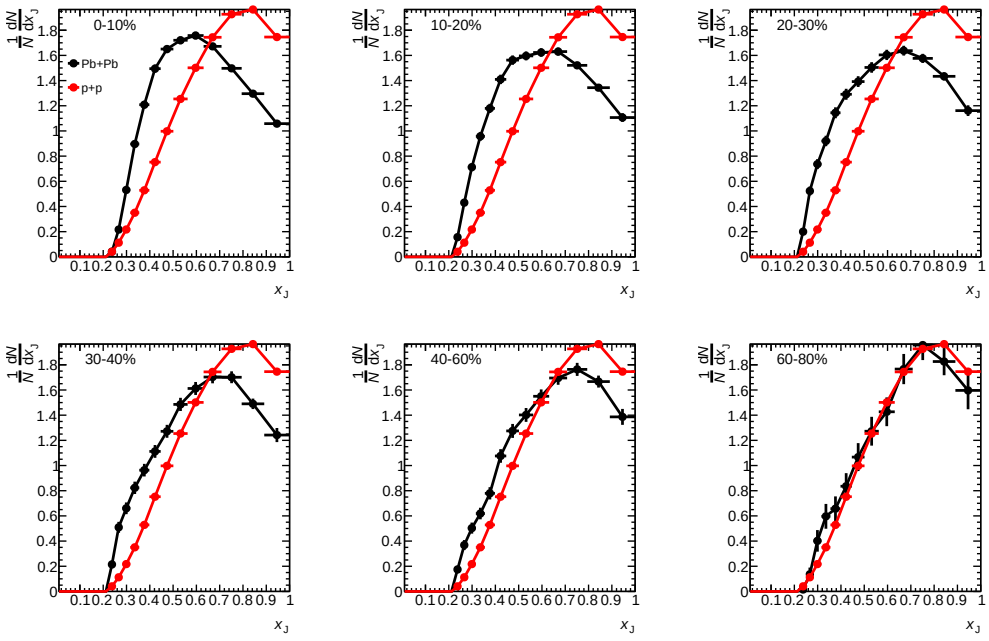

Figure 5.33: The Pb+Pb x_{J} distributions for $R = 0.4$ jets in different centrality bins compared to the pp data in the 100-112 GeV leading jet p_{T} bin.

the unfolding is done separately as well. The data is unfolded with the response matrix for a given number of iterations that is determined based on the dependence of the unfolding on the prior and the statistical uncertainties (described in general in Section 4.6.1 and in this analysis in Section 5.4.4). Iterating too much can cause amplification of statistical fluctuations in the data so a careful balance has to be obtained between the prior dependence and the statistical fluctuations in the unfolded result. The statistical errors in the unfolding are calculated by generating 100 toys (or MC sampling) using gaussian statistics which accounts for the error due to many different variations of the data. This uses the initial covariance in the raw data and also calculates the final covariance in the $\frac{1}{N}\frac{dN}{dx_J}$ distributions. The covariance is discussed in detail in Appendix B.

5.4.1 Response Matrix

The response matrix was built from truth level pairs that are matched to reconstructed pairs in the MC. The truth level dijet pairs are selected by finding the two highest jets in the event that have $|\eta| < 2.1$ and $p_{\mathrm{T}} > 10$ GeV. In order to keep the event the jets in the truth level dijet pair have to be within $\Delta\phi > 7\pi/8$. Each of these truth jets were then matched to the nearest reconstructed jet (within $\Delta R < 0.3$) that has $p_{\mathrm{T}} > 25$ GeV and $\eta < 2.1$. The reconstructed jets in the MC are reconstructed the same way as the data and receive the same JES and JER level calibrations and corrections. These reconstructed jets need to be within $\Delta\phi > 7\pi/8$ for the event to be considered for the response. The truth and reconstructed dijet pairs only contribute to the response if the previous conditions are fulfilled.

The response is filled symmetrically with ${p_{\mathrm{T}_1}}^{\mathrm{truth}}$, ${p_{\mathrm{T}_2}}^{\mathrm{truth}}$, ${p_{\mathrm{T}_1}}^{\mathrm{reco}}$, and ${p_{\mathrm{T}_2}}^{\mathrm{reco}}$ since the bin migration across the diagonal can cause the leading jet distinction to switch. The 2D truth and reconstructed distributions are shown in Figure 5.34 for Pb+Pb and Figure 5.35 for *pp*. The distributions are shown as a symmetric distribution and folded over the diagonal. The symmetric distribution is used in the unfolding and the folded distribution is the correct physical result. The response was made such that each axis has 40 logarithmic bins starting at 10 GeV and going to 1 TeV. This was chosen so that the reconstructed axes match those in the data. The response is filled in the same way for the $R = 0.4$ and $R = 0.3$ jets so the

$R = 0.3$ jets are shown Appendix C. The response in different centrality bins in the truth and in the reconstructed jets are also shown in Appendix C.

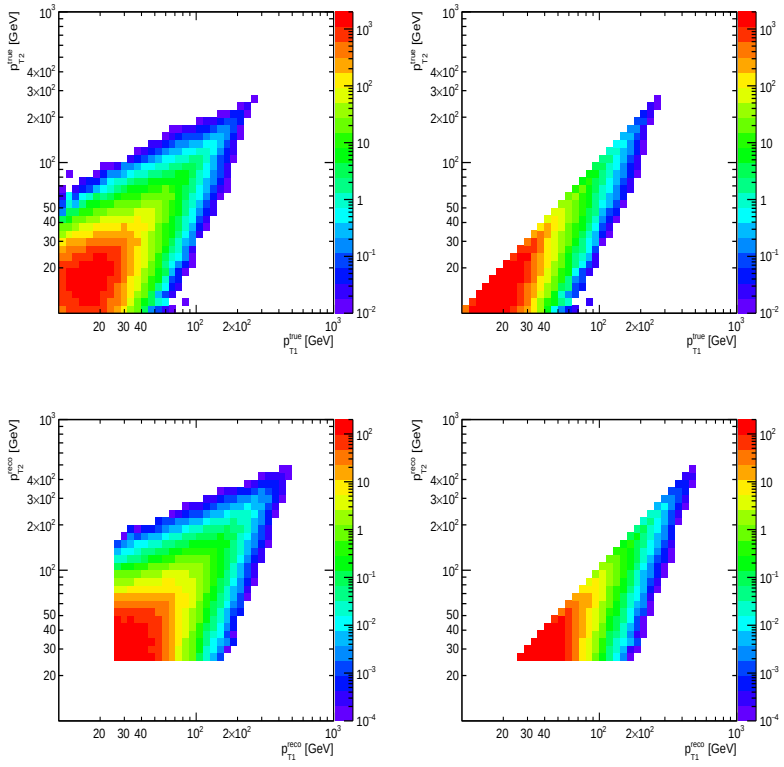

Figure 5.34: The top left panel is the truth level symmetric 2D distribution $(p_{\mathrm{T}_1}, p_{\mathrm{T}_2})$ and the top right panel is the truth folded over the diagonal. The bottom left panel is the reconstructed symmetric 2D distribution $(p_{\mathrm{T}_1}, p_{\mathrm{T}_2})$ and the bottom right panel is the reconstructed folded over the diagonal. All the distributions are for Pb+Pb in the 0–10% centrality bin and for $R = 0.4$ jets.

The actual response for the jets are demonstrated in the reconstructed versus truth distributions so the response in the reconstructed to the truth is shown in Figure 5.36 for Pb+Pb as a function of centrality and in Figure 5.37 for *pp*.

The response is a complicated four-dimensional object that is subject to many fluctuations. The response was sliced into different truth 1 and truth 2 bins so that the 2D reconstructed distributions could be investigated further. This is shown in Figure 5.38 for Pb+Pb in the left-hand panels. Since fluctuations were found in the response and the unfolding is very sensitive to these fluctuations, smoothing was attempted on the response in

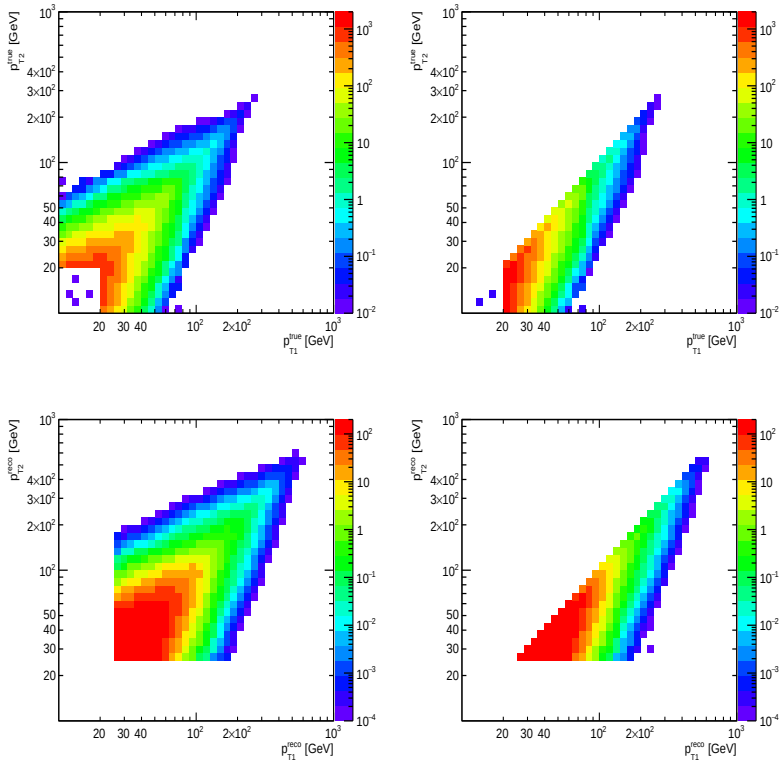

Figure 5.35: The top left panel is the truth level symmetric 2D distribution$p_{\mathrm{T}_1}/p_{\mathrm{T}_2}$ and the top right panel is the truth folded over the diagonal. The bottom left panel is the reconstructed symmetric 2D distribution $p_{\mathrm{T}_1}/p_{\mathrm{T}_2}$ and the bottom right panel is the reconstructed folded over the diagonal. All the distributions are for pp $R = 0.4$ jets.

the reconstructed distribution for each truth jet 1 and jet 2 bin. Bins are smoothed only if the bin didn't pass a significance cut that is based on the ratio of the error in that bin to the number of counts in that bin. Here the significance cut was chosen to be 2.0. The right-hand side of the previously described figures show the distributions after smoothing. The main part of the distribution with the most counts is unaltered but the fluctuations on the edges get smoothed out. Each row in the figures is a different bin in truth p_{T} 1 and 2. Another attempt to account for the fluctuations was made by implementing a filter in the JX-sample weighting in the MC. Anytime there was low counts in a bin in the response that would be amplified by the weighting of that particular J-sample that contribution was not included. Another improvement on the response was made by filling out the sparsely

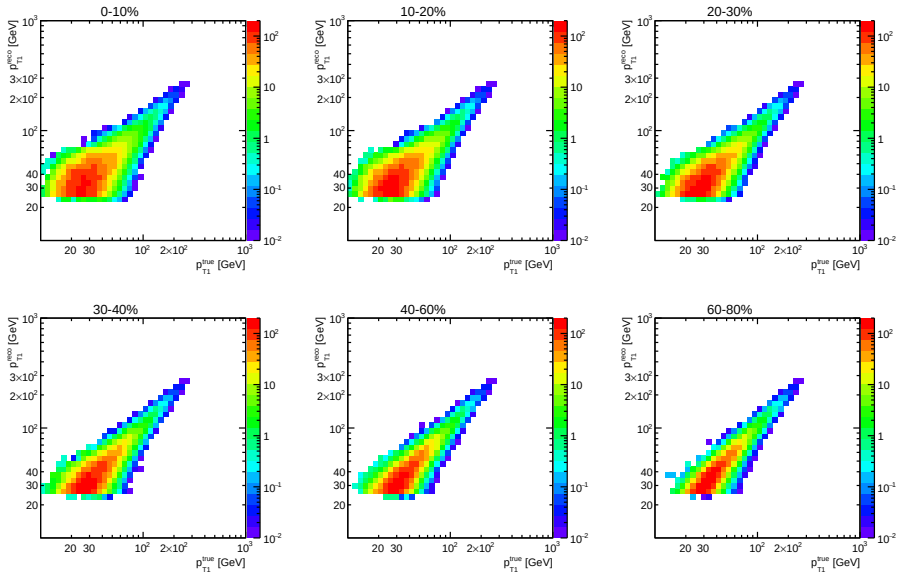

Figure 5.36: The response of the reconstructed jets to the truth jets in the MC for $R = 0.4$ jets in different centrality bins for the Pb+Pb.

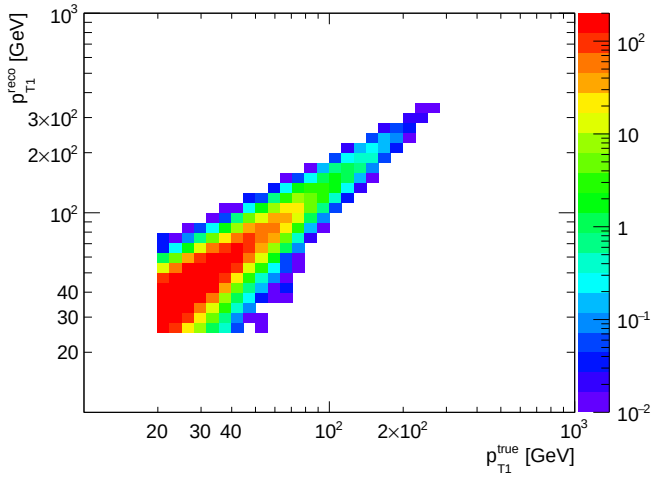

Figure 5.37: The response of the reconstructed jets to the truth jets in the MC for $R = 0.4$ *pp* jets.

populated bins in the 2D truth distribution that could be populated by data when unfolded. These bins were filled using a factorized response generated from the single jet response so that there is no correlation in the truth or reconstructed distribution but there is still cor-

relation between the truth and reconstructed jets. Bins were chosen to be filled based on a significance cut and different significance cuts were investigated. The largest variation from all of these modifications to the response was chosen to be a systematic due to alternative responses (more details in Section 5.5) and the difference between this and the nominal unfolded x_{J} distribution in different centrality bins is shown in Figure 5.39. The biggest difference in the unfolded result was observed for implementing the factorization with a significance of 2.0.

5.4.2 MC Closure

The unfolding procedure was verified by looking at the closure in the MC. This was done by splitting the MC in half and using one half to fill the response and the other half as the "data" to unfold. The "data" was unfolded using the response from half the MC and this result was compared to the original truth in x_{J}. Figure 5.40 demonstrates this for increasing number of iterations in 0–10% centrality for 100–126 GeV leading jet p_{T}. As the number of iterations increases the amount non-closure (difference in the ratio from unity) becomes within the statistical error indicating good MC closure.

The closure can also be investigated by comparing the statistical error due to the MC closure. This is demonstrated in Figure 5.41 where the relative statistical error, relative error from the MC closure, and the quadrature sum are shown as a function of iterations for a selection of x_{J} bins. The MC closure becomes smaller than the statistical error at a particular large number of iterations in each x_{J} bin indicating more evidence for closure.

5.4.3 Reweight Prior

The response was reweighted because the MC truth distribution is significantly different from the data. Therefore, the following reweighting was used as the nominal MC:

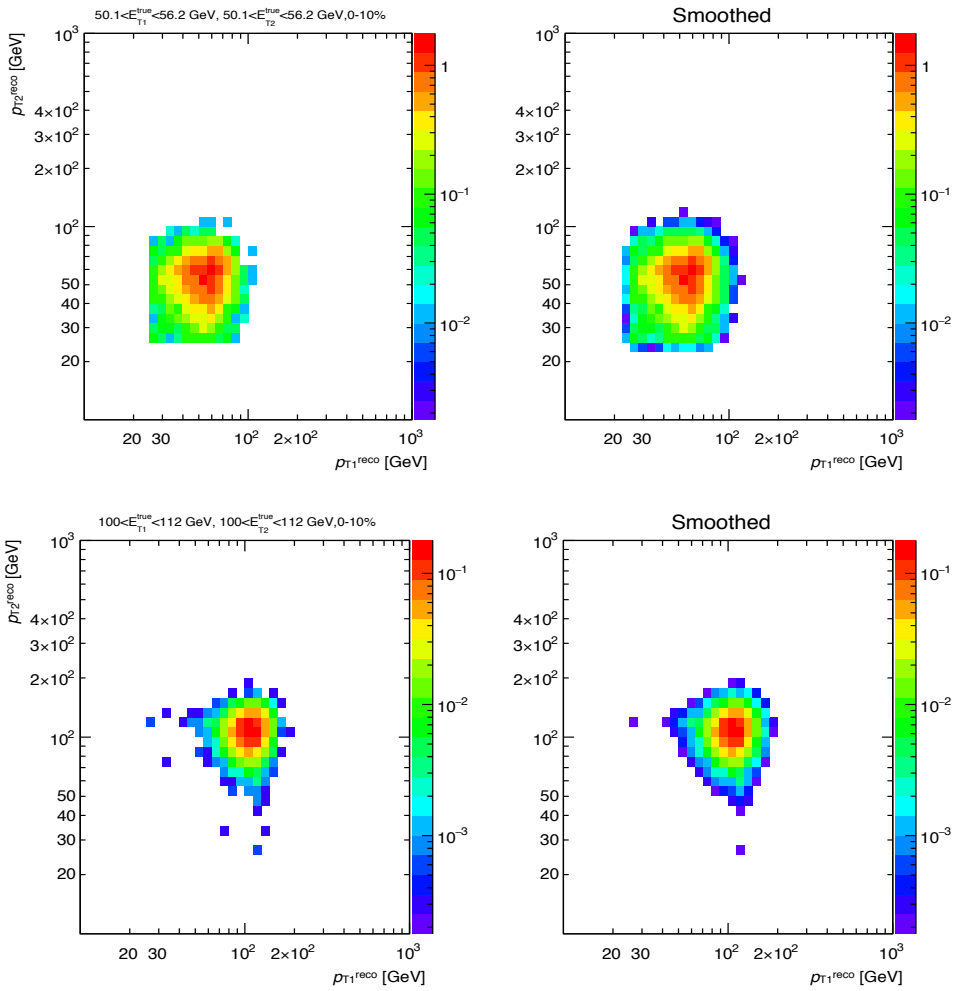

Figure 5.38: The reconstructed 2D distributions from the 4D response is shown in 2 different p_{T} truth 1 and 2 bins for the 0-10 % centrality $R = 0.4$ jets. The left panel shows the distribution before smoothing and the right panel after.

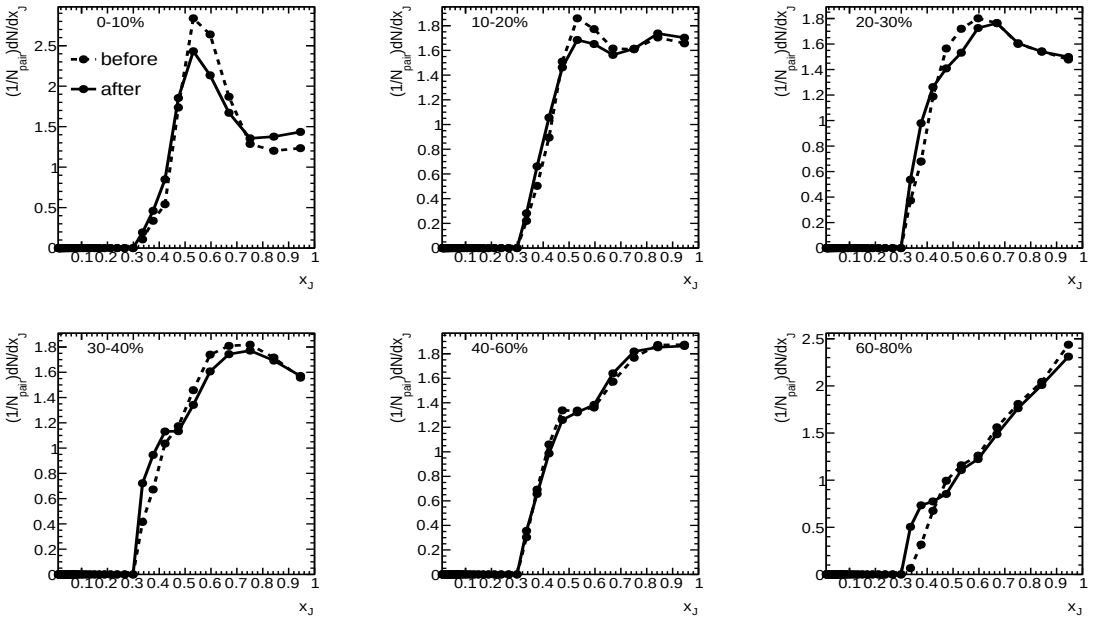

Figure 5.39: The unfolded x_{J} distributions in data using the nominal response and the most drastic alteration to the response (factorization with significance of 2.0) are overlaid. This is for $R = 0.4$ Pb+Pb jets with leading jet p_{T} between 100-126 GeV in the 0-10% centrality bin.

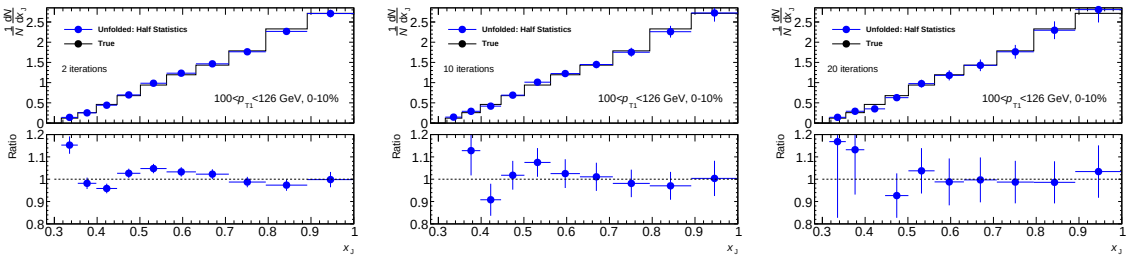

Figure 5.40: The closure in the unfolding is demonstrated in the MC for the 0–10% centrality and 100–126 GeV bin for different number of iterations: 2 (left), 10 (center), and 20 (right). The top sub-panel overlays x_{J} distributions where the black is the truth distribution from half the response matrix and the blue is the unfolded distribution for the other half of the MC. The bottom sub-panel has the ratio between the unfolded distribution and the truth.

$$
\begin{aligned}
w(x_{\mathrm{J}}, p_{\mathrm{T}_1}, \mathrm{cent}) = & \quad \frac{0.5^2 + C(p_{\mathrm{T}_1}, \mathrm{cent})}{(x_{\mathrm{J}} - 0.5)^2 + C(p_{\mathrm{T}}, \mathrm{cent})} \\
C(p_{\mathrm{T}}, \mathrm{cent}) = & \quad C_0(\mathrm{cent})(\frac{p_{\mathrm{T}}}{p_{\mathrm{T}}^{\mathrm{min}}})^5 \\
C_0 = & \quad (0.01, 0.02, 0.04, 0.08, 0.1, 0.5) \\
p_{\mathrm{T}}^{\mathrm{min}}|_{\mathrm{R}=0.4} = & \quad 100 \text{ GeV} \\
p_{\mathrm{T}}^{\mathrm{min}}|_{\mathrm{R}=0.2} = & \quad 79 \text{ GeV}
\end{aligned}
\tag{5.5}
$$

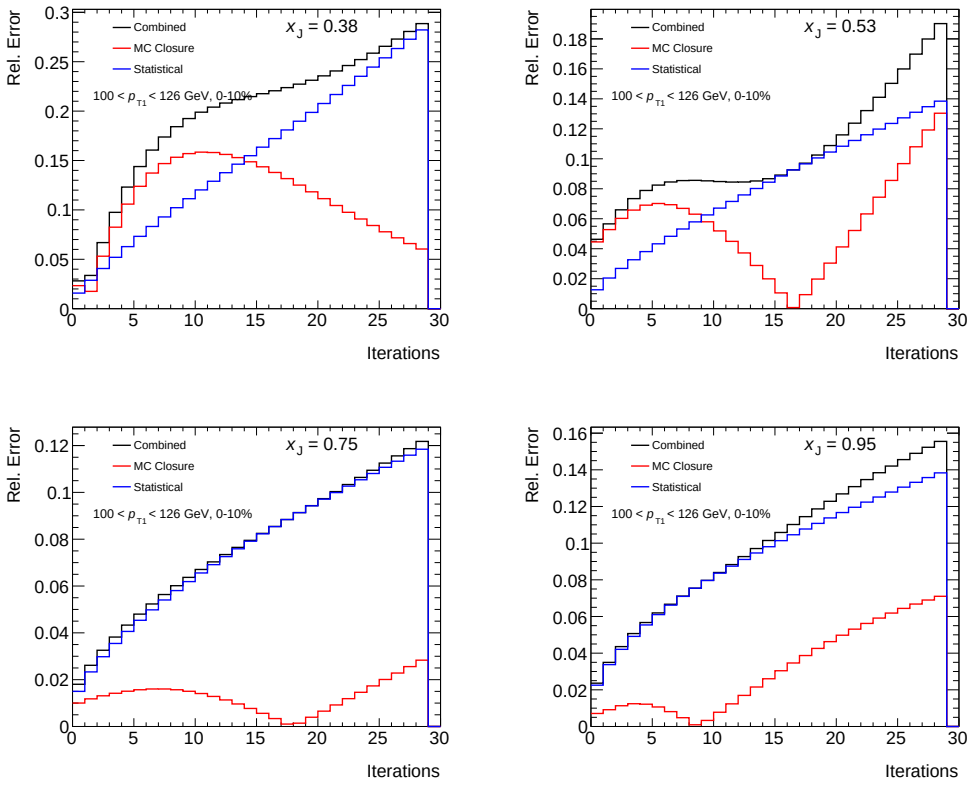

Figure 5.41: The relative statical, relative MC closure, and their quadrature sum as a function of number of iterations for x_J=0.38, 0.53, .75, and 0.95. This is in the 0–10% centrality and 100-126 GeV leading p_T bin.

where $w(x_J, p_{T_1}, \text{cent})$ is a weight that is applied to the response in each truth p_{T_1}, p_{T_1}, and centrality bin. This is shown for different centrality and leading jet p_T bins in Figure 5.42.

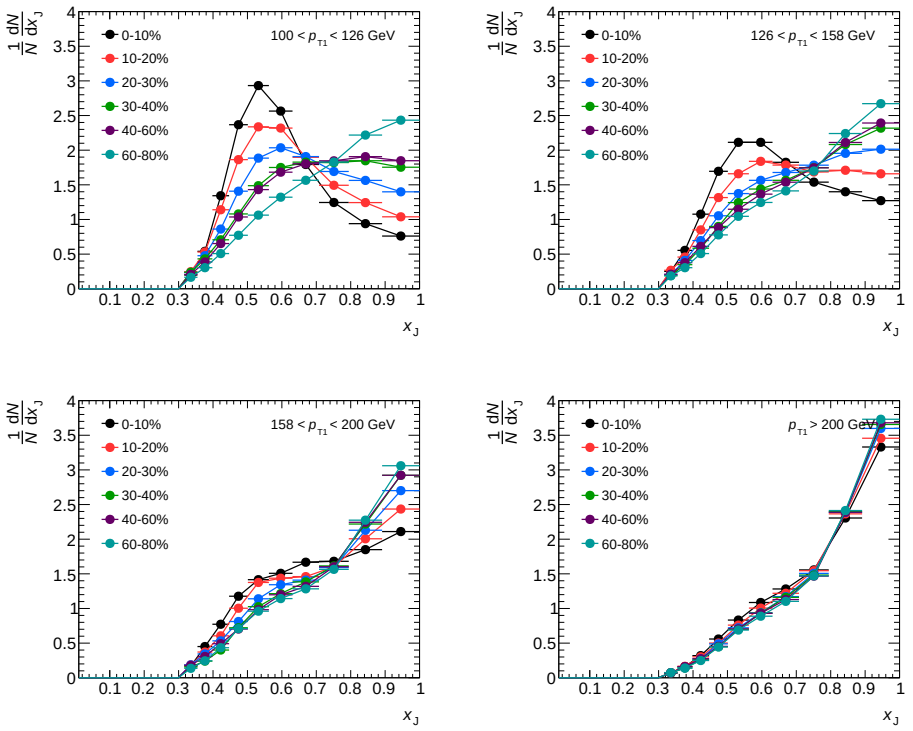

Figure 5.42: The weighted prior that is used as the nominal in the unfolding (equation 5.5) in different leading jet p_T bins: 100-126 GeV (top left), 126-158 GeV (top right), 158-200 GeV (bottom left), >200 (bottom right) overlaid for different centrality bins: 0-10% (black), 10-20% (red), 20-30% (blue), 30-40% (green), 40-60% (purple), 60-80% (teal).

To investigate the stability of the unfolding result to the choice of prior the values of C_0 were changed to generate a substantial difference from the nominal. This was used as systematic due to the reweighting procedure. The C_0 values are as follows:

$$C_0 = (0.1, 0.1, 0.01, 0.01, 0.02, \text{pythia}) \tag{5.6}$$

The MC with the reweighting systematic in centrality and leading jet p_T intervals is shown in Figure 5.43.

In order to validate this procedure, the unfolded results for the original unweighted MC, the nominal weighted MC, and the weighted MC for the systematic were compared as a

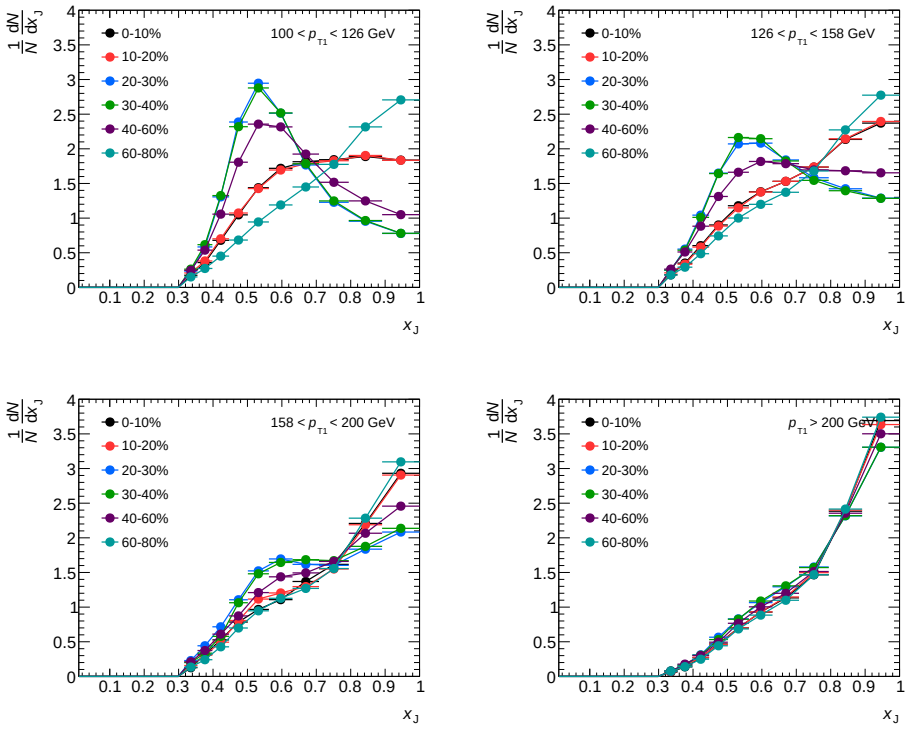

Figure 5.43: The weighted prior that is used as the systematic in the unfolding (equation 5.6) in different leading jet p_T bins: 100-126 GeV (top left), 126-158 GeV (top right), 158-200 GeV (bottom left), >200 (bottom right) overlaid for different centrality bins: 0-10% (black), 10-20% (red), 20-30% (blue), 30-40% (green), 40-60% (purple), 60-80% (teal).

function of centrality in Figure 5.44. There are small disagreements between the unfolded results for the different weightings indicating that the sensitivity of the result to the choice of prior is small even though the reweighting significantly modifies the prior as seen in Figure 5.42. The ratio on the right is the ratio of the unfolded result using the nominal weighted response to the unfolded result using the systematic weighted response.

The stability of the response weighting was also investigated in the MC closure as shown in Figure 5.45. The top sub-panels show the x_J distributions, where the black curve is the truth in the MC systematic and the blue is the MC systematic as the "data" which has been unfolded with the nominal response for different number of iterations in the corresponding figures. The unfolding should eventually return the truth associated with the "data" regardless of what the prior is in the response.

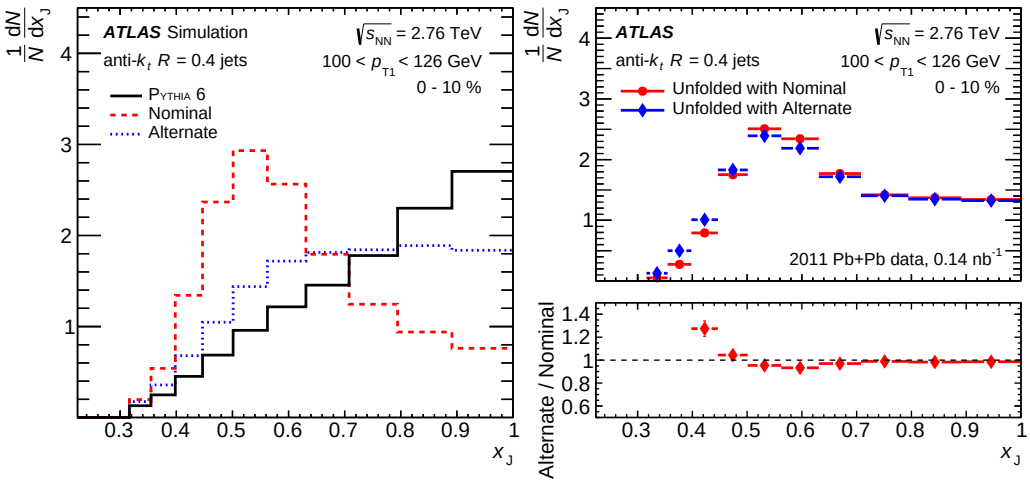

Figure 5.44: Left: the $(1/N)\mathrm{d}N/\mathrm{d}x_\mathrm{J}$ distributions used as priors in the unfolding for the nominal (red) and systematic (blue) for the $100 < p_{\mathrm{T}_1} < 126$ GeV and 0–10% centrality interval. The same distribution from the PYTHIA MC sample is shown in black. Right: the unfolded $(1/N)\mathrm{d}N/\mathrm{d}x_\mathrm{J}$ distributions from data using the nominal (red) and systematic (blue) priors. The ratio of nominal to systematic is shown in the bottom panel.

5.4.4 Convergence with Iterations

After the response matrix was generated from the MC and the closure was checked the data was then unfolded using the 2D Bayesian unfolding method (described in Section 4.6). In Bayesian unfolding the unfolding procedure is iterated until convergence is reached. The result needs to be stable with the number of iterations. Figure 5.46 shows the Pb+Pb data for $R = 0.4$ jets with leading jet p_T between 100–112 GeV in different centrality bins with different numbers of iterations in increments of two overlaid.

Another important aspect of the unfolding is that statistical fluctuations can be amplified through the unfolding procedure. The number of iterations has to be chosen in a way that carefully considers the point at which this effect dominates. This effect can be seen in the 60–80% bin for 30 iterations in orange where the statistical uncertainties have become very large. Figure 5.47 is also looking at the stability of the number of iterations but now at fixed centrality (0–10% where we saw the most instability from the previous figure) and in different leading jet p_T bins. Fluctuations like the point at 35 GeV in the 126–141 GeV

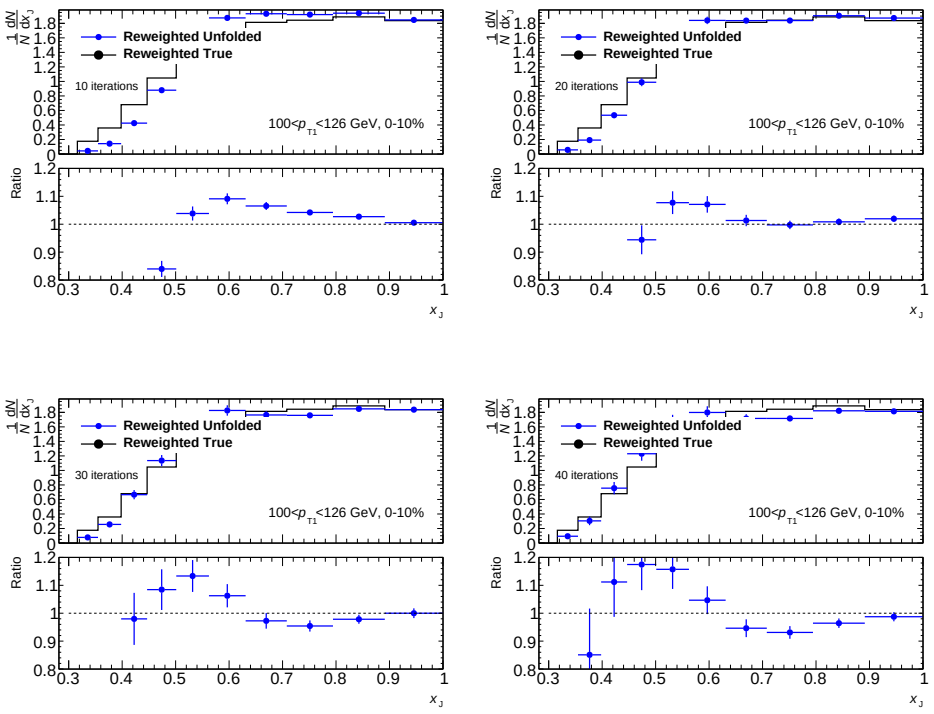

Figure 5.45: The closure in the reweighting is demonstrated in the MC for the 0-10% centrality and 100-126 GeV bin for different number of iterations: 10 (top left), 20 (top right), 30 (bottom left), and 40 (bottom right). The top sub-panel overlays x_{J} distributions where the black is the truth distribution from the original MC and the blue is the unfolded distribution using the $1/x_{\mathrm{J}}$ weighted response. The bottom sub-panel has the ratio between the unfolded distribution and the truth.

are due to fluctuations in the response that get amplified each time the result is unfolded. Smoothing reduced this effect but will not completely remove it in the final unfolded result. Also, the result is less stable in the lower p_{T} bins because here the data is the most different from the prior in the MC.

Figure 5.48 shows the stability with the number of iterations in pp collisions in leading jet p_{T} bins. The pp is very stable with number of iterations because the data is very close to the prior from the MC in pp collisions.

In order to investigate the stability with number of iterations further the ratio of all the unfolded results to the nominal result was taken. Figure 5.49 shows this for the centrality dependence and Figure 5.50 for the p_{T_1} dependence in Pb+Pb collisions. These indicate

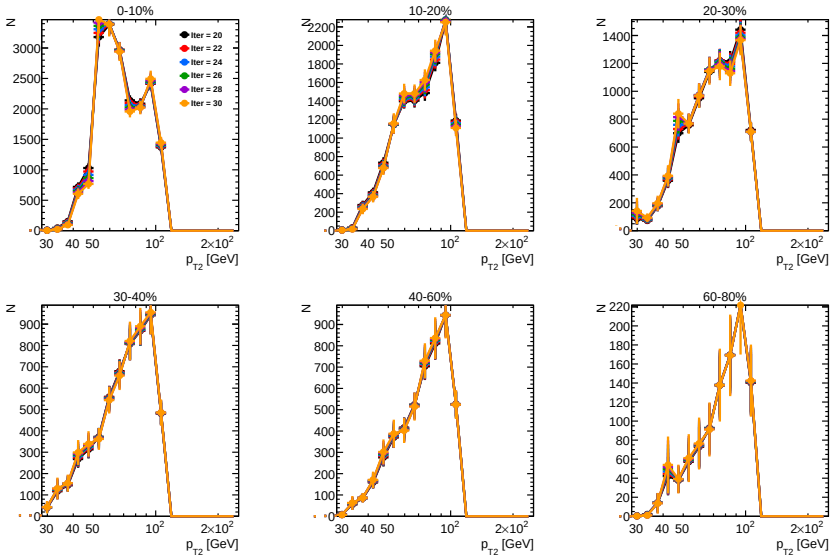

Figure 5.46: Projections onto the p_{T_2} axis of the unfolded jet 1/jet 2 distribution in different centrality bins for Pb+Pb $R = 0.4$ jets with leading jet p_T between 100-112 GeV. Different number of iterations from 20 to 30 in increments of 2 are overlaid.

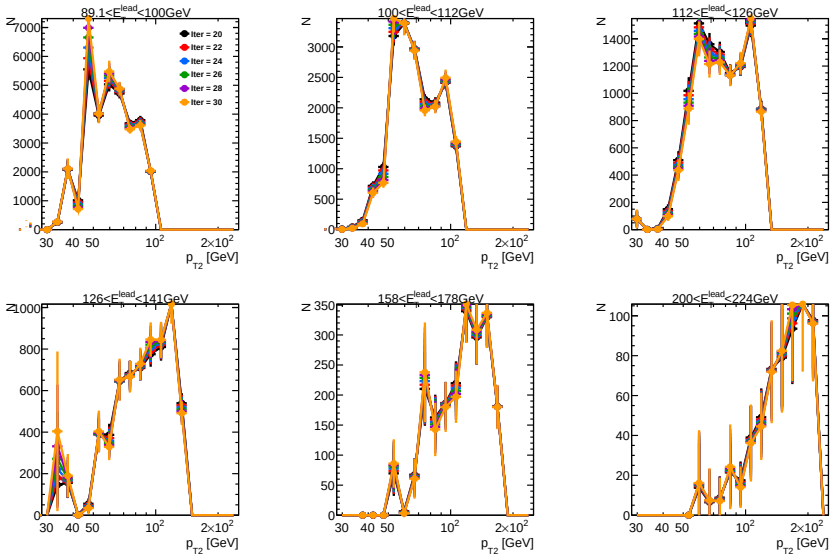

Figure 5.47: Projections onto the p_{T_2} axis of the unfolded jet 1/jet 2 distribution in different leading jet p_T bins for Pb+Pb $R = 0.4$ jets in 0-10% centrality. Different number of iterations from 20 to 30 in increments of 2 are overlaid.

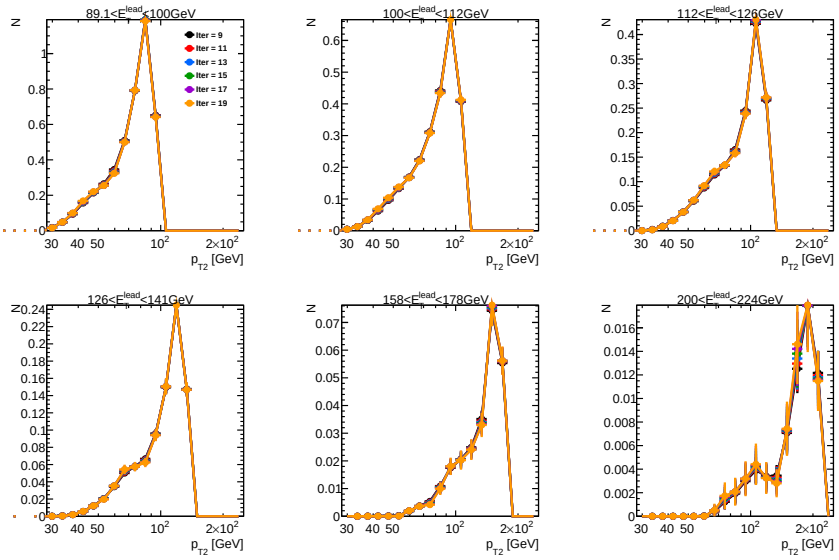

Figure 5.48: Projections onto the p_{T_2} axis of the unfolded jet 1/jet 2 distribution in different leading jet p_T bins for pp $R = 0.4$ jets. Different number of iterations from 9 to 19 in increments of 2 are overlaid.

that the results are stable to within 5% above 50 GeV in the sub-leading jet except at higher leading jet p_T. The instability in higher p_T bins can be attributed to low statistics.

Figure 5.51 shows this for the p_{T_1} dependence in pp collisions. The results are stable to within 5% for sub-leading jets above 40 GeV until the highest p_T bins in the leading jet.

5.4.5 Refolding

The stability of the result can also be investigated by looking at the refolded result compared to the original data. The refolded result is taking the unfolding result and multiplying it by the inverse of the response matrix. The `RooUnfold` software package has a method to refold the unfolded data. This is demonstrated in 2D in Figure 5.52 where the left panel is the original data, the middle panel is the unfolded result for the nominal number of iterations and the right is the refolded result.

Figure 5.53 has the centrality dependence and Figure 5.54 has the leading jet p_T dependence of the ratio of the refolded result for different numbers of iterations to the original data in slices of sub-leading jet p_T in Pb+Pb collisions. The refolded shows closure to

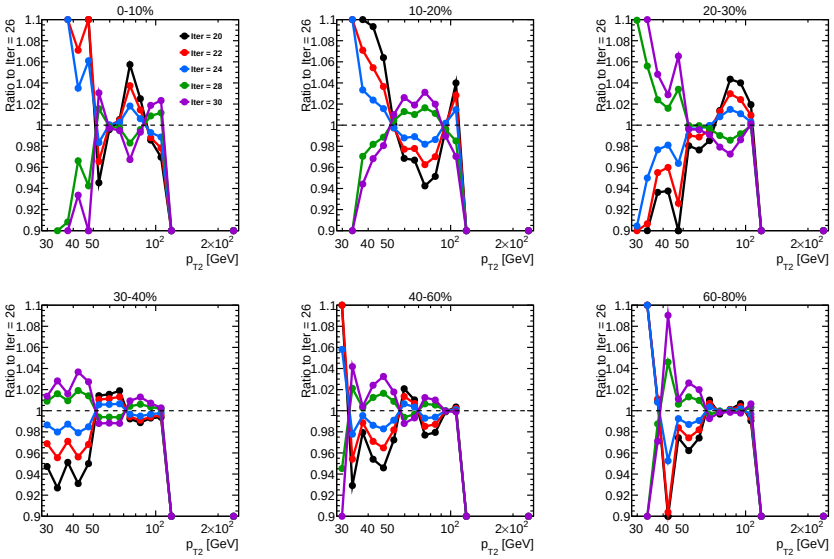

Figure 5.49: Ratio of projections onto the p_{T_2} axis of different number of iterations in the unfolded jet 1/jet 2 distribution to the nominal result at 26 iterations. This is shown in different centrality bins for Pb+Pb $R = 0.4$ jets with leading jet p_{T} between 100-112 GeV.

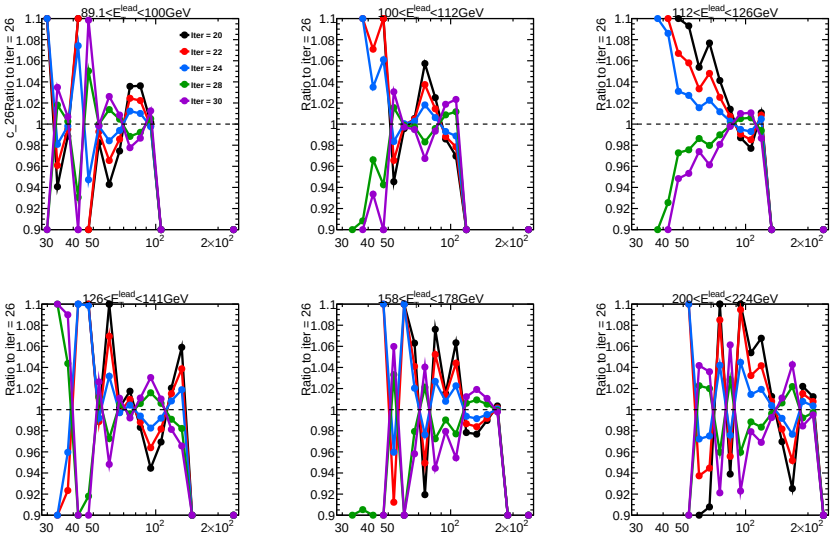

Figure 5.50: Ratio of projections onto the p_{T_2} axis of different number of iterations in the unfolded jet 1/jet 2 distribution to the nominal result at 26 iterations. This is shown in different leading jet p_{T} bins for Pb+Pb $R = 0.4$ jets in 0-10% centrality.

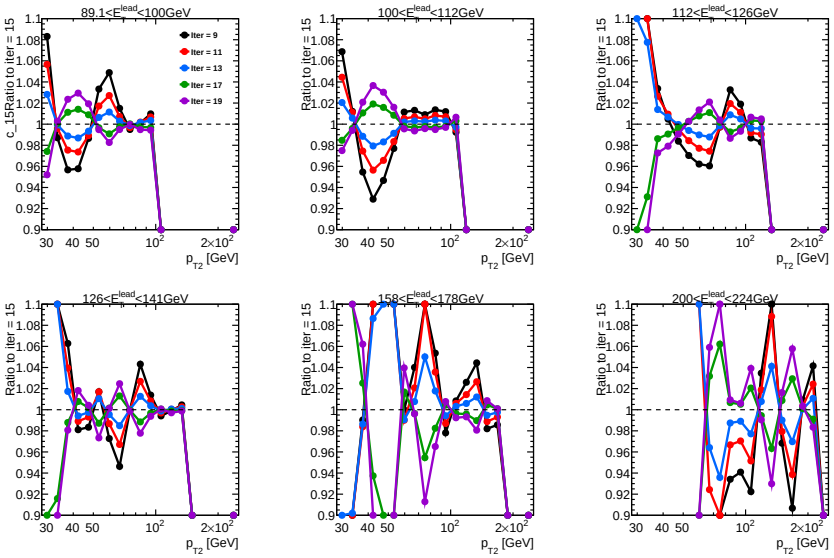

Figure 5.51: Ratio of projections onto the p_{T_2} axis of different number of iterations in the unfolded jet 1/jet 2 distribution to the nominal result at 15 iterations. This is shown in different leading jet p_T bins for pp $R = 0.4$ jets.

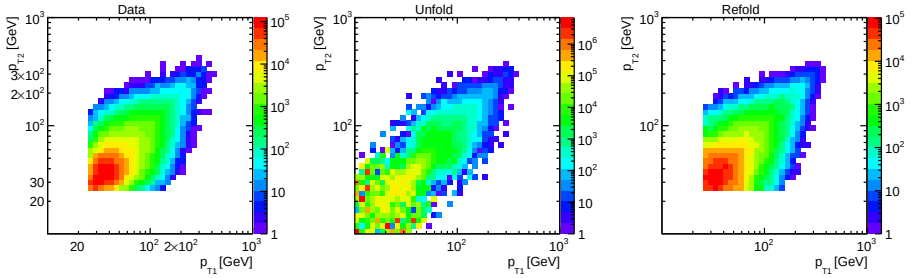

Figure 5.52: 2D distributions for the rata data in the left panel, unfolded result in the middle panel and refolded result in right panel. This is for $R = 0.4$ Pb+Pb jets in the 0-10% centrality bin.

within 10% except at p_T value below 40 GeV. The refolding result is also stable with the number of iterations indicating that the stability to the number of iterations is uncorrelated with the refolding.

Figure 5.55 has the leading jet p_T dependence of the ratio of the refolded result for different numbers of iterations to the original data in slices of sub-leading jet p_T in the $R = 0.4$ jets in pp. The pp has better closure in the refolding than the Pb+Pb and also becomes worse at low p_T.

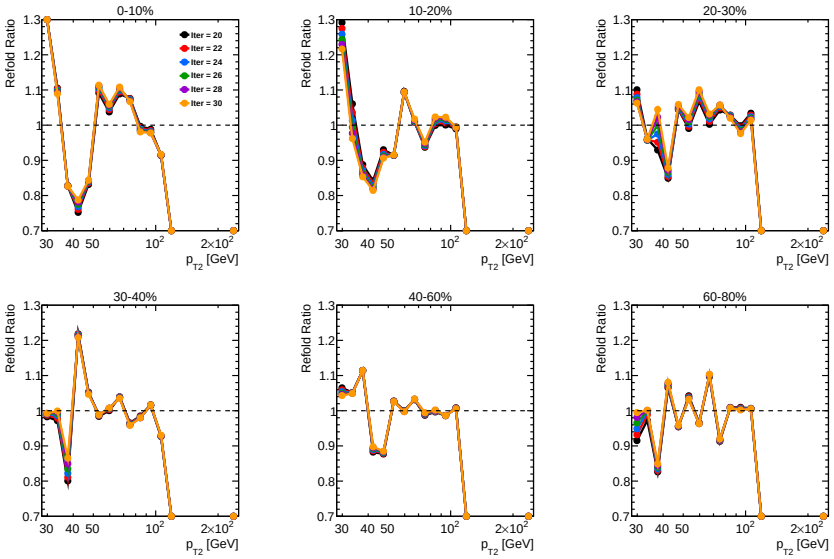

Figure 5.53: Ratio of projections onto the p_{T_2} axis of different number of iterations in the refolded jet 1/jet 2 distribution to the original raw data. This is shown in different centrality bins for Pb+Pb $R = 0.4$ jets with leading jet p_T between 100-112 GeV.

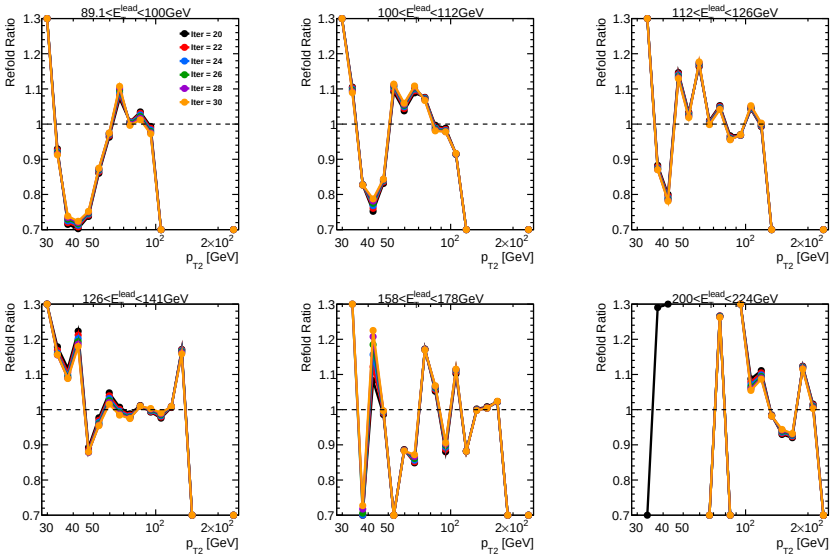

Figure 5.54: Ratio of projections onto the p_{T_2} axis of different number of iterations in the refolded jet 1/jet 2 distribution to the original raw data. This is shown in different leading jet p_T bins for Pb+Pb $R = 0.4$ jets in 0-10% centrality.

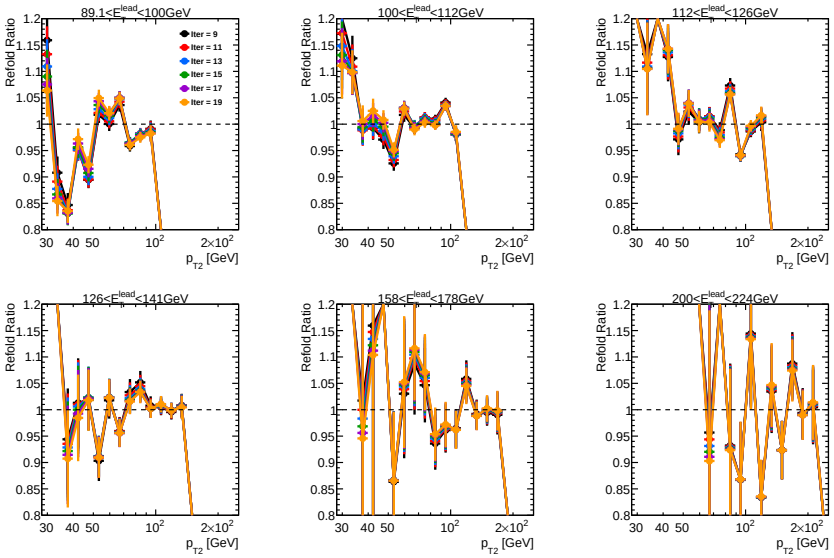

Figure 5.55: Ratio of projections onto the p_{T_2} axis of different number of iterations in the refolded jet 1/jet 2 distribution to the original raw data. This is shown in different leading jet p_{T} bins for pp $R = 0.4$ jets.

5.4.6 Method to Determine n_{iter}

In order to determine the number of iterations in a quantitative way, a method was developed to evaluate the different factors that contribute to determining the number of iterations as a function of number of iterations. The full spectra of different number of iterations from 1 to 60 were investigated. The sum of the square of each source of error was computed for each bin in the x_{J} distribution. This was them summed over all x_{J} bins for each leading jet p_{T} bin and each centrality bin. The sources of error that were taken into account to determine the number of iterations are the statistical error and the error due to the reweighting discussed in Section 5.4.3. The following formulas demonstrates how each error was calculated for each iteration i at each x_{J} value and then how the total error was found by summing over each error and over each x_{J} bin:

Table 5.5: The final number of iterations for each jet radius and centrality bin.

Collision Type	Jet Radius	Centrality [%]	Iterations
Pb+Pb	0.4	0-10	20
Pb+Pb	0.4	10-20	17
Pb+Pb	0.4	20-30	12
Pb+Pb	0.4	30-40	10
Pb+Pb	0.4	40-60	8
Pb+Pb	0.4	60-80	6
pp	0.4	*pp*	8
Pb+Pb	0.3	0-10	21
Pb+Pb	0.3	10-20	15
Pb+Pb	0.3	20-30	12
Pb+Pb	0.3	30-40	10
Pb+Pb	0.3	40-60	8
Pb+Pb	0.3	60-80	6
pp	0.3	*pp*	12

$$
\begin{aligned}
\sigma_i^2|^{\text{reweight}} &= (\frac{1}{N}\frac{dN}{dx_{\text{J}}}|_i^{\text{nom}} - \frac{1}{N}\frac{dN}{dx_{\text{J}}}|_i^{\text{sys}})^2 \\
\sigma_i^2|^{\text{stat}} &= (\sigma_i^{\text{nom}})^2 \\
\sigma_i^2|^{x_J} &= \sigma_i^2|^{\text{reweight}} + \sigma_i^2|^{\text{stat}} \\
\sigma_i^2|^{p_{\text{T}}} &= \sum_{x_J} \sigma_i^2|^{x_{\text{J}}}
\end{aligned}
$$

Figures 5.56– 5.57 show the different contributions to the error as a function of number of iterations in the lowest leading jet p_{T} bin on the left for each centrality bin. The total errors for $R = 0.4$ jets in different p_{T_1} bins are shown on the right of each figure. The black curve shows the total errors with all the different p_{T} bins added in quadrature. In order to determine the optimum number of iterations (which has to be determined separately for each centrality bin but not in each p_{T} bin) the minima in the different curves were determined. The minima is not the same in each p_{T} bins so the place that minimizes there error in all four bins should be used. The distribution of the total errors for *pp* for $R = 0.4$ is shown in Figure 5.58. A table summarizing the chosen number of iterations for all the jet samples is shown in Table 5.5.

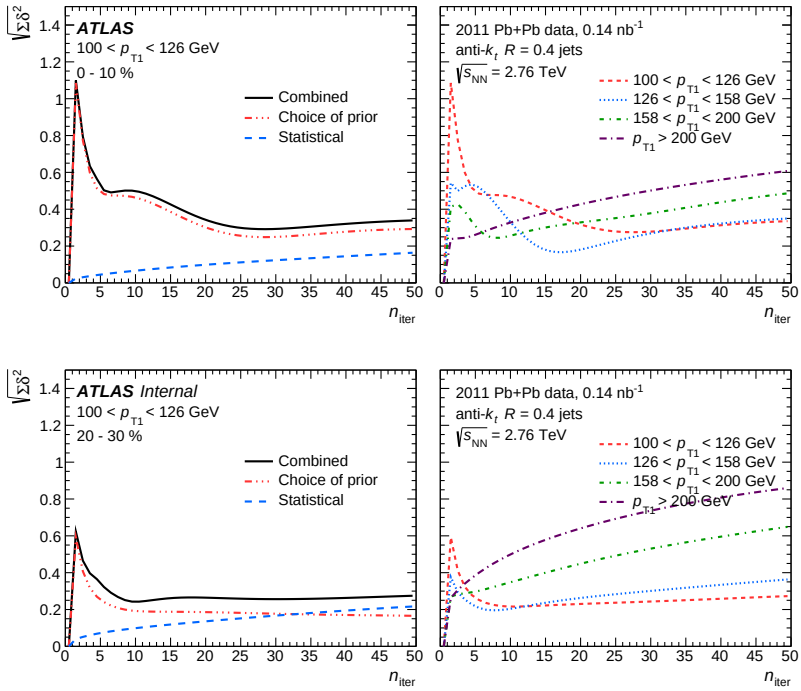

Figure 5.56: The left panel shows the different contributions to the error for $100 < p_{\mathrm{T}} < 126$ GeV. The reweighting error is shown in red, the statistical error is shown in blue, and the quadrature sum in black. The right panel shows the total errors overlaid for different leading jet p_{T} bins for $R = 0.4$ jets. The 0–10% bin is on the top and the 20–30% bin is on the right.

5.4.7 Unfolding Results

The final 2D unfolded results for the nominal number of iterations in different centrality bins are shown in Figure 5.59 for $R = 0.4$ jets. The final 2D unfolded result for pp jets for $R = 0.4$ jets at the nominal number of iterations is shown in Figure 5.60. Figure 5.61 shows the 2D distributions after unfolding for central Pb+Pb, peripheral Pb+Pb, and pp collisions, where the distributions have been folded back over the diagonal.

The unfolded results were compared to the raw data in Figures 5.62 and 5.63 in 0–10% on the left, 60–80% in the middle, and pp on the right. This is shown for all the p_{T} bins in the corresponding figures. The effect of the unfolding is stronger in the more central bins and lower leading jet p_{T} intervals. In general, the unfolding sharpens in pp and peripheral Pb+Pb to more symmetric configurations at $x_{\mathrm{J}} = 1$, which is expected since $x_{\mathrm{J}} = 1$ should

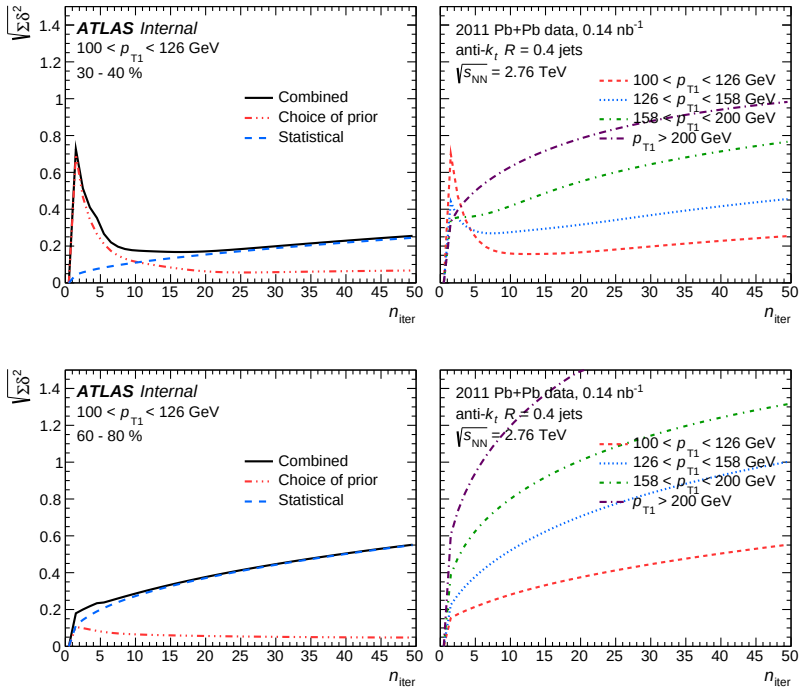

Figure 5.57: The left panel shows the different contributions to the error for $100 < p_{\mathrm{T}} < 126$ GeV. The reweighting error is shown in red, the statistical error is shown in blue, and the quadrature sum in black. The right panel shows the total errors overlaid for different leading jet p_{T} bins for $R = 0.4$ jets. The 30–40% bin is on the top and the 60–80% bin is on the right.

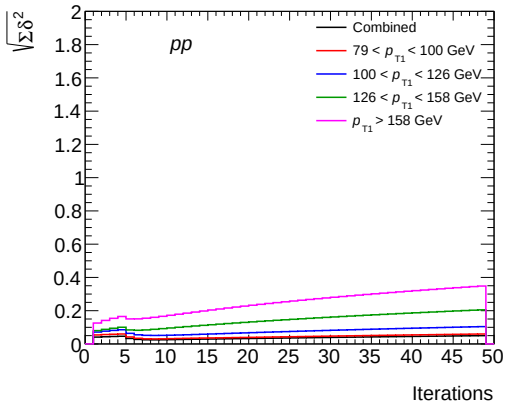

Figure 5.58: The total errors overlaid for different leading jet p_{T} bins for pp $R = 0.4$ jets.

be the most probable configuration for balanced jets. In central Pb+Pb the unfolding moves some jets to symmetric configurations but also pushes jets into a peak at lower asymmetry

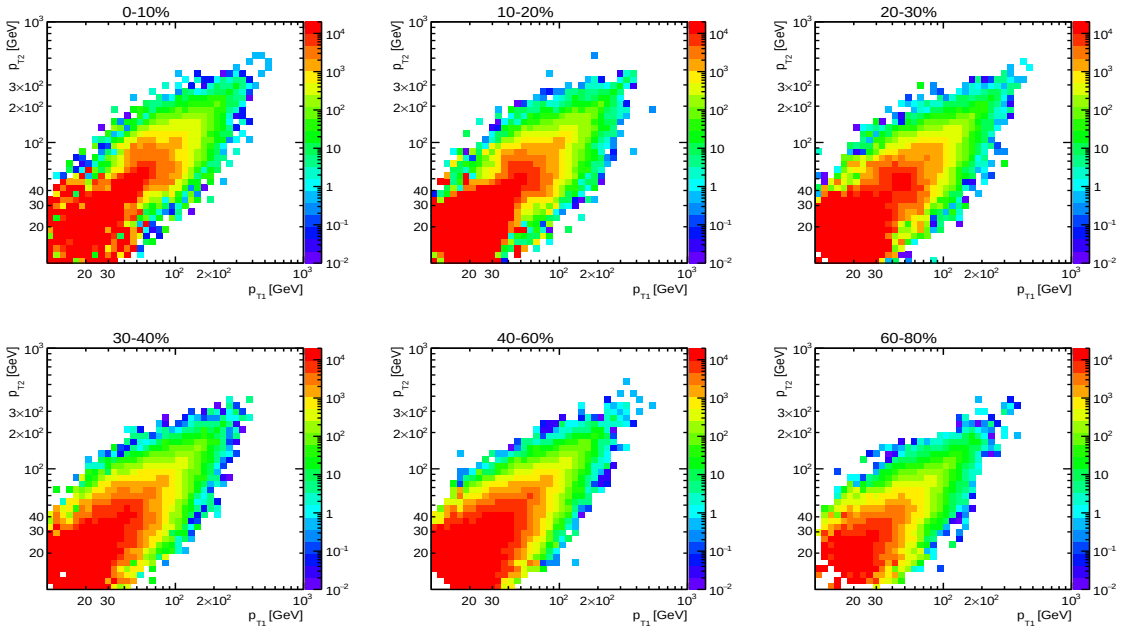

Figure 5.59: 2D unfolded distribution for $R = 0.4$ Pb+Pb jets for different centrality bins for 20 iterations.

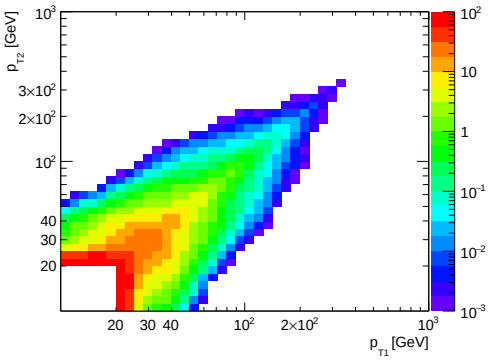

Figure 5.60: 2D unfolded distribution for $R = 0.4$ pp jets for 8 iterations (left) and for $R = 0.3$ for 12 interactions (right).

around $x_J = 0.5$. Here is a clear example of an interesting feature that was smeared out by the unfolding. In the reverse comparison, before and after smearing, the peak looks like it has been smeared out by detector effects.

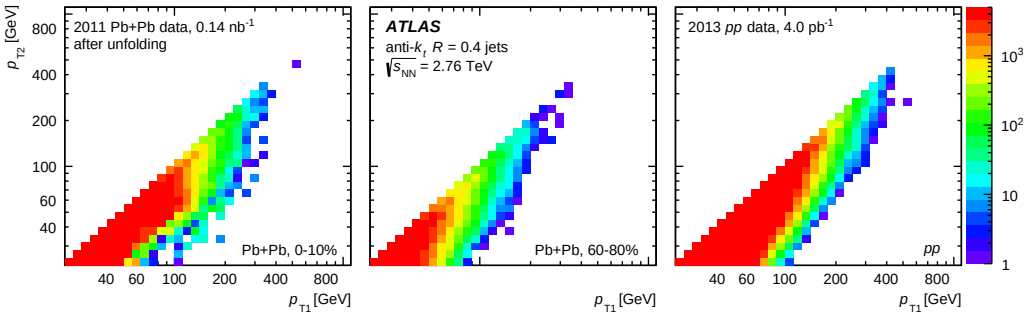

Figure 5.61: The two-dimensional p_{T_1}-p_{T_2} distributions after unfolding for Pb+Pb data in the 0–10% (left) and 60–80% (center) centrality bins and for pp data (right) for $R = 0.4$ jets.

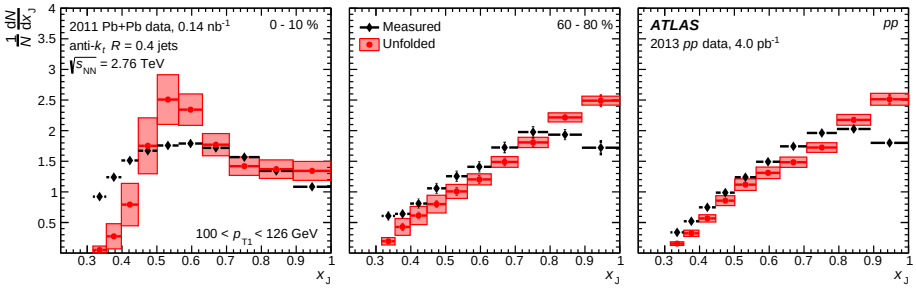

Figure 5.62: Comparing the $R = 0.4$ jets before (black) and after (red) unfolding for 100 ¡p_{T_1}¡126 GeV jets in 0-10% Pb+Pb (left), 60-80% (middle), and pp(right).

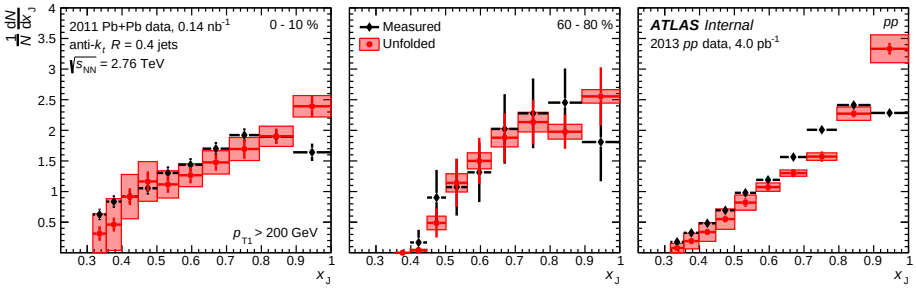

Figure 5.63: Comparing the $R = 0.4$ jets before (black) and after (red) unfolding for p_{T_1}¿200 GeV jets in 0-10% Pb+Pb (left), 60-80% (middle), and pp(right).

5.5 Systematic Uncertainties

The systematic uncertainties in the measurement are due to the following sources:

1. Jet energy scale (JES)

2. Jet energy resolution (JER)

3. Combinatoric subtraction

4. Unfolding: choice of Bayesian prior

5. Unfolding: factorization of response

The JES and JER uncertainties were evaluated by rebuilding the response matrix with a systematically varied relationship between the truth and reconstructed jet kinematics using standard tools.

5.5.1 Jet energy scale

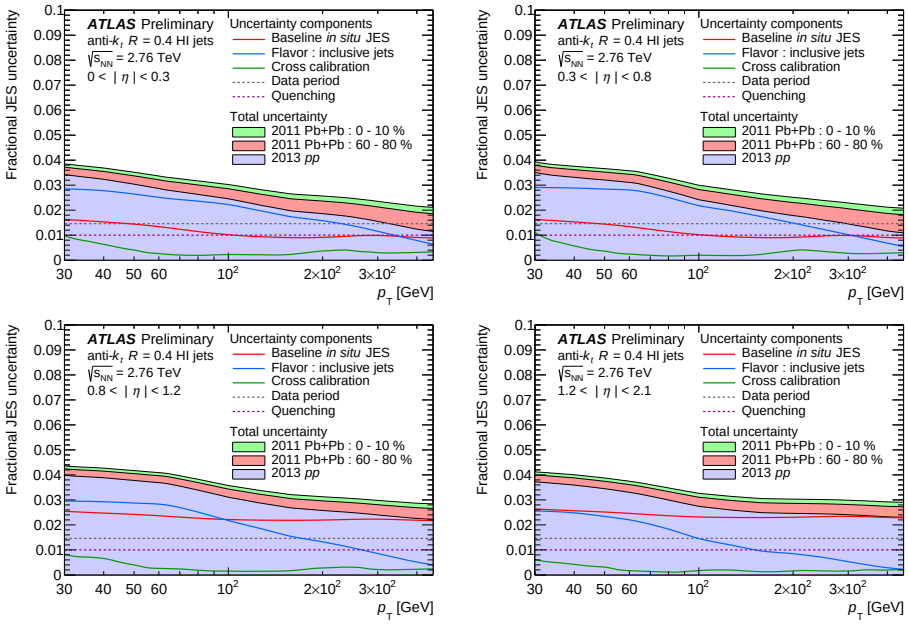

Figure 5.64: The total JES uncertainty on the 2013 $\sqrt{s} = 2.76$ TeV pp data (filled blue), with the total uncertainty in 2011 $\sqrt{s_{\mathrm{NN}}} = 2.76$ TeV Pb+Pb data in the 60–80% (filled blue plus red) and 0–10% (filled blue plus red plus green) show for different ranges of $|\eta|$.

In HI jet analyses there are a set of standard JES uncertainties that are applied. These are described in detail in Ref. [218] and summarized in Figure 5.64. First there are a standard set of uncertainties that are used in standard pp EMTopo jets that are implemented in both pp and Pb+Pb HI data. These uncertainties were derived using the existing calibration for EMTopo jets from 2012 8 TeV data. This includes an uncertainty associated with

the cross calibration due to using the JES and uncertainties from one dataset in another (described in Section 4.4), which comes from the differences in the jets, differences in detector settings, and statistics. The uncertainties inherited from EMTopo are called "baseline" and are broken down into 8 nuisance parameters. These "baseline" uncertainties are due to the *in situ* calibration and are derived using Z/γ+jets. There are additional uncertainties due the difference in the flavor response and composition since quarks and gluons have different responses and the different generators (Herwig++ and PYTHIA) which use different fragmentation models (string vs. cluster). The difference in the JES is seen in Figure 4.16. This is evaluated using flavor fractions from this beam energy and the differences in the response for quarks and gluons in PYTHIA and Herwig++.

All of the above uncertainties are common to both Pb+Pb and pp data, but there are two HI specific uncertainties used in Pb+Pb only. The first is the uncertainty due to the response to quenched jets, which is centrality dependent. This is evaluated by using `PYQUEN` [161], which is a generator that applies medium energy loss to parton showers from PYTHIA 6, to evaluate the JES. This generator produces a FF that is different from the PYTHIA in a similar way that the FF evaluated in Pb+Pb data is different from pp [229]. The difference in the JES is at most 1% in central collisions and decreases linearly with centrality and thus was parameterized as

$$\delta = \delta_{\text{cent}} \frac{60 - \text{C}}{60} \tag{5.7}$$

where $\delta_{\text{cent}} = 1\%$ and C is the centrality in the event in percent. The peripheral collisions starting at about 60% get no quenching uncertainty. The last uncertainty on the JES is due to the difference in the data-taking periods between Pb+Pb and pp collisions. This was evaluated by comparing the response of the calorimeter with respect to the p_{T} of the matched track jets (sum of the track p_{T} associated with the jets) in pp and peripheral Pb+Pb.

5.5.2 Jet energy resolution

There are also uncertainties due to the JER which consists of a centrality independent and centrality dependent component. The JER systematic uncertainties are applied to the

reconstructed p_{T} by smearing it out with a gaussian with mean 0 and standard deviation of $\sigma_{\mathrm{sys}} = \sqrt{(\sigma + \delta\sigma)^2 - \sigma^2}$, where σ is the JER and $\delta\sigma$ is the uncertainty on the JER.

$$p_{\mathrm{T}}^{\mathrm{sys}} = p_{\mathrm{T}}^{\mathrm{reco}} + N(0, \sigma_{\mathrm{sys}}) \tag{5.8}$$

This is motivated from equation 4.11, where the a and c terms are not centrality dependent and the b term is such that

$$\sigma(\Delta p_{\mathrm{T}})|_{\mathrm{tot}} = \sqrt{\sigma(\Delta p_{\mathrm{T}})^2|_{\mathrm{peri,pp}} + \sigma(\Delta p_{\mathrm{T}})^2|_{\mathrm{cent}}} \tag{5.9}$$

where the centrality dependent part can be separated out from the centrality independent part which is the JER in peripheral or *pp*. The uncertainty on the first term comes from the standard *pp* JER from EMTopo jets, which is derived through the cross calibration in Ref. [218].

The second term is evaluated by comparing the resolution in the MC (where the UE is the same as the data due to the overlay) to a data-driven analysis of the fluctuations that uses a non-overlapping sliding window analysis (discussed in Section 7.2). The b term in equation 4.11 represents the fluctuations in the MC. This can be calculated by

$$\frac{\sigma}{p_{\mathrm{T}}}|_{\mathrm{cent}} - \frac{\sigma}{p_{\mathrm{T}}}|_{\mathrm{peri}} = \frac{\Delta b^2_{\mathrm{MC}}}{p^2_{\mathrm{T}}} \tag{5.10}$$

where Δb^2_{MC} is the fluctuations, which is shown in Figure 5.65. These are fit and Δb^2_{MC} is extracted and compared to the values of the fluctuations extracted from data, $\Delta b^2_{\mathrm{data}}$, in the left panel of Figure 5.66. The value used for $\delta\sigma$ to vary the response is $|\Delta b^2_{\mathrm{MC}} - \Delta b^2_{\mathrm{data}}|$, which is shown in the right panel of Figure 5.66.

5.5.3 Additional scale and resolution uncertainties for R=0.3 jets

This analysis was performed for both $R = 0.3$ and $R = 0.4$ jets but all of the JES and JER systematics were derived for $R = 0.4$ jets but then also applied to the $R = 0.3$ jets. Therefore, a systematic uncertainty was derived to account for this by matching the $R = 0.3$ and $R = 0.4$ jets in MC and data and comparing the relative response. The fractional difference between the p_{T} in truth and reconstructed is,

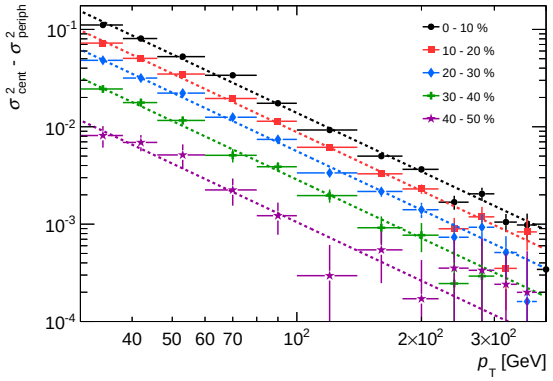

Figure 5.65: The quadratic difference of the fractional JER between central and peripheral collisions, shown as a function of p_{T}, for different centrality bins. Each centrality interval is fit with a $\Delta b^2_{\mathrm{MC}}/p^2_{\mathrm{T}}$ functional form with the extracted fit parameters compared to data.

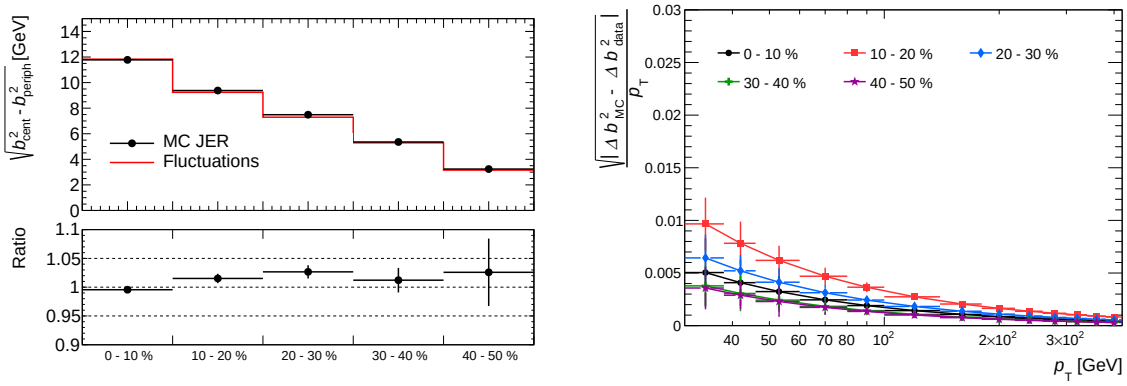

Figure 5.66: Left: the quadratic difference between the central and peripheral b terms in data and in the MC JER study. Right: Additional JER contribution arising from data/MC difference as a function of jet p_{T}, shown for different centralities.

$$R = \left.\frac{p_{\mathrm{T}}^{R=0.4} - p_{\mathrm{T}}^{R=0.3}}{p_{\mathrm{T}}^{R=0.4}}\right|_{\mathrm{reco}} \qquad T = \left.\frac{p_{\mathrm{T}}^{R=0.4} - p_{\mathrm{T}}^{R=0.3}}{p_{\mathrm{T}}^{R=0.4}}\right|_{\mathrm{truth}} . \tag{5.11}$$

and the response is $R - T$, so the variance and mean of the response are,

$$\delta_{R-T} = \langle R-T\rangle|_{\mathrm{Data}} - \langle R-T\rangle|_{\mathrm{MC}} = \langle R\rangle|_{\mathrm{Data}} - \langle R\rangle|_{\mathrm{MC}} + \langle T\rangle|_{\mathrm{Data}} - \langle T\rangle|_{\mathrm{MC}} = \delta_R - \delta_T\,. \tag{5.12}$$

where δ_R can be evaluated by comparing $< R >$ in the data and MC, which is shown in Figure 5.67. Each ratio was fit to a constant and the largest value found yields an estimate

of $\delta_R = 0.27\%$.

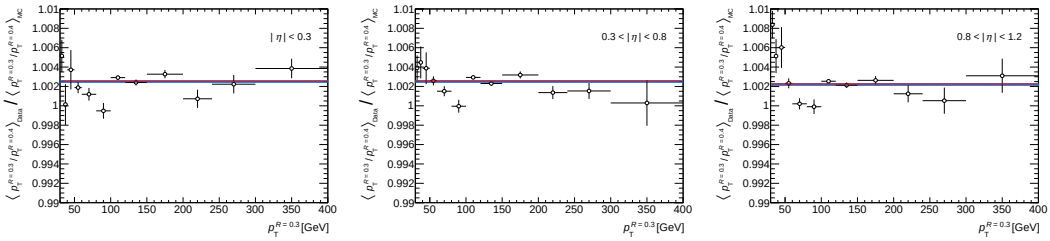

Figure 5.67: The ratio between of the average values $p_{\mathrm{T}}^{R=0.3}/p_{\mathrm{T}}^{R=0.4}$ evaluated in data and the MC sample at the reconstructed level for three different ranges of jet η. The horizontal lines indicate a fit to a constant. The largest value, including the fit uncertainties was in the $|\eta| < 0.3$ bin and was found to be 1.0027.

The δ_T term comes from the fact that the angular distribution of particles in the jet between $0.3 < R < 0.4$ from PYTHIA can differ in data and MC. This is estimated using a differential jet shape in ATLAS at $\sqrt{s}$=7 TeV using the 2010 data [230]. This is compared to the jet shape in MC in Figure 5.68, where the agreement is expected to be good because the data was used to tune this MC. The uncertainty was estimated by providing an upper limit to equation 5.12,

$$\delta_{R-T} \leq |\delta_R - \delta_T| \leq |\delta_R| + |\delta_T| \leq |\delta_R| + d\int_{0.3}^{0.4} \rho(r)\mathrm{d}r\,. \tag{5.13}$$

where d was set to 10% and the integral was evaluated from the ATLAS measurement in bins of p_{T} and then fit as a function of p_{T} as shown in Figure 5.69. The uncertainty is shown in Figure 5.70, along with the individual contributions in truth and reconstructed.

The JER uncertainty is evaluated by,

$$\sigma^2_{R-T} = \sigma^2_R - (2\mathrm{Cov}[R,T] - \mathrm{Var}[T]) = \sigma^2_R - \Gamma\,, \tag{5.14}$$

where σ^2_R can be found in both data and MC. There is no data analogy for Γ so it can only be evaluated in the MC. The different terms in MC are shown in Figure 5.70 and the uncertainty becomes,

$$\delta\sigma^2_{R-T} = \delta\sigma^2_R - \delta\Gamma \leq |\delta\sigma^2_R - \delta\Gamma| \leq |\delta\sigma^2_R| + |\delta\Gamma|\,. \tag{5.15}$$

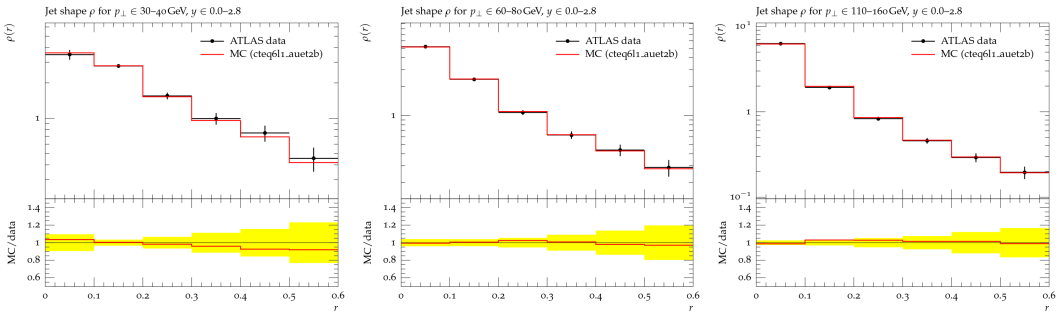

Figure 5.68: Comparison between the ATLAS differential jet shape measurement and PYTHIA 6 AUET2B tune for three bins in jet p_{T}. A similar level of agreement is present in those not shown with the difference between the central value of the data and the PYTHIA 6 much smaller than the experimental uncertainty.

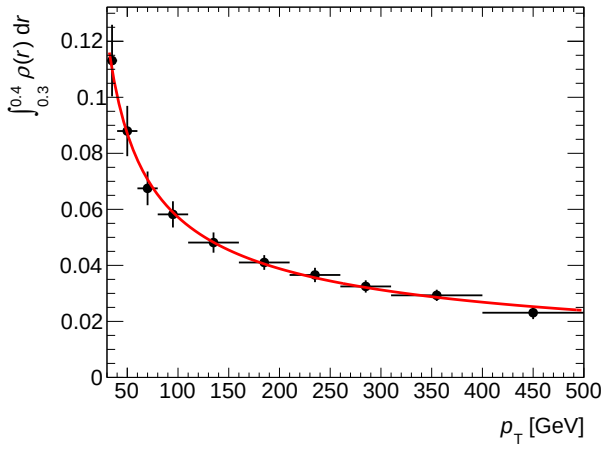

Figure 5.69: Values of $\int_{0.3}^{0.4} \rho(r)\mathrm{d}r$ as a function of p_{T} extracted from the ATLAS jet shape measurement along with a fit to the form $\sqrt{a^2/{p_{\mathrm{T}}}^2 + b^2/p_{\mathrm{T}} + c^2}$.

The $\delta\Gamma$ gets a conservative upper limit of,

$$|\delta\Gamma| \leq |\Gamma_{\mathrm{MC}}\,, \tag{5.16}$$

since it is only evaluated in the MC. This says that the data and MC could differ by 100%. This conservative estimate of the uncertainty, a less conservative estimate that is proportional to the uncertainty on σ_R^2, and the data/MC difference for σ_R^2 are shown on the left panel in Figure 5.71.

This uncertainty is added as an additional smearing and is just the square root of the σ^2 values. This is shown to be small on the right panel of Figure 5.71 and have no observable

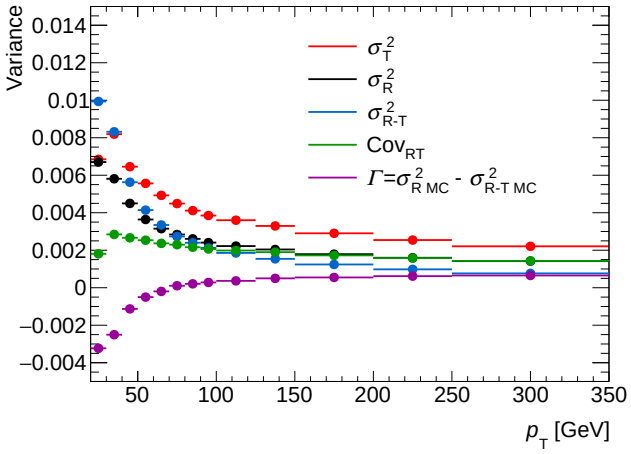

Figure 5.70: The variances of R, T and $R-T$ along with the correlation terms as a function of p_{T} in the MC sample.

impact on the total uncertainty.

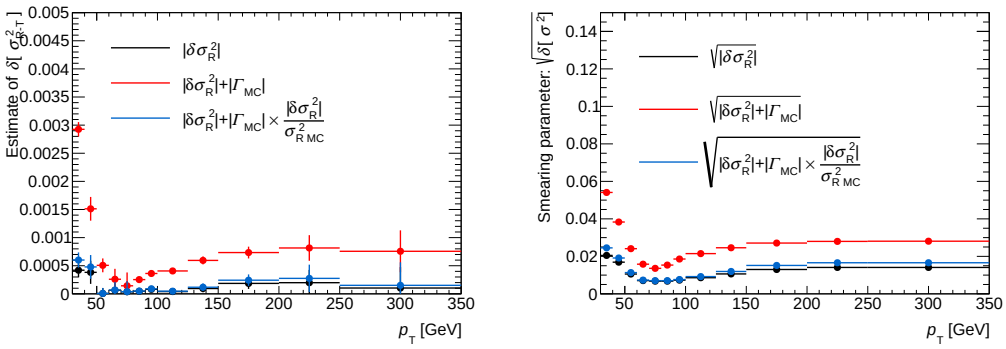

Figure 5.71: The left panel shows the $\delta\sigma_R^2$ and two estimates of the uncertainty using different estimates for $|\delta\Gamma|$. The most conservative uncertainty (red) is used in the analysis. The right panel shows the smearing parameters corresponding to the various uncertainty estimates.

5.5.4 Combinatoric subtraction

The uncertainty in the measurement due to uncertainties in the combinatoric subtraction procedure was evaluated by changing the procedure used to estimate the combinatoric contribution. This was performed by changing the $\Delta\phi$ region used in the estimation from $1.0-1.4$ to $1.1-1.5$. This change varies the contribution of the flow modulation and any residual contribution from the di-jet signal leaking into the background region. The effects

of this change on the raw distributions were shown in Section 5.3.1.3. The raw distributions with this alternate subtraction were propagated through the unfolding procedure and the difference between the resulting distributions and the unfolded distributions using the nominal subtraction were used as a systematic uncertainty.

5.5.5 Unfolding

Uncertainties in the unfolding procedure account for the sensitivity of the unfolded result to the choice of prior. The unfolding was repeated by using a prior that was reweighted. Following the discussion in Section 5.4.3, this reweighting was chosen to be the "alternate" prior in Figures 5.56– 5.57 and the uncertainty comes from the ratio in the bottom of the right-hand panel of each of the figures.

The method of populating the response matrix, using samples with different $\hat{p_{\mathrm{T}}}$ ranges and applying a weighting, suffers from the fact that large fluctuations may occur in bins where two samples contribute with one containing many fewer counts but a much larger cross section. As the response matrix is sparsely populated (containing 40^4 bins), such fluctuations could introduce instabilities in the unfolding. To evaluate the sensitivity to such effects, along with any other defects in the response, a new response matrix was constructed as a factorised product of single jet response distributions, i.e. assuming the response in p_{T_1} and p_{T_2} were independent. The data were unfolded using this new response and the differences in the unfolded distributions were taken as a systematic.

5.5.6 Summary

A summary of the different contributions to the total systematic uncertainty is shown for $100 < p_{\mathrm{T}_1} < 126$ GeV in the 0–10% centrality interval and for pp collisions in Figure 7.16. In general, the uncertainties tend to decrease with increasing x_{J}, where the total uncertainty at $x_{\mathrm{J}} \sim 1$ reaches $\approx 12\%$ in most of the p_{T_1} and centrality bins in the Pb+Pb data. The relative uncertainty becomes large for $x_{\mathrm{J}} < 0.4$, but this region is a small part of the total $(1/N)\mathrm{d}N/\mathrm{d}x_{\mathrm{J}}$ distribution. The largest contribution is from the JER, where in Pb+Pb data it reaches values of $\approx 10\%$ at $x_{\mathrm{J}} \sim 1$ and 15% at $x_{\mathrm{J}} = 0.5$. The next largest contribution is from the JES which is between 5% and 10%. The unfolding uncertainty can becomes as

large as the JES in central collisions.

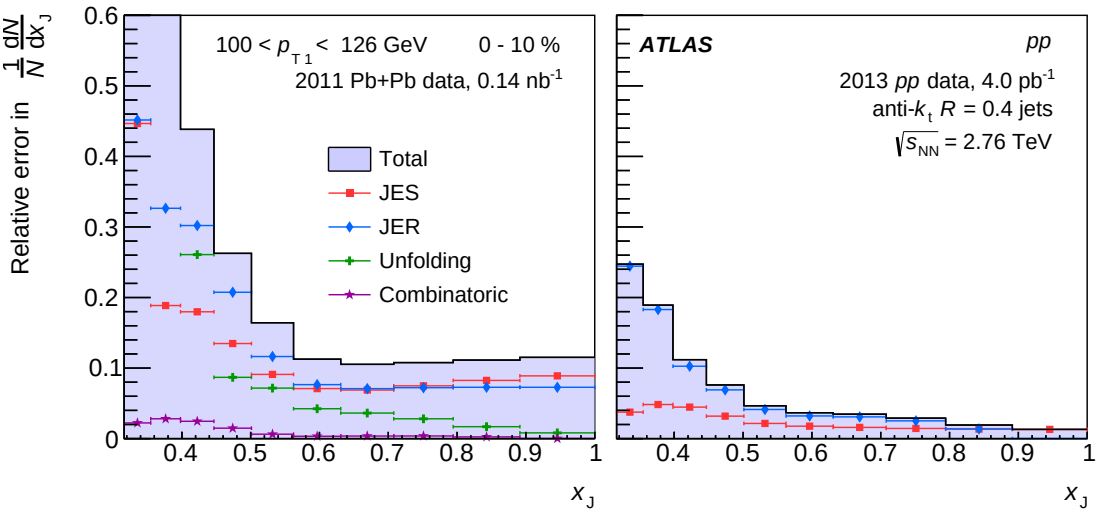

Figure 5.72: The total systematic uncertainty and its various components for $100 < p_{T_1} < 126$ GeV for $R = 0.4$ jets in Pb+Pb collisions with 0–10% centrality (left) and pp collisions (right). In the figure on the left the first two bins are off scale with bins centers of x_J=0.34 and 0.38 and bins contents of 1.25 and 0.75, respectively.

The other centrality intervals and the pp data have similar trends as those in the 0–10% centrality interval, but the uncertainties are smaller in more peripheral collisions. In the pp data they are smaller by about a factor of two compared to the 0–10% Pb+Pb data. This is shown for the other centrality bins in Pb+Pb (and different p_{T_1} intervals) in Figures 5.73 and 5.74. The different p_{T_1} intervals in pp collisions are shown in Figure 5.75. The trends are similar in the different p_{T_1} bins as well. A more detailed breakdown of the various components that contribute to the total uncertainty is shown in Figure 5.76, where it is seen that for the unfolding uncertainty the factorization dominates and for the JES/JER uncertainties the data period dominates.

The $R = 0.3$ uncertainties have similar features as the $R = 0.4$ uncertainties but they are slightly larger due to the two additional $R = 0.3$ sources of uncertainties.

5.6 Results and Discussion

The centrality dependence of the fully unfolded $(1/N)\mathrm{d}N/\mathrm{d}x_J$ distributions normalized to the number of dijet pairs for pp $R = 0.4$ jets are compared to Pb+Pb $R = 0.4$ jets in

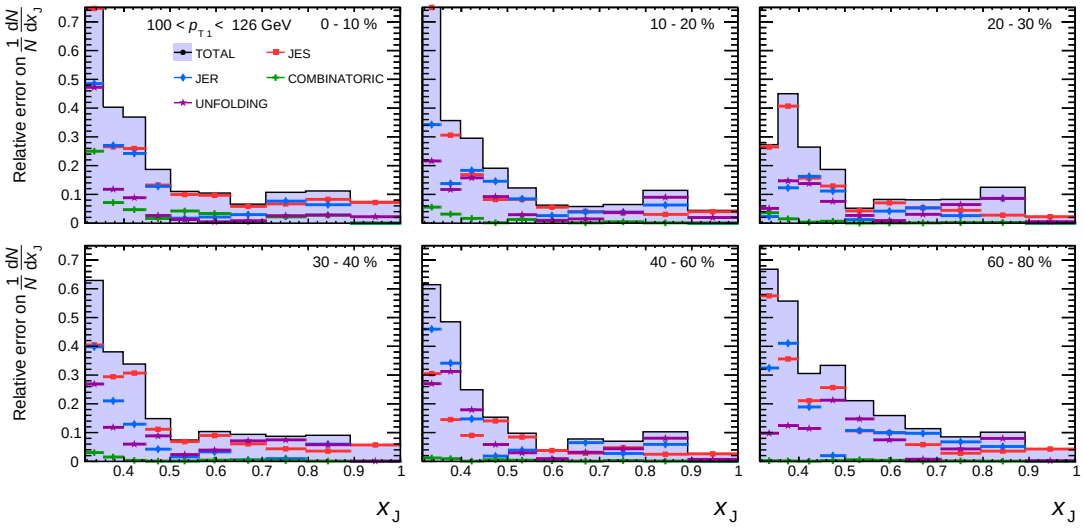

Figure 5.73: The total systematic uncertainty and its various components for $100 < p_{T_1} < 126$ GeV for the 0–10% centrality bin.

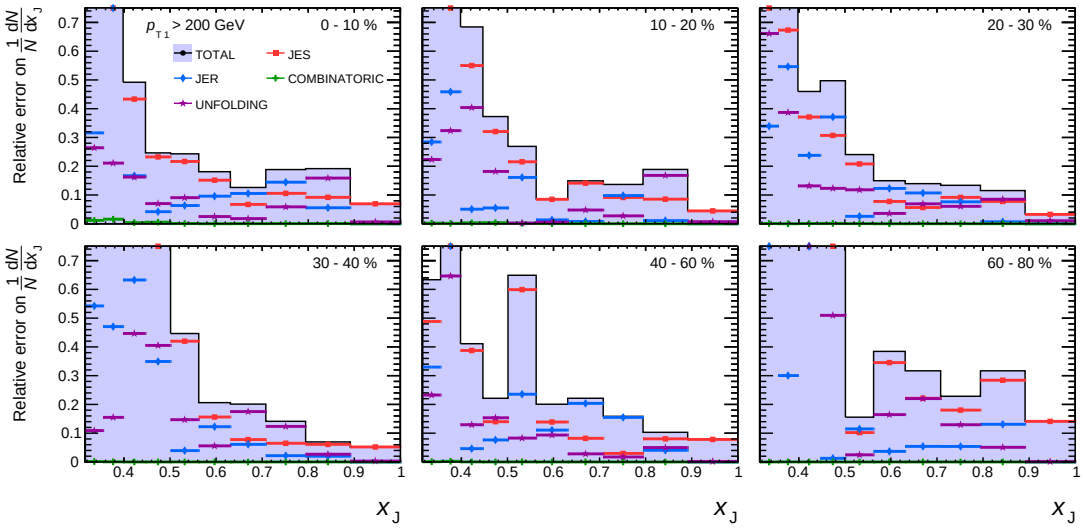

Figure 5.74: The total systematic uncertainty and its various components for $p_{T_1} > 200$ GeV for the 0–10% centrality bin.

Figure 5.77 for the 100–126 GeV leading jet p_T bin. Here the error bars indicate statistical errors and the bands represent systematic errors. The Pb+Pb dijets differ substantially from the *pp* jets in the most central bins and then agree with the *pp* jets in the most peripheral bin (60–80%).

The same distributions are showing for the R=0.3 jets in Figure 5.78. The p_T of an

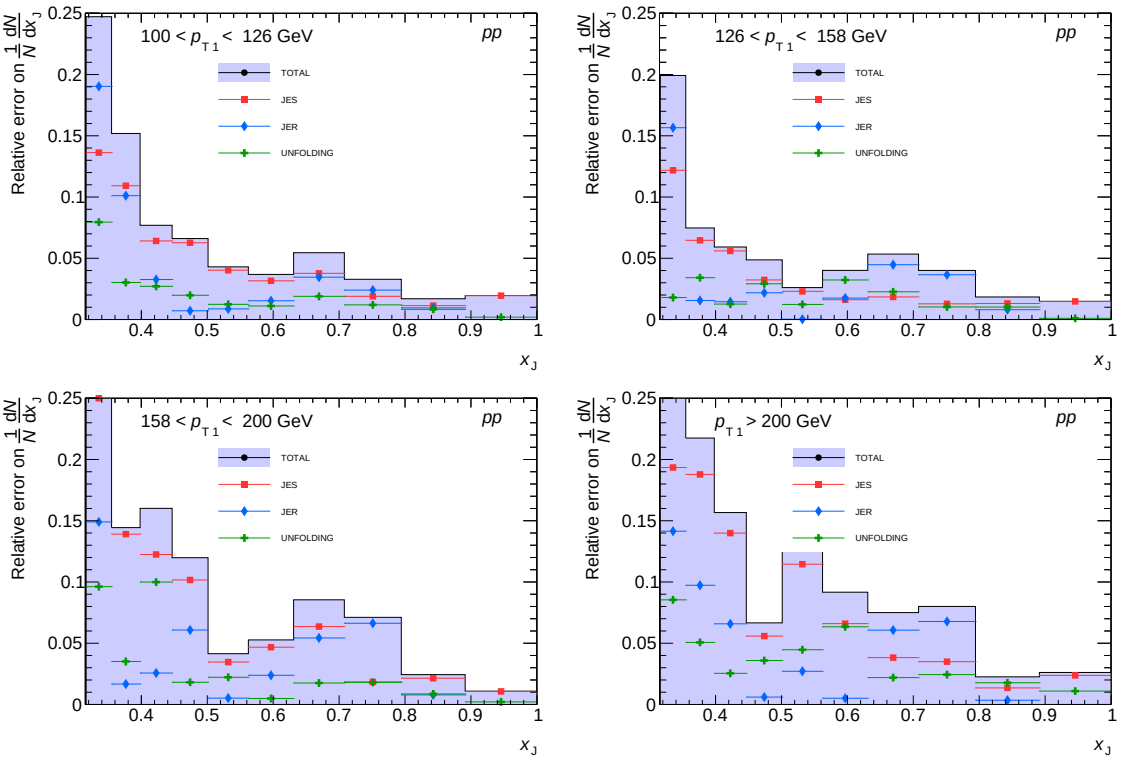

Figure 5.75: The total systematic uncertainty and its various components in various p_{T_1} bins for the pp analysis.

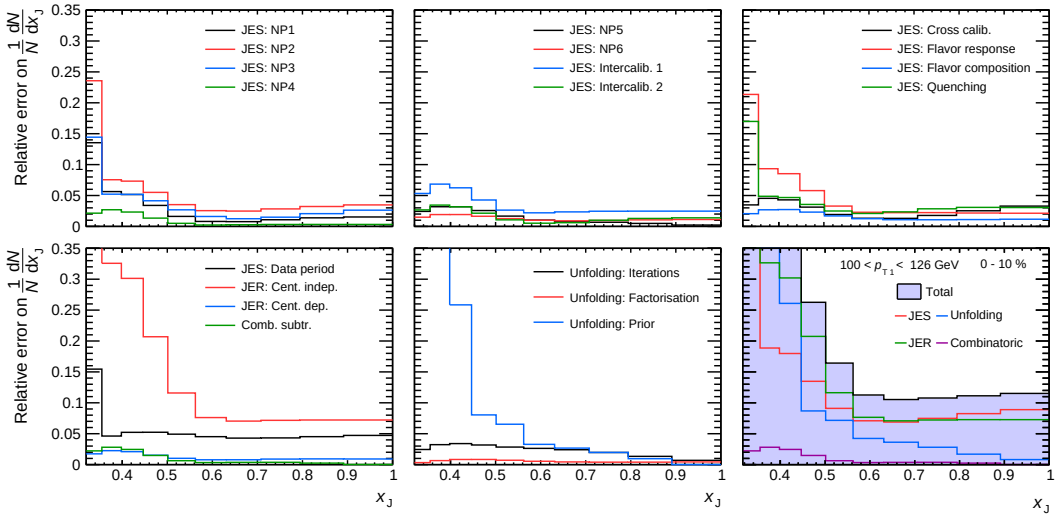

Figure 5.76: The total systematic uncertainty and its various components for $100 < p_{T_1} < 126$ GeV for the 0–10% centrality bin.

$R = 0.3$ jet is generally lower than that of an $R = 0.4$ jet originating from the same hard scattering, so features in the $(1/N)\mathrm{d}N/\mathrm{d}x_{\mathrm{J}}$ distributions for $R = 0.4$ jets should appear at lower values of p_{T_1} for $R = 0.3$ jets. In order to compare the two R values, the $R = 0.3$ jet results include an additional p_{T_1} interval, $79 < p_{\mathrm{T}_1} < 100$ GeV. The $R = 0.3$ results show similar qualitative trends as the $R = 0.4$ jets when the lower p_{T} bin in the $R = 0.3$ dijets is included. The $R = 0.3$ jets should have less contribution from the UE due to the smaller cone size, so observing similar trends between the two cone sizes implies that the results are robust with respect to the UE. This indicates that the data analysis properly account for UE effects through the combinatoric subtraction and unfolding procedures. The distributions are flatter for $R = 0.3$ jets, including in pp collisions, which is consistent with the expectation that the correlation between the jets in the pair is weaker for smaller-R jets due to parton radiation outside the jet cone.

The centrality dependence shows a clear decrease in asymmetric jets with increasing centrality. This effect is most significant in the 100–126 GeV bin in $R = 0.4$ jet and the 79.4–100 GeV bin in $R = 0.3$ jets. In the 0–10% bin there is a sharp peak in the x_{J} distribution at around 0.55 that decreases with centrality and with leading jet p_{T}. This decrease is particularly distinct when moving from 0–10% to 10–20% in both $R = 0.3$ and $R = 0.4$ jets and when moving from 100–126 GeV to 126–158 GeV for $R = 0.4$ and when moving from 79.4–100 GeV to 100–126 GeV in $R = 0.3$.

The $R = 0.4$ pp jets are compared to the most peripheral (60–80%) Pb+Pb jets for different leading jet p_{T} bins in the panels in Figure 5.79. The Pb+Pb agrees with the pp in all of the p_{T} bins. A similar trend is demonstrated in Figure 5.80 for the $R = 0.3$ jets.

The $R = 0.4$ pp dijets are also compared to the most central (0–10%) Pb+Pb jets for different leading jet p_{T} bins in the panels in Figure 5.81. The difference between the two is most distinctive in the 100–126 GeV bin and then becomes less significant as the leading jet p_{T} is increased. In the highest p_{T_1} bin the Pb+Pb dijet pairs become better balanced in momentum. This is showing relative energy loss though and doesn't mean that the high energy jets didn't lose energy, it just means they lost approximately the same amount of energy. The same trend is seen in Figure 5.82 for the $R = 0.3$ jets except the $R = 0.3$ jets start at one lower leading jet p_{T} bin. Appendix D shows these results in all the different

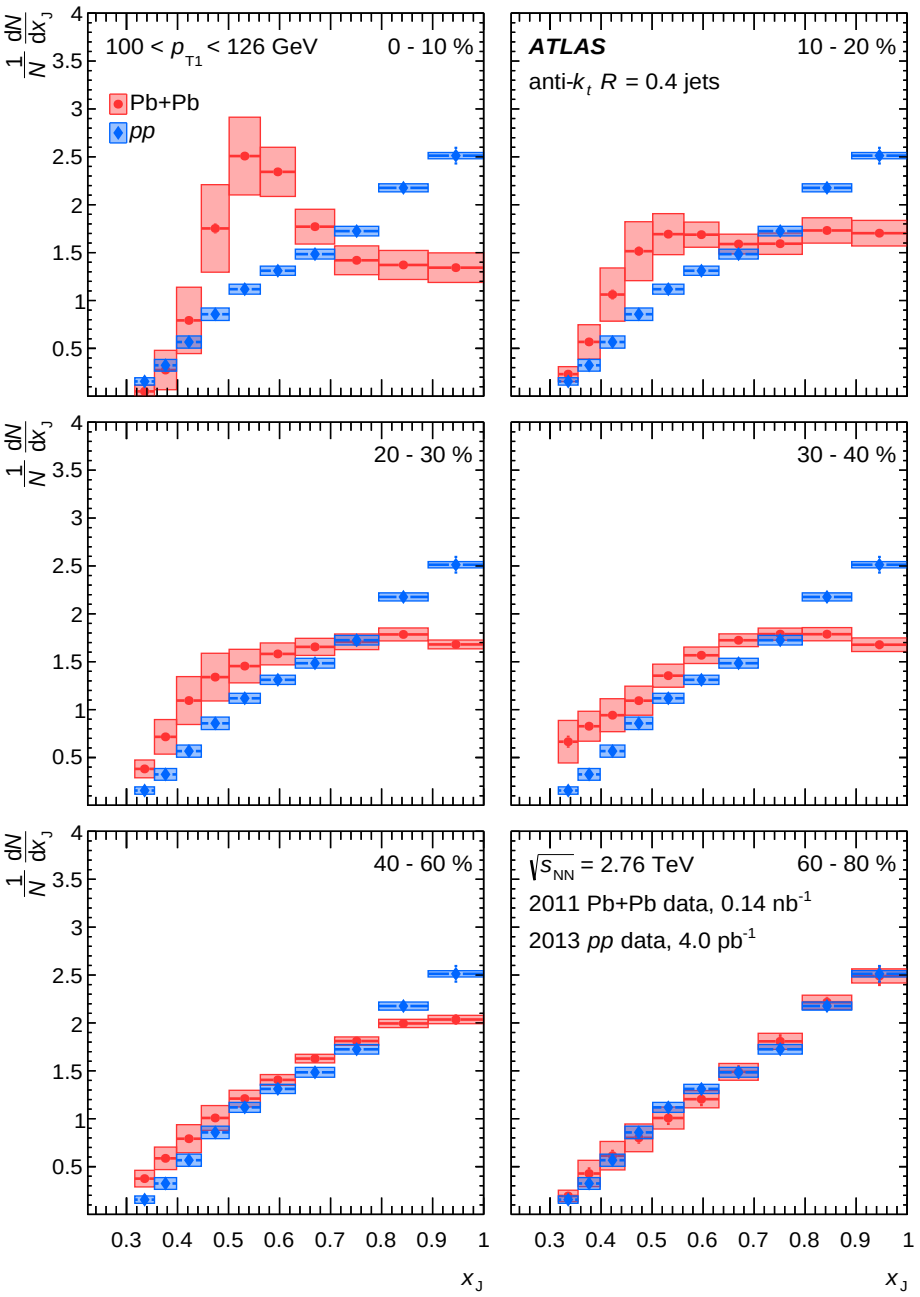

Figure 5.77: The unfolded $(1/N)\mathrm{d}N/\mathrm{d}x_\mathrm{J}$distribution normalized to the number of dijet pairs for Pb+Pb $R = 0.4$ jets (black) and pp $R = 0.4$ jets (red). Each panel is a different centrality bin in the Pb+Pb with the pp being the same in each panel: 0-10% (top left), 10-20% (top middle), 20-30% (top right), 30-40% (top right), 40-60% (bottom middle), and 60-80% (bottom right). Each curve is for leading jet p_T from 100-126 GeV. The statistical errors are given by the error bars on each curve and the systematics are given by the error bands.

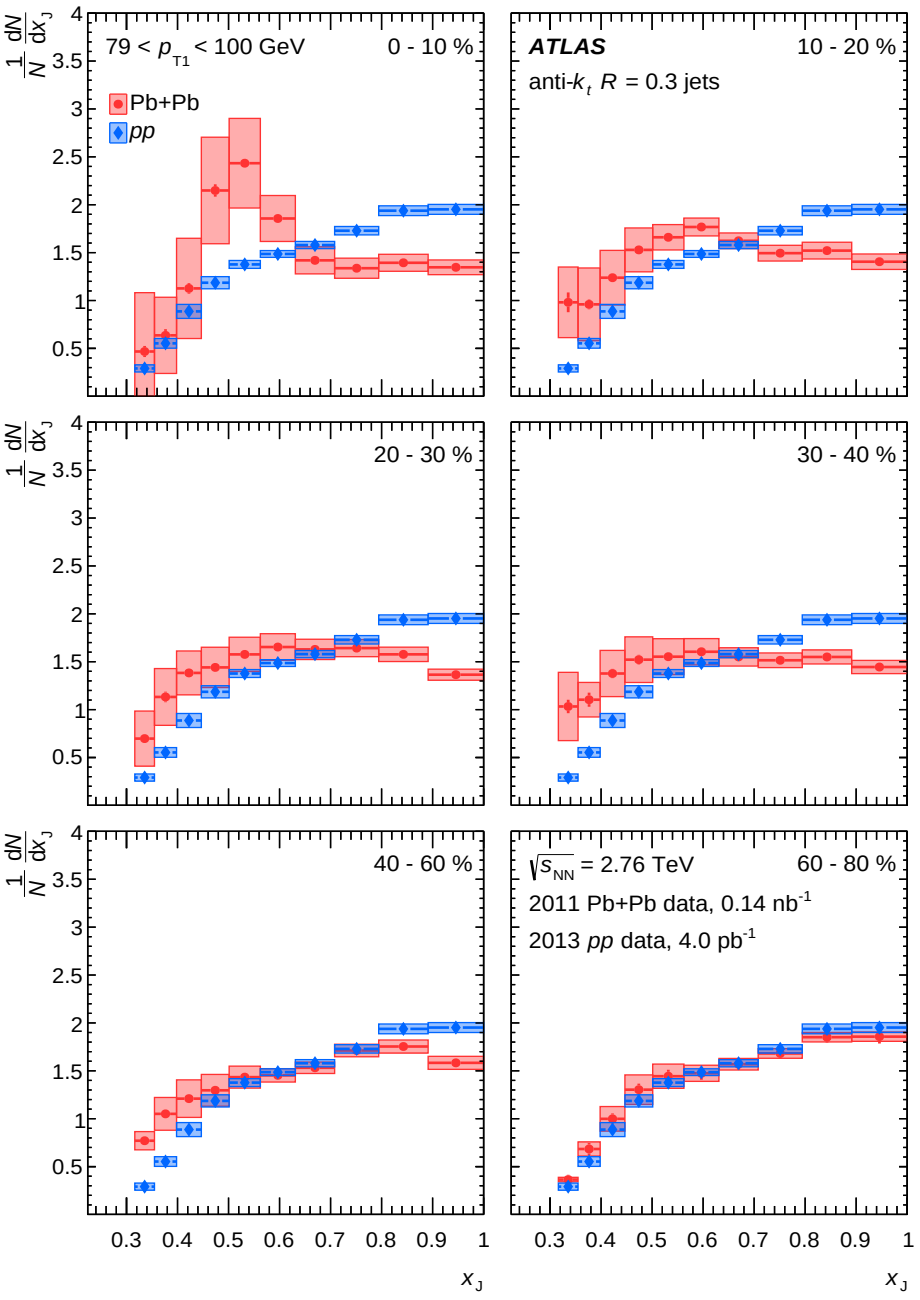

Figure 5.78: The unfolded $(1/N)\mathrm{d}N/\mathrm{d}x_\mathrm{J}$distribution normalized to the number of dijet pairs for Pb+Pb $R = 0.3$ jets (black) and pp $R = 0.3$ jets (red). Each panel is a different centrality bin in the Pb+Pb with the pp being the same in each panel: 0-10% (top left), 10-20% (top middle), 20-30% (top right), 30-40% (top right), 40-60% (bottom middle), and 60-80% (bottom right). Each curve is for leading jet p_T from 79-100 GeV. The statistical errors are given by the error bars on each curve and the systematics are given by the error bands.

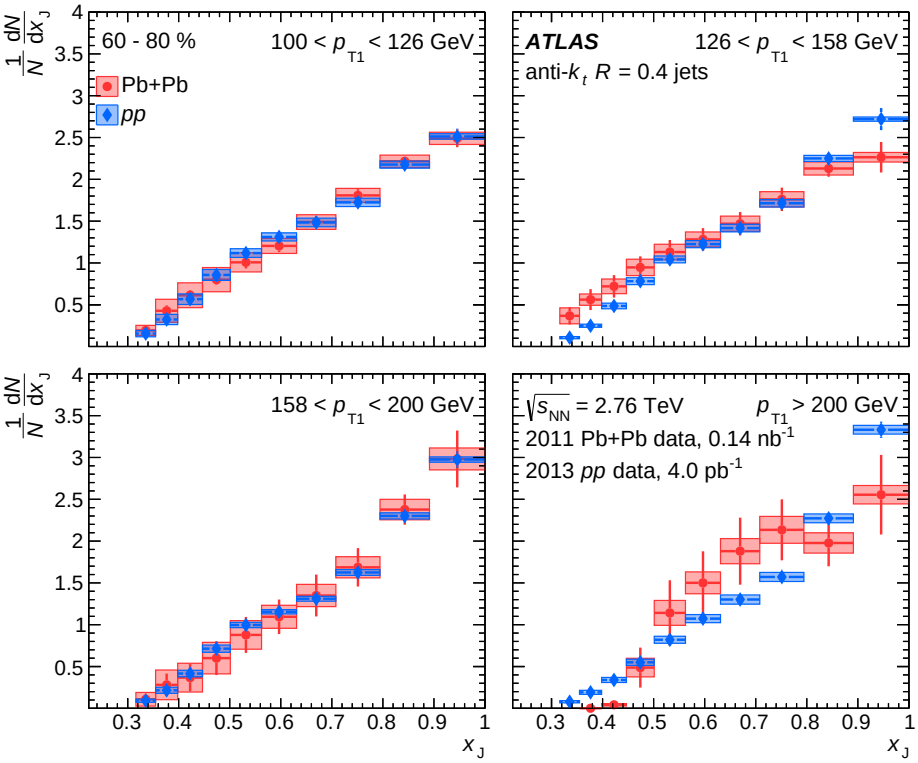

Figure 5.79: The unfolded $(1/N)\mathrm{d}N/\mathrm{d}x_\mathrm{J}$distribution normalized to the number of dijet pairs for peripheral Pb+Pb (60-80%) $R = 0.4$ jets (black) and pp $R = 0.4$ jets (red) where each panel is a different leading jet bin: 100-126 GeV (top left), 126-158 GeV (top right), 158-200 GeV (bottom left), and >200 GeV (bottom right). The statistical errors are given by the error bars on each curve and the systematics are given by the error bands.

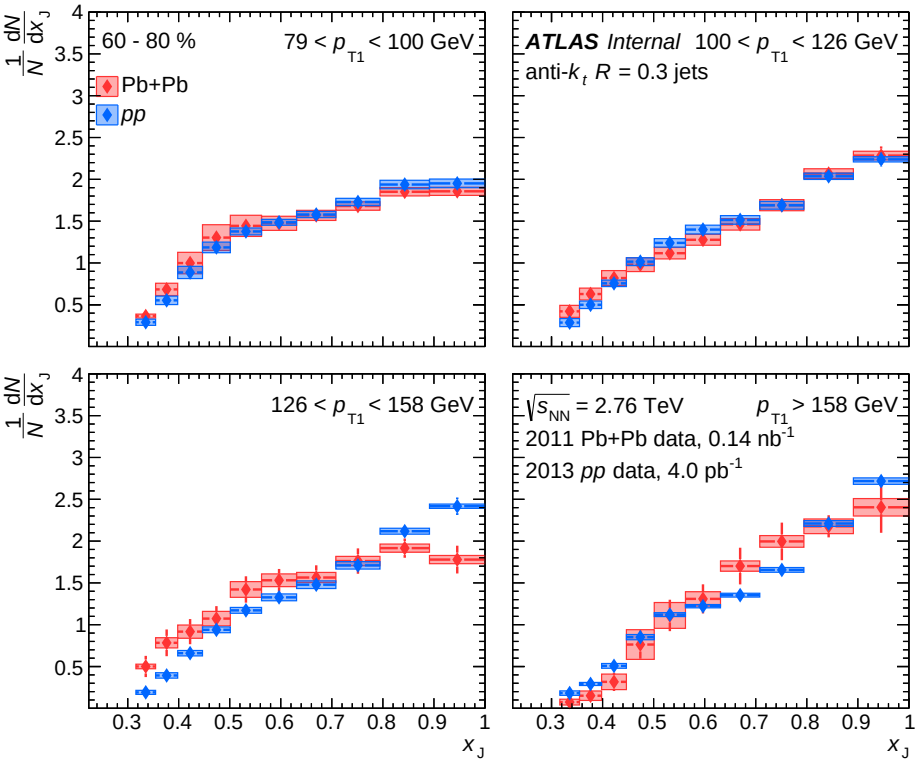

Figure 5.80: The unfolded $(1/N)\mathrm{d}N/\mathrm{d}x_\mathrm{J}$distribution normalized to the number of dijet pairs for peripheral Pb+Pb (60-80%) $R = 0.3$ jets (black) and pp $R = 0.3$ jets (red) where each panel is a different leading jet bin: GeV 79-100 (top left), 100-126 GeV (top right), 126-158 GeV (bottom left), and >158 GeV (bottom right). The statistical errors are given by the error bars on each curve and the systematics are given by the error bands.

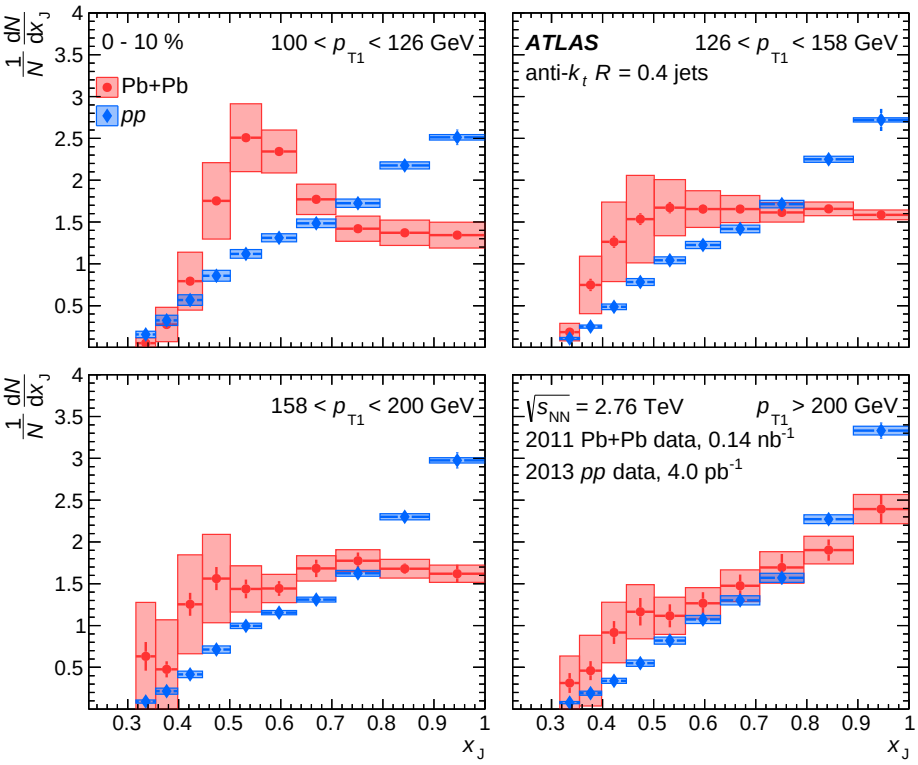

Figure 5.81: The unfolded $(1/N)\mathrm{d}N/\mathrm{d}x_\mathrm{J}$distribution normalized to the number of dijet pairs for central Pb+Pb (0-10%) $R = 0.4$ jets (black) and pp $R = 0.4$ jets (red) where each panel is a different leading jet bin: 100-126 GeV (top left), 126-158 GeV (top right), 158-200 GeV (bottom left), and >200 GeV (bottom right). The statistical errors are given by the error bars on each curve and the systematics are given by the error bands.

centrality and p_T bins included in the analysis. This drastic p_{T_1} dependence could possibly be attributed to the changing flavor composition of the pairs, as shown in the right panel of Figure 2.35, since the energy loss depends on flavor. The figure implies that gg pairs dominate at low p_T, qq pairs at high p_T, and qg and gq at intermediate p_T. It should be noted that this is based on the p_{T_1} of dijets where the leading jet has not undergone in-medium energy loss. The leading jet has undergone some energy loss in this result and thus originally comes from a higher p_T jet. The qg pairs are expected to be the most imbalanced so it is possible that the lowest p_{T_1} bin is dominated by these pairs and then the flavor fractions quickly change such that qq pairs dominate at high p_T.

The interesting features in the unfolded x_J distribution in Pb+Pb collisions can be in-

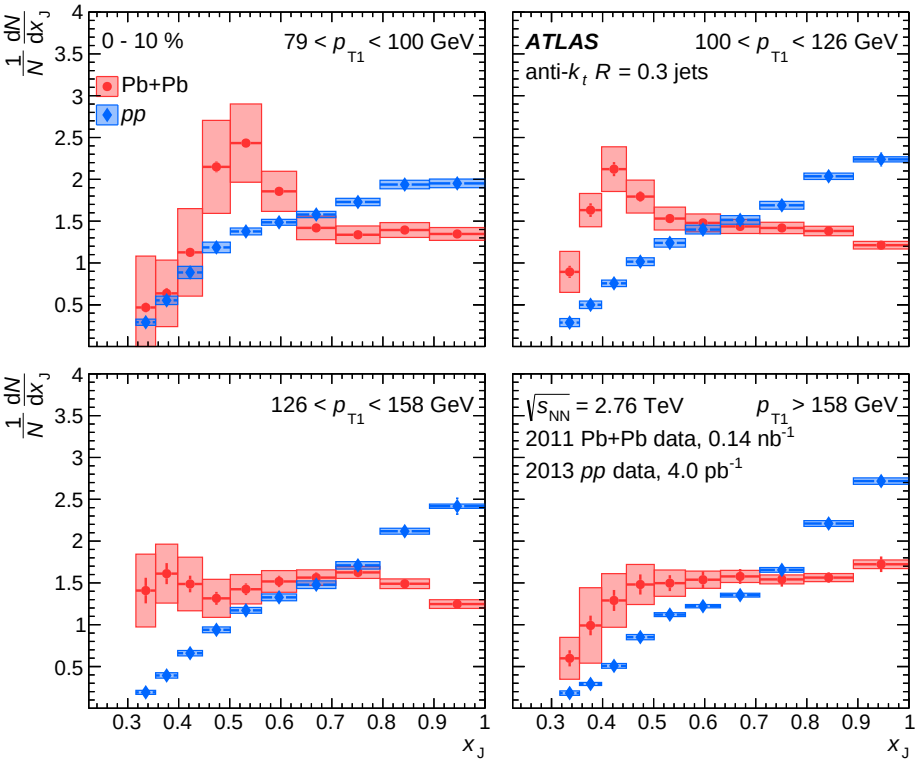

Figure 5.82: The unfolded $(1/N)\mathrm{d}N/\mathrm{d}x_\mathrm{J}$ distribution normalized to the number of dijet pairs for central Pb+Pb (0-10%) $R = 0.3$ jets (black) and pp $R = 0.3$ jets (red) where each panel is a different leading jet bin: 79-100 GeV (top left), 100-126 GeV (top right), 126-158 GeV (bottom left), and >158 GeV (bottom right). The statistical errors are given by the error bars on each curve and the systematics are given by the error bands.

vestigated by comparing to theoretical models of jet energy loss. The distinct x_J shape and dependence on p_{T_1} can be used to constrain different jet quenching models and help the field better understand jet energy loss in the medium. Unfortunately, not many theoretical comparisons have been made to this result since it was published. The only cited comparison is shown in Figure 5.83 from Ref. [138], which uses the BDMPS-Z formalism (radiative energy loss in the multiple soft-scattering limit) with Sudakov resummation to correctly account for the broadening effect in back-to-back dijet azimuthal correlations. The theoretical model for pp collisions is compared to the pp data in different p_{T_1} intervals, where it mostly describes the low x_J region of the data but over predicts the high x_J region indicating that NNLO effects should be included. The model for Pb+Pb collisions is compared to central Pb+Pb data, where it describes the three higher p_{T_1} intervals fairly well but misses the peak structure in the lowest p_{T_1} interval. This demonstrates that a model with strictly radiative energy loss in the limit of multiple soft gluon emmission doesn't fully describe the energy loss in this p_{T_1} range. Given that radiative energy loss models rely heavily on a path length dependence to energy loss, the path length may not be the dominant effect in jet energy loss. The dominant effect could instead be from jet-by-jet fluctuations in the energy loss due to medium fluctuations or fluctuations in the energy loss mechanisms themselves.

The $R = 0.4$ pp results were compared to different MC generators for 100–126 GeV leading jet p_T in Figure 5.84. The MC generators used for the comparison are the PYTHIA 6 sample that is used in the MC studies in this analysis, a sample from Pythia 8 using the AU2 tune, a sample using Herwig++ with the UE-EE-3 tune, and a sample using POWHEG which is accurate to next-to-leading order in perturbative QCD and interfaced with the Pythia 8 to provide a description of the parton shower and hadronization. The ratio of each MC generator to the pp data is shown in the bottom panel where the shaded grey represents the error on the ratio from the data. All of the generators are in good agreement with the data with most of the higher x_J points agree within error. POWHEG+Pythia 8 shows the best agreement, which is most likely due to the inclusion of the NLO calculations. Appendix D shows these results in all the leading jet p_T bins used in the analysis.

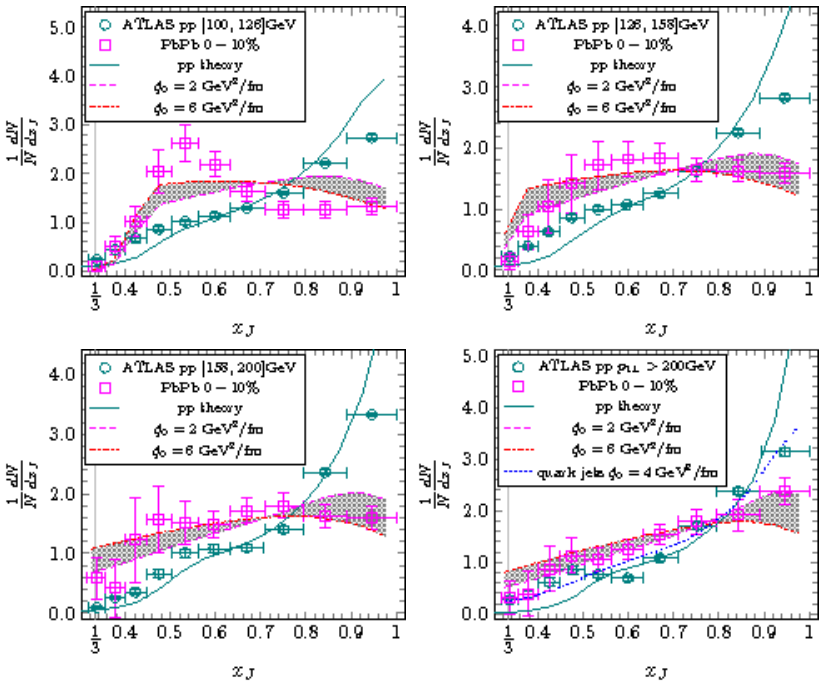

Figure 5.83: The leading jet p_{T} dependence of the x_{J} distribution in 0–10% Pb+Pb collisions and pp collisions compared to a theoretical model from Ref. [138].

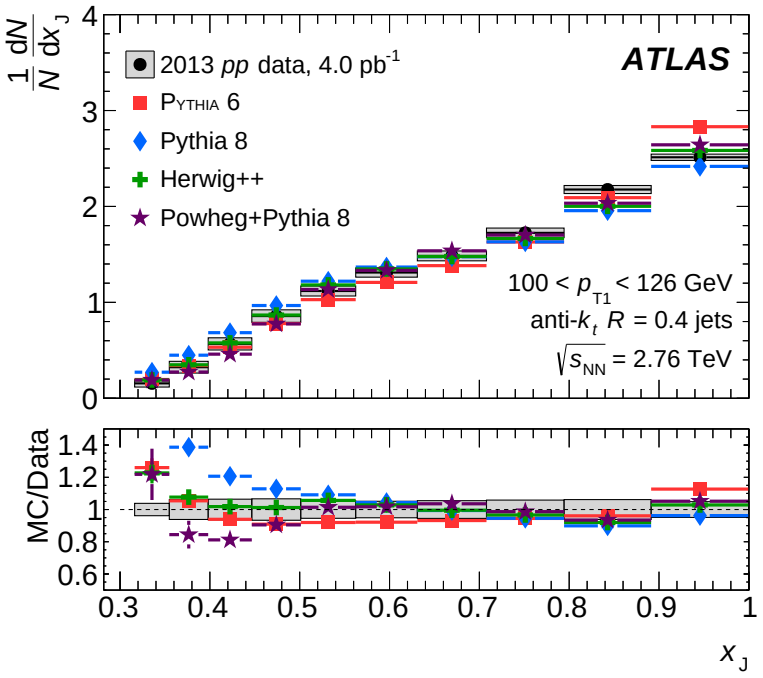

Figure 5.84: The unfolded $(1/N)\mathrm{d}N/\mathrm{d}x_\mathrm{J}$distribution normalized to the number of dijet pairs is shown in the top panel for pp $R = 0.4$ jets (black) in the 100-126 GeV leading jet p_T bin compared to the following MC generators: Pythia 6 (red squares), Pythia 8 (blue diamonds), Herwig++ (green crosses), and POWHEG+Pythia 8 (purple stars). The statistical errors are given by the error bars on the points and the systematics are given by the error bands (only for the data). The bottom panel represents the ratio of each MC generator (same colors apply) to the data and the shaded band represents to error on the ratio from the systematic errors on the data.

Chapter 6

Inclusive Jet Suppression

6.1 Data and MC Samples

This analysis used data from 2015 of Pb+Pb and pp collisions at $\sqrt{s_{\mathrm{NN}}} = 5.02$ TeV.

6.1.1 2015 Pb+Pb Data

The Pb+Pb data used is this analysis was taking during run 2 in 2015 at $\sqrt{s_{\mathrm{NN}}} = 5.02$ TeV with a total luminosity of 0.52 nb^{-1}. A combination of minimum bias and jet-triggered high level triggers (HLT) were used. The minimum bias events were selected using a logical OR between the `HLT_noalg_mb_L1TE50`, which is a transverse energy (TE) trigger with an $E_{\mathrm{T}}^{\mathrm{tot}} = 50$ GeV and `HLT_mb_sptrk_ion_L1ZDC_A_C_VTE50`, which is ZDC coincidence trigger. When just the ZDC trigger is fired, empty events are removed by imposing a requirement of at least one track. The data is also composed of multiple triggers from the `HardProbes` stream that have different p_{T} thresholds and different prescales as indicated in Table 6.1. These are seeded off the L1 trigger and then use the jet reconstruction algorithm as in the Pb+Pb reconstruction (Section 4.1). The highest trigger (j75) is an unprescaled trigger that sees the full luminosity. The p_{T} ranges are based on where the trigger is fully efficient ($> 99\%$) for $R = 0.4$ jets, which are shown in Figure 6.1.

The events were also required to pass typical HI event-level selection criteria which was outline in the list 5.1.1 in Chapter 5. Pile-up was rejected by cutting out the end of the $\Sigma E_{\mathrm{T}}^{\mathrm{FCal}}$ distribution at $\Sigma E_{\mathrm{T}}^{\mathrm{FCal}} > 4.9$ which is less than 1% of the data in the 0–

Table 6.1: The rigger scheme for the 2015 Pb+Pb data including the trigger names and p_{T} ranges over which the triggers were used.

Trigger	p_{T} range
`MinBias`	< 68.1
`HLT_j50_ion_L1TE20`	68.1–79.4
`HLT_j60_ion_L1TE50`	79.4–89.1
`HLT_j75_ion_L1TE50`	> 89.1

10% centrality bin since the 0.1% centrality bin starts at an $\Sigma E_{\mathrm{T}}^{\mathrm{FCal}}$ of 4.54 TeV. If the pile-up rates in this region are extrapolated to the $\Sigma E_{\mathrm{T}}^{\mathrm{FCal}} < 4.9$ TeV region the residual pile-up rate in the measurement region ends up being less than 0.1%, which indicates this cut is sufficient for cutting out the pile-up. Also, there are no expectation of real events in the region being rejected which was determined through extrapolations of the $\Sigma E_{\mathrm{T}}^{\mathrm{FCal}}$ distribution into the rejected region.

It is extremely important to make sure the analysis is using every event in each run of the data-taking period with the correct luminosity. Figure 6.2 shows the cross section as a function of run number for jets above 100 GeV that fire the highest jet trigger (j75). This cross section is calculated from the total number of jets that fired the trigger scaled by the luminosity (also shown in the figure). The cross section should be constant as a function of run number, which is shown to be true except for a small fraction of events ($< 1\%$) that are due to broken data sets that were not analyzed. The average number of collisions per

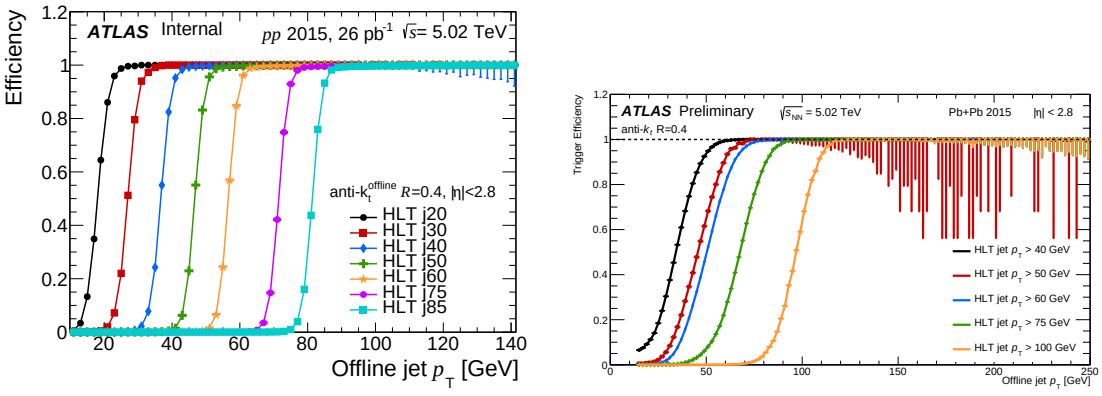

Figure 6.1: The left panel shows the trigger efficiencies for $R = 0.4$ offline jets for pp HLT jet triggers at 5.02 TeV. The right panel shows the trigger efficiencies for $R = 0.4$ offline jets for Pb+Pb HLT jets at 5.02 TeV.

Centrality	$\Sigma E_{\mathrm{T}}^{\mathrm{FCal}}$ [TeV]	N_{part}	$\langle T_{\mathrm{AA}} \rangle$ [1/mb]
70-80%	0.144–0.064	15.4±1.0	0.22±0.02
60-70%	0.290–0.144	30.6±1.6	0.57±0.04
50-60%	0.525–0.290	53.9±2.0	1.28±0.07
40-50%	0.875–0.525	87.0±2.3	2.63±0.11
30-40%	1.369–0.875	131.4±2.6	4.94±0.15
20-30%	2.047–1.369	189.2±2.8	8.64±0.17
10-20%	2.989–2.047	264.0±2.8	14.33±0.18
0-10%	$>$ 2.989	358.8±2.2	23.35±0.20

Table 6.2: The centrality ranges used for the 2015 Pb+Pb data and their corresponding $\Sigma E_{\mathrm{T}}^{\mathrm{FCal}}$ ranges, N_{part}, and $\langle T_{\mathrm{AA}} \rangle$ values.

bunch crossing μ was less than 0.0001.

6.1.1.1 Centrality

The centrality was determined by the same methods as discussed in Section 5.1.1.1 but for the 2015 Pb+Pb data. The $\Sigma E_{\mathrm{T}}^{\mathrm{FCal}}$ distribution with the corresponding quantiles is shown in Figure 6.3. The minimum bias trigger and event selection sampled 84.5% of the total inelastic cross section. In this analysis 8 centrality interval were used: 0-10%, 10-20%, 20-30%, 30-40%, 40-50%, 50-60%, 60-70% and 70-80%. The R_{AA} also needs to $\langle T_{\mathrm{AA}} \rangle$ factors and is analyzed as a function of N_{part}, which were discussed in Section 2.4.2, and are given in Table 6.2.

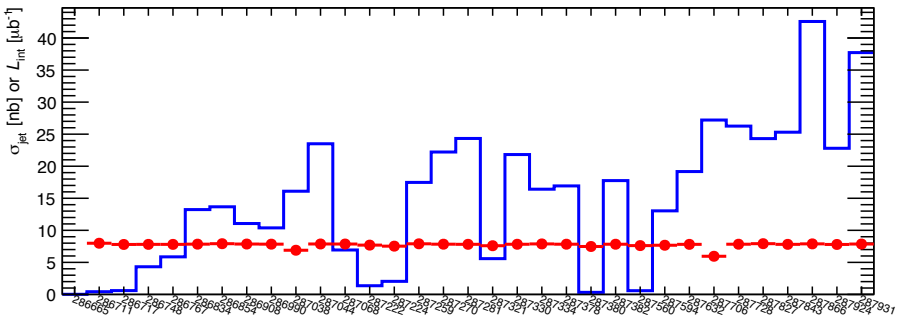

Figure 6.2: The jet cross section for jets with $p_{\mathrm{T}} > 100$ GeV as a function of run number for Pb+Pb collision data. The blue line represents the integrated luminosity and the red points are the cross sections.

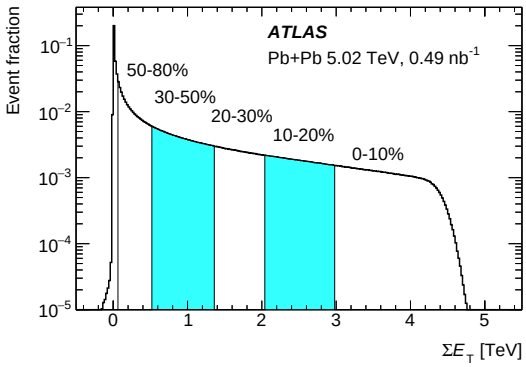

Figure 6.3: The $\Sigma E_{\mathrm{T}}^{\mathrm{FCal}}$ distributions for 2015 Pb+Pb data at $\sqrt{s_{\mathrm{NN}}} = 5.02$ TeV partitioned into centrality quantiles [231].

Table 6.3: The trigger scheme in the pp data, including the names of the triggers and the p_{T} ranges over which the triggers were used.

Trigger	p_{T} range
HLT_j30_L1TE5	34.1–44.5
HLT_j40_L1TE10	44.5–59
HLT_j50_L1J12	59–70
HLT_j60_L1J15	70–79
HLT_j75_L1J20	79–89
HLT_j85	$> 89.$

6.1.2 2015 *pp* Data

The pp data used in this analysis was taken in run 2 during 2015 at $\sqrt{s_{\mathrm{NN}}} = 5.02$ TeV with a total luminosity of 25 pb^{-1}.The data is also composed of multiple triggers from the HardProbes stream that have different p_{T} thresholds and different prescales as indicated in Table 6.3. These are seeded off the L1 trigger and then uses jets build from topoclusters with no UE subtraction. The highest trigger (j85) is an unprescaled trigger that sees the full luminosity. The p_{T} ranges are based on where the trigger is fully efficient ($> 99\%$) for $R = 0.4$ jets, which are shown in Figure 6.1.

The pp data was also required to have a reconstructed primary vertex and be in the GRL. Figure 6.4 shows the cross section as a function of run number for jets above 100 GeV that fires the highest jet trigger (j85). This was also found to be constant. The μ for the pp data-taking period was less than 1.4.

6.1.2.1 Cleaning

The *pp* jets were cleaned using standard cleaning tools to remove non-collisional background, cosmic ray background, and noise. The "BadLoose" cut level from Ref. [232] was used which is defined to have a high efficiency for real jets while still having as high a fake rejection as possible.

A tag and probe method was used to evaluate the cleaning efficiency in the 2015 *pp* dataset. This method identities balanced dijet pairs with $A_{\mathrm{J}} < 0.3$ and $\Delta\phi > 3$. In each pair one of the jets had to pass the cleaning cut and was designated the probe. Then the other jet (the tag) is checked to see if it passes the cleaning cut as well. The efficiency is evaluated based on this and is shown as a function of p_{T} on the left panel of Figure 6.5 and as a function of η on the right.

The *pp* jets before and after cleaning are shown in Figure 6.6. The jets that failed the cleaning are shown in blue.

6.1.3 MC Samples

The MC samples in this analysis use a signal from POWHEG+Pythia 8 where muti-jet processes were simulated using POWHEG-BOX v2 [72, 226, 227] interfaced with Pythia 8.186 [74] using the A14 tune [233] and CT10 PDFs [224] along with NNPDF2.3LO PDFs [234] to model non-perturbative effects. As mentioned in Section 4.3, the Pythia events are divided into ranges of $\hat{p_{\mathrm{T}}}$, which is the p_{T} of the outgoing partons in a $2 \to 2$ hard scattering, and

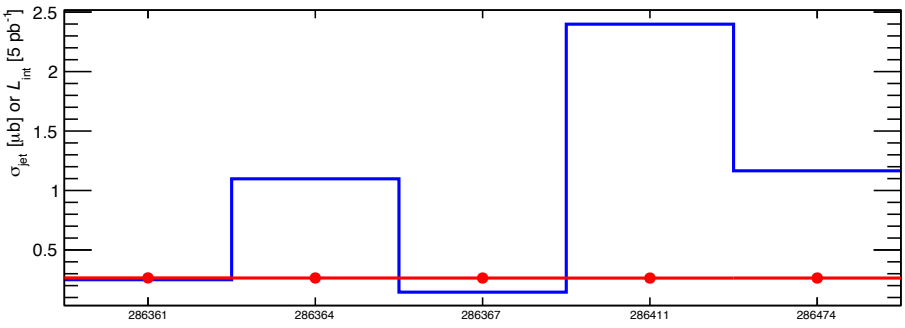

Figure 6.4: The jet cross section for jets with $p_{\mathrm{T}} > 100$ GeVas a function of run number for the *pp* collision data. The blue line represents the integrated luminosity and the red points are the cross sections.

combined using weights from their cross sections. The J slices and their cross sections for the PYTHIA used to generate the pp MC are shown in Table 6.4. For the Pb+Pb MC, the same signal was used but overlaid with real minimum bias Pb+Pb data as discussed in Section 4.3. Table 6.5 shows the p_{T} ranges, cross sections, and total number of events for the Pb+Pb MC.

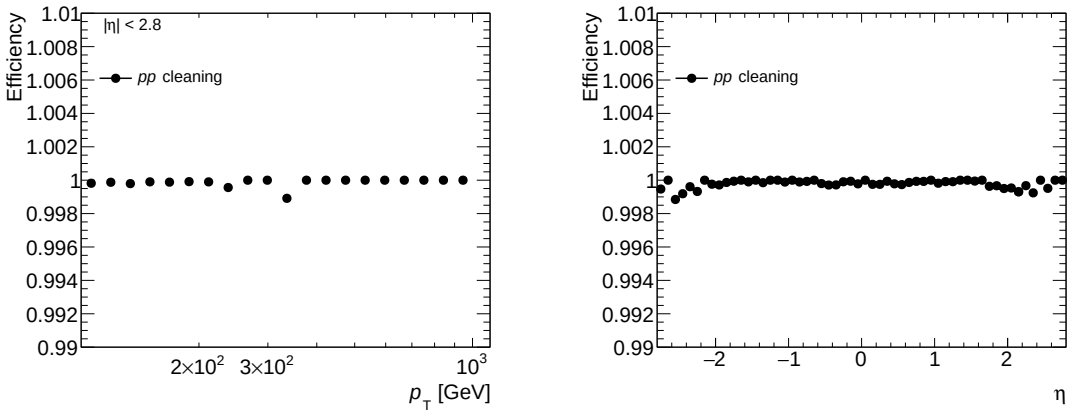

Figure 6.5: The cleaning efficiency for jets in pp collisions as a function of p_{T} (left) and η (right).

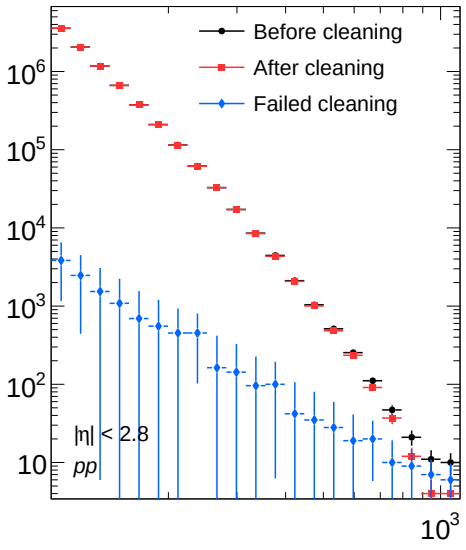

Figure 6.6: The p_{T} spectrum for pp jets before (black) and after (red) cleaning. The jets that were removed by the cleaning are also shown in blue.

J	$R = 0.4$ $p_{\mathrm{T}}^{\mathrm{truth}}$ [GeV]	σ [nb] $\times$ ϵ	#events
1	20–60	(1.28×10^{8}) $\times$ (1.59×10^{-3})	5.9 M
2	60–160	(1.97×10^{7}) $\times$ (1.30×10^{-4})	5.9 M
3	160–400	(5.76×10^{5}) $\times$ (4.21×10^{-5})	5.9 M
4	400–800	(4.15×10^{4}) $\times$ (2.86×10^{-6})	5.4 M
5	800–1300	(8.43×10^{2}) $\times$ (5.99×10^{-7})	5.9 M

Table 6.4: MC samples for simulation of dijets in pp events.

J	$R = 0.4$ $p_{\mathrm{T}}^{\mathrm{truth}}$ [GeV]	σ [nb] $\times$ ϵ	#events
1	20–60	(1.28×10^{8}) $\times$ (1.59×10^{-3})	5.9 M
2	60–160	(1.97×10^{7}) $\times$ (1.30×10^{-4})	5.8 M
3	160–400	(5.76×10^{5}) $\times$ (4.21×10^{-5})	5.9 M
4	400–800	(4.15×10^{4}) $\times$ (2.86×10^{-6})	5.8 M
5	800–1300	(8.43×10^{2}) $\times$ (5.99×10^{-7})	5.9 M

Table 6.5: MC samples for simulation of inclusive jets in Pb+Pb events based on POWHEG+PYTHIA8 dijets embedded to minimum bias heavy ion data. The ϵ represents the filtering efficiency from AMI which is applied at the level of sample generation.

6.2 Jet Reconstruction

The jet reconstruction procedure was described in detail in Section 4.1 and in this analysis the run 2 jet reconstruction was used. In addition to all the corrections mentioned in that section, there were some additional corrections applied.

The first is an η-ϕ dependent weighting which accounts for a large ϕ dependence to the JES. These weights were applied cluster by cluster during the reconstruction and were derived from the average response in the calorimeter as a function of η-ϕ. The jet yield as a function of ϕ is shown in Figure 6.7 after the weights were applied. This shows that the JES no longer has a large ϕ dependence and this effect has been effectively removed.

6.2.1 Fake Rejection

There is also a contribution from "fake" jets, especially at low p_{T}. This was discussed in Section 4.6.3. A procedure to remove the fake jets from the p_{T} spectrum was developed and is described here.

A way to remove fake jets is by requiring that the jet is associated with a track jet, since this is consistent with a hard particle production from the jet. The procedure looks

for tracks with $p_{\mathrm{T}} > 4$ GeV that pass standard track selections and that are associated with the jet. The sum of the p_{T} of all of the tracks associated with the jet that follow these requirements, $\sum p_{\mathrm{T}}$, is evaluated. Different cuts on this $\sum p_{\mathrm{T}}$ value are investigated as a potential fake rejection where the idea is to remove as much fakes as possible without biasing the spectrum. Therefore, the first cut where the fakes are removed is used for the cut.

First the effect of this cut on the p_{T} spectrum was investigated in Figure 6.8, where the p_{T} spectrum before any fake rejection, with fake rejection, and the jets that were rejected are shown in data for two different cuts. It can be seen here that the fakes start to dominate at less than 80 GeV, implying that even with a fake rejection, jets below this shouldn't be used in the analysis because those jets are dominated by fakes. The fake rejection is applied in both the data and MC and the efficiency as a function of $p_{\mathrm{T}}^{\mathrm{truth}}$ is shown in Figure 6.9. The fake rejection is fully efficient around 100 GeV for the 4 GeV cut and 125 GeV for the

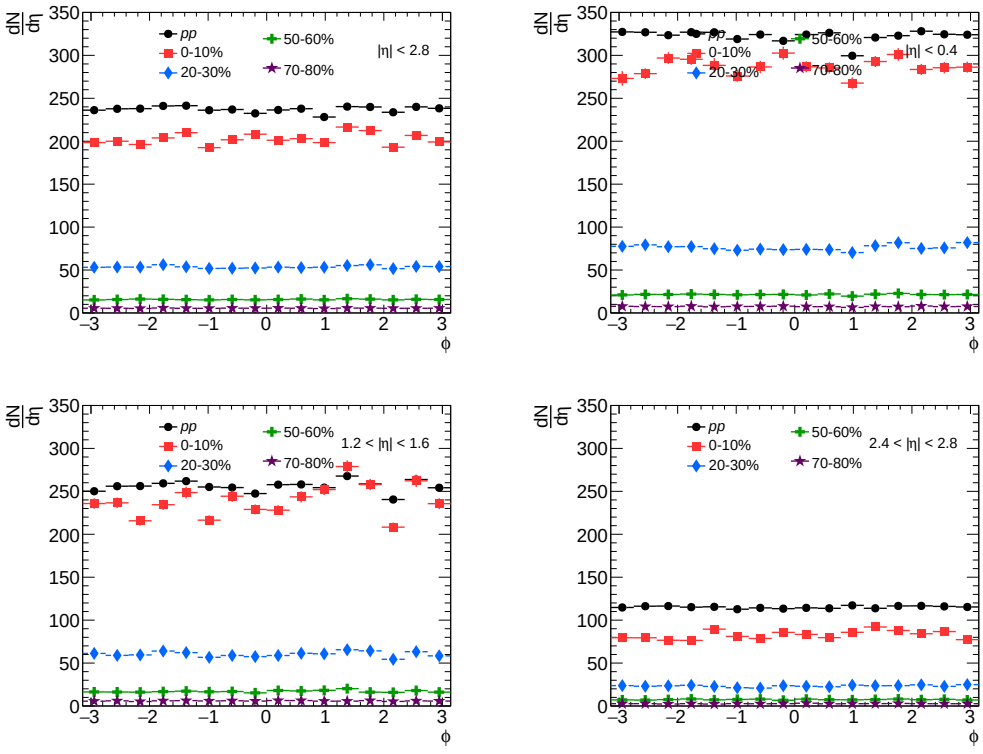

Figure 6.7: The jet yield as a function of ϕ for truth $p_{\mathrm{T}} > 50$ GeV in different η intervales with pp (black) and centrality bins in the colors.

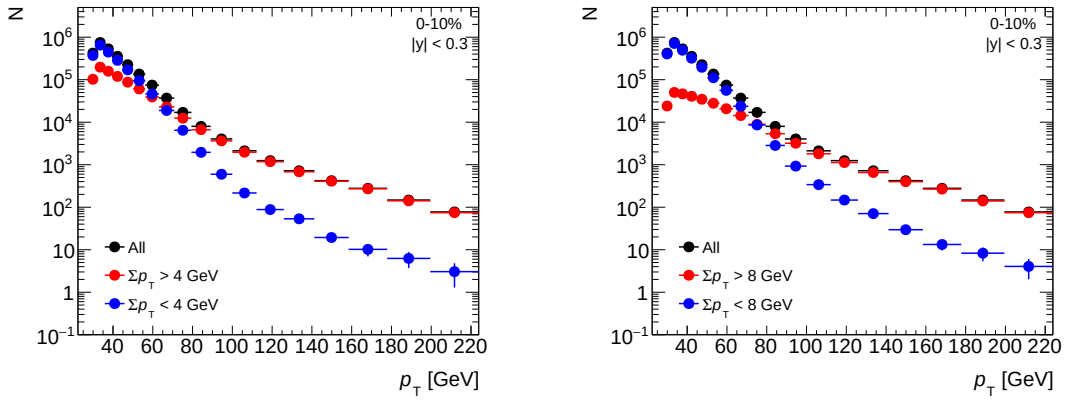

Figure 6.8: The p_{T} spectrum with no fake rejection (black), with fake rejection (red), and for jets rejected by fake rejection (blue) in central collisions with $y < 0.3$ for $\sum p_{\mathrm{T}} = 4$ GeV (left) and 8 GeV (right).

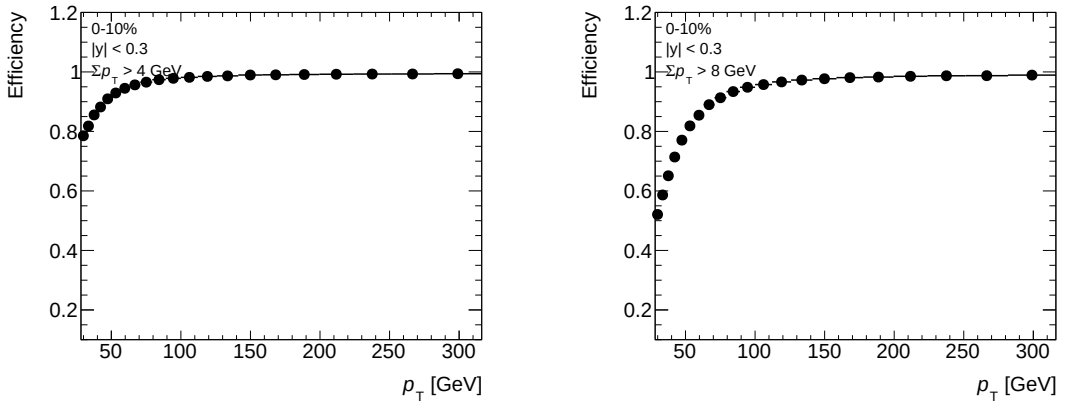

Figure 6.9: The efficiency of the fake rejection in the MC as a function of $p_{\mathrm{T}}^{\mathrm{truth}}$ in central collisions with $y < 0.3$ for $\sum p_{\mathrm{T}} = 4$ GeV (left) and 8 GeV (right).

8 GeV cut, which means that in either case an efficiency correction should be used after the cut is applied.

Determining if the fakes are effectively rejected can be done by looking at the stability of the unfolding since (as discussed in Section 4.6.3) backgrounds can distort the shape of the distributions which causes problems for unfolding. Therefore, the unfolding was investigated as a function of the number of iterations. Figures 6.10, 6.11, and 6.12 include four panels demonstrating the unfolding in central Pb+Pb collisions and $|y| < 2.8$. The first panel shows the unfolded p_{T} spectrum for different numbers of iterations, the second panel shows the refolded p_{T} spectra, the third panel shows the unfolded to truth ratio, and the

fourth panel shows the refolded to data ratio. The refolded to truth ratio shows instability in Figure 6.10, where no fake rejection has been applied. Figure 6.11 is for a fake rejection of 4 GeV and shows a slight improvement to the instability. Finally, Figure 6.12 is for a fake rejection of 8 GeV and shows the instability removed. This indicates that a fake rejection of 8 GeV is removing the fake contribution to the data, making the unfolding stable.

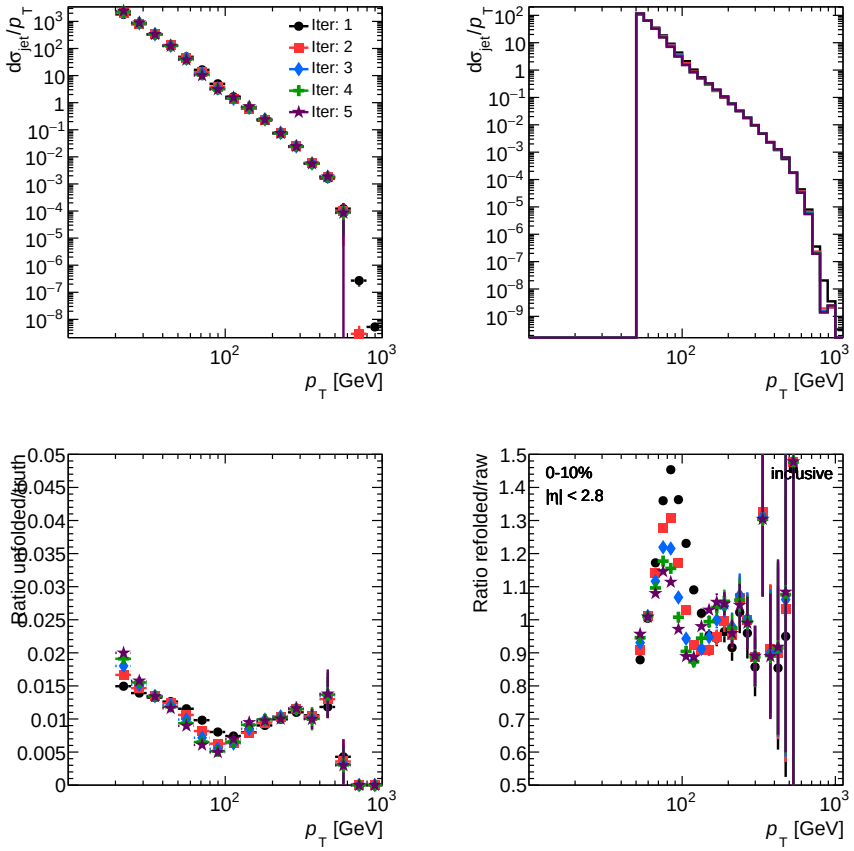

Figure 6.10: This figure is only shown to demonstrate how the fake rejection cut was determined and shows what the unfolding looks like when no fake rejection is applied. The figure is showing the unfolding results for different numbers of iterations in central Pb+Pb collisions within $|y| < 2.8$. The top left panel shows the unfolded p_{T} spectra and the top right panel shows the refolded p_{T} spectra. The bottom left panel shows the ratio of the unfolded to truth distribution and bottom right panel shows the ratio of the refolded to data distribution. The unfolding is shown to be unstable in this case.

The effect of the fake rejection can also be investigated by looking at the effect of the different cuts on the unfolded R_{AA}. This was done for different cuts between 5 and 12 GeV,

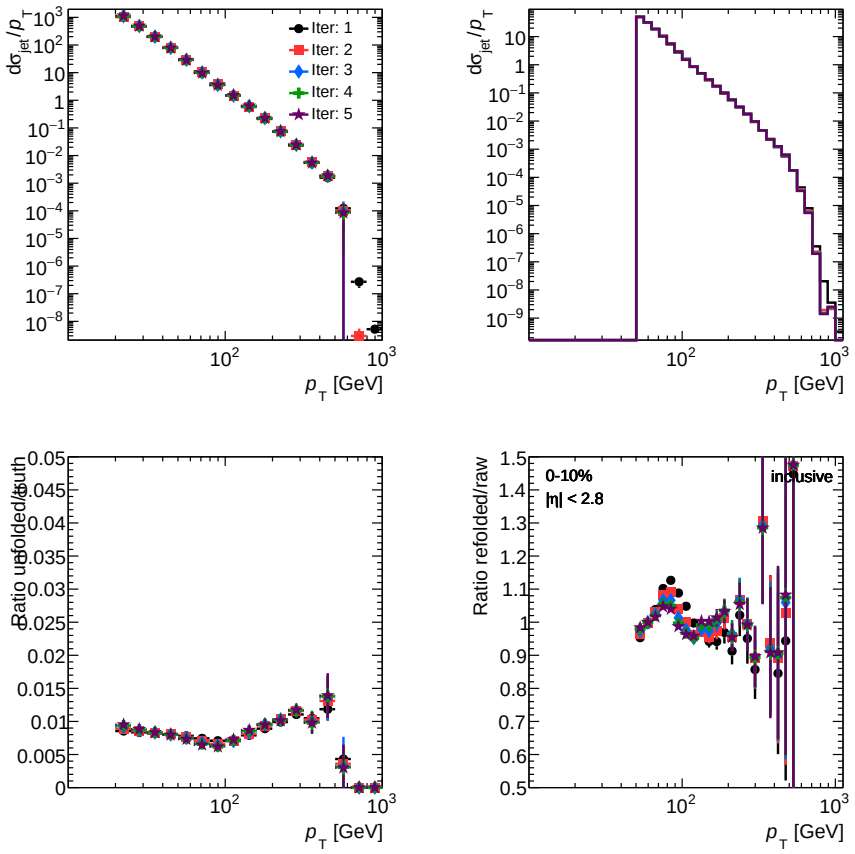

Figure 6.11: This figure is only shown to demonstrate how the fake rejection cut was determined and shows what the unfolding looks like when only a $\sum p_{\mathrm{T}} > 4$ GeV is applied. The figure is showing the unfolding results for different numbers of iterations in central Pb+Pb collisions within $|y| < 2.8$. The top left panel shows the unfolded p_{T} spectra and the top right panel shows the refolded p_{T} spectra. The bottom left panel shows the ratio of the unfolded to truth distribution and bottom right panel shows the ratio of the refolded to data distribution. The unfolding is still shown to be unstable but is an improvement from Figure 6.10.

in Figure 6.13. It can be seen in the top panel for 0–10% that the R_{AA} changes dramatically for the different cuts below ≈ 80 GeV. This indicates that the fakes are still contributing significantly in this region since the R_{AA} increases with decreasing fake rejection (which is allowing more fakes to contribute). Figure 4.23 demonstrates that fakes broaden the p_{T} distribution at low p_{T} and thus raise the number of jets at low p_{T} causing a higher R_{AA}. Above 80 GeV, the R_{AA} is unchanged with the different rejections, indicating that the fakes are not contributing significantly in this region. Therefore, the fake rejection is applied but

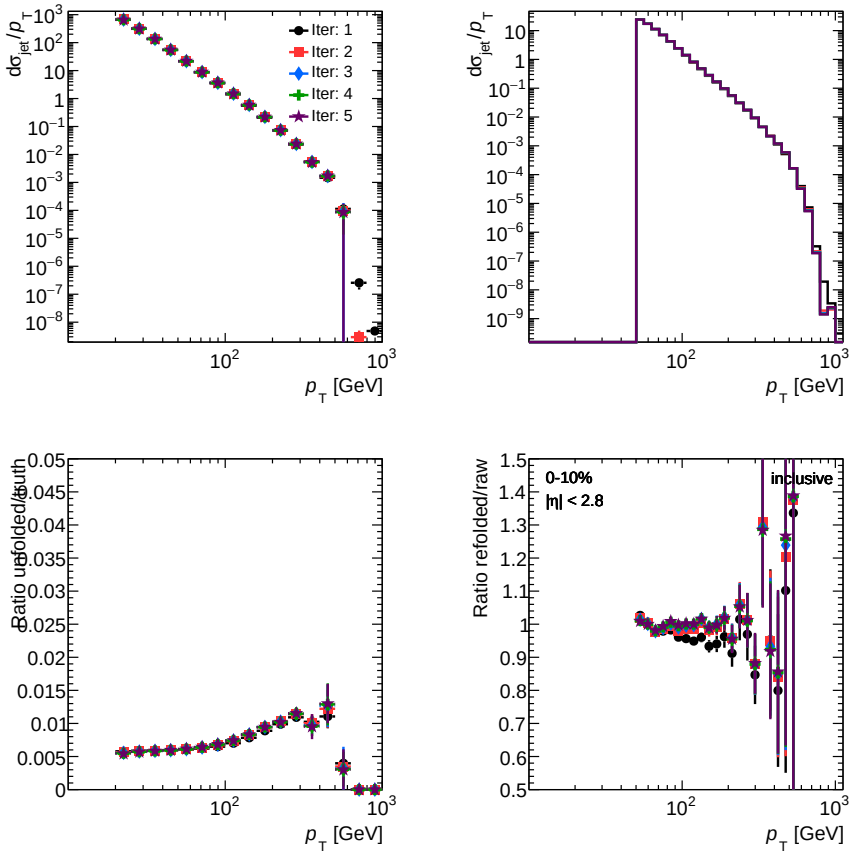

Figure 6.12: This figure is only shown to demonstrate how the fake rejection cut was determined and shows what the unfolding looks like when only a $\sum p_{\mathrm{T}} > 8$ GeV is applied. The figure is showing the unfolding results for different numbers of iterations in central Pb+Pb collisions within $|y| < 2.8$. The top left panel shows the unfolded p_{T} spectrum and the top right panel shows the refolded p_{T} spectrum. The bottom left panel shows the ratio of the unfolded to truth distribution and bottom right panel shows the ratio of the refolded to data distribution.The unfolding is shown to be stable in this case.

a cut is made at 80 GeV in the data analysis. The effect of fakes decrease as the collisions becomes less central. This is shown in the remaining figures where, for example for 40–50%, the effect is not significant and the cut can be at 40 GeV. These cuts are at the reconstructed level (before unfolding), but the unfolding needs room for bin migration (Section 4.6). Both the reconstructed and truth cuts are given in Table 6.6.

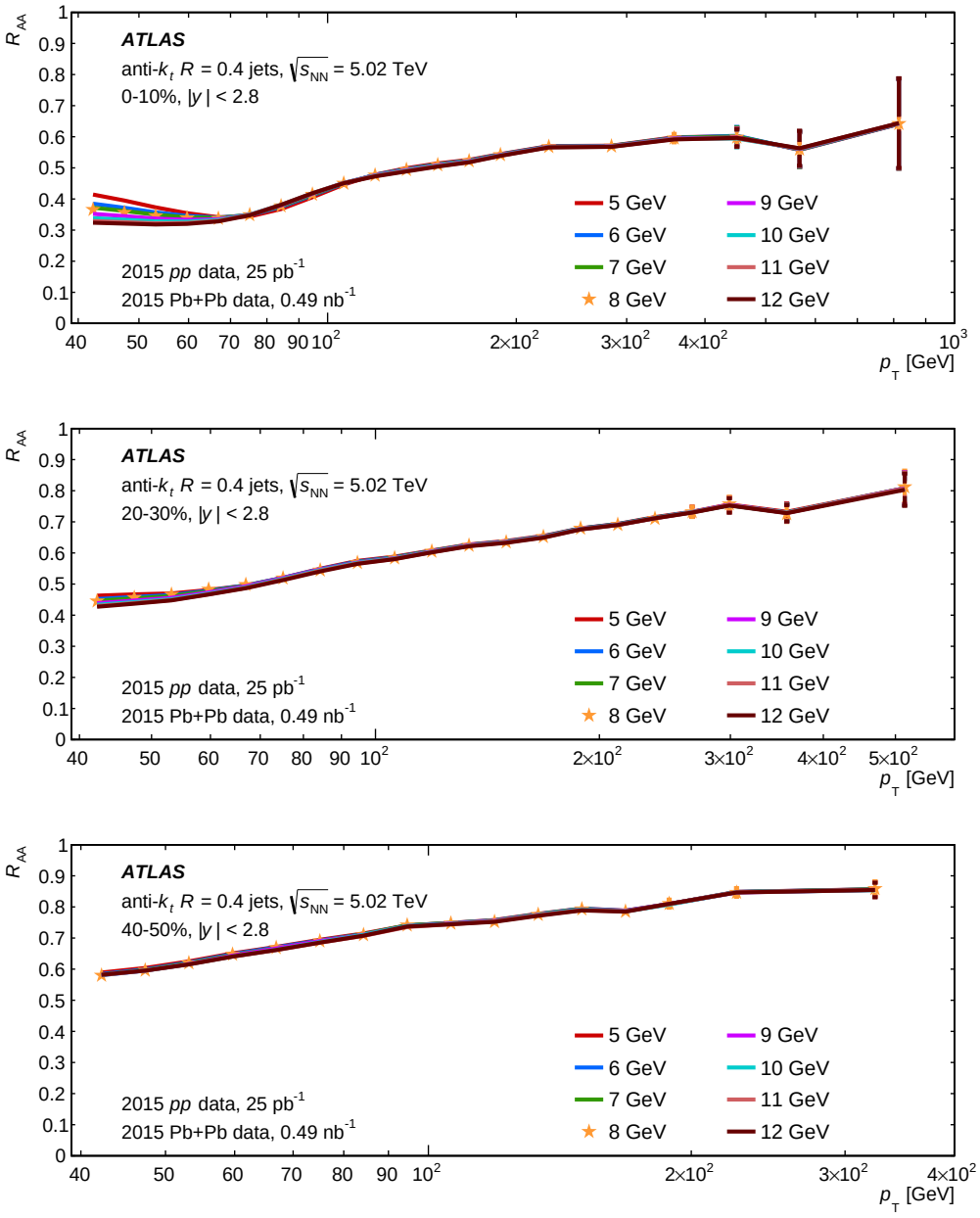

Figure 6.13: The R_{AA} as a function of p_{T} for different $\sum p_{\mathrm{T}}$ cuts (or fake rejection cuts). This is shown in 0–10% in the top panal, 20–30% in the center panel, and 50–60% in the bottom panel.

6.3 Data Analysis

The first step in the analysis is to measure the jet spectra in pp and Pb+Pb collisions in various kinematic intervals. The spectra is measured six bins of rapidity for both Pb+Pb and pp, $|y| < 0.3$, $0.3 < |y| < 0.8$, $0.8 < |y| < 1.2$, $1.2 < |y| < 1.6$, $1.6 < |y| < 2.1$, and $2.1 < |y| < 2.8$ and between 40 and 1000 GeV in jet p_{T}. The Pb+Pb jet spectra is also measured differentially in eight bins of centrality: 0-10%, 10-20%, 20-30%, 30-40%, 50-60%, 60-70%, and 70-80%. This is the raw jet spectra and any corrections are made at this level before unfolding and evaluating the ratio to obtain the final R_{AA}.

In order to validate the jets going into the analysis, the $\eta - \phi$ distributions for jets with $p_{\mathrm{T}} > 100$ GeV are checked for irregularities. This is shown in Figure 6.14 for pp and for central and peripheral collisions in Pb+Pb. There is a clear hole in the region $0 < y < 1$ and $\pi/4 < \phi < 11\pi/32$. To fix this, jets in the hole are removed in the data analysis and the remaining jets in that y region are scaled by the amount removed in ϕ, which ends up being $(2\pi/(2\pi - 3\pi/32)$. This needs to be done in both the analysis and for the reconstructed jets in the MC since the MC is overlaid with the same data. The projection of this onto the y axis is shown in Figure 6.15 for pp and various centrality bins in Pb+Pb. The rapidity distribution is shown to be smooth except for in places that are known to be transition regions in the ATLAS detector (or the holes mentioned above). Therefore, the rapidity intervals in the analysis are chosen to avoid irregularities such that the response does not dramatically change within one bin since the detector response in different regions of the calorimeter can be different. These rapidity intervals are also selected to match those used in the previous R_{AA} result in Ref. [5] such that comparisons between the two can easily be made.

6.3.1 Raw Inclusive Jet Yields

The raw p_{T} distributions before unfolding are shown in Figure 6.16 for the different rapidity intervals in pp in the left panel and central Pb+Pb in the central panel. The right panel shows all the centrality intervals in Pb+Pb but inclusive in rapidity ($|y| < 2.8$). Each centrality bin begins at a different p_{T} based on where the fake rates were found to contribute.

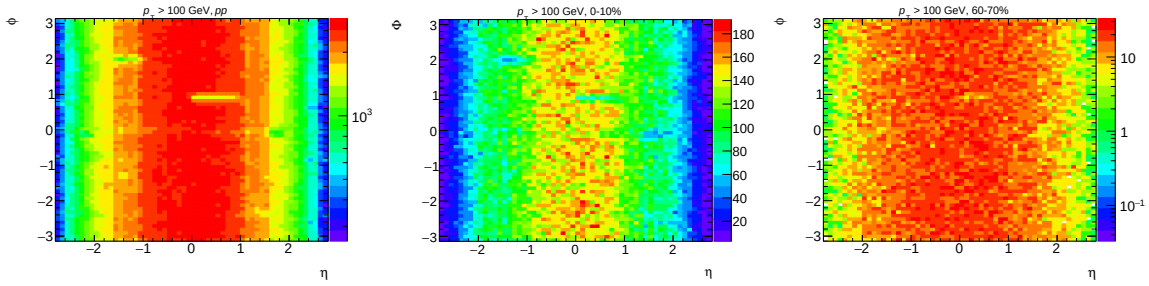

Figure 6.14: The $\eta - \phi$ distribution for $R = 0.4$ jets with $p_{\mathrm{T}} > 100$ GeVand $|y| < 2.8$ in pp data (top left), Pb+Pb data in 0-10% (center), and Pb+Pb data in 60-70% (right).

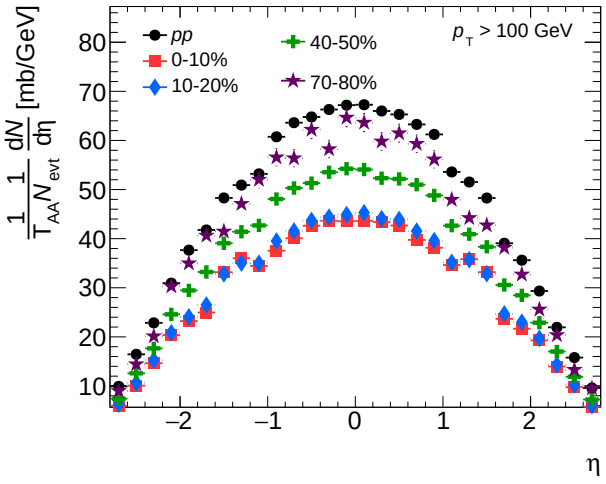

Figure 6.15: The y distribution for $R = 0.4$ jets with $p_{\mathrm{T}} > 100$ GeVin pp and different centrality intervals in Pb+Pb.

These values are given in Table 6.6. Here the pp data, also inclusive in rapidity, is overlaid with each centrality bin in black lines for comparison. The y dependence is as expected in that the distributions are steeper in the more forward rapidity intervals. In the central Pb+Pb bins a suppression can already be observed when comparing the pp. Appendix E provides the rapidity dependence for additional centrality bins in Pb+Pb.

Table 6.6: The various p_{T} cuts made before unfolding (reconstructed p_{T}) and after unfolding (unfolded p_{T}) for each centrality bin.

Centrality [%]	Reconstructed p_{T} GeV	Unfolded p_{T} GeV
0–10	79	100
10–20	79	100
20–30	60	79
30–40	60	79
40–50	40	50
50–60	40	50
60–70	40	50
70–80	40	50

6.3.1.1 MC Weighting

The Pb+Pb MC needs to be weighted by the $\Sigma E_{\mathrm{T}}^{\mathrm{FCal}}$ distribution in the data before it can be used for the response matrix when unfolding because of the different total energy triggers in the MC overlay. The trigger boundaries can be seen in MC distribution before weighting in Figure 6.17. The ratio of the distribution in the data (in red) to the MC (black) is shown on the right panel and is used to weight to the MC. The weighted version of the MC is shown in blue and is in agreement with the data which verifies that the weighting is valid.

The Pb+Pb MC needs an additional re-weighting in order to get the correct `POWHEG`

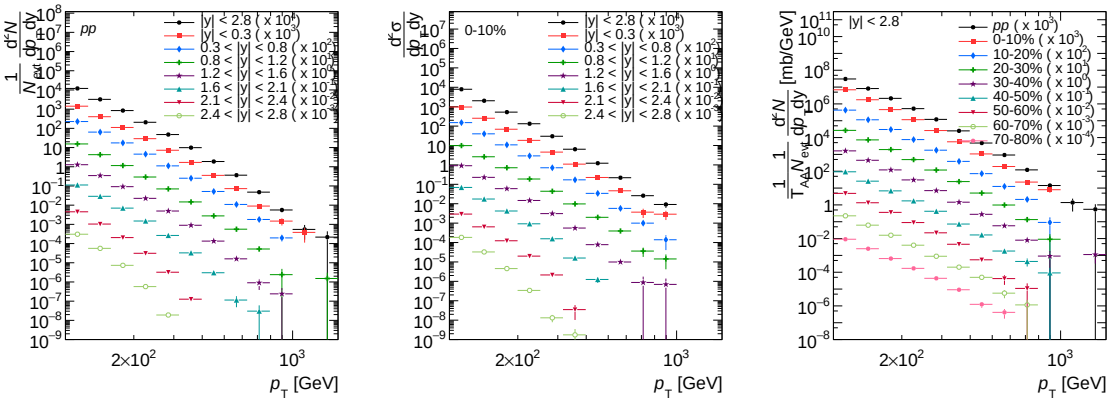

Figure 6.16: The raw p_{T} distributions for jets with $p_{\mathrm{T}} > 40$ GeV in different rapidity bins for pp on the left and central Pb+Pb in the center. The raw p_{T} distribution for jets with $p_{\mathrm{T}} > 40$ GeV for all centrality classes in Pb+Pb within $|y| < 2.8$ is shown on the right (the pp distribution is overlaid in the black lines for comparison).

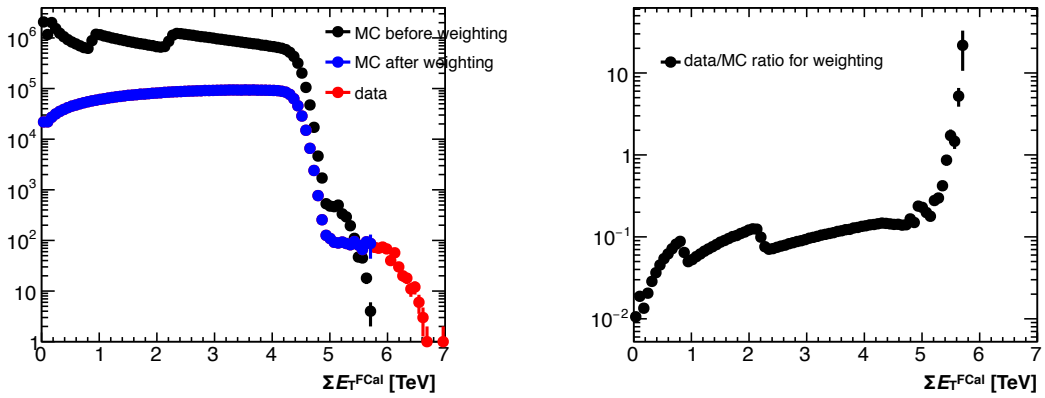

Figure 6.17: The left panel shows $\Sigma E_{\mathrm{T}}^{\mathrm{FCal}}$ distributions in Pb+Pb MC (black) and data (red). The right panel is the ratio of the data to the MC. This ratio is then applied to the MC and the result is shown in blue on the left.

weights such that the underlying p_{T} distribution in the MC represents a cross section. The correct weights can be obtained from the *pp* MC. The weighting is performed by taking the ratio of the *pp* to the Pb+Pb MC is each centrality bin, as shown in the left panel of Figure 6.18 for central collions and the middle panel for peripheral collisions. The spikes in the ratio are the incorrect weights in `POWHEG`. The average ratio is evaluated and plotted as a function of centrality in the right panel. This weight is applied jet-by-jet based on the p_{T} of the jet in order to correct for the difference in the shape between the Pb+Pb and *pp* MC, as well as rescale the Pb+Pb MC appropriately.

Figure 6.19 shows a comparison between the Pb+Pb data and truth MC on the top panel and the ratio of the two on the bottom panel for different centrality bins in the panels. Figure 6.20 shows a comparison between the Pb+Pb data and reconstructed MC on the top panel and the ratio of the two on the bottom panel for different centrality bins in the panels.

6.3.2 Raw R_{AA}

The raw (before unfolding) Pb+Pb and *pp* spectra were used to evaluate the R_{AA} before unfolding, which is shown in Figure 6.21 for different centrality bins. There is a clear suppression seen in each centrality bin, with the largest suppression in the most central bin.

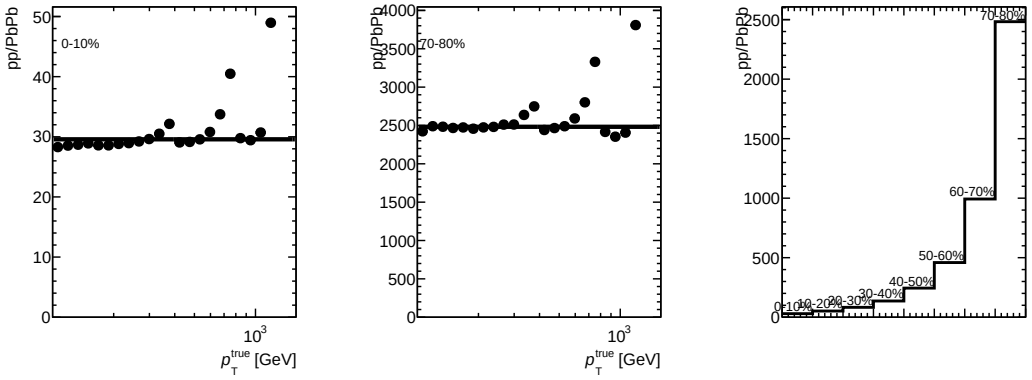

Figure 6.18: The left panel shows the ratio of the pp to the Pb+Pb MC as a function of $p_{\mathrm{T}}^{\mathrm{truth}}$ in the 0-10% interval. The middle panel shows the same thing but for the 70-80% interval. The right panel shows the average ratio as a function of centrality, which is applied to the Pb+b MC to correct for the `POWHEG` weights.

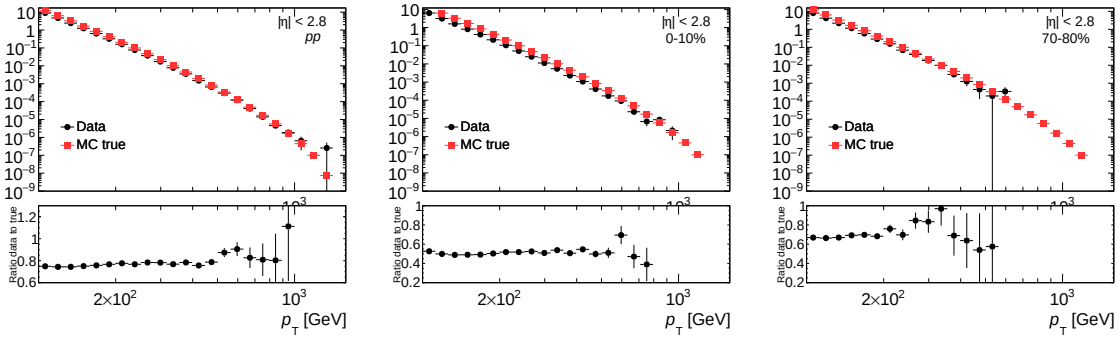

Figure 6.19: The p_{T} distributions (before unfolding) for jets with $p_{\mathrm{T}} > 100$ GeV and $|y| < 2.8$ in data (black) and MC truth (red) in pp (left) and the centrality bins in Pb+Pb (other panels).

The R_{AA} also has a dependence on the jet p_{T}, which implies that the pp distributions are steeper than the Pb+Pb distributions.

6.3.3 Unfolding

The jet yields and cross sections are unfolded using 1D Bayesian unfolding [219] as discussed in Section 4.6 to account for bin migration due the JER and a residual JES. The cross section is unfolded in pp using a response generated from the pp MC in the six rapidity bins. The

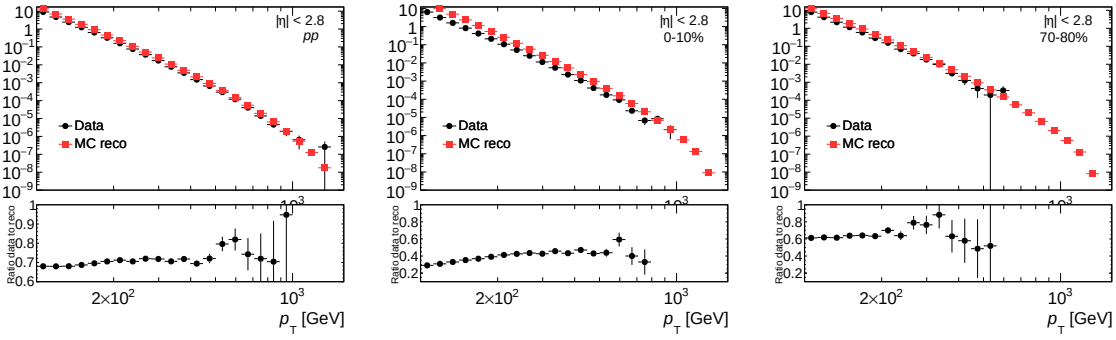

Figure 6.20: The p_{T} distributions for jets (before unfolding) with $p_{\mathrm{T}} > 100$ GeV and $|y| < 2.8$ in data (black) and reconstructed MC (red) in pp (left) and the centrality bins in Pb+Pb (other panels).

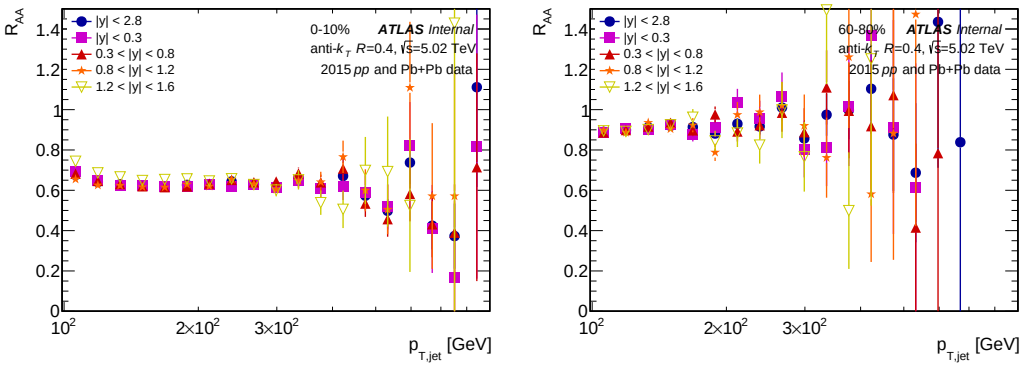

Figure 6.21: The raw (before unfolding) R_{AA} as a function of p_{T} for jets with $p_{\mathrm{T}} > 100$ GeV in central and peripheral collisions in the two panels and different rapidity intervals in the colored points.

jet yield in Pb+Pb is unfolded in the eight bins of centrality and the six rapidity intervals using a response generated from the Pb+Pb MC.

6.3.3.1 Response

The response is generated by matching truth jets to reconstructed jets in the MC within a $\Delta R < 0.2$. The truth jets are selected to be above 25 GeV and the reconstructed jets have different p_{T} cuts depending on where they are cut in the data and listed in Table 6.6. Each rapidity and centrality bin in the analysis get it's own response matrix. Some examples of

the response matrix for pp collisions and central and peripheral Pb+Pb collisions are shown in Figure 6.22.

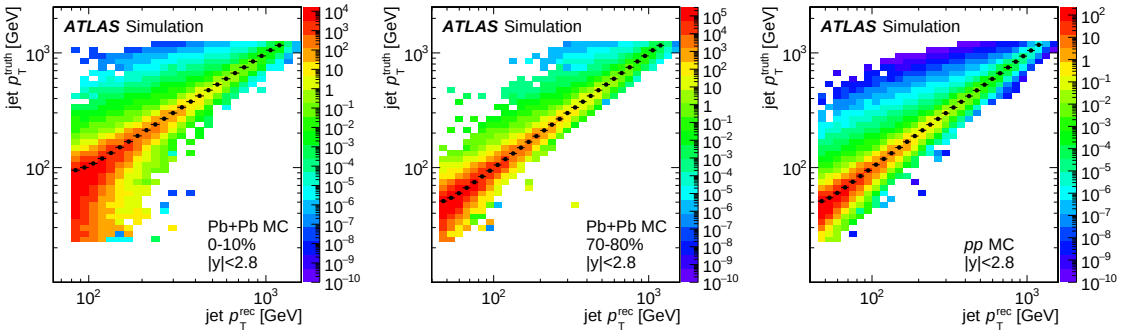

Figure 6.22: The response matrixes ($p_{\mathrm{T}}^{\mathrm{truth}}$ vs. $p_{\mathrm{T}}^{\mathrm{reco}}$) generated from the MC in central Pb+Pb (left), peripheral Pb+Pb (middle), and pp collisions (right).

6.3.3.2 Reweight Prior

The response matrixes are reweighted before unfolding to better represent the data. This reweighting is applied to the prior (or truth distribution) but the effect is to redistribute counts in the entire response. Reweighting the prior to be closer to the data allows for the unfolding to converge more quickly when iterating. A faster convergence can reduce the statistical uncertainties, as discussed in Section 4.6.1. The reweighting used in this analysis is taken from the ratio of the reconstructed data to the reconstructed MC. This ratio is taken as a function of the p_{T} and is shown in Figure 6.23 for pp and central Pb+Pb collisions. This ratio was fit with a linear function and the parameters (slope and offset) of the fits are saved for each centrality and rapidity interval. These parameters are shown in Figure 6.24. As the respones matrix is filled in the analysis, the truth p_{T} of each jet is used to calculate the weight from these parameters and the weight is then applied to the response. This reweighted version of the response is the response used to unfold the nominal result. The unfolded result with the reweighted response is compared to the unfolded result with the unweighted response in Figure 6.25 as a function of iterations. The result is shown to converge after 2–3 iterations and the difference between the two results is within 2%. This confirms the choice of the number of iterations at 3 and this difference is taken as a systematic uncertainty on the final result.

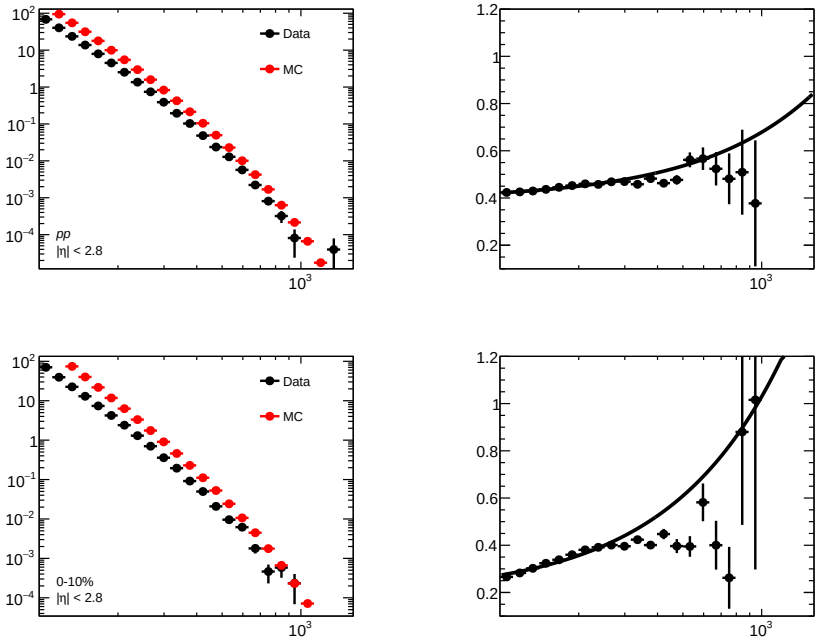

Figure 6.23: The left panel shows the overlay and the right panel shows the ratio of Pb+Pb data to MC as a function of p_{T} in pp (top) and 0-10% Pb+Pb (bottom). The ratio is fitted with a linear function.

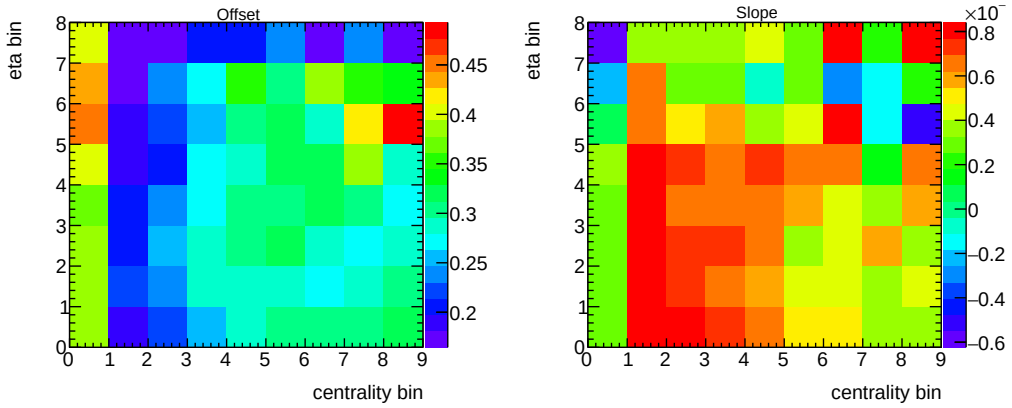

Figure 6.24: The left panel shows the values of the offset in the linear fit of the data/MC ratios in each y and centrality bin in the analysis. The first bin in y, $|y| < 2.8$ is included. The first bin on the centrality axis is pp collisions and then it increases in 8 bins of 10% centrality. The right panel is the same thing but for the slope from the fit.

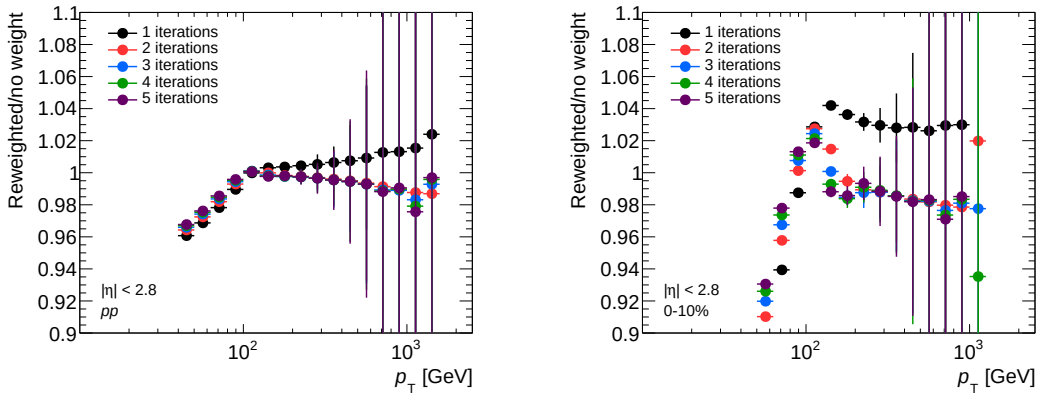

Figure 6.25: The ratio of the unfolded result with and without reweighting as a function of number of iterations for *pp* on the left and 0–10% Pb+Pb on the right.

6.3.3.3 MC Closure

The closure in the MC was investigated by splitting the MC in half and using one half as the response and the other half as the "data", as described in Section 5.4.2. This is shown in Figures 6.26– 6.28, which are similar figures as in Figure 6.12. The MC closure is in the bottom left plot which is the ratio of the unfolded truth distribution to the original truth from the MC. This ratio is shown to be unity within statistical fluctuations and is stable with the number of iterations for the bins shown. Additional centralities are shown in Appendix E.

6.3.3.4 Stability with Iterations

The stability with the number of iterations was investigated in the unfolded data by unfolding for different number of iterations and evaluating the ratio of each successive iteration to the result at 3 iterations. This is shown in Figure 6.29 for central Pb+Pb and *pp* collisions. The result is shown to be stable with the number of iterations after 2-3 iterations to within 3%. This set the number of iterations at 3.

6.3.3.5 Unfolding Summary

Figure 6.30– 6.32 show a summary of the unfolding. The top left panel shows the components of the response, including the reconstructed MC, the truth MC that match to the

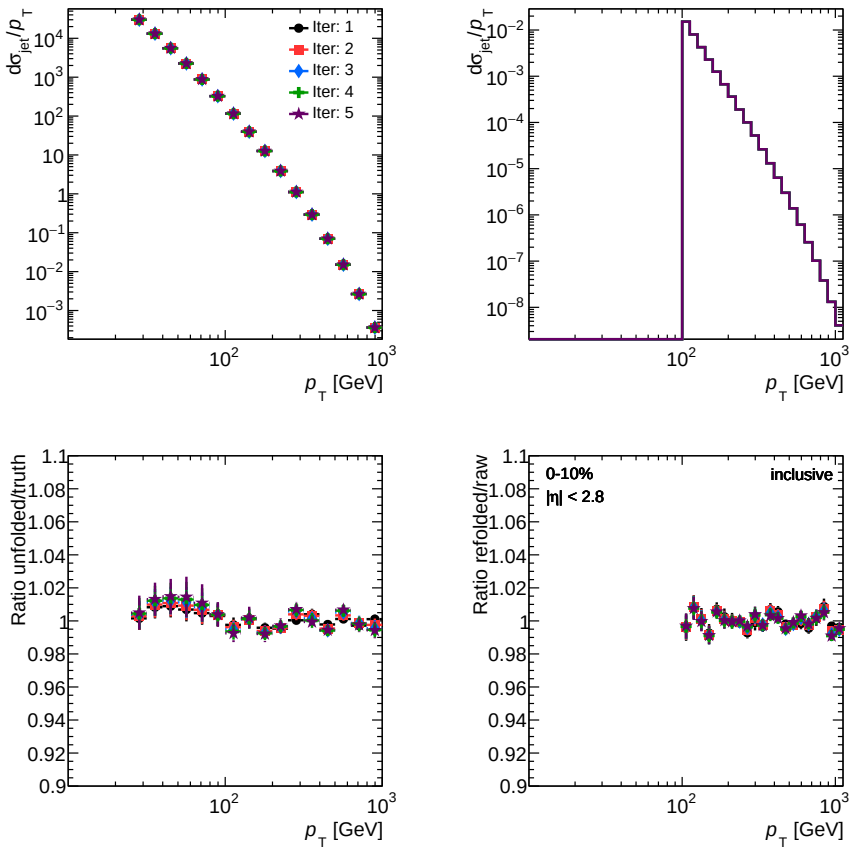

Figure 6.26: Unfolding results for the MC closure test for different numbers of iterations in central Pb+Pb collisions within $|y| < 2.8$. The top left panel shows the unfolded p_{T} spectra and the top right panel shows the refolded p_{T} spectra. The bottom left panel shows the ratio of the unfolded truth to truth distribution (the MC closure) and bottom right panel shows the ratio of the refolded to data distribution.

reconstructed, the full truth spectrum, and the measured reconstructed data. The top right panel shows the 2D response. The bottom left panel shows full truth distribution and the reconstructed data again along with the unfolded data and the refolded data. These distributions are the spectra that go into making the bottom right panel figure which shows details of the unfolding.

The first distribution is the unfolded to raw ratio which is the distribution in the data before and after unfolding. This shows the effect of unfolding which is to lower the distribution, especially at low p_{T} values. This makes sense because the JER has the largest effect on the unfolding (Figure 4.9), especially at low p_{T}. The effect of the JER on the p_{T}

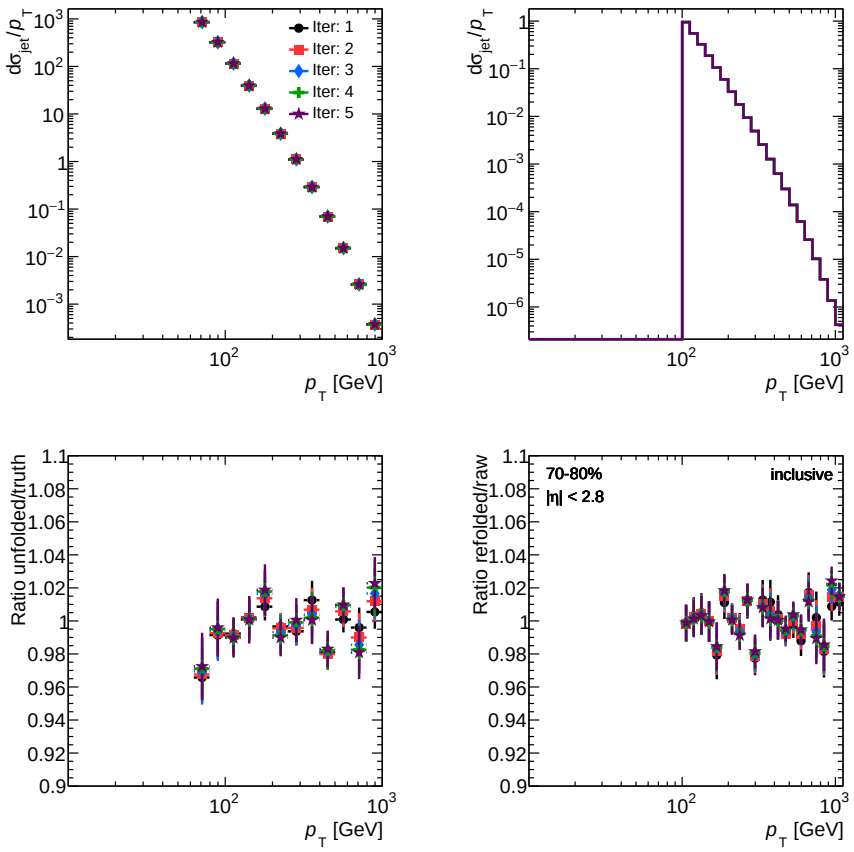

Figure 6.27: Unfolding results for the MC closure test for different numbers of iterations in peripheral Pb+Pb collisions within $|y| < 2.8$. The top left panel shows the unfolded p_{T} spectra and the top right panel shows the refolded p_{T} spectra. The bottom left panel shows the ratio of the unfolded truth to truth distribution (the MC closure) and bottom right panel shows the ratio of the refolded to data distribution.

spectrum is demonstrated in a schematic in Figure 6.33, where the JER originally pushed jets out in p_{T} (blue to red) such that the unfolding pushes jets back to lower p_{T} (green line). This effect is shown to be larger at lower p_{T}. When the Pb+Pb results in Figure 6.30 are taken with the *pp* results in Figure 6.32, the overall effect on the unfolded R_{AA} can be determined. It can be seen that the effect of unfolding in *pp* is much less drastic than in Pb+Pb in the unfolded/raw ratios. Therefore, the Pb+Pb spectrum gets shifted down in p_{T} significantly more than the *pp* spectrum during the unfolding as shown in top panels in Figure 6.34 where the left is before unfolding and the right is after. The ratio of the two, or the R_{AA}, is shown on the bottom panels and the effect of unfolding is to decrease to R_{AA},

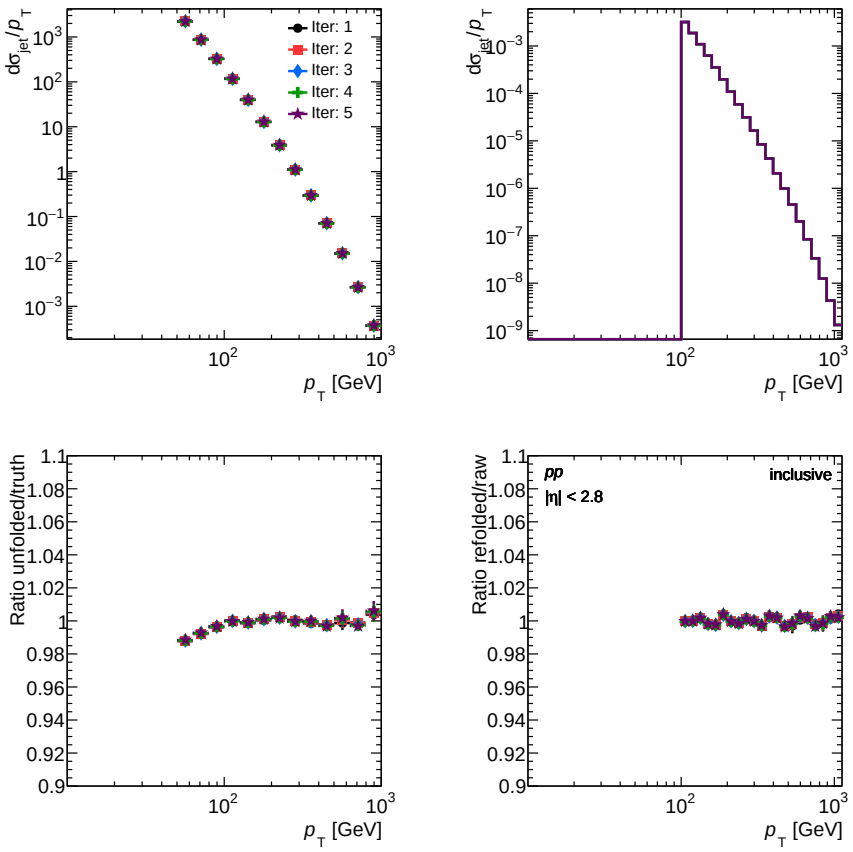

Figure 6.28: Unfolding results for the MC closure test for different numbers of iterations in pp collisions within $|y| < 2.8$. The top left panel shows the unfolded p_{T} spectra and the top right panel shows the refolded p_{T} spectra. The bottom left panel shows the ratio of the unfolded truth to truth distribution (the MC closure) and bottom right panel shows the ratio of the refolded to data distribution.

especially at lower p_{T}.

The second ratio is the bin-by-bin correction factors which are the factors that would be applied if the unfolding was done by just using the ratio of the reconstructed to truth distribution and applying this to the data. The factor is evaluated by taking the ratio of the truth to the reconstructed MC. This can be compared to the effect of unfolding to see how much non-linear bin migration exists. The pp unfolding is closer to the bin-by-bin unfolding than the Pb+Pb which makes sense since the pp data is much closer to the MC than the Pb+Pb data.

The third ratio is a check that the unfolding is working through refolding (described in

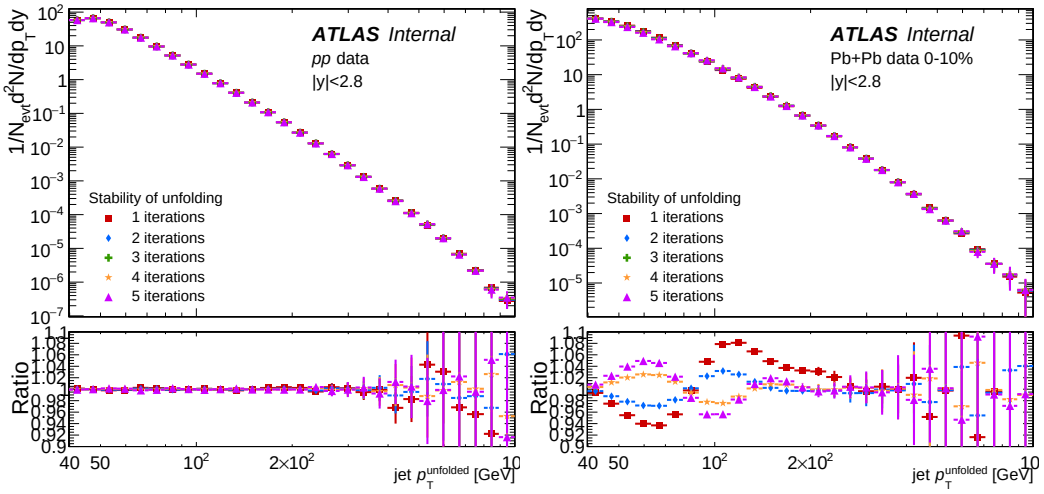

Figure 6.29: The unfolded spectra for different number of iterations is shown on the top panel of each figure. The bottom panels show the stability of the unfolding through the ratio of the unfolded spectra using a given number of iterations with respect to 3 iterations for central Pb+Pb collisions (right) and *pp* collisions (left).

Section 5.4.5), which is evaluated by taking the ratio of the refolded result to the original data. The refolding should return the original data so this ratio should be close to unity. It can be seen that the refolding ratio is approximately unity in Pb+Pb and *pp* collisions which gives confidence that the unfolding is working.

6.4 Systematic Uncertainties

The systematic uncertainties in the measurement are due to the following sources:

1. Jet energy scale (JES)
2. Jet energy resolution (JER)
3. Unfolding: choice of Bayesian prior
4. $\langle T_{\mathrm{AA}} \rangle$ and luminosity

The JES and JER uncertainties were evaluated by rebuilding the response matrix with a systematically varied relationship between the truth and reconstructed jet kinematics using

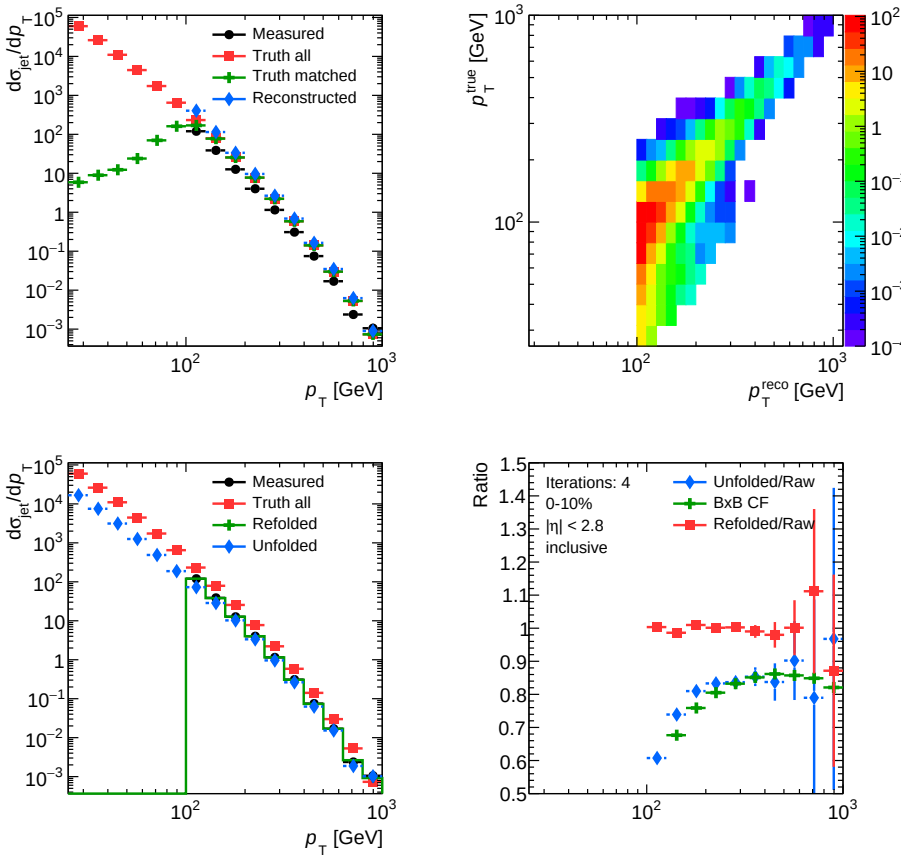

Figure 6.30: Unfolding results summary plot for central Pb+Pb collisions in $|y| < 2.8$. The top left panel shows the reconstructed MC (blue), the reconstructed data (black), the matched truth MC (green), and the full truth MC distribution (blue). The top right panel shows the 2D response ($p_{\mathrm{T}}^{\mathrm{truth}}$ vs. $p_{\mathrm{T}}^{\mathrm{reco}}$). The bottom left panel shows the reconstructed data (black), the refolded data (green), the full truth MC (red), and the unfolded data (blue). The bottom right panel shows the effect of unfolding through the unfolded/data ratio (blue), the bin-by-bin correction factors through the ratio of the truth MC to the reconstructed MC (green), and the refolded to raw ratio (red).

standard tools. The difference between the data unfolded with the new response and the nominal result is the systematic uncertainty on the p_{T} spectra. These uncertainties need to be propagated through the R_{AA}.

All the uncertainties, except for ones that just effect the normalization are broken up again into two categories. The first case is uncertainties that are common between the numerator and denominator and thus are correlated uncertainties in pp and Pb+Pb. For this case the uncertainty propagation to the R_{AA} is done in the following way, where $R =$

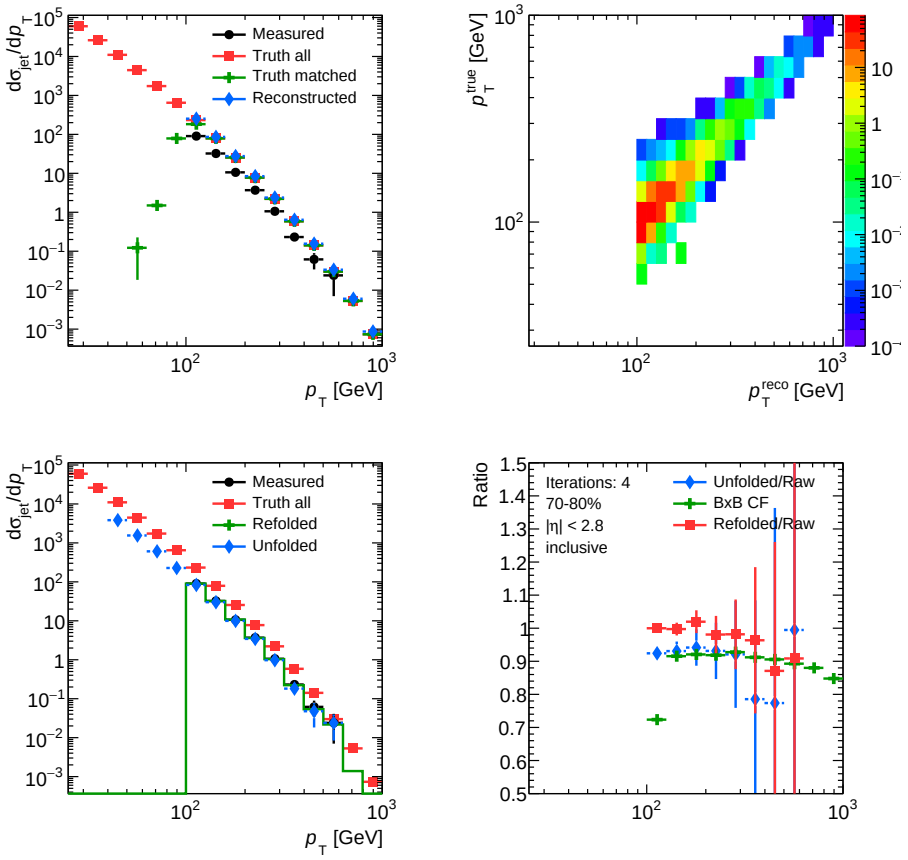

Figure 6.31: Unfolding results summary plot for peripheral Pb+Pb collisions in $|y| < 2.8$. The top left panel shows the reconstructed MC (blue), the reconstructed data (black), the matched truth MC (green), and the full truth MC distribution (blue). The top right panel shows the 2D response ($p_{\mathrm{T}}^{\mathrm{truth}}$ vs. $p_{\mathrm{T}}^{\mathrm{reco}}$). The bottom left panel shows the reconstructed data (black), the refolded data (green), the full truth MC (red), and the unfolded data (blue). The bottom right panel shows the effect of unfolding through the unfolded/data ratio (blue), the bin-by-bin correction factors through the ratio of the truth MC to the reconstructed MC (green), and the refolded to raw ratio (red).

A/B:

$$\delta \equiv \frac{A \pm \delta A}{B \pm \delta B} - \frac{A}{B}\,. \tag{6.1}$$

The uncertainties that are not common between the numerator and denominator are uncorrelated between pp and Pb+Pb and the uncertainty is propagated by

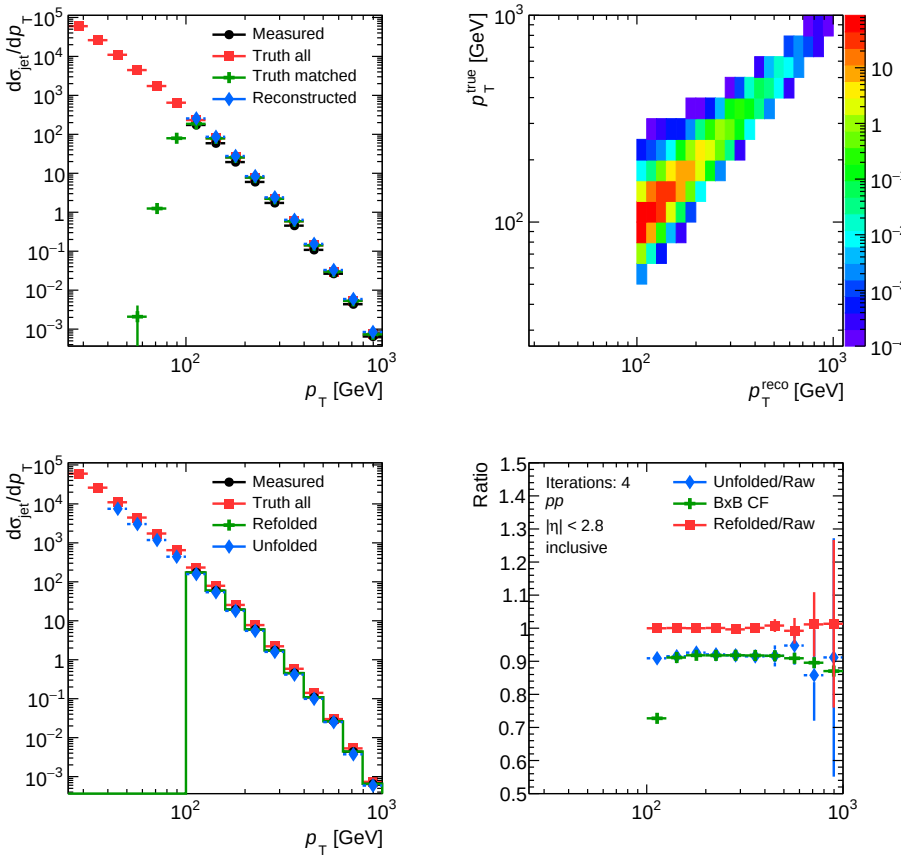

Figure 6.32: Unfolding results summary plot for pp collisions in $|y| < 2.8$. The top left panel shows the reconstructed MC (blue), the reconstructed data (black), the matched truth MC (green), and the full truth MC distribution (blue). The top right panel shows the 2D response ($p_{\mathrm{T}}^{\mathrm{truth}}$ vs. $p_{\mathrm{T}}^{\mathrm{reco}}$). The bottom left panel shows the reconstructed data (black), the refolded data (green), the full truth MC (red), and the unfolded data (blue). The bottom right panel shows the effect of unfolding through the unfolded/data ratio (blue), the bin-by-bin correction factors through the ratio of the truth MC to the reconstructed MC (green), and the refolded to raw ratio (red).

$$\delta \equiv \frac{A}{B}\sqrt{\left(\frac{\delta A}{A}\right)^2 + \left(\frac{\delta B}{B}\right)^2}. \tag{6.2}$$

After taking the ratio, the uncertainties are broken down again into three categories. The first was already mentioned (overall normalization) and are typically represented by one band on the figure at $R_{\mathrm{AA}} = 1$ since they are common to every point. These uncertainties are fully correlated such that the points move up and down together within the uncertainties.

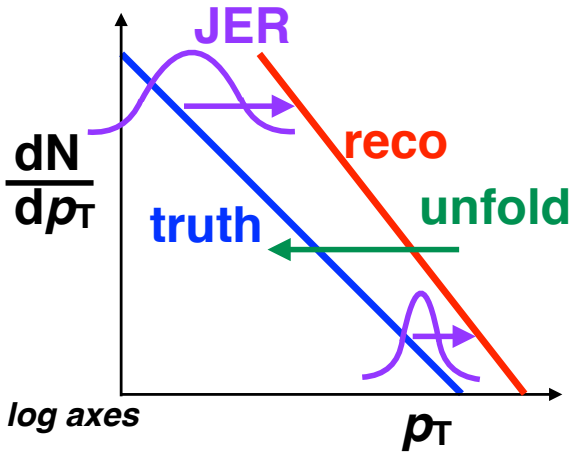

Figure 6.33: A schematic showing the effect of the JER (purple gaussians and arrows) on the "truth" spectrum (blue) to make the reconstructed data (red). The effect of the unfolding (green) to reverse the effect of the JER is also shown.

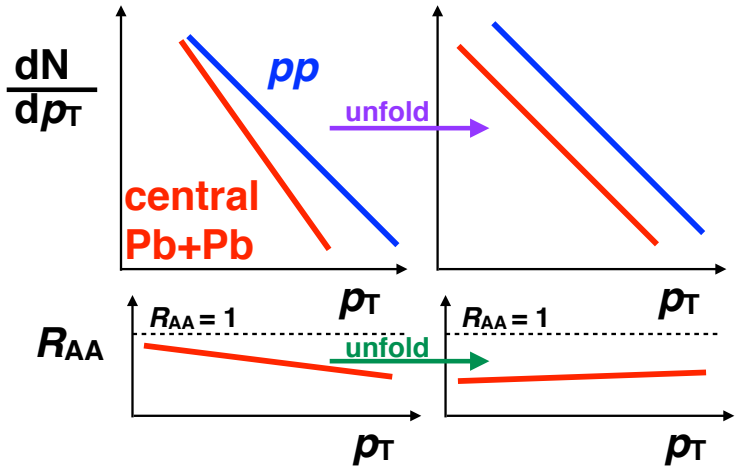

Figure 6.34: A schematic showing the effect of unfolding (purple) on the p_{T} spectrums in Pb+Pb (red) and pp (blue) on the top panels (before unfolding is on the left and after is on the right). The effect of unfolding (green) on the R_{AA} (red) is also shown on the bottom panels.

The second is the uncertainties that are correlated in p_{T} or y. These uncertainties are combined to be one correlated uncertainty and are indicated by shaded boxes on the R_{AA}

figures. The third is uncertainties that are uncorrelated in p_{T} and y. These are separately combined into one uncorrelated uncertainty and are indicated by open boxes on the R_{AA} figures.

6.4.1 Jet Energy Scale

The standard JES uncertainties are very similar to the ones described in Section 5.5.1, except they were derived in run 2 with some slight differences. First the standard baseline uncertainties came from 2015 pp data at 13 TeV [235]. All the JES uncertainties (except for the Pb+Pb specific ones discussed next) were found to be correlated between Pb+Pb and pp and the break-down on pp collisions is shown in Fig. 6.35.

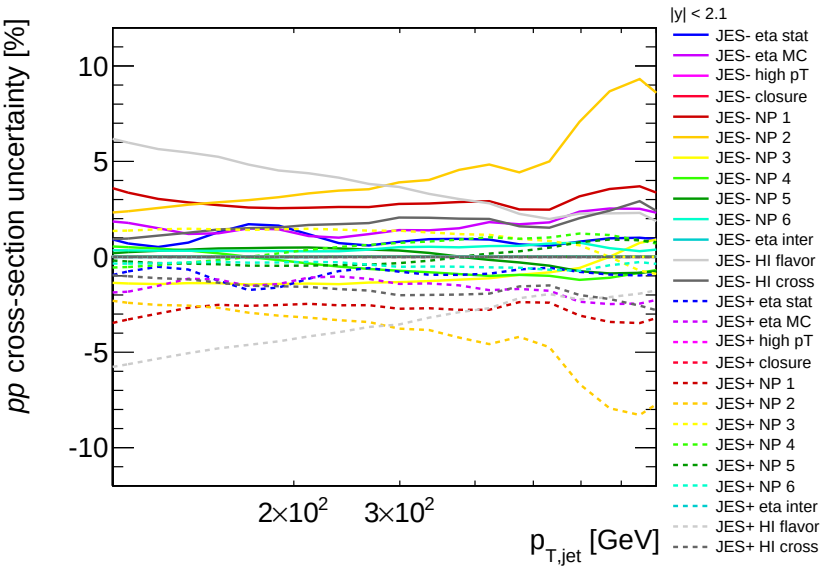

Figure 6.35: A break down of different systematic uncertainties due to JES on the pp cross-section.

This analysis also has a JES uncertainty due to quenching but does not have a data period uncertainty since the Pb+Pb and pp data were taken during the same data-taking period.

The uncertainty due to quenching was derived in a different way for run 2. This procedure uses the r_{trk} which is the ratio of the p_{T} of the calorimeter jets to the $\sum p_{\mathrm{T}}^{\mathrm{trk}}$ of track jets. The systematic uncertainty was evaluated through the double ratio

$$\sigma = \frac{(r_{\rm trk}^{\rm data}/r_{\rm trk}^{\rm MC})|_{\rm Pb+Pb}}{r_{\rm trk}^{\rm data}/(r_{\rm trk}^{\rm MC})|_{pp}} \ . \tag{6.3}$$

The $r_{\rm trk}$ distributions in data and MC for pp and central Pb+Pb collisions in two panels on the left and the center of Figure 6.36. The ratio of the average $r_{\rm trk}$ as a function of $\sum p_{\rm T}^{\rm trk}$ is shown in the right panels. The average of these ratios is calculated and then used to evaluated the double ratio of each centrality bin to the average ratio in pp. This is shown in Figure 6.37. This ends up being a measure of the difference in the FFs in Pb+Pb and pp which represents the difference in the JES in Pb+Pb and pp. It is seen that the maximum value is 0.5% in forward rapidity and that it decreases with centrality. The following parameterization was chosen for the uncertainty

$$\delta = \delta_{\rm cent}\frac{60 - {\rm C}}{60} \tag{6.4}$$

where $\delta_0 = 0.5\%$. This uncertaintiy is uncorrelated between Pb+Pb and pp collisions.

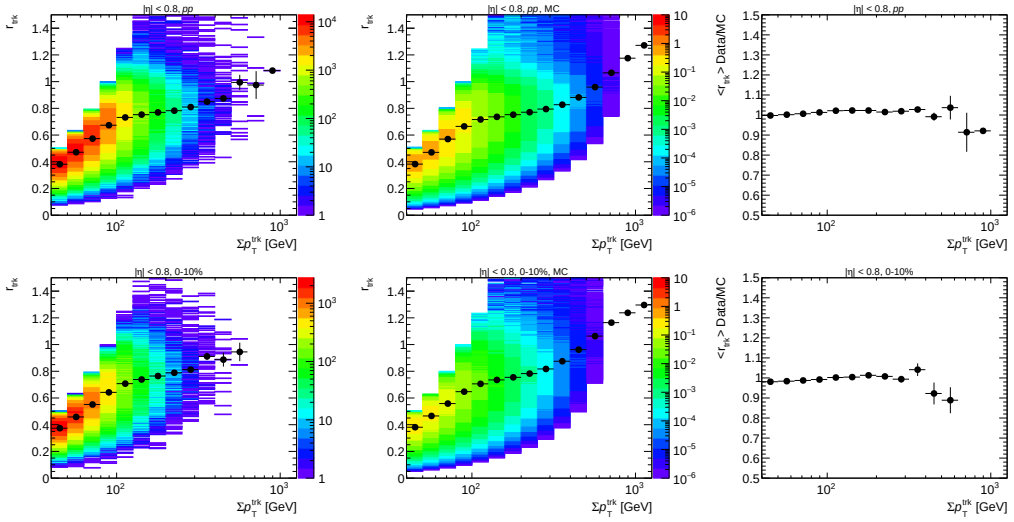

Figure 6.36: The 2D distribution (and average) $r_{\rm trk}$ as a function of $\sum p_{\rm T}^{\rm trk}$ in data (left) and MC (middle) are shown for pp (top) and central Pb+Pb (bottom) for $|\eta| < 0.8$. The ratio of $\langle r_{\rm trk}\rangle$ in the data to MC is shown in right panels.

For each component of the JES uncertainty a new response matrix is generated with the $p_{\rm T}^{\rm reco}$ shifted both up and down by each JES uncertainty in the following way:

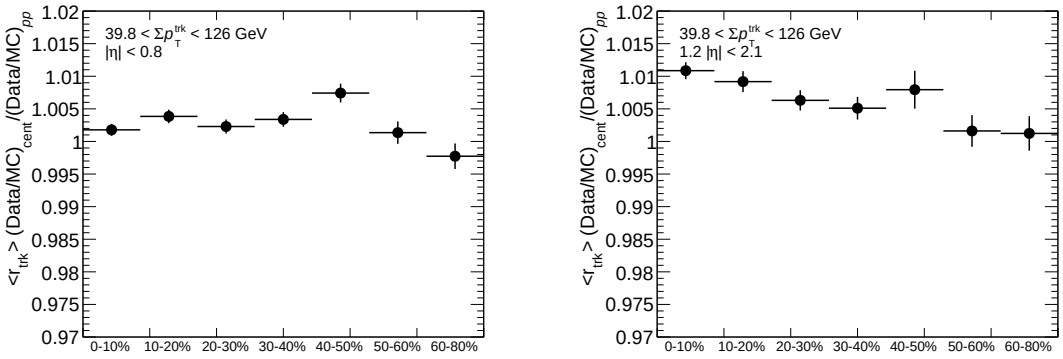

Figure 6.37: The data-to-MC r_{trk} double ratio between Pb+Pb and pp as a function of centrality for $|\eta| < 0.8$ (left) and $1.2 < |\eta| < 2.1$ (right).

$$p_{\mathrm{T}}^{\star,\mathrm{reco}} = p_{\mathrm{T}}^{\mathrm{reco}}(1 \pm U^{\mathrm{JES}}(p_{\mathrm{T}}^{\mathrm{truth}}, \eta)). \tag{6.5}$$

This new response matrix is then used to unfold the data and this unfolded result is compared to the nominal result where the difference is taken as the uncertainty.

6.4.2 Jet Energy Resolution

The uncertainties due to the JER are also similar to what was described in Section 5.5.2 except using run 2 derivations from Ref. [236]. There is also an additional HI uncertainty that is calculated in the same way as in Section 5.5.2 except using the run 2 data and MC at $\sqrt{s_{\mathrm{NN}}} = 5.02$ TeV. The JER uncertainties are used to smear the $p_{\mathrm{T}}^{\mathrm{reco}}$ as in equation 5.8 and generate a new response matrix. This response matrix is used to unfold the data and this result is compared to the nominal result where the difference is taken as the uncertainty.

6.4.3 Unfolding

As mentioned in Section 6.3.3.2 the response was reweighted for the nominal result (and all of the above systematic uncertainties) in order to better represent the data and converge quicker in the unfolding. The response without any weighting is used to evaluated to systematic due to reweighting and the difference between the two results, as shown in Figure 6.25, is used for the uncertainty due to the unfolding procedure, or specifically the

range	$\langle T_{AA} \rangle$[1/mb]	AbsErr($\langle T_{AA} \rangle$)	RelErr($\langle T_{AA} \rangle$)
0-10%	23.35	0.20	0.0087
10-20%	14.33	0.18	0.012
20-30%	8.64	0.17	0.020
30-40%	4.95	0.15	0.030
40-50%	2.63	0.11	0.043
50-60%	1.28	0.07	0.058
60-70%	0.56	0.04	0.076
70-80%	0.22	0.02	0.095

Table 6.7: The nuclear thickness function $\langle T_{AA} \rangle$ and its uncertainty.

sensitivity to the prior.

6.4.4 $\langle T_{AA} \rangle$ and Luminosity

The uncertainty on the nuclear thickness function $\langle T_{AA} \rangle$ comes from geometric modeling which includes an uncertainty on the nucleon-nucleon cross section and an uncertainty on the nucleon positions evaluated in the Woods-Saxon parameterization. There was also an uncertainty due to the efficiency of selecting real inelastic Pb+Pb collisions. These uncertainty values are shown in Table 6.7.

The 2015 *pp* luminosity was calibrated using a specific set of data generated during vdM scans which are described in Section 3.1.4. The systematic uncertainty on the *pp* luminosity is the uncertainty on the calibration and is also derived using the dedicated scans. The relative uncertainty is $\delta\mathcal{L}/\mathcal{L} = 5.4\%$ [237].

6.4.5 Summary

The breakdown of the systematic uncertainties for *pp* and central Pb+Pb is shown in Figure 6.38, where the uncertainty due to the JES is shown to be the largest. The right panel shows the uncertainties propagated to the R_{AA}. Here the standard JES and JER are shown to decrease due to the near cancellation of the correlated uncertainties. The largest uncertainty on the R_{AA} is the HI uncertainty on the JES due to the difference in the response of quenched jets. The systematic uncertainties on the R_{AA} for additional centrality bins are shown in Appendix E.

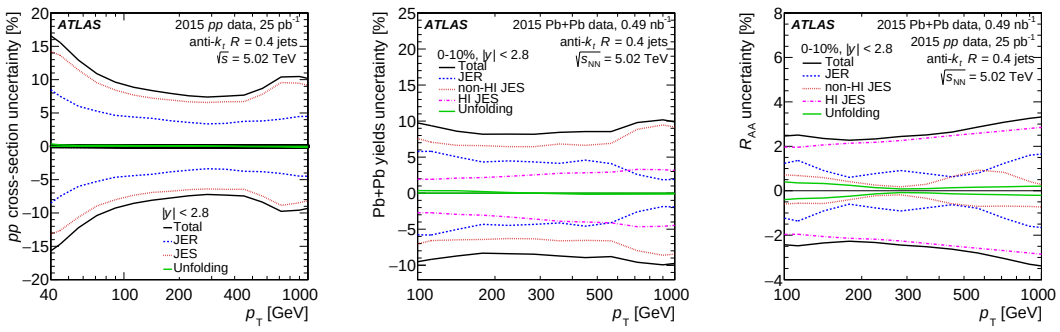

Figure 6.38: The systematic uncertainty breakdown in the pp jet cross-section (left), the central Pb+Pb jet yields (middle), and the R_{AA} (right).

6.5 Results and Discussion

6.5.1 Inclusive Jet Cross-section

The inclusive jet cross-section obtained from pp data is shown in the left panel of Figure 6.39. The cross-section is reported for six intervals of rapidity. The error bars in the figure represent statistical uncertainties while the shaded boxes represent systematic uncertainties. Systematic uncertainties also include the uncertainty due to the luminosity which is correlated for all the data points.

6.5.2 Inclusive Jet Yields in Pb+Pb Collisions

The right panel of Figure 6.39 shows the Pb+Pb jet yields scaled by $\langle T_{\mathrm{AA}} \rangle$. These are shown for all centrality intervals for jets with $|y| < 2.8$. For a direct comparison with the jet production in pp collisions, the values of pp cross-section are included on the figure int the black lines (scaled appropriately). Some additional rapidity intervals are shown in Appendix E.

6.5.3 Unfolded R_{AA}

The nuclear modification factor evaluated as a function of jet p_{T} is shown in the upper panels of Figure 6.40 for all centrality intervals. The R_{AA} is evaluated for jets with p_{T} between 100–1000 GeV and within $|y| < 2.8$. The higher p_{T} intervals are combined in the cross section and yields before evaluating the R_{AA} because of the large statistical uncertainties

at high p_{T}. The error bars in the figure represent the statistical uncertainties. The shaded boxes represent fully correlated systematic uncertainties for which all the data-points can move up or down together for a given change in the uncertainty. A clear suppression of the jet production in central Pb+Pb collisions with respect to pp collisions is observed. In the 0–10% centrality the R_{AA} is approximately 0.45 near $p_{\mathrm{T}} = 100$ GeV. The R_{AA} is then observed to grow slowly with increasing jet momentum reaching a value of approximately 0.6 for jets with p_{T} around 800 GeV.

The R_{AA} was seen to be less than unity in all centrality intervals. In the most peripheral interval it was ≈ 0.9, which is expected because the energy loss (for radiative models) is proportional to $N_{\mathrm{part}}^{2/3}$ and the peripheral collisions have $N_{\mathrm{part}} \approx 15$. From equation 2.105, $R_{\mathrm{AA}} \approx (1 - \kappa N_{\mathrm{part}}^{2/3})^5 \approx (1 - 6.1 * \kappa)^5$, where κ is some constant. Therefore, unless κ is very small, the R_{AA} will be less than one even for peripheral collisions. In the most central

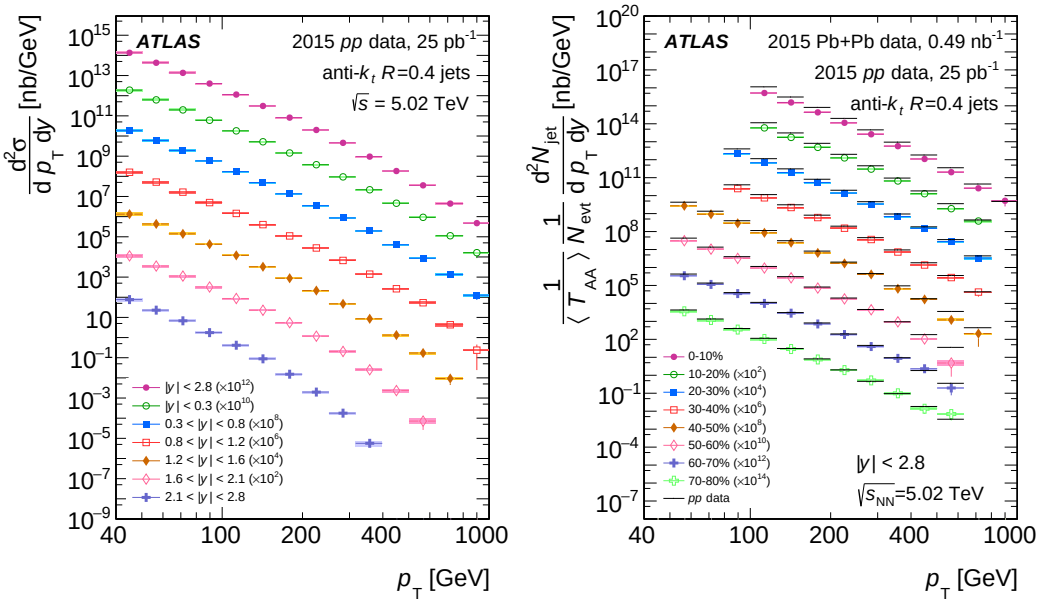

Figure 6.39: Left: Inclusive jet cross-section in pp data evaluated as a function of jet p_{T} scaled by successive powers of 10^2. Right: Per event jet yield in Pb+Pb collisions, multiplied by $\langle T_{\mathrm{AA}} \rangle$, as a function of jet p_{T} scaled by successive powers of 10^2. The solid lines represent the pp cross-section for the same rapidity selection scaled by the same factor to allow for a comparison with the Pb+Pb data at different centralities. The error bars represent statistical uncertainties, shaded boxes represent systematic uncertainties including uncertainties on $\langle T_{\mathrm{AA}} \rangle$ and luminosity.

collisions the R_{AA} was found to be ≈ 0.6, which results in an energy loss, $\epsilon_{\mathrm{loss}} \approx 0.097$, from equation 2.106. Given that for central collisions $N_{\mathrm{part}} \approx 359$, this results in $\kappa \approx 0.0019$. Using this value and going back to peripheral collisions, the R_{AA} in peripheral collisions is predicted to be ≈ 0.94, which is consistent within the uncertainties of the measurement. This suggests that radiative energy loss is dominating the jet suppression in this particular kinematic range since the N_{part} dependence is derived from the L^2 path length dependence

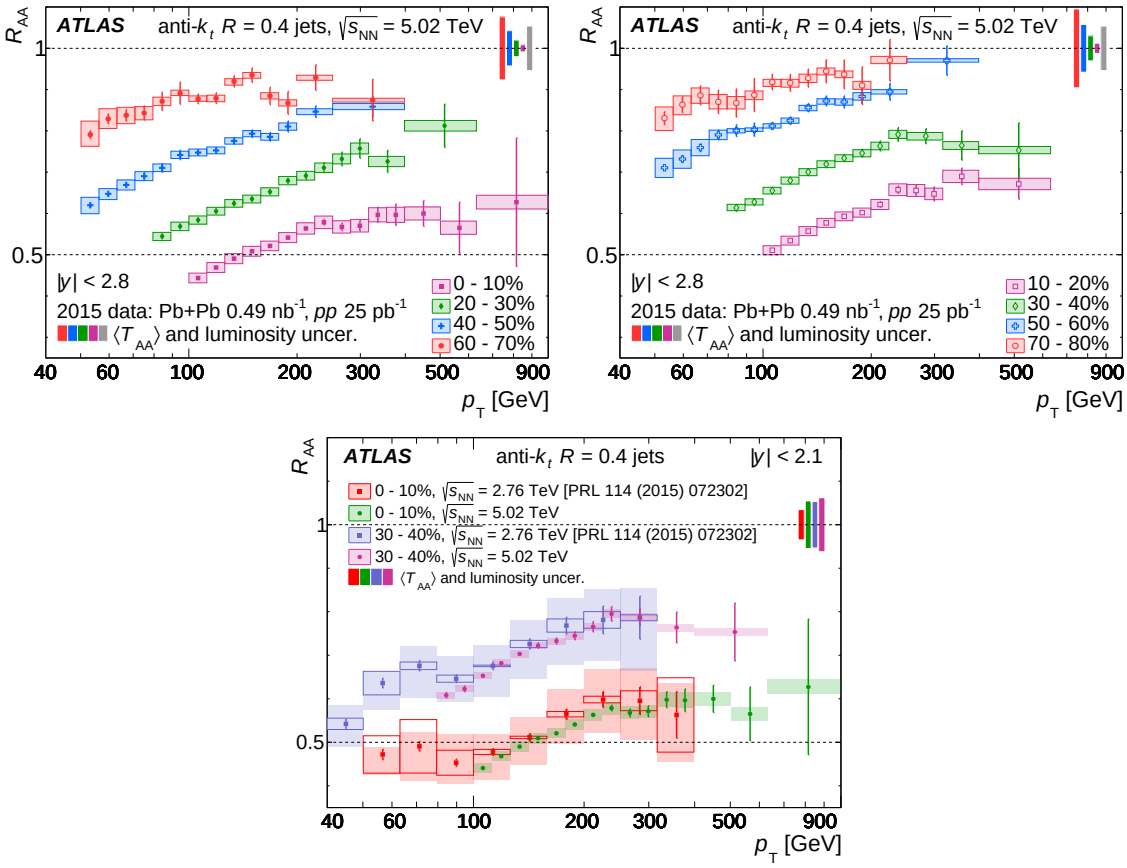

Figure 6.40: Upper panel: The R_{AA} as a function of jet p_{T} for jets with $|y| < 2.8$ for different centrality bins. Bottom panel: The R_{AA} as a function of jet p_{T} for jets with $|y| < 2.1$ in 0-10% central collisions compared to the same quantity measured in $\sqrt{s_{\mathrm{NN}}} = 2.76$ Pb+Pb collisions published in Ref. [5]. The error bars represent statistical uncertainties, the shaded boxes around the data points represent correlated systematic uncertainties. In the upper panel, the colored shaded boxes at unity represent $\langle T_{\mathrm{AA}} \rangle$ uncertainties and the gray shaded box represents the uncertainty on pp luminosity. The horizontal width on the shaded boxes represent the width of the p_{T} interval and the horizontal width on the open boxes are arbitrary for better visibility. In the bottom panel, the colored shaded boxes at unity represent the combined $\langle T_{\mathrm{AA}} \rangle$ uncertainties with the uncertainties on pp luminosity.

for radiative energy loss.

As mentioned above, the R_{AA} also demonstrates an interesting dependence with the jet p_{T}. First, the R_{AA} shows jet suppression out to a TeV which is striking because it suggests that those jets are still losing approximately 10% of their energy, despite being at such high p_{T}. The R_{AA} is observed to increase with increasing jet p_{T} until around 400 GeV where it begins to level off, although this is hard to discern within the statistical uncertainties. This suggests that the energy loss could have a slight dependence on the parton energy until very high energies where it could become independent of parton energy. Equation 2.82 shows that different kinematic regimes have either a logarithmic or no dependence on the parton energy which could explain the behavior. Also, some models, like the collisional and radiative energy loss mechanisms or the DGLV model, predict a logarithmic dependence on the energy of the parton, while others, like the strong coupling energy loss mechanism or the BDMPS-Z model, predict no dependence.

The p_{T} dependence and overall suppression can be further investigated by comparing to various jet quenching models. This is shown in Figure 6.41, where the central R_{AA} is compared to multiple theoretical predictions. The LBT model (described in Section 2.5.2.5) incorporates both radiative and collisional energy loss and jet-medium interactions, including the jet recoil. This model describes the high p_{T} dependence but misses the lower p_{T} dependence. The SCET$_G$ model (described in Section 2.5.2.4) extends beyond the typical radiative energy loss models to include calculations beyond the small x limit where only multiple gluon emissions can cause energy loss. It also incorporates CNM effects into the calculation. When the coupling constant, $g = 2.2$, this model describes the lower p_{T} dependence but underestimates the suppression at high p_{T}. The third model, the Effective Quenching (EQ) model [170] (introduced in Section 2.5.3), is an analytical model that incorporates energy loss through two downward shifts to the p_{T} spectrum, a larger one for gluons and a smaller one for quarks. This model requires energy loss parameters that are extracted from data, where here the values were taken from $\sqrt{s_{\mathrm{NN}}} = 2.76$ TeV. This could explain why the predicted suppression is higher than the data since the quenching should be stronger at 5.02 TeV. This model seems to describe the p_{T} dependence well which can be attributed to treating the energy loss differently for quarks and gluons, having the quark

fraction increase with p_{T}, and including a p_{T} dependent power law distribution. In this model, including both the difference in the energy loss for quarks and gluons and the non-constant power law distribution but assuming a constant energy loss with jet p_{T} gives the wrong dependence of the R_{AA} on the jet p_{T}. Interestingly, when instead the energy loss is assumed to depend on the jet p_{T} (in potentially different ways for quarks and gluons) the R_{AA} dependence on jet p_{T} is restored. In this model the energy loss ΔE actually varies like $\sqrt{p_{\mathrm{T}}}$. This can explain why the R_{AA} begins to flatten at higher jet p_{T} since the fractional energy loss decreases (increasing the R_{AA}) but the spectra become steeper (decreasing the R_{AA}). These two effects could cancel at high p_{T}.

The R_{AA} evaluated for jets with $|y| < 2.1$ can be compared with the previous measurement of the R_{AA} at $\sqrt{s_{\mathrm{NN}}} = 2.76$ TeV [5]. This is shown for both central and peripheral collisions in the bottom panel of Figure 6.40. The two measurements are observed to agree within uncertainties, implying that jet suppression is independent of the center-of-mass energy within this narrow range. The new measurement also has significantly reduced uncertainties, which is mainly attributed to the pp data being taken at the same time as the Pb+Pb data (no data period uncertainty), and has a much further reach in jet p_{T}.

The R_{AA} as a function of N_{part} is shown in Figure 6.42 for two jet p_{T} bins. The error band here represents the correlated systematic uncertainties which include the uncertainty on

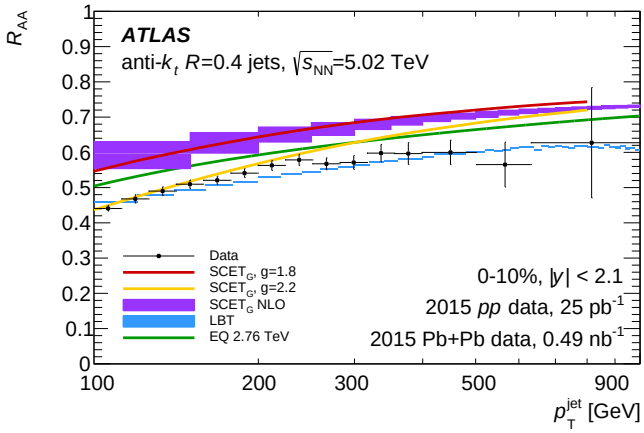

Figure 6.41: The R_{AA} as a function of jet p_{T} for jets with $|y| < 2.1$ in 0–10% collisions compared to theoretical predictions. The error bars on the data represent combined statistical and systematic uncertainties.

$\langle T_{\mathrm{AA}} \rangle$. The open boxes represent the uncorrelated systematic uncertainties. The statistical uncertainties are smaller than the data points for all R_{AA} values. A smooth evolution of the R_{AA} is seen, where the largest values are in the most peripheral collision and the smallest values are in the most central collisions. The R_{AA} is shown to be lower at all values of N_{part} in the lower p_{T} interval.

6.5.4 Rapidity Dependence

The rapidity dependence is interesting because it can probe the flavor dependence of energy loss since the quark and gluon fraction changes with jet p_{T} and rapidity. There are more quarks at high jet p_{T} and forward rapidity, as seen in the left panel of Figure 2.35. Quark jets should lose less energy than gluon jets, as discussed in Section 2.5.3, so the R_{AA} at forward rapidity and high p_{T} should be higher. This competes with the effect of the p_{T} spectrum becoming steeper at more forward rapidity, as seen in left panel of Figure 6.39, which will lead to a lower R_{AA} for the same amount of energy loss. Therefore, there are two competing effects so the question is which one dominates or do they cancel each other

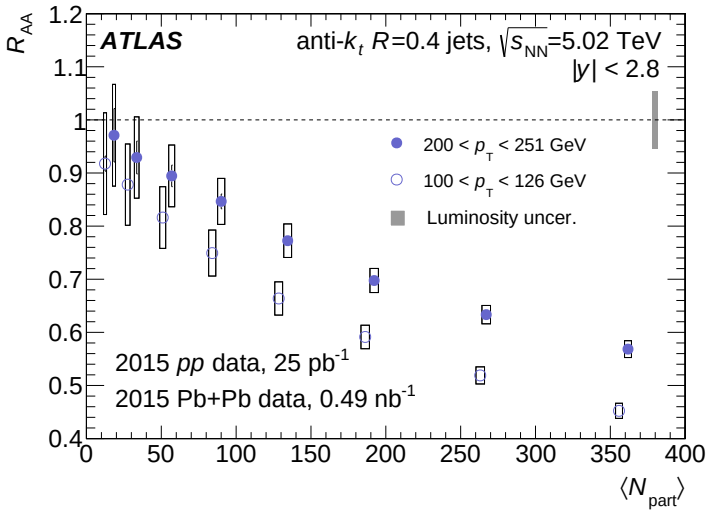

Figure 6.42: The R_{AA} for jets with $p_{\mathrm{T}} = 100 - -125$ GeV and $p_{\mathrm{T}} = 200 - -251$ GeV within $|y| < 2.8$ evaluated as a function of $\langle N_{\mathrm{part}} \rangle$. The black and red open boxes represent correlated and uncorrelated systematic uncertainties, respectively. The horizontal size of error boxes represents the uncertainty in the determination of $\langle N_{\mathrm{part}} \rangle$. The statistical uncertainties are smaller than the data-points. Gray shaded box represents the uncertainty on pp luminosity.

out.

The rapidity dependence of the R_{AA} is shown in Figure 6.43 by evaluating the ratio of the R_{AA} as a function of rapidity to the R_{AA} at $|y| < 0.3$. This representation was chosen because all systematic uncertainties largely cancel in the ratio. This is shown in intervals of increasing values of p_{T} in the four panels. The rapidity dependence is shown to be flat with rapidity at lower p_{T}. As the p_{T} is increased the R_{AA} starts to decrease with rapidity and this decrease is the most significant in the highest p_{T} interval. This is consistent with the steepness of the spectrum causing a lower R_{AA} at forward rapidity. This is the first time a significant rapidity dependence has been observed.

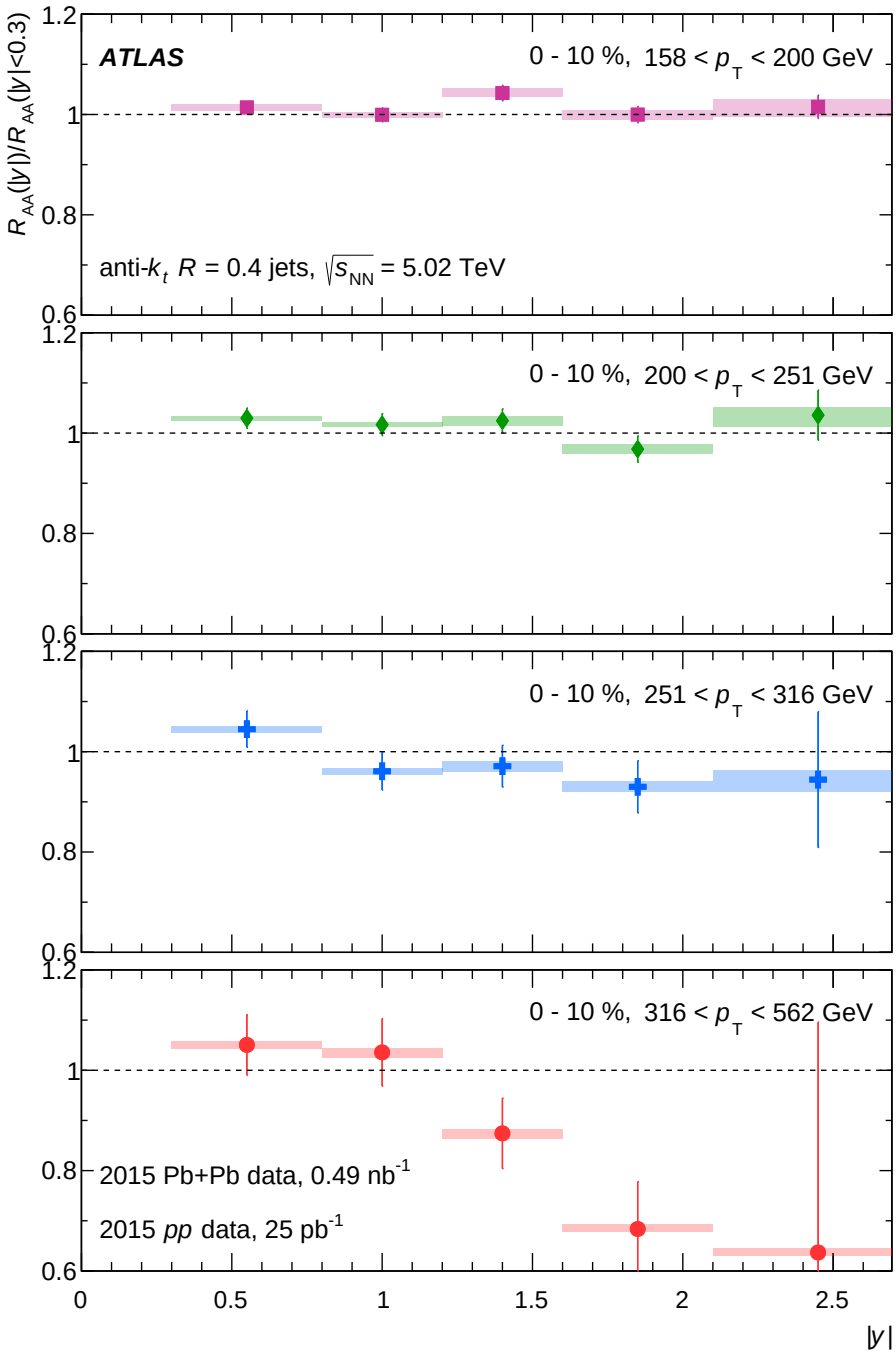

Figure 6.43: The ratio of the R_{AA} as a function of $|y|$ to the R_{AA} at $|y| < 0.3$ for jets with centrality of 0-10% in the following p_{T} bins on each panel: $158 < p_{\mathrm{T}} < 200$ GeV (red squares), $200 < p_{\mathrm{T}} < 251$ GeV (blue diamonds), $251 < p_{\mathrm{T}} < 316$ GeV (green crosses), and $316 < p_{\mathrm{T}} < 562$ GeV (purple stars). The error bars represent statistical uncertainties, the shaded boxes around the data points represent correlated systematic uncertainties.

Chapter 7

Dijet Asymmetry in Xe+Xe Collisions

7.1 Data and MC Samples

This analysis used data from 2015 Pb+Pb collisions (described in Section 6.1.1), and 2017 pp collisions at $\sqrt{s_{\mathrm{NN}}} = 5.02$ TeV and Xe+Xe collisions at $\sqrt{s_{\mathrm{NN}}} = 5.44$ TeV. The Pb+Pb data only consists of higher p_{T} jets above 100 GeV so the highest unprescaled jet trigger is used (`HLT_j75_ion_L1TE50`) which is fully efficient above 91 GeV.

7.1.1 2017 Xe+Xe Data

The Xe+Xe data used is this analysis was taking during a short run during the 2017 data-taking period at $\sqrt{s_{\mathrm{NN}}} = 5.44$ TeV with a total luminosity of $3\,\mu\mathrm{b}^{-1}$. The Xe+Xe events are selected with two minimum-bias triggers. If the total calorimeter $\sum E_{\mathrm{T}} < 4$ GeV then the `HLT_mb_sptrk_L1VTE4` is used which requires at least one reconstructed track in the ID. If the $\sum E_{\mathrm{T}}$ in the calorimeter is higher than this cut then the `HLT_noalg_mb_L1TE4` is used, which requires no additional cuts on the events except that the $\sum E_{\mathrm{T}} > 4$ GeV. The `HLT_noalg_mb_L1TE5` is also used for the first seven LB.

The events were also required to pass typical HI event-level selection criteria which was outlined in the list 5.1.1. An additional cut to remove a small number of pile-up events is

made through a simple cut that assumes a tight correlation between the $\Sigma E_{\mathrm{T}}^{\mathrm{FCal}}$ and the number of reconstructed tracks. This correlation is shown in Figure 7.1 along with a line that represents the cut where anything below the line is rejected

$$\text{FCal } E_{\mathrm{T}} < 0.21047 + 0.0015335 \cdot N_{\mathrm{trk}},$$

where N_{trk} is number of tracks with $p_{\mathrm{T}} > 0.5\,\mathrm{GeV}$ that pass standard track selections with "HILoose". This cut was derived previously for the centrality estimate. The right panel of Figure 7.1 shows the fraction of events without pile-up after the rejection has been applied and indicates that the fraction of removed jets is very small at most $\Sigma E_{\mathrm{T}}^{\mathrm{FCal}}$ values. At it's largest, events with $\Sigma E_{\mathrm{T}}^{\mathrm{FCal}} \sim 2.9\,\mathrm{TeV}$have around 1% contamination, while events with lower $\Sigma E_{\mathrm{T}}^{\mathrm{FCal}}$ have even smaller contamination.

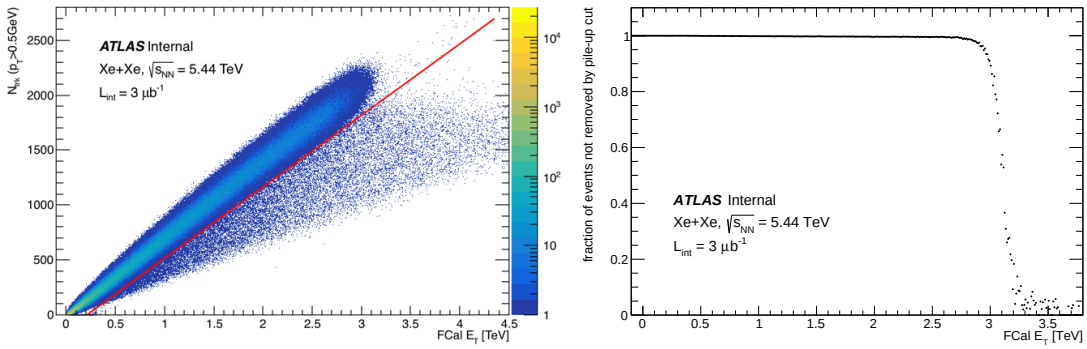

Figure 7.1: Left: Correlation between $\Sigma E_{\mathrm{T}}^{\mathrm{FCal}}$ and track multiplicity. The line represents a cut to remove pile-up events. Right: The fraction of of events without pile-up.

7.1.1.1 Centrality

The centrality was determined by the same methods as discussed in Section 5.1.1.1 but for the 2017 Xe+Xe data. The $\Sigma E_{\mathrm{T}}^{\mathrm{FCal}}$ distribution with the corresponding quantiles is shown in Figure 7.2, overlaid with the 2015 Pb+Pb distribution since the two collisions systems are compared in this analysis. There were 15.3 million events recorded and the event selections and trigger sampled 82.4% of the total inelastic cross-section in Xe+Xe with an uncertainty of 1% [238, 239]. In this analysis 8 centrality interval were used: 0-10%, 10-20%, 20-30%, 30-40%, 40-50%, 50-60%, 60-70% and 70-80% and the $\Sigma E_{\mathrm{T}}^{\mathrm{FCal}}$ values are shown in Table 7.1

Table 7.1: The centrality ranges used to the analysis with their corresponding $\Sigma E_{\mathrm{T}}^{\mathrm{FCal}}$ values.

Centrality [%]	$\Sigma E_{\mathrm{T}}^{\mathrm{FCal}}$ [TeV]
0–10	>1.887
10–20	1.887–1.303
20–30	1.303–0.881
30–40	0.881–0.572
40–60	0.572–0.200
60–80	0.200–0.049

for Xe+Xe and in Table 6.2 for Pb+Pb.

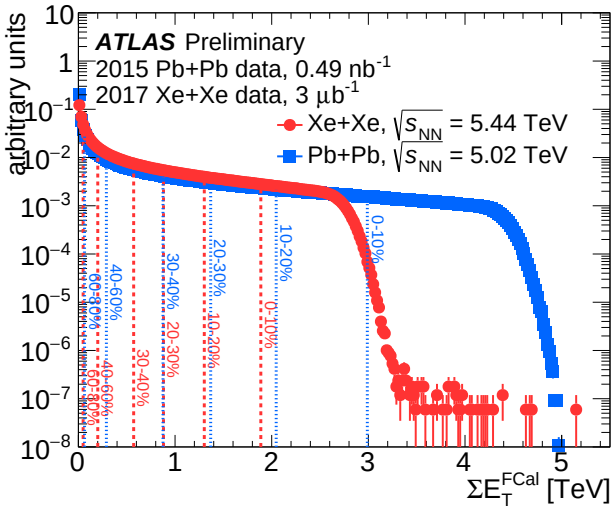

Figure 7.2: The $\Sigma E_{\mathrm{T}}^{\mathrm{FCal}}$ distributions in Xe+Xe in round and Pb+Pb in square points. The lines on the figure indicate the respective centrality intervals for each collision system: 0–10%, 10–20%, 20–30%, 30–40%, 40–60%, and 60–80%.

7.1.2 2017 *pp* Data

The *pp* data used in this analysis was taken in run 2 during the 2017 at $\sqrt{s_{\mathrm{NN}}} = 5.02$ TeV with a total luminosity of 278 pb^{-1}. The jets are selected using only the highest prescale jet trigger (similar definition as in Section 6.1.2) `HLT_j85` which is fully efficient above 95 GeV. The *pp* data was alo required to have a reconstructed primary vertex and be in the GRL.

7.1.3 MC Samples

The MC samples used in the Xe+Xe and pp analysis used signal from PYTHIA 8.215 [74] with the A14 set of tuned parameters [233] and NNPDF2.3 LO PDFs [234]. As mentioned in Section 4.3, the PYTHIA events are divided into ranges of $\hat{p}_{\mathrm{T}}$, which is the p_{T} of the outgoing partons in a $2 \to 2$ hard scattering, and combined using weights from their cross sections. The J slices and their cross sections for the PYTHIA used to generate the pp MC are shown in Table 7.2. For the Pb+Pb MC, the same signal was used but overlaid onto HIJING-simulated [158] Xe+Xe collisions (as discussed in Section 4.3) at $\sqrt{s_{\mathrm{NN}}} = 5.44$ TeV generated at five fixed vertex positions. The J slices and their cross sections for the PYTHIA used to generate the pp MC are shown in Table 7.3. The MC samples used for the 2015 Pb+Pb jets are described in Section 6.1.3.

MC sample	N_{evt}	$\sigma \times \varepsilon$ [nb]	jet p_{T} [GeV]
JZ1	20k	6.8E+07 × 2.9E-03	20–60
JZ2	20k	6.4E+05 × 4.3E-03	60–160
JZ3	20k	4.7E+03 × 5.3E-03	160–400
JZ4	20k	27 × 4.6E-03	400–700
JZ5	20k	0.22 × 2.2E-03	700+

Table 7.2: 5.02 TeV pp MC samples. Column "$\sigma \times \varepsilon$" denotes samples' cross sections and filtering efficiencies.

MC sample	N_{evt}	$\sigma \times \varepsilon$ [nb]	jet p_{T} [GeV]
JZ1	1M	6.872E+07 × 3.25E-03	20–60
JZ2	1.5M	7.21E+05 × 4.51E-02	60–160
JZ3	1.5M	5.52E+03 × 5.64E-02	160–400

Table 7.3: 5.44 TeV Xe+Xe MC samples. Column "$\sigma \times \varepsilon$" denotes samples' cross sections and filtering efficiencies. Only the total number of events for all vertex positions combined is listed.

7.2 Underlying Event Study

The HI events have a large UE that is removed in the jet reconstruction but there are UE fluctuations that cause a large JER (discussed in detail in Chapter 4). These UE fluctuations are dependent on the centrality or the N_{part}. This is usually removed by an

unfolding procedure that is sensitive to how well the MC describes these UE fluctuations, where the difference between the UE fluctuations in the data and the MC is evaluated by comparing the b term in the MC (equation 4.11) and the size of the fluctuations in the data. This procedure was described in Section 5.5.2. In this analysis the results have not been unfolded and thus are not sensitive to this effect. The analysis does compare Pb+Pb and Xe+Xe collisions which are expected to have different sizes of UE fluctuations in a fixed centrality since the UE is characterized by the $\Sigma E_{\mathrm{T}}^{\mathrm{FCal}}$ and the two collisions systems will have different values of the $\Sigma E_{\mathrm{T}}^{\mathrm{FCal}}$ in the same centrality interval (see Figure 7.2). At the same $\Sigma E_{\mathrm{T}}^{\mathrm{FCal}}$ value the size of the UE fluctuations are expected to be more comparable but the difference between the system size can also change the size of the fluctuations.

This difference is studied by comparing the size of the UE in data between Pb+Pb and Xe+Xe. The fluctuation size in data is estimated using a non-overlapping sliding window analysis like in Ref. [240]. It this analysis, the $\sum E_{\mathrm{T}}$ at the electromagnetic scale of the towers in defined windows in $\eta-\phi$ in the calorimeter are evaluated. First 1×1 single towers were used and then those were further combined into 7×7 windows which are comparable to the size of $R=0.4$ jets. This window is slid through the entire $\eta-\phi$ space in each event (making sure to not have overlapping windows), as illustrated in Figure 7.3, and the average $<\sum E_{\mathrm{T}}>$ and standard deviation $\sigma(\sum E_{\mathrm{T}})=\sqrt{<\sum E_{\mathrm{T}}^2>-<\sum E_{\mathrm{T}}>^2}$ of all the windows was evaluated in each event. At this point there is a $\sigma(\sum E_{\mathrm{T}})$ for each event and this is shown as a function of the $\Sigma E_{\mathrm{T}}^{\mathrm{FCal}}$ in Pb+Pb in Figure 7.4 and in Xe+Xe in Figure 7.5 for both window sizes discussed.

The correlation can be seen to be tight and thus the average standard deviation ($\overline{\sigma(\sum E_{\mathrm{T}})}$) in slices of $\Sigma E_{\mathrm{T}}^{\mathrm{FCal}}$ in each of these distributions was evaluated and then compared between Pb+Pb and Xe+Xe in Figure 7.6. The ratio of the two is in the bottom panel, where they are seem to be comparable with the difference being as large as 3% for single towers and 13% for the windows. This difference in the 7×7 window is represents the difference in the UE event contribution in the JER and is used in the data analysis to smear to Xe+Xe results to the Pb+Pb results to take into account the difference in the UE so that a better comparison between the two systems can be made.

The UE fluctuation estimate in the data can be compared to the b term in the MC. The

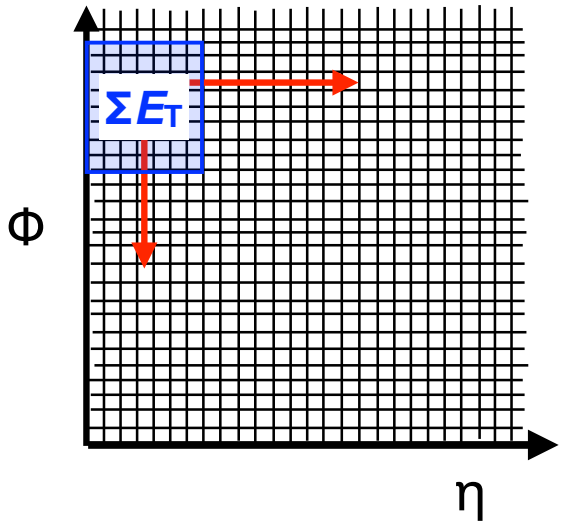

Figure 7.3: A schematic of the sliding window analysis for 7×7 windows of calorimeter towers in $\eta - \phi$.

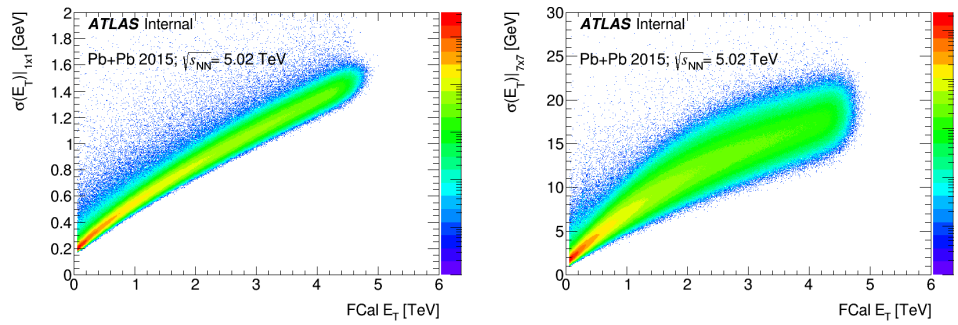

Figure 7.4: Distribution of per-event single-tower (left) and 7×7 tower sums (right) standard deviation versus event FCal ΣE_T obtained from Pb+Pb data.

b term in the MC is evaluated in Figure 4.15. The comparison is shown in Figure 7.7, where they are shown to be in good agreement which verifies that the `HIJING` overlay describes the UE in the data well.

7.3 Data Analysis

Jets selected in this analysis are required to have $|\eta| < 2.1$ and $p_{\mathrm{T}} > 30$ GeV. The left panels of Figures 7.8 and 7.9 show the p_{T} distribution and the η distribution for jets having

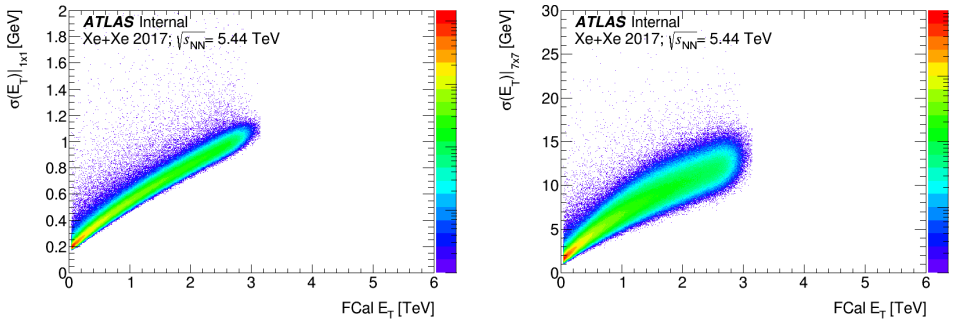

Figure 7.5: Distribution of per-event single-tower (left) and 7×7 tower sums (right) standard deviation versus event FCal ΣE_T obtained from Xe+Xe data.

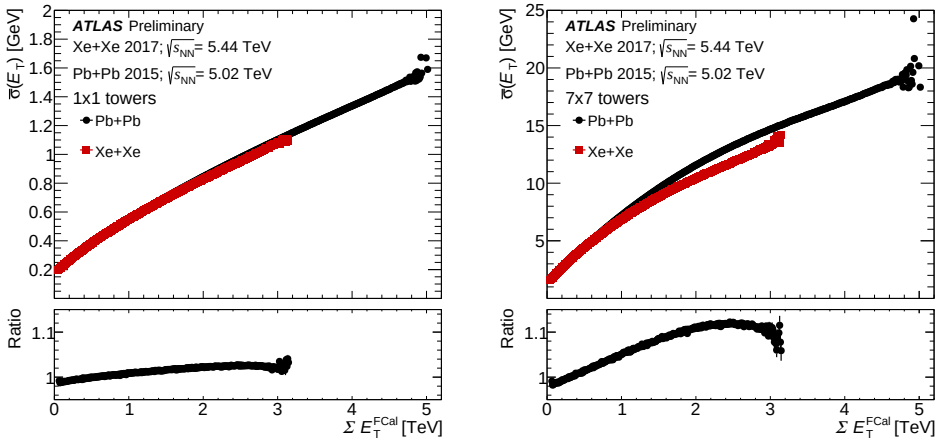

Figure 7.6: Comparison of $\overline{\sigma}(\Sigma E_T)$ (top) and $\overline{\sigma}(\langle E_T \rangle)$ (bottom) in single towers (left) and in 7 × 7 tower sums (right) evaluated in Xe+Xe and Pb+Pb collisions.

$p_{\mathrm{T}} > 75$ GeV, respectively, in the different centrality intervals used in the analysis. This is shown for Xe+Xe since the 2015 Pb+Pb jets have been validated in previous analyses of 2015 data in Chapter 6. The same thing is show in the right panels in Figures 7.8 and 7.9 but for pp jets in data. These figures have the expected features for jets and indicate that are jets are working in the analysis.

The jet with the highest p_{T} value in each event is the leading jet and the jet having the highest p_{T} value within, $|\Delta\phi| > 7\pi/8$ of the leading jet, is the sub-leading jet. For events selected by a jet trigger, the leading jet is required to match a jet identified by the trigger algorithm responsible for selecting the jet where the trigger is fully efficient. Distributions

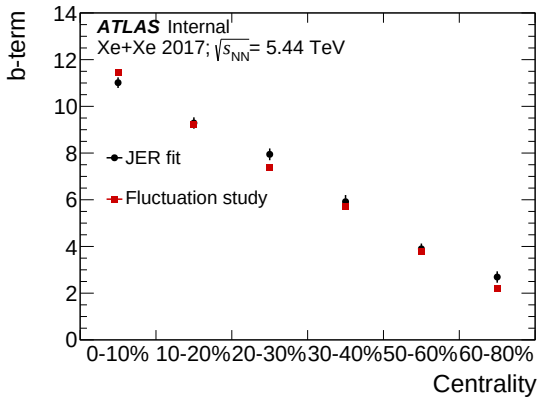

Figure 7.7: Comparison of the $b-$term estimated from the fitting of the JER evaluated in the MC HIJING and from the fluctuation study as a function of centrality.

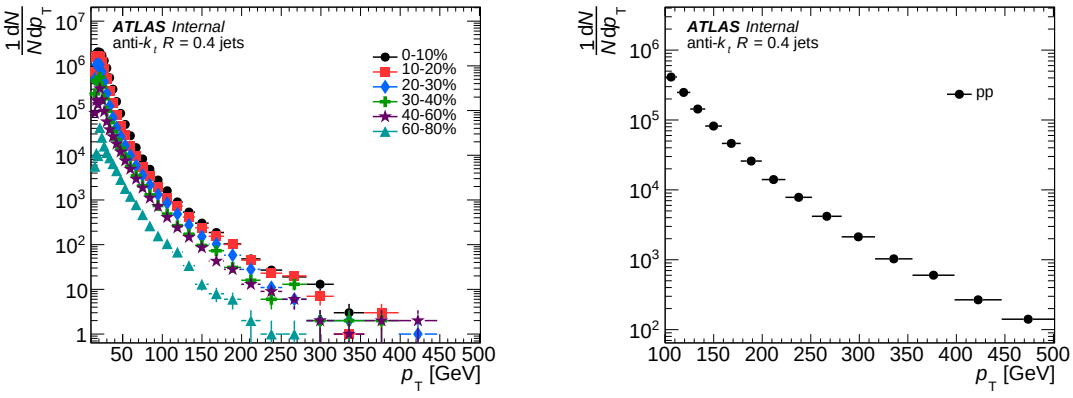

Figure 7.8: Distributions of p_{T} for reconstructed jets in Xe+Xe data in the different centrality intervals used in the analysis (left) and pp (right).

of leading jet p_{T} are shown in Figure 7.10. The kinematic cuts for this analysis are the same as for the 2.76 TeV Pb+Pb analysis described in Section 5.3.1 that are made after unfolding. After unfolding typically means that the cuts were made at the truth level but in this measurement the results are not unfolded so these cuts are made at the reconstructed level.

The dijet $x_{\mathrm{J}}^{\mathrm{meas}}$ is defined, $x_{\mathrm{J}}^{\mathrm{meas}} \equiv p_{\mathrm{T}}^{\mathrm{sub}}/p_{\mathrm{T}}^{\mathrm{lead}}$, where $p_{\mathrm{T}}^{\mathrm{lead}}$ and $p_{\mathrm{T}}^{\mathrm{sub}}$ represent the leading and sub-leading jet p_{T} values, respectively. The results are presented as area-normalized distributions of $(1/N)\mathrm{d}N/\mathrm{d}x_{\mathrm{J}}$.

The measurement of the $x_{\mathrm{J}}^{\mathrm{meas}}$ distributions is performed in four intervals of $p_{\mathrm{T}}^{\mathrm{lead}}$: 100–

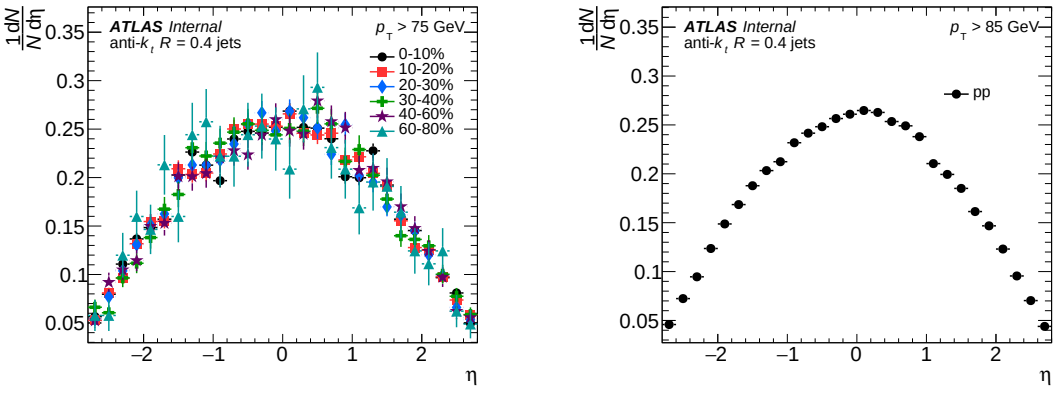

Figure 7.9: Distributions of η for reconstructed jets in Xe+Xe having $p_{\mathrm{T}} > 75$ GeV for the different centrality selections used in the analysis (left) and pp (right).

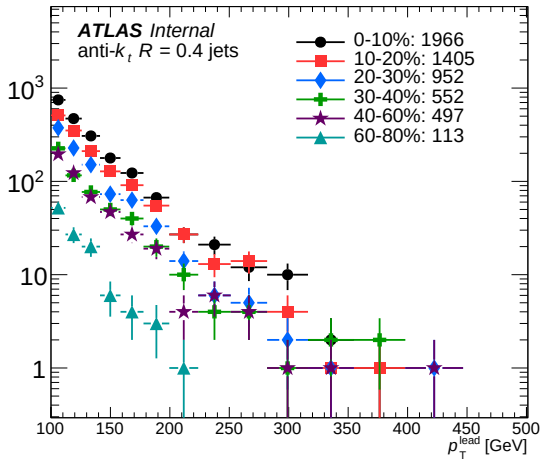

Figure 7.10: Distributions of leading jet p_{T} for the different centrality selections used in the analysis. The number of leading jets in each centrality bin is given in the legend.

126 GeV, 126–158 GeV, 158–200 GeV, and >200 GeV, and centrality intervals: 0–10%, 10–20%, 20–30%, 30–40%, 40–60%, 60–80%. These intervals are selected to be the same as those used for the dijet asymmetry at 2.76 TeV, described in Chapter 5. For the 0–10% centrality interval, a total of 1637, 511, 406, and 77 pairs were obtained for the 100–126 GeV, 126–158 GeV, 158–200 GeV, and >200 GeV $p_{\mathrm{T}}^{\mathrm{lead}}$intervals, respectively. The measurement was also performed in the centrality intervals defined for the 2015 Pb+Pb data so that a comparison can be made between Pb+Pb and Xe+Xe in the same $\Sigma E_{\mathrm{T}}^{\mathrm{FCal}}$ intervals. The

entire measurement is also done in 2015 Pb+Pb data at 5.02 TeV for comparison. The measurement is also compared to the same $p_{\mathrm{T}}^{\mathrm{lead}}$ intervals in pp data.

7.4 Systematic Uncertainties

The systematic uncertainties in the measurement are due to the following sources:

- Jet energy scale
- Jet energy resolution

The systematic uncertainties are evaluated separately for Xe+Xe, Pb+Pb, and pp and as a function of p_{T_1} and centrality. The systematic uncertainty procedure and components are similar to those in the x_{J} analysis in Section 5.5, except this analysis is not unfolded so the systematic variations are evaluated as a function of the reconstructed jet p_{T} and not the truth p_{T} so there are no response matrices to re-unfold with and there are no uncertainties due to unfolding or due to the response. Here the analysis procedure is repeated for each systematic variation by varying the reconstructed data. Then the difference between the upward variation and the nominal result is the upper bound of the uncertainty and the difference between the downward variation and the nominal result is the lower bound on the uncertainty. All of the systematic uncertainties are treated as uncorrelated and thus combined in quadrature to obtain the total systematic uncertainty on the final result.

7.4.1 Jet Energy Scale

The description of the JES uncertainties are the same as in Section 6.4.1 and Section 5.5.1, where the Pb+Pb, pp, and Xe+Xe data received all the standard baseline JES uncertainties, as well as the flavor uncertainties using flavor fractions from the corresponding datasets. The Xe+Xe and Pb+Pb data also have the HI specific uncertainty due to the difference in the response to quenched jets that is described in Section 6.4.1.

There is an additional JES uncertainty due to a residual non-closure in the MC as seen in Fig. 4.10 for Xe+Xe and pp. This is accounted for by parameterizing the JES in pp and in each centrality interval in Xe+Xe as shown in Fig. 7.11.

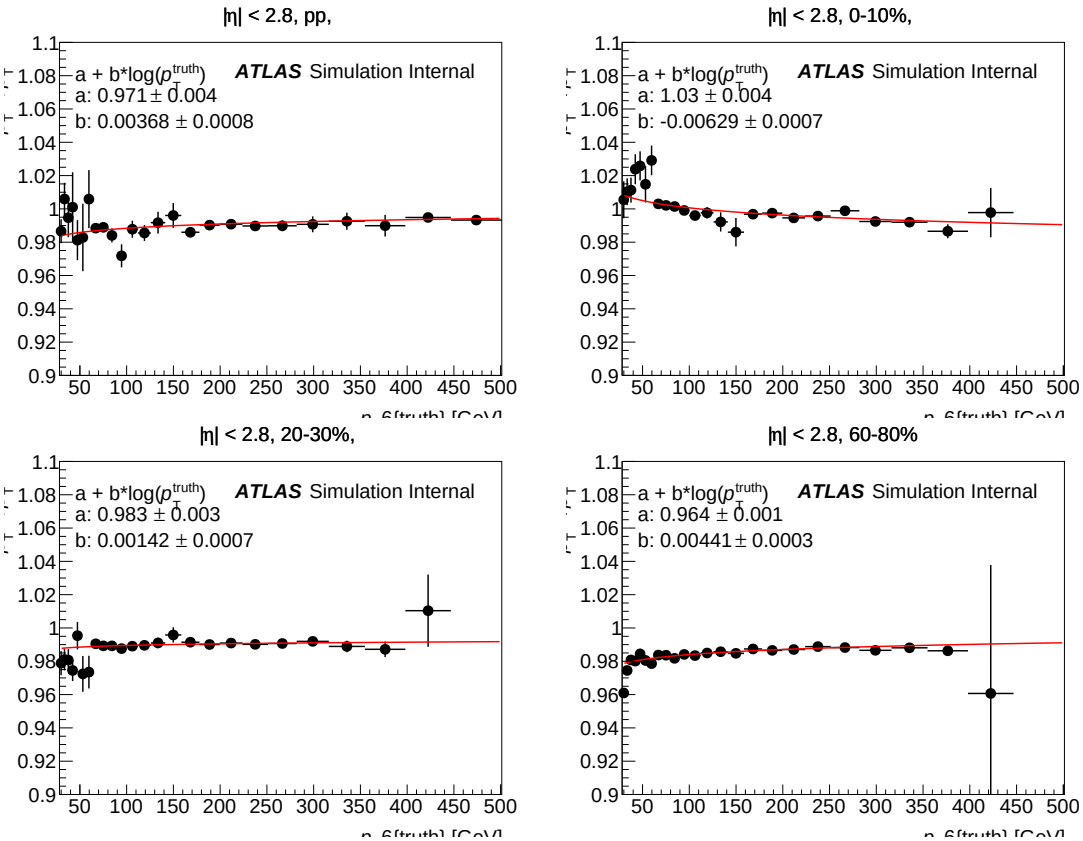

Figure 7.11: JES as a function of truth p_{T} fit with a logaritm for residual non-closure in pp and centrality intervals in Xe+Xe.

For each component of the variation the p_{T} is shifted in the same way as equation 6.5, except the variation is performed on the reconstructed jets in data and it is evaluated as function of that reconstructed jet p_{T} instead of $p_{\mathrm{T}}^{\mathrm{truth}}$ according to,

$$p_{\mathrm{T}}^{\star,\mathrm{reco}} = p_{\mathrm{T}}^{\mathrm{reco}}(1 \pm U^{\mathrm{JES}}(p_{\mathrm{T}}, \eta)). \tag{7.1}$$

The variation in the x_{J} distributions with the uncertainty applied and without is taken as the systematic uncertainty.

7.4.2 Jet energy resolution

The uncertainties due to the JER are also similar to what was described in Section 5.5.2 and Section 6.4.2. This includes the HI specific JER uncertainty due to the difference between

the reconstruction procedure in pp and HI, which is only applied to Xe+Xe and Pb+Pb.

An additional systematic in Xe+Xe accounts for the difference between the UE fluctuations and data. This is an evaluation of the accuracy of `HIJING` to describe the UE fluctuations in the data. This was described in Section 7.2 and shown in Figure 7.7. A similar uncertainty to this is also present in the Pb+Pb data but here it is comparing the UE fluctuations in data to the minimum bias overlay in MC. This is described in Section 5.5.2.

The JER uncertainties are used to smear the $p_{\mathrm{T}}^{\mathrm{reco}}$ as in equation 5.8 and the analysis is redone and the difference between the x_{J} distributions with the varied p_{T} and the nominal result is taken as the systematic uncertainty to the JER.

7.4.3 Summary and Correlations

The systematics in pp data are shown in Figure 7.12 in the lowest leading p_{T} interval in the analysis. The uncertainty on the JER was found to be the largest.

The systematics in Xe+Xe data are shown in Figure 7.13 for central collisions in the lowest leading jet p_{T} interval in the analysis. The systematics for the lowest leading jet p_{T} interval in peripheral collisions are shown in Figure 7.14. The uncertainty on the JER was also found to be the largest in most p_{T} bins with the pp baseline JES and the flavor response JES also contributing significantly.

The systematics in Pb+Pb data are shown in Figure 7.15 for central collisions in the lowest leading jet p_{T} interval in the analysis. The uncertainty on the JER was also found to be the largest in most p_{T} bins with the pp baseline JES and the flavor response JES also contributing significantly.

Due to the common analysis and reconstruction procedure, and detector conditions, the systematic uncertainties are correlated between the Pb+Pb and Xe+Xe collisions in many cases. Table 7.4 summarizes correlations between pp Xe+Xe, and Pb+Pb collisions and also point-to-point correlations of individual distributions.

The Pb+Pb and pp results are only used as a comparison to the Xe+Xe results so only the uncertainties that are different between them and the Xe+Xe results are actually shown on the data points. The breakdown of the systematic uncertainty is shown in Figure 7.16 for the $100<p_{\mathrm{T}_1}<126\,\mathrm{GeV}$ interval in pp collisions and for the 0–10% centrality interval

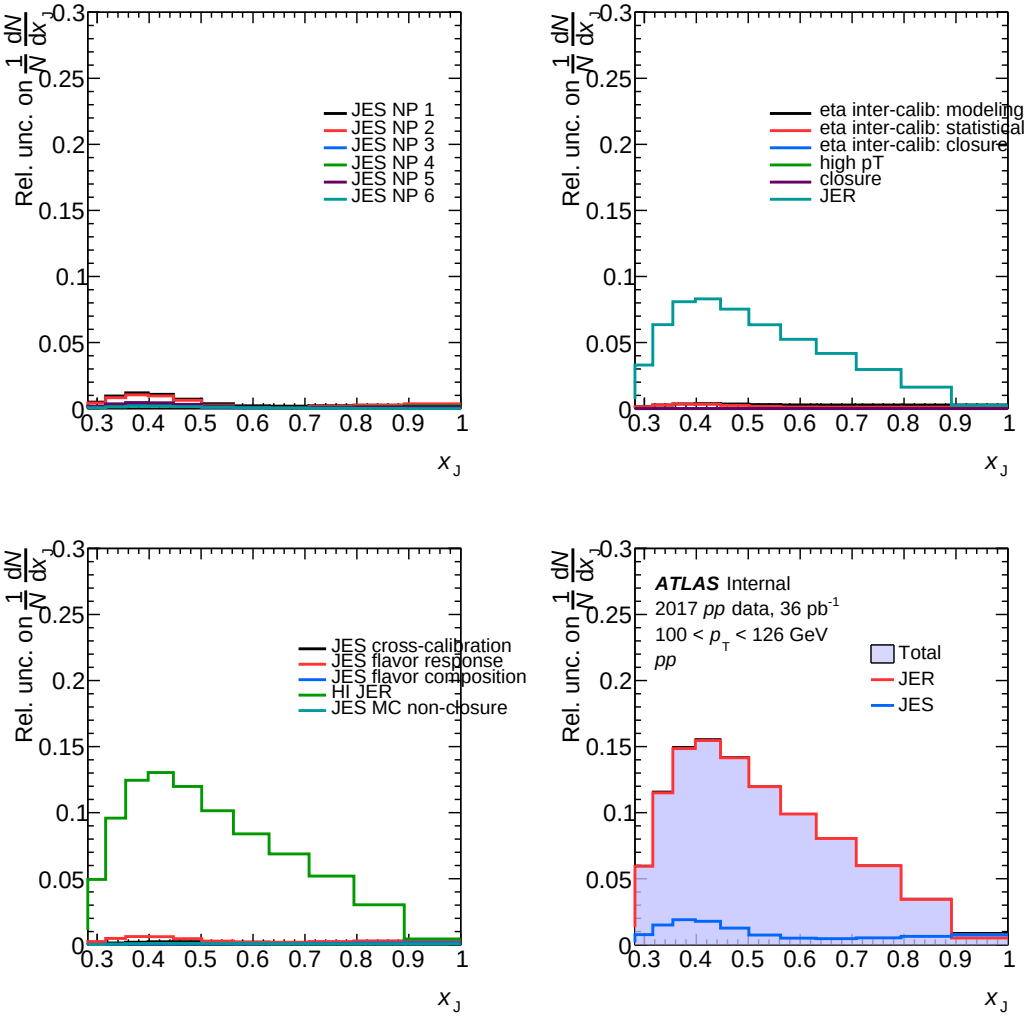

Figure 7.12: Relative systematic uncertainties on $1/NdN/dx_{\mathrm{J}}$ as a function of x_{J} for pp collisions for $100 < p_{\mathrm{T}} < 126$ GeV used in the analysis.

in Xe+Xe and Pb+Pb collisions. For the Xe+Xe results in the left panel, the systematic uncertainties are shown for both the JES and JER contributions as well as the combination. For the Pb+Pb results in the center panel, the systematics uncertainties that are uncorrelated with those in Xe+Xe collisions are shown. This includes the difference between the non-closure in the JES evaluated in the MC in Pb+Pb and Xe+Xe collisions and the heavy-ion specific JES uncertainty due to quenching in Pb+Pb collisions. For the pp results in the right panel, the systematic uncertainties that are uncorrelated with those in Xe+Xe colli-

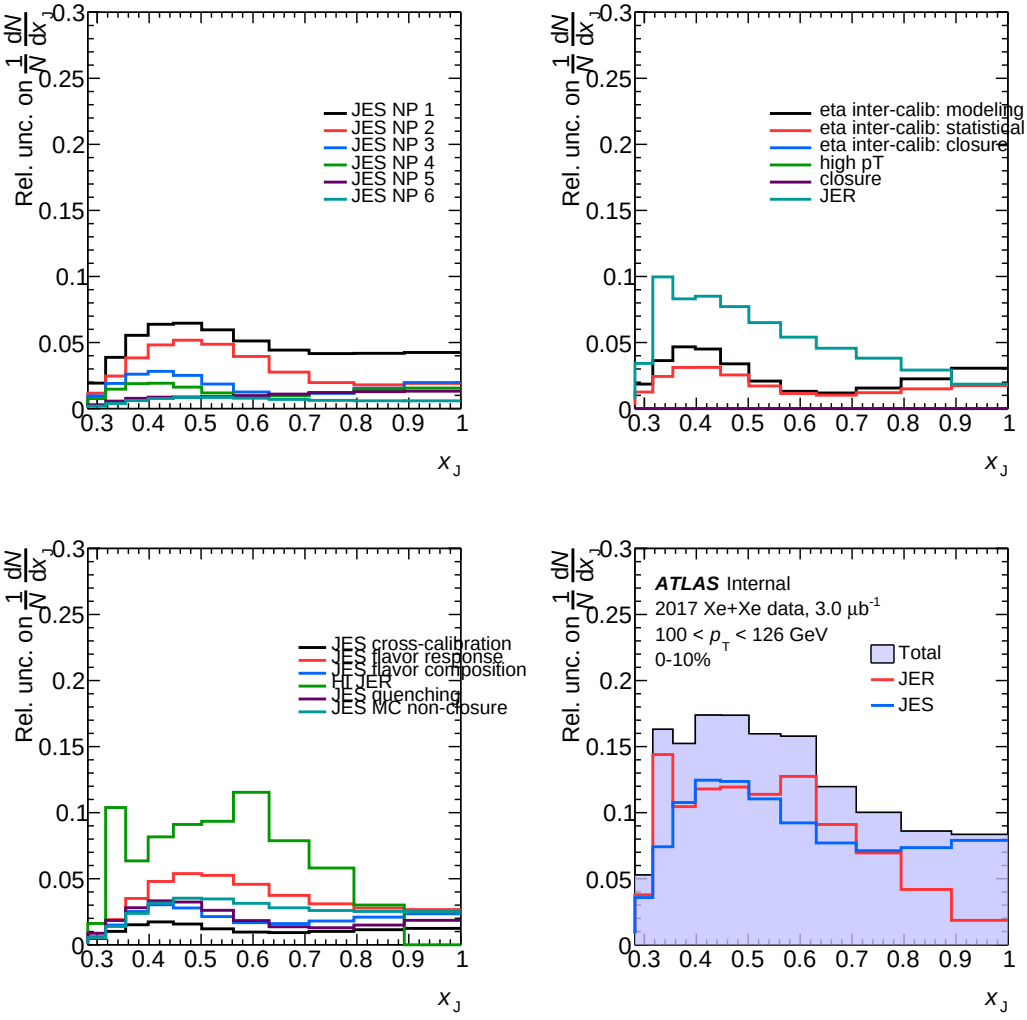

Figure 7.13: Relative systematic uncertainties on $1/NdN/dx_J$ as a function of x_J for 0–10% Xe+Xe collisions for $100 < p_{T1} < 126$ GeV jets.

sions are shown. Similarly, this includes the difference between the non-closure in the JES evaluated in the MC in pp and Xe+Xe collisions and the heavy-ion specific JES uncertainty due to quenching in Xe+Xe collisions. The uncertainty tends to decrease with increasing x_J. The total uncertainty at $x_J \sim 1$ reaches approximately 10% in the Xe+Xe data. For $x_J < 0.4$, the relative uncertainty on Xe+Xe becomes large, but this region represents only a small contribution to the total $(1/N)\mathrm{d}N/\mathrm{d}x_J$ distribution.

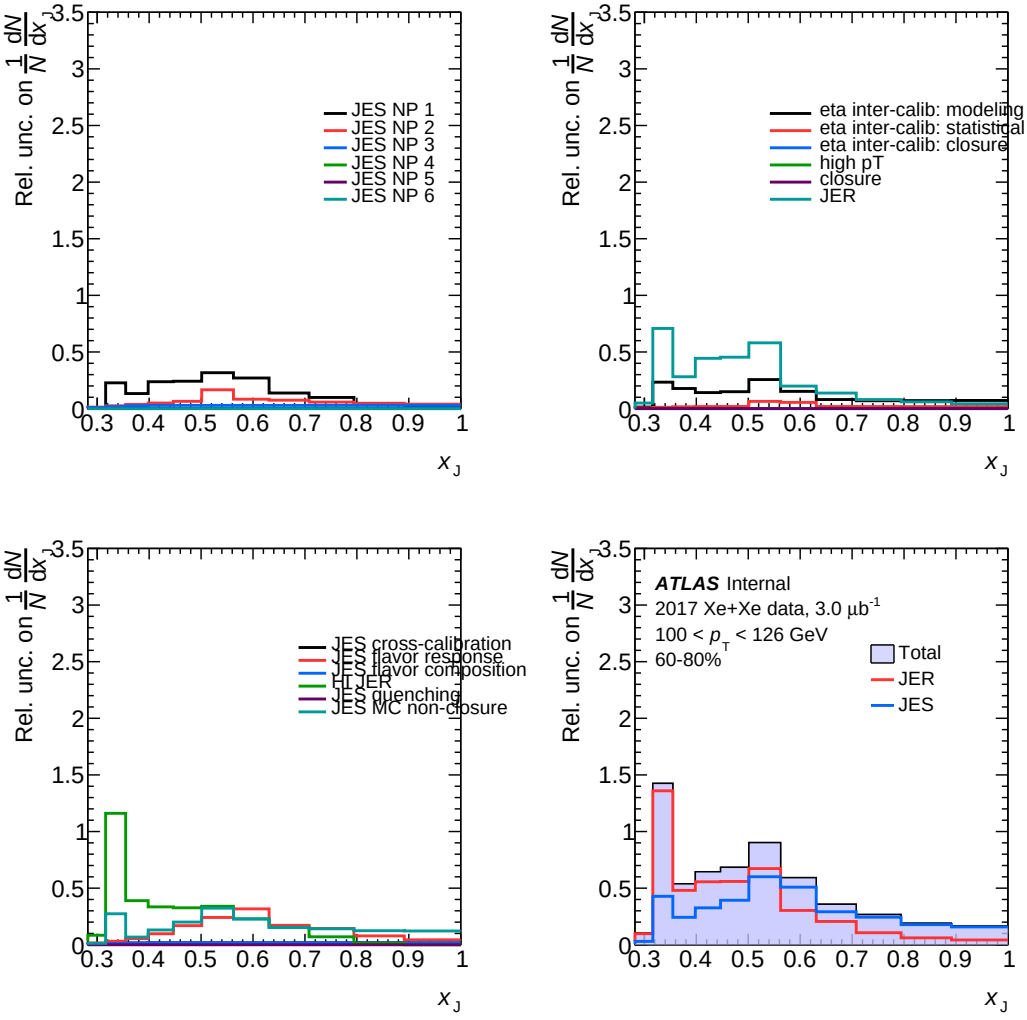

Figure 7.14: Relative systematic uncertainties on $1/NdN/dx_J$ as a function of x_J for 60–80% Xe+Xe collisions for $100 < p_{T1} < 126$ GeV jets.

7.5 Results and Discussion

The $1/NdN/dx_J^{\text{meas}}$ in Xe+Xe collisions are compared to pp collisions at the same center-of-mass energy. This is show in Figure 7.17 for the centrality dependence in the lowest p_T^{lead} bin. The trend is similar to that seen in 2.76 TeV Pb+Pb collisions where the jets are more asymmetric in more central collisions as compared to pp but become like the pp in more peripheral collisions in Section 5.6. Figure 7.18 shows results for the 0–10% centrality interval for different p_T^{lead} intervals. This is also similar to what is seen in Pb+Pb collisions

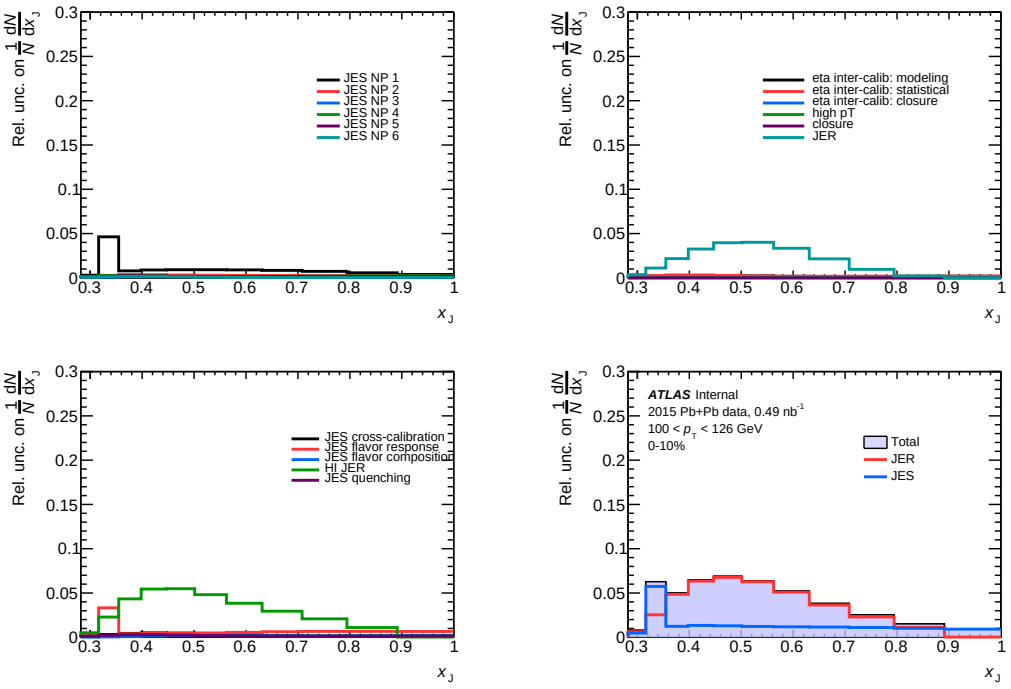

Figure 7.15: Relative systematic uncertainties on $1/NdN/dx_{\mathrm{J}}$ as a function of x_{J} for 0–10% Pb+Pb collisions for $100 < p_{T1} < 126$ GeV jets.

in Section 5.6.

The different mass numbers for Xe_{129} and Pb_{208} indicate that the medium produced in Xe+Xe collisions will have a lower medium density and associated path length than in Pb+Pb collisions. Based on discussions in Section 2.5.3, this should result in less energy loss in Xe+Xe than in Pb+Pb collisions. The primary results of the analysis are shown in Figures 7.19 and 7.20. The figures show the differential $x_{\mathrm{J}}^{\mathrm{meas}}$ distributions normalized by the total number of pairs $1/NdN/dx_{\mathrm{J}}^{\mathrm{meas}}$ in Xe+Xe collisions compared to the same distribution in 5.02 TeV Pb+Pb collisions. Figure 7.19 shows the $x_{\mathrm{J}}^{\mathrm{meas}}$ distribution in different centrality bins for the lowest $p_{\mathrm{T}}^{\mathrm{lead}}$ interval, while Figure 7.20 shows results for the 0–10% centrality interval for different $p_{\mathrm{T}}^{\mathrm{lead}}$ intervals. Fixing the centrality of the collision means that the collision systems are being compared at different medium densities, which means that the Pb+Pb collisions would be expected to be more asymmetric than in Xe+Xe collisions. In both figures, the Xe+Xe and Pb+Pb data are consistent within statistical and systematic uncertainties. The black line represents the results after applying the additional

uncertainty	*pp* and HI	Pb+Pb and Xe+Xe	point-to-point	one/two sided/symmetrized
JES (*pp*)	correlated	correlated	correlated	two sided
JES (HI)	uncorrelated	uncorrelated	correlated	two sided
JER (intrinsic)	correlated	correlated	correlated	symmetrized
JER (UE)	uncorrelated	uncorrelated	correlated	one sided

Table 7.4: Summary of correlation of different systematic uncertainties.

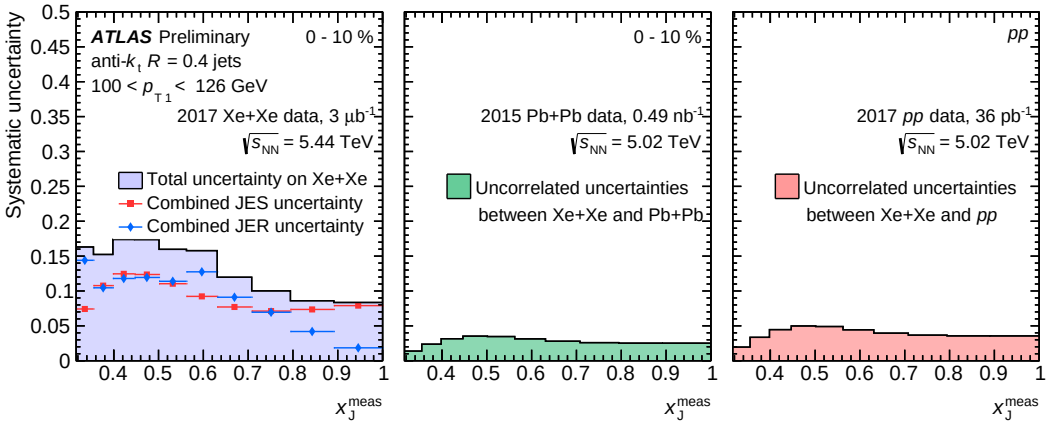

Figure 7.16: The systematic uncertainty for $100 < p_{T_1} < 126\,\text{GeV}$ jets in Xe+Xe (left) and Pb+Pb (centre) collisions in the 0–10% interval and *pp* collisions (right). The left panel includes all the JES and JER uncertainties on Xe+Xe data. The middle panel includes only the uncertainties that are uncorrelated between Xe+Xe and Pb+Pb which include the difference between the JES non-closure uncertainty in Pb+Pb and Xe+Xe and the JES uncertainty due to quenching in Pb+Pb. The right panel only includes the uncertainties that are uncorrelated between Xe+Xe and *pp* which include the difference between the JES non-closure uncertainty in *pp* and Xe+Xe and the JES uncertainty due to quenching in Xe+Xe.

smearing to account for a difference between Pb+Pb and Xe+Xe in the JER induced by small differences in the UE fluctuations as discussed in Section 7.2. This also doesn't deviate from the Pb+Pb results. The energy loss should be proportional to $A^{2/3}$ such that $\epsilon_{\text{Xe}}/\epsilon_{\text{Pb}} \propto (129/208)^{2/3} = 0.7$. This is potentially not a large enough difference to be seen when using the x_{J} variable since the effect was seen in the hadron R_{AA} where the jets in Pb+Pb were more suppressed than the jets in Xe+Xe collisions [4]. Also, the lack of difference could be attributed to the large uncertainties in the Xe+Xe data.

The $1/NdN/dx_{\text{J}}^{\text{meas}}$ in Xe+Xe collisions were also evaluated in the same $\Sigma E_{\text{T}}^{\text{FCal}}$ intervals as the 2015 Pb+Pb analysis to get a better direct comparison of the results. This is

useful because the two collision systems should have a comparable UE. This also probes the geometry dependence (discussed in Section 2.4.3.1 and Section 2.5.3) because at a fixed value of $\Sigma E_{\mathrm{T}}^{\mathrm{FCal}}$ (or N_{part}), the Xe+Xe collisions will be more central than the Pb+Pb collisions. The $\Sigma E_{\mathrm{T}}^{\mathrm{FCal}}$ dependence is shown in Figure 7.21 and the $p_{\mathrm{T}}^{\mathrm{lead}}$ dependence for a fixed $\Sigma E_{\mathrm{T}}^{\mathrm{FCal}}$ interval is shown in Figure 7.22. These results show that Xe+Xe and Pb+Pb are still consistent within statistical and systematic uncertainties. The black line again represents the results after applying the additional smearing, but now for the $\Sigma E_{\mathrm{T}}^{\mathrm{FCal}}$ intervals. These result also doesn't deviate systematically from the Xe+Xe results.

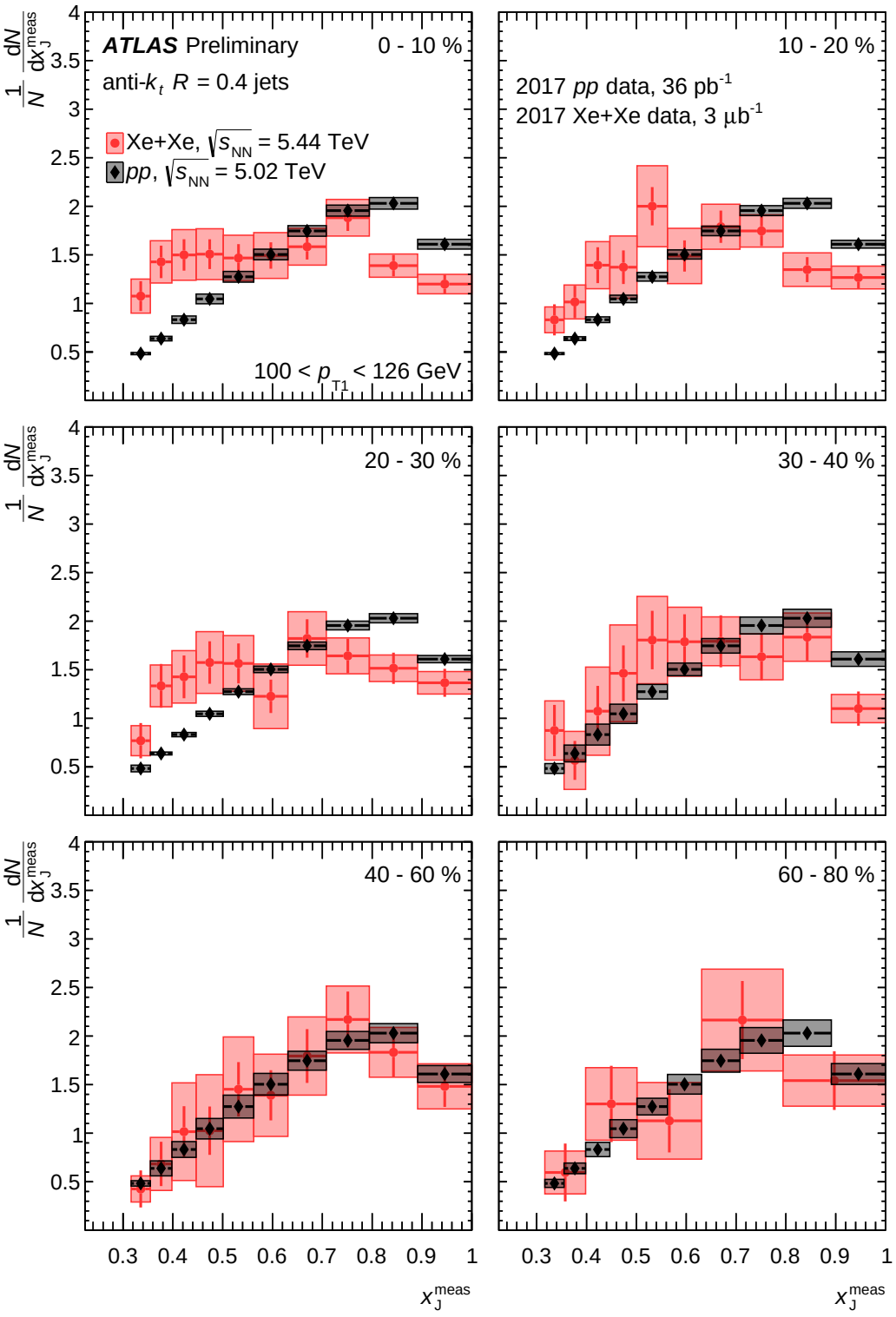

Figure 7.17: Xe+Xe and pp dijet $x_{\mathrm{J}}^{\mathrm{meas}}$ distributions for $100 < p_{\mathrm{T}}^{\mathrm{lead}} < 126$ GeV in the different collision centrality intervals used in this analysis.

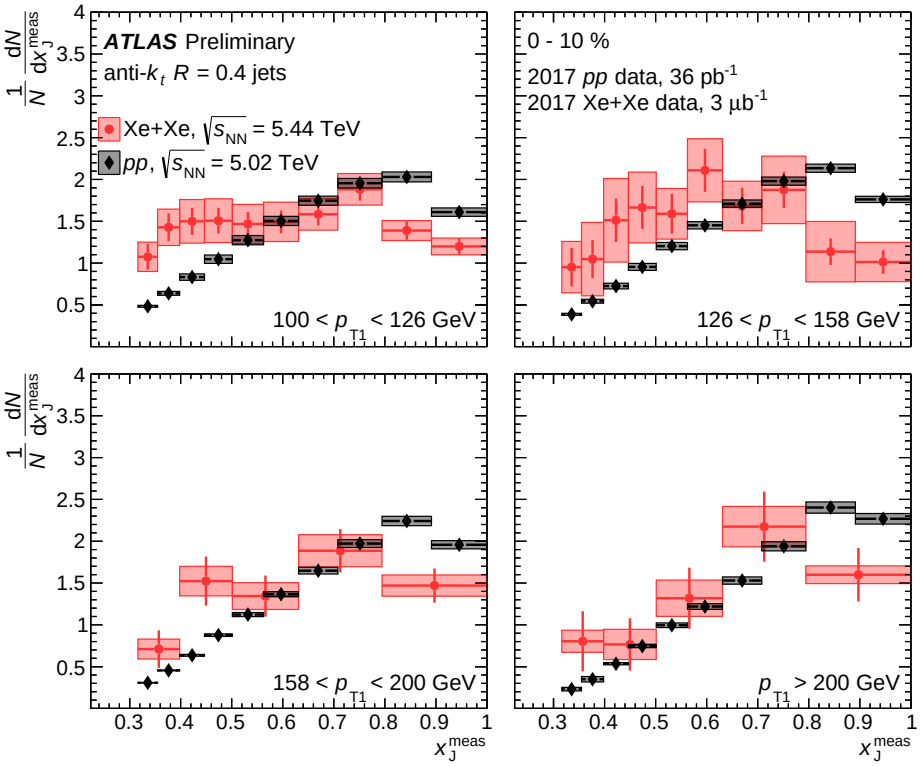

Figure 7.18: Xe+Xe and pp dijet $x_{\mathrm{J}}^{\mathrm{meas}}$ distribution in different $p_{\mathrm{T}}^{\mathrm{lead}}$ intervals for the 0–10% centrality interval.

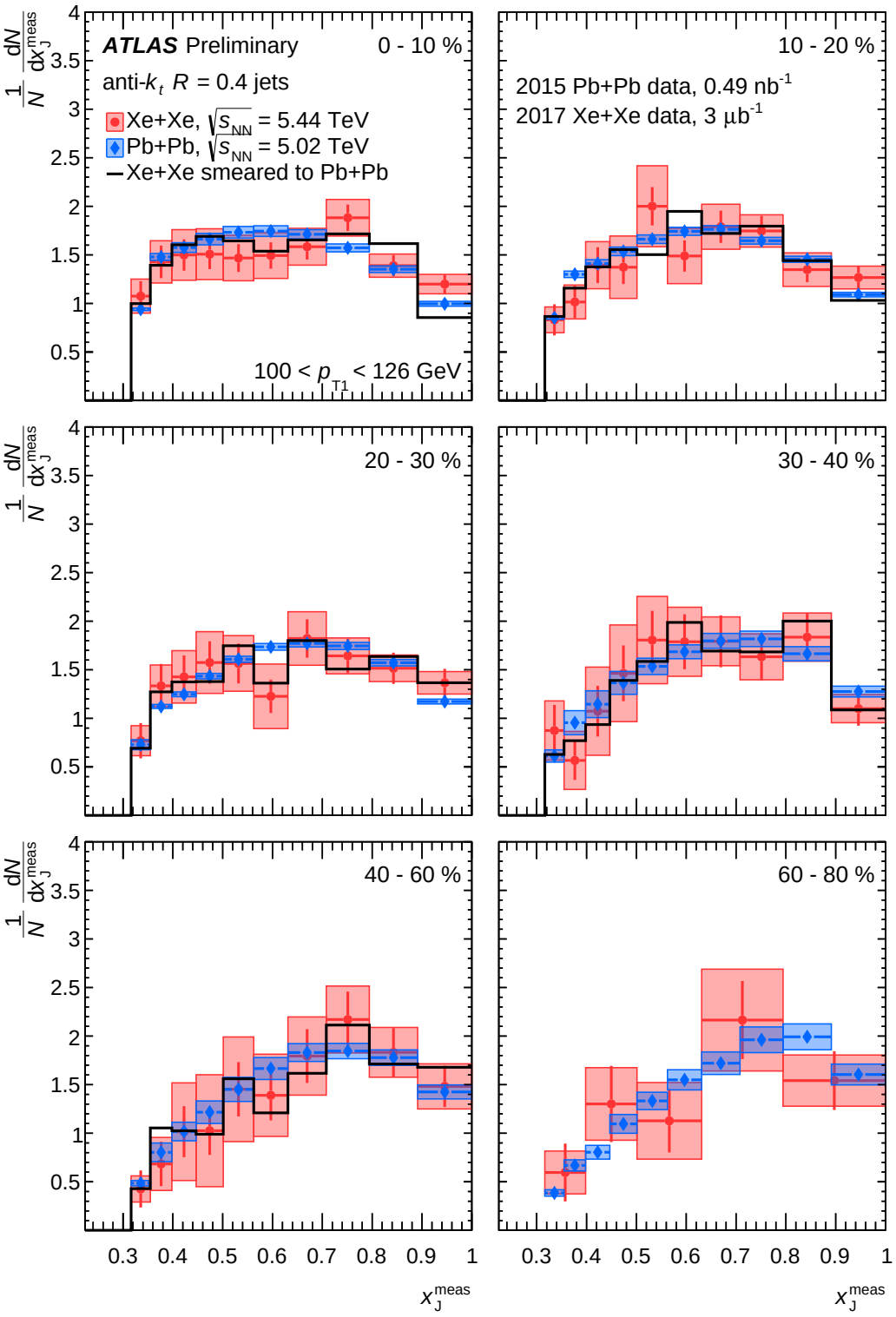

Figure 7.19: Xe+Xe and Pb+Pb dijet $x_{\mathrm{J}}^{\mathrm{meas}}$ distributions for $100 < p_{\mathrm{T}}^{\mathrm{lead}} < 126$ GeV in the different collision centrality intervals used in this analysis. The black line represents the results after applying the additional smearing.

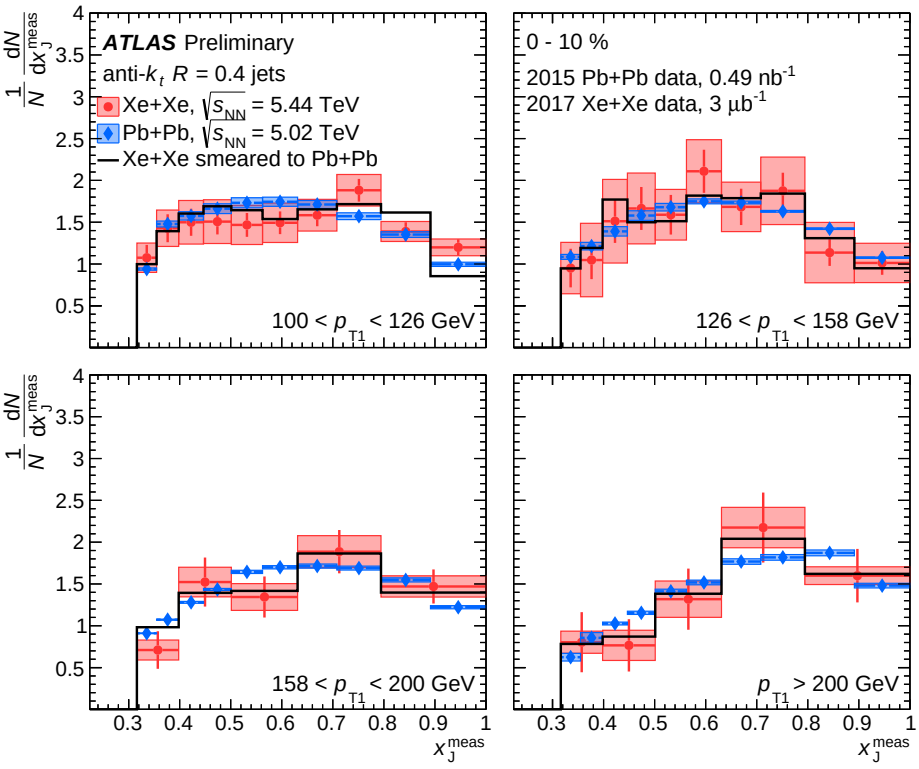

Figure 7.20: Xe+Xe and Pb+Pb dijet $x_{\mathrm{J}}^{\mathrm{meas}}$ distribution in different $p_{\mathrm{T}}^{\mathrm{lead}}$ intervals for the 0–10% centrality interval. The black line represents the results after applying the additional smearing.

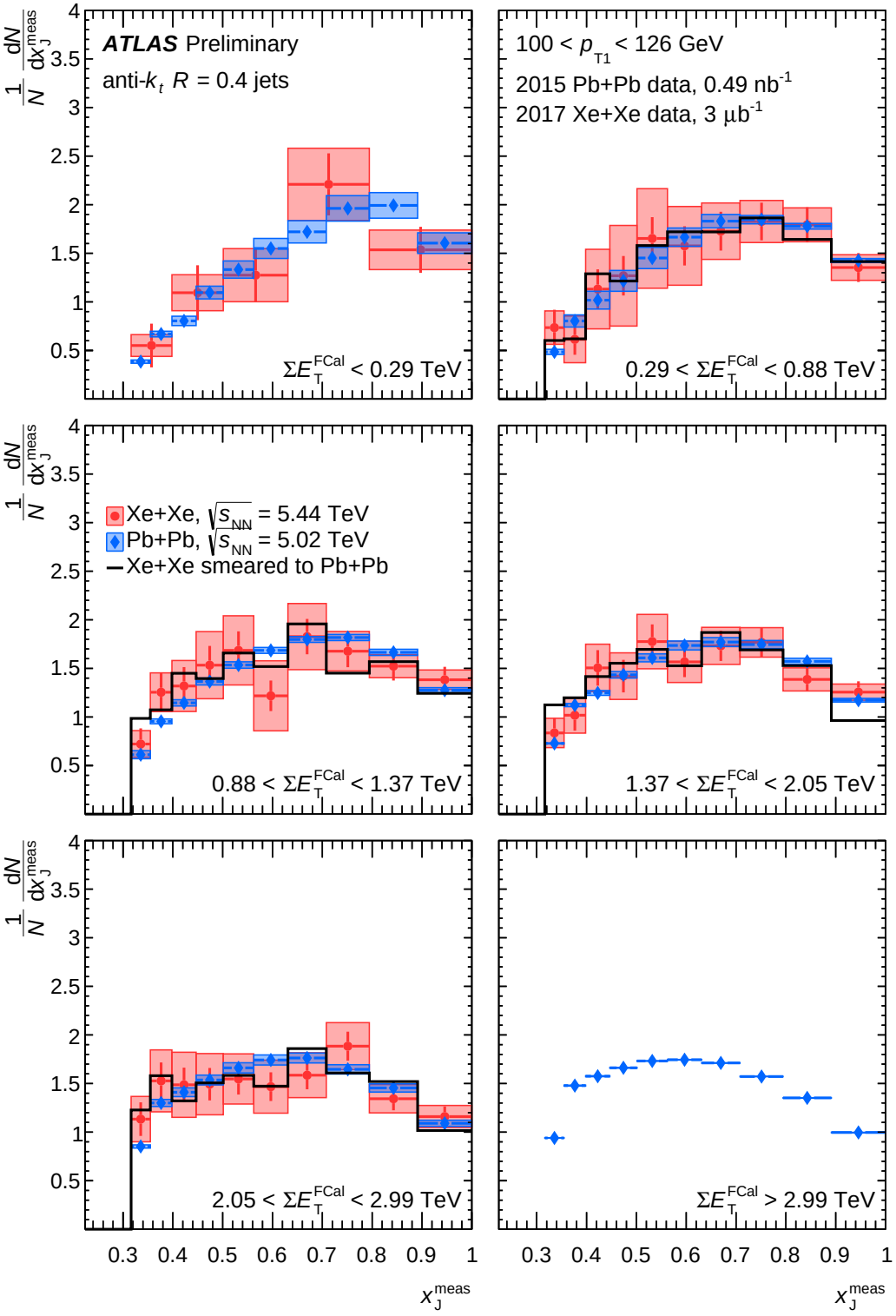

Figure 7.21: Xe+Xe and Pb+Pb dijet $x_{\mathrm{J}}^{\mathrm{meas}}$ distributions for $100 < p_{\mathrm{T}}^{\mathrm{lead}} < 126$ GeV in the same $\Sigma E_{\mathrm{T}}^{\mathrm{FCal}}$ (obtained from the Pb+Pb defined centrality bins). The black line represents the results after applying the additional smearing.

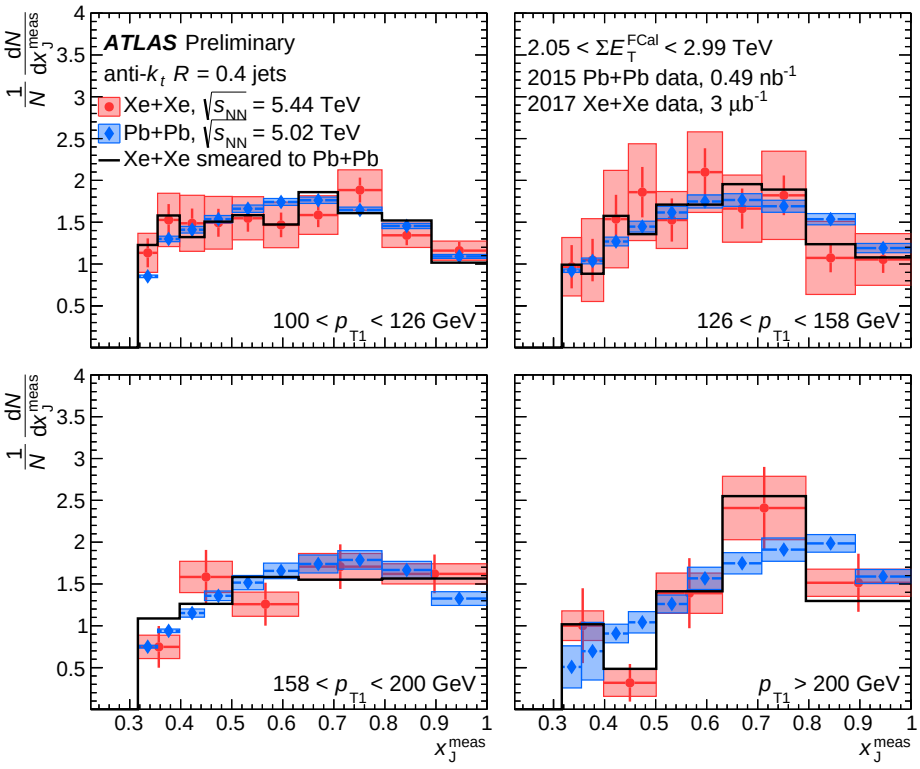

Figure 7.22: Xe+Xe and Pb+Pb dijet $x_{\mathrm{J}}^{\mathrm{meas}}$ distribution in different $p_{\mathrm{T}}^{\mathrm{lead}}$ intervals for $2.05 < \Sigma E_{\mathrm{T}}^{\mathrm{FCal}} < 2.99$ TeV. The black line represents the results after applying the additional smearing.

Chapter 8

Conclusions

This thesis presented precision measurements of jet suppression and imbalance in relativistic heavy ion collisions with the ATLAS detector. All the measurements presented here take advantage of increased statistics and improved measurement techniques to build upon previous measurements of jet quenching. Specifically, the measurements emphasize unfolding techniques to remove the detector effects such that the results can be compared directly to theoretical models of jet quenching. As discussed in Section 2.5.1, there are many mechanisms for jet energy loss that are expected to contribute in different kinematic regimes and have different dependencies on jet and medium parameters, which are modeled through a wealth of theoretical frameworks (Section 2.5.2). These models need to be constrained in order to understand the mechanisms behind energy loss. The higher statistics measurements not only provide better measurements with reduced uncertainties, but also allow for more differential measurements in the jet kinematics. Energy loss depends on various parameters of the jets and the medium like the flavor, path length, and medium density that can be probed through differential measurements in the jet p_{T}, rapidity, and even the collision system size (Section 2.5.3).

Inclusive jet suppression addresses the question of how single jets lose energy in the medium on average. In this thesis, jet suppression was measured through the nuclear modification factor (R_{AA}) in Pb+Pb collisions at $\sqrt{s_{\mathrm{NN}}} = 5.02$ TeV. This measurement improved upon a previous measurement of the R_{AA} at $\sqrt{s_{\mathrm{NN}}} = 2.76$ TeV through increased statistics that allowed the R_{AA} to be measured out to a TeV in jet p_{T} and more differential

in jet p_{T} and rapidity. It is also benefited from a significant reduction in the systematic uncertainties. The R_{AA} as a function of p_{T} was compared to the R_{AA} at $\sqrt{s_{\mathrm{NN}}} = 2.76$ TeV, where it was shown to be consistent within uncertainties in central and peripheral collisions, but with significantly reduced uncertainties and a further reach in jet p_{T}. This indicates that jet suppression is independent of the center-of-mass of the collisions over a narrow range. The R_{AA} was seen to be less than unity in all centrality intervals. In the most peripheral interval $R_{\mathrm{AA}} \approx 0.9$, while in the most central interval $R_{\mathrm{AA}} \approx 0.6$. This was found to be consistent with radiative energy loss with an $\epsilon_{\mathrm{loss}} \approx 0.097$ for central collisions and an $\epsilon_{\mathrm{loss}} \approx 0.021$ for peripheral collisions, meaning that jets loss approximately 10% of their energy in central collisions and 2% in peripheral collisions.

The R_{AA} was found to have a slight p_{T} dependence. It slowly increases before leveling off at high p_{T}, with significant suppresion still present out to TeV. This might be explained through different models of energy loss where some predict a logarithmic dependence on parton energy (collisional and radiative e-loss, DGLV) and some predict no dependence on parton energy (strong coupling e-loss, BDMPS-Z). Also, radiative energy loss predicts both dependencies in different kinematic regimes. This could also be explained by the EQ model, where the energy loss is no longer fractional with jet p_{T} but increases slower than linearly with jet p_{T} which would cause the R_{AA} to increase with jet p_{T}. This model also incorporates a jet p_{T} dependence to the power law distribution which causes the spectra to become steeper at high jet p_{T} and would cause the R_{AA} to decrease with jet p_{T}. These two effects could cancel resulting in a R_{AA} that flattens at high p_{T}. The R_{AA} was also compared to various jet quenching models in central collisions, which can help understand the p_{T} dependence and magnitude of the suppression. It was found that both the LBT and SCET$_G$ models describe the overall magnitude of the suppression fairly well, but the LBT model best describes the high p_{T} behavior and the SCET$_G$ model best describes the low p_{T} behavior. In general, the models may not describe the full p_{T} dependence because, as shown in the EQ model, the R_{AA} depends significantly on the definition of the steeply falling nature of the p_{T} spectra and the treatment of the flavor dependence of energy loss. The flavor dependence of energy loss was probed by looking at the dependence of the R_{AA} on rapidity. There are two competing effects here: the high quark fraction at forward rapidity

and the steeper spectra at forward rapidity. The R_{AA} was found to decrease with rapidity at high p_{T}, which is probably caused by the steepness of the spectrum. This is the first to measurement of the rapidity dependence of the R_{AA} with enough statistics to see an effect and the first measurement to reach a TeV in jet energy.

Relative energy loss is investigated through measurements of jet correlations. In this thesis, the jet imbalance was measured using the variable x_{J} in Pb+Pb and pp collisions at $\sqrt{s_{\mathrm{NN}}} = 2.76$ TeV and 5.02 TeV and in Xe+Xe collisions at 5.44 TeV. The $\sqrt{s_{\mathrm{NN}}} = 2.76$ TeV measurement is an improvement on the first measurement of the dijet asymmetry by ATLAS due to the increased statistics and the comparison to pp collisions at the same center-of-mass energy. Also, a full background subtraction for the UE effects was implemented and the results were unfolded for detector effects. The x_{J} distribution was shown to change significantly before and after unfolding, where a peak-like feature in central Pb+Pb collisions was revealed once smearing from the resolution was removed. This peak indicates that the most probable value for central Pb+Pb collisions is at $x_{\mathrm{J}} \approx 0.5$. In contrast, in pp collisions the most probable configuration is at $x_{\mathrm{J}} \approx 1$, which is expected since pp dijets should be mostly balanced. The centrality dependence of the x_{J} distribution demonstrated that the Pb+Pb dijets were most asymmetric in central collisions and became like the pp dijets in peripheral collisions. The peripheral Pb+Pb isn't expected to be exactly like pp since the R_{AA} is less than unity for peripheral collisions indicating that some energy loss still occurs.

The leading jet p_{T} dependence showed a drastic $p_{\mathrm{T_1}}$ dependence to the x_{J} distribution where the Pb+Pb dijets became like the pp dijets at high p_{T}. This does not contradict the R_{AA} result that demonstrated that the jets are still significantly suppressed at high p_{T} because x_{J} measures relative energy loss. Both of the jets still lost energy, they just lost approximately the same amount of energy at high $p_{\mathrm{T_1}}$. The $p_{\mathrm{T_1}}$ dependence can be attributed to the changing flavor composition of the pairs, where potentially the distribution is dominated by qg pairs a lower p_{T} which should have the most imbalance but then quickly changes to qq pairs at higher p_{T} which should be more balanced. This drastic $p_{\mathrm{T_1}}$ dependence and peak structure can be further investigated by comparing to theoretical models. One comparision (BDMPS-Z with Sudakov resummation) was shown to describe the high $p_{\mathrm{T_1}}$ intervals, but not the lowest $p_{\mathrm{T_1}}$ interval where the peak at $x_{\mathrm{J}} \sim 0.5$ is the

most prominent.

Despite the desire to have the fully unfolded result to compare directly to theoretical models, most of the models are still comparing to uncorrected data that have detector effects, which does not allow for detailed quantitive comparisons. Therefore, theoretical models are encouraged to compare to these unfolded results. It has been suggested that the reason these comparisons haven't been made is that the models have difficulties getting the shape of the peak as well as the drastic leading jet p_{T_1} dependence. This could be due to an incorrect dependence on the flavor since the flavor composition could be different in the lower p_{T_1} interval. It could also indicate that other energy loss mechanisms like collisional energy loss or strongly coupled energy loss are needed at lower p_{T}. The strongly coupled energy loss could be particularly useful because it predicts a cubic dependence on the path length, although it also predicts less dependence on the flavor and no dependence on the initial parton energy. The lack of agreement with these results could also indicate that our understanding of the path length dependence of the energy loss is either flawed or too simple. The fluctuations in the medium and the energy mechanisms could instead be the dominate effect here.

Finally, the collision system and path length dependence of energy loss was probed by looking at the jet imbalance in a different collision system. An analysis of the dijet asymmetry in Xe+Xe collisions at $\sqrt{s_{\mathrm{NN}}} = 5.44$ TeV was compared to pp and Pb+Pb collisions at 5.02 TeV. The different mass numbers for Xe_{129} and Pb_{208} indicate that the medium produced in Xe+Xe collisions will have a lower medium density and path length than in Pb+Pb collisions. This should result in less energy loss in Xe+Xe than in Pb+Pb collisions. The x_{J} distributions were first compared between Xe+Xe and Pb+Pb collisions as a function of centrality. At a fixed value of the centrality (or fixed geometry) the $\Sigma E_{\mathrm{T}}^{\mathrm{FCal}}$ and N_{part} values (and thus the density) and the path length should be different between the two collision systems. This should result in the Xe+Xe being more symmetric than the Pb+Pb pairs, but the Xe+Xe and Pb+Pb data were shown to have comparable x_{J} distributions at all values of centrality and p_{T_1} within the measurement uncertainties. This again suggests that the path length dependence is not the dominant effect in jet energy loss. More statistics for the Xe+Xe collisions or a smaller system size would be useful

to understand the lack of a system-size dependence in this result. The x_{J} distributions were also compared between Xe+Xe and Pb+Pb collisions at a fixed value of $\Sigma E_{\mathrm{T}}^{\mathrm{FCal}}$ (or N_{part}). This is a comparison of the geometry of the collision since at a fixed value of N_{part} the Xe+Xe collisions will be more "central" than the Pb+Pb collisions. It was seen, once again, that there is no significant difference between the Xe+Xe and Pb+Pb collisions in any p_{T_1} or $\Sigma E_{\mathrm{T}}^{\mathrm{FCal}}$ intervals within the measurement uncertainties.

The Xe+Xe analysis was not unfolded for detector effects so the next step in this measurement is to unfold the Pb+Pb and Xe+Xe x_{J} distributions to remove the effect of the detector resolution. This should allow for a more direct comparison and also could reduce the systematic uncertainties. This is also useful because x_{J} distributions could be compared directly to theoretical predictions. The unfolded Pb+Pb results will be particularly useful for further model comparisons because of the reduced systematic and statistical uncertainties at 5.02 TeV from the previous measurement at 2.76 TeV.

In general, the measurements presented in this thesis have contributed to our understanding jet energy loss through differential studies in the jet kinematics that allow the flavor and p_{T} dependence of energy loss to be probed. The dijet asymmetry measurements also further our understanding of the medium density and path length dependence of energy loss. These results are part of a new era of precision jet quenching measurements that allow for detailed comparisons to theoretical models and other experiments due careful unfolding and reduced uncertainties.

In the future, the higher statistics data that will be taken in 2018 and during Run 3 will allow for more precision measurements of jet quenching to be performed. The careful unfolding performed here will allow for comparisons to other experiments, especially to sPHENIX [241], which is the next generation HI detector at RHIC. sPHENIX will measure fully reconstructed jets at lower energies which, when combined with LHC results at higher p_{T}, allow for a more complete understanding of energy loss over the full jet p_{T} spectrum. These precision results are also useful for comparisons using JETSCAPE (Jet Energy-loss Tomography with a Statistically and Computationally Advanced Program Envelope) [242], which is a theoretical framework designed to model the full evolution of a HI collision including multiple models of jet energy loss. JETSCAPE is designed to be very usable for

a non-expert and contains advanced statistical tools that allow for detailed comparisons between experiment and theory. Also, it has been proposed to collide oxygen ions during the 2018 data-taking period which will be useful for understanding the xenon and lead results since oxygen (A=16) will produce a much smaller system.

Finally, the missing piece of the puzzle for a complete picture of jet quenching from this thesis is jet substructure measurements. The medium is expected to modify the internal structure of the jet as the jet moves through the plasma. The different theoretical models have different predictions for the modification of the internal structure and thus combined with the inclusive and relative energy loss calculations can help constrain the models even more. It is also useful to understand what actually happens to the constituents of the jet as it moves through the plasma because this can shine light into how the partons and the medium interact. Many measurements of this have already been performed, for example measurements of the jet shape [243], jet mass [244] and FFs [229, 245, 246] with ATLAS and jet splitting functions and other related substructure variables with ALICE and CMS [247]. It will be useful to perform additional substructure measurements with ATLAS at higher statistics and using the unfolding techniques from Section 4.6 so the results can be compared to theory.

Bibliography

[1] ATLAS Collaboration, *Observation of a Centrality-Dependent Dijet Asymmetry in Lead-Lead Collisions at* $\sqrt{s_{NN}} = 2.77$ *TeV with the ATLAS Detector at the LHC*, Phys. Rev. Lett. **105** (2010) 252303, arXiv:1011.6182 [hep-ex].

[2] ATLAS Collaboration, *Measurement of jet* p_{T} *correlations in Pb+Pb and pp collisions at* $\sqrt{s_{\mathrm{NN}}} = 2.76$ *TeV with the ATLAS detector*, Phys. Lett. **B774** (2017) 379–402, arXiv:1706.09363 [hep-ex].

[3] ATLAS Collaboration, *Some Interesting Events from Lead-Lead Collisions in ATLAS at the LHC (individual captions in abstract)*, Nov, 2010.

[4] ATLAS Collaboration, *Measurement of the azimuthal anisotropy of charged particle production in Xe+Xe collisions at* $\sqrt{s_{\mathrm{NN}}}$*=5.44 TeV with the ATLAS detector*, Tech. Rep. ATLAS-CONF-2018-011, CERN, Geneva, May, 2018. http://cds.cern.ch/record/2318870.

[5] ATLAS Collaboration, *Measurements of the Nuclear Modification Factor for Jets in Pb+Pb Collisions at* $\sqrt{s_{\mathrm{NN}}} = 2.76$ *TeV with the ATLAS Detector*, Phys. Rev. Lett. **114** (2015) 072302, arXiv:1411.2357 [hep-ex].

[6] ATLAS Collaboration, *Measurement of the nuclear modification factor for inclusive jets in Pb+Pb collisions at* $\sqrt{s_{\mathrm{NN}}} = 5.02$ *TeV with the ATLAS detector*, arXiv:1805.05635 [nucl-ex].

[7] C. N. Yang and R. L. Mills, *Conservation of Isotopic Spin and Isotopic Gauge Invariance*, Phys. Rev. **96** (1954) 191–195.

[8] C. Patrignani et al. (Particle Data Group), *Review of Particle Physics*, Chin. Phys. **C40** (2016) 100001.

[9] M. E. Peskin and D. V. Schroeder, *An Introduction to quantum field theory*. Addison-Wesley, Reading, USA, 1995. http://www.slac.stanford.edu/~mpeskin/QFT.html.

[10] M. L. Mangano, *Introduction to QCD*. No. CERN-OPEN-2000-255. 1999. https://cds.cern.ch/record/454171.

[11] R. K. Ellis and W. J. Stirling, *QCD and collider physics*. 1992. http://lss.fnal.gov/cgi-bin/find_paper.pl?conf-90-164.

[12] G. S. Bali, *QCD forces and heavy quark bound states*, Phys. Rept. **343** (2001) 1–136, arXiv:hep-ph/0001312 [hep-ph].

[13] Y. Sumino, *QCD potential as a 'Coulomb plus linear' potential*, Phys. Lett. **B571** (2003) 173–183, arXiv:hep-ph/0303120 [hep-ph].

[14] E. Eichten, K. Gottfried, T. Kinoshita, J. B. Kogut, K. D. Lane, and T.-M. Yan, *The Spectrum of Charmonium*, Phys. Rev. Lett. **34** (1975) 369–372.

[15] A. Laschka, N. Kaiser, and W. Weise, *Quark-antiquark potential to order 1/m and heavy quark masses*, Phys. Rev. **D83** (2011) 094002, arXiv:1102.0945 [hep-ph].

[16] TXL, T(X)L Collaboration, G. S. Bali, B. Bolder, N. Eicker, T. Lippert, B. Orth, P. Ueberholz, K. Schilling, and T. Struckmann, *Static potentials and glueball masses from QCD simulations with Wilson sea quarks*, Phys. Rev. **D62** (2000) 054503, arXiv:hep-lat/0003012 [hep-lat].

[17] G. M. Prosperi, M. Raciti, and C. Simolo, *On the running coupling constant in QCD*, Prog. Part. Nucl. Phys. **58** (2007) 387–438, arXiv:hep-ph/0607209 [hep-ph].

[18] H. D. Politzer, *Reliable Perturbative Results for Strong Interactions?*, Phys. Rev. Lett. **30** (1973) 1346–1349.

[19] D. J. Gross and F. Wilczek, *Ultraviolet Behavior of Nonabelian Gauge Theories*, Phys. Rev. Lett. **30** (1973) 1343–1346.

[20] K. G. Wilson, *Confinement of Quarks*, Phys. Rev. **D10** (1974) 2445–2459.

[21] J. Casalderrey-Solana, H. Liu, D. Mateos, K. Rajagopal, and U. A. Wiedemann, *Gauge/String Duality, Hot QCD and Heavy Ion Collisions*. 2011. arXiv:1101.0618 [hep-th].

[22] J. M. Maldacena, *The Large N limit of superconformal field theories and supergravity*, Int. J. Theor. Phys. **38** (1999) 1113–1133, arXiv:hep-th/9711200 [hep-th].

[23] E. Witten, *Anti-de Sitter space and holography*, Adv. Theor. Math. Phys. **2** (1998) 253–291, arXiv:hep-th/9802150 [hep-th].

[24] P. Colangelo and A. Khodjamirian, *QCD sum rules, a modern perspective*, arXiv:hep-ph/0010175 [hep-ph].

[25] Y. Nambu and G. Jona-Lasinio, *Dynamical Model of Elementary Particles Based on an Analogy with Superconductivity. 1.*, Phys. Rev. **122** (1961) 345–358.

[26] Y. Nambu and G. Jona-Lasinio, *Dynamical Model of Elementary Particles Based on an Analogy with Superconductivity. II*, Phys. Rev. **124** (1961) 246–254.

[27] J. Gasser and H. Leutwyler, *Chiral Perturbation Theory to One Loop*, Annals Phys. **158** (1984) 142.

[28] C. W. Bauer, S. Fleming, D. Pirjol, and I. W. Stewart, *An Effective field theory for collinear and soft gluons: Heavy to light decays*, Phys. Rev. **D63** (2001) 114020, arXiv:hep-ph/0011336 [hep-ph].

[29] R. Gupta, *Introduction to lattice QCD: Course*. 1997. arXiv:hep-lat/9807028 [hep-lat].

[30] H. B. Nielsen and M. Ninomiya, *Absence of Neutrinos on a Lattice. 1. Proof by Homotopy Theory*, Nucl. Phys. **B185** (1981) 20.

[31] H. B. Nielsen and M. Ninomiya, *No Go Theorem for Regularizing Chiral Fermions*, Phys. Lett. **105B** (1981) 219–223.

[32] CTEQ Collaboration, R. Brock et al., *Handbook of perturbative QCD: Version 1.0*, Rev. Mod. Phys. **67** (1995) 157–248.

[33] A. S. Kronfeld and C. Quigg, *Resource Letter: Quantum Chromodynamics*, Am. J. Phys. **78** (2010) 1081–1116, arXiv:1002.5032 [hep-ph].

[34] D. E. Soper, *Basics of QCD perturbation theory*, arXiv:hep-ph/0011256 [hep-ph].

[35] J. C. Collins, D. E. Soper, and G. F. Sterman, *Factorization of Hard Processes in QCD*, Adv. Ser. Direct. High Energy Phys. **5** (1989) 1–91, arXiv:hep-ph/0409313 [hep-ph].

[36] G. Altarelli and G. Parisi, *Asymptotic Freedom in Parton Language*, Nucl. Phys. **B126** (1977) 298–318.

[37] Y. L. Dokshitzer, *Calculation of the Structure Functions for Deep Inelastic Scattering and e+ e- Annihilation by Perturbation Theory in Quantum Chromodynamics.*, Sov. Phys. JETP **46** (1977) 641–653.

[38] V. N. Gribov and L. N. Lipatov, *Deep inelastic e p scattering in perturbation theory*, Sov. J. Nucl. Phys. **15** (1972) 438–450.

[39] S. Moch, *Expectations at LHC from hard QCD*, J. Phys. **G35** (2008) 073001, arXiv:0803.0457 [hep-ph].

[40] L. A. Harland-Lang, A. D. Martin, P. Motylinski, and R. S. Thorne, *Parton distributions in the LHC era: MMHT 2014 PDFs*, Eur. Phys. J. **C75** (2015) 204, arXiv:1412.3989 [hep-ph].

[41] NNPDF Collaboration, R. D. Ball et al., *Parton distributions for the LHC Run II*, JHEP **04** (2015) 040, arXiv:1410.8849 [hep-ph].

[42] S. Dulat, T.-J. Hou, J. Gao, M. Guzzi, J. Huston, P. Nadolsky, J. Pumplin, C. Schmidt, D. Stump, and C. P. Yuan, *New parton distribution functions from a*

global analysis of quantum chromodynamics, Phys. Rev. **D93** (2016) 033006, arXiv:1506.07443 [hep-ph].

[43] ZEUS, H1 Collaboration, H. Abramowicz et al., *Combination of measurements of inclusive deep inelastic $e^{\pm}p$ scattering cross sections and QCD analysis of HERA data*, Eur. Phys. J. **C75** (2015) 580, arXiv:1506.06042 [hep-ex].

[44] S. Alekhin, J. Blumlein, S. Klein, and S. Moch, *The 3, 4, and 5-flavor NNLO Parton from Deep-Inelastic-Scattering Data and at Hadron Colliders*, Phys. Rev. **D81** (2010) 014032, arXiv:0908.2766 [hep-ph].

[45] M. Gluck, P. Jimenez-Delgado, and E. Reya, *Dynamical parton distributions of the nucleon and very small-x physics*, Eur. Phys. J. **C53** (2008) 355–366, arXiv:0709.0614 [hep-ph].

[46] NNPDF Collaboration, R. D. Ball et al., *Parton distributions from high-precision collider data*, Eur. Phys. J. **C77** (2017) 663, arXiv:1706.00428 [hep-ph].

[47] D. Jorrin, N. Kovensky, and M. Schvellinger, *Towards 1/N corrections to deep inelastic scattering from the gauge/gravity duality*, JHEP **04** (2016) 113, arXiv:1601.01627 [hep-th].

[48] E. D. Bloom, D. H. Coward, H. DeStaebler, J. Drees, G. Miller, L. W. Mo, R. E. Taylor, M. Breidenbach, J. I. Friedman, G. C. Hartmann, and H. W. Kendall, *High-Energy Inelastic $e-p$ Scattering at 6 degrees and 10 degrees*, Phys. Rev. Lett. **23** (1969) 930–934.

[49] J. I. Friedman and H. W. Kendall, *Deep inelastic electron scattering*, Ann. Rev. Nucl. Part. Sci. **22** (1972) 203–254.

[50] J. D. Bjorken and E. A. Paschos, *Inelastic Electron-Proton and γ-Proton Scattering and the Structure of the Nucleon*, Phys. Rev. **185** (1969) 1975–1982.

[51] B. R. Webber, *Fragmentation and hadronization*, Int. J. Mod. Phys. **A15S1** (2000) 577–606, arXiv:hep-ph/9912292 [hep-ph].

[52] A. Ali and G. Kramer, *Jets and QCD: A Historical Review of the Discovery of the Quark and Gluon Jets and its Impact on QCD*, Eur. Phys. J. **H36** (2011) 245–326, arXiv:1012.2288 [hep-ph].

[53] Y. L. Dokshitzer, V. A. Khoze, A. H. Mueller, and S. I. Troian, *Basics of perturbative QCD*. 1991.

[54] J. Casalderrey-Solana, Y. Mehtar-Tani, C. A. Salgado, and K. Tywoniuk, *New picture of jet quenching dictated by color coherence*, Phys. Lett. **B725** (2013) 357–360, arXiv:1210.7765 [hep-ph].

[55] Y. L. Dokshitzer, V. A. Khoze, and S. I. Troian, *Inclusive particle spectra from QCD cascades*, Int. J. Mod. Phys. **A7** (1992) 1875–1906.

[56] A. H. Mueller, *Multiplicity and Hadron Distributions in QCD Jets: Nonleading Terms*, Nucl. Phys. **B213** (1983) 85–108.

[57] B. R. Webber, *Hadronization*, arXiv:hep-ph/9411384 [hep-ph].

[58] D. Amati and G. Veneziano, *Preconfinement as a Property of Perturbative QCD*, Phys. Lett. **83B** (1979) 87–92.

[59] D. d'Enterria, *Jet quenching*, Landolt-Bornstein **23** (2010) 471, arXiv:0902.2011 [nucl-ex].

[60] G. P. Salam, *Towards Jetography*, Eur. Phys. J. **C67** (2010) 637–686, arXiv:0906.1833 [hep-ph].

[61] D. Yu. Grigoriev, E. Jankowski, and F. V. Tkachov, *Towards a standard jet definition*, Phys. Rev. Lett. **91** (2003) 061801, arXiv:hep-ph/0301185 [hep-ph].

[62] S. D. Ellis and D. E. Soper, *Successive combination jet algorithm for hadron collisions*, Phys. Rev. **D48** (1993) 3160–3166, arXiv:hep-ph/9305266 [hep-ph].

[63] M. Cacciari, G. P. Salam, and G. Soyez, *The anti-k_t jet clustering algorithm*, JHEP **04** (2008) 063, arXiv:0802.1189 [hep-ph].

[64] Y. L. Dokshitzer, G. D. Leder, S. Moretti, and B. R. Webber, *Better jet clustering algorithms*, JHEP **08** (1997) 001, arXiv:hep-ph/9707323 [hep-ph].

[65] M. Cacciari, G. P. Salam, and G. Soyez, *FastJet User Manual*, Eur. Phys. J. **C72** (2012) 1896, arXiv:1111.6097 [hep-ph].

[66] U. A. Wiedemann, *Jet Quenching in Heavy Ion Collisions*. 2010. arXiv:0908.2306 [hep-ph].

[67] K. C. Zapp, *Monte Carlo simulations of jet quenching in heavy ion collisions*, Nucl. Phys. **A855** (2011) 60–66, arXiv:1012.0177 [hep-ph].

[68] T. Sjostrand, S. Mrenna, and P. Z. Skands, *PYTHIA 6.4 Physics and Manual*, JHEP **05** (2006) 026, arXiv:hep-ph/0603175 [hep-ph].

[69] G. Corcella, I. G. Knowles, G. Marchesini, S. Moretti, K. Odagiri, P. Richardson, M. H. Seymour, and B. R. Webber, *HERWIG 6.5 release note*, arXiv:hep-ph/0210213 [hep-ph].

[70] M. Bahr et al., *Herwig++ Physics and Manual*, Eur. Phys. J. **C58** (2008) 639–707, arXiv:0803.0883 [hep-ph].

[71] T. Gleisberg, S. Hoeche, F. Krauss, M. Schonherr, S. Schumann, F. Siegert, and J. Winter, *Event generation with SHERPA 1.1*, JHEP **02** (2009) 007, arXiv:0811.4622 [hep-ph].

[72] P. Nason, *A New method for combining NLO QCD with shower Monte Carlo algorithms*, JHEP **11** (2004) 040, arXiv:hep-ph/0409146 [hep-ph].

[73] J. C. Collins, *Sudakov form-factors*, Adv. Ser. Direct. High Energy Phys. **5** (1989) 573–614, arXiv:hep-ph/0312336 [hep-ph].

[74] T. Sjostrand, S. Mrenna, and P. Z. Skands, *A Brief Introduction to PYTHIA 8.1*, Comput. Phys. Commun. **178** (2008) 852–867, arXiv:0710.3820 [hep-ph].

[75] E. V. Shuryak, *Quantum Chromodynamics and the Theory of Superdense Matter*, Phys. Rept. **61** (1980) 71–158.

[76] HotQCD Collaboration, A. Bazavov et al., *Equation of state in (2+1)-flavor QCD*, Phys. Rev. **D90** (2014) 094503, arXiv:1407.6387 [hep-lat].

[77] J. I. Kapusta, *Quark - gluon plasma in the early universe*, arXiv:astro-ph/0101516 [astro-ph].

[78] C. Schmidt, F. Karsch, and E. Laermann, *The Chiral critical point in 3 flavor QCD*, Nucl. Phys. Proc. Suppl. **106** (2002) 423–425, arXiv:hep-lat/0110039 [hep-lat].

[79] Y. Aoki, G. Endrodi, Z. Fodor, S. D. Katz, and K. K. Szabo, *The Order of the quantum chromodynamics transition predicted by the standard model of particle physics*, Nature **443** (2006) 675–678, arXiv:hep-lat/0611014 [hep-lat].

[80] M. Cheng et al., *Baryon Number, Strangeness and Electric Charge Fluctuations in QCD at High Temperature*, Phys. Rev. **D79** (2009) 074505, arXiv:0811.1006 [hep-lat].

[81] S. Ejiri, *Canonical partition function and finite density phase transition in lattice QCD*, Phys. Rev. **D78** (2008) 074507, arXiv:0804.3227 [hep-lat].

[82] E. S. Bowman and J. I. Kapusta, *Critical Points in the Linear Sigma Model with Quarks*, Phys. Rev. **C79** (2009) 015202, arXiv:0810.0042 [nucl-th].

[83] STAR Collaboration, *STAR Note 0598: BES-II whitepaper: Studying the phase diagram of QCD matter with RHIC*, http://drupal.star.bnl.gov/STAR/starnotes/public/sn0598.

[84] PHENIX Collaboration, *Beam Energy Scan II (2018-2019) PHENIX collaboration white paper*, https://www.phenix.bnl.gov/phenix/WWW/publish/dave/sPHENIX/BES_II_whitepaper.pdf.

[85] A. Chodos, R. L. Jaffe, K. Johnson, C. B. Thorn, and V. F. Weisskopf, *A New Extended Model of Hadrons*, Phys. Rev. **D9** (1974) 3471–3495.

[86] C. Y. Wong, *Introduction to high-energy heavy ion collisions*. 1995.

[87] H. C. Chandola, G. Punetha, and H. Dehnen, *Dual QCD thermodynamics and quarkgluon plasma*, Nucl. Phys. **A945** (2016) 226–247.

[88] A. Bazavov et al., *Equation of state and QCD transition at finite temperature*, Phys. Rev. **D80** (2009) 014504, arXiv:0903.4379 [hep-lat].

[89] A. Bazavov, *Lattice QCD at Non-Zero Temperature*, arXiv:1505.05543 [hep-lat].

[90] Evans, Lyndon and Bryant, Philip, *LHC Machine*, JINST **3** (2008) S08001.

[91] J. D. Bjorken, *Highly Relativistic Nucleus-Nucleus Collisions: The Central Rapidity Region*, Phys. Rev. **D27** (1983) 140–151.

[92] F. Gelis, E. Iancu, J. Jalilian-Marian, and R. Venugopalan, *The Color Glass Condensate*, Ann. Rev. Nucl. Part. Sci. **60** (2010) 463–489, arXiv:1002.0333 [hep-ph].

[93] B. Schenke, P. Tribedy, and R. Venugopalan, *Fluctuating Glasma initial conditions and flow in heavy ion collisions*, Phys. Rev. Lett. **108** (2012) 252301, arXiv:1202.6646 [nucl-th].

[94] C. Gale, S. Jeon, B. Schenke, P. Tribedy, and R. Venugopalan, *Event-by-event anisotropic flow in heavy-ion collisions from combined Yang-Mills and viscous fluid dynamics*, Phys. Rev. Lett. **110** (2013) 012302, arXiv:1209.6330 [nucl-th].

[95] U. W. Heinz and M. Jacob, *Evidence for a new state of matter: An Assessment of the results from the CERN lead beam program*, arXiv:nucl-th/0002042 [nucl-th].

[96] PHENIX Collaboration, *Measurement of the mid-rapidity transverse energy distribution from s(NN)**(1/2) = 130-GeV Au + Au collisions at RHIC*, Phys. Rev. Lett. **87** (2001) 052301, arXiv:nucl-ex/0104015 [nucl-ex].

[97] B. Schenke, S. Jeon, and C. Gale, *Higher flow harmonics from (3+1)D event-by-event viscous hydrodynamics*, Phys. Rev. **C85** (2012) 024901, arXiv:1109.6289 [hep-ph].

[98] I. Karpenko, P. Huovinen, and M. Bleicher, *A 3+1 dimensional viscous hydrodynamic code for relativistic heavy ion collisions*, Comput. Phys. Commun. **185** (2014) 3016–3027, arXiv:1312.4160 [nucl-th].

[99] G. Policastro, D. T. Son, and A. O. Starinets, *The Shear viscosity of strongly coupled N=4 supersymmetric Yang-Mills plasma*, Phys. Rev. Lett. **87** (2001) 081601, arXiv:hep-th/0104066 [hep-th].

[100] P. Kovtun, D. T. Son, and A. O. Starinets, *Holography and hydrodynamics: Diffusion on stretched horizons*, JHEP **10** (2003) 064, arXiv:hep-th/0309213 [hep-th].

[101] M. L. Miller, K. Reygers, S. J. Sanders, and P. Steinberg, *Glauber modeling in high energy nuclear collisions*, Ann. Rev. Nucl. Part. Sci. **57** (2007) 205–243, arXiv:nucl-ex/0701025 [nucl-ex].

[102] R. J. Glauber, *Lecture on Theoretical Physics*, ed. W.E. Brittin, L.G. Dunham, 1:315. New York: Interscience (1959).

[103] R. J. Glauber and G. Matthiae, *High-energy scattering of protons by nuclei*, Nucl. Phys. **B21** (1970) 135–157.

[104] J.-Y. Ollitrault, *Anisotropy as a signature of transverse collective flow*, Phys. Rev. **D46** (1992) 229–245.

[105] S. Voloshin and Y. Zhang, *Flow study in relativistic nuclear collisions by Fourier expansion of Azimuthal particle distributions*, Z. Phys. **C70** (1996) 665–672, arXiv:hep-ph/9407282 [hep-ph].

[106] A. M. Poskanzer and S. A. Voloshin, *Methods for analyzing anisotropic flow in relativistic nuclear collisions*, Phys. Rev. **C58** (1998) 1671–1678, arXiv:nucl-ex/9805001 [nucl-ex].

[107] ATLAS Collaboration, *Measurement of the azimuthal anisotropy for charged particle production in* $\sqrt{s_{NN}} = 2.76$ *TeV lead-lead collisions with the ATLAS detector*, Phys. Rev. **C86** (2012) 014907, arXiv:1203.3087 [hep-ex].

[108] ATLAS Collaboration, *Z boson production in Pb+Pb collisions at* $\sqrt{s_{NN}}$ *= 5.02 TeV with the ATLAS detector at the LHC*, Tech. Rep. ATLAS-CONF-2017-010, CERN, Geneva, Feb, 2017. http://cds.cern.ch/record/2244821.

[109] T. Matsui and H. Satz, *J/ψ Suppression by Quark-Gluon Plasma Formation*, Phys. Lett. **B178** (1986) 416–422.

[110] ATLAS Collaboration, *Study of* $J/\psi \to \mu^+\mu^-$ *and* $\psi(2S) \to \mu^+\mu^-$ *production with 2015 Pb+Pb data at* $\sqrt{s_{\rm NN}} = 5.02$ TeV *and pp data at* $\sqrt{s} = 5.02$ TeV *with the ATLAS detector*, Tech. Rep. ATLAS-CONF-2016-109, CERN, Geneva, Sep, 2016. http://cds.cern.ch/record/2220771.

[111] A. Mocsy, *Potential Models for Quarkonia*, Eur. Phys. J. **C61** (2009) 705–710, arXiv:0811.0337 [hep-ph].

[112] J. W. Cronin, H. J. Frisch, M. J. Shochet, J. P. Boymond, R. Mermod, P. A. Piroue, and R. L. Sumner, *Production of hadrons with large transverse momentum at 200, 300, and 400 GeV*, Phys. Rev. **D11** (1975) 3105–3123.

[113] D. Antreasyan, J. W. Cronin, H. J. Frisch, M. J. Shochet, L. Kluberg, P. A. Piroue, and R. L. Sumner, *Production of Hadrons at Large Transverse Momentum in 200-GeV, 300-GeV and 400-GeV p p and p n Collisions*, Phys. Rev. **D19** (1979) 764–778.

[114] S. J. Brodsky and H. J. Lu, *Shadowing and antishadowing of nuclear structure functions*, Phys. Rev. Lett. **64** (1990) 1342–1345.

[115] D. F. Geesaman, K. Saito, and A. W. Thomas, *The nuclear EMC effect*, Ann. Rev. Nucl. Part. Sci. **45** (1995) 337–390.

[116] L. L. Frankfurt and M. I. Strikman, *Hard Nuclear Processes and Microscopic Nuclear Structure*, Phys. Rept. **160** (1988) 235–427.

[117] K. J. Eskola, H. Paukkunen, and C. A. Salgado, *EPS09: A New Generation of NLO and LO Nuclear Parton Distribution Functions*, JHEP **04** (2009) 065, arXiv:0902.4154 [hep-ph].

[118] J. D. Bjorken, *Energy Loss of Energetic Partons in Quark - Gluon Plasma: Possible Extinction of High p(t) Jets in Hadron - Hadron Collisions*. 1982. FERMILAB-PUB-82-059-THY.

[119] J. Casalderrey-Solana, D. C. Gulhan, J. G. Milhano, D. Pablos, and K. Rajagopal, *A Hybrid Strong/Weak Coupling Approach to Jet Quenching*, JHEP **10** (2014) 019, arXiv:1405.3864 [hep-ph].

[120] E. Braaten and M. H. Thoma, *Energy loss of a heavy quark in the quark - gluon plasma*, Phys. Rev. **D44** (1991) R2625.

[121] E. Braaten and M. H. Thoma, *Energy loss of a heavy fermion in a hot QED plasma*, Phys. Rev. D **44** (1991) 1298–1310.

[122] S. Peigne and A. Peshier, *Collisional energy loss of a fast heavy quark in a quark-gluon plasma*, Phys. Rev. **D77** (2008) 114017, arXiv:0802.4364 [hep-ph].

[123] A. Peshier, *Running coupling and screening in the (s)QGP*. 2006. arXiv:hep-ph/0601119 [hep-ph].

[124] M. H. Thoma and M. Gyulassy, *Quark Damping and Energy Loss in the High Temperature QCD*, Nucl. Phys. **B351** (1991) 491–506.

[125] B. G. Zakharov, *Parton energy loss in an expanding quark-gluon plasma: Radiative versus collisional*, JETP Lett. **86** (2007) 444–450, arXiv:0708.0816 [hep-ph].

[126] S. Peigne and A. V. Smilga, *Energy losses in a hot plasma revisited*, Phys. Usp. **52** (2009) 659–685, arXiv:0810.5702 [hep-ph].

[127] H. Bethe and W. Heitler, *On the Stopping of fast particles and on the creation of positive electrons*, Proc. Roy. Soc. Lond. **A146** (1934) 83–112.

[128] A. B. Migdal, *Bremsstrahlung and pair production in condensed media at high-energies*, Phys. Rev. **103** (1956) 1811–1820.

[129] R. Baier, Y. L. Dokshitzer, A. H. Mueller, S. Peigne, and D. Schiff, *Radiative energy loss of high-energy quarks and gluons in a finite volume quark - gluon plasma*, Nucl. Phys. **B483** (1997) 291–320, arXiv:hep-ph/9607355 [hep-ph].

[130] C. A. Salgado and U. A. Wiedemann, *Calculating quenching weights*, Phys. Rev. **D68** (2003) 014008, arXiv:hep-ph/0302184 [hep-ph].

[131] Y. L. Dokshitzer, V. A. Khoze, and S. I. Troian, *On specific QCD properties of heavy quark fragmentation ('dead cone')*, J. Phys. **G17** (1991) 1602–1604.

[132] H. Liu, K. Rajagopal, and U. A. Wiedemann, *Wilson loops in heavy ion collisions and their calculation in AdS/CFT*, JHEP **03** (2007) 066, arXiv:hep-ph/0612168 [hep-ph].

[133] J. Casalderrey-Solana and C. A. Salgado, *Introductory lectures on jet quenching in heavy ion collisions*, Acta Phys. Polon. **B38** (2007) 3731–3794, arXiv:0712.3443 [hep-ph].

[134] J. Brewer, K. Rajagopal, A. Sadofyev, and W. Van Der Schee, *Evolution of the Mean Jet Shape and Dijet Asymmetry Distribution of an Ensemble of Holographic Jets in Strongly Coupled Plasma*, JHEP **02** (2018) 015, arXiv:1710.03237 [nucl-th].

[135] P. M. Chesler and K. Rajagopal, *Jet quenching in strongly coupled plasma*, Phys. Rev. **D90** (2014) 025033, arXiv:1402.6756 [hep-th].

[136] R. Baier, Y. L. Dokshitzer, A. H. Mueller, S. Peigne, and D. Schiff, *Radiative energy loss and p(T) broadening of high-energy partons in nuclei*, Nucl. Phys. **B484** (1997) 265–282, arXiv:hep-ph/9608322 [hep-ph].

[137] R. Baier, Y. L. Dokshitzer, A. H. Mueller, and D. Schiff, *Quenching of hadron spectra in media*, JHEP **09** (2001) 033, arXiv:hep-ph/0106347 [hep-ph].

[138] L. Chen, G.-Y. Qin, S.-Y. Wei, B.-W. Xiao, and H.-Z. Zhang, *Dijet Asymmetry in the Resummation Improved Perturbative QCD Approach*, Phys. Lett. **B782** (2018) 773–778, arXiv:1612.04202 [hep-ph].

[139] B. G. Zakharov, *Radiative energy loss of high-energy quarks in finite size nuclear matter and quark - gluon plasma*, JETP Lett. **65** (1997) 615–620, arXiv:hep-ph/9704255 [hep-ph].

[140] B. G. Zakharov, *Light cone path integral approach to the Landau-Pomeranchuk-Migdal effect*, Phys. Atom. Nucl. **61** (1998) 838–854, arXiv:hep-ph/9807540 [hep-ph].

[141] B. G. Zakharov, *Fully quantum treatment of the Landau-Pomeranchuk-Migdal effect in QED and QCD*, JETP Lett. **63** (1996) 952–957, arXiv:hep-ph/9607440 [hep-ph].

[142] M. Gyulassy, P. Levai, and I. Vitev, *Jet tomography of Au+Au reactions including multigluon fluctuations*, Phys. Lett. **B538** (2002) 282–288, arXiv:nucl-th/0112071 [nucl-th].

[143] M. Gyulassy, P. Levai, and I. Vitev, *Reaction operator approach to nonAbelian energy loss*, Nucl. Phys. **B594** (2001) 371–419, arXiv:nucl-th/0006010 [nucl-th].

[144] M. Gyulassy, P. Levai, and I. Vitev, *NonAbelian energy loss at finite opacity*, Phys. Rev. Lett. **85** (2000) 5535–5538, arXiv:nucl-th/0005032 [nucl-th].

[145] S. Wicks, W. Horowitz, M. Djordjevic, and M. Gyulassy, *Elastic, inelastic, and path length fluctuations in jet tomography*, Nucl. Phys. **A784** (2007) 426–442, arXiv:nucl-th/0512076 [nucl-th].

[146] M. Djordjevic and M. Gyulassy, *Heavy quark radiative energy loss in QCD matter*, Nucl. Phys. **A733** (2004) 265–298, arXiv:nucl-th/0310076 [nucl-th].

[147] X.-f. Guo and X.-N. Wang, *Multiple scattering, parton energy loss and modified fragmentation functions in deeply inelastic e A scattering*, Phys. Rev. Lett. **85** (2000) 3591–3594, arXiv:hep-ph/0005044 [hep-ph].

[148] X.-N. Wang and X.-f. Guo, *Multiple parton scattering in nuclei: Parton energy loss*, Nucl. Phys. **A696** (2001) 788–832, arXiv:hep-ph/0102230 [hep-ph].

[149] A. Majumder and M. Van Leeuwen, *The Theory and Phenomenology of Perturbative QCD Based Jet Quenching*, Prog. Part. Nucl. Phys. **66** (2011) 41–92, arXiv:1002.2206 [hep-ph].

[150] P. B. Arnold, G. D. Moore, and L. G. Yaffe, *Photon and gluon emission in relativistic plasmas*, JHEP **06** (2002) 030, arXiv:hep-ph/0204343 [hep-ph].

[151] C. W. Bauer, S. Fleming, and M. E. Luke, *Summing Sudakov logarithms in B —¿ X(s gamma) in effective field theory*, Phys. Rev. **D63** (2000) 014006, arXiv:hep-ph/0005275 [hep-ph].

[152] C. W. Bauer and I. W. Stewart, *Invariant operators in collinear effective theory*, Phys. Lett. **B516** (2001) 134–142, arXiv:hep-ph/0107001 [hep-ph].

[153] C. W. Bauer, D. Pirjol, and I. W. Stewart, *Soft collinear factorization in effective field theory*, Phys. Rev. **D65** (2002) 054022, arXiv:hep-ph/0109045 [hep-ph].

[154] C. W. Bauer, D. Pirjol, and I. W. Stewart, *Power counting in the soft collinear effective theory*, Phys. Rev. **D66** (2002) 054005, arXiv:hep-ph/0205289 [hep-ph].

[155] A. Idilbi and A. Majumder, *Extending Soft-Collinear-Effective-Theory to describe hard jets in dense QCD media*, Phys. Rev. **D80** (2009) 054022, arXiv:0808.1087 [hep-ph].

[156] G. Ovanesyan, *Medium-induced splitting kernels from SCETG*, Nucl. Phys. **A904-905** (2013) 981c–984c, arXiv:1210.4945 [hep-ph].

[157] Y.-T. Chien, A. Emerman, Z.-B. Kang, G. Ovanesyan, and I. Vitev, *Jet Quenching from QCD Evolution*, Phys. Rev. **D93** (2016) 074030, arXiv:1509.02936 [hep-ph].

[158] X.-N. Wang and M. Gyulassy, *HIJING: A Monte Carlo model for multiple jet production in p p, p A and A A collisions*, Phys. Rev. **D44** (1991) 3501–3516.

[159] W.-T. Deng, X.-N. Wang, and R. Xu, *Hadron production in p+p, p+Pb, and Pb+Pb collisions with the HIJING 2.0 model at energies available at the CERN Large Hadron Collider*, Phys. Rev. **C83** (2011) 014915, arXiv:1008.1841 [hep-ph].

[160] I. P. Lokhtin, L. V. Malinina, S. V. Petrushanko, A. M. Snigirev, I. Arsene, and K. Tywoniuk, *Heavy ion event generator HYDJET++ (HYDrodynamics plus JETs)*, Comput. Phys. Commun. **180** (2009) 779–799, arXiv:0809.2708 [hep-ph].

[161] I. P. Lokhtin and A. M. Snigirev, *A Model of jet quenching in ultrarelativistic heavy ion collisions and high-p(T) hadron spectra at RHIC*, Eur. Phys. J. **C45** (2006) 211–217, arXiv:hep-ph/0506189 [hep-ph].

[162] K. Zapp, G. Ingelman, J. Rathsman, J. Stachel, and U. A. Wiedemann, *A Monte Carlo Model for 'Jet Quenching'*, Eur. Phys. J. **C60** (2009) 617–632, arXiv:0804.3568 [hep-ph].

[163] N. Armesto, L. Cunqueiro, and C. A. Salgado, *Q-PYTHIA: A Medium-modified implementation of final state radiation*, Eur. Phys. J. **C63** (2009) 679–690, arXiv:0907.1014 [hep-ph].

[164] N. Armesto, G. Corcella, L. Cunqueiro, and C. A. Salgado, *Angular-ordered parton showers with medium-modified splitting functions*, JHEP **11** (2009) 122, arXiv:0909.5118 [hep-ph].

[165] T. Renk, *Parton shower evolution in a 3-d hydrodynamical medium*, Phys. Rev. **C78** (2008) 034908, arXiv:0806.0305 [hep-ph].

[166] T. Renk, *A comparison study of medium-modified QCD shower evolution scenarios*, Tech. Rep. arXiv:0901.2818, Jan, 2009. https://cds.cern.ch/record/1156560.

[167] B. Schenke, C. Gale, and S. Jeon, *MARTINI: An Event generator for relativistic heavy-ion collisions*, Phys. Rev. **C80** (2009) 054913, arXiv:0909.2037 [hep-ph].

[168] Y. He, T. Luo, X.-N. Wang, and Y. Zhu, *Linear Boltzmann Transport for Jet Propagation in the Quark-Gluon Plasma: Elastic Processes and Medium Recoil*, Phys. Rev. **C91** (2015) 054908, arXiv:1503.03313 [nucl-th].

[169] S. Cao, T. Luo, G.-Y. Qin, and X.-N. Wang, *Heavy and light flavor jet quenching at RHIC and LHC energies*, Phys. Lett. **B777** (2018) 255–259, arXiv:1703.00822 [nucl-th].

[170] M. Spousta and B. Cole, *Interpreting single jet measurements in Pb + Pb collisions at the LHC*, Eur. Phys. J. **C76** (2016) 50, arXiv:1504.05169 [hep-ph].

[171] H. Stoecker, *Collective flow signals the quark gluon plasma*, Nucl. Phys. **A750** (2005) 121–147, arXiv:nucl-th/0406018 [nucl-th].

[172] J. Casalderrey-Solana, E. V. Shuryak, and D. Teaney, *Conical flow induced by quenched QCD jets*, J. Phys. Conf. Ser. **27** (2005) 22–31, arXiv:hep-ph/0411315 [hep-ph].

[173] J. Ruppert and B. Muller, *Waking the colored plasma*, Phys. Lett. **B618** (2005) 123–130, arXiv:hep-ph/0503158 [hep-ph].

[174] L. M. Satarov, H. Stoecker, and I. N. Mishustin, *Mach shocks induced by partonic jets in expanding quark-gluon plasma*, Phys. Lett. **B627** (2005) 64–70, arXiv:hep-ph/0505245 [hep-ph].

[175] PHENIX Collaboration, *Suppression of hadrons with large transverse momentum in central Au+Au collisions at* $\sqrt{s_{NN}}$ *= 130-GeV*, Phys. Rev. Lett. **88** (2002) 022301, arXiv:nucl-ex/0109003 [nucl-ex].

[176] PHENIX Collaboration, *Suppression pattern of neutral pions at high transverse momentum in Au + Au collisions at s(NN)**(1/2) = 200-GeV and constraints on medium transport coefficients*, Phys. Rev. Lett. **101** (2008) 232301, arXiv:0801.4020 [nucl-ex].

[177] STAR Collaboration, *Disappearance of back-to-back high* p_T *hadron correlations in central Au+Au collisions at* $\sqrt{s_{NN}}$ *= 200-GeV*, Phys. Rev. Lett. **90** (2003) 082302, arXiv:nucl-ex/0210033 [nucl-ex].

[178] STAR Collaboration, *Transverse momentum and collision energy dependence of high p(T) hadron suppression in Au+Au collisions at ultrarelativistic energies*, Phys. Rev. Lett. **91** (2003) 172302, arXiv:nucl-ex/0305015 [nucl-ex].

[179] BRAHMS Collaboration, I. Arsene et al., *Transverse momentum spectra in Au+Au and d+Au collisions at s**(1/2) = 200-GeV and the pseudorapidity dependence of*

high p(T) suppression, Phys. Rev. Lett. **91** (2003) 072305, arXiv:nucl-ex/0307003 [nucl-ex].

[180] PHENIX Collaboration, D. Sharma, *Measurement of light mesons by the PHENIX experiment at the RHIC*, J. Phys. **G38** (2011) 124082.

[181] STAR Collaboration, *Evidence from d + Au measurements for final state suppression of high p(T) hadrons in Au+Au collisions at RHIC*, Phys. Rev. Lett. **91** (2003) 072304, arXiv:nucl-ex/0306024 [nucl-ex].

[182] STAR Collaboration, *Experimental and theoretical challenges in the search for the quark gluon plasma: The STAR Collaboration's critical assessment of the evidence from RHIC collisions*, Nucl. Phys. **A757** (2005) 102–183, arXiv:nucl-ex/0501009 [nucl-ex].

[183] I. Vitev, *Testing the mechanism of QGP-induced energy loss*, Phys. Lett. **B639** (2006) 38–45, arXiv:hep-ph/0603010 [hep-ph].

[184] O. S. Bruning, P. Collier, P. Lebrun, S. Myers, R. Ostojic, J. Poole, and P. Proudlock, *LHC Design Report Vol.1: The LHC Main Ring*. 2004. http://cds.cern.ch/record/782076.

[185] O. Buning, P. Collier, P. Lebrun, S. Myers, R. Ostojic, J. Poole, and P. Proudlock, *LHC Design Report. 2. The LHC infrastructure and general services*. 2004. http://cds.cern.ch/record/815187.

[186] M. Benedikt, P. Collier, V. Mertens, J. Poole, and K. Schindl, *LHC Design Report. 3. The LHC injector chain*. 2004. http://cds.cern.ch/record/823808.

[187] E. Mobs, *The CERN accelerator complex. Complexe des acclrateurs du CERN*, https://cds.cern.ch/record/2197559, General Photo.

[188] CERN, *LEP design report*. Geneva, 1984. https://cds.cern.ch/record/102083.

[189] R. Bailey and P. Collier, *Standard Filling Schemes for Various LHC Operation Modes*. No. LHC-PROJECT-NOTE-323. Geneva, Sep, 2003. http://cds.cern.ch/record/691782.

[190] ATLAS Collaboration, *The ATLAS Experiment at the CERN Large Hadron Collider*, JINST **3** (2008) S08003.

[191] CMS Collaboration, *The CMS Experiment at the CERN LHC*, JINST **3** (2008) S08004.

[192] ALICE Collaboration, *The ALICE experiment at the CERN LHC*, JINST **3** (2008) S08002.

[193] LHCb Collaboration, *The LHCb Detector at the LHC*, JINST **3** (2008) S08005.

[194] TOTEM Collaboration, *The TOTEM experiment at the CERN Large Hadron Collider*, JINST **3** (2008) S08007.

[195] LHCf Collaboration, *The LHCf detector at the CERN Large Hadron Collider*, JINST **3** (2008) S08006.

[196] MoEDAL Collaboration, B. Acharya et al., *The Physics Programme Of The MoEDAL Experiment At The LHC*, Int. J. Mod. Phys. **A29** (2014) 1430050, arXiv:1405.7662 [hep-ph].

[197] ATLAS Collaboration, *Luminosity Determination in pp Collisions at $\sqrt{s} = 7$ TeV Using the ATLAS Detector at the LHC*, Eur. Phys. J. **C71** (2011) 1630, arXiv:1101.2185 [hep-ex].

[198] S. van der Meer, *Calibration of the Effective Beam Height in the ISR*. 1968. CERN-ISR-PO-68-31.

[199] B. Cole, L. B. Havener, and W. Kozanecki, *Luminosity calibration for November 2015 5.02 TeV pp measurements*, Tech. Rep. ATL-COM-DAPR-2016-008, CERN, Geneva, Jul, 2016. https://cds.cern.ch/record/2199372.

[200] B. Cole, L. Havener, D. Perepelitsa, and W. Kozaneck, *Luminosity calibration for February 2013 s = 2.76 TeV pp measurements*, Tech. Rep. ATL-COM-DAPR-2014-009, CERN, Geneva, Aug, 2014. https://cds.cern.ch/record/1747966.

[201] M. Arratia, *Luminosity determination for the 2015 PbPb run*, Tech. Rep. ATL-COM-DAPR-2016-004, CERN, Geneva, May, 2016. https://cds.cern.ch/record/2152730.

[202] B. B. Rossi, *High-energy particles*. New York : Prentice-Hall, 1952. Bibliography: p. 547-561.

[203] B. Martin and G. Shaw, *Particle Physics*. Manchester Physics Series. Wiley, 2008. https://books.google.com/books?id=whIbrWJdEJQC.

[204] C. Grupen and B. Shwartz, *Particle Detectors*. Cambridge Monographs on Particle Physics, Nuclear Physics and Cosmology. Cambridge University Press, 2 ed., 2008.

[205] ATLAS Liquid Argon Collaboration, K.-J. Grahn, *A Layer Correlation Technique for Pion Energy Calibration at the 2004 ATLAS Combined Beam Test*, arXiv:0911.2639 [physics.ins-det].

[206] ATLAS Collaboration, *ATLAS liquid-argon calorimeter: Technical Design Report*. Technical Design Report ATLAS. CERN, Geneva, 1996. http://cds.cern.ch/record/331061.

[207] ATLAS Collaboration, *ATLAS tile calorimeter: Technical Design Report*. Technical Design Report ATLAS. CERN, Geneva, 1996. https://cds.cern.ch/record/331062.

[208] V. Cindro et al., *The ATLAS beam conditions monitor*, JINST **3** (2008) P02004.

[209] ATLAS Collaboration, *Performance of the Minimum Bias Trigger in p-p Collisions at Sqrt(s) = 900 GeV*, Tech. Rep. ATLAS-CONF-2010-025, CERN, Geneva, Jul, 2010. https://cds.cern.ch/record/1277657.

[210] ATLAS Collaboration, A. Krasznahorkay, *The evolution of the Trigger and Data Acquisition System in the ATLAS experiment*, J. Phys. Conf. Ser. **523** (2014) 012019.

[211] ATLAS Collaboration, *Performance of the ATLAS Trigger System in 2015*, Eur. Phys. J. **C77** (2017) 317, arXiv:1611.09661 [hep-ex].

[212] ATLAS Collaboration, *Measurement of the jet radius and transverse momentum dependence of inclusive jet suppression in lead-lead collisions at* $\sqrt{s_{NN}}$*= 2.76 TeV with the ATLAS detector*, Phys. Lett. **B719** (2013) 220–241, arXiv:1208.1967 [hep-ex].

[213] A. Angerami, B. Cole, D. Perepelitsa, P. Balek, T. Kosek, M. Rybar, M. Spousta, A. Galan, and H. Santos, *Performance of Jet Reconstruction in Heavy Ion Collisions*, Tech. Rep. ATL-COM-PHYS-2011-1733, CERN, Geneva, Dec, 2011. https://cds.cern.ch/record/1409453.

[214] ATLAS Collaboration, *Measurement of the pseudorapidity and transverse momentum dependence of the elliptic flow of charged particles in lead-lead collisions at* $\sqrt{s_{NN}} = 2.76$ *TeV with the ATLAS detector*, Phys. Lett. **B707** (2012) 330–348, arXiv:1108.6018 [hep-ex].

[215] S. Agostinelli et al., *GEANT4: A simulation toolkit*, Nucl. Instrum. Meth. A **506** (2003) 250–303.

[216] A. Angerami, B. Cole, and D. Perepelitsa, *Measurement of the inclusive jet spectrum and jet suppression using 2011 Pb+Pb data: Jet RAA measurement*, Tech. Rep. ATL-COM-PHYS-2013-1370, CERN, Geneva, Sep, 2013. https://cds.cern.ch/record/1604232.

[217] ATLAS Collaboration, *Jet energy measurement and its systematic uncertainty in proton-proton collisions at* $\sqrt{s} = 7$ *TeV with the ATLAS detector*, Eur. Phys. J. **C75** (2015) 17, arXiv:1406.0076 [hep-ex].

[218] ATLAS Collaboration, *Jet energy scale and its uncertainty for jets reconstructed using the ATLAS heavy ion jet algorithm*, Tech. Rep. ATLAS-CONF-2015-016, CERN, Geneva, Apr, 2015. https://cds.cern.ch/record/2008677.

[219] G. D'Agostini, *A Multidimensional unfolding method based on Bayes' theorem*, Nucl. Instrum. Meth. A **362** (1995) 487–498.

[220] ATLAS Collaboration, *The performance of the jet trigger for the ATLAS detector during 2011 data taking*, Eur. Phys. J. **C76** (2016) 526, arXiv:1606.07759 [hep-ex].

[221] ATLAS Collaboration, *ATLAS tunes of PYTHIA 6 and Pythia 8 for MC11*, Tech. Rep. ATL-PHYS-PUB-2011-009, CERN, Geneva, Jul, 2011. http://cds.cern.ch/record/1363300.

[222] J. Pumplin, D. R. Stump, J. Huston, H. L. Lai, P. M. Nadolsky, and W. K. Tung, *New generation of parton distributions with uncertainties from global QCD analysis*, JHEP **07** (2002) 012, arXiv:hep-ph/0201195 [hep-ph].

[223] ATLAS Collaboration, *Summary of ATLAS Pythia 8 tunes*, Tech. Rep. ATL-PHYS-PUB-2012-003, CERN, Geneva, Aug, 2012. https://cds.cern.ch/record/1474107.

[224] H.-L. Lai, M. Guzzi, J. Huston, Z. Li, P. M. Nadolsky, J. Pumplin, and C. P. Yuan, *New parton distributions for collider physics*, Phys. Rev. **D82** (2010) 074024, arXiv:1007.2241 [hep-ph].

[225] S. Gieseke, C. Rohr, and A. Siodmok, *Colour reconnections in Herwig++*, Eur. Phys. J. **C72** (2012) 2225, arXiv:1206.0041 [hep-ph].

[226] S. Frixione, P. Nason, and C. Oleari, *Matching NLO QCD computations with Parton Shower simulations: the POWHEG method*, JHEP **11** (2007) 070, arXiv:0709.2092 [hep-ph].

[227] S. Alioli, P. Nason, C. Oleari, and E. Re, *A general framework for implementing NLO calculations in shower Monte Carlo programs: the POWHEG BOX*, JHEP **06** (2010) 043, arXiv:1002.2581 [hep-ph].

[228] T. Adye, *Unfolding algorithms and tests using RooUnfold*. CERN, Geneva, 2011. arXiv:1105.1160 [physics.data-an].

[229] ATLAS Collaboration, *Measurement of inclusive jet charged-particle fragmentation functions in Pb+Pb collisions at* $\sqrt{s_{NN}} = 2.76$ *TeV with the ATLAS detector*, Phys. Lett. **B739** (2014) 320–342, arXiv:1406.2979 [hep-ex].

[230] ATLAS Collaboration, *Study of Jet Shapes in Inclusive Jet Production in pp Collisions at* $\sqrt{s} = 7$ *TeV using the ATLAS Detector*, Phys. Rev. **D83** (2011) 052003, arXiv:1101.0070 [hep-ex].

[231] ATLAS Collaboration, *Measurement of photon-jet transverse momentum correlations in 5.02 TeV Pb+Pb and pp collisions with ATLAS*, arXiv:1809.07280 [nucl-ex].

[232] ATLAS Collaboration, *Selection of jets produced in 13TeV proton-proton collisions with the ATLAS detector*, Tech. Rep. ATLAS-CONF-2015-029, CERN, Geneva, Jul, 2015. https://cds.cern.ch/record/2037702.

[233] ATLAS Collaboration, *ATLAS Run 1 Pythia8 tunes*, Tech. Rep. ATL-PHYS-PUB-2014-021, CERN, Geneva, Nov, 2014. https://cds.cern.ch/record/1966419.

[234] R. D. Ball et al., *Parton distributions with LHC data*, Nucl. Phys. **B867** (2013) 244–289, arXiv:1207.1303 [hep-ph].

[235] ATLAS Collaboration, *Jet energy scale measurements and their systematic uncertainties in proton-proton collisions at* $\sqrt{s} = 13$ *TeV with the ATLAS detector*, Phys. Rev. **D96** (2017) 072002, arXiv:1703.09665 [hep-ex].

[236] ATLAS Collaboration, *Data-driven determination of the energy scale and resolution of jets reconstructed in the ATLAS calorimeters using dijet and multijet events at* $\sqrt{s} = 8$ *TeV*, Tech. Rep. ATLAS-CONF-2015-017, CERN, Geneva, Apr, 2015. https://cds.cern.ch/record/2008678.

[237] ATLAS Collaboration, *Luminosity determination in pp collisions at* $\sqrt{s} = 8$ *TeV using the ATLAS detector at the LHC*, Eur. Phys. J. **C76** (2016) 653, arXiv:1608.03953 [hep-ex].

[238] ATLAS Collaboration, *Measurement of the pseudorapidity and transverse momentum dependence of the elliptic flow of charged particles in lead–lead collisions at* $\sqrt{s_{\mathrm{NN}}} = 2.76$ *TeV with the ATLAS detector*, Phys. Lett. B **707** (2012) 330, arXiv:1108.6018 [hep-ex].

[239] ATLAS Collaboration, *Study of photon-jet momentum correlations in Pb+Pb and pp collisions at* $\sqrt{s_{\mathrm{NN}}} = 5.02$ *TeV with ATLAS*, ATLAS-CONF-2016-110, 2016, https://cds.cern.ch/record/2220772.

[240] ATLAS Collaboration, *Transverse energy fluctuations in Pb+Pb collisions at* $\sqrt{s_{NN}}$*=2.76 TeV with the ATLAS detector at the LHC*, Tech. Rep. ATLAS-CONF-2012-045, CERN, Geneva, Apr, 2012. https://cds.cern.ch/record/1440894.

[241] PHENIX Collaboration, *An Upgrade Proposal from the PHENIX Collaboration*, arXiv:1501.06197 [nucl-ex].

[242] JETSCAPE Collaboration, K. Kauder, *JETSCAPE v1.0 Quickstart Guide*, arXiv:1807.09615 [hep-ph].

[243] ATLAS Collaboration, *Measurement of angular and momentum distributions of charged-particles within and around jets in Pb+Pb and pp collisions at* $\sqrt{s_{NN}} = 5.02$ *TeV with ATLAS at the LHC*, Tech. Rep. ATLAS-CONF-2018-010, CERN, Geneva, May, 2018. http://cds.cern.ch/record/2318869.

[244] ATLAS Collaboration, *Measurement of* $R = 0.4$ *jet mass in Pb+Pb and pp collisions at* $\sqrt{s_{\mathrm{NN}}} = 5.02$ *TeV with the ATLAS detector*, Tech. Rep. ATLAS-CONF-2018-014, CERN, Geneva, May, 2018. http://cds.cern.ch/record/2319867.

[245] ATLAS Collaboration, *Measurement of jet fragmentation in Pb+Pb and pp collisions at* $\sqrt{s_{\mathrm{NN}}} = 2.76$ *TeV with the ATLAS detector at the LHC*, Eur. Phys. J. **C77** (2017) 379, arXiv:1702.00674 [hep-ex].

[246] ATLAS Collaboration, *Measurement of jet fragmentation in 5.02 TeV proton-lead and proton-proton collisions with the ATLAS detector*, Nucl. Phys. **A978** (2018) 65, arXiv:1706.02859 [hep-ex].

[247] CMS Collaboration, *Measurement of the Splitting Function in pp and Pb-Pb Collisions at* $\sqrt{s_{\mathrm{NN}}} = 5.02$ *TeV*, Phys. Rev. Lett. **120** (2018) 142302, arXiv:1708.09429 [nucl-ex].

Appendices

Appendix A

Dijet Asymmetry Analysis $R = 0.3$

The data analysis for the $R = 0.3$ jets is the same as the $R = 0.4$ jets. The trigger efficiencies in different centralities are shown with the fits between 60-100 GeV in Figure A.1. The minimum bias and jet triggered samples were combined at 85 GeV as shown in Figure A.3. The ratio of the minimum bias to jet triggered samples is shown in Figure A.2.

The $\Delta\phi$ distributions for $R = 0.3$ jets are shown in Figures A.5. There is stil a modulation here but it is smaller the for $R = 0.4$.

The raw p_{T_2} slices for $R = 0.3$ jets are shown in Figure A.6 and Figure A.7. The trends for the $R = 0.3$ jets are qualitatively the same as for the $R = 0.4$ jets just shifted to lower p_T. This is due to the difference in the energy scales for the $R = 0.3$ and $R = 0.4$ jets. The

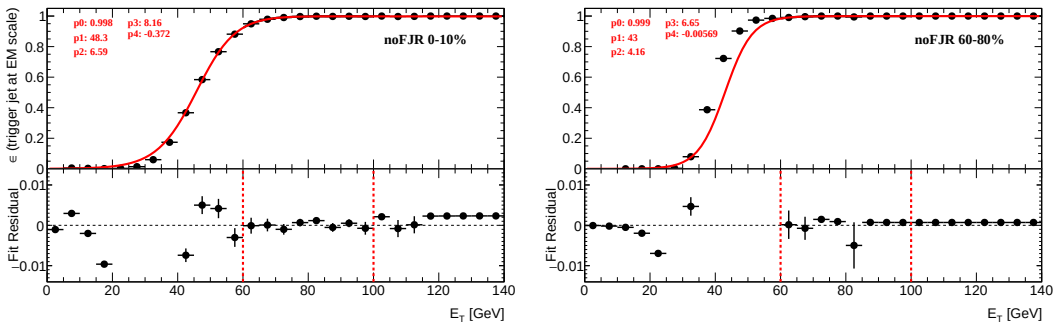

Figure A.1: Trigger efficiencies fit between 60-100 GeV for different centralities in $R = 0.4$ jets. The fix parameters are given on each plot in red. The fit residuals (data-fit) are shown below each efficiency distribution.

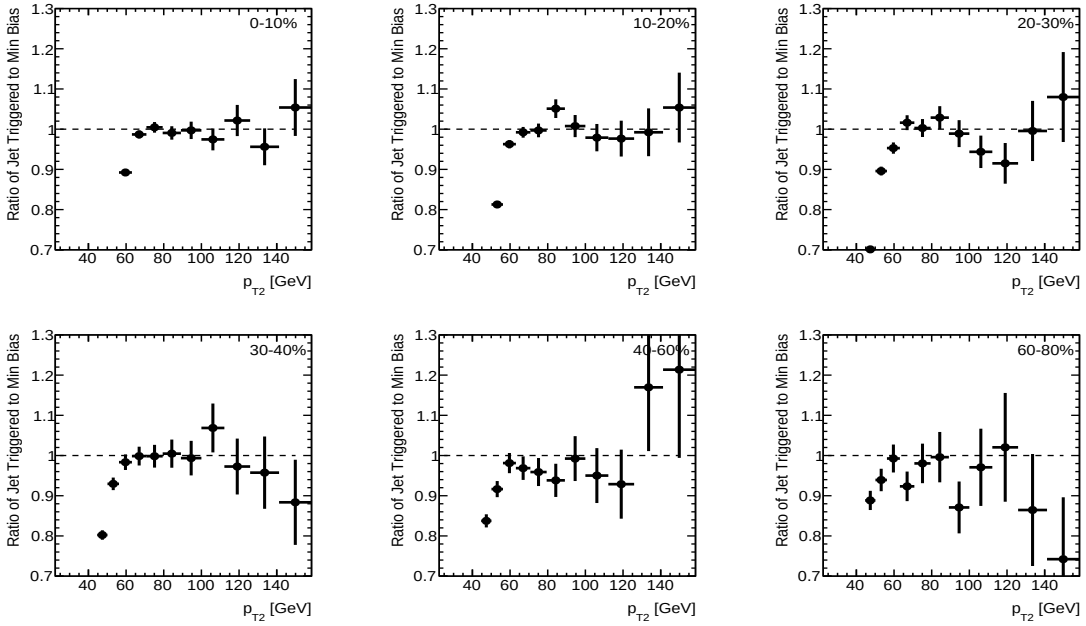

Figure A.2: Ratio of the minimum bias to jet triggered samples in centrality bins for $R = 0.3$ jets. The transition region was chosen from this plot to be 85 GeV.

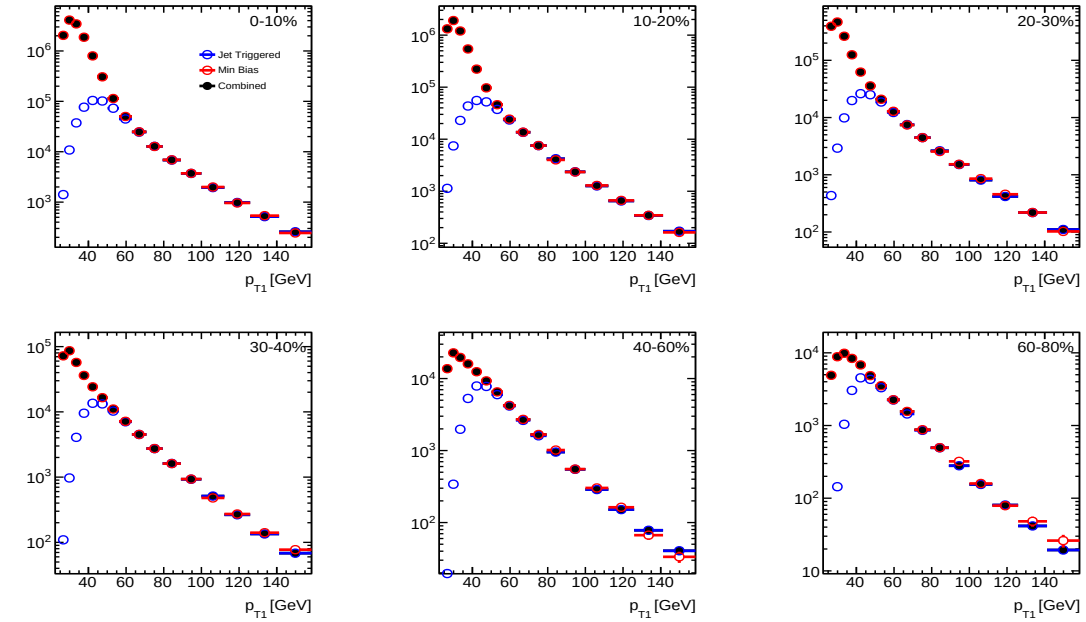

Figure A.3: The minimum bias, jet triggered, and combined samples overlaid in centrality bins for $R = 0.3$ jets.

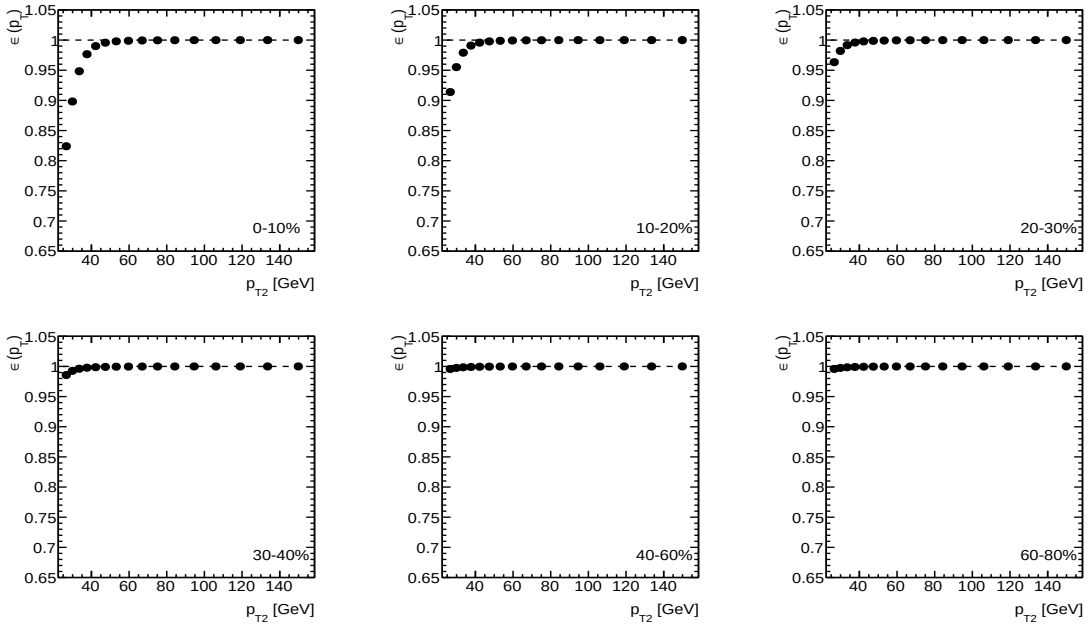

Figure A.4: The inefficiency as a function of sub-leading jet p_{T} in different centrality bins centrality for $R = 0.3$ Pb+Pb jets.

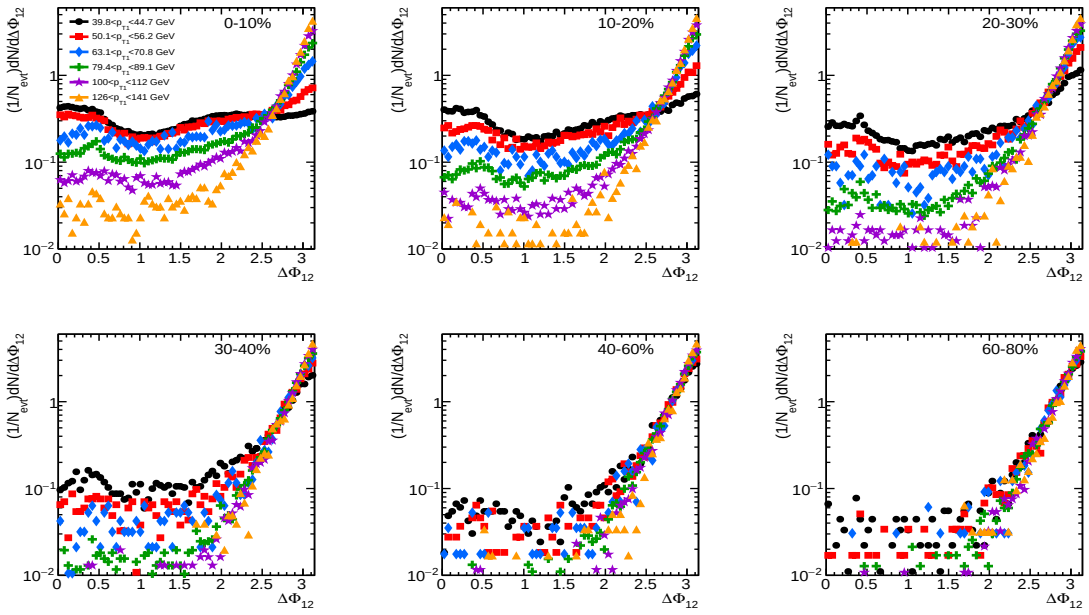

Figure A.5: The $\Delta\phi$ distribution binned in centrality as a function of leading jet p_{T} for $R = 0.3$ jets.

$R = 0.3$ jets will contain less energy for the same jet due to the smaller jet cone.

The x_{J} distributions for $R = 0.3$ jets are shown in Figure A.8 and Figure A.9.

The pp trigger boundaries are shown for the $R = 0.3$ jets in Figure A.10. It was determined that the same trigger boundaries worked for the $R = 0.3$ as the $R = 0.4$ sample.

Figure 5.32 shows the p_{T_2} distribution on the left and the x_{J} distributions on right for pp $R = 0.3$ jets.

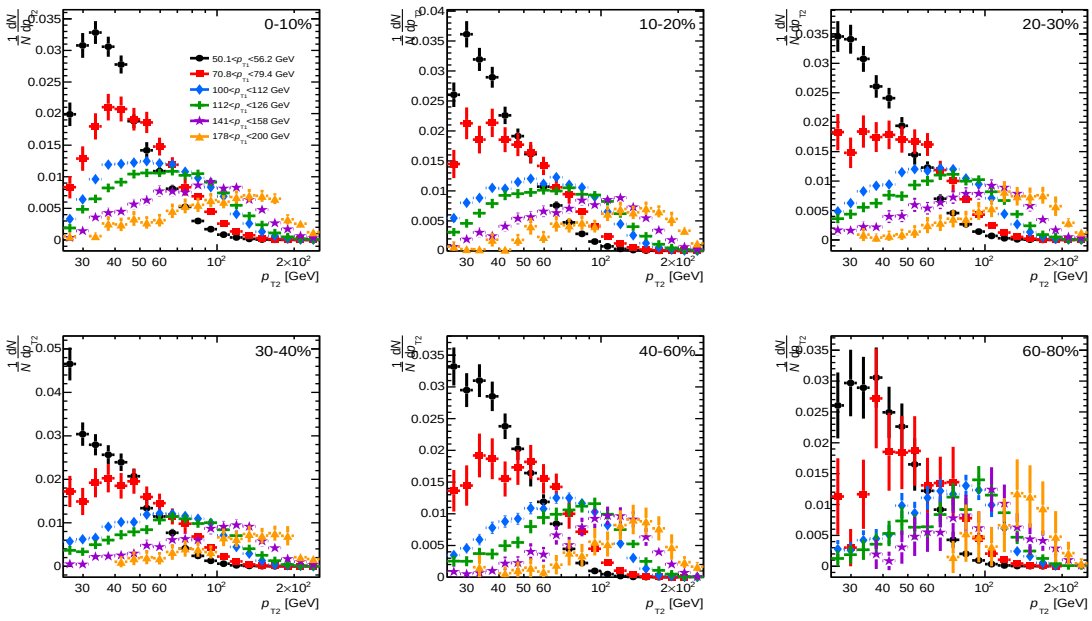

Figure A.6: The raw data sub-leading jet distributions binned in centrality as a function of leading jet p_{T} for $R = 0.3$ jets.

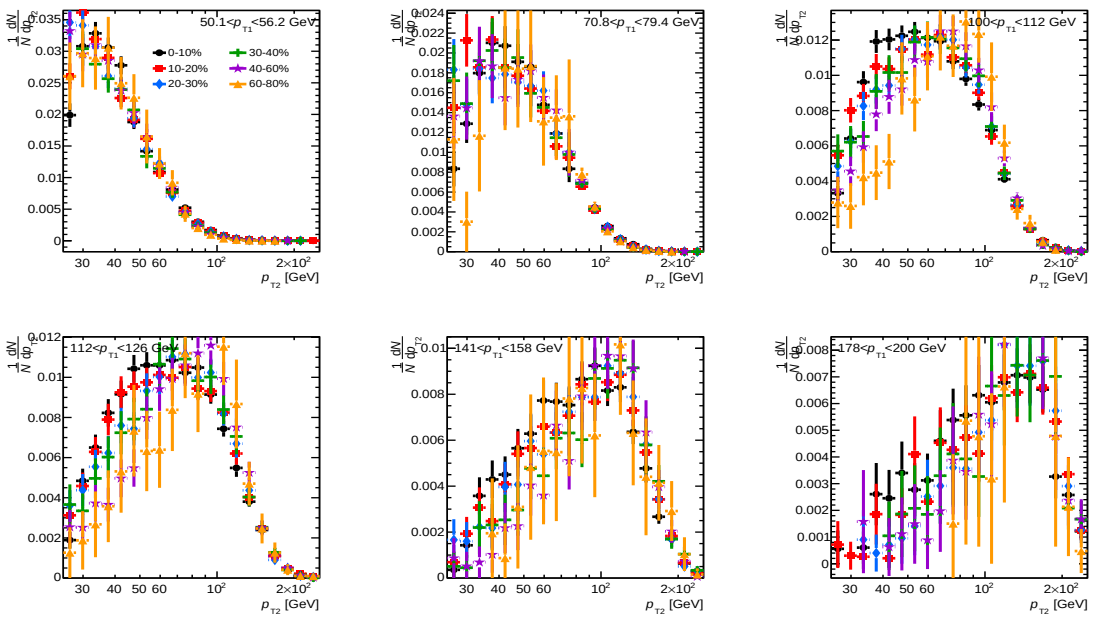

Figure A.7: The raw sub-leading jet distributions binned in leading jet p_{T} as a function of centrality for $R = 0.3$ jets.

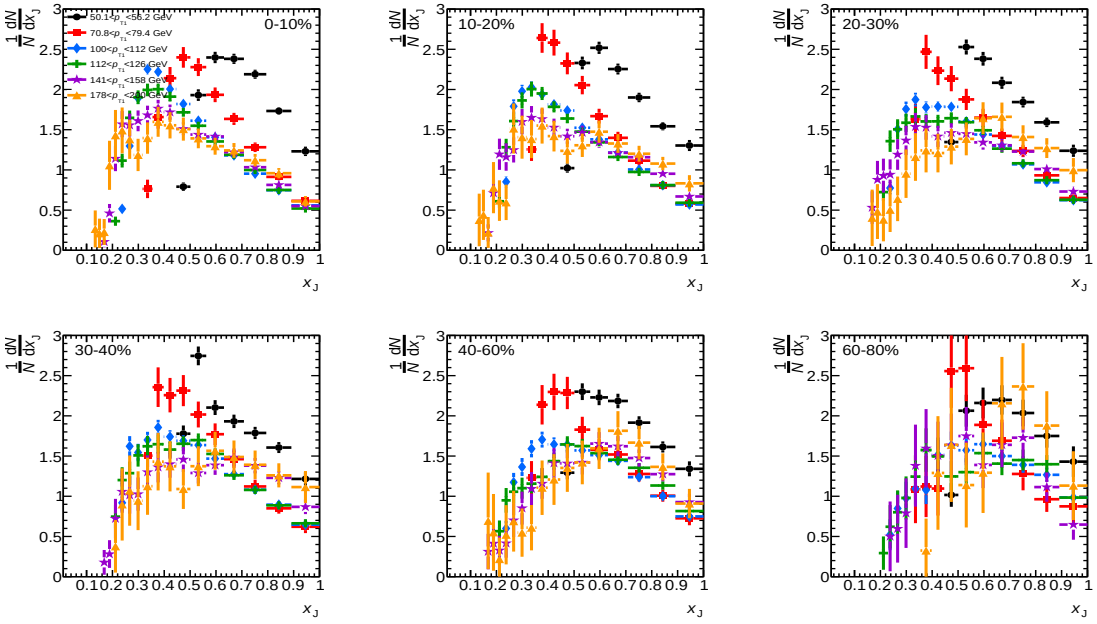

Figure A.8: The raw x_{J} distributions binned in centrality as a function of leading jet p_{T} for $R = 0.3$ jets.

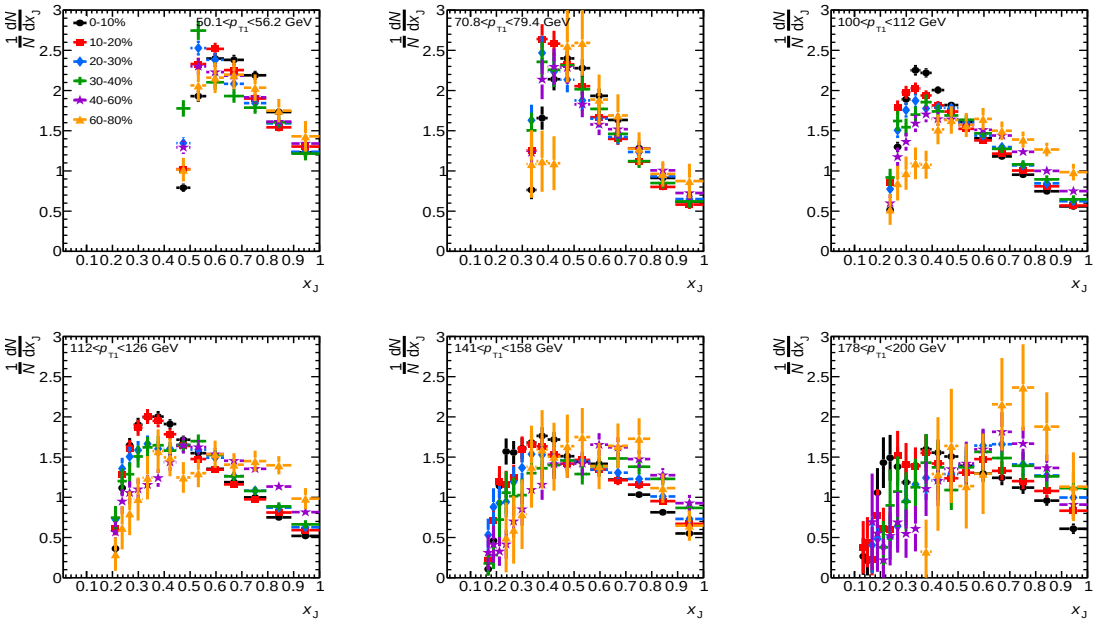

Figure A.9: The raw x_{J} distributions binned in leading jet p_{T} as a function of centrality for $R = 0.3$ jets.

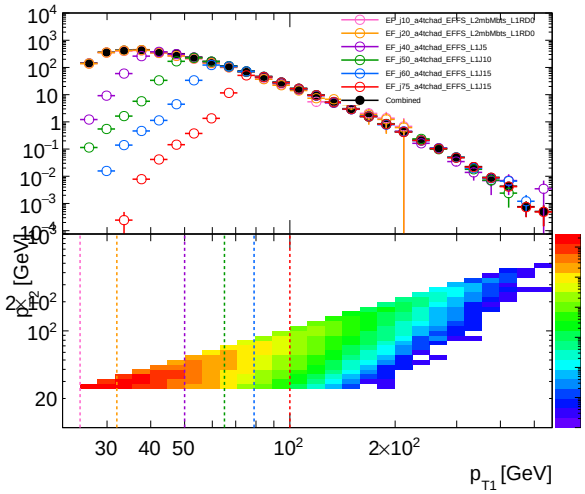

Figure A.10: The top panel is an overlay of the different $R = 0.3$ trigger sample leading jet p_{T} spectrums with the combined spectrum in black. The bottom panel is the combined spectrum 2D jet 1/jet 2 distribution.

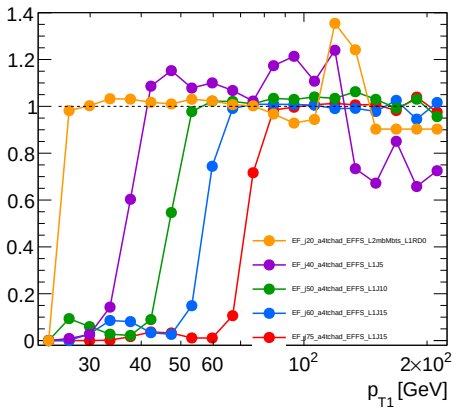

Figure A.11: The ratio of each $R = 0.3$ trigger sample leading jet p_{T} distribution to the lower p_{T} sample (for example j75/j60 and j20/j10.)

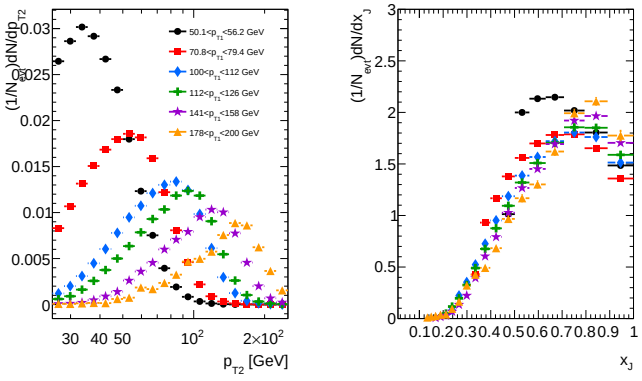

Figure A.12: Left panel is the distribution of the sub-leading jet p_{T} in bins of leading jet p_{T} for $R = 0.3$ jets. Right panel is the x_J distributions in bins of leading jet p_{T}.

Appendix B

Dijet Asymmetry Covariance

The individual point in the normalized $(1/N)\mathrm{d}N/\mathrm{d}x_{\mathrm{J}}$ distributions have a covariance between each of the points. This was evaluated by generating 100 toys on the raw data before unfolding based on gaussian fluctuations on the errors. Then the covariance was evaluated between the 100 unfolded results from the toys. Figure B.1 - B.6 show all of the covariances for $R = 0.3$ and $R = 0.4$ Pb+Pb and pp results for every centrality and p_{T} bins. The covariance is normalized such that each point is $\rho_{ij} = \frac{\sigma_{ij}^2}{\sigma_{ii}^2 \sigma_{jj}^2}$ where σ_{ij}^2 is (i, j) element of the covariance matrix which can be positive or negative. The diagonal elements of covariance were used as the final statistic errors on the unfolded $(1/N)\mathrm{d}N/\mathrm{d}x_{\mathrm{J}}$ distributions.

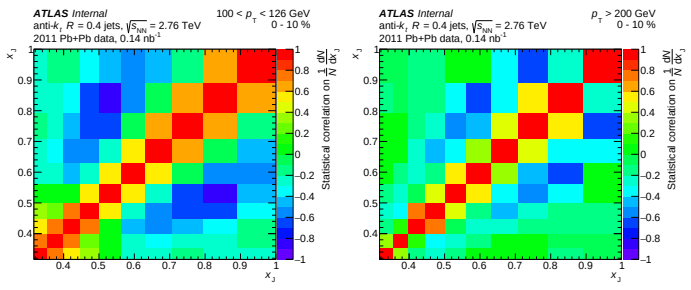

Figure B.1: The normalized covariance for $R = 0.4$ jets on $(1/N)\mathrm{d}N/\mathrm{d}x_{\mathrm{J}}$ for 0-10% centrality in different leading jet p_{T} bins.

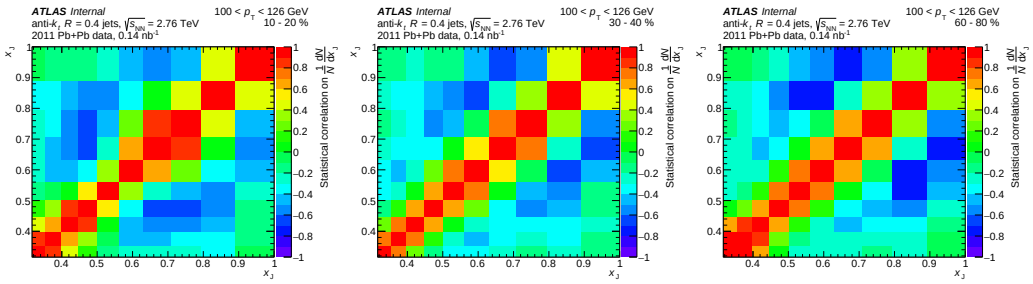

Figure B.2: The normalized covariance for $R = 0.4$ jets on $(1/N)\mathrm{d}N/\mathrm{d}x_\mathrm{J}$ for p_{T_1} between 100–126 GeV in different centrality bins.

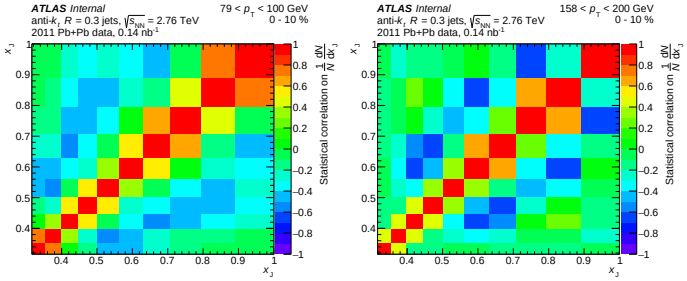

Figure B.3: The normalized covariance for $R = 0.3$ jets on $(1/N)dN/dx_J$ for 0-10% centrality in different leading jet p_T bins.

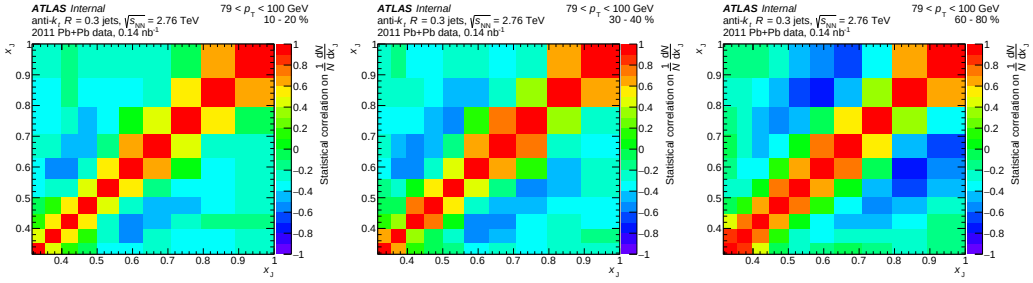

Figure B.4: The normalized covariance for $R = 0.3$ jets on $(1/N)\mathrm{d}N/\mathrm{d}x_\mathrm{J}$ for p_{T_1} between 79–100 GeV in different centrality bins.

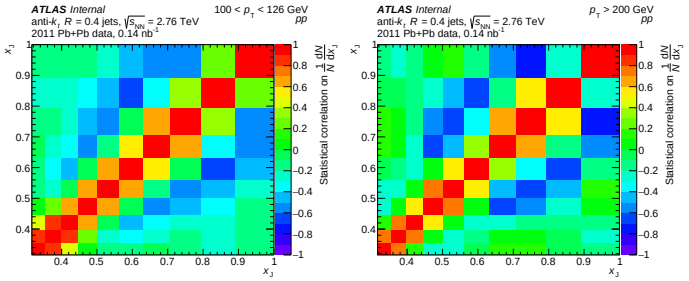

Figure B.5: The normalized covariance for $R = 0.4$ pp jets on $(1/N)dN/dx_J$ in different leading jet p_{T} bins.

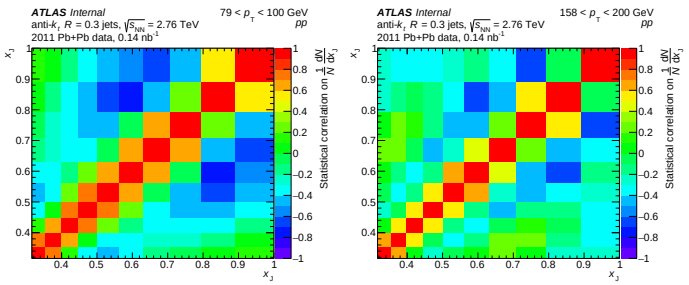

Figure B.6: The normalized covariance for $R = 0.3$ pp jets on $(1/N)dN/dx_J$ in different leading jet p_{T} bins.

Appendix C

Dijet Asymmetry Additional Response

Figure C.1 shows the 2D truth and reconstructed distributions before and after folding over the diagonal for $R = 0.3$ jets. Figure C.2 and Figure C.4 demonstrates the centrality dependence of the truth $(p_{\mathrm{T}_1}, p_{\mathrm{T}_2})$ distributions from the response matrix for $R = 0.4$ and $R = 0.3$ respectively. Figure C.3 and Figure C.4 are the same figures but now with the reconstructed $(p_{\mathrm{T}_1}, p_{\mathrm{T}_2})$ distributions from the response matrix.

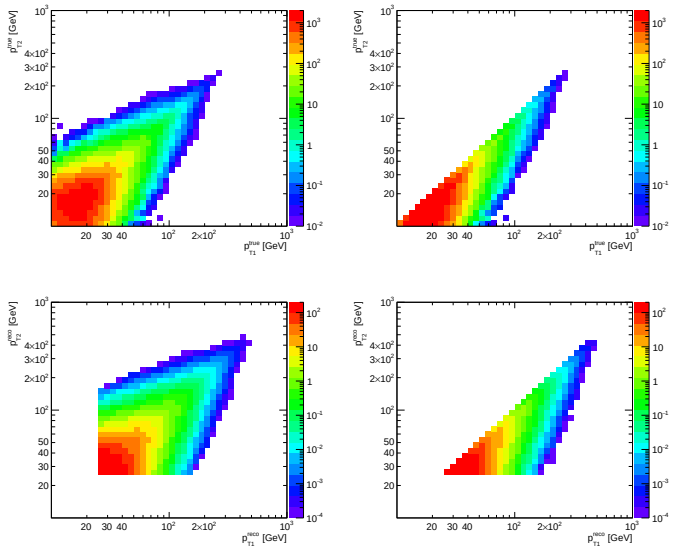

Figure C.1: The top left panel is the truth level symmetric 2D distribution $(p_{\mathrm{T}_1}, p_{\mathrm{T}_2})$ and the top right panel is the truth folded over the diagonal. The bottom left panel is the reconstructed symmetric 2D distribution$(p_{\mathrm{T}_1}, p_{\mathrm{T}_2})$ and the top right panel is the reconstructed folded over the diagonal. All the distributions are for Pb+Pb in the 0-10% centrality bin and for $R = 0.3$ jets.

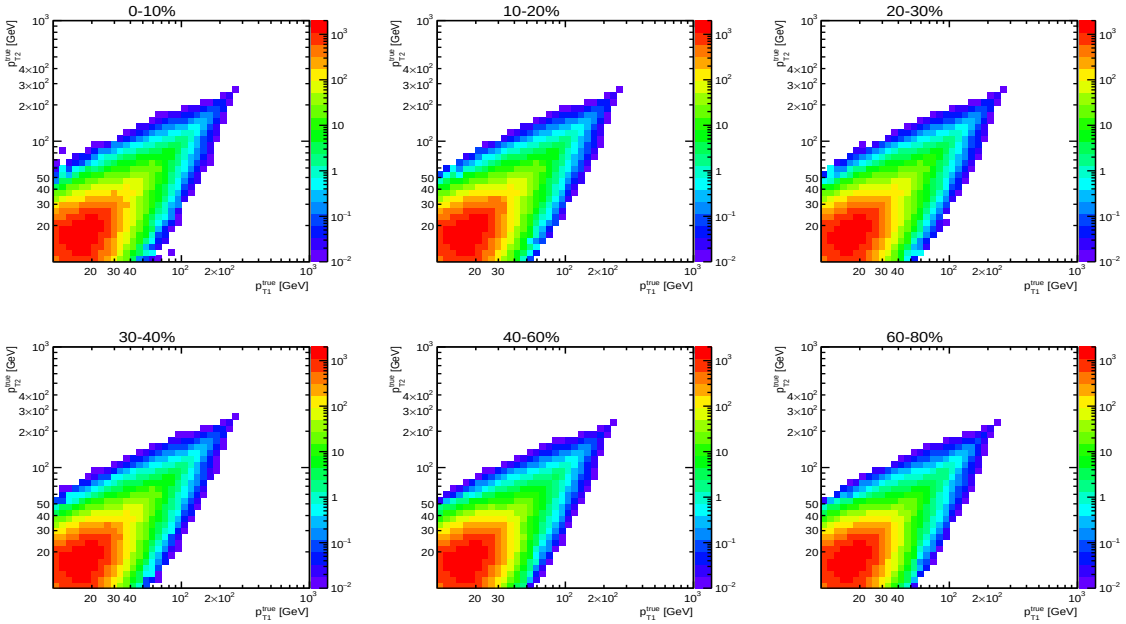

Figure C.2: The 2D jet 1/jet 2 truth distribution from the 4D response matrix $R = 0.4$ jets in different centrality bins.

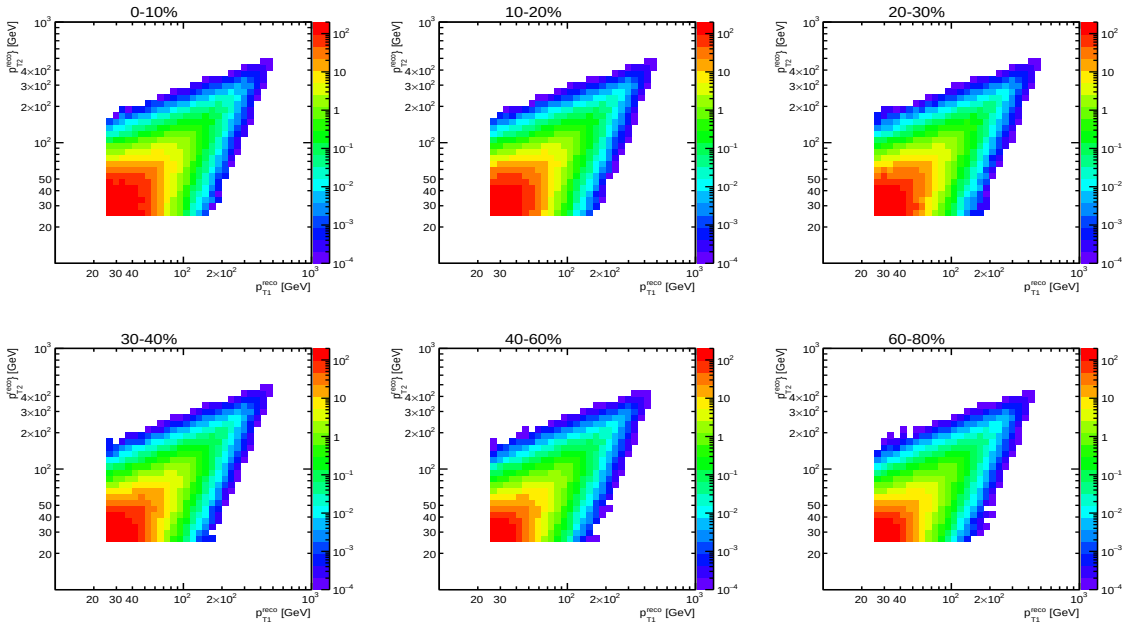

Figure C.3: The 2D jet 1/jet 2 reconstructed distribution from the 4D response matrix $R = 0.4$ jets in different centrality bins.

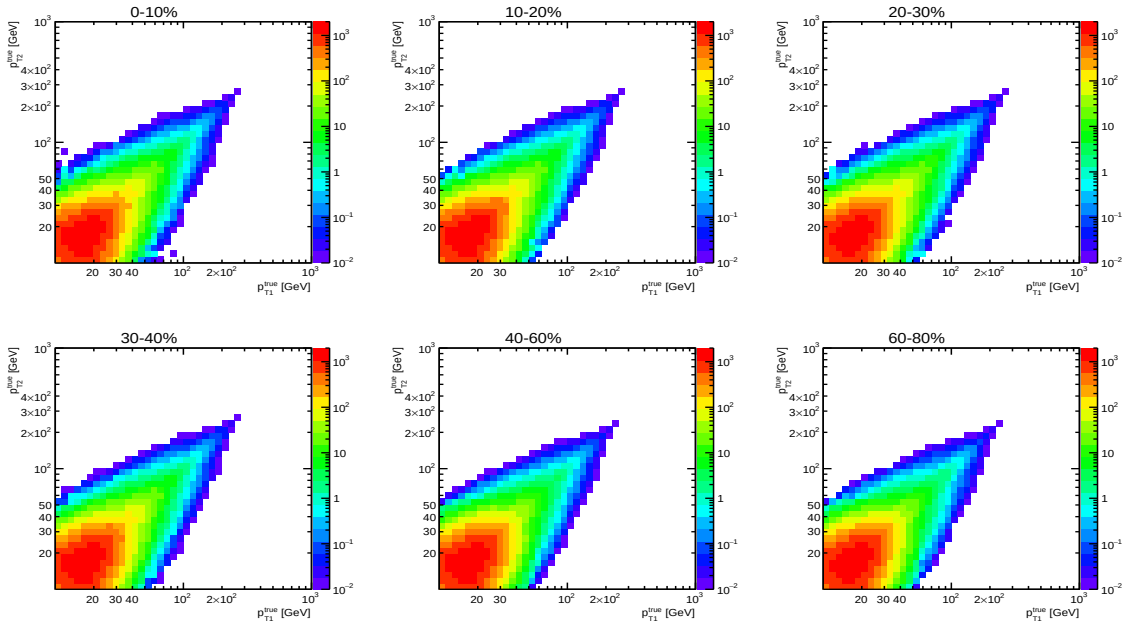

Figure C.4: The 2D jet 1/jet 2 truth distribution from the 4D response matrix $R = 0.3$ jets in different centrality bins.

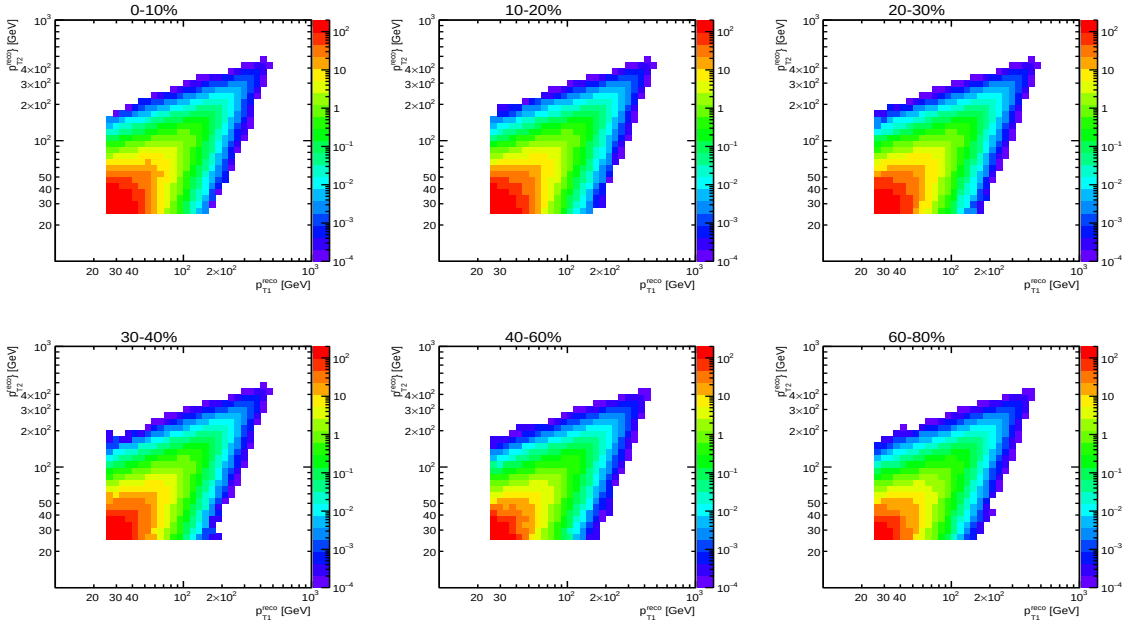

Figure C.5: The 2D jet 1/jet 2 reconstructed distribution from the 4D response matrix $R = 0.3$ jets in different centrality bins.

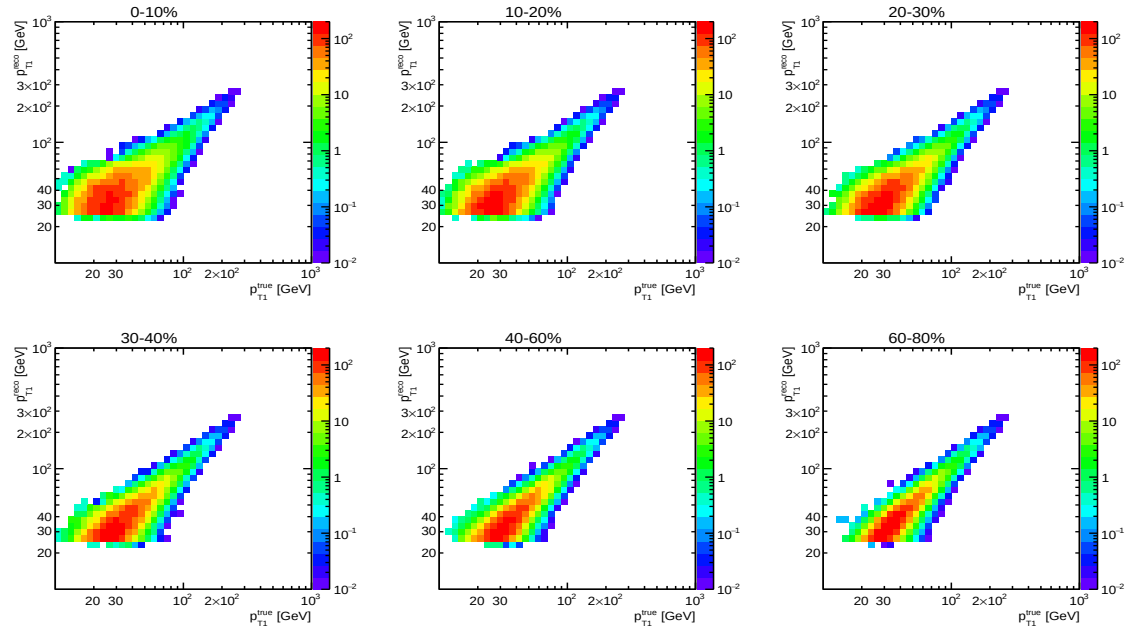

Figure C.6: The response of the reconstructed jets to the truth jets in the MC for $R = 0.3$ jets in different centrality bins for the Pb+Pb.

Appendix D

Dijet Asymmetry Additional Results

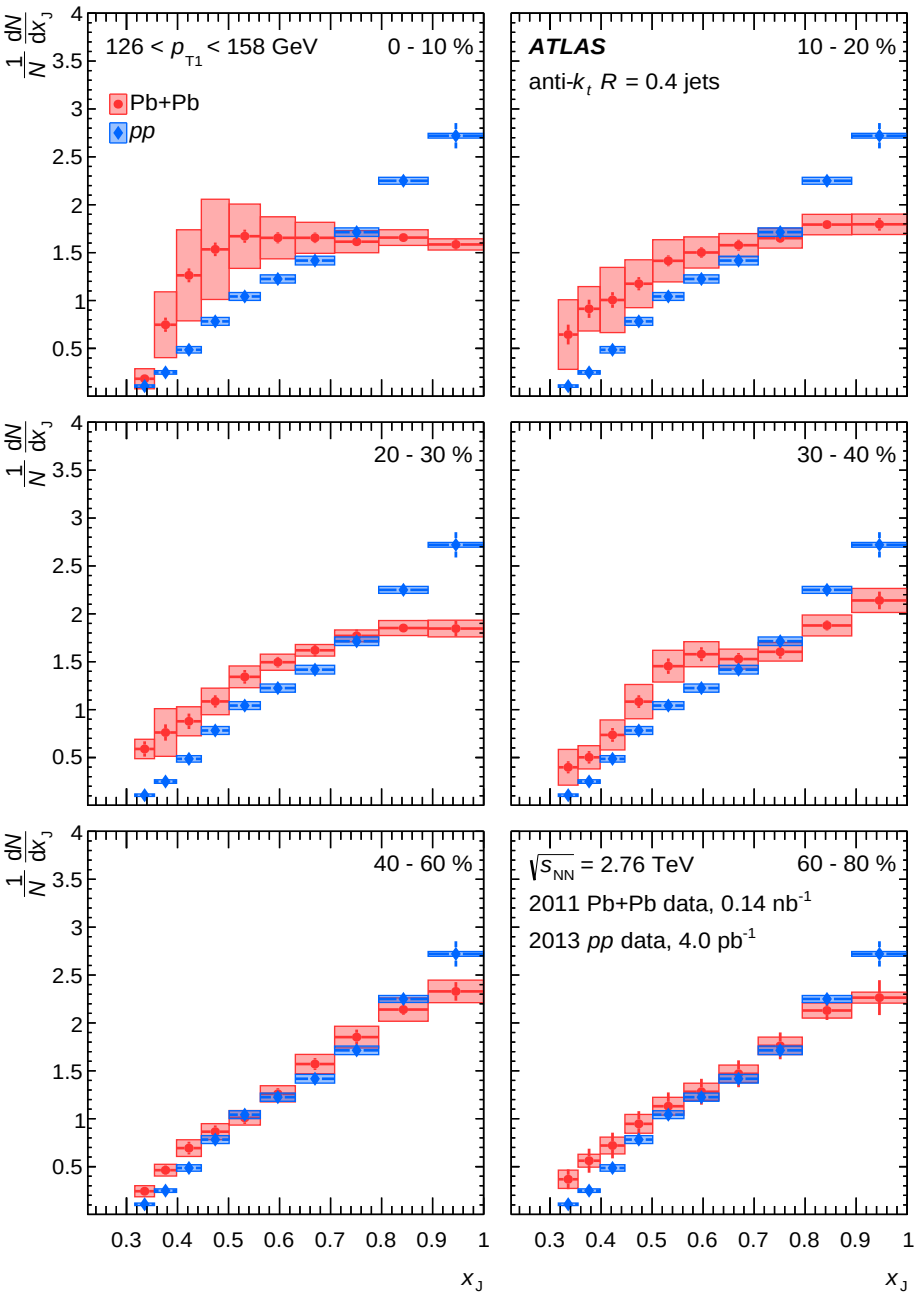

Figure D.1: The unfolded dN/dx_J distribution normalized to the number of dijet pairs for Pb+Pb R=0.4 jets (black) and *pp* R=0.4 jets (red). Each panel is a different centrality bin in the Pb+Pb with the *pp* being the same in each panel: 0-10% (top left), 10-20% (top middle), 20-30% (top right), 30-40% (top right), 40-60% (bottom middle), and 60-80% (bottom right). Each curve is for leading jet p_T from 126-158 GeV. The statistical errors are given by the error bars on each curve and the systematics are given by the error bands.

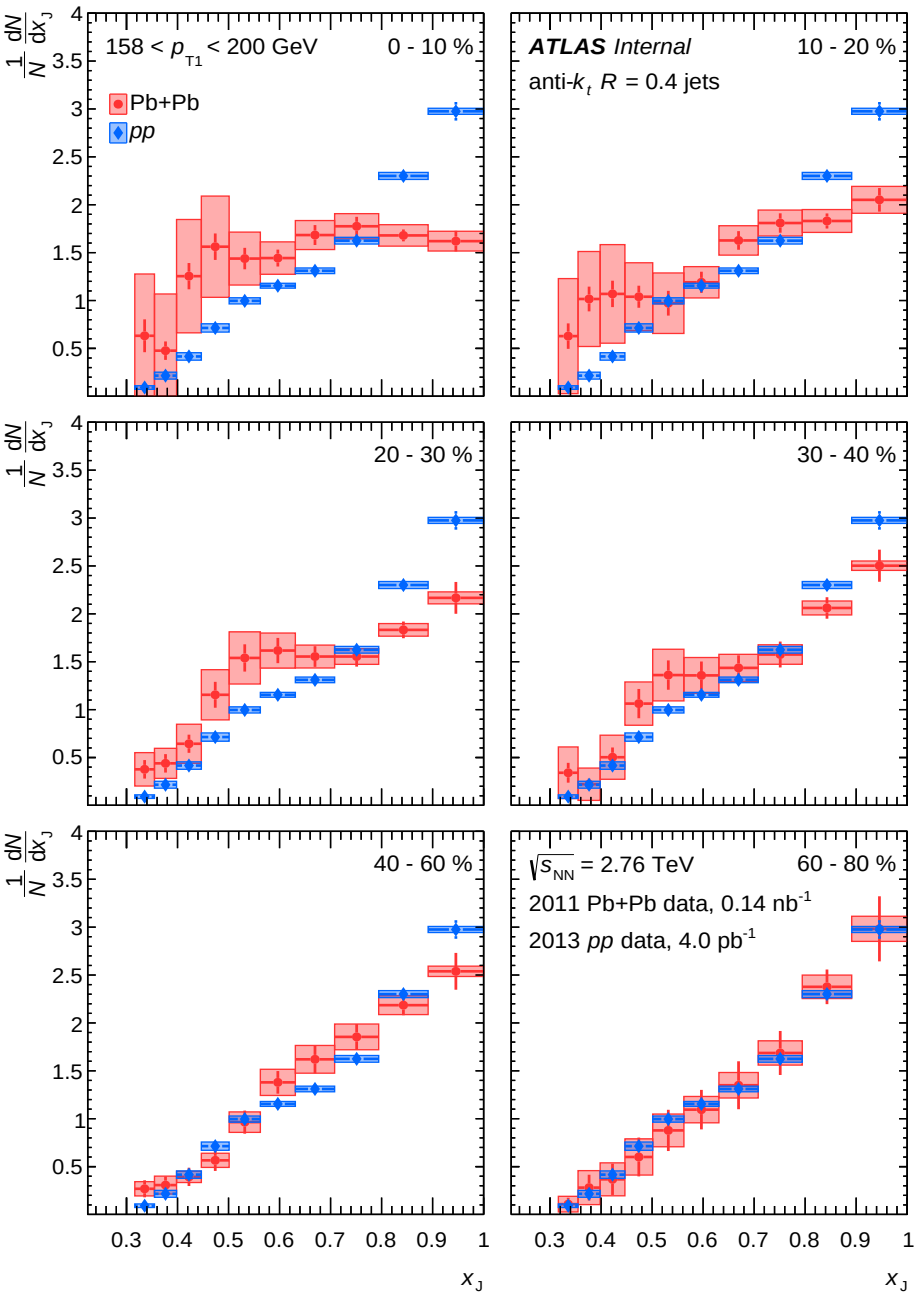

Figure D.2: The unfolded dN/dx_J distribution normalized to the number of dijet pairs for Pb+Pb R=0.4 jets (black) and *pp* R=0.4 jets (red). Each panel is a different centrality bin in the Pb+Pb with the *pp* being the same in each panel: 0-10% (top left), 10-20% (top middle), 20-30% (top right), 30-40% (top right), 40-60% (bottom middle), and 60-80% (bottom right). Each curve is for leading jet p_T from 158-200 GeV. The statistical errors are given by the error bars on each curve and the systematics are given by the error bands.

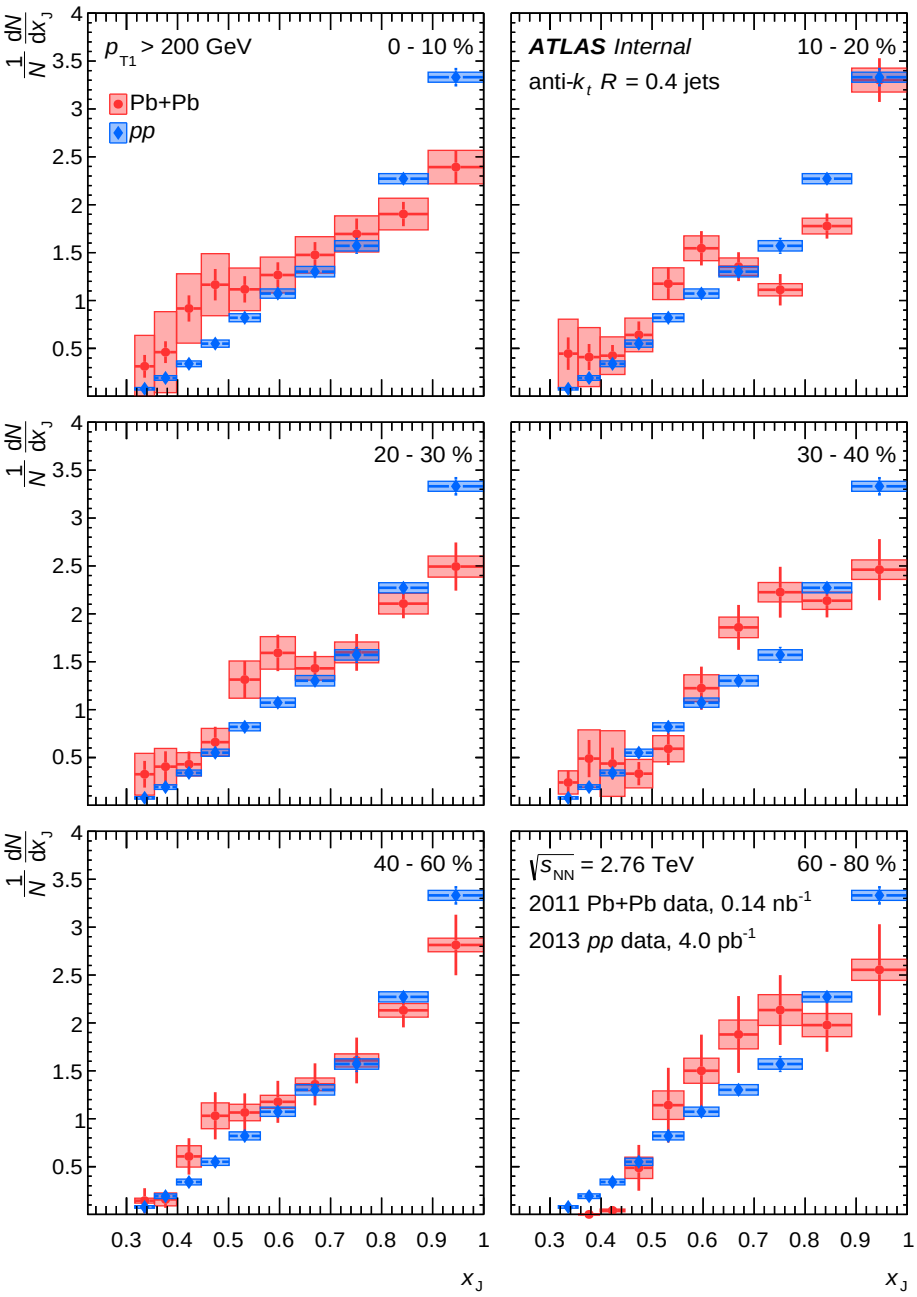

Figure D.3: The unfolded dN/dx_J distribution normalized to the number of dijet pairs for Pb+Pb R=0.4 jets (black) and *pp* R=0.4 jets (red). Each panel is a different centrality bin in the Pb+Pb with the *pp* being the same in each panel: 0-10% (top left), 10-20% (top middle), 20-30% (top right), 30-40% (top right), 40-60% (bottom middle), and 60-80% (bottom right). Each curve is for leading jet p_{T} ¿200 GeV. The statistical errors are given by the error bars on each curve and the systematics are given by the error bands.

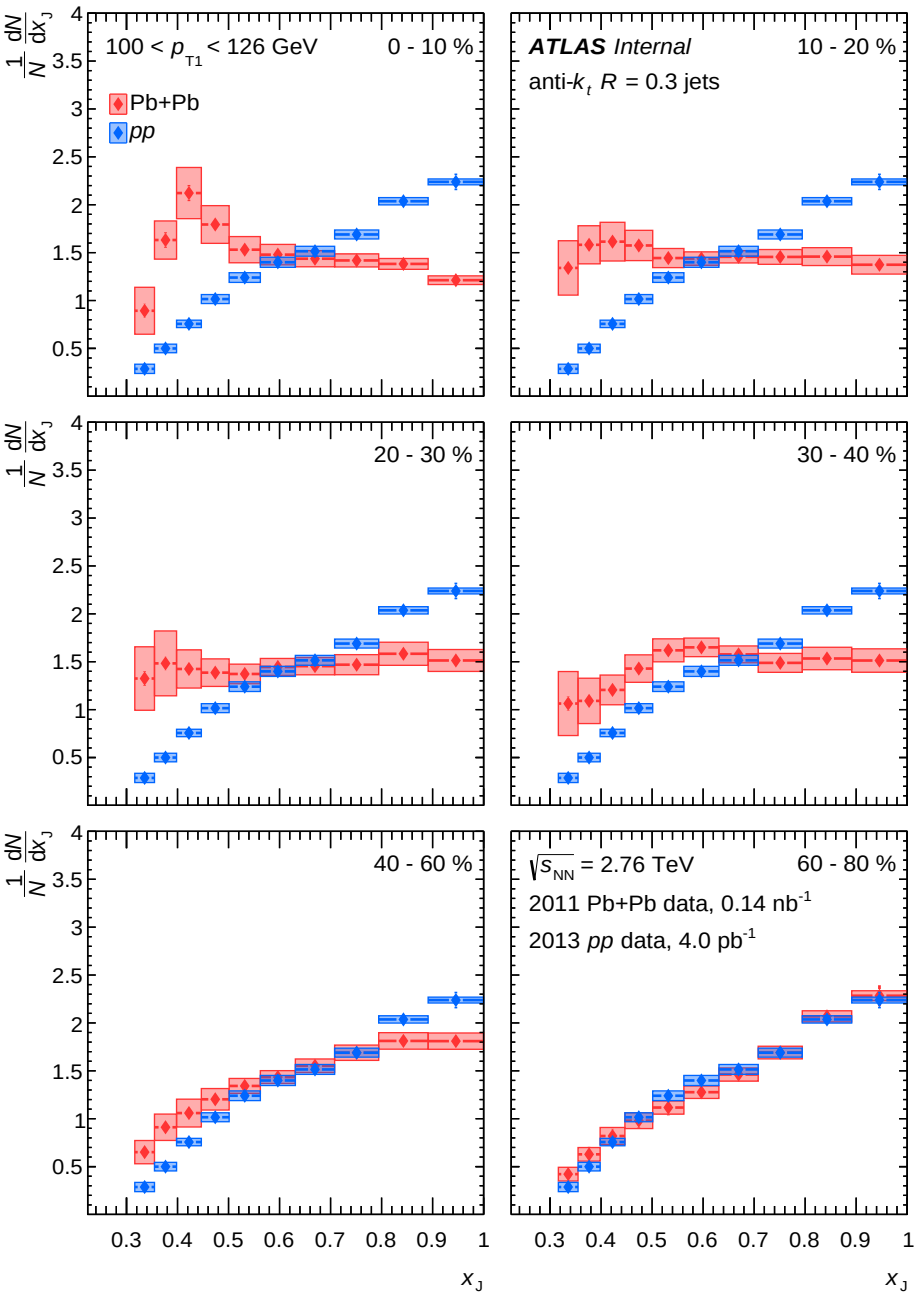

Figure D.4: The unfolded dN/dx_J distribution normalized to the number of dijet pairs for Pb+Pb R=0.3 jets (black) and *pp* R=0.3 jets (red). Each panel is a different centrality bin in the Pb+Pb with the *pp* being the same in each panel: 0-10% (top left), 10-20% (top middle), 20-30% (top right), 30-40% (top right), 40-60% (bottom middle), and 60-80% (bottom right). Each curve is for leading jet p_T from 100-126 GeV. The statistical errors are given by the error bars on each curve and the systematics are given by the error bands.

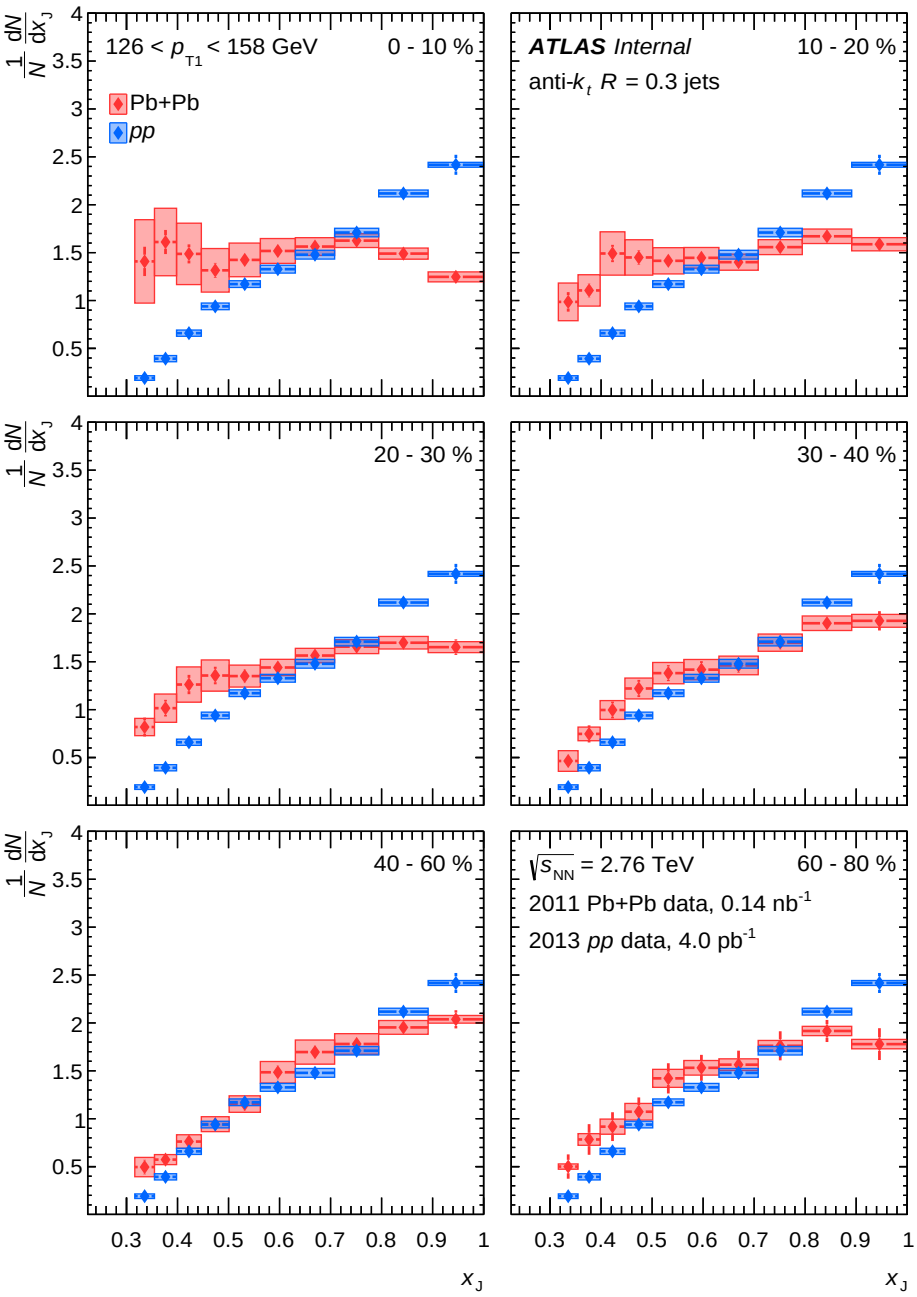

Figure D.5: The unfolded dN/dx_J distribution normalized to the number of dijet pairs for Pb+Pb R=0.3 jets (black) and *pp* R=0.3 jets (red). Each panel is a different centrality bin in the Pb+Pb with the *pp* being the same in each panel: 0-10% (top left), 10-20% (top middle), 20-30% (top right), 30-40% (top right), 40-60% (bottom middle), and 60-80% (bottom right). Each curve is for leading jet p_T from 126-158 GeV. The statistical errors are given by the error bars on each curve and the systematics are given by the error bands.

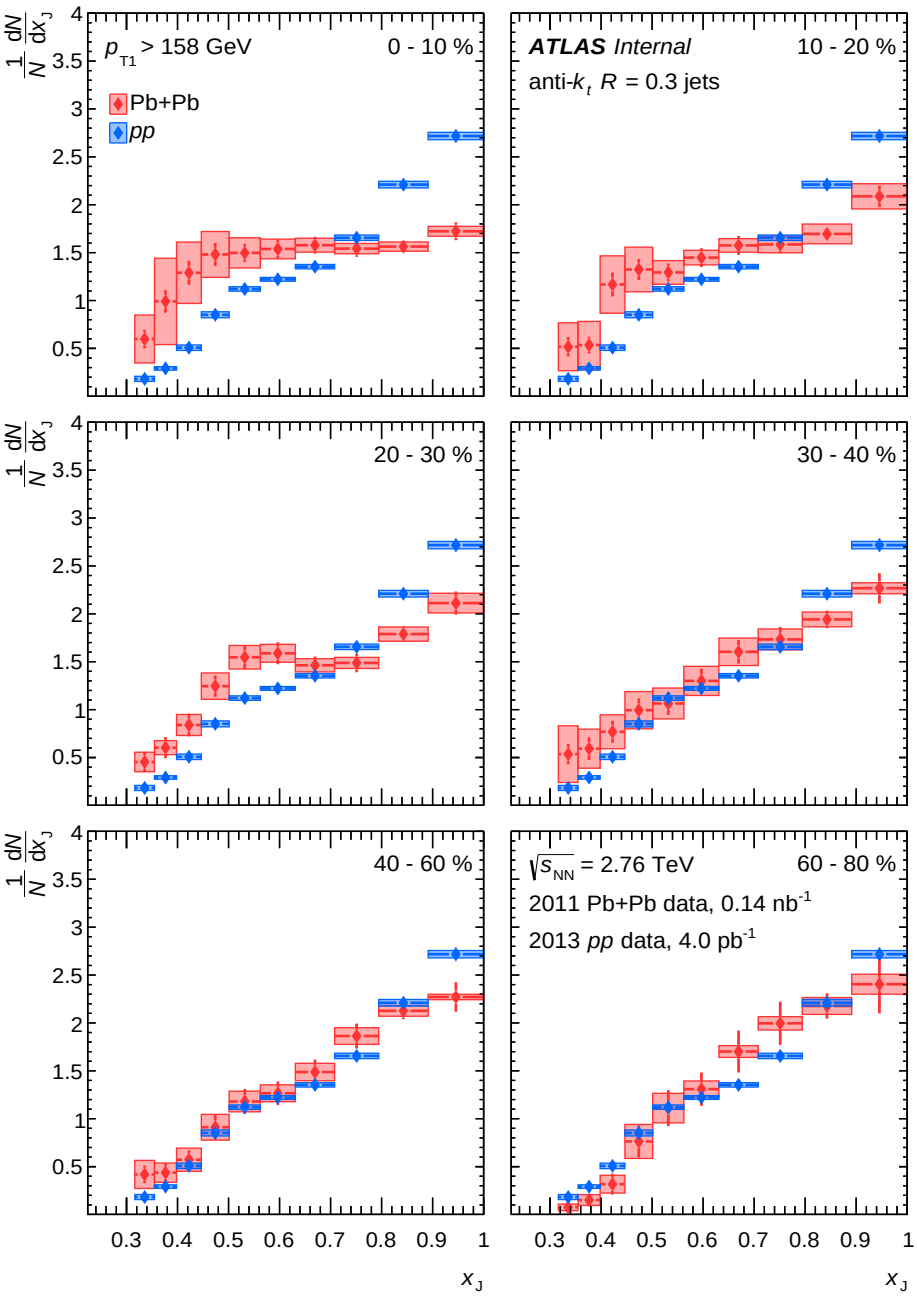

Figure D.6: The unfolded dN/dx_J distribution normalized to the number of dijet pairs for Pb+Pb R=0.3 jets (black) and *pp* R=0.3 jets (red). Each panel is a different centrality bin in the Pb+Pb with the *pp* being the same in each panel: 0-10% (top left), 10-20% (top middle), 20-30% (top right), 30-40% (top right), 40-60% (bottom middle), and 60-80% (bottom right). Each curve is for leading jet p_T ¿158 GeV. The statistical errors are given by the error bars on each curve and the systematics are given by the error bands.

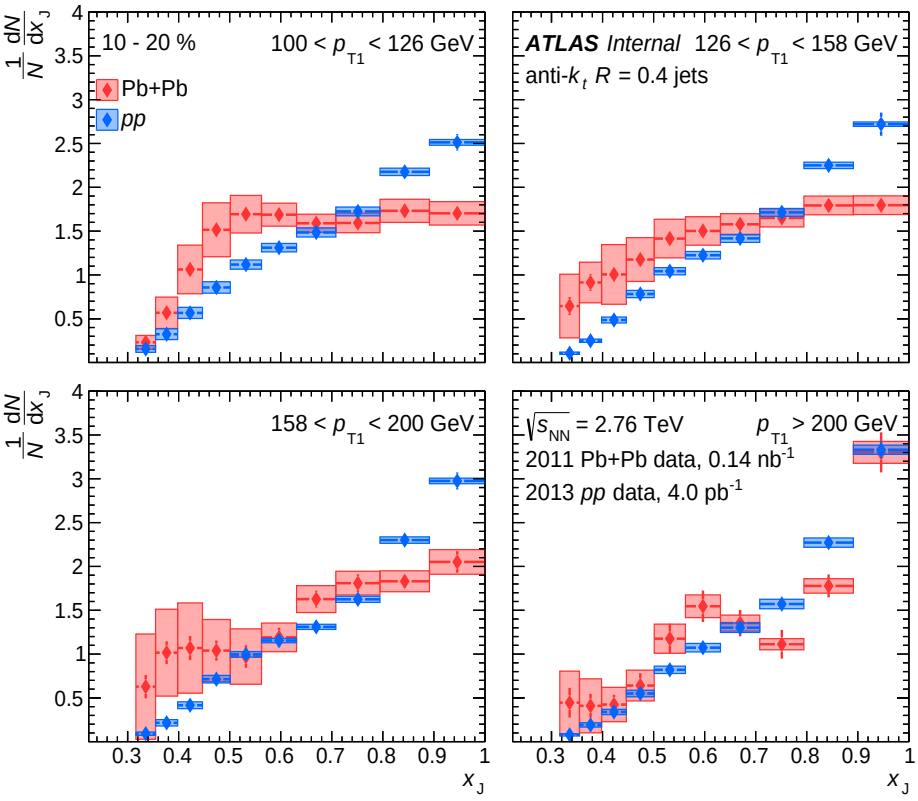

Figure D.7: The unfolded dN/dx_J distribution normalized to the number of dijet pairs for Pb+Pb (10-20%) R=0.4 jets (black) and *pp* R=0.4 jets (red) where each panel is a different leading jet bin: 100-126 GeV (top left), 126-158 GeV (top right), 158-200 GeV (bottom left), and ¿200 GeV (bottom right). The statistical errors are given by the error bars on each curve and the systematics are given by the error bands.

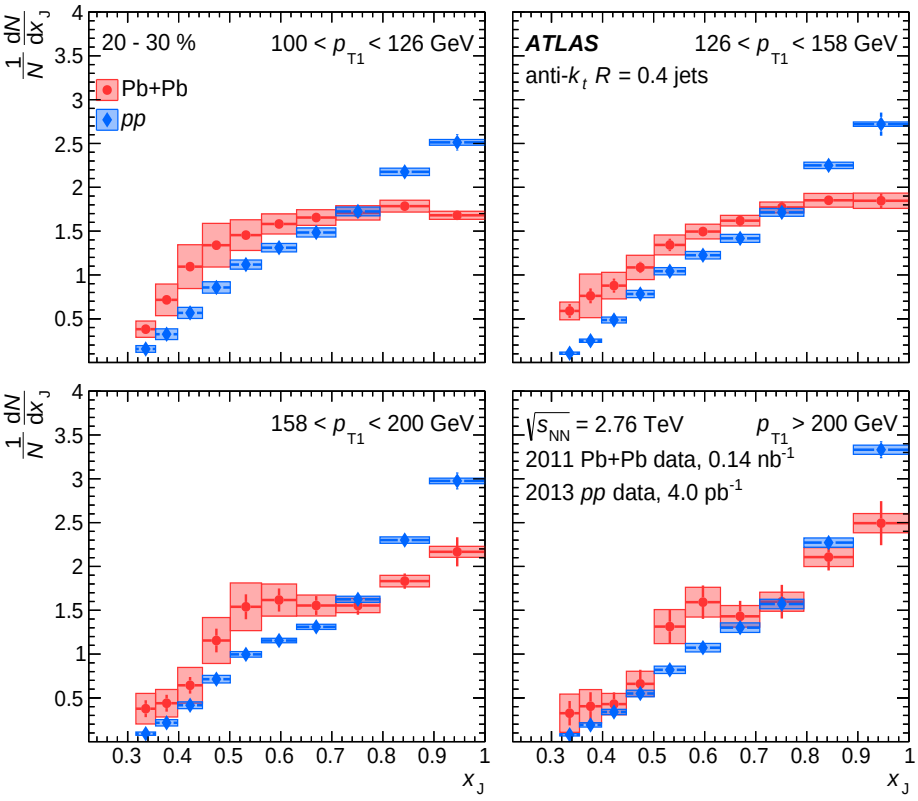

Figure D.8: The unfolded dN/dx_J distribution normalized to the number of dijet pairs for Pb+Pb (20-30%) R=0.4 jets (black) and *pp* R=0.4 jets (red) where each panel is a different leading jet bin: 100-126 GeV (top left), 126-158 GeV (top right), 158-200 GeV (bottom left), and ¿200 GeV (bottom right). The statistical errors are given by the error bars on each curve and the systematics are given by the error bands.

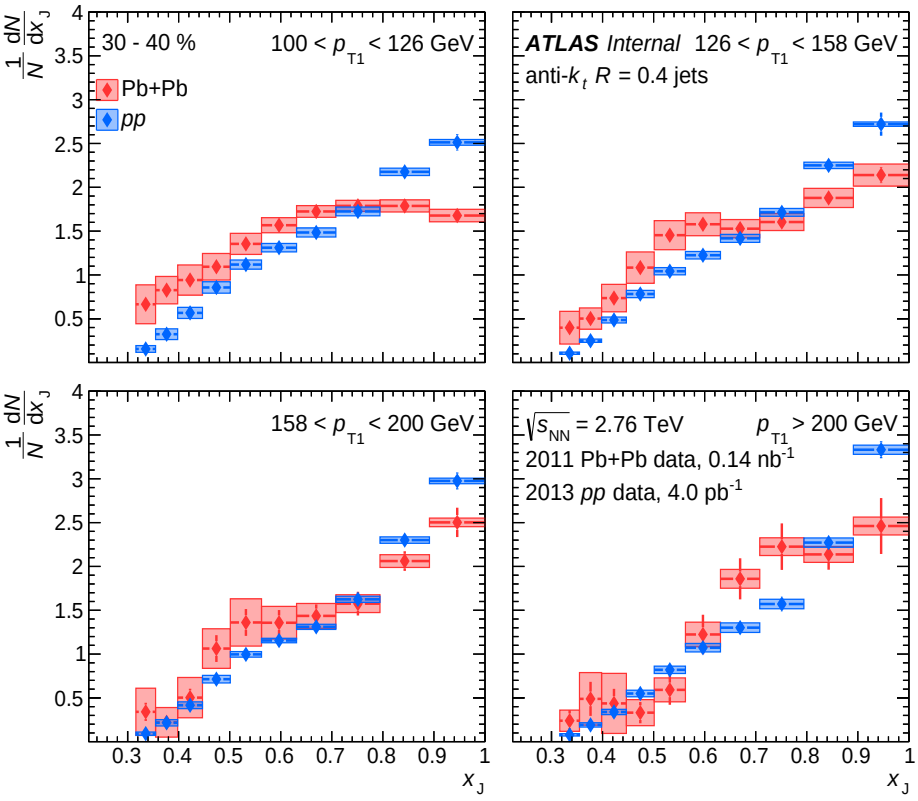

Figure D.9: The unfolded dN/dx_J distribution normalized to the number of dijet pairs for Pb+Pb (30-40%) R=0.4 jets (black) and *pp* R=0.4 jets (red) where each panel is a different leading jet bin: 100-126 GeV (top left), 126-158 GeV (top right), 158-200 GeV (bottom left), and ¿200 GeV (bottom right). The statistical errors are given by the error bars on each curve and the systematics are given by the error bands.

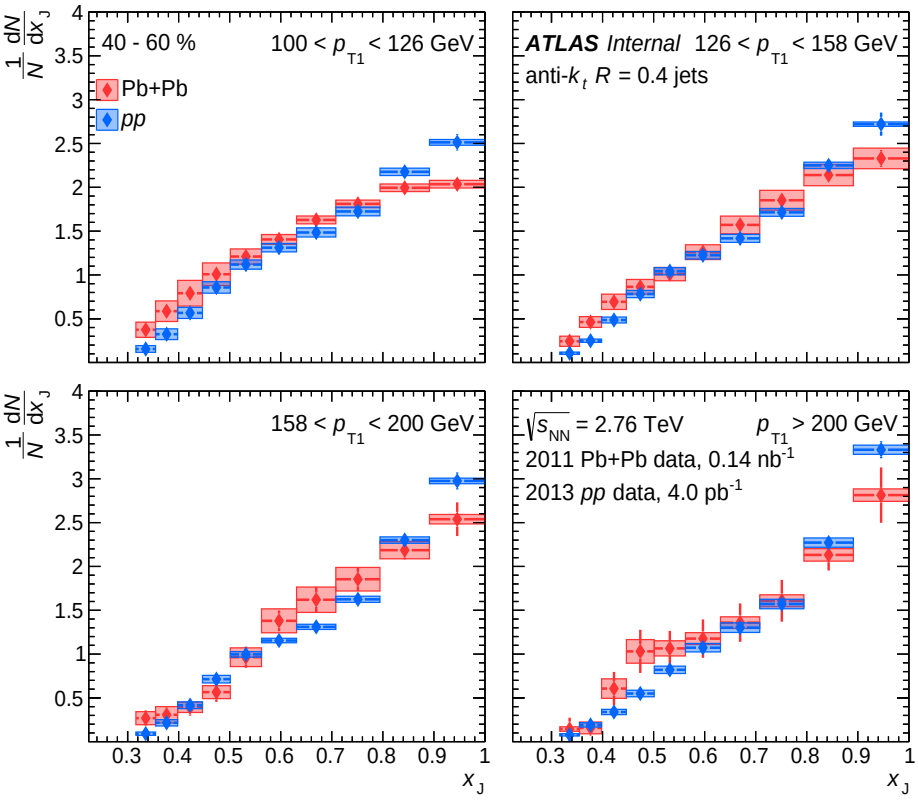

Figure D.10: The unfolded dN/dx_J distribution normalized to the number of dijet pairs for Pb+Pb (40-60%) R=0.4 jets (black) and *pp* R=0.4 jets (red) where each panel is a different leading jet bin: 100-126 GeV (top left), 126-158 GeV (top right), 158-200 GeV (bottom left), and ¿200 GeV (bottom right). The statistical errors are given by the error bars on each curve and the systematics are given by the error bands.

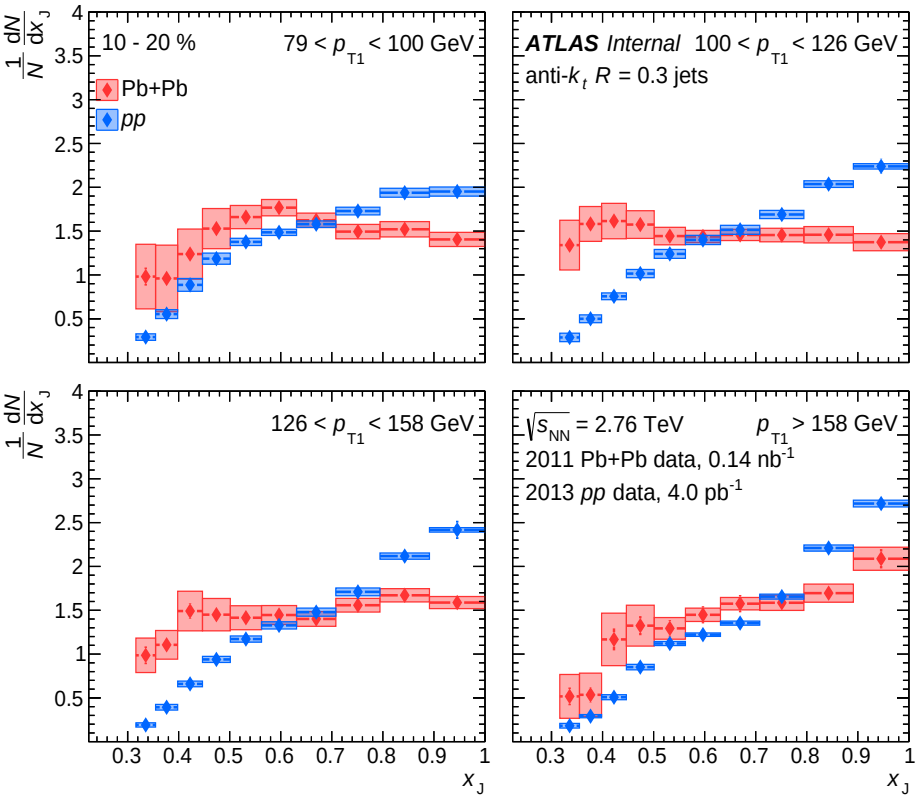

Figure D.11: The unfolded dN/dx_J distribution normalized to the number of dijet pairs for Pb+Pb (10-20%) R=0.3 jets (black) and *pp* R=0.3 jets (red) where each panel is a different leading jet bin: 79-100 GeV (top left), 100-126 GeV (top right), 126-158 GeV (bottom left), and ¿158 GeV (bottom right). The statistical errors are given by the error bars on each curve and the systematics are given by the error bands.

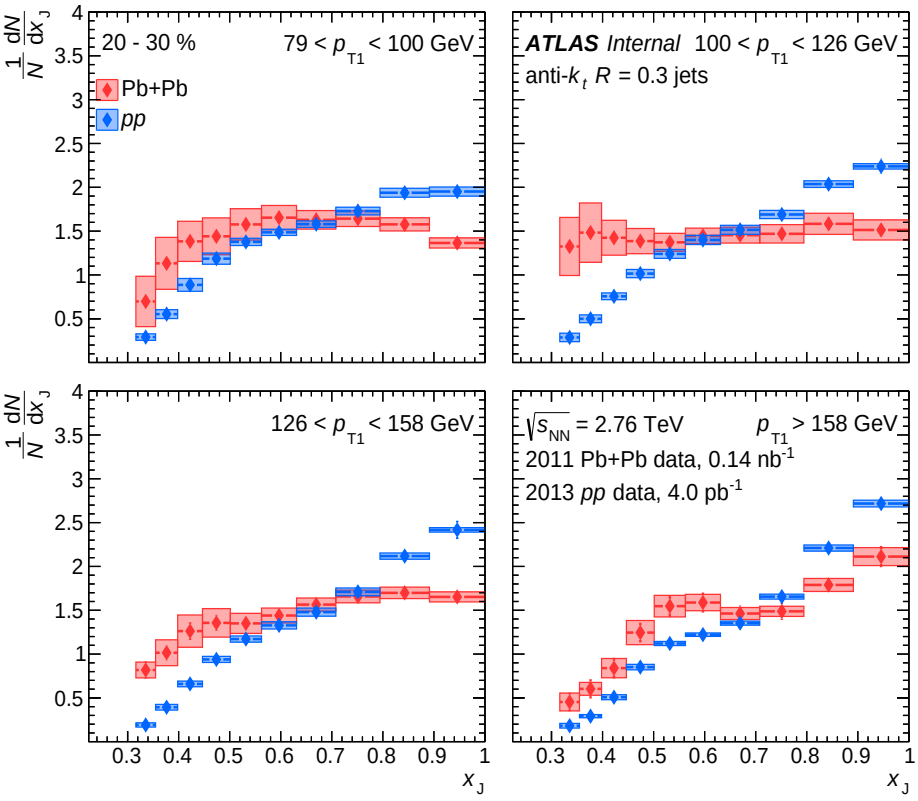

Figure D.12: The unfolded dN/dx_J distribution normalized to the number of dijet pairs for Pb+Pb (20-30%) R=0.3 jets (black) and *pp* R=0.3 jets (red) where each panel is a different leading jet bin: 79-100 GeV (top left), 100-126 GeV (top right), 126-158 GeV (bottom left), and ¿158 GeV (bottom right). The statistical errors are given by the error bars on each curve and the systematics are given by the error bands.

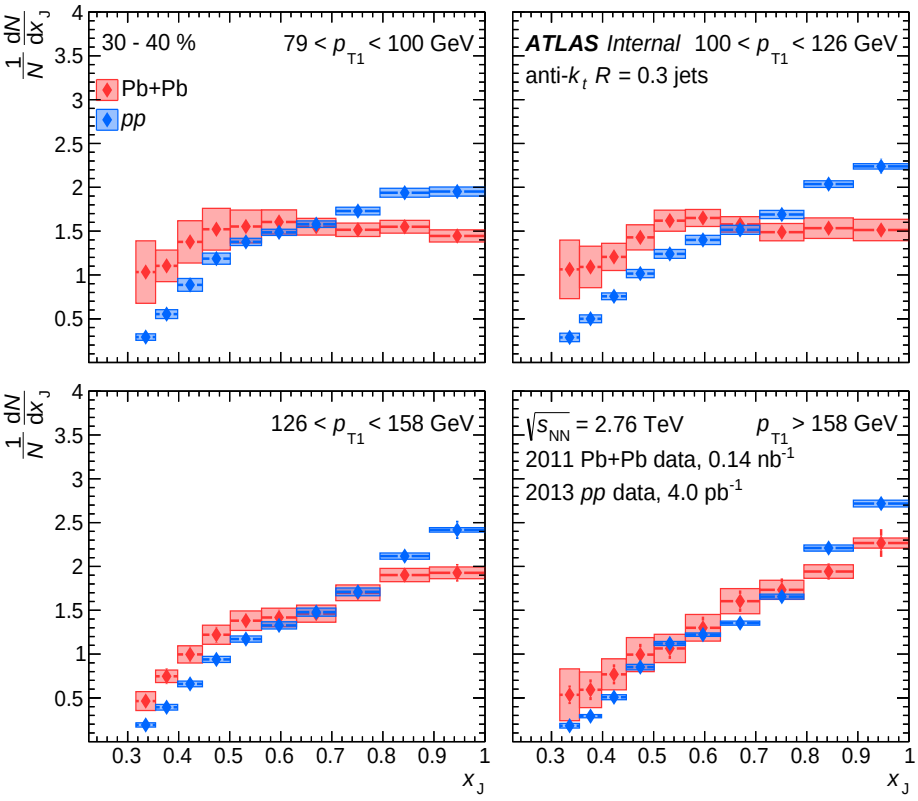

Figure D.13: The unfolded dN/dx_J distribution normalized to the number of dijet pairs for Pb+Pb (30-40%) R=0.3 jets (black) and *pp* R=0.3 jets (red) where each panel is a different leading jet bin: 79-100 GeV (top left), 100-126 GeV (top right), 126-158 GeV (bottom left), and ¿158 GeV (bottom right). The statistical errors are given by the error bars on each curve and the systematics are given by the error bands.

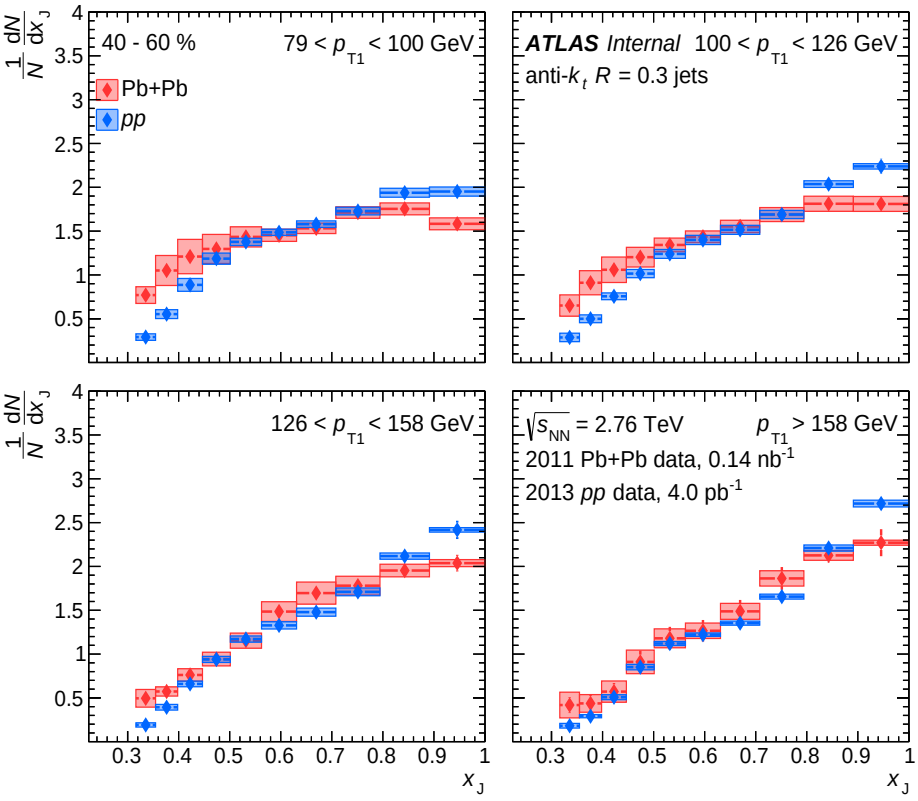

Figure D.14: The unfolded dN/dx_J distribution normalized to the number of dijet pairs for Pb+Pb (40-60%) R=0.3 jets (black) and *pp* R=0.3 jets (red) where each panel is a different leading jet bin: 79-100 GeV (top left), 100-126 GeV (top right), 126-158 GeV (bottom left), and ¿158 GeV (bottom right). The statistical errors are given by the error bars on each curve and the systematics are given by the error bands.

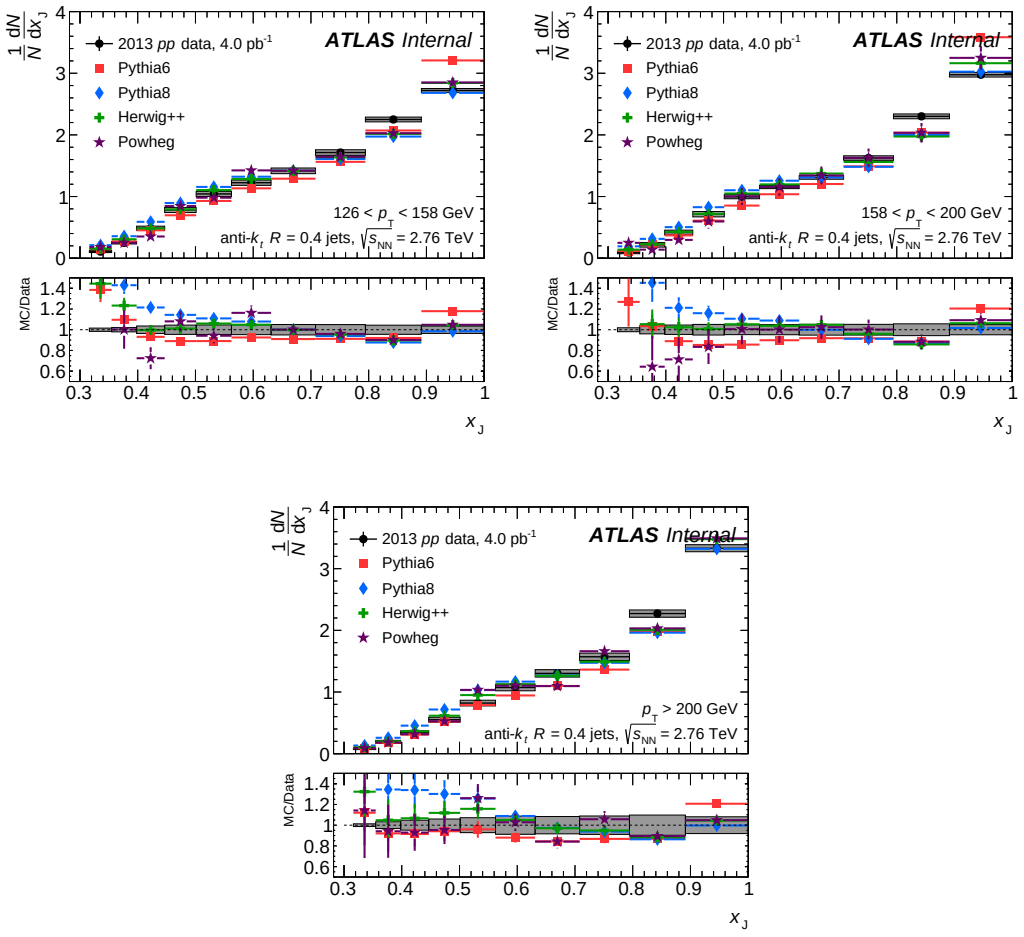

Figure D.15: The unfolded $\mathrm{d}N/\mathrm{d}x_J$ distribution normalized to the number of dijet pairs is shown in the top panel for pp R=0.4 jets (black) in different leading jet p_{T} bins in the panels compared to the following MC generators: PYTHIA6 (red squares), PYTHIA8 (blue diamonds), HERWIG++ (green crosses), and POWHEG+PYTHIA8 (purple stars). The statistical errors are given by the error bars on the points and the systematics are given by the error bands (only for the data). The bottom panel represents the ratio of each MC generator (same colors apply) to the data and the shaded band represents to error on the ratio from the systematic errors on the data.

Appendix E

Jet Suppression Additional Figures

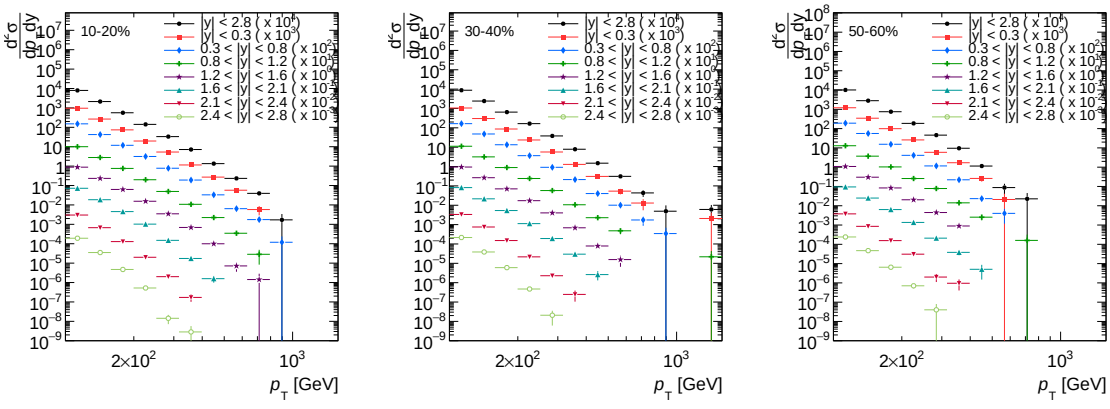

Figure E.1: The raw p_{T} distribution for jets with $p_{\mathrm{T}} > 40$ GeV in different rapidity bins for 10–20% (left),30–40% (center), and 60–70% (right) Pb+Pb collisions.

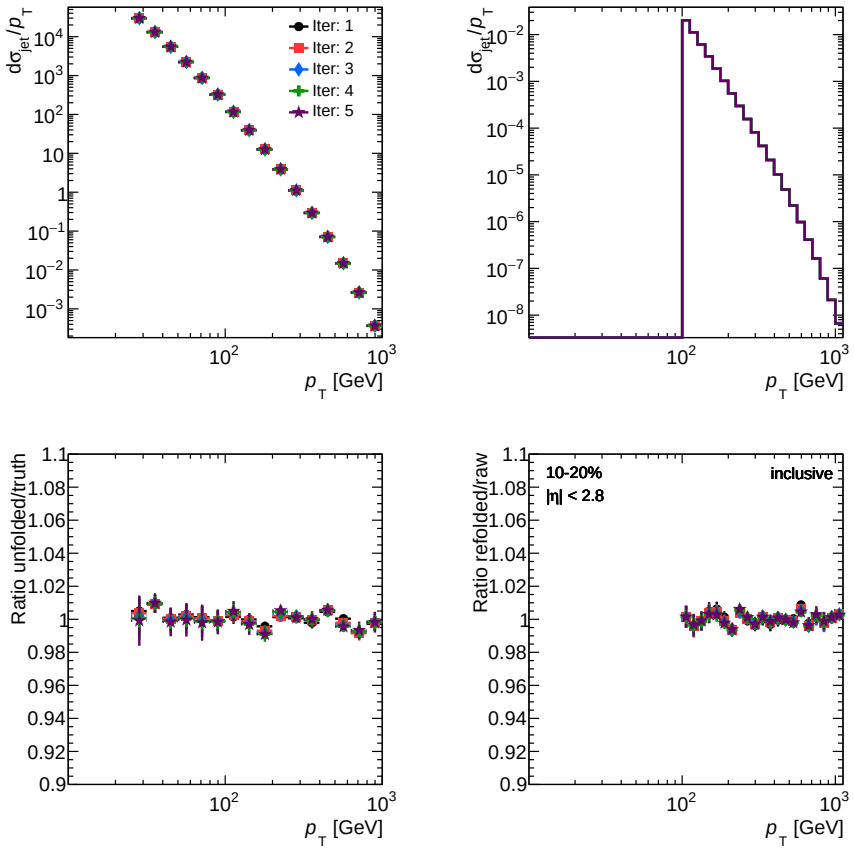

Figure E.2: Unfolding results for the MC closure test for different numbers of iterations in 10–20% Pb+Pb collisions within $|y| < 2.8$. The top left panel shows the unfolded p_{T} spectrum and the top right panel shows the refolded p_{T} spectrum. The bottom left panel shows the ratio of the unfolded truth to truth distribution (the MC closure) and bottom right panel shows the ratio of the refolded to data distribution.

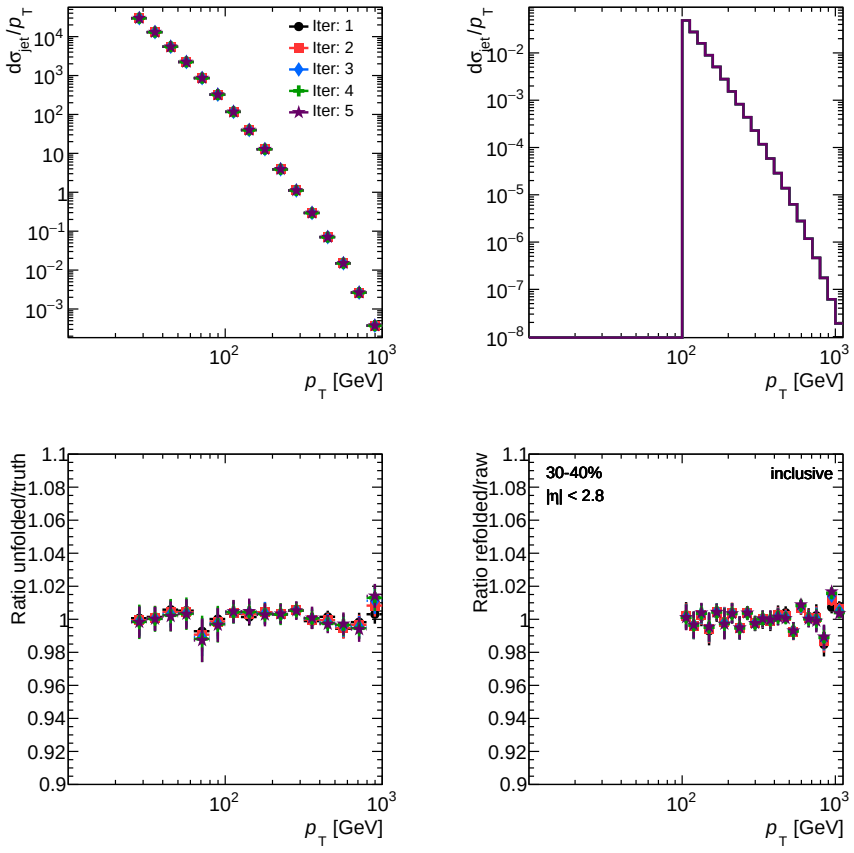

Figure E.3: Unfolding results for the MC closure test for different numbers of iterations in 30–40% Pb+Pb collisions within $|y| < 2.8$. The top left panel shows the unfolded p_{T} spectrum and the top right panel shows the refolded p_{T} spectrum. The bottom left panel shows the ratio of the unfolded truth to truth distribution (the MC closure) and bottom right panel shows the ratio of the refolded to data distribution.

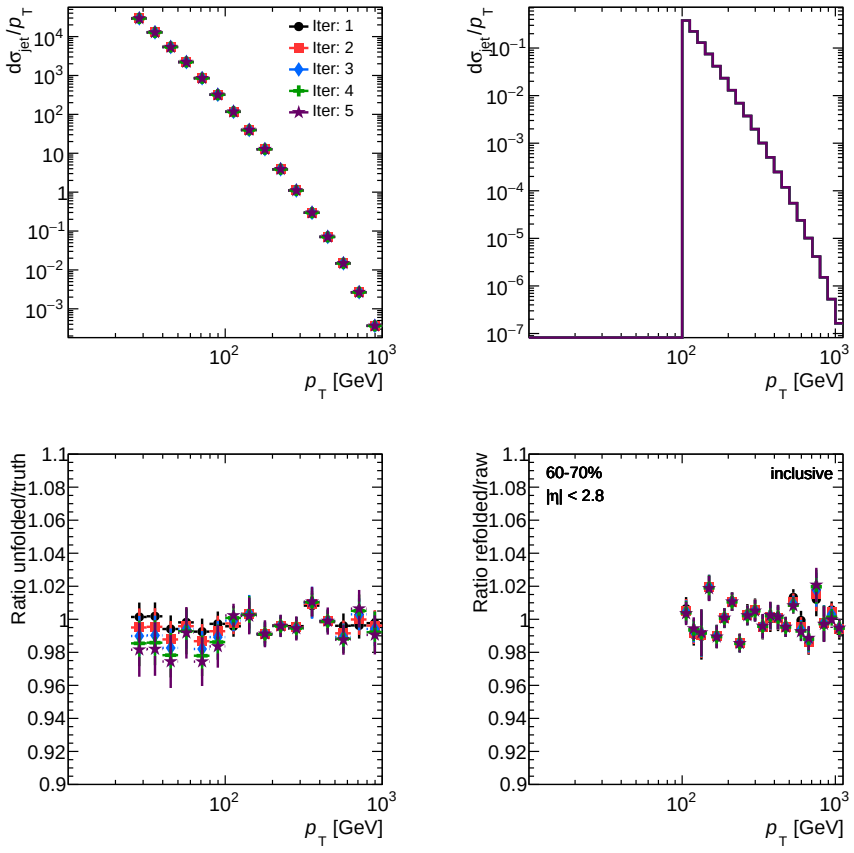

Figure E.4: Unfolding results for the MC closure test for different numbers of iterations in 60–70% Pb+Pb collisions within $|y| < 2.8$. The top left panel shows the unfolded p_{T} spectrum and the top right panel shows the refolded p_{T} spectrum. The bottom left panel shows the ratio of the unfolded truth to truth distribution (the MC closure) and bottom right panel shows the ratio of the refolded to data distribution.

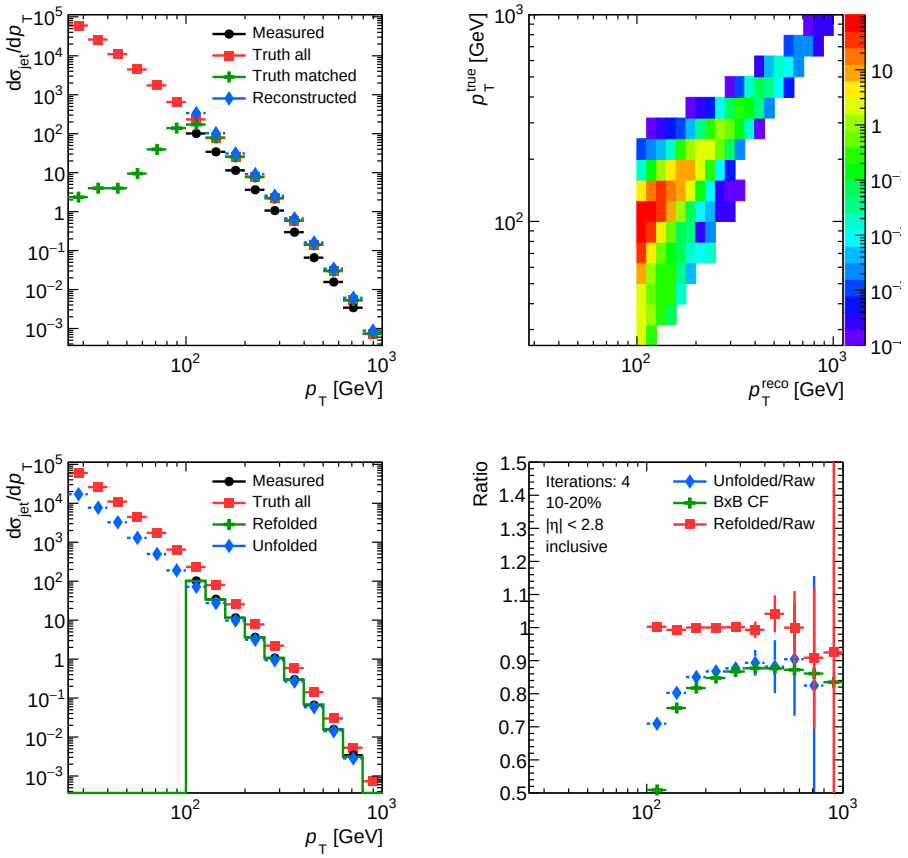

Figure E.5: Unfolding results summary plot for 10–20% Pb+Pb collisions in $|y| < 2.8$. The top left panel shows the reconstructed MC (blue), the reconstructed data (black), the matched truth MC (green), and the full truth MC distribution (blue). The top right panel shows the 2D response ($p_{\mathrm{T}}^{\mathrm{truth}}$ vs. $p_{\mathrm{T}}^{\mathrm{reco}}$). The bottom left panel shows the reconstructed data (black), the refolded data (green), the full truth MC (red), and the unfolded data (blue). The bottom right panel shows the effect of unfolding through the unfolded/data ratio (blue), the bin-by-bin correction factors through the ratio of the truth MC to the reconstructed MC (green), and the refolded to raw ratio (red).

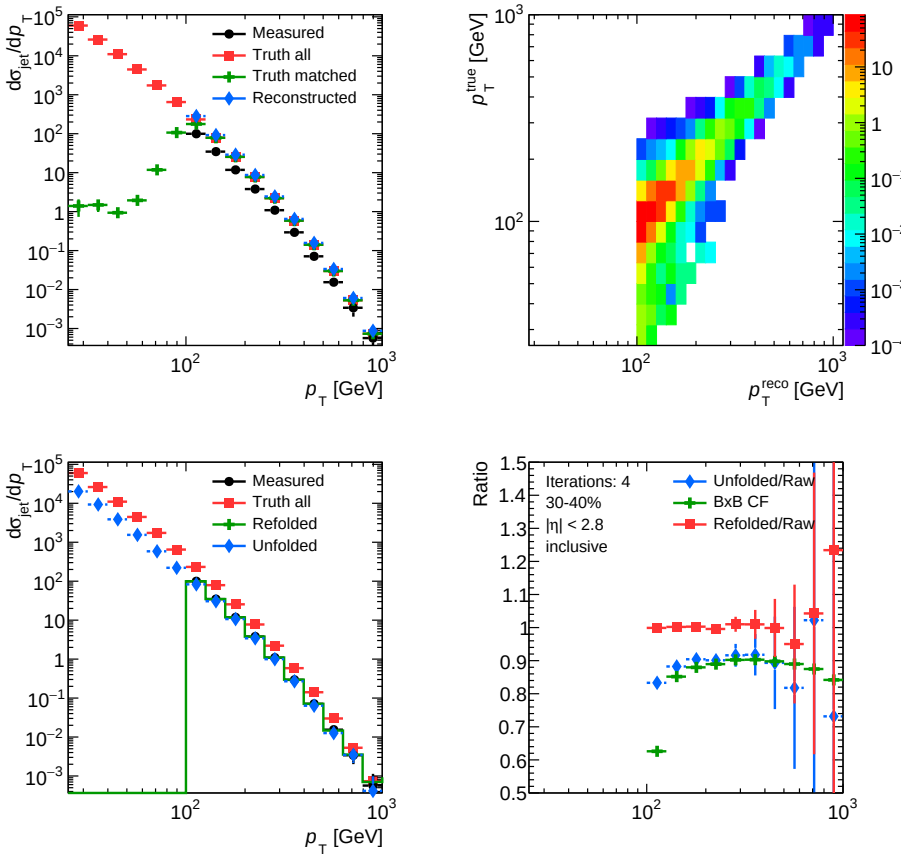

Figure E.6: Unfolding results summary plot for 30–40% Pb+Pb collisions in $|y| < 2.8$. The top left panel shows the reconstructed MC (blue), the reconstructed data (black), the matched truth MC (green), and the full truth MC distribution (blue). The top right panel shows the 2D response ($p_{\mathrm{T}}^{\mathrm{truth}}$ vs. $p_{\mathrm{T}}^{\mathrm{reco}}$). The bottom left panel shows the reconstructed data (black), the refolded data (green), the full truth MC (red), and the unfolded data (blue). The bottom right panel shows the effect of unfolding through the unfolded/data ratio (blue), the bin-by-bin correction factors through the ratio of the truth MC to the reconstructed MC (green), and the refolded to raw ratio (red).

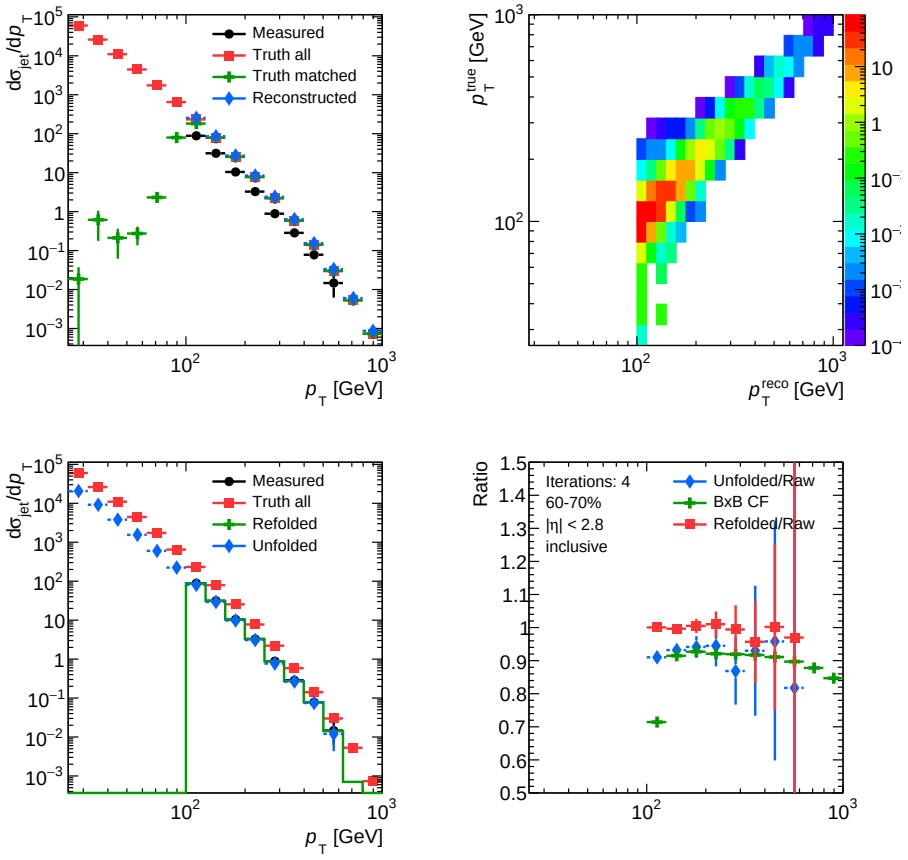

Figure E.7: Unfolding results summary plot for 60–70% Pb+Pb collisions in $|y| < 2.8$. The top left panel shows the reconstructed MC (blue), the reconstructed data (black), the matched truth MC (green), and the full truth MC distribution (blue). The top right panel shows the 2D response ($p_{\mathrm{T}}^{\mathrm{truth}}$ vs. $p_{\mathrm{T}}^{\mathrm{reco}}$). The bottom left panel shows the reconstructed data (black), the refolded data (green), the full truth MC (red), and the unfolded data (blue). The bottom right panel shows the effect of unfolding through the unfolded/data ratio (blue), the bin-by-bin correction factors through the ratio of the truth MC to the reconstructed MC (green), and the refolded to raw ratio (red).

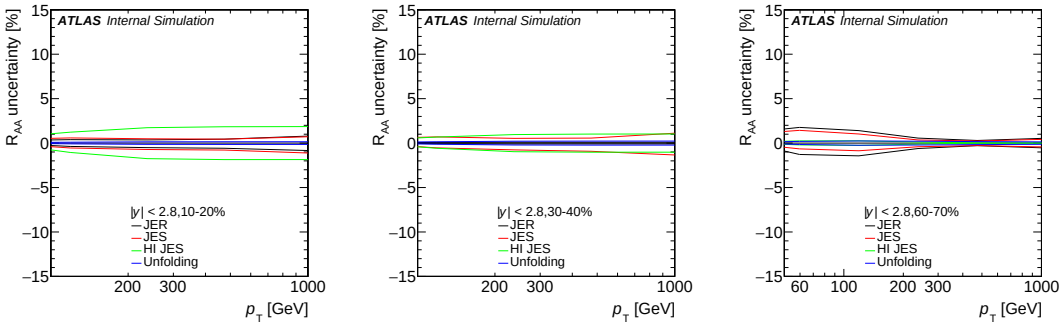

Figure E.8: The systematic uncertainty breakdown in for the R_{AA} in 10–20% (left), 30–40% (center), and 60–70% (right).

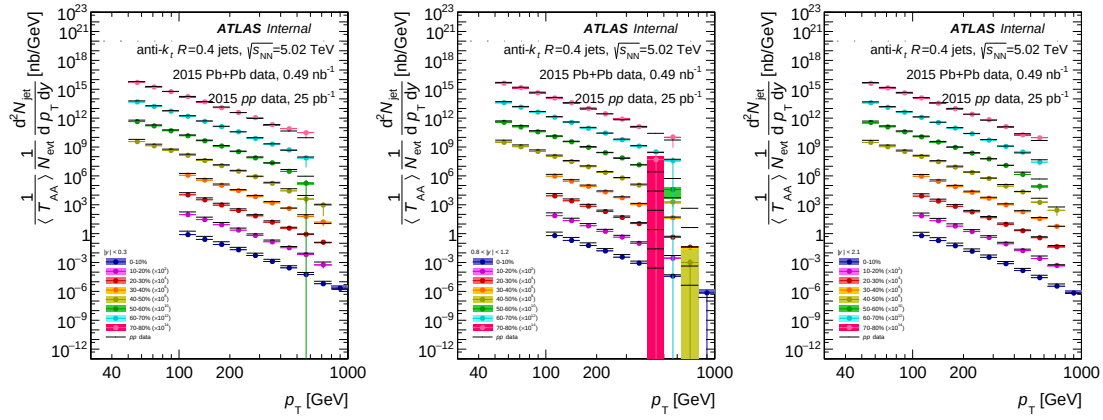

Figure E.9: Per event jet yield in Pb+Pb collisions, multiplied by $\langle T_{\mathrm{AA}} \rangle$, as a function of jet p_{T} scaled by successive powers of 10^2. The solid lines represent the pp cross-section for the same rapidity selection scaled by the same factor to allow for a comparison with the Pb+Pb data at different centralities. The error bars represent statistical uncertainties, shaded boxes represent systematic uncertainties including uncertainties on $\langle T_{\mathrm{AA}} \rangle$ and luminosity. This is shown in $|y| < 0.3$ (left), $0.8 < |y| < 1.2$ (center), and $|y| < 2.1$.